Numerical Modelling of Compressible Turbulent Premixed Hydrogen Flames

Charles TURQUAND D'AUZAY

Supervisors : Dr. A. Aspden, Dr. I. Moulitsas, Dr. B. Thornber

A Dissertation submitted for the degree of *Philosophiæ Doctor*

Center for Fluid Mechanics and Computational Sciences
School of Aerospace, Transport and Manufacturing
Cranfield University

2016

Abstract

Turbulent combustion has a profound effect on the way we live our lives; homes and businesses predominantly rely on power generated by burning some form of fuel, and the vast majority of transport of passengers and cargo are driven by combustion. Fossil fuels remain readily available and relatively cheap, and so will continue to power the modern world for the foreseeable future. Combustion of fossil fuels produces emissions that detrimentally affect air quality, particularly in highly-populated cities, and are also widely believed to be contributing to global climate change. Consequently, increasing attention is being focused on alternative fuels, increased efficiency and reduced emissions. One alternative fuel is hydrogen, which introduces challenges in end-usage, storage and safety that are not encountered with more conventional fuels. Advances in computational power and software technology means that numerical simulation has a growing role in the development of combustors and safety evaluation. Despite these advances, many challenges remain; the broad range of time and length scales involved are coupled with complex thermodynamics and chemistry on top of turbulent fluid mechanics, which means that detailed simulations of even relatively-simple burners are still prohibitively expensive. Engineering turbulent flame models are required to reduce computational expense, and the challenge is to retain as much of the flow physics as possible. Furthermore, the choice of numerical approach has a significant effect on the quality of simulation, and different target applications place different demands on the numerical scheme. In the case of hydrogen explosion, the approach needs to be able to capture a range of physical behaviours including turbulence, low-speed deflagration, high-speed shock waves and potentially detonations. One such numerical approach that has enjoyed widespread success is finite volumes schemes based on the Godunov method. These methods perform well at all speeds, and have positive shock-capturing capability, but recent studies have demonstrated difficulties with numerical stability for more complex thermodynamics, specifically in the case of fully-conservative methods for multi-component fluids with varying thermodynamic properties. A recent development is the so-called double-flux method, which retains many of the positive properties of the fully-conservative approaches and does not suffer from the same numerical instabilities, but is quasi-conservative and involves additional computational expense. The present work consolidates the state-of-the-art in the literature, and considers two equation sets, based on mass fraction and volume fraction, respectively, along with fully-conservative and quasi-conservative schemes. Comprehensive validation and evaluation of the different approaches is presented. It was found that both quasi-conservative approaches performed well, with a better conservative behaviour for the quasi-conservative volume fraction, but a better stability for the quasi-conservative mass fraction. Finally, the numerical tool developed is applied to turbulent combustion of premixed hydrogen in the context of the semi-confined experiments from the University of Sydney. The LES results showed an good overall agreement with the experimental data, and the critical parameters such as overpressure and flame speed where globally well captured, highlighting the large potential of LES for safety analysis.

keywords : Turbulent Premixed Combustion, Large Eddy Simulation, Deflagration, Hydrogen, Volume Fraction, Fully-Compressible Shock-Capturing

Acknowledgements

I have once been told that the path of research was long and arduous. I should have believed the wise man that told me that, but I did not and neither do I regret it. This has truly been an exhilarating experience, with moments of incommensurable joy (when the code is finally working), to moments of intense doubts and crushed certitudes.

Completing this work has taken both time, dedication and the help and support of a great number of amazing people, most of whom I feel privileged to know.

Without any doubt the first one is Dr. Andy Aspden (or Andy) whose patience, support, guidance and knowledge have been key in the success of this research. No word can express the gratitude I feel towards him for what he has given me, and for standing by my side even though he was under no obligation of doing so. Dr. Irene Moulitsas and Prof. Stephen James should also be largelly thanked for they gave me what was most precious in a time of serious doubts and needs, a peaceful and calm working environment. For this, I thank them deeply. Dr. Ben Thornber must also be thanked for providing the spark that started this journey. His support, help and guidance provided during the first year and a half of this project were most welcome.

Andy Gittings, the manager of the High Performance Computing (HPC) center at Cranfield is deeply thanked for providing me the tools, computational time and help needed to run what appears to be close to 50 years worth of computational time on a single CPU.

I feel equally in debt to many of my friends and colleagues at Cranfield University. Ranking high in the list is the "Dream Team" originally composed of Olivier Bouzigues, Camille Burban before the arrival of Zoi Georgakopoulou without whom this long journey would not have been possible. Time with them always provided the relaxation and joy that were needed after long hours or days of work. My PhD brother Mike holds a special place for the all the time we spent together trying to solve each other problems, and often succeeding, but also for the moral support sessions held around a cup of tea or a pint.

For similar reasons and for his continuous support and words of advice, Mustapha Gourma is greatly thanked. Francis Salama and Mark Picciani will remain the best office mates, roomates, friends, etc. that I had in Cranfield and should be thanked for the fun time, brainstorming sessions, memorable moments spent together, and especially the Battlefield nights. Neither will I forget Laetitia Stephan, Sue Richardson, Robin McGrath, Kirsty Wallis, and numerous other colleagues at the CSA bar, for all the enjoyable and awkward moments spent together.

I would also like to thank the coaching team of the Cranfield Rugby Club for all the mud baths, third half-times and long nights spent in the CSA laughing, so Martin and Lewis, thank you !

I must also thank Mr. Bayet and Seghezzi, my maths and physics lecturers during my first year at CPE Lyon who showed me that with hard work and dedication, one could overcome any problems. Without them and their harsh support, I would never have found my way to Cranfield.

Kindest thanks now goes to my all family, especially my parents Marc and Florence, my grand-parents, my brothers, for their unconditional support and words of consolation in time of doubts, but also for their encouragements no matter which way I choose to pursue. Pierre and Monique Coulet should also be thanked for their interest in my project and for all their advices.

Finally, but certainly not least this list can not end without the world most expert person in combustion that I know. Thank you, Célia, for keeping that little flame lit between us, thank you for standing by me through thick and thin, thank you for your every day support, and finally thank you for accepting to live the rest of you life with me. MERCI ...

Contents

List of Figures

List of Tables

List of Symbols

Acronyms

ANRS	Approximative Noniterative Riemann Solver
ATF	Artificially Thickened Flame
AUSM	Advection Upstream Splitting Method
BML	Bray-Moss-Libby
(S)CFD	(Safety) Computational Fluid Dynamics
CERFACS	Centre Europeen de Recherche et de Formation Avancee en Calculs Scientifiques
CFL	Courant Friedrichs Lewy number
CFM	Coherent Flame Model
CGDT	Counter Gradient Turbulent Diffusion
CMC	Conditional Moment Closure
CNG	Compressed Natural Gas
CVR	Constant Volume Reactor
DDT	Deflagration to Detonation Transition
DFSD	Dynamic Flame Surface Density
DNS	Direct Numerical Simulation
DTF	Dynamic Thickened Flame
EBU	Eddy Break-Up
EoS	Equation of State
FCMF	Fully-Conservative Mass Fraction
FCVF	Fully-Conservative Volume Fraction
FSD	Flame Surface Density
G	Gibson scale
GFM	Ghost Fluid Method
HLL	Harten Lax von Leer
HLLC	Harten Lax van Leer Contact
IBVP	Initial Boundary-Value Problem
IEA	International Energy Agency
IRC	Istituto di Recerche sulla Combustione

ITER	International Thermonuclear Experimental Reactor
LAD	Localised Artificial Dissipation
LES	Large Eddy Simulation
LIF-OH	Laser Induced Fluorescence - OH
LMC	Low-Mach Correction
LODI	Local One Dimensional Inviscid
LPG	Liquefied Petroleum Gas
MUSCL	Monotone Upwind
NASA	National Aeronautics and Space Administration
NFPA	National Fire Protection Association
NSCBC	Navier-Stokes Characteristic Boundary Conditions
OC	Obukhov-Corrsin scale
ODE	Ordinary Differential Equation
ONERA	Office National d'Etudes et de Recherches en Aeronautique
PDF	Probability Density Function
PVRS	Primitive Variable Riemann Solver
QCMF	Quasi-Conservative Mass Fraction
QCVF	Quasi-Conservative Volume Fraction
(U)RANS	(Unsteady) Reynolds Averaged Navier-Stokes
RK	Runge-Kutta
RMS	Root Mean Square
SCM	Split Coefficient Matrix
SGS	Sub-Grid Scale
SSP	Strong-Stability Preserving
TCFC	Thermodynamically Consistent and Fully Conservative
TFLES	Thickened Flame for LES
ThCM	Total Enthalpy Conservation of the Mixture
TKE	Turbulent Kinetic Energy
TRRS	Two-Rarefaction Riemann Solver
TRZ	Thin Reaction Zone
TSRS	Two-Shock Riemann Solver
UK	United Kingdom
VOF	Volume of Fluid
WENO	Weighted Essentially Non-Oscillatory

ZFK	Zeldovich Frank-Kamenetski and Von Karman

Greek Symbols

α	Parameter measuring the flame heat release
β	Parameter measuring the activation energy, second coefficient of viscosity, Boger's FSD model parameter
β_j	Temperature exponent for reaction j (Arrhenius' law)
$\bar{\Delta}$	Filter size
δ	Laminar flame thickness or time variation
$\Delta_{x,y,z}$	Cell size in x, y or z direction
η_k	Kolmogorov scale
ε	Turbulent kinetic energy dissipation rate or internal energy
ϕ	Equivalence ratio
Φ_{ij}	Inter-collisional parameter between species i and j (Wilke's law)
Γ	Efficiency function for flame wrinkling estimation
γ	Specific heat ratio, adiabatic index
κ	Flame stretch
λ	Eigenvalues
$\underline{\mathbf{\Lambda}}$	Eigenvalue matrix, Characteristic variables Jacobian matrix
μ	Dynamic viscosity
ν	Kinematic viscosity, ratio of time step size over cell size
ν'	Reactants stoichiometric coefficients
ν''	Products stoichiometric coefficients
ν_t	SGS turbulent kinematic viscosity
ρ	Density
Σ	Flame Surface Density
τ_c	Chemical time scale
τ_{SGS}	SGS turbulent time scale
$\underline{\boldsymbol{\tau}}$	Viscous stress tensor
$\dot{\omega}_k$	Production rate of species k
$\dot{\omega}_T$	Net heat release for a chemical reaction
ω	Turbulent kinetic energy specific dissipation rate
χ	Scalar dissipation rate
Ξ	Flame wrinkling factor
ξ, η, ζ	Curvilinear coordinate system

Latin Symbols

$\underline{\mathbf{A}}^x$	Conservative variables Jacobian matrix
A	Flame element surface
a_1, b_1	Charlette's model constants
a_k^m, b_k^m	Tabulated coefficients for the linear C_{p_k} approximation used in the QCMF
A_{f_j}	Pre-exponential factor for reaction j (Arrhenius' law)
$a_{i_k}^r$, $b_{i_k}^r$	JANNAF C_p and C_v tabulated coefficients
$b_k^{\bar{m}}i$	Constant value of C_p in interval m for the QCMF tabulated C_p
$\mathcal{C}^m$	Coefficient needed in the resolution of the implicit pressure polynomial equation
c	Progress variable or speed of sound
C_k	Charlette's model constant
c_m	BML model constant
C_p	Constant pressure heat capacity
C_s	Smagorinsky constant
C_v	Constant volume heat capacity
C_{EBU}	LES-EBU model constant
$\mathbf{d}$	Boundary normal terms vector
D	Diffusion coefficient, Diameter, Fractal dimension
Da	Damköhler number
$\mathcal{E}$	Thickened Flame model efficiency, Conservation errors of mass/momentum/energy
$\underline{\mathbf{E}}^x$	Primitive variables Jacobian matrix
E	Total energy
E_{a_j}	Activation energy for reaction j (Arrhenius' law)
$\mathbf{F}_\mathbf{i}^\xi$, $\mathbf{G}_\mathbf{i}^\eta$, $\mathbf{H}_\mathbf{i}^\zeta$	Inviscid flux vectors in curvilinear coordinates
$\mathbf{F_i}$, $\mathbf{G_i}$, $\mathbf{H_i}$	Inviscid flux vectors in Cartesian coordinates
$\mathbf{F}_\mathbf{v}^\xi$, $\mathbf{G}_\mathbf{v}^\eta$, $\mathbf{H}_\mathbf{v}^\zeta$	Viscous flux vectors in curvilinear coordinates
$\mathbf{F_v}$, $\mathbf{G_v}$, $\mathbf{H_v}$	Viscous flux vectors in Cartesian coordinates
$\mathbf{F}$, $\mathbf{G}$, $\mathbf{H}$	Flux vectors in x, y and z directions
$\mathcal{F}$	Thickened Flame model thickening factor, LES filter function
f_u, f_Δ, f_{Re}	Blending function for Charlette's wrinkling model
G	Flame tracking level-set function - Scalar field
$g1$, $g2$, $g3$	Obstacles in the Masri geometry

$\Delta h^0_{f_k}$	Species formation enthalpy at the reference temperature
h	Sensible enthalpy, height
h_0^m	Mixture total non-chemical enthalpy for the QCMF
$\underline{\mathbf{I}}$	Identity tensor
I_m	Temperature interval for the tabulated C_p for the QCMF
$\mathbf{J}_k$	Species mass diffusion flux vector
J	Jacobian (determinant of the Jacobian matrix)
k	Wave number or turbulent kinetic energy
K_j^{eq}	Equilibrium constant for reaction j
K_k^ϕ	$\sum_{i=1}^{5} \frac{1000^i}{i} \left(a_{i_k}^1 - a_{i_k}^2\right)$ if $\phi = \varepsilon$ and $\sum_{i=1}^{5} \frac{1000^i}{i} \mathcal{R}_k \left(b_{i_k}^1 - b_{i_k}^2\right)$ if $\phi = h$
K_{f_j}	Forward reaction j rate constant
K_{r_j}	Backward reaction j rate constant
Ka	Karlovitz number
$\mathcal{L}_a$	Markstein length
$\mathcal{L}_i$	Wave amplitude at the boundaries
$\underline{\mathbf{L}}$	Left eigenvectors matrix
L	Characteristic dimension of computational domain
L_Σ	Flame wrinkling scale
l_t	Integral length scale
Le	Lewis number
$\mathcal{M}$	Face normal vector magnitude
$\underline{\mathbf{M}}$	Conversion matrix from primitive to conservative variables
M	Mach number
m	Mass
m_i	Coefficient for the implicit 5^{th} order polynomial equation for pressure
$\mathbf{n}$	Flame normal vector
N	Species number
$N_{x,y,z}$	Cell number in x, y and z direction
$\mathcal{P}$	Probability Density Function
P	Pressure
Pe	Peclet number (Cell Reynolds number)
Pr	Prandtl number
Pr_t	Turbulent Prandtl number

$\mathbf{q}_c$	Heat conduction vector
$\mathbf{q}_d$	Energy transport by molecular diffusion
$\mathcal{Q}_j$	Rate of progress of chemical reaction j
$\mathcal{R}_k$	Specific gas constant
$\mathcal{R}_u$	Universal perfect gas constant
$\underline{\mathbf{R}}$	Right eigenvectors matrix
r	Radius
Re	Reynolds number
$\lvert\underline{\mathbf{S}}\rvert$	Strain rate magnitude
$\underline{\mathbf{S}}$	Symmetric strain rate tensor
S	Entropy, wave speeds in the HLLC solver
s	Stoichiometric ratio
S_k	Suntherland's constant
s_l^0	Laminar flame speed
Sc	Schmidt number
Sc_t	Turbulent Schmidt number
T	Temperature
t	Time
T^m	Lower bound temperature of interval I^m
T_0	Reference temperature (constant for all species) or different (Suntherland's law)
t_f	Final time of the computation
$T_{0_k}^{\phi}$	$\sum_{i=1}^{5} \frac{a_{i_k}^1 T_0}{i} + \mathcal{R}_k T_0$ if $\phi = \varepsilon$ and $\sum_{i=1}^{5} \frac{\mathcal{R}_k b_{i_k}^1 T_0}{i}$ if $\phi = h$
$\mathbf{U}$	Conserved variables vector
$\mathbf{u}$	Local flow speed vector, $\mathbf{u} = [u,\, v,\, w]^T$
U	Characteristic velocity
$\mathbf{V}$	Primitive variables vector
$\mathbf{V}_k$	Species diffusion velocity vector
$\mathbf{V}_k^c$	Species diffusion correction velocity vector
$\mathbf{W}$	Characteristic variables vector
$\mathcal{V}$	Venting rates
V	Volume or speed
$\mathbf{w}$	Absolute speed vector
W	Molar mass

$[X]$	Molar concentration
$\mathbf{x}$	Position vector in cartesian space, $\mathbf{x} = [x,\ y,\ z]^T$
X	Molar fraction
x_0	Initial position
Y	Mass fraction
z	Volume fraction, Low-Mach Correction blending parameter

Operators

$\boldsymbol{\phi} \cdot \boldsymbol{\phi}$	Scalar product
$\langle \phi \rangle_s$	Surface Favre-averaged or statistical mean in interval s
$(\mathbf{nn} : \nabla)\, \boldsymbol{\phi}$	Gradients normal to the flame surface
$\nabla_t \cdot \boldsymbol{\phi}$	Tangential components of ∇
$\Delta\phi$	Variation of ϕ
LHS	Left-Hand Side
$\nabla\boldsymbol{\phi}$	Dyadic of $\boldsymbol{\phi}$
$\nabla \cdot \boldsymbol{\phi}$	Divergence
$\nabla\phi$	Gradient
RHS	Right-Hand Side
RP	Riemann Problem

Subscripts, Superscripts and Accents

$\bar{\phi}$	RANS : Reynolds average, LES : Reynolds filtered
$\hat{\phi}$	Computed with filtered values
$\tilde{\phi}$	RANS : Favre average, LES : Favre filtered
ϕ_a	Absolute
ϕ_{ad}	Adiabatic
ϕ_b	Burned mixture
ϕ_c	Progress variable or consumption (speed)
ϕ_Δ	Sub-grid quantity
ϕ_d	Displacement
ϕ_{df}	Double-flux value
ϕ'	Fluctuations
ϕ_F	Fuel
ϕ_∞	Far-field value
ϕ_i	ϕ at cell/interface i

ϕ_{in}	Inlet
ϕ_k	Species or Kolmogorov
ϕ_l, ϕ_L	Left state
ϕ_l^0	Laminar
ϕ^n	ϕ at iteration/time-step n
ϕ_O	Oxidizer
ϕ_r, ϕ_R	Right state
ϕ_{res}	Resolved on the computational grid
ϕ_*	Intermediate state
ϕ_{sgs}	Modelled on the computational grid
ϕ^T	Transpose
ϕ_l^{th}	Thermal total
ϕ_T	Turbulent (usually for flame speed)
ϕ_t	Turbulent (usually at the integral length scale)
ϕ_{th}	Heat / Thermal
ϕ_u	Unburned mixture

CHAPTER 1

Introduction

1.1 Problem statement

1.1.1 Introduction to accidental explosions

For hundreds of thousands of years dating back to the dawn of mankind, controlling fire has represented a constant challenge. In the early stages of humanity, men were unable to produce it, they had to wait for natural causes to provide it. Evidences of a widespread control of fire by humans were found to date back approximately 125 000 years, but the first hints of a mastered use are much older, originating some 400 000 years ago.

Control of fire led to the development of today's society as we know it, by allowing humans to cook food and secure warmth and protection. It also helped the expansion of human activity during the coldest hours of the night and the winter allowing populations to move to cooler climates. Furthermore, for more than 5 000 years, it has been one of the main methods of processing raw materials (pottery, iron, steel, etc.) available to humans. Until recently, the available mechanical power produced by humans, animals, wind and water was greater than the mechanical power produced by combustion (steam, spark-ignition) engines, gas turbines, etc. [91].

The combustion process essentially refers to a transformation of energy between the internal energy of the burned materials and a secondary energy being either heat, processed materials electrical or mechanical power. This process initiates when a mixture of a combustible material and oxygen-rich compound is exposed to an energy source (heat, spark, ...) of higher intensity than the auto-ignition energy of the mixture (Fig. 1.1).

There are numerous applications to combustion or fire in its broadest sense. It is widely present in every day life for most of mankind, starting with its domestic usage (electricity, food, heating), to internal combustion (IC) engines of cars and the several manufacturing processes of steel, plastic, etc. For most of known human history, the primary energy source was composed by so-called "fossil fuels" starting with wood, then charcoal and since the 1850's, oil and even more recently, since the 1950's natural gas. According to the International Energy Agency (IEA), oil and natural gas account nowadays for respectively 41% and 16% of the total energy consumed, and 96% for the oil in transportation.

Current estimations predict that the world population at the middle of the XXIst century will reach approximately 137% of the 2014 one, thereby indicating that the energy demand will continue increasing for the next 50 to 100 years [282]. On a shorter term, the IEA estimates that the oil demand will increase by 50% over the next 15 years.

However, accumulating evidences pointing in the direction of a human responsibility in the currently observed global warning due to the ever increasing amounts of CO_2 released in the atmosphere by the

combustion of fossils fuels, as well as the finite nature of fossil fuels supplies have recently led both the public and governments to think about replacing the combustion of fossil fuels by alternative ways of producing energy. Solar and wind energies are the obvious replacement solutions having both the advantages of being in unlimited supply, despite a great difficulty in storing them. The possibility of using hydrogen as a energy carrier has also received an increased interest as it represent a storable energy source coupled with an unlimited supply. Fusion facilities being build in France (ITER project[1]) and Germany (Wendelstein 7-X[2]) use hydrogen isotopes as their primary energy source, but fuel-cells could also be used to use hydrogen as a fuel.

Apart from its use as an energy carrier, hydrogen is a widely used chemical compound in numerous applications ranging from the fertilizer industry (ammonia production uses an estimated 28 million tons of hydrogen per year on an estimated production of 50 million tons according to the IEA), oil refinement industry for upgrading fuel, food industry to increase the saturation levels of unsaturated fat in margarine for example, but also in the production of ethanol, spatial propulsion in so-called "cryogenic" engines, etc. It is also widely used in welding and metal refinement industry. At the moment, most of the hydrogen production occurs in oil extraction plants where it is removed from hydrocarbon by a process referred to as "steam reforming" (Fig. 1.1).

(a) *Combustion tetrahedron*

(b) *Air Liquide hydrogen production plant - Chempark Dormagen, Germany*

Figure 1.1: *Combustion and hydrogen*

This increasing use and production of hydrogen rises two challenges,

- Producing, transporting and consuming it with a minimal environmental impact
- Enforcing the safety and security of the different infrastructures involved in the hydrogen life-cycle (extraction, storage, transportation and consumption)

The safety and security of the infrastructures involved in the hydrogen-life cycle remains a major issue concerning all the users of this compound. Hydrogen indeed features a wider flammability range than conventional fuels (4% of lower limit to 75% of upper limit), it would have to accumulate first to reach the proper concentration and only then could the mixture be ignited. However, the overall level of risk associated with hydrogen is often similar to gasoline and arguably safer as hydrogen is not inherently explosive, nor does it easily self-ignite. Oil products tend to auto-ignite around $230 - 500°C$ while hydrogen auto-inflammability temperature is $550°C$ [1].

In regards to safety properties, hydrogen diffusivity is both an asset and a risk. In unconfined areas, it is an asset, as it will be extremely difficult to obtain a mixture within the flammability range, however, in confined or semi-confined areas, it becomes a risk as inflammable clouds are more likely to form. Similarly to gasoline, methane and other petroleum products, hydrogen is a tasteless, colourless, odourless

[1] www.iter.org
[2] http://www.ipp.mpg.de/16900/w7x

and non-toxic gas. It also features a very low ignition energy, meaning that a small spark would be enough to ignite a cloud that would be neither too rich nor too lean, but also a very high laminar flame speed which indicates an high explosive potential associated with the difficulty of confining hydrogen flames. Both of these factors imply that in a confined area, hydrogen storage poses the hazards of both combustion and explosions [1].

However rare, due to the stringent regulations put in place at a national and international levels (e.g. NFPA68[3]), incidents leading to explosions feature a high risk on both the people and infrastructures within the explosion radius, and the damages induced by the large over-pressures resulting from such events can be extremely extended. Numerous occurrences of accidents that occurred during the past decades pushed forward the development of safety and security measures to mitigate the impact of such events. Below is presented a non-exhaustive list of accidents involving either hydrogen or more conventional fuels,

- May 6^{th} 1937 - Lakehurst, New Jersey - Fire started near the tail in an hydrogen filled airship (LZ 129 Hindenburg) and propagated at $50\,[m/s]$ with a complete destruction after $32\,[s]$ - 36 fatalities
- January 4^{th}, 1966 - Feyzin, France - A LPG spill occurred during the draining of a tank, and the inflammable cloud generated was ignited by a car passing on the adjoining motorway - 18 fatalities, 81 injured and extensive damages to the site
- April 19^{th} 1984 - Sarnia, Canada - Hydrogen explosion in the benzene unit of the Polysar petrochemical complex from $30\,[kg]$ of hydrogen released and ignited 20-30 seconds later leading to a small detonation in near field - 3 fatalities and extensive damages to the side plus minor structural damages up to $1\,[km]$ away
- March 2000 - Blainville, Quebec - Hydrogen tank mounted in a car test model exploded during pressure adjustment - 3 casualties and extensive damages to the car and building
- December 11^{th} 2005 - Buncefield, UK - Explosions in the Hertfordshire Oil Storage Terminal (one of the largest in Europe) with subsequent detonation due to the flame acceleration by the turbulence generated by the surroundings hedgerows and trees leading the remaining vapours to detonate - 43 injuries and large structural damages
- April 20^{th} 2010 - Mexico Gulf - Deepwater Horizon off-shore oil drilling rig exploded and took fire following the rise of a methane bubble from the well - 11 fatalities, extensive damages to the rig, world largest marine oil spill and largest environmental disaster in US history
- March 11^{th} 2011 - Fukushima Daiichi, Japan - Following the loss-of-coolant accidents and the nuclear meltdown, the Fukushima powerplant was shut, but while struggling to restore power to the plant, accumulated $1000\,[kg]$ of hydrogen resulting from the reaction between hot zirconium and water exploded destroying the upper part of multiple units - No fatalities but additional damages to the already badly severed plant

In order to establish the regulations and apply them, but also to mitigate the risks of unacceptable accidents, it is necessary to be able to predict these risks. Research on gas explosions started in the 1970's [28] with the first objective of building a knowledge database and tools allowing the prediction of the effects of such accidents. The first results were obtained based on experimental measurements, while the use of computational resources for such studies is much more recent, and features the advantage of being both safer and cheaper in addition to providing a larger amount of usable data. The Safety CFD (or SCFD) is a field that has now been active for approximately 30 to 35 years.

An explosion can be defined as a rapid transformation of the chemical energy in kinetic energy inducing a fast expansion of gas. During such an event, the critical factor is the overpressure generated which will determine the extent of the damages to the surrounding structures and environment. It is then of prime importance to predict it accurately. In this research work, we will only be interested in the

[3]National Fire Protection Association, http://www.nfpa.org/about-nfpa

simulation of explosions driven by a reactive propagating front.

In this type of explosion, an external energy source ignites a inflammable mixture. Once started, the process converts the chemical energy in heat, and the lighter dense products of the combustion expand pushing the fresh mixture in front of the flame. The presence of obstacles in front of the flame would generate turbulence in the inflammable mixture, which upon interaction with the flame will wrinkle it thus increasing strongly its reaction rate and total surface. This will further increase the amount of hot expanding products pushing the reactants faster, who will in turn generate more turbulence, thus increasing the flame speed even more, and so on. This powerful feedback loop is what makes this type of semi-confined explosions so dangerous and so strong.

Two main parameters have been found to strongly influence the pressure increase during the flame propagation, which are the flame laminar properties (flame speed) and its subsequent acceleration under the influence of turbulence, and the level of confinement. In the most critical accidents, both of these mechanisms are responsible for the large damages inflicted to the structures, but also to the potential fatalities. Two main propagation regimes of flame during these events can be defined,

- **Deflagration** : The flame propagates at a subsonic speed with respect to the inflammable mixture speed of sound. The propagation is driven by diffusion effects of reactants and heat. It is mainly characterised by a decrease of the density and an increase in velocity as the reactants pass through the flame front.
- **Detonation** : Propagation of a reaction zone coupled with a shock-system preceding it and moving at a supersonic speed with respect to the inflammable mixture speed of sound. Both the pressure and the density are increasing dramatically through the shock and reaction zone. The velocity is decreasing continuously in the tail of the detonation after the very large acceleration induced by the shock. The propagation is driven by an auto-inflammation of the mixture heated by the shock passing through the fresh mixture.

Although the detonation mode is by far the most devastating in terms of structural damages due to the very large overpressure generated, only the deflagration mode which represent the first stage of the flame acceleration will be studied in details in this work. More details on detonations can be found in the numerical simulations of Deiterding [73] or Oran and Gamezo [101–104], but also in the experimental work of Dorofeev [82–85] and references therein.

Deflagrations which are at the centre of this research are very complex multi-scale multi-physics phenomena, with a strong coupling between chemical reactions, heat and species diffusion, turbulence, flame-obstacles interactions, compressibility effects, etc. Each of these phenomena must be reproduced correctly in numerical simulations of explosions, such that the critical parameter (over-pressure) can be accurately predicted. This is done either by solving it directly, or by modelling it.

1.1.2 Explosion experimental studies

Several organisms and research centres devote their time to the analysis of methodologies, but also the definition of guidelines and safety measures in the case of explosions. One of the largest is the non-lucrative NFPA who published more than 300 guidelines to date for limiting risks associated with fire and explosions in different configurations. Collaborations between research centres and laboratories on the development of methods for predicting the effects of explosion exist. The Hysafe project[4] regroups 26 organisations across 12 countries to improve the knowledge about risks associated with the use of hydrogen as a energy source. The MERGE project financed by the European Commission allows a collaboration between companies and organisations developing explosion codes. These are then compared on common explosion configurations [16], such that guidelines can be defined.

[4] http://www.hysafe.org

Before developing the numerical techniques and models predicting these phenomena, it is necessary to obtain experimental measurements of these events such that empirical correlations can be extracted or such that they can be used as reference points for the validation of numerical tools. Due to the complexity, cost and levels of risk involved, no experimental data can be obtained on real configurations. Indirect measurements can still be obtained by using the on-site probes and sensors, such as pressure taps in oil tanks, gathering witnesses testimony, evaluation of the damages, etc.

To gain insight into these explosions, carefully instrumented experiments have been designed, following a similar *modus operandi*. A semi-confined geometry is filled with a stagnant inflammable mixture, and ignited. The flame then propagates in the geometry with a laminar behaviour at first, but under the influence of the obstacle positioned in the chamber, it accelerates and generates large overpressure. The main driving parameters of an explosion highlighted above are both well reproduced in such set-up, i.e. the flame confinement and large speed reached due to the turbulence generated by the obstacles.

Experimental studies for semi-confined explosions can be grouped in two categories, with the medium to large-scale ones where the chamber volume is of the order of the cubic meter or larger, and the small-scale where the volume is measured in litres. In the first case [28, 114, 130, 131, 225, 292], overpressures are measured in different positions, but experimental visualisations or velocity measurements can not be obtained because of the rigs large size. In the second case, however, the experimental apparatus is smaller and allows for more precise measurements and the study of numerous different configurations [44, 94, 123, 138, 151, 185, 199, 200].

The Sydney combustion chamber experimented since 2005 [151] and illustrated in Fig. 1.2 is one of the small-scale experiments with a length of 25 $[cm]$. This is the configuration chosen as the test case for the simulations presented at the end of this work. It is one of the very few small-scale experiments using hydrogen as fuel, when most of the others use either methane or propane. The large number of publications on this chamber [3, 115–118, 123, 136, 137, 156, 200, 249] and the wide variety of geometrical configurations experimentally measured (number, position and obstacle shape) make this test case a very good test for the current work.

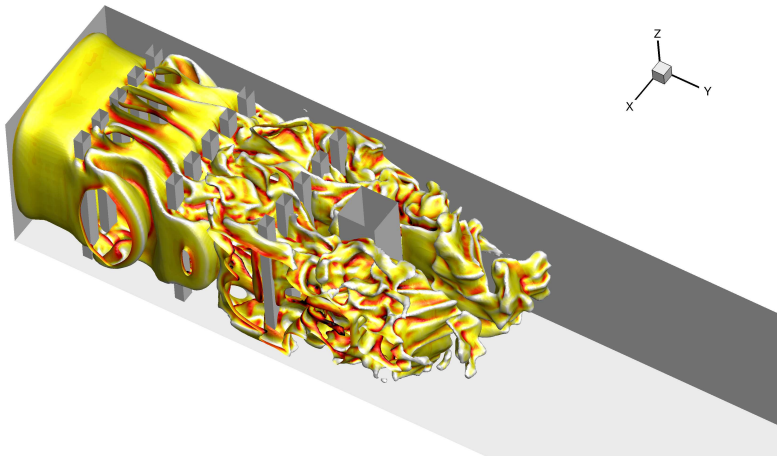

Figure 1.2: *Schematic illustrating the small-scale combustion chamber of Sydney University*

1.1.3 Modelling of explosions

The method chosen for modelling such phenomena must be able to reproduce correctly the flow physics, as well as be able to predict the resulting overpressure accurately. Moreover, it has to account correctly for the influence of the different parameters (fuel, obstacle shape, confinement, etc.). The number of modelling constants should be kept to a minimum, its use must be relatively easy and that the computational time associated it with must remain manageable.

Of course, most of these requests are contradictory, it is not possible to simultaneously reproduce the entirety of the physics in a short time, and the methods featuring short restitution times will only yield approximate results. The methods are thus classified in three categories [176] of increasing complexity, precision and computational time

- *Empirical methods* : Extracted from experimental results and used mainly in the design of vents in buildings to reduce the overpressure generated in such confined spaces
- *Phenomenological models* : Simplified physical models representing only the "relevant" physics but unable to account for the geometry other than by adjusting model constants and the turbulence is usually modelled using empirical correlations
- *Computational Fluid Dynamics (CFD)* : The governing equations of the flow and the combustion physics are solved numerically

Historically, (U)RANS methods have been considered for the CFD simulation of both large and small-scale configurations. Although mostly overlooked in safety analysis a decade ago, CFD is now more and more accepted as the solution and is widely used in the safety analysis of real configurations. The physics of the flow is reproduced accurately, and the prediction are of good quality. Its downside resides in its restitution time which is much larger than the empirical and phenomenological approaches. Despite some drawbacks and an increased cost compared to previous techniques, (U)RANS methods still remain today the industry workhorse thanks to its low computational cost compared to the more accurate LES and DNS approaches. However it suffers from the inaccuracy of the turbulence models used that are based on an assumption of statistical mean of the turbulence and are not adapted to all flows. They are not capable of predicting the transition of the flame from a laminar to a turbulent propagation mode for example, while this constitutes one of the critical point of semi-confined explosions where the flame starts in a fluid at rest and accelerates in the turbulence generated by its propagation. With the increase of computational power, LES is slowly becoming a promising tool for safety analysis, and has already shown promising results on medium-scale geometries [193, 209]. Additionally, it has been successfully applied to small-scale simulations of methane and propane explosions on the Sydney chamber [115–118, 123, 136, 137, 156, 200, 249]. For these reasons, LES is employed in this work for the simulation of hydrogen explosions on the Sydney University combustion chamber.

1.1.4 Compressible methods

As already pointed out, hydrogen is a very reactive compound with a large flame speed, whose explosions usually result in very large overpressure. Both of these characteristics make hydrogen a fuel very prone to detonate under the right conditions due to its very low detonation energy limit [1]. In order to simulate hydrogen explosions it is therefore necessary to use numerical methods able to tackle compressible problems, where large overpressure are encountered and potentially shock-waves. The widely used Godunov method [109, 278] allows the simulation of both slow and fully compressible flows, i.e. it can accurately capture shock-waves. Numerous pieces of work have contributed to make it a very efficient and accurate numerical technique [273, 275, 276, 278].

The main driver behind the use of compressible methods is the accurate capture of the potential shock waves in the flow, but also of the strong pressure waves. One of the key parameter of shock waves is their speed which determines for example whether a shock would be powerful enough to ignite a certain mixture (initiation of detonation). Predicting the shock speed incorrectly leads to different results in most compressible flow simulations where depending on the precise nature of the flow, the discrepancies could be quite large [269]. An inaccurate prediction of the shock properties would also lead to errors in the prediction of the speed at which the pressure wave are travelling, which corresponds to the speed of sound. As the overpressure constitutes the most critical parameter of semi-confined explosions, its accurate prediction is also highly critical.

The shock speed is determined solely by the thermodynamic properties of the flow it is travelling into, such as the specific heat ratio and molar mass. These two parameters therefore need to be accounted for precisely in the computations. The molar mass variations can be relatively easily taken into account by introducing additional equations for the transport of the different species in the flow. This first step increases the cost and complexity of the computation but helps increasing its accuracy by simulating the variation of one of the parameters. This is the approach used in the detonation simulations of Gamezo *et al.* [101–104] where the adiabatic index was held constant in the whole flow and adjusted prior to the computations to the fuel-oxidizer mixture under consideration, and leaves the shock speed as a parameter partially controlled by the user and not exclusively by the flow physic.

In order to have a shock structure fully determined by the flow physics, an additional step has to be taken, and the variation of the adiabatic index taken into account. This can be done by fixing its value for each chemical compound present in the flow, such that the mixture value can be recovered using some mixing rule. This allows for a more precise determination of the sound speed, or shock speed, but remains inaccurate when dealing with a large range of temperature in the flow as the adiabatic index is a direct function of the temperature. The second solution consists in using polynomial functions of the temperature whose coefficients are tabulated [59]. This constitutes a comprehensive way of accounting for the variations of the shock speed as a function of both the temperature and composition of the flow. The former solution consists in using the so-called calorically perfect equation of state (where the thermodynamic coefficients are independent of the temperature), while the second consists in using a more complex equation of state, usually referred to as thermally perfect.

However, one of the known drawbacks of fully conservative methods such as the Godunov method is that they can not be directly applied to the simulation of flows where the adiabatic index is allowed to be a function of the composition and/or temperature [4, 5, 147, 170]. Direct application of these methods results in large temperature spikes at the species interface (mixing zone), but also in pressure and velocity oscillations (Fig. 1.3) and was shown to be related to the inability of the pressure equilibrium to be maintained when numerical diffusion is present. These can eventually crash the computations, but even if this extreme case is not reached, they are very problematic in flows where temperature plays an important role (such as combustion), but also where small-scale structures are important (mixing of the species in combustion).

This issue forms part of the motivation of the present work, and addressing it has sparkled a whole new area of research in numerical methods for multi-component flows, resulting in numerous new techniques [6, 7, 139, 143, 146, 183, 219, 222, 250, 260] using either shock-capturing or shock-tracking methods. The vast majority of these methods relies at some stage or another on the abandon of strict conservation near material interface, following the analysis of Abgrall and Karni [6] showing that abandoning strict conservation allows to circumvent this issue. An additional issue is that the extension of most of these methods to viscous reacting flows is far from being straightforward, such that one of the only method available in the literature to compute compressible reacting multi-component flows is the Double-Flux model of Abgrall and Karni [6] and Billet and Abgrall [25], while the compact-central differencing of Kawai and Terashima [149] could probably be extended to mixture of non-calorically perfect gas as well.

1.2 Aims and objectives

The present work aims at proposing a new method for addressing the pressure oscillations issue arising in fully-compressible multi-component flows and some of the drawbacks of the double-flux model. Indeed, the double-flux model requires the evaluation of the Riemann problem twice at each cell interface, which in three-dimensional simulations would convert to evaluating it 12 times per cell, compared with the 6 times of a normal Godunov approach. Furthermore, relatively large energy conservation errors have been reported for this model, which could potentially become problematic in some applications.

The new approach derived in this work is based on the work of Allaire *et al.* [7], where one addi-

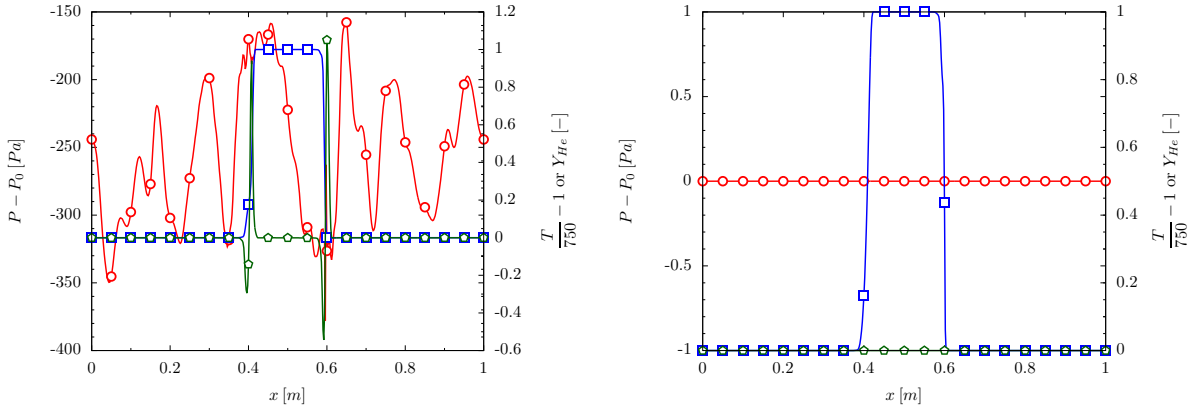

(a) *Fully-conservative approach* **(b)** *Quasi-conservative approach*

Figure 1.3: *Advection of an helium bubble in a nitrogen coflow at* $T = 750\ K$, $M = 0.3$ *and* $P_0 = 101325\ Pa$ - $P - P_0$, $\frac{T}{750} - 1$, Y_{He}

tional equation is solved for each species. The computational cost is thus expected to be lower than the double-flux at the cost of an increased memory usage. This new approach will be integrated within a fully-compressible flow solver able to deal with slow to fast compressible reacting flows as well as precisely accounting for shock-waves.

Thus the objectives of this research work can be separated in two steps, the first one concerned with the derivation and development of a new numerical technique,

- Derivation of a new fully compressible multi-component approach based on the 5-equation model of Allaire *et al.* [7] to address the issue of pressure oscillations in such flows. The proposed method will use the thermally perfect equation of state and be high-order accurate, low dissipation and shock-capturing, able to deal with slow and fast reacting flows
- Validation of the proposed method on a wide range of problems ranging from simple advection-like tests to fully compressible detonations in one and multiple space dimensions. Its performance will be compared with the double-flux model of Abgrall and Karni [6] and Billet and Abgrall [25] in terms of accuracy, conservation properties and computational cost

and the second with the application of these techniques to hydrogen explosions simulation,

- Implementation of the proposed numerical technique within a block-structured compressible LES solver for turbulent premixed combustion able to deal with a wide range of flame speed and compressible features in complex geometries based on the Flame Surface Density combustion model
- Simulation of the Sydney University hydrogen explosion test case to confirm that LES is well adapted to the prediction of compressible strongly turbulent and reacting transient flows such as hydrogen explosions in semi-confined geometries

1.3 Thesis layout

This work is split in three parts, where the first part describes the theoretical and numerical approaches employed in this work. General knowledge about premixed laminar and turbulent flames, as well as a detailed description of the failure of the Godunov method in compressible multi-component flow simulations and the published techniques to circumvent the problem are given in Chapter 2. The governing equations for all the methods considered in this work, from the newly developed volume fraction approach to the classical Navier-Stokes equations are presented in details in Chapter 3. In depth review of the

thermodynamic relations and closures considered in this work are introduced. The filtered equations for the LES framework are also presented and the modelling of the different sub-grid terms is discussed. Finally, a detailed description of the numerical methods developed and implemented within the course of the current research work is given in Chapter 4. A special attention is given to the numerical treatment of both quasi-conservative methods used here as their use forms the main motivation of the research. A special emphasis is also made on the implementation of the newly derived characteristic boundary conditions for the quasi-conservative volume fraction approach.

The second part is concerned solely with the validation of the algorithm detailed in the first part. Chapter 5 uses a one-dimensional code written by the author to verify and validate the different algorithms considered in problems of increasing complexity, from simple advection problem to fully compressible viscous reacting detonations. The strengths and weaknesses of the different models are highlighted and an in-depth review of their capabilities is given. Chapter 6 presents the extension of the validation and verification process to multi-dimensional problems, and in particular the well-known inert and reacting shock-bubble interactions.

Finally, the last part concentrates on the application of the validated methods to the problem of hydrogen explosions in the Sydney University small-scale combustion chamber. Chapter 7 introduces the relevant concepts of flame phenomenology in semi-confined explosions as well as a description of the numerous experimental studies published to date on the problem of hydrogen explosions. The choice of the test case is thus presented and justified in view of the existing available database. The experimental Sydney University explosion chamber is then detailed and the governing equations and numerical methods used in the present research for the modelling of compressible turbulent combustion within the implemented LES framework are presented. Finally, Chapter 8 presents a short theoretical and one-dimensional analysis of the turbulent models considered before their application to the full geometry of the Sydney experiment. The LES results are then validated and the quality of the computations is assessed. A short study of the impact of different parameters on the flame behaviour is then presented.

PART I

Theory and modelling of turbulent compressible multi-component reacting flows

CHAPTER 2

Literature Review

2.1 Premixed combustion phenomenology

2.1.1 Characterisation of the combustion

Combustion can be defined as a series of sequential and simultaneous exothermic or endothermic chemical reactions between a fuel and an oxidant, a release of heat. A transformation of chemical species occurs during this process, where the heat can potentially be converted into light. The mass and energy are conserved, only the chemical bond energy is transformed to thermal energy.

In order to understand reacting flows, the combustion community identified several canonical combustion situations as a mean to classify the different types of flames [21] :

- **Non-Premixed Combustion**, or diffusion flames : The combustion is non-premixed when the fuel and the oxidizer are initially separated and then brought together by means of mixing. It usually only involves two streams, one of fuel and the other of an oxidant. The flame is then present at the mixing between the two streams, usually along the line of stoichiometric mixture (Fig. 2.1). The non-premixed combustion has been widely studied by the industry as it is intrinsically a simpler problem, and thus it has been far more investigated than the premixed one. It is of particular importance in diesel engines, liquid fuelled gas turbines, fires, furnaces.
- **Premixed Combustion** : Premixed combustion on the other hand does not need any streams to burn. Fuel and oxidant are already mixed together forming a flammable mixture, and combustion occurs by the propagation of a flame front separating the burnt and unburnt mixtures (Fig. 2.1). Although more complex than non-premixed combustion, the interest in its modelling is rapidly growing due to its relevance in applications such as modern gas-fuelled turbine engines, spark-ignition engines, jet afterburners and explosion or accident scenarios.

More recently, evidences of a third behaviour were observed [23]. In some practical combustion systems, the most basic assumption of either asymptotic theories can not be assumed to suffice any more, for example, when the gas entering in localised reaction zones is not fully premixed into a uniform mixture, or when the gas can no longer be considered as pure fuel or oxidiser. The combustion is then described as **partially premixed**. It is important to distinguish between the different partial premixing cases existing. Amongst these, an essential distinction must be made between the non-uniform burnable mixtures which may or may not include a stoichiometric mixture within their range of compositions. For those that do, the flame is expected to behave as a premixed flame and will be referred to as *stratified premixed flame*, whereas for those that do not (more challenging case), the flame will most probably display the behaviour of both a premixed and a non-premixed flame, it is therefore called a *premixed/non-premixed* combustion.

A second distinction can be made based on the turbulence level of the flow. A laminar or turbulent behaviour of the flame can be observed, and this distinction will have a significant impact on the modelling of the problem. Either of the propagation modes (laminar or turbulent) might need to be simulated, or

in several cases, both simultaneously which could lead to several problems as most combustion models are designed to tackle a single one.

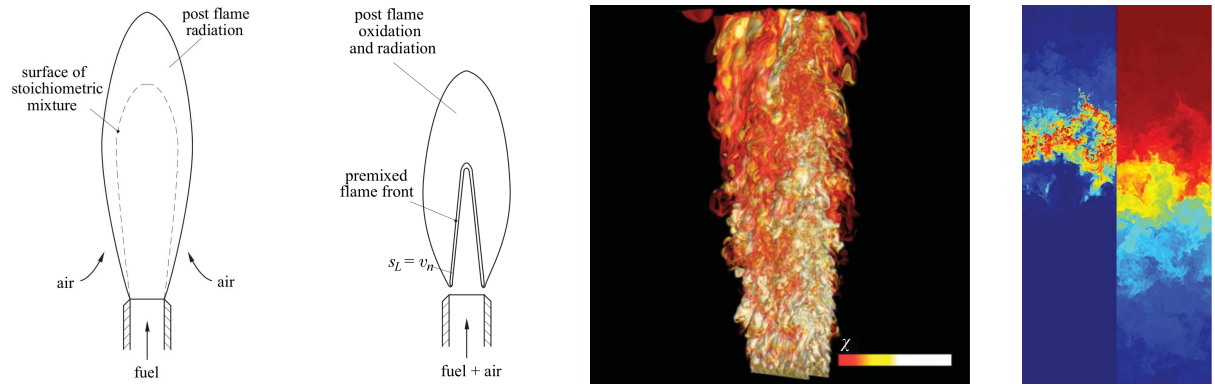

(a) *Laminar non-premixed flame [232]*

(b) *Laminar premixed flame [232]*

(c) *Turbulent non-premixed flame [300]*

(d) *Turbulent premixed flame [11]*

Figure 2.1: *Flame classification*

Theoretical properties of premixed laminar flames are presented in §. 2.1.2, while turbulent premixed flames are described in §. 2.1.4.

2.1.2 Premixed laminar flames

The study, both theoretical and numerical of simple laminar flames is of particular relevance towards the investigation of combustion modelling. Indeed, in the case of fairly simple flames, where the proper assumptions have been made, some analytical results can be derived for the flame's speed, reaction rate, structure, etc. For more complex cases, computed results can be obtained and provide insight into the sensitivity of the flame to different parameters, such as the species' diffusivities, chemical schemes, etc. Furthermore, many turbulent combustion models consider laminar flames as the basis upon which the closure of the unclosed terms can be derived. Therefore it is important to have the most comprehensive knowledge possible on these flames.

Mixture composition

One of the key parameter driving the premixed laminar combustion is the equivalence ratio of the flame describing the content of the burnable mixture. Even though numerous (up to thousands) chemical species are involved in the combustion process, it is primarily a reaction between an oxidant and a fuel. For a single-step chemical mechanism, where ν'_O and ν'_F are the stoichiometric coefficients of the oxidant and fuel respectively, we have,

$$\nu'_O O + \nu'_F F \rightarrow \text{Products} \tag{2.1}$$

and the stoichiometric ratio s is defined as,

$$s = \left(\frac{Y_O}{Y_F}\right)_{st} = \frac{\nu'_O W_O}{\nu'_F W_F} \tag{2.2}$$

while the equivalence ratio is given by,

$$\phi = s\frac{Y_F}{Y_O} \tag{2.3}$$

The equivalence ratio is used to characterise the regime of laminar combustion, i.e. either rich (fuel in excess, $\phi > 1$) or lean (oxidant in excess, $\phi < 1$).

Flame structure

The laminar flame properties have been widely studied for more than 150 years [295, 301], using the simplified Navier-Stokes set of equations [238] in 1D, neglecting the transient effects.

The structure of a laminar premixed flame is presented on Fig. 2.2, showing that the flame front can be viewed as a wave propagating from the burnt to the fresh gases with a constant speed of displacement usually referred to as the laminar flame speed, and noted s_l^0. The fresh mixture of reactants is at the left of the picture, while the hot products are on the right, separated by a thin reaction zone characterised by large temperature gradients. Several zones can be identified,

- **Cold reactants zone** where the fuel and oxidant are perfectly mixed at the molecular level and where the mixture is chemically inert.
- **Preheat zone** where by diffusion of temperature, the reactant mixture is heated but still chemically inert.
- **Reaction zone** characterised by large temperature and species concentration gradients, where the fuel reacts with the radicals (H, O atoms) to form intermediate species (CO, H_2, etc.). It has a thickness δ_r.
- **Post-Flame zone** (also called oxidation zone), where slow chemical reactions occurs, and the secondary fuels are converted in final products (CO_2, H_2O, etc.). As the fuel consumption is several order of magnitude faster than the recombination reactions, the reaction zone thickness is very small compared to the oxidation zone thickness.

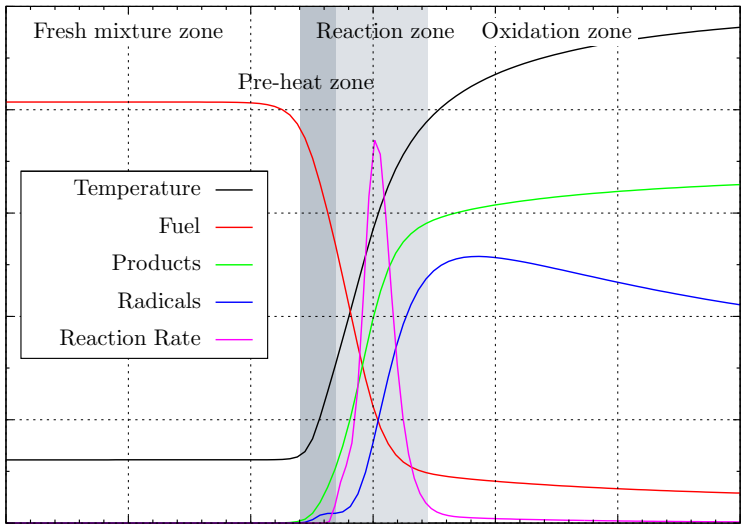

Figure 2.2: *Premixed laminar flame structure*

General behaviour

As stated previously, a simplified set of equations is used to model the unstrained laminar flame. The transient effects are neglected by studying the flame in a reference frame moving at speed s_l^0 and making the following additional hypothesis [295],

- All species have the same molecular weight, constant heat capacity and molecular diffusion. This amounts to an equal Lewis number (Le) for all species. Adding the simplification of equal mass and heat diffusivities, this finally leads to a unity Lewis number for all species.

- The chemical reaction scheme is composed by a single irreversible reaction and the reaction rate constant follows an Arrhenius law.
- The reaction rate is assumed to be limited by the fuel mass fraction, such that the flame is very lean and the oxidizer mass fraction is assumed constant.

These assumptions, although quite stringent, still represent the basic phenomena encountered in combustion such as highly non-linear heat release, gas expansion and temperature increase. Based on these simplifications and by solving the resulting system of equations, general trends for premixed combustion can be obtained and summarised as follows [295],

- The maximum temperature and reaction speed are completely decoupled even for complex chemical schemes and turbulent combustion. This implies that the maximum temperature obtained in a premixed flame can be entirely determined by the thermo-chemistry of the mixture, i.e. its composition, species formation enthalpies and heat capacities. Furthermore, the reaction speed is only function of the chemical parameters such as the Arrhenius pre-exponential factor, activation energy and temperature exponent.
- The adiabatic flame temperature obtained via the use of these assumptions provides satisfactory orders of magnitude, although in the case of complex chemical schemes, endothermic dissociation reactions of some products take place at high temperature, thus reducing the maximum achievable temperature of the flame (Fig. 2.3). It has been shown that using variable heat capacities contributes in reducing this error in rich mixtures where the temperature is high enough to trigger dissociation reactions.
- The reacting zone in a premixed flame is rather thin, of the order of $2/\beta$, where β represents the activation temperature of a reaction ($\beta = \alpha T_a/T_{ad}$ with $\alpha = (T_{ad} - T_u)/T_{ad}$ a measure of the heat release, where T_u is the fresh gas temperature, T_a the activation temperature and T_{ad} the adiabatic temperature), and usually displays value around 20. This implies that if a mesh is designed to solve a non-reacting flow at a given Reynolds number, its cell size has to be divided by about $\beta/2 \approx 10$ in each direction to accurately solve for the structure of the premixed flame.

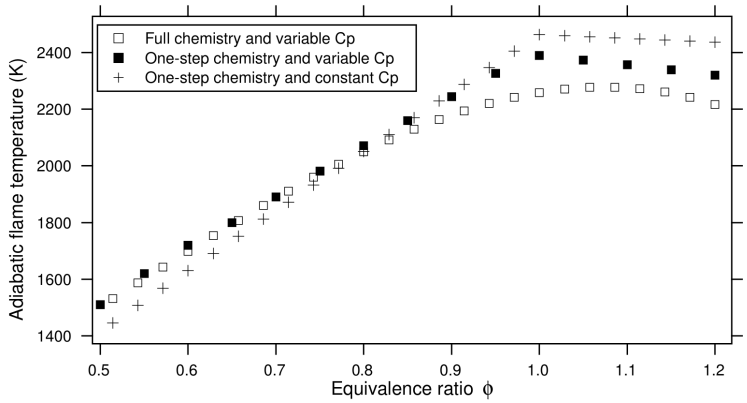

Figure 2.3: *Adiabatic flame temperature of a propane-air mixture under different assumptions [238]*

Laminar flame speed

An asymptotic analysis derived by Zeldovich, Frank-Kamenetski and Von Karman (ZFK) in the 1940s [301] and based on the previously mentioned assumptions allows the derivation of explicit equations solving for the flame speed. It was shown to be controlled by the heat diffusivity and chemical parameters. Different expressions (ZFK [301], Williams [295], van Kalmthout [283], Poinsot and Veynante [238]) have been derived, and although featuring different formulations, they all exhibit the same dependency [238],

$$s_l^0 \propto (D_{th} R_r)^{1/2} \propto \left(\frac{\lambda_u}{\rho_u C_{p,u}} R_r \right)^{1/2} \tag{2.4}$$

where D_{th} is the heat diffusivity in the fresh gas, $R_r = \frac{2B}{\beta}\exp(-\beta/\alpha)$ and B is the rate constant from the Arrhenius' law.

Further work (Mitani (1980) [208]) unveiled more general expressions, enabling the pressure and temperature effects to be taken into account. It was found that flame speed would rapidly increase with the temperature of fresh gas, while it was shown to decrease with pressure.

The laminar flame speed is an essential parameter of laminar flames and is widely used for validating the numerical results obtained by comparison with experimentally measured values, and as a parameter in turbulent combustion models.

The definition of the flame speed has been based until now on the intuitive image of an interface moving at a speed s_l^0 in the local flow. Poinsot *et al.* [236, 281] showed that two alternative definitions could be introduced using either a global or a local definition of the speed. By supposing that the flame front can be tracked using a progress variable c given by,

$$c = \frac{T - T_u}{T_b - T_u} \quad \text{or} \quad c = \frac{Y_F - Y_{u,F}}{Y_{b,F} - Y_{u,F}} \tag{2.5}$$

which takes the value $c = 0$ in reactants and $c = 1$ in products, we can define a local normal to the flame surface directed towards the reactants as,

$$\mathbf{n} = -\frac{\nabla c}{|\nabla c|} \tag{2.6}$$

The speed at which a point on the flame front moves in a fixed reference frame to remain on the flame front is denoted $\mathbf{w}$ while the local flow velocity is referred to as $\mathbf{u}$, thus leading to several definitions based on either the flame kinematic or chemical properties and summarised in Table 2.1.

Name	Symbol	Definition	Formula
Laminar	s_l^0	Speed at which a 1D unstrained laminar flame propagates in a fixed reference frame. Reference speed in combustion	–
Absolute	s_a	Projection of $\mathbf{w}$ along the flame normal	$s_a = \mathbf{w}\cdot\mathbf{n}$
Displacement	s_d	Speed at which a flame front moves in the local flow field, i.e. the difference between $\mathbf{w}$ and $\mathbf{u}$	$s_d = s_a - \mathbf{u}\cdot\mathbf{n}$
Consumption	s_c	Speed at which a flame consumes the reactants	$s_c = -\frac{1}{\rho_u Y_{u,F}}\int_{\mathbb{R}} \dot{\omega}_F \, \mathrm{d}\mathbf{n}$

Table 2.1: *Several flame speed definitions for a premixed laminar flame*

Flame thickness

In LES and a fortiori in all turbulent combustion modelling techniques, another key parameter is the flame thickness. Indeed, knowing an estimate of the flame thickness prior to any computation is essential to discretise properly the computational domain. It is also a useful quantity for modelling transport, chemistry, etc. Similarly to the flame speed, several definitions of the flame thickness can be found as shown in Fig. 2.4 and summarised in Table 2.2.

Amongst the different definitions presented in Table 2.2, the diffusive one is very easy to estimate but appears quite approximative (usually gives a fivefold estimation of the thermal thickness), while the thermal thickness is usually the reference length of the flame but requires a temperature profile to be estimated. The total thermal thickness is found to be always larger than the thermal thickness, and often leads to an overestimation due to the slow recombination reactions taking place in the oxidation zone, while the reaction thickness is always the smallest of all.

Name	Symbol	Definition	Formula
Diffusive	δ	Similar scaling laws as Eq. 2.4	$\delta = \frac{D_{th}}{s_l^0}$
Thermal	δ_l^0	Based on the temperature profile across the flame	$\delta_l^0 = \frac{T_b - T_u}{\lvert \max(\nabla T) \rvert}$
Thermal total	δ_l^{th}	Distance over which the temperature varies between $1.01T_u$ and $0.99T_b$	–
Reaction	δ_r	Reaction zone thickness	–

Table 2.2: *Several flame thickness definitions for a premixed laminar flame*

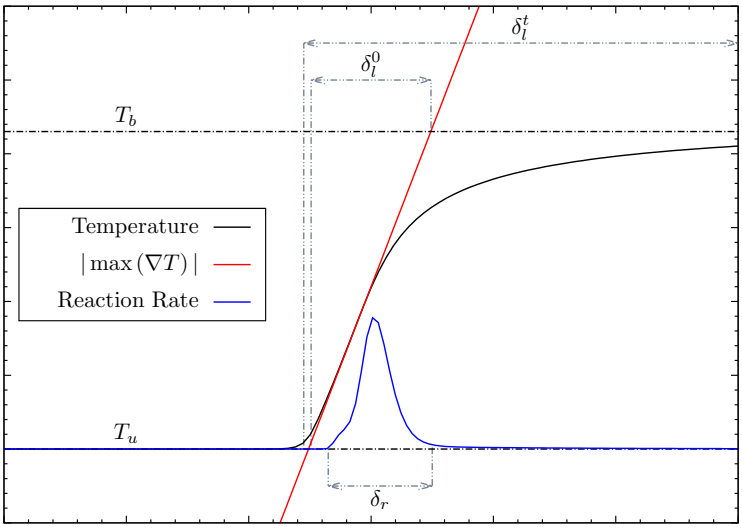

Figure 2.4: *Definition of the different laminar flame thickness*

Flame stretch

A flame propagating in a flow is under the influence of its curvature and the strain, which could both have an impact on the flame speed. This can be related to the stretch of the flame κ defined as the rate of change of a flame surface element A by Matalon and Matkowsky [203] by,

$$\kappa = \frac{1}{A}\frac{\mathrm{d}A}{\mathrm{d}t} \tag{2.7}$$

Kinematic considerations on a thin flame front led Candel and Poinsot [45] to give the following general expression,

$$\kappa = -\mathbf{nn} : \nabla\mathbf{w} + \nabla \cdot \mathbf{w} \tag{2.8}$$

where the operator $(\mathbf{nn} : \nabla)$ represents the gradient normal to the flame surface. This formulation can be recast using the definition of the displacement speed (Table 2.1),

$$\kappa = -\mathbf{nn} : \nabla\mathbf{u} + \nabla \cdot \mathbf{u} + s_d \nabla \cdot \mathbf{n} \tag{2.9}$$

Chung and Law [63] further defined $\nabla_t \cdot \mathbf{u} = -\mathbf{nn} : \nabla\mathbf{u} + \nabla \cdot \mathbf{u}$ as being the tangential component of the ∇ operator referring to the strain in the plane locally parallel to the flame front, leading to,

$$\kappa = \nabla_t \cdot \mathbf{u} + s_d \nabla_t \cdot \mathbf{n} \tag{2.10}$$

Stretch is thus defined as the sum of two components, the first being due to the local flow non-uniformity (strain), and the second due to the flame curvature $(\nabla \cdot \mathbf{n})$.

Stretch can influence the flame speed in several ways, but as it is very challenging both numerically and experimentally to precisely estimate the different speeds of the flame, only asymptotic analysis can give information on the stretch-flame speed coupling. Under several hypothesis, but most notably small stretch values [40], it can be shown that both displacement and consumption speeds are linearly related to stretch by a new length referred to as Markstein length ($\mathcal{L}_a$). Additionally, stretch also has an impact on the burnt gas temperature as shown by Law [172].

2.1.3 Turbulence properties

The first question typically asked when considering a fluid flow and its simulation is typically about its Reynolds number. It allows to determine approximately whether a flow is laminar or turbulent.

$$Re = \frac{UL}{\nu} \tag{2.11}$$

A laminar flow is characterised by a smooth aspect with large coherent structures. As the flow Reynolds number increases, large scale motions become unstable and eventually transition to a highly chaotic turbulent state. This occurs when inertial forces (UL) overcome viscous dampening (ν). A fully turbulent flow is then characterised by a highly complex flow field across a very large range of scales.

Another remarkable feature of fully turbulent flows is the energy distribution across scales, with a continuous spectra of small eddies convected by the mean flow. Eddies of all sizes are interacting through an energy cascade, enhancing mass, momentum and species diffusion as well as heat transfer compared to a laminar flow. This energy cascade is famously described by the short poem of Richardson,

Big whirls have little whirls,
which feed on their velocity.
Little whirls have lesser whirls,
and so on to viscosity

Fig. 2.5 shows the typical distribution of turbulent kinetic energy $E(k)$ over the different scales in wavenumber space ($k = 1/r$, where r is the eddy size). For high Reynolds, this energy distribution can be split in three regimes [244],

- **Integral zone**, characterised by the largest eddies (low wavenumbers) containing the most energetic structures associated with the integral length scale l_t. Large scales are typically problem dependant and usually formed by an external mechanism. The flow is inhomogeneous and anisotropic. The velocity ($u'(l_t) = u'$) and length scales in this range are not affected by viscosity and are usually used to estimate the turbulent Reynolds number

$$Re_t = \frac{u'\left(l_t\right) l_t}{\nu} \tag{2.12}$$

- **Sub-inertial zone**, characterised by a behaviour independent of both viscous effects and the mechanism injecting energy at large scales. In this zone, large unstable eddies break up into smaller eddies through an energy cascade. The energy flux from one scale to the other is constant through the different scales, and the energy at each scale is given by the famous Kolmogorov law [164],

$$E(k) \propto K_0 \varepsilon^{2/3} k^{-5/3} \tag{2.13}$$

  The turbulent kinetic energy dissipation rate (ε) of an eddy of size r is estimated by the ratio between its turbulent kinetic energy ($u'^2(r)$) and its time scale ($r/u'(r)$), leading to,

$$\varepsilon = \frac{u'^3(r)}{r} \tag{2.14}$$

- **Dissipative zone**, characterised by a Reynolds number close to unity and large wavenumbers. In this zone, the turbulent kinetic energy passed from the large scales is dissipated by viscosity and converted into heat. The balance between inertial and viscous forces determines the smallest scales of the flow, referred to as the Kolmogorov scale (η_k) and estimated by,

$$\eta_k = \left(\frac{\nu^3}{\varepsilon}\right)^{1/4} \tag{2.15}$$

while the smallest eddies speed is given by,

$$u'(\eta_k) = u'_k = (\nu\varepsilon)^{1/4} \tag{2.16}$$

and the Reynolds number becomes,

$$Re(\eta_k) = Re_k = \frac{u'_k \eta_k}{\nu} = \frac{\varepsilon^{1/3}\eta_k^{4/3}}{\nu} = 1 \tag{2.17}$$

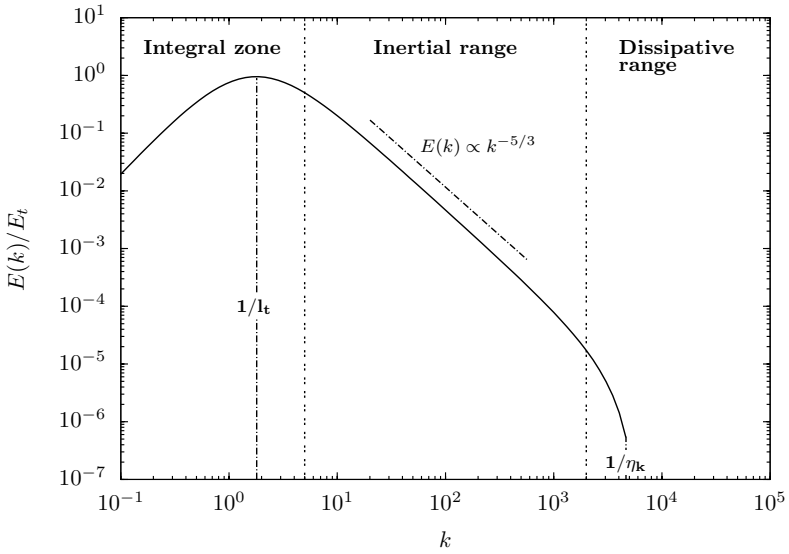

Figure 2.5: *Typical turbulent kinetic energy spectrum for homogeneous turbulence*

2.1.4 Turbulent premixed flames

Turbulence influence

When considering flames in a turbulent flow, which occurs in most practical combustion systems (combustion chambers, rockets, internal combustion engines, etc.), the laminar relations previously presented no longer hold true due to a non-negligible interaction with the turbulence. This interaction works both ways, as combustion can either increase the turbulence (acceleration of the flow due to the heat release) or decrease it (expansion of hot gases), and turbulence enhance (through enhanced mixing and diffusion of species and heat diffusion) or stop (flame quenching) the combustion process [238].

Turbulence also increases widely the range of length scales and speed values obtained for the flame. A laminar flame features a typical thickness of the order of $\delta_l^0 \approx 0.3\,[mm]$, while a turbulent one usually starts at a few millimetres and can grow up to several meters. The laminar flame speed for a stoichiometric hydrocarbon flame is approximately $s_l^0 \approx 0.40\,[m/s]$, while a turbulent flame speed of several hundreds of meters per second can easily be achieved in semi-confined explosions, up to supersonic speeds in detonations.

Regime diagrams

The need to account for the wide range of time and length scales encountered in turbulent premixed flames led to a classification of the turbulence/combustion interaction into different categories delimited by several dimensionless numbers, summarised in the so-called "turbulent combustion diagrams" [238].

In these, combustion is described in terms of ratios of lengths and velocity scales, while turbulence is characterised by its integral length, turbulent kinetic energy, dissipation rate, etc. This enables to determine whether the flow contains flamelets (thin reaction zones), pockets or distributed reactions zones. This provides very useful information for the development and selection of combustion models as a continuous front cannot be modelled in a similar way as one broken in many small pockets, or even burning in a more distributed fashion. Amongst numerous diagrams presented in the literature, one can mention Peters with the first version of his diagram [229] and its revision [230], Williams [295] and Pitsch [234] whose diagram is an extension of Peters' one designed to take the computational mesh effects into account.

Three time scales can be identified within a turbulent premixed flame, a chemical one associated with the flame characteristics, and two kinematic associated with the largest and smallest eddies of the flow. The chemical time scale is related to the laminar flame properties by $\tau_c = \delta_l^0/s_l^0$. The flame interacts with eddies whose size ranges from the integral length scale to the Kolmogorov scale, and whose characteristic speed ranges from the integral RMS speed to the Kolmogorov speed, thus defining the integral ($\tau_t = l_t/u'$) and the Kolmogorov ($\tau_k = \eta_k/u'_k$) time scales.

Their respective magnitudes (i.e. the strength of each phenomena) can be compared using three dimensionless numbers,

- The **Damköhler number** compares the integral and chemical time scales,

$$Da = \frac{\tau_t}{\tau_c} = \frac{l_t}{\delta_l^0}\frac{s_l^0}{u'} \tag{2.18}$$

- The **Karlovitz number** compares the Kolmogorov and chemical time scales,

$$Ka = \frac{\tau_c}{\tau_k} = \frac{\delta_l^0}{\eta_k}\frac{u'_k}{s_l^0} \tag{2.19}$$

  By combining Eq. 2.16 and the flame Reynolds number definition $\left(Re_f = \delta_l^0 s_l^0/\nu \approx 1\right)$, it can be reformulated in terms of the integral velocity and time scale,

$$Ka = \left(\left(\frac{u'}{s_l^0}\right)^3 \frac{\delta_l^0}{l_t}\right)^{1/2} \tag{2.20}$$

- The **turbulent Reynolds number** linking together the Damköhler and the Karlovitz numbers,

$$Re_t = \frac{u' l_t}{\nu} = \left(\frac{u'}{s_l^0}\right)\left(\frac{l_t}{\delta_l^0}\right) = Da^2 Ka^2 \tag{2.21}$$

Two diagrams are presented in Fig. 2.6 showing different classifications based on turbulent characteristics for Peters [230] and on computational parameters for Pitsch [234] where the integral length scale is replaced by the filter (or cell) size (Δ) and the RMS speed is replaced by the subgrid velocity fluctuations (u'_Δ).

Following Peters [230], the following combustion regimes can be defined,

- $\mathbf{Re_t < 1}$ **- Laminar flame regime** : Laminar flow and weakly wrinkled flame

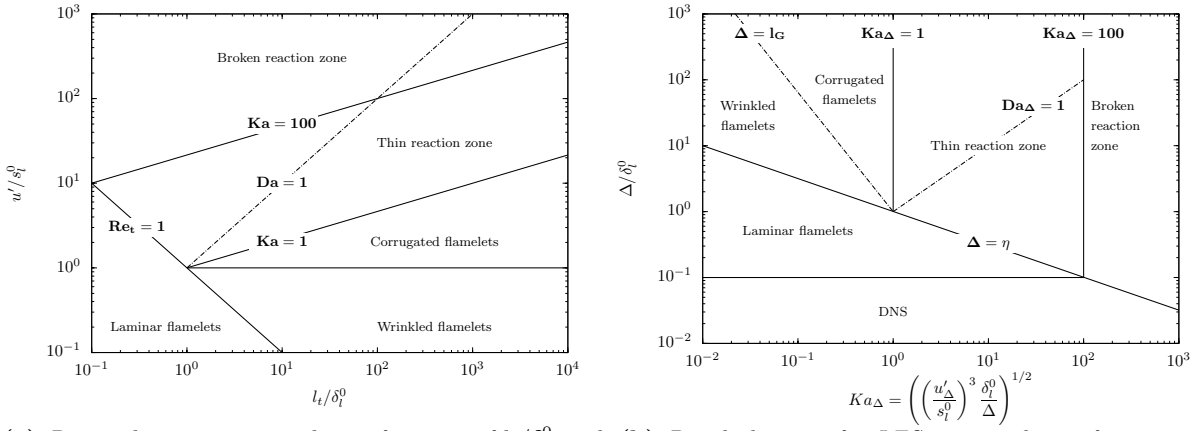

(a) *Peters diagram expressed as a function of* l_t/δ_l^0 *and* u'/s_l^0 *[230]*

(b) *Pitsch diagram for LES expressed as a function of* Ka_Δ *and* u'_Δ/s_l^0 *[234]*

Figure 2.6: *Turbulent combustion diagrams for premixed combustion*

- **$\mathbf{Re_t} > 1$ - Turbulent flame regime**
  - **$\mathbf{Ka} < 1$ - Flamelet regime** : The flame thickness is smaller than any turbulent scales and the chemical time scale is shorter than any turbulent time scale. The flame front is therefore thin and features an inner structure close to a laminar flame. It is wrinkled by turbulent motion, and depending on the turbulence level, this regime can be separated in two sub-regimes,
    - **$\mathbf{u' < s_l^0}$ - Wrinkled flamelet regime** : Turbulent eddies are too weak to disturb the flame front and interact with its structure. The flame curvature is small and its inner structure is very similar to a laminar flame.
    - **$\mathbf{u' > s_l^0}$ - Corrugated flamelet regime** : The flamelet regime is still valid, but the strongest eddies are able to interact with the flame and could lead to the formation of pockets of products or reactants
  - **$1 < \mathbf{Ka} < 100$ - Thin reaction zone regime** (or thickened-wrinkled regime) : The smallest eddies (η_k) are smaller than the flame thickness (δ_l^0) and are able to interact with the preheat zone thus increasing heat transfer and mass diffusion. The preheat zone thickness increases but the reaction thickness remains smaller than the Kolmogorov length and retains its laminar structure.
  - **$\mathbf{Ka} > 100$ - Broken reaction zone regime** (or well-stirred reactor) : The Kolmogorov length becomes smaller than the reaction zone thickness. The small eddies are thus able to interact strongly with both the preheat and reaction zones of the flame. No laminar structure can be identified any more. It corresponds to an extreme case that is rarely met in combustion devices.

It shall be noted that this classification remains qualitative as it has been conducted using dimensional analysis, order of magnitude estimations and various limiting hypothesis such as,

- Turbulence is not influenced by the flame heat release (homogeneous, isotropic frozen turbulence)
- Stretch, curvature and unsteady effects are neglected
- The order of magnitude analysis could be different, i.e. the flamelet regime limit could be $Ka > 0.1$ or $Ka > 10$
- One-step irreversible chemistry is assumed
- Kolmogorov length and velocity may be too small or too weak (compared to the laminar flame properties) to affect the flame significantly

Several other diagrams can be derived, especially based on a spectral analysis of flame-vortex interactions DNS studies. Additional physical effects can then be taken into account (quenching, heat losses, etc.) to adjust regimes limits [61, 239].

Turbulent flame speed

Similarly to the definition of the consumption speed in a laminar flow, it is interesting to describe and determine flame speeds in a turbulent flow. However, it is much more complex as turbulence characteristics and their potential interactions with the inner flame structure have to be taken into account in addition to the diffusive and chemical properties of the laminar flame.

Careful measurements in combustion vessels by Abdel-Gayed *et al.* [2] and Gülder [121] led to the following relation,

$$\frac{s_T}{s_l^0} \approx 1 + \frac{u'}{s_l^0} \tag{2.22}$$

showing that flame speed is enhanced by turbulent motions.

In the more specific case of the flamelet regime, where the flame inner structure remains laminar, it is possible to estimate this speed in a more precise way. Indeed, the main effect of turbulence in this regime is the wrinkling or stretching of the flame front by the large eddies of the flow, therefore increasing the total flame surface. The volumetric consumption rate therefore increases, increasing the flame front speed. In the flamelet regime, it can be assumed that the local speed of the flame front is close to the laminar flame speed. The mean flame front therefore moves at a turbulent speed corresponding to the laminar flame speed weighted by the ratio of the total wrinkled flame surface (A_T) by its mean area (A) as illustrated on Fig. 2.7 and given by,

$$\frac{s_T}{s_l^0} \approx \frac{A_T}{A} \tag{2.23}$$

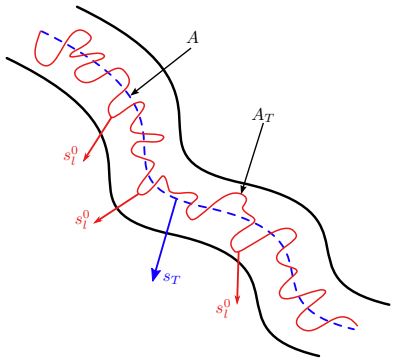

Figure 2.7: *Turbulent flame speed definition in the flamelet regime - The total wrinkled flame surface A_T and mean area A are shown along with the flamelet consumption (s_l^0) and turbulent (s_T) speeds*

Many expressions have been proposed for turbulent flame speeds over the years, usually as a function of several turbulent (l_t, u', etc.) and flame (s_l^0, δ_l^0, Le, etc.) parameters. The problem remains open nowadays and is a field of active research as it constitutes one of the major block of turbulent reacting flows modelling where several models exist to represent the turbulence influence on the flame.

2.2 Numerical approaches for the simulation of turbulent reacting flows

Analytical solutions to the Navier-Stokes equations do not exist in the general case, and even less so in the case of turbulent reacting flows in complex geometries. It is thus necessary to use numerical simulations

to obtain approximate solutions. This helps us in understanding and predicting the phenomena involved. Furthermore, they also provide a viable alternative to the costly and sometimes dangerous experiments, especially in semi-confined explosions.

Several techniques have been developed over the years to model turbulence and turbulent combustion, of which a brief overview is given below.

2.2.1 Numerical methods for turbulent flows : DNS/LES/RANS approaches

The different methods used to simulate turbulent flows mainly differ by the ratio between resolved and modelled turbulent scales. There are mainly three different methods used in the computation of turbulent flows, whose approximation' range of the turbulent scales of the spectrum goes from empty (DNS) to full (RANS) through partial (LES). This is illustrated in Fig. 2.8 and described in more details below by order of decreasing complexity and cost.

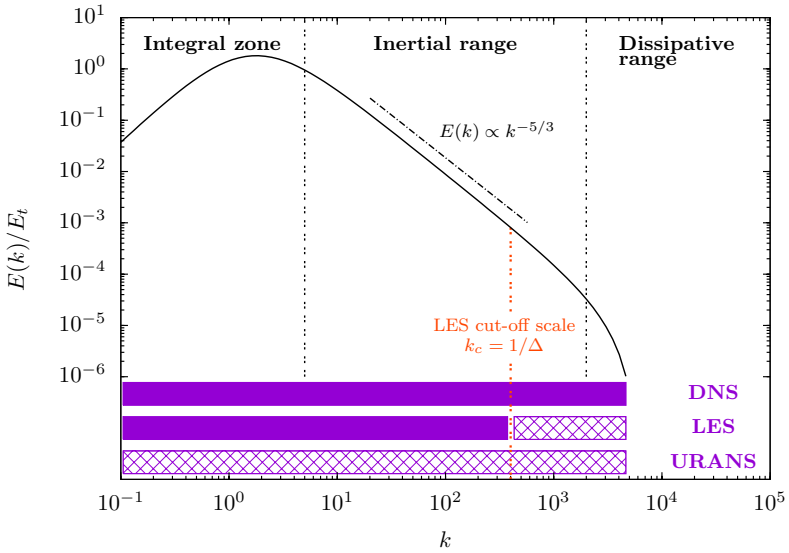

Figure 2.8: *Comparison of resolved (filled) and modelled (pattern) scales for the different numerical methods modelling turbulent flows : DNS, LES, RANS - k_c is the cut-off wavenumber used in LES (Poinsot and Veynante (2005) [238])*

DNS - Direct Numerical Simulation

Direct Numerical Simulation is the most comprehensive way of simulating turbulent flows. The full instantaneous Navier-Stokes equations are solved on every point of the computational domain, such that all turbulent scales are resolved, and no turbulence model used. The full frequency content of the flow is thus obtained and can be directly compared with experimental data (Fig. 2.9). DNS grids need to be extremely fine to capture all turbulent scales, from the integral to the Kolmogorov one, and even if super-computer capabilities are increasing at a fast pace, it still remains a challenge to compute a DNS case at moderate Reynolds number.

Using the different relations presented in §. 2.1.3, it can be shown that $l_t/\eta_k = Re^{3/4}$, which correspond to the scaling of DNS grids with Reynolds number, as all scales have to be resolved. On a three-dimensional grid, this lead to a cost proportional to $Re^{9/4}$, and by taking the time-stepping procedure into account, this yields a total cost scaling with Re^3. This converts in turn in months or years of computation for any practical Reynolds number ($\approx 10^6$). In combustion in particular, every chemical species have to be simulated, giving N additional transport equations to solve ($N > 10$ for any meaningful chemical mechanism, and $N >> 50$ for comprehensive large hydrocarbons mechanisms).

However, DNS is nowadays extensively used in the combustion community on academic test cases [11, 126, 256] as it brings valuable data to validate and develop combustion models for LES. It is still too expensive to be used on industrial test cases, although some results begin to appear, such as a very finely resolved LES presented by Quillatre [249] on the small explosion chamber experiment of Masri *et al.* [200].

LES - Large Eddy Simulation

LES is in a sense the best compromise between RANS that is fast but lacks precision in the resolution of instantaneous fields and the very expensive DNS providing the best solution possible. It allows the computation of an accurate solution while featuring an affordable cost. Its principle lies in the turbulence description given by Kolmogorov and presented in §. 2.1.3, showing that small scales statistics can be directly extracted from the large scales.

Large, geometry dependant turbulent scales are solved directly on the computational grid. Only the small diffusive scales, featuring an isotropic and homogeneous behaviour are modelled through the known energy of the large resolved scales. The main operation of the LES is thus a low-pass filtering, essentially removing the explicit integration of the small scales in the governing equations. This reduces significantly the modelling error compared to RANS, as only scales presenting an universal behaviour are modelled. This is done through a subgrid-scale (SGS) model, which is essentially a model for sub-filter turbulence. Higher frequencies than RANS are explicitly resolved, as shown in Fig. 2.9.

The governing equations are obtained through a physical or spectral filtering of the instantaneous Navier-Stokes equations [238] instead of an averaging. The variable decomposition proposed for RANS modelling (Eqs. 2.25-2.26) can be adapted to LES with a mean, an unsteady term, a resolved random fluctuation and finally an unresolved filtered random fluctuation, yielding,

$$\Phi(\mathbf{x},t) = \bar{\Phi}(\mathbf{x}) + \Phi_{uns}(\mathbf{x},t) + \Phi''_{res}(\mathbf{x},t) + \Phi''_{filt}(\mathbf{x},t) = \bar{\Phi}(\mathbf{x},t) + \Phi''_{filt}(\mathbf{x},t) \tag{2.24}$$

LES is by definition unsteady and requires a computational grid much finer than RANS due to the direct link between the filtering operation and grid size. To obtain an accurate LES solution, it is necessary to solve the widest range possible of turbulent scales, such that only the smallest are modelled. It is usually advised that the cell size lies in the inertial range of the Kolmogorov spectrum. Numerical methods used to solve the equations are usually high-order (3^{rd} and more) to reduce the non-physical dissipation added to the solution. These two facts combined increase quite significantly the cost of LES compared to RANS. More details are given about the methodology in §. 3.7 and its application to combustion in §. 2.2.2.

(U)RANS - (Unsteady) Reynolds-Averaged Navier-Stokes

RANS has been developed to compute the mean field of each variable. It is the cheapest of the methods aforementioned, and as such is the most popular for solving turbulent flows. The governing equations for the Reynolds ($\bar{\Phi}$, or Favre in compressible flows $\tilde{\Phi} = \overline{\rho\Phi}/\bar{\rho}$) averages are obtained by taking a time-average of the instantaneous Navier-Stokes equations [238]. Each time (t) and space ($\mathbf{x}$) dependant variables $\Phi(\mathbf{x},t)$ can be decomposed in a time-average $\bar{\Phi}$ and a random fluctuation Φ' giving,

$$\Phi(\mathbf{x},t) = \bar{\Phi}(\mathbf{x}) + \Phi'(\mathbf{x},t) \tag{2.25}$$

$$\overline{\Phi'}(\mathbf{x},t) = 0 \tag{2.26}$$

Turbulent models must then account for all turbulent scales lost in the averaging process. Computation results are time-averaged fields featuring no transient or unsteady behaviour as one could observe experimentally. Using them for studying semi-confined explosions or turbulent combustion in general is then highly debatable by nature, as results will not be representative of a single explosion but the average

of a great number of realisations.

A time-dependant version of RANS have been developed and is referred to as Unsteady RANS or URANS. The average of the Navier-Stokes equations is here not a time-average any more but an ensemble average (or statistical mean). This approach is based on the hypothesis that the turbulence characteristic time (τ_{turb}) is very small compared to the mean flow characteristic time (τ_{flow}). It is then supposed that the ensemble average characteristic time (τ_{RANS}) is larger than τ_{turb} but very small compared to τ_{flow}. The previous decomposition of Φ can then be rewritten by adding an unsteady term, or coherent fluctuation as follows,

$$\Phi(\mathbf{x},t) = \bar{\Phi}(\mathbf{x}) + \Phi_{uns}(\mathbf{x},t) + \Phi'(\mathbf{x},t) = \bar{\Phi}(\mathbf{x},t) + \Phi'(\mathbf{x},t) \tag{2.27}$$

$$\overline{\Phi'}(\mathbf{x},t) = 0 \tag{2.28}$$

Resolved variables $\bar{\Phi}$ are now time and space dependant, thus allowing the capture of low-frequency unsteady phenomena, as illustrated in Fig. 2.9. When using (U)RANS, coarse grids and low-order methods are usually used, making its use very cheap and robust, and thus very appreciated by industrials (COBRA by Mantis Numerics ltd, FLACS by CMR/GexCon, REAGAS by TNO, EXSIM by Tel-Tek, ANSYS Fluent, etc.).

Turbulence is modelled in (U)RANS through the computation of a turbulent viscosity (or eddy viscosity) added to the fluid viscosity to model unclosed terms effects (Reynold stress terms), using the Boussinesq assumption. Eddy viscosity is estimated either by the determination of the flow speed and length scales (algebraic models, Cebeci-Smith [50], Baldwin-Lomax [14]), or by computing the transport of turbulent quantities such as turbulent kinetic energy (k), its dissipation rate (ε) or its specific dissipation rate (ω) (one- and two-equation models, Spalart-Allmaras [264], $k-\varepsilon$ of Launder and Spalding [171], $k-\omega$ of Wilcox [293] and Menter [205]).

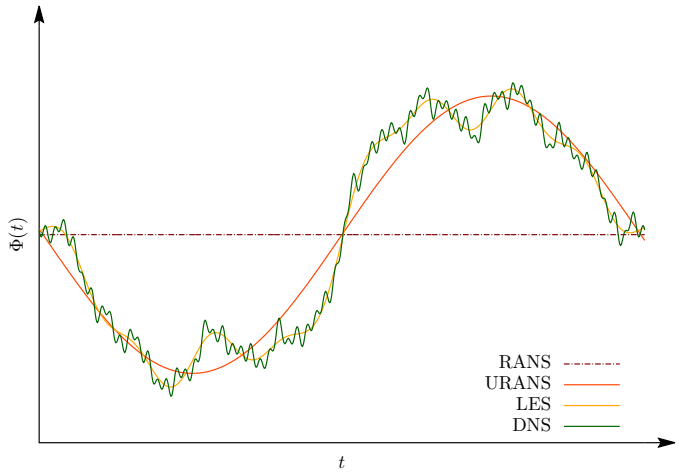

Figure 2.9: Φ *profiles obtained with RANS, LES or DNS in a given point of a turbulent flow*

2.2.2 LES of turbulent premixed combustion

It has been shown that LES provides numerous advantages over RANS, by reducing modelling errors thanks to the resolution of a higher-wave number than RANS. It also increases greatly the resolution of scalars mixing which is of paramount importance in combustion modelling. The Kolmogorov analysis of turbulence is used to compute the small-scales (modelled) statistics using the large (resolved) energy containing ones. However, it has been shown that in LES, similarly to RANS, in high Reynolds flows, there is no resolved part of the filtered chemical source term. This implies that in LES (and in RANS), the source term has to be modelled entirely. Consequently combustion models proposed and applied in LES have great similarities with their RANS counterparts.

Additionally, it has been shown in Poinsot and Veynante [238] that a simple mathematical closure could not be obtained for the mean reaction rate in a turbulent flame as there is still a random non-resolved fluctuation part in the LES solution. This means that a simple extension of the chemical source term as a Taylor series of the temperature fluctuations will still lead to large truncation errors, in addition to several additional unclosed terms.

The main challenge of modelling turbulent combustion in LES is to deal with the fact that on a substantial part of the regime diagram, the flame is entirely sub-filter. Although the filter width and the Damkölher number might be locally small enough to resolve a part of the preheat zone, there will always be large flow regions where the flame is under-resolved. According to Pitsch [234], this is not a problem in itself if explicit filtering is used, as the flame can be filtered and discretised on a mesh with a typical cell size smaller by an order of magnitude compared to the filter width. However, this now poses the problem of the computational cost. If implicit filtering (the most common approach) is used, then temperature and progress variable change from their burnt to their unburnt value within roughly a single cell, which is clearly unacceptable from a numerical point of view. Under-resolving some of these fields will generate numerical diffusion which will in turn enhance the flame speed.

According to Veynante and Vervisch [286], three approaches can be used to derive combustion models, as illustrated in Fig. 2.10 and described below. It has also been highlighted by Veynante and Vervisch [286] that although based on different physical concepts, these approaches are closely related, and none of them feature decisive advantages over the others. The results they provide will mainly depend on their ability to model the unclosed quantities.

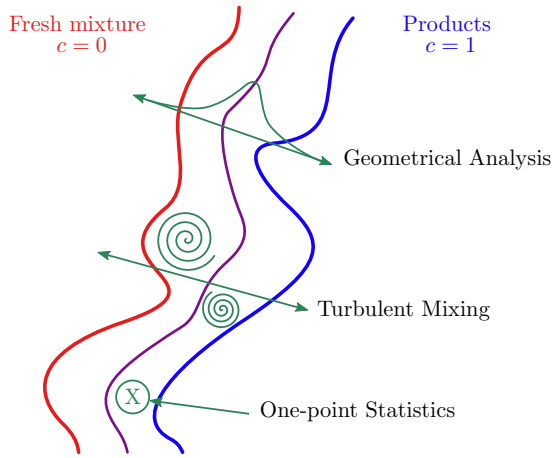

Figure 2.10: *Modelling approaches for turbulent premixed combustion - **Geometrical analysis** : G-equation, Flame Surface Density (FSD), Thickened Flame (TF) - **Turbulent Mixing** : Scalar Dissipation Rate, Bray-Moss-Libby (BML), Eddy Break-Up (LES-EBU) - **One-point Statistics** : Probability Density Function (PDF), Conditional Moment Closure (CMC) - Reproduced after Veynante and Vervisch [286]*

- **Geometrical Analysis :** The flame is here considered as a geometrical surface propagating in a turbulent flow. Its internal structure is usually considered to be very similar to a laminar flame, or flamelet. From this, several treatments of the flame surface have been proposed to study its front propagation : it can be tracked (**G-equation**), filtered (**Flame Surface Density (FSD)**), or thickened (**Thickened Flame Model (ATF)**).
- **Turbulent Mixing :** In the limit of large Damköhler (chemical time is very small compared to the turbulent one) and infinitely thin flame fronts, the mean or filtered reaction rates are only controlled by turbulent mixing. Hence, the scalar dissipation rate (species mixing rate at small scales, Eq. 2.29) is the controlling quantity, but it is quite difficult to model. **Eddy Break-Up (EBU)**-type models are based on this principle, as well as the famous **Bray-Moss-Libby (BML)**

approach.

$$\rho\chi = \rho\frac{\partial c}{\partial x_i}\frac{\partial c}{\partial x_i} \tag{2.29}$$

- **One-point Statistics :** Based on the **joint Probability Density Function (j-PDF)** of the flow, this approach does not require any assumption on the flame structure, and is therefore regime independent, unlike the two previous ones. It closes the reaction rate by combining individual Arrhenius rates with the j-PDF of the thermodynamic variables. Scalar fields statistics are collected in each point of the domain upon which means and correlations are extracted using PDFs.

A brief description of the main approaches is given below, based on the previously discussed classification. Further details on subgrid modelling for premixed turbulent combustion can be found in the review papers of Bilger *et al.* [23], Candel *et al.* [46], Pitsch [234], Cant [49], Veynante and Vervisch [286] amongst others. In this work, only the FSD approach has been used to model turbulent premixed combustion but other approaches are presented for comparison and illustration purposes.

2.2.3 Turbulent mixing approaches for the LES of premixed combustion

LES-EBU model

Simple algebraic closure are worth considering given their low computational cost. The EBU class of models have been first introduced by Spalding (1971) [265] and used extensively in RANS [100, 211] and in LES [100, 211, 245]. It relies on the separation of scales using an infinitely fast chemistry assumption, as does the EDM (Eddy Dissipation Model) of Magnussen and Hjertager [192].

The underlying concept of the EBU is that chemistry is infinitely fast, and thus the reaction rate is limited by the rate at which turbulent mixing can bring together products and reactants, which depends on the turbulent time scale. As such, the reaction zone is considered as a series of pockets of gas (reactants or products) convected by turbulent motions. The reaction rate is then assumed to be proportional to the intermittency between fresh and burnt mixtures, and inversely proportional to the turbulent time scale. In LES, it is expressed by,

$$\bar{\dot{\omega}}_c = C_{EBU}\overline{\rho}\frac{1}{\tau_{SGS}}\tilde{c}\,(1-\tilde{c}) \tag{2.30}$$

where C_{EBU} is a model constant close to unity, and $\tau_{SGS} \approx k/\varepsilon \approx \Delta/u'_\Delta$ is the SGS turbulent time scale.

Several drawbacks of the LES-EBU model are known, especially that as it does not address the aforementioned problem of flame thickness. It is used in addition to a gradient model for the SGS transport of $\tilde{c}$ to ensure a resolved flow field. It is also completely independent of chemistry effects, although some modifications have been implemented to limit its reaction rate with an Arrhenius law. Additionally, in LES simulations, a strong dependency of the EBU constant was observed with the filter size and flow conditions, thus highlighting the need for length scale ratios to be accounted for (flame wrinkling, flame thickness, etc.). Finally, it is intrinsically based on an hypothesis of a turbulence driven combustion, making it ill suited to simulate accurately a laminar flame front propagation and its transition towards a turbulent propagation mode.

Bray-Moss-Libby (BML) approach

Similarly to the EBU approach, the large Damköhler number and infinitely thin flame fronts hypothesis are made for the derivation of this model, along with a large Reynolds number, unity Lewis number and constant heat capacities (C_p and C_v) for all species. This allows the chemical and thermodynamic state of the mixture description by a scalar referred to as *progress variable* (Bray *et al.* [35, 37–39], Libby *et al.* [179, 180]). The model combines a statistical approach (use of a PDF) and a physical analysis. It was

mainly used in RANS, where it helped uncovering several behaviours of turbulent premixed combustion such as counter-gradient diffusion turbulent transport (CGDT) and flame generation of turbulence.

In this approach, three reaction rate closures can be obtained, based on scalar dissipation (presented here), flame crossing frequencies and flame surface density (covered in §. 2.2.4 and §. 7.3.3). The closure is thus as follows,

$$\bar{\dot{\omega}}_c = \frac{\overline{\rho}\tilde{\chi}}{2c_m - 1} \tag{2.31}$$

where the scalar dissipation rate can be modelled using a transport equation (Mantel and Borghi [196]), or by postulating a linear relaxation of the fluctuations as, $\bar{\rho}\tilde{\chi} = \bar{\rho}\widetilde{c''^2}/\tau_{SGS}$ and introducing a turbulent time scale. Under the assumption of infinitely thin flame fronts and an intermittency between products and reactants ($c^2 = c$, as $c = 0$ and $c = 1$ are the only values possible), it can be shown that $\bar{\rho}\widetilde{c''^2} = \bar{\rho}\tilde{c}(1-\tilde{c})$, yielding,

$$\bar{\dot{\omega}}_c = \frac{1}{2c_m - 1}\bar{\rho}\frac{1}{\tau_{SGS}}\tilde{c}\,(1-\tilde{c}) \tag{2.32}$$

The careful reader would have recognised in Eq. 2.32 an LES-EBU type closure (Eq. 2.30), thus establishing that the BML approach can be seen as an extension of the EBU model, but explicitly taking chemistry effects into account through $c_m = \overline{c\dot{\omega}_c}/\bar{\dot{\omega}}_c$. However, it suffers from a similar problem as the LES-EBU model, in the sense that the flame thickness is not accounted for, and gradient subgrid scalar transport models need to be used to obtain a resolved field of progress variable. Additionally, it is also unable to simulate a laminar flame propagation and its transition towards turbulent burning.

2.2.4 Geometrical analysis approaches for the LES of premixed combustion

Flame tracking : G-equation

The G-equation approach is a level-set method, i.e. the flame front is explicitly tracked. This formalism adopts a point of view opposite to the thickened flame approach, the flame thickness is here zero and the propagating flame front is described by the scalar field G. Chemistry is also supposed infinitely fast, such that chemical reactions occur in a very small thickness compared to the flow length scales. As such, it is a kinematic approach. A progress variable is not transported here, but a function $G = G(\mathbf{x}, t)$ is considered, such that $G = G_0$ represents the flame surface separating reactants and products. Away from the flame, the function values are commonly taken as a signed distance to the flame front, where $G > G_0$ corresponds to the products and $G < G_0$ to the reactants.

The transport equation for G has first been proposed by Williams [296] and later extended by Peters to RANS [230]. Its extension to LES was provided by Pitsch [233] and Pitsch and Duchamp de Lageneste [87, 88, 235], where its Favre filtered equation reads,

$$\frac{\partial\overline{\rho}\tilde{G}}{\partial t} + \frac{\partial\overline{\rho}\tilde{u}_i\tilde{G}}{\partial x_i} = \rho_0\overline{s}_T\left|\nabla\overline{G}\right| \tag{2.33}$$

Two remarks can be made on this equation, the first one being that as no diffusion term appears, the solution at G_0 does not depend on the flow field, but only on local flow conditions. Secondly, the $\tilde{G}$ field does not need to follow progress variable gradients, and can thus be filtered to be resolved on the computational grid.

The main closure challenge associated with the G-equation formalism is the subgrid scale turbulent flame speed estimation. As it has already been pointed out, the turbulent flame speed is not a well defined quantity and no universal model is available. In general, the closure is based on a correlation

following,

$$\frac{\overline{s}_T}{s_l^0} = 1 + \alpha \left(\frac{\overline{u'}}{s_l^0} \right)^n \tag{2.34}$$

where α and n are constant to be specified, and $\overline{u'}$ is the subgrid turbulence level. In general, $\overline{u'} - \overline{s}_T$ correlations extracted in experiments (Abdel-Gayed [2], Gülder [121]) or used in RANS are directly applied to LES without further justification, by replacing the RMS velocity by the subgrid turbulent velocity. It can be noted that theoretical analysis have led to some relations for α and n as presented by Yakhot *et al.* [298] with the Renormalisation Group Theory. Finally, applying this method in variable density codes leads to stability issues, which are resolved in practice by either thickening the flame front to smooth gradients or by using "ghost-fluid" type methods [74, 212, 213]. It is worth mentioning that the G-equation formalism has already been applied with success to deflagration-to-detonation transition simulations in confined geometries [262].

Flame thickening : Artificial Thickened Flame

In the Artificially Thickened Flame (ATF) or TFLES (Thickened Flame for LES) [8, 9, 41, 66, 257] approach, the solution retained to propagate a premixed flame on a coarse grid was first proposed by Butler and O'Rourke [41], and consists in thickening the flame front until it is sufficiently thick to be resolved on the LES mesh while maintaining its speed constant. With this method, species mass fractions can be explicitly resolved, thus allowing to account for differential diffusion and finite-rate chemistry effects.

Recalling the dimensional analysis proposed by Williams [295] and presented in §. 2.1.2, flame speed and flame thickness are controlled by the reaction rate and diffusion coefficient such that,

$$s_l^0 \propto \sqrt{D\dot{\omega}_c} \tag{2.35}$$

$$\delta_l^0 \propto \frac{D}{s_l^0} = \sqrt{\frac{D}{s_l^0}} \tag{2.36}$$

The ATF model consists in multiplying all diffusion coefficients by the thickening factor $\mathcal{F}$ while reaction rates are divided by the same amount. This gives a modified set of equations governing species transport,

$$\frac{\partial \rho Y_c}{\partial t} + \frac{\partial}{\partial x_i}\left(\rho u_i Y_c\right) = \frac{\partial}{\partial x_j}\left(\rho \mathcal{F} D_c \frac{\partial Y_c}{\partial x_j}\right) + \frac{1}{\mathcal{F}}\dot{\omega}_{Y_c} \tag{2.37}$$

Previous relations show that by applying these modifications, the thickened laminar flame thickness becomes $\delta_l^1 = \mathcal{F}\delta_l^0$ while its laminar speed remains constant $s_l^1 = s_l^0$, and where $\mathcal{F}$ is chosen such that the flame front can be resolved on a LES grid of size Δ.

In turbulent flows, however, due to an increased flame thickness, the flame/turbulent interaction is altered. Eddies smaller than $\mathcal{F}\delta_l^0$ are now unable to interact with the flame front, which can be related to a decrease of the local Damköhler number,

$$Da^1 = \frac{l_t s_l^1}{u' \delta_l^1} = \frac{Da^0}{\mathcal{F}} \tag{2.38}$$

As already pointed out, when the Damköhler number decreases, flame fronts become less and less sensitive to turbulent motions, more and more sensitive to strain effects (as investigated by Angelberger *et al.* [9] and Colin *et al.* [66]) and less and less sensitive to Lewis number effects and thus to species diffusion. The loss of wrinkling due to the thickening process is partially recovered by an efficiency function $\mathcal{E}$ corresponding to a subgrid wrinkling factor, and defined as the ratio between the non-thickened and thickened flame wrinkling,

$$\mathcal{E} = \frac{\Xi\left(\delta_l^0\right)}{\Xi\left(\delta_l^1\right)} \tag{2.39}$$

Species transport equations thus become,

$$\frac{\partial \rho Y_c}{\partial t} + \frac{\partial}{\partial x_i}\left(\rho u_i Y_c\right) = \frac{\partial}{\partial x_j}\left(\rho \mathcal{E}\mathcal{F} D_c \frac{\partial Y_c}{\partial x_j}\right) + \frac{\mathcal{E}}{\mathcal{F}}\dot{\omega}_{Y_c} \tag{2.40}$$

Wrinkling factor formulations have been given by numerous authors such as Angelberger [8, 9], Colin [65, 66] and Charlette [56, 57] amongst others. These formulations mostly consists in fitting functions and coefficients being either statically or dynamically defined, and historically extracted from DNS of flame-vortex interactions.

This method features several strong points, such as a correct degeneration towards the DNS limit, i.e. when the grid size decreases, the thickening also decreases, as well as the efficiency function. As already stated, finite-rate chemistry effects can be accounted for which allows a correct simulation of stretch effects on the flame speed. The laminar to turbulent transition of the flame propagation mode is also well reproduced. Finally, its numerical stability arising from the thickening process is an appreciable feature.

However, it also suffers from weaknesses, such as its cost, and its dependency to the efficiency function. This methods requires the computation of N additional transport equations, where N is the number of species needed by the chemical mechanism, which is more costly than progress variable approaches. In practice, reduced mechanisms are considered in the TFLES approach. Mechanisms involving short-life radicals are also difficult to use as they would result in very large thickening factors, whose adverse effects on the chemistry/turbulence interaction could not necessarily be recovered by an efficiency function. Additionally, this function is built upon an equilibrium hypothesis between the flame surface and the turbulence which is not always found in practice. Finally, away from the flame, the thickening factor changes both heat and species transport, where it should be unity. To partially alleviate the last two points, it has been shown by Charlette *et al.* [56, 57] that the Dynamic Thickened Flame (DTF) model could be used, in addition to a flame sensor.

Flame filtering : Flame Surface Density

Approaches based on the concept of Flame Surface Density (FSD) have also been proposed. They are based on the filtering of the progress variable (c) transport equation given by,

$$\frac{\partial \rho c}{\partial t} + \frac{\partial}{\partial x_i}\left(\rho u_i c\right) = \frac{\partial}{\partial x_j}\left(\rho D_c \frac{\partial c}{\partial x_j}\right) + \dot{\omega}_c \tag{2.41}$$

Similarly to G-equation models, combustion is described using a kinematic point of view, instead of a diffusion/reaction balance. This approach relies on the estimation of the filtered FSD (which is the limit of the flame surface to local volume ratio, when the volume tends to zero) for an infinitely thin interface separating products and reactants. It has been originally derived for RANS (Cant *et al.* [48], Bray *et al.* [36], Pope [241], Candel *et al.* [47]) based on the Coherent Flame Model (CFM) developed for non-premixed combustion by Marble and Broadwell [197].

The infinitely thin flame front hypothesis allows a decoupling between turbulence and chemistry, as the flame internal structure is mostly ignored. The filtered reaction rate can then be closed as a product between a flame displacement speed and its mean surface area (FSD), yielding,

$$\overline{\dot{\omega}}_c = \overline{\rho s_d \left|\nabla c\right|} = \int_0^1 \left\langle \rho s_d \right\rangle_s \Sigma_{sgs}\, \mathrm{d}c^* \tag{2.42}$$

where Σ_{sgs} represents the filtered FSD which is essentially the flame surface area per unit volume contained within a LES filtering volume, $\left\langle \rho s_d \right\rangle_s$ is the surface Favre-averaged displacement speed of the propagating flame in the reactants defined as $\left\langle \rho s_d \right\rangle_s = \overline{\rho s_d \left|\nabla c\right|}/\overline{\left|\nabla c\right|}$ [31, 286] and $c = c^*$ denotes the

flame surface.

It has been shown by Hawkes and Cant [125] that for very thin flames, $\langle \rho s_d \rangle_s$ and Σ_{sgs} are both independent of the progress variable choice, allowing the previous relation to be recast without the integral,

$$\int_0^1 \langle \rho s_d \rangle_s \, \Sigma_{sgs} \, \mathrm{d}c^* \approx \langle \rho s_d \rangle_s \, \Sigma \tag{2.43}$$

where Σ is the generalised Flame Surface Density (FSD independent of the choice of the iso-contour c^*) defined by $\Sigma = \overline{|\nabla c|}$. By further assuming laminar flame elements, the displacement speed can be modelled as $\langle \rho s_d \rangle_s \approx \rho^0 s_l^0$, where ρ^0 denotes the reactants density. Boger *et al.* [31] presented a validation of this approximation based on the filtering of DNS results and obtained a good agreement. The use of the un-stretched laminar flame speed suggests that this approximation mainly applies to the corrugated flamelets and thin reaction zone regimes where curvature effects are not expected to significantly affect the displacement speed.

The main term to model is then the generalised FSD (hereafter referred to as FSD for brevity). Several closures have been derived based on heuristic approaches [197], algebraic closures close in spirit to the BML and LES-EBU approaches [30,31], similarity analysis [161] or transport equations [30,124,125,251] adapted from RANS models [89,246] to LES by adding terms accounting for the resolved FSD production and destruction. Further details on the FSD closures considered in this work are given in §. 7.3.3.

Similarly to the TFLES model, this approach degenerates correctly towards a laminar propagation mode when turbulence is weak, or when the flame wrinkling is fully resolved. This allows for a correct representation of both turbulent and laminar flames. However, a major limitation of this type of models is to be accounted for, the mixture description by a progress variable c does not allow the simulation of species diffusion. Algebraic closures also make it difficult to account for curvature and stretch effects on the flame propagation speed. It shall finally be noted that most models are using similar wrinkling relations to the TFLES based on a local flame surface/turbulence equilibrium.

2.2.5 One-point statistics for the LES of premixed combustion

PDF method

The different approaches described up to this point have all been widely used both in industry and within the research community, featuring accurate and reliable predictions. However, they all rely to some extent on fundamental assumptions, such as a certain validity range within regime diagrams (infinitely thin flame front, infinitely fast chemistry, etc.). The PDF approach, on the other hand takes a completely different point of view by modelling the turbulence impact on a quantity φ by a Probability Density Function (PDF) and aims to provide a method that is both general and robust to model turbulent combustion.

The PDF of any scalar is defined as,

$$\mathcal{P}(\varphi^*) \, \mathrm{d}\varphi^* = \text{Probability} \left(\varphi^* \leqslant \varphi < \varphi^* + \mathrm{d}\varphi^* \right) \tag{2.44}$$

and is normalised, such that

$$\int \mathcal{P}(\varphi^*) \, \mathrm{d}\varphi^* = 1 \tag{2.45}$$

Information contained within PDFs are essential for combustion modelling, as moments of any orders

can be extracted from them, following,

$$\widetilde{\varphi} = \int_0^1 \varphi^* \widetilde{\mathcal{P}}\left(\varphi^*\right) \mathrm{d}\varphi^* \tag{2.46}$$

$$\widetilde{\varphi''^2} = \widetilde{\varphi^2} - \widetilde{\varphi}^2 = \int_0^1 \left(\varphi^{*^2} - \widetilde{\varphi^*}^2\right) \widetilde{\mathcal{P}}\left(\varphi^*\right) \mathrm{d}\varphi^* \tag{2.47}$$

For a single-step adiabatic reaction and unity Lewis number, mean reaction rates can be obtained from the progress variable knowledge as,

$$\overline{\dot{\omega}}_c = \int_0^1 \dot{\omega}_c(c^*)\mathcal{P}(c^*)\,\mathrm{d}c^* \tag{2.48}$$

The previous expressions are easily extended to any number of scalar, such as the temperature, composition (in case of non-unity Lewis number), etc. by considering the joint-PDF of the relevant scalars, which in the reaction rate case would read,

$$\overline{\dot{\omega}}_k = \int_0^1 \dot{\omega}_k\left(\boldsymbol{\varphi}^*\right) \mathcal{P}_{\dot{\omega}}\left(\boldsymbol{\varphi}^*\right) \mathrm{d}\boldsymbol{\varphi}^* \tag{2.49}$$

where the source term appears in closed form ($\dot{\omega}_k\left(\boldsymbol{\varphi}^*\right)$) as a function of the different thermochemical variables φ_k^* and the chemical mechanism.

The main challenge associated with this method is the PDF determination which changes are every point and at every time instant in the flow. Two main paths have been identified to tackle this problem [242, 243],

- An exact transport equation for the relevant scalar's PDF can be derived [242, 285, 286], where the PDF is transported both in physical space by the flow field and in composition space by diffusion and combustion. The source term appears in closed form and does not need any modelling, which is the key strength of this method. However, molecular diffusion is unclosed and difficult to model due to the one-point (local) knowledge provided by PDFs. Spatial gradients information are not contained within PDFs. The resolution of such equations is usually very costly and carried out using Monte-Carlo type methods.
- PDF's shape can be presumed. In general, PDFs can take any shape and even feature multiple extrema, but in the particular case of combustion, they often present common features suggesting that their shape can be described using a limited number of parameters. Williams [295] proposed to assume a fixed shape parametrised with only one or two parameters (e.g. mean and variance). This has been done in the BML model where the PDF is assumed to be bimodal with only two states (reactants or products). Multiple examples of PDF shapes can be found in the literature [22, 32, 36, 97] but the most common within the combustion community is the β PDF first applied to LES by Cook and Riley [69].

Conditional Moment Closure

This last method is briefly presented here as some recent work by Thornber *et al.* [274] extended it to the LES of turbulent premixed combustion, from its original derivation for diffusion flames. The main idea behind the CMC approach derived independently by both Bilger [20] and Klimenko [158] is to take advantage of the strong correlation observed between reactive scalars (temperature, mass fractions, etc.) and progress variable (or mixture fraction) [160]. This allows the linking of reactive scalar fluctuations with progress variable (or mixture fraction) fluctuations in conditional space, via a transport equation for the conditional species mass fractions. A first order closure is used to close the reaction rate using the mass fractions conditional values,

$$\dot{\omega}_k|\eta \approx \dot{\omega}_k\left(\mathbf{Q}, \eta\right) \tag{2.50}$$

where $\mathbf{Q} = \mathbf{Y}|\eta$, η denotes the conditional variable and $\mathbf{Y}$ the vector of reacting variables.

Two challenges are present in the method, the first one being the PDF determination, which is generally done using a presumed β shape [12, 217, 218, 279, 280], and the second is the conditional scalar dissipation rate closure representing the subgrid scales mixing. CMC's cost also represents a significant challenge given that the method dimensionality is quite large. Indeed, a normal simulation would feature $Nx \times Ny \times Nz \times N\eta$ cells with N species transport equations to solve. Fortunately, Klimenko [159] showed that conditional gradient were much smoother than physical ones, allowing the use of a somewhat coarser CMC grid, and thereby reducing the method's cost, which remains high nonetheless.

Several simulations of bluff-body stabilised flames both non-premixed [12, 217, 280, 297] and premixed [274] flames have been performed successfully, showing the soundness and accuracy of the approach. Higher-order extensions [154, 155, 166, 167, 202] and the addition of a second conditioning variable [52, 166] have also been used in hydrocarbon flame calculations to improve the predictions.

2.3 Compressible multi-component flow modelling

2.3.1 Introduction

Understanding the dynamics of flows consisting of several fluid components is of great interest in a large range of applications, including the dynamics and stability of bubbles, interfaces, mixing processes, combustion, etc. Compressibility is also an important flow feature, as it accounts for any acoustic phenomena, shock wave propagation, combustion acoustic instabilities, detonation, deflagration-to-detonation transition (DDT), etc. However, such flows give rise to challenging problems, both theoretically and computationally [6].

The complete approach for multi-component flows would be to have a different set of equations for each component (momentum, energy and continuity), however this work is concerned solely with the simulation of miscible, single phase gaseous flows. With these restrictions in mind, several simplifications can be made to the system of governing equations,

- All components within a computational cell share a common velocity, thus allowing the computation of a single set of momentum equations, which is a valid assumption as long as the density difference between components is not too large, which is verified is most gaseous mixtures [250]
- An instantaneous thermodynamic equilibrium is reached between the different gases, so that a single continuity and energy equations are required [206]

Thus, for inviscid flows, the system of equation is now the compressible Euler, to which one or more equations are added to transport a quantity (φ) describing the mixture composition, and to compute the parameters required by the equation of state (EoS), yielding,

$$\frac{\partial \mathbf{U}}{\partial t} + \frac{\partial \mathbf{F}(\mathbf{U})}{\partial x} + \frac{\partial \mathbf{G}(\mathbf{U})}{\partial y} + \frac{\partial \mathbf{H}(\mathbf{U})}{\partial z} = 0 \tag{2.51}$$

where,

$$\mathbf{U} = [\rho,\ \rho\varphi,\ \rho u,\ \rho v,\ \rho w,\ \rho E]^T \tag{2.52}$$

$$\mathbf{F}(\mathbf{U}) = \left[\rho u,\ \rho\varphi u,\ \rho u^2 + P,\ \rho uv,\ \rho uw,\ (\rho E + P)\, u\right]^T \tag{2.53}$$

$$\mathbf{G}(\mathbf{U}) = \left[\rho v,\ \rho\varphi v,\ \rho uv,\ \rho v^2 + P,\ \rho vw,\ (\rho E + P)\, v\right]^T \tag{2.54}$$

$$\mathbf{H}(\mathbf{U}) = \left[\rho w,\ \rho\varphi w,\ \rho uw,\ \rho vw,\ \rho w^2 + P,\ (\rho E + P)\, w\right]^T \tag{2.55}$$

and the total non-chemical energy is given by $\rho E = \rho\varepsilon + \frac{1}{2}\rho\mathbf{u}^2$. The EoS for perfect gases reads,

$$\rho\varepsilon = \frac{P}{\gamma - 1} \tag{2.56}$$

It was suggested by Roe [252–254] to take φ to be the specific heat ratio of the fluid γ or $1/\gamma - 1$ [5], Abgrall [4, 5, 55], Larrouturou [170] and others suggested to use species mass fractions instead amongst others choices. The resulting equations sets written in one space dimension and for two species without loss of generality are thus,

- *Symmetric formulation* [147, 170] using species mass fractions,

$$\begin{pmatrix} \rho Y_1 \\ \rho Y_2 \\ \rho u \\ \rho E \end{pmatrix}_t + \begin{pmatrix} \rho Y_1 u \\ \rho Y_2 u \\ \rho u^2 + P \\ (\rho E + P)\, u \end{pmatrix}_x = 0 \tag{2.57}$$

- *Unsymmetric formulation* [4] using $Y_1 + Y_2 = 1$ and $\rho = \rho Y_1 + \rho Y_2$,

$$\begin{pmatrix} \rho \\ \rho Y \\ \rho u \\ \rho E \end{pmatrix}_t + \begin{pmatrix} \rho u \\ \rho Y u \\ \rho u^2 + P \\ (\rho E + P)\, u \end{pmatrix}_x = 0 \tag{2.58}$$

- γ *formulation* [254],

$$\begin{pmatrix} \rho \\ \rho\gamma \\ \rho u \\ \rho E \end{pmatrix}_t + \begin{pmatrix} \rho u \\ \rho\gamma u \\ \rho u^2 + P \\ (\rho E + P)\, u \end{pmatrix}_x = 0 \tag{2.59}$$

As γ is an homographic function of species mass fractions, the three previous formulations lead to similar weak solutions.

Several choices for the general computational framework can be considered for solving these systems, **(i)** a front-tracking method can be used, with the upside of preserving interfaces as sharp discontinuities, but the downside of being very complex to use for multidimensional problems, **(ii)** front-capturing methods are obtained from the governing equations integral form and are simple enough to implement in multiple space dimensions, but with the drawback of smearing discontinuities over multiple cells.

Two major computational difficulties are associated with front-capturing methods applied to the previous multi-component models (Eqs. 2.57-2.59), thus preventing the naive extension of state-of-the-art schemes developed for single component flows,

- Species mass fractions (Y_k) obtained numerically from $Y_k = (\rho Y_k)/\rho$ are not guaranteed to remain positive and bounded by $Y_k \in [0\,;\,1]$ as observed by Larrouturou [170], who attributed this deficiency to the fact that ρ and ρY_k were not varying *"in phase"* across material discontinuities. The author has also shown that using a Godunov scheme [109] would preserve mass fractions positivity.
- Velocity and pressure profiles feature a persistent and non-physical oscillation across material fronts, which was identified by Abgrall [4, 5] and others [54, 147, 170] as a pure numerical artefact, present even in first-order schemes. This problem is presented in more details in §. 2.3.2 and the solutions published to address it in §. 2.3.3.

2.3.2 Problem description

The naive implementation of high-order shock-capturing schemes (e.g. Godunov scheme) to compressible multi-component flow problems gives rise to pressure oscillations at material interfaces. These small (or large) artefacts are particularly problematic in flows where small scales are important features (e.g. acoustic, combustion, turbulence), or when an accurate temperature estimation is critical (e.g. reacting flows). Additionally, diffusive effects tend to initially accentuate such oscillations, thus contaminating a large portion of the solution domain. Hence, the difficulty resides in maintaining the pressure equilibrium across material interfaces in spite of the numerical diffusion. Indeed, even if all conserved variables remain monotone, there is no guarantee that a derived quantity will also be monotone, and so pressures corresponding to artificial intermediate states can differ from the equilibrium pressures, as illustrated in Fig. 2.11.

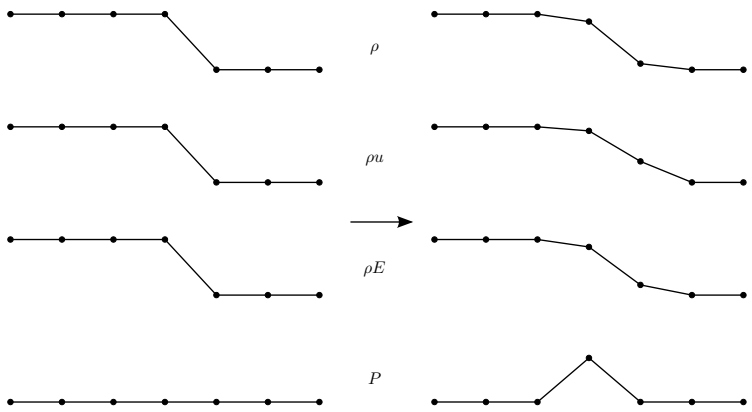

Figure 2.11: *Pressure fluctuations generated at interfaces due to numerical diffusion (reproduced after Quirk and Karni [250])*

A brief analysis of the pressure field evolution is presented below, first for a single fluid (where no pressure oscillations are observed), and secondly for a mixture, where oscillations develop at material discontinuities as presented by Abgrall [6]. For the sake of brevity, the analysis is restricted to the case of an inviscid flow in a one dimensional domain. It shall be noted that the results obtained are general and apply to any Godunov-type scheme which is fully conservative [4].

Constitutive relations and notations

The mass fraction model is considered here with two calorically perfect species in thermal equilibrium with specific heat constants C_{p_k} and C_{v_k}. The species internal energies are given by,

$$\rho Y_k \varepsilon_k = \rho Y_k C_{v_k} T \tag{2.60}$$

$$\rho Y_k \varepsilon_k = \frac{P_k}{\gamma_k - 1} \tag{2.61}$$

where Dalton's law of pressure gives $P = P_1 + P_2$, yielding $\rho\varepsilon = \rho Y_1 \varepsilon_1 + \rho Y_2 \varepsilon_2 = \rho C_v T$, where $C_v(Y_k) = Y_1 C_{v_1} + Y_2 C_{v_2}$ and,

$$\rho\varepsilon = \frac{P}{\gamma - 1} \tag{2.62}$$

$$\gamma = \gamma(Y_k) = \frac{Y_1 C_{p_1} + Y_2 C_{p_2}}{Y_1 C_{v_1} + Y_2 C_{v_2}} \tag{2.63}$$

$$P = \left(\rho E - \frac{1}{2}\rho u^2\right)(\gamma - 1) \tag{2.64}$$

The Godunov scheme writes,

$$\mathbf{U}_j^{n+1} = \mathbf{U}_j^n - \frac{\Delta t}{\Delta x}\left(\mathbf{F}_{i+1/2}^n - \mathbf{F}_{i-1/2}^n\right) \tag{2.65}$$

where $\mathbf{F}$ is the inter-cell numerical flux. More details on the Godunov scheme are given in §. 4.2.

For any quantity φ, we note,

- $\delta\varphi = \varphi^{n+1} - \varphi^n$ the time changes
- $\Delta\varphi = \varphi_{i+1/2} - \varphi_{i-1/2}$ the spatial variations

Therefore, the Godunov scheme applied to the Euler equations leads to,

$$\begin{pmatrix} \rho \\ \rho u \\ \rho E \end{pmatrix}^{n+1} = \begin{pmatrix} \rho \\ \rho u \\ \rho E \end{pmatrix}^{n} + \begin{pmatrix} \delta\rho \\ \delta(\rho u) \\ \delta(\rho E) \end{pmatrix} \tag{2.66}$$

where,

$$\begin{pmatrix} \delta\rho \\ \delta(\rho u) \\ \delta(\rho E) \end{pmatrix} = -\frac{\Delta t}{\Delta x}\begin{pmatrix} \Delta(\rho u) \\ \Delta\left(\rho u^2 + P\right) \\ \Delta\left((\rho E + P)\, u\right) \end{pmatrix} \tag{2.67}$$

and $\dfrac{\Delta t}{\Delta x}$ is noted ν.

Single fluid case

In this case, we have $\gamma^n = \gamma$ in the whole domain, pressure and velocity are initially uniform ($P_i^n = P_{i\pm1/2} = P$ and $u_i^n = u_{i\pm1/2} = u$), and the solution at time-step $n+1$ is obtained from Eq. 2.67 (the subscript and superscripts are dropped for convenience),

$$\begin{cases} \delta\rho = -\nu u \Delta\rho \\ \delta(\rho u) = -\nu\Delta\left(\rho u^2\right) - \nu\Delta P = -\nu u^2\Delta\rho = u\delta\rho \\ \delta(\rho E) = -\nu\Delta\left((\rho E + P)\, u\right) = -\nu\left(\Delta(\rho E u) + \Delta(P u)\right) = -\nu u\Delta(\rho E) \end{cases} \tag{2.68}$$

The spatial variation of the total energy is calculated as,

$$\begin{aligned} \Delta(\rho E) &= \Delta(\rho\varepsilon) + \frac{1}{2}\Delta\left(\rho u^2\right) = \Delta(\rho\varepsilon) + \frac{1}{2}u^2\Delta\rho = \Delta\left(\frac{P}{\gamma - 1}\right) + \frac{1}{2}u^2\Delta\rho \\ &= \frac{1}{2}u^2\Delta\rho \end{aligned} \tag{2.69}$$

and so,

$$\delta(\rho E) = -\frac{1}{2}\nu u^3\Delta\rho = -\frac{1}{2}u^2\delta\rho \tag{2.70}$$

From Eq. 2.68 and the chain rule, $\delta(\rho u) = u\delta\rho + \rho\delta u$, it easily follows that,

$$\delta u = 0 \tag{2.71}$$

Now concentrating on pressure, we have $P^{n+1} = P^n + \delta P$, and the time variation of the internal energy is given by,

$$\begin{aligned} (\rho\varepsilon)^{n+1} &= \frac{P^{n+1}}{\gamma - 1} = \frac{P^n + \delta P}{\gamma - 1} \\ &= (\rho E)^n + \delta(\rho E) - \frac{1}{2}\left(\rho^n + \delta\rho\right)(u + \delta u)^2 \end{aligned} \tag{2.72}$$

using Eq. 2.70 and Eq. 2.71 we further obtain,

$$\begin{aligned}(\rho\varepsilon)^{n+1} &= (\rho E)^n - \frac{1}{2}u^2\delta\rho - \frac{1}{2}\left(\rho^n + \delta\rho\right)u^2 \\ &= (\rho E)^n - \frac{1}{2}\rho^n u^2 \\ &= (\rho\varepsilon)^n \end{aligned} \tag{2.73}$$

The obvious conclusion is thus $\delta P = 0$, and so the computed pressure (P^{n+1}) and velocity (u^{n+1}) fields remain uniform at all times as they should.

Mixture or multi-component case

In this case, a moving discontinuity with velocity $u > 0$ separating two ideal gases is considered in a constant pressure field. The situation is similar to Fig. 2.11, where the left (l) and right (r) initial states are described by,

$$\mathbf{U}_l = \left[\rho,\ \rho u,\ (\rho E)_l,\ \rho Y_l\right]^T \tag{2.74}$$

$$\mathbf{U}_r = \left[\rho,\ \rho u,\ (\rho E)_r,\ \rho Y_r\right]^T \tag{2.75}$$

with $Y_l = 0$ and $Y_r = 1$.

In this case, numerical fluxes reduce to upwind fluxes, where $\mathbf{F}_{i+1/2} = \mathbf{F}\left(\mathbf{U}_i\right)$, and after a single time step, one get,

$$\mathbf{U}_r^1 = \mathbf{U}_r^0 - \nu\left(\mathbf{F}\left(\mathbf{U}_r^0\right) - \mathbf{F}\left(\mathbf{U}_l^0\right)\right) \tag{2.76}$$

with the following time variations,

$$\begin{cases} \delta\rho = -\nu\Delta\left(\rho u\right) = 0 \\ \delta\left(\rho u\right) = -\nu\left(\rho u^2 + P\right) = -\nu\Delta\left(\rho u^2\right) - \nu\Delta P = -\nu\left(u^2\Delta\rho + \rho\Delta u^2\right) = 0 \\ \delta\left(\rho E\right) = -\nu\Delta\left(\left(\rho E + P\right)u\right) = -\nu\Delta\left(\rho u E\right) - \nu\Delta\left(uP\right) = -\nu u\Delta E = -\nu u P\Delta\left(\dfrac{1}{\gamma - 1}\right) \\ \delta\left(\rho Y\right) = -\nu\Delta\left(\rho u Y\right) = -\nu\rho u\Delta Y \end{cases} \tag{2.77}$$

Values of momentum, density and species mass fractions at the next time step are thus,

$$\rho_r^1 = \rho_r^0 - \nu \times 0 = \rho_r^0 \tag{2.78}$$

$$(\rho u)_r^1 = (\rho u)_r^0 - \nu \times 0 = (\rho u)_r^0 \tag{2.79}$$

$$(\rho Y)_r^1 = (\rho Y)_r^0 - \nu\rho u\left(Y_r^0 - Y_l^0\right) = (\rho Y)_r^0 - \nu\rho u Y_r^0 \tag{2.80}$$

This also yields $u_r^1 = (\rho u)_r^1 / \rho_r^1 = u_r^0 = u$ and the new mass fraction is then,

$$Y_r^1 = \frac{(\rho Y)_r^1}{\rho_r^1} = \frac{(\rho Y)_r^0 - \nu\rho u Y_r^0}{\rho_r^0} = Y_r^0 - \nu u Y_r^0 = 1 - \nu u \tag{2.81}$$

which is the correct solution behaviour (velocity is uniform and mass fraction is advected). However, when using the EoS, the new value of pressure can be expressed as,

$$P + \delta P = (\gamma + \delta\gamma - 1)\left((\rho E + \delta\left(\rho E\right)) - \frac{1}{2}\left(\rho + \delta\rho\right)\left(u + \delta u\right)^2\right) \tag{2.82}$$

which using Eq. 2.77 can be re-written as,

$$\begin{aligned} P + \delta P &= (\gamma + \delta\gamma - 1)\left(\rho E - \nu u P\Delta\left(\frac{1}{\gamma - 1}\right) - \frac{1}{2}\rho u^2\right) \\ &= \left(\gamma^1 - 1\right)\left(\left(\rho\varepsilon\right)^0 - \nu u P\Delta\left(\frac{1}{\gamma - 1}\right)\right) \end{aligned} \tag{2.83}$$

$$\frac{P_r^1}{\gamma_r^1 - 1} = \frac{P_r^0}{\gamma_r^0 - 1} - \nu u P_r^0\left(\frac{1}{\gamma_r^0 - 1} - \frac{1}{\gamma_l^0 - 1}\right) \tag{2.84}$$

Using Eq. 2.63 and Eq. 2.81, γ_1^1 can be computed,

$$\begin{aligned}\gamma_r^1 = \gamma\left(Y_r^1\right) &= \frac{\left(Y_r^1\right)_1 C_{p_1} + \left(Y_r^1\right)_2 C_{p_2}}{\left(Y_r^1\right)_1 C_{v_1} + \left(Y_r^1\right)_2 C_{v_2}} = \frac{(1-\nu u)\, C_{p_1} + (1-1+\nu u)\, C_{p_2}}{(1-\nu u)\, C_{v_1} + (1-1+\nu u)\, C_{v_2}} \\ &= \frac{C_{p_1} - \nu u\,(C_{p_1} - C_{p_2})}{C_{v_1} - \nu u\,(C_{v_1} - C_{v_2})}\end{aligned} \tag{2.85}$$

where the $k-$species mass fraction in cell r at time step 1 is denoted $(Y_r^1)_k$.

For obvious reasons, one has $0 < \nu u < 1$, leading to $\gamma_l < \gamma_r^1 < \gamma_r$ and thus $P_r^1 \neq P$. The pressure equilibrium is thus perturbed, and although velocity remains uniform at time-step 1, it will not be so at time step 2 as the pressure perturbation will trigger a velocity perturbation and so on and so forth, thereby contaminating the solution.

As this demonstration holds for any Godunov-type schemes in conservative form, this suggest that fully-conservative methods are not suited for the simulation of compressible multi-component flows and that one may need to move towards non-conservative formulations, as described in the next paragraph.

2.3.3 Numerical methods for compressible multi-component flows

A brief review of both front-tracking and front-capturing methods successfully applied to the compressible multi-component flow problem detailed above is presented below, showing the diversity of approaches available in the literature to tackle this problem.

Front-tracking methods

Front-tracking methods, as already pointed out, avoid pressure oscillations by explicitly tracking discontinuities, thus keeping them sharp and removing numerical diffusion. A level set function is usually used to track the position and topology of the front [72, 215, 223]. However, modifications of the governing equations are often required. Two major types of front tracking methods are,

- The *Volume of Fluid Model* (VOF) was first described by Noh and Woodward [219], formalised by Collela, Glaz and Ferguson (CGF) [67] and is further discussed in [206]. It is essentially equivalent to a multiphase model where the individual species mass and energies are tracked and the momentum is solved for the mixture. The algorithm reconstructs material interfaces within the computational cell using the different components volume fractions, such that the appropriate local thermodynamic properties of the mixture can be recovered. The fluid mixture is thus evolved as a single fluid, and the pressure equilibrium is maintained. However, its implementation is very complex due to the logistics of having to deal with arbitrary shaped interfaces.
- The *Ghost Fluid Method* (GFM) is a level-set based approach which treats interfaces as internally moving boundaries [95, 183, 222]. It keeps track of two sets of variables, both real and "ghost". Real variables correspond to cell variables in the region where they belong, while "ghost" variables correspond to data across interfaces extrapolated from the real ones. The equations are then solved as usual, with the notable exception that ghost variables are now used within the near-interfaces stencils. This effectively transforms the multi-component model into a single fluid type model. Extrapolation in the ghost cells affects conservation, but refinement tests have shown that convergence is obtained [95].

Front-capturing methods

Following on the apparent failure of fully-conservative schemes, numerous non- or quasi-conservative methods have been proposed in the literature for shock-capturing models.

Karni [146] proposed to use a primitive formulation of hyperbolic laws (Euler equations) modified to account for leading order term conservation errors, and further enforcing the convergence on consistent weak solutions. This was further extended by Quirk and Karni [250] by correcting the formulation at shock waves. Jenny *et al.* [139] altered the energy equation to modify the conservative variables calculation and make it single-fluid like, thus reducing oscillations amplitude. Karni [148] also proposed to solve the Euler equations separately on each side of the interface using a method designed for single-fluid flows, while the interface was being dealt with by a pressure evolution equation derived from the energy conservation.

Abgrall [5] proposed a "quasi-conservative" method, so called due to the extremely small conservation errors generated. The Euler equations augmented by an advection equation are written in a "quasi-conservative" form and solved using a predictor-corrector approach. An advection equation transports a thermodynamic quantity which does not allow pressure oscillations at interfaces, such as $1/\gamma - 1$.

Most of the above presented models were not, or could not be extended to high-resolution state-of-the-art shock-capturing schemes. Shyue [260] used a similar approach as Abgrall [5] albeit transporting species mass fractions instead of $1/\gamma - 1$, and using high-resolution wave propagation methods showing that the pressure equilibrium could be conserved with high-order methods.

Allaire *et al.* [7] presented a new set of equations re-writing the species mass transport in terms of the species volume fraction, and adding an advection equation for the volume fraction. The system represents an extension of the work of Abgrall [5] and Karni [147] and is closed by computing γ from the species volume fractions.

More recently, building upon Shyue [260] and Abgrall [5] work, Johnsen and Colonius [143] extended the quasi-conservative method to the WENO [184] (Weighted Essentially Non Oscillatory) framework in which the average primitive variables must be reconstructed to prevent spurious oscillations. They also modified the HLLC Riemann solver [278] to treat advection equations. This work is further generalised to all material discontinuities by Johnsen [142] and Johnsen and Ham [144]. However, this methodology has been shown to fail in the case of strong shock waves by Thornber [273].

Another approach has been proposed by Abgrall and Karni [6] for calorically perfect gas, extended to thermally perfect gas by Billet and Abgrall [25], to high-order WENO methods by Houim and Kuo [133] and to the Discontinuous Galerkin framework by Billet and Ryan [27]. It relies on the computation of two fluxes at interfaces while maintaining a constant specific heat ratio across the stencil. This allows the computation of the Riemann fluxes in a single-fluid like fashion therefore removing pressure oscillations, at the cost of quasi-conserving total energy, as energy fluxes will not be equal any more from the interface left and right sides. This method is usually referred to as the "double-flux" method.

Kawai and Terashima [149] suggested the use of the fully compressible system (Navier-Stokes equations) using compact central differencing schemes and the Localised Artificial Diffusivity (LAD) method [68], thus adding dissipation where needed to remove pressure oscillations. This method has proved its accuracy in shock-bubble type test cases, as well as in Richtmyer-Meshkov instability simulations.

Numerous valuable pieces of work published on this problem are also worth mentioning, such as the work of Wang *et al.* [289] with the Total Enthalpy Conservation of the mixture (ThCM) model and its extension by Cael *et al.* [43] and Bates *et al.* [17] into the Thermodynamically Consistent and Fully Conservative (TCFC) model, Housman *et al.* [134,135] and his use of the Split Coefficient Matrix method (SCM) of Chakravarthy *et al.* [53], Marquina and co-authors [81,198], amongst others.

Application to multi-component compressible reacting flows

Simulating multi-component compressible turbulent combustion is a challenging endeavour, and as such, robust and accurate numerical methods are needed. If momentum and energy conservations are important, the most important requirement would be total mass conservation. An even more restrictive condition in the case of reacting flows is the mass conservation of each species, as even trace amounts of radical species (HO_2, H_2O_2, OH, O, H, etc.) do have large effects on the overall combustion process, and need to be accounted for precisely.

Amongst the front-tracking methods presented above, it can be noted that both have already been applied successfully to combustion of premixed slow deflagrations and detonation discontinuities. One could cite the work of Ton *et al.* [277] for the VOF, and Fedkiw *et al.* [96] and Desjardins *et al.* [74] for the GFM. One could also cite Smiljanovski's work on detonations using level-set methods [262]. However, it can be noted, that although the governing equations are solved in strong conservation form in the GFM method, it is discretely non-conservative due to variables extrapolations across interfaces [6,183].

At the exception of Kawai and Terashima's method [149] which is fully conservative, all the above front-capturing methods suffer from the non-conservation of at least one conserved variable. The non-conservative integration scheme of Karni [148], and the quasi-conservative method of Abgrall [5] (non-conservative form of the advection equation) suffer from poor mass conservation as shown by Johnsen [141]. Additionally, non-conservative methods do not always predict accurately shock positions, and potentially fail at large Mach numbers, while the quasi-conservative ones revert to a non-conservative formulation in a small number of cells and thus potentially feature similar deficiencies. Hence, it seems complex to apply these methods to viscous reacting flows. To the author knowledge, no such problem has been identified in the literature for the models of Allaire *et al.* [7] (where each species mass is conserved but each species energy is not necessarily) and Abgrall and Karni [6] (where total energy is not conserved).

If the combustion needs to be solved accurately, the calorically perfect gas EoS might need to be replaced by the more precise thermally perfect gas EoS. Amongst the previously mentioned models, the methods of Shyue [260], Allaire *et al.* [7], Abgrall and Karni [6] have been demonstrated with mixtures of non-calorically perfect gases, and only the double-flux has been applied to combustion by Billet and co-authors [24–27], Houim and co-authors [133, 269] and Lv and Ihme [188–190].

2.4 Conclusion

In this chapter, different fundamental concepts related to premixed laminar flames were introduced (§. 2.1.1). The flame structure was discussed as well as the different characteristics of laminar premixed combustion such as flame speed and flame thickness that are essential parameters in the modelling of turbulent combustion. Different properties of turbulence were also discussed (§. 2.1.3), and the combustion-turbulence interaction was characterised using the so-called regime diagrams (§. 2.1.4).

The three different computational approximation levels of turbulence modelling (RANS, LES and DNS) have been detailed (§. 2.2.1), before presenting in some details the different techniques developed to simulate turbulent combustion within the LES framework (§. 2.2.3 - 2.2.5). These are the methods relying on the estimation of the flow mixing properties, on the approximation of the flame front as a geometrical surface propagating in a turbulent flow or on the evaluation of flow statistics. Their strengths and weaknesses have been reviewed to highlight the choice made in this work §. 7.3.1.

Finally, the modelling of compressible multi-component flows has been reviewed (§. 2.3). The failure of the classical numerical methods (Godunov-type methods) derived for compressible flows when applied to multi-component flows and resulting in spurious pressure and velocity oscillations at interfaces between species was explained and demonstrated on a simple test case (§. 2.3.2). The need for moving towards

quasi- or non-conservative methods for the simulations of such flows was also presented. The two families of techniques derived to overcome this particular issue, shock-tracking and shock-capturing methods, have then been presented. Their application to the case of compressible reacting flows is further discussed (§. 2.3.3), and the selection of some of the models considered in this work was also highlighted.

CHAPTER 3

Governing equations and models formulation

As described in the literature review (§. 2.3), the simulation of compressible turbulent combustion with complex thermodynamic requires either a specific treatment of the governing equations or a specific set of equations. The models retained for the current analysis have been selected amongst the one presented in §. 2.3.3. This chapter presents the model choice, as well as their respective mathematical descriptions, along with the considered EoS. Firstly, the equation are presented in the case of an inviscid flow for simplicity, before the introduction of the terms used to model both the diffusive and reactive processes. Finally, the filtered equation sets will be presented and the closure of the different unclosed terms will be discussed.

3.1 Introduction

3.1.1 Choice of governing equations

A viscous reacting Newtonian flow behaviour follows the compressible Navier-Stokes equations augmented with source terms accounting for chemical reactions. As described in the literature review and in the introduction, combustion is a multi-species process, and as such, multi-component models presented in §. 2.3.3 have to be employed.

As already pointed out (§. 2.3.3), only the methods of Shyue [260], Allaire *et al.* [7] and Abgrall and Karni [6] have been demonstrated with thermally perfect EoS. Due to its formulation, Shyue's model seems difficult to extend to reacting viscous flows, and will not be considered in this work. The work of Abgrall and Karni [6] having already been applied to combustion seems a good candidate as a baseline model used to assess the performance of other approaches. Its main known deficiency resides in its quite poor conservation of total energy as reported by the different authors that have been using it [24–27, 133, 188–190]. A second concern could also be raised about its computational cost, as the Riemann solver is solved twice at each interface, which converts to twelve times per cell in three-dimensional computations. It seems therefore interesting to extend the approach of Allaire *et al.* [7] to viscous reacting flows, as it has been reported to be almost perfectly conservative for the total mass, energy and momentum, and more importantly each species mass, only the species energy could be potentially non-conserved. Furthermore, it has already been used in the computation of turbulent mixing in compressible inviscid flows by Probyn *et al.* [247].

Following these observations, it has been decided to put to the test four different formulations or models in this work. They are as follows,

- **Fully-conservative mass fraction** (FCMF) method, which is the classical set of equations referred to as the compressible viscous reacting Navier-Stokes equations [238] solved using the classical Godunov method and is used to highlight its deficiencies in multi-species flows, but also as a baseline in some cases
- **Quasi-conservative mass fraction** (QCMF) method, which is the double-flux method of Abgrall

and Karni [6] and uses the same governing equations as the FCMF albeit featuring a different numerical method to solve them

- **Quasi-conservative volume fraction** (QCVF) method, which is the author's novel extension of Allaire's model [7] to the case of viscous and reacting flows
- **Fully-conservative volume fraction** (FCVF) method, which is an reformulation of the QCVF method into a fully-conservative equation set

3.1.2 Variable definitions and thermodynamic coefficients

In the multi-species formulations employed in this work, each species k is characterised by,

- Either its **mass fraction** $Y_k = m_k/m$ defined as the ratio between its mass and the total mass contained in the volume V, or by its **volume fraction** defined by $z_k = V_k/V = \rho Y_k/\rho_k$ defined as the amount of volume it occupies in the volume V, or by the ratio between its mass and density, and ρ is the mixture density. It shall be noted that in this work ρ_k does not refer to the usual partial density $\rho_k = \rho Y_k$ as defined in Poinsot and Veynante [238], but to the density of species k occupying the volume V_k at its own pressure and temperature,
- Its molar mass W_k,
- Its specific gas constant $\mathcal{R}_k$ defined by,

$$\mathcal{R}_k = \frac{\mathcal{R}_u}{W_k} \tag{3.1}$$

  where $\mathcal{R}_u$ is the universal perfect gas constant with $\mathcal{R}_u = 8.31445\ [J/mol.K]$,
- Its heat capacity coefficients at constant pressure (C_{p_k}) and constant volume (C_{v_k}), which are either considered constant (calorically perfect gases) or temperature dependant (thermally perfect gases). In the first case, they are just constant functions of the species k, while in the latter they are computed using the NASA polynomials gathered into the JANNAF tables [59] as,

$$\frac{C_{p_k}}{\mathcal{R}_k} = \sum_{i=1}^{5} b_{i_k}^r T_k^{i-1} \tag{3.2}$$

$$C_{v_k} = \sum_{i=1}^{5} a_{i_k}^r T_k^{i-1} \tag{3.3}$$

  where $b_{i_k}^r$ are coefficients provided in tables. They are usually split in two ranges of temperature, $r \equiv 1$ corresponds to $T \in [300\,;\,1000]\,[K]$, while $r \equiv 2$ corresponds to $T \in [1000\,;\,5000]\,[K]$. Both heat capacity coefficients are related by the usual relation,

$$\mathcal{R}_k = C_{p_k} - C_{v_k} \tag{3.4}$$

  leading to $a_{1_k}^r = \mathcal{R}_k \left(b_{1_k}^r - 1\right)$ and $a_{i_k}^r = \mathcal{R}_k b_{i_k}^r$ for $i \in [2\,;\,5]$.
- Its formation enthalpy at reference temperature $\Delta h_{f_k}^0$. In general $T_0 = 298.15\,[K]$, but in some situations, $T_0 = 0\,[K]$ is used. In this work, $T_0 = 298.15\,[K]$ is used for the FCMF, QCVF and FCVF models, while $T_0 = 0\,[K]$ is used for the QCMF following the available literature for this model.

By definition, in a mixture, we have,

$$\sum_{k=1}^{N} Y_k = 1 \tag{3.5}$$

$$\sum_{k=1}^{N} \rho Y_k = \rho \tag{3.6}$$

and,

$$\sum_{k=1}^{N} z_k = 1 \tag{3.7}$$

$$\sum_{k=1}^{N} \rho_k z_k = \rho \tag{3.8}$$

Furthermore, the molar mass of a mixture of N species is given by,

$$\frac{1}{W} = \sum_{k=1}^{N} \frac{Y_k}{W_k} \tag{3.9}$$

while the molar fraction X_k is defined as,

$$X_k = \frac{W}{W_k} Y_k \tag{3.10}$$

and the molar concentration reads,

$$[X_k] = \rho \frac{Y_k}{W_k} = \rho \frac{X_k}{W} \tag{3.11}$$

3.2 Inviscid Mass fraction formulation

As already pointed out, both the QCMF and FCMF approach feature the same set of governing equations, which in this case is based on the well-known compressible inviscid Navier-Stokes equations, or Euler equations [278]. This is a fully conservative system where total momentum, mass and energy are perfectly conserved as well as species mass and energy. In fully conservative compact form, it reads,

$$\frac{\partial \mathbf{U}}{\partial t} + \frac{\partial \mathbf{F}(\mathbf{U})}{\partial x} + \frac{\partial \mathbf{G}(\mathbf{U})}{\partial y} + \frac{\partial \mathbf{H}(\mathbf{U})}{\partial z} = 0 \tag{3.12}$$

where,

$$\mathbf{U} = \left[\rho Y_k,\ \rho u,\ \rho v,\ \rho w,\ \rho E\right]^T \tag{3.13}$$

$$\mathbf{F}(\mathbf{U}) = \left[\rho Y_k u,\ \rho u^2 + P,\ \rho uv,\ \rho uw,\ (\rho E + P)\, u\right]^T \tag{3.14}$$

$$\mathbf{G}(\mathbf{U}) = \left[\rho Y_k v,\ \rho uv,\ \rho v^2 + P,\ \rho vw,\ (\rho E + P)\, v\right]^T \tag{3.15}$$

$$\mathbf{H}(\mathbf{U}) = \left[\rho Y_k w,\ \rho uw,\ \rho vw,\ \rho w^2 + P,\ (\rho E + P)\, w\right]^T \tag{3.16}$$

where the total non-chemical energy is given by $\rho E = \rho\varepsilon + \frac{1}{2}\rho\mathbf{u}^2$, u, v, w denote the velocity components, ρ and P are the mixture density and pressure respectively. The internal energy is discussed in depth in §. 3.4.4.

3.3 Inviscid Volume fraction formulations

3.3.1 Quasi-conservative volume fraction (QCVF)

This model proposed by Allaire *et al.* [7] features the usual energy and momentum conservation equations supplemented with two transport equations per species, one for the mass conservation and the second for the advection of the volume fraction. The system reads,

$$\begin{cases} \dfrac{\partial \mathbf{U}}{\partial t} + \dfrac{\partial \mathbf{F}(\mathbf{U})}{\partial x} + \dfrac{\partial \mathbf{G}(\mathbf{U})}{\partial y} + \dfrac{\partial \mathbf{H}(\mathbf{U})}{\partial z} = 0 \\ \dfrac{\partial z_k}{\partial t} + \mathbf{u} \cdot \nabla z_k = 0 \end{cases} \tag{3.17}$$

where,

$$\mathbf{U} = \left[\rho_k z_k,\ \rho u,\ \rho v,\ \rho w,\ \rho E\right]^T \tag{3.18}$$

$$\mathbf{F}\left(\mathbf{U}\right) = \left[\rho_k z_k u,\ \rho u^2 + P,\ \rho uv,\ \rho uw,\ \left(\rho E + P\right) u\right]^T \tag{3.19}$$

$$\mathbf{G}\left(\mathbf{U}\right) = \left[\rho_k z_k v,\ \rho uv,\ \rho v^2 + P,\ \rho vw,\ \left(\rho E + P\right) v\right]^T \tag{3.20}$$

$$\mathbf{H}\left(\mathbf{U}\right) = \left[\rho_k z_k w,\ \rho uw,\ \rho vw,\ \rho w^2 + P,\ \left(\rho E + P\right) w\right]^T \tag{3.21}$$

where the total non-chemical energy is similarly defined as $\rho E = \rho\varepsilon + \frac{1}{2}\rho\mathbf{u}^2$ while the internal energy definition is discussed in §. 3.4.3. The transport of volume fraction is not written in conservative form, thus justifying the method being referred to as "quasi-conservative".

It is worth noting that as $\rho_k z_k = \rho Y_k$, the species mass conservation equation is merely the usual species conservation equation rewritten with a new set of variables. Additionally, it can be noted that by expanding the species mass transport, it yields,

$$\rho_k \left(\frac{\partial z_k}{\partial t} + \mathbf{u}\cdot\nabla z_k\right) + z_k \left(\frac{\partial \rho_k}{\partial t} + \nabla\cdot\left(\rho_k\mathbf{u}\right)\right) = 0 \tag{3.22}$$

which using the volume fraction advection equation gives,

$$\frac{\partial \rho_k}{\partial t} + \nabla\cdot\left(\rho_k\mathbf{u}\right) = \frac{D\rho_k}{Dt} = 0 \tag{3.23}$$

This means that when using the QCVF formulation, Eq. 3.23 is always implicitly valid and species densities are materially advected.

3.3.2 Fully-conservative volume fraction (FCVF)

A fully-conservative derivation of the model of Allaire *et al.* [7] is proposed here for the purpose of trying to overcome the quasi-conservative behaviour of the original model. Although Karni [147], Abgrall [5] and Abgrall and Karni [6] showed that fully-conservative methods would produce spurious oscillations in multi-species flows, it is interesting to observe the behaviour of this new formulation. The momentum and energy equations are left untouched as they are already written in fully-conservative form, while species transport is modified as presented below.

The starting point of the derivation is thus the system,

$$\begin{cases} \dfrac{\partial \rho_k z_k}{\partial t} + \nabla\cdot\left(\rho_k z_k\mathbf{u}\right) = 0 \\ \dfrac{\partial z_k}{\partial t} + \mathbf{u}\cdot\nabla z_k = 0 \end{cases} \tag{3.24}$$

By expanding the mass transport equation, we get,

$$\begin{cases} \rho_k\dfrac{\partial z_k}{\partial t} + z_k\dfrac{\partial \rho_k}{\partial t} + \left(\rho_k\mathbf{u}\right)\cdot\nabla z_k + z_k\nabla\cdot\left(\rho_k\mathbf{u}\right) = 0 \\ \dfrac{\partial z_k}{\partial t} + \mathbf{u}\cdot\nabla z_k = 0 \end{cases} \tag{3.25}$$

yielding,

$$\begin{cases} \rho_k \left(\dfrac{\partial z_k}{\partial t} + \mathbf{u}\cdot\nabla z_k\right) + z_k \left(\dfrac{\partial \rho_k}{\partial t} + \nabla\cdot\left(\rho_k\mathbf{u}\right)\right) = 0 \\ \dfrac{\partial z_k}{\partial t} + \mathbf{u}\cdot\nabla z_k = 0 \end{cases} \tag{3.26}$$

As this system needs to be valid for any value of the species volume fraction, it leads to,

$$\frac{\partial \rho_k}{\partial t} + \nabla \cdot (\rho_k \mathbf{u}) = 0 \tag{3.27}$$

which needs to be always valid. Therefore, the original quasi-conservative system of Allaire *et al.* [7] can be rewritten with two fully conservative equations per species, one for the transport of its mass and the second for its density.

This new system is now presented in strong conservation form,

$$\frac{\partial \mathbf{U}}{\partial t} + \frac{\partial \mathbf{F}(\mathbf{U})}{\partial x} + \frac{\partial \mathbf{G}(\mathbf{U})}{\partial y} + \frac{\partial \mathbf{H}(\mathbf{U})}{\partial z} = 0 \tag{3.28}$$

where,

$$\mathbf{U} = [\rho_k,\ \rho_k z_k,\ \rho u,\ \rho v,\ \rho w,\ \rho E]^T \tag{3.29}$$

$$\mathbf{F}(\mathbf{U}) = \left[\rho_k u,\ \rho_k z_k u,\ \rho u^2 + P,\ \rho uv,\ \rho uw,\ (\rho E + P)\, u\right]^T \tag{3.30}$$

$$\mathbf{G}(\mathbf{U}) = \left[\rho_k v,\ \rho_k z_k v,\ \rho uv,\ \rho v^2 + P,\ \rho vw,\ (\rho E + P)\, v\right]^T \tag{3.31}$$

$$\mathbf{H}(\mathbf{U}) = \left[\rho_k w,\ \rho_k z_k w,\ \rho uw,\ \rho vw,\ \rho w^2 + P,\ (\rho E + P)\, w\right]^T \tag{3.32}$$

3.4 Thermodynamic closures and equation of state

3.4.1 Equation of state for perfect gases

The systems of equations presented in the previous section are not closed, and one needs to add an extra relation to do so. Given that in this work, we are interested in the simulation of reacting flows composed of a mixture of perfect gases, two main relations can be used,

- The **calorically perfect EoS**, whose main feature is the constant value of the species heat capacity coefficients who are not pressure nor temperature dependent. As such, the mixture heat capacity coefficients is only a function of the mixture composition $C_p = C_p(Y_k)$ as is the mixture heat capacity ratio γ.
- The **thermally perfect EoS** (or thermal EoS) features an extra degree of freedom compared to the calorically perfect EoS. In this case, both the species heat capacity coefficients and heat capacity ratio are function of temperature. The mixture properties (C_p, C_v and γ) are thus composition and temperature dependent, yielding $C_p = C_p(Y_k,\ T)$, $C_v = C_v(Y_k,\ T)$ and $\gamma = \gamma(Y_k,\ T)$.

The heat capacity coefficients are related by Eq. 3.4, while the heat capacity ratio is defined as,

$$\gamma_k = \frac{C_{p_k}}{C_{v_k}} = \frac{C_{p_k}}{C_{p_k} - \mathcal{R}_k} \tag{3.33}$$

Both previous relations are valid for calorically and thermally perfect gas assumptions. The relation linking the different thermodynamic variables (P, T, ρ) is the same in both cases and reads,

$$P_k = P_k(\rho_k,\ T_k) = \rho_k \mathcal{R}_k T_k \tag{3.34}$$

Another important property of perfect gases is the relation between their speed of sound and thermodynamic variables, namely

$$c = \sqrt{\left.\frac{\partial P}{\partial \rho}\right|_S} = \sqrt{\gamma \mathcal{R} T} = \sqrt{\frac{P\gamma}{\rho}} \tag{3.35}$$

The EoS choice depends on the type of application considered. In combustion, where both low ($\sim$ 300 $[K]$) and high ($\sim$ 2500 $[K]$) temperatures are encountered, and in many other situations (detonations, shock-driven flows, fast deflagrations, etc.) one cannot any more assume that heat capacities coefficients are not temperature dependent. In these cases (and numerous others), it becomes of prime importance to take this temperature dependence into account as coefficients values at high temperatures can deviate quite significantly from their low temperature values as shown in Fig. 3.1 (C_p values can vary by more than 250% in the temperature range, while γ could vary by $10-15\%$).

Furthermore, as the speed of sound is directly linked with the value of γ, is appears quite clearly that the temperature (in)dependence of C_p and C_v coefficients is a significant issue for the pressure wave speed, and by referring to Fig. 2.3 on the flame temperature as well. Both these effects combined can potentially lead to vastly different results.

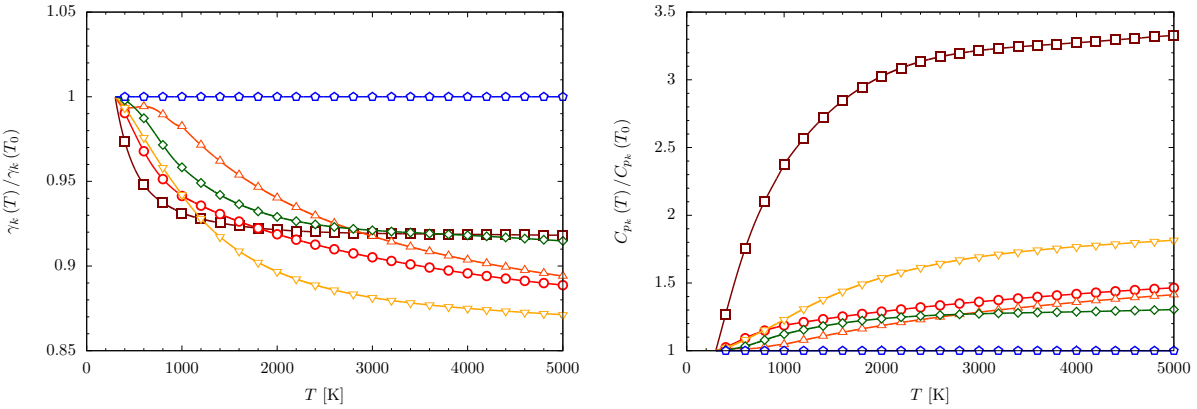

(a) *Heat capacity ratio* **(b)** *Heat capacity coefficient at constant pressure*

Figure 3.1: *Heat capacity ratio and heat capacity at constant pressure normalised by their values at* $T_0 = 298.15\ [K]$ *for several species as a function of temperature -* C_3H_8, O_2, H_2, H_2O, N_2, He

3.4.2 Thermodynamic closure

The last piece of information needed to fully close the different systems of equations presented earlier is the link between pure species and mixture properties. To this end, a thermodynamic closure need to be chosen.

In most codes, the classical isothermal hypothesis is made, where all the species are supposed to be in thermal equilibrium, such that $T_k = T$, and each species features its own partial pressure P_k. The mixture pressure is then recovered using Dalton's law as the sum of all partial pressures. Each species energy can also be computed, and the mixture energy is taken as the sum of each species energy weighted by its mass fraction as follows,

$$\begin{cases} T_k = T \\ \rho = \sum_{k=1}^{N} \rho Y_k \\ P = \sum_{k=1}^{N} P_k \\ \varepsilon = \sum_{k=1}^{N} Y_k \varepsilon_k \\ h = \sum_{k=1}^{N} Y_k h_k \end{cases} \tag{3.36}$$

where h is the mixture enthalpy. This is the closure that will be used for both mass fraction models, i.e. FCMF and QCMF models.

However, it has been shown by Allaire *et al.* [7] that this closure was not suitable for the volume fraction model as it would lead to pressure oscillations at material interfaces. Therefore, a second closure is used, namely, the isobaric closure. As its name implies, in this case, the pressure is shared by all species while their temperature (and density) can vary. This leads to new relations for the mixture energy and enthalpy,

$$\begin{cases} P_k = P \\ \rho = \sum_{k=1}^{N} \rho_k z_k \\ \rho\varepsilon = \sum_{k=1}^{N} \rho_k z_k \varepsilon_k \\ \rho h = \sum_{k=1}^{N} \rho_k z_k h_k \end{cases} \tag{3.37}$$

This closure features a "multiphase flavour" in the sense that it seems to imply that species present in a given cell are separated and occupy respectively a fraction z_k of the overall cell volume with a density ρ_k. Therefore, they can have their own temperature and density while sharing a common pressure (similarly to a gas and a fluid sharing an interface, different temperature and density, but similar pressure). This closure will be considered in the present work for both volume fraction models, i.e. FCVF and QCVF formulations.

3.4.3 Volume fraction models - Isobaric closure

As shown by Allaire *et al.* [7], when the volume fraction formulation is used with the isobaric closure, solutions free of pressure oscillations can be obtained for multi-species computations. In the present section, thermodynamic relations used for the computation of the mixture temperature, mixture heat capacity ratio or mixture pressure when the gas is considered either calorically or thermally perfect are presented in details. It is assumed that the vector of conserved variables is known, $\mathbf{U} = [\rho_k z_k,\ \rho u,\ \rho v,\ \rho w,\ \rho E]^T$ as well as the volume fraction z_k.

Computing internal energy and pressure

The pressure can be computed using the EoS. The mixture density is first extracted from the species mass using Eq. 3.8, and the internal energy of the mixture can be extracted from the total energy as,

$$\rho\varepsilon = (\rho E) - \frac{1}{2\rho}(\rho \mathbf{u})^2 \tag{3.38}$$

Depending on the formulation chosen for the heat capacities, pressure is recovered as follows,

- *Calorically perfect gas* : Species internal energy can be computed as,

$$\rho_k \varepsilon_k = \rho_k C_{v_k} T_k = C_{v_k} \frac{P}{\mathcal{R}_k} \tag{3.39}$$

  which for the mixture gives,

$$\rho\varepsilon = \sum_{k=1}^{N} \rho_k z_k \varepsilon_k = \sum_{k=1}^{N} z_k C_{v_k} \frac{P}{\mathcal{R}_k} \tag{3.40}$$

by recalling the definition of γ (Eq. 3.33), we have $C_{v_k}/\mathcal{R}_k = (\gamma_k - 1)^{-1}$, and this yields,

$$P = \rho\varepsilon \left(\sum_{k=1}^{N} \frac{z_k}{\gamma_k - 1} \right)^{-1} \tag{3.41}$$

- *Thermally perfect gas* : In this case, the computation is slightly demanding, as an iterative procedure is needed to find the solution. The following details the derivation of the equation for pressure and its solution. Species internal energy is defined as,

$$\rho_k \varepsilon_k = \rho_k \left(\int_0^{T_k} C_{v_k}(\xi_k)\,\mathrm{d}\xi_k - \int_0^{T_0} C_{v_k}(\xi_k)\,\mathrm{d}\xi_k - \mathcal{R}_k T_0 \right) = \rho_k \left(\int_{T_0}^{T_k} C_{v_k}(\xi_k)\,\mathrm{d}\xi_k - \mathcal{R}_k T_0 \right) \tag{3.42}$$

which yields for the mixture,

$$\rho\varepsilon = \sum_{k=1}^{N} \rho_k z_k \left(\int_{T_0}^{T_k} C_{v_k}(\xi_k)\,\mathrm{d}\xi_k - \mathcal{R}_k T_0 \right) \tag{3.43}$$

where $T_0 = 298.15\,[K]$. Using the definitions of C_{p_k} and C_{v_k} given in Eq. 3.2 and Eq. 3.3, species internal energy can be rewritten as follows,

$$\varepsilon_k = \begin{cases} \displaystyle\sum_{i=1}^{5} \frac{a_{i_k}^1}{i} T_k^i - T_{0_k}^{\varepsilon} & \text{if } T_k < 1000\,[K] \\ \displaystyle\sum_{i=1}^{5} \frac{a_{i_k}^2}{i} T_k^i + K_k^{\varepsilon} - T_{0_k}^{\varepsilon} & \text{if } T_k \geqslant 1000\,[K] \end{cases} \tag{3.44}$$

where K_k^{ε} represents the difference between the C_{v_k} computed using both set of coefficients at $T_k = 1000\,[K]$, and $T_{0_k}^{\varepsilon}$ stands for $\displaystyle\int_0^{T_0} C_{v_k}(\xi_k)\,\mathrm{d}\xi_k + \mathcal{R}_k T_0$,

$$T_{0_k}^{\varepsilon} = \sum_{i=1}^{5} \frac{a_{i_k}^1 T_0}{i} + \mathcal{R}_k T_0 \tag{3.45}$$

$$K_k^{\varepsilon} = \sum_{i=1}^{5} \frac{1000^i}{i} \left(a_{i_k}^1 - a_{i_k}^2 \right) \tag{3.46}$$

By further recasting Eq. 3.44 in terms of pressure, we get,

$$\varepsilon_k = \begin{cases} \displaystyle\sum_{i=1}^{5} \frac{a_{i_k}^1}{i} \left(\frac{P}{\rho_k T_k} \right)^i - T_{0_k}^{\varepsilon} & \text{if } T_k < 1000\,[K] \\ \displaystyle\sum_{i=1}^{5} \frac{a_{i_k}^2}{i} \left(\frac{P}{\rho_k T_k} \right)^i + K_k^{\varepsilon} - T_{0_k}^{\varepsilon} & \text{if } T_k \geqslant 1000\,[K] \end{cases} \tag{3.47}$$

By combining the last expression with Eq. 3.43, we obtain a polynomial equation where the pressure is the only unknown. It can be written as follows,

$$\sum_{i=0}^{5} m_i P^i = 0 \tag{3.48}$$

where the m_i's coefficients are given by,

$$m_0 = -\rho\varepsilon + \sum_{k=1}^{N} \begin{cases} -\rho_k z_k T_{0_k}^{\varepsilon} & \text{if } T_k < 1000\,[K] \\ \rho_k z_k \left(K_k^{\varepsilon} - T_{0_k}^{\varepsilon} \right) & \text{if } T_k \geqslant 1000\,[K] \end{cases} \tag{3.49}$$

$$m_i = \frac{1}{i} \sum_{k=1}^{N} \left[\rho_k z_k \left(\frac{1}{\rho_k \mathcal{R}_k} \right)^i a_{i_k}^r \right] \tag{3.50}$$

where $r \in [1,2]$ depending on the value of T_k. As it is well known that no analytical solution exists for 5^{th} order polynomials, an iterative Newton-Raphson procedure is applied to find an approximate solution. This procedure is detailed in Appendix A.1.

Computing enthalpy

As already pointed out, the mixture enthalpy is obtained by,

$$\rho h = \sum_{k=1}^{N} \rho_k z_k h_k \tag{3.51}$$

where, depending on the EoS chosen, species enthalpy are computed differently following,

- *Calorically perfect gas*

$$h_k = C_{p_k} T_k \tag{3.52}$$

- *Thermally perfect gas* : Reminding that $\varepsilon_k = h_k - P_k/\rho_k$, it follows,

$$\rho_k h_k = \rho_k \left(\int_0^{T_k} C_{p_k}(\xi_k)\,\mathrm{d}\xi_k - \int_0^{T_0} C_{p_k}(\xi_k)\,\mathrm{d}\xi_k \right) = \rho_k \int_{T_0}^{T_k} C_{p_k}(\xi_k)\,\mathrm{d}\xi_k \tag{3.53}$$

Similarly to Eqs. 3.44-3.46, it can be written as a function of the JANNAF polynomial coefficients,

$$h_k = \begin{cases} \displaystyle\sum_{i=1}^{5} \frac{b_{i_k}^1}{i} \mathcal{R}_k T_k^i - T_{0_k}^h & \text{if } T_k < 1000\,[K] \\ \displaystyle\sum_{i=1}^{5} \frac{b_{i_k}^2}{i} \mathcal{R}_k T_k^i + K_k^h - T_{0_k}^h & \text{if } T_k \geqslant 1000\,[K] \end{cases} \tag{3.54}$$

where we have,

$$T_{0_k}^h = \sum_{i=1}^{5} \frac{\mathcal{R}_k b_{i_k}^1 T_0}{i} \tag{3.55}$$

$$K_k^h = \sum_{i=1}^{5} \frac{1000^i}{i} \mathcal{R}_k \left(b_{i_k}^1 - b_{i_k}^2 \right) \tag{3.56}$$

Computing temperature and specific heat ratio

In the paper by Allaire *et al.* [7], two different methodologies are proposed to compute both temperature and specific heat ratio. The first one is based on the analysis carried out by Allaire *et al.* [7] and uses mixture quantities, while the second consists in a simple volume averaging of species properties weighted by their volume fraction. This last approach assumes a linear relationship between the amount of a given species in the mixture and its influence on it. This latter will not be presented in further details as it has not been retained for this work. It is more suited in the case of tabulated EoS, where no simple relation can be established between the different quantities. This is not the case here, as only the simple perfect gas EoS is considered.

In a similar fashion as the computations of pressure, enthalpy and energy, the heat capacity ratio is dependent on the choice of the EoS, yielding different relations described below. On the other hand, temperature is obtained in a similar way for both EoS,

- *Calorically perfect gas* : Pressure and density of the mixture are both known at this point, leading to,

$$\frac{1}{\gamma - 1} = \sum_{k=1}^{N} \frac{z_k}{\gamma_k - 1} \tag{3.57}$$

where $\gamma_k = 1 + \mathcal{R}_k / C_{v_k}$, and the mixture specific heat ratio becomes,

$$\gamma = 1 + \left(\sum_{k=1}^{N} \frac{z_k}{\gamma_k - 1} \right)^{-1} \tag{3.58}$$

- *Thermally perfect gas* : In this case, Eq. 3.57 still holds true, but γ_k is now given by,

$$\gamma_k = 1 + \mathcal{R}_k \left(\sum_{i=1}^{5} a_{i_k}^r \left(\frac{P}{\rho_k \mathcal{R}_k} \right)^{i-1} \right)^{-1} \tag{3.59}$$

where $r \equiv [1\,;\,2]$ depending on the value of $\dfrac{P}{\rho_k \mathcal{R}_k} = T_k$.

For both perfect gas formulations, temperature is simply obtained by using the mixture EoS,

$$T = \frac{P}{\rho \mathcal{R}} \tag{3.60}$$

where the mixture perfect gas constant is computed as,

$$\mathcal{R} = \sum_{k=1}^{N} \mathcal{R}_k \frac{\rho_k z_k}{\rho} \tag{3.61}$$

3.4.4 FCMF - Isothermal closure

In the case of the FCMF model, the classical isothermal (temperature equilibrium) thermodynamic closure is used. The mixture temperature is then shared by all species, while each has its own pressure, and the relations presented by Poinsot and Veynante [238] are applicable. It is worth noticing that these partial pressures do not appear explicitly in the current algorithm, and as such do not need to be computed, only the mixture pressure is relevant. The present section presents the relations needed to compute the mixture pressure, temperature and specific heat ratio for both EoS considered, while having the knowledge of the conserved variables vector $\mathbf{U} = [\rho Y_k,\ \rho u,\ \rho v,\ \rho w,\ \rho E]^T$.

Computing temperature and specific heat ratio

When using the thermally perfect EoS, temperature calculation is slightly involved as it requires the solution of a 5^{th} order polynomial equation. In the case of a calorically perfect gas, it can simply be extracted from internal energy computed following Eq. 3.38.

- *Calorically perfect gas*

$$T = \frac{\rho \varepsilon}{\sum_{k=1}^{N} (\rho Y_k)\, C_{v_k}} = \frac{\rho \varepsilon}{\rho C_v} \tag{3.62}$$

The specific heat ratio is simply computed using species heat capacities and the mixture composition as follows,

$$\gamma = \frac{\sum_{k=1}^{N} (\rho Y_k)\, C_{p_k}}{\sum_{k=1}^{N} (\rho Y_k)\, C_{v_k}} = \frac{C_p}{C_v} \tag{3.63}$$

- *Thermally perfect gas* : In this case, the temperature cannot be directly obtained from internal energy, as C_p is not a constant any more for each species. The iterative procedure used to compute it relies on a Newton-Raphson algorithm, highlighted in Appendix A.2. The specific heat ratio is obtained using Eq. 3.63 which is still valid, and rewritten as,

$$\gamma = \frac{\displaystyle\sum_{k=1}^{N} (\rho Y_k) \left(\sum_{i=1}^{5} b_{i_k}^r T^{i-1} \mathcal{R}_k \right)}{\displaystyle\sum_{k=1}^{N} (\rho Y_k) \left(\sum_{i=1}^{5} a_{i,k}^r T^{i-1} \right)} \tag{3.64}$$

Computing pressure and internal energy

As temperature is known, pressure can be directly computed from the EoS for both calorically and thermally perfect assumptions. It is given by,

$$P = \mathcal{R}_u T \sum_{k=1}^{N} \frac{\rho Y_k}{W_k} \tag{3.65}$$

Using a form of internal energy similar to the volume fraction approach, internal energy is computed by,

- *Calorically perfect gas*

$$\varepsilon = \sum_{k=1}^{N} \left(C_{p_k} T - \frac{\mathcal{R}_u T}{W_k} \right) Y_k \tag{3.66}$$

- *Thermally perfect gas* : Eq. 3.42 is used, but replacing C_v by C_p leading to,

$$\varepsilon_k = \int_0^T C_{p_k}(\xi)\,\mathrm{d}\xi - \int_0^{T_0} C_{p_k}(\xi)\,\mathrm{d}\xi - \mathcal{R}_k T = \int_{T_0}^T C_{p_k}(\xi)\,\mathrm{d}\xi - \mathcal{R}_k T \tag{3.67}$$

which leads to the following relations with JANNAF coefficients,

$$\varepsilon_k = \begin{cases} \displaystyle\sum_{i=1}^{5} \frac{\mathcal{R}_k b_{i_k}^1}{i} T^i - T_{0_k}^{\varepsilon} & \text{if } T < 1000\,[K] \\ \displaystyle\sum_{i=1}^{5} \frac{\mathcal{R}_k b_{i_k}^2}{i} T^i + K_k^{\varepsilon} - T_{0_k}^{\varepsilon} & \text{if } T \geqslant 1000\,[K] \end{cases} \tag{3.68}$$

where K_k^{ε} represents the difference between the C_{p_k} at $T = 1000\,[K]$ computed with both sets of coefficients, while $T_{0_k}^{\varepsilon}$ stands for $\displaystyle\int_0^{T_0} C_{p_k}(\xi)\,\mathrm{d}\xi - \mathcal{R}_k T$ and are expressed as,

$$T_{0_k}^{\varepsilon} = \left(\sum_{i=1}^{5} \frac{\mathcal{R}_k b_{i_k}^1 T_0^i}{i} \right) + \mathcal{R}_k T \tag{3.69}$$

$$K_k^{\varepsilon} = \sum_{i=1}^{5} \frac{1000^i}{i} \mathcal{R}_k \left(b_{i_k}^1 - b_{i_k}^2 \right) \tag{3.70}$$

Computing enthalpy

As pointed out in §. 3.4.2, mixture enthalpy is simply expressed as the sum of species enthalpy weighted by their mass fractions,

$$h = \sum_{k=1}^{N} \rho Y_k h_k \tag{3.71}$$

where species enthalpy is evaluated as follows, depending on the EoS,

- *Calorically perfect gas*

$$h_k = C_{p_k} T \tag{3.72}$$

- *Thermally perfect gas* : by definition it is given by

$$h_k = \int_0^T C_{p_k}(\xi)\,\mathrm{d}\xi - \int_0^{T_0} C_{p_k}(\xi)\,\mathrm{d}\xi = \int_{T_0}^T C_{p_k}(\xi)\,\mathrm{d}\xi \tag{3.73}$$

which using JANNAF coefficients yields,

$$h_k = \begin{cases} \displaystyle\sum_{i=1}^{5} \frac{b^1_{i_k}}{i} \mathcal{R}_k T^i - T^h_{0_k} & \text{if } T < 1000\,[K] \\ \displaystyle\sum_{i=1}^{5} \frac{b^2_{i_k}}{i} \mathcal{R}_k T^i + K^h_k - T^h_{0_k} & \text{if } T \geqslant 1000\,[K] \end{cases} \tag{3.74}$$

where K^h_k and $T^h_{0_k}$ are given by Eq. 3.56 and Eq. 3.55 respectively.

3.4.5 QCMF - Isothermal closure

As explained in §. 4.3.4, the double-flux model consists in two main steps, an energy projection and a thermal quantity correction step. In the energy projection step, species heat capacities are approximated as piecewise linear functions of temperature, such that total energy for thermally perfect gas can be recast in a form similar to the calorically perfect EoS.

This tabulation of heat capacities calculations in linear functions of temperature leads to a simplification of the temperature computation (no iterative procedure needed), and thus in a decrease of the overall computational time, which is quite welcome to balance the increase of computational cost resulting from the governing equations special numerical treatment.

The temperature range is split in intervals of size ΔT and denoted I_l where $I_l = \left[T^l\,;\,T^{l+1}\right] = [(l-1)\,\Delta T\,;\,l\Delta T]$ (Fig. 3.2). The interval size can be adjusted to reduce interpolation errors. Species heat capacities are computed as,

$$C_{p_k} = a^l_k T + b^l_k \tag{3.75}$$

where a^l_k and b^l_k are constants on the interval I_l.

Similarly to the FCMF model, the total non-chemical energy is expressed by,

$$E = \sum_{k=1}^{N} Y_k \varepsilon_k + \frac{\mathbf{u}^2}{2} \tag{3.76}$$

$$= \left(\sum_{k=1}^{N} \int_{T_0}^{T} Y_k C_{p_k}(\xi)\,\mathrm{d}\xi \right) - \frac{P}{\rho} + \frac{\mathbf{u}^2}{2} \tag{3.77}$$

Recalling Eq. 3.73, when $T \in I_m$, the enthalpy is obtained as,

$$\begin{aligned} h_k &= \sum_{l=1}^{m-1} \int_{T^l}^{T^{l+1}} C^l_{p_k}\,\mathrm{d}\xi + \int_{T^m}^{T} C^m_{p_k}\,\mathrm{d}\xi \\ &= \sum_{l=1}^{m-1} \int_{T^l}^{T^{l+1}} \left(a^l_k \xi + b^l_k\right)\mathrm{d}\xi + \int_{T^m}^{T} \left(a^m_k \xi + b^m_k\right)\mathrm{d}\xi \\ &= h^{m'}_{0_k} + \frac{a^m_k}{2}\left(T^2 - (T^m)^2\right) + b^m_k\left(T - T^m\right) \\ &= h^{m'}_{0_k} + \frac{a^m_k}{2}\left(T^m + T\right)\left(T - T^m\right) + b^m_k\left(T - T^m\right) \end{aligned} \tag{3.78}$$

In the last interval I_m, the linear evolution of C_{p_k} is replaced by a constant evolution, $C_{p_k} = \overline{b_k^m}$. To keep the correct value of enthalpy, and using Eq. 3.78, we can express the enthalpy in interval I_m (h_k^m) as,

$$h_k^m = \int_{T^m}^{T} \overline{b_k^m}\, \mathrm{d}\xi = \frac{a_k^m}{2}\left(T^m + T\right)\left(T - T^m\right) + b_k^m\left(T - T^m\right) \tag{3.79}$$

$$= \overline{b_k^m}\left(T - T^m\right) = \left(T - T^m\right)\left(\frac{a_k^m}{2}\left(T^m + T\right) + b_k^m\right) \tag{3.80}$$

and by identification, it comes,

$$\overline{b_k^m} = \frac{a_k^m}{2}\left(T^m + T\right) + b_k^m \tag{3.81}$$

Further noting $h_{0_k}^m = h_{0_k}^{m'} - \overline{b_k^m} T^m$ and $h_0^m = \sum_{k=1}^{N} Y_k h_{0_k}^m$, the total non-chemical energy of the mixture becomes,

$$\begin{aligned} E &= h_0^m + \sum_{k=1}^{N} Y_k \overline{b_k^m} T - \frac{P}{\rho} + \frac{\mathbf{u}^2}{2} \\ &= h_0^m + C_p T - \frac{P}{\rho} + \frac{\mathbf{u}^2}{2} \\ &= h_0^m + \frac{P}{\rho\left(\gamma - 1\right)} + \frac{\mathbf{u}^2}{2} \end{aligned} \tag{3.82}$$

which is a form equivalent to that of calorically perfect gas.

It shall be noted that $h_{0_k}^m$ can be precomputed and tabulated over the intervals spanning $T_0 \leqslant T \leqslant T^m$, and we have thus,

$$h_k = h_{0_k} + \overline{b_k^m}\left(T - T^m\right) \tag{3.83}$$

which is extremely fast to compute during the simulation. The mixture internal energy is computed using,

$$\rho\varepsilon = \frac{P}{\gamma - 1} \tag{3.84}$$

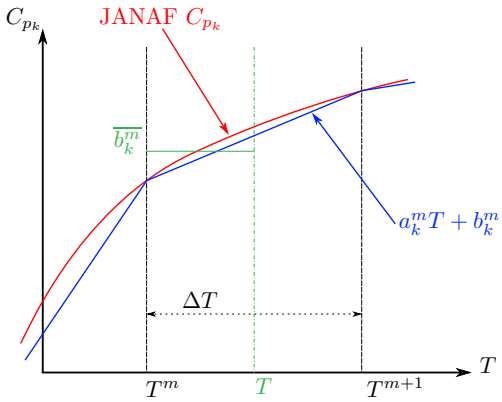

Figure 3.2: *Approximation of species C_{p_k} and enthalpy h_k*

Further details on the QCMF approach are given in §. 4.3.4.

3.5 Diffusion and reactions terms

All systems presented up to now (QCMF and FCMF (§. 3.2), QCVF (§. 3.3.1), FCVF (§. 3.3.2)) were presented for inviscid flows. In combustion, diffusion phenomena and source terms are of prime importance

and need to be accounted for in the equation sets. The different diffusion fluxes and source terms are presented in this section for all models, along with the calculation of the different transport coefficients.

3.5.1 Diffusion fluxes for gaseous species

Species diffusion occurs at a molecular level and is one of the main driving mechanisms of premixed combustion. Reactants are already mixed at the macroscopic level, but it is only when species are mixed at a molecular level that combustion occurs. The mass diffusive fluxes estimation for the different equation sets considered is presented here.

Mass fraction formulations (FCMF and QCMF)

Species diffusion is modelled using species diffusion velocities given by,

$$-\nabla \cdot \mathbf{J}_k = -\nabla \cdot (\rho Y_k \mathbf{V}_k) \tag{3.85}$$

where $\mathbf{V}_k$ is the diffusion velocity of species k, and $\mathbf{J}_k$ represents the diffusive mass flux. This term is present at the right-hand side of the species mass transport equations. The global mass conservation is ensured by,

$$\sum_{k=1}^{N} Y_k \mathbf{V}_k = 0 \tag{3.86}$$

To obtain the diffusion velocities values, an exact system of $N \times N$ equations has to solved which proves overly expensive in practical applications. Species diffusion velocities are therefore approximated by the Hirschfelder and Curtis [128] equation representing the best first-order closure of the full system and reads,

$$Y_k \mathbf{V}_k = -D_k \frac{W_k}{W} \nabla X_k \tag{3.87}$$

where D_k is the species diffusion coefficient. Pressure and temperature gradients effects (Soret effect) on the species diffusion velocities are neglected [107].

An outstanding issue of the Hirschfelder and Curtis approximation is that it does not satisfy global mass conservation when species Schmidt numbers are not equal. Two solutions can be used to overcome this issue,

- The solution of the $N-1$ first species transport equations is computed and the last species mass fraction is recovered by using the fact that the species mass fractions sum is always unity. This means that all diffusion errors are absorbed by one species, which is usually N_2, as it is the flame diluent in air. However, this is dangerous and should only be used for very diluted flames
- A correction term is added to the species diffusion velocity to enforce the conservation of global mass [238]. The diffusion velocity of species k is then expressed by,

$$\mathbf{J}_k = -\rho \left(D_k \frac{W_k}{W} \nabla X_k - Y_k \mathbf{V}_k^c \right) \tag{3.88}$$

  where $\mathbf{V}_k^c$ is a correction velocity computed as,

$$\mathbf{V}_k^c = \sum_{k=1}^{N} D_k \frac{W_k}{W} \nabla X_k \tag{3.89}$$

The second solution is retained in the present work, and as such the diffusive mass fluxes are given by,

$$\nabla \cdot \mathbf{J}_k = -\nabla \cdot \left(\rho D_k \frac{W_k}{W} \nabla X_k - Y_k \left(\sum_{k=1}^{N} D_k \frac{W_k}{W} \nabla X_k \right) \right) \tag{3.90}$$

and the estimation of the diffusion coefficient D_k is discussed in §. 3.5.3.

QCVF formulation

In the QCVF formulation, two equations are considered for each species, the first one being the species mass conservation which is similar to the mass fraction model, therefore the diffusive term presented above is also used. The main difference arises in the treatment of the species volume fraction advection equations where the diffusion fluxes formulation has to be modified. The addition of diffusion terms to this equation set represents one of the novelty of this work as, to the author knowledge, the 5-equation model of Allaire *et al.* [7] was only used for inviscid non-reacting simulations so far. A similar comment can be made regarding the source term addition as discussed in §. 3.5.4.

By expanding the species mass conservation equation, as presented in Eq. 3.22, but accounting for the diffusive fluxes, we have,

$$\rho_k \left(\frac{\partial z_k}{\partial t} + \mathbf{u} \cdot \nabla z_k \right) + z_k \left(\frac{\partial \rho_k}{\partial t} + \nabla \cdot (\rho_k \mathbf{u}) \right) = -\nabla \cdot \mathbf{J}_k \tag{3.91}$$

which can be rearranged as,

$$\frac{\partial z_k}{\partial t} + \mathbf{u} \cdot \nabla z_k = -\frac{1}{\rho_k} \nabla \cdot \mathbf{J}_k - z_k \left(\frac{\partial \rho_k}{\partial t} + \nabla \cdot (\rho_k \mathbf{u}) \right) \tag{3.92}$$

By remembering that species density are materially advected (Eq. 3.23), we end up with,

$$\frac{\partial z_k}{\partial t} + \mathbf{u} \cdot \nabla z_k = -\frac{1}{\rho_k} \nabla \cdot \mathbf{J}_k \tag{3.93}$$

and by identification with the volume fraction transport equation accounting for species diffusion given by,

$$\frac{\partial z_k}{\partial t} + \mathbf{u} \cdot \nabla z_k = -\left(\nabla \cdot \mathbf{J}_k \right)^z \tag{3.94}$$

we have,

$$\left(\nabla \cdot \mathbf{J}_k \right)^z = \frac{1}{\rho_k} \nabla \cdot \mathbf{J}_k \tag{3.95}$$

The volume fraction diffusive fluxes in the QCVF model are thus the mass diffusive fluxes scaled by the species density.

FCVF formulation

Similarly to the QCVF model, the FCVF formulation features two transport equations per species, one similar to the mass fraction models transporting species mass, and the second transporting species density. The treatment of the partial density transport is discussed here.

By adding a diffusive term to the partial density transport, Eq. 3.24 becomes,

$$\begin{cases} \dfrac{\partial \rho_k z_k}{\partial t} + \nabla \cdot (\rho_k z_k \mathbf{u}) = -\nabla \cdot \mathbf{J}_k \\ \dfrac{\partial z_k}{\partial t} + \mathbf{u} \cdot \nabla z_k = -\left(\nabla \cdot \mathbf{J}_k \right)^\rho \end{cases} \tag{3.96}$$

where by expanding the first relation and using Eq. 3.95, we end up with,

$$\left(\nabla \cdot \mathbf{J}_k \right)^\rho = 0 \tag{3.97}$$

The species density are not diffusing, but are materially advected.

3.5.2 Diffusion fluxes for the momentum and energy equations

Both momentum and energy equations are common to all approaches highlighted earlier. Several diffusive processes have to be taken into account in these equations, such as momentum dissipation by viscous stresses, energy diffusion due to viscous stresses work, temperature diffusion (heat fluxes) or even species diffusion (enthalpy fluxes).

Momentum diffusion

Momentum is dissipated by viscous stresses ($\nabla \cdot \underline{\boldsymbol{\tau}}$) estimated by the viscous stress tensor $\underline{\boldsymbol{\tau}}$ calculated as follows when considering a Newtonian fluid,

$$\underline{\boldsymbol{\tau}} = \beta \left(\nabla \cdot \mathbf{u}\right) \underline{\mathbf{I}} + 2\mu \underline{\mathbf{S}} \tag{3.98}$$

where β denotes the second coefficient of viscosity, μ is the dynamic viscosity, $\underline{\mathbf{I}}$ represents the identity tensor ($I_{ij} = \delta_{ij}$, where δ_{ij} denotes the Kronecker function) and $\underline{\mathbf{S}}$ stands for the symmetric strain rate tensor given by,

$$\underline{\mathbf{S}} = \frac{1}{2}\left(\nabla \mathbf{u} + \left(\nabla \mathbf{u}\right)^T\right) \tag{3.99}$$

and $\left(\nabla \mathbf{u}\right)^T$ is the transpose of the dyadic $\nabla \mathbf{u}$. In index notation, it is given by,

$$S_{ij} = \frac{1}{2}\left(\frac{\partial u_i}{\partial x_j} + \frac{\partial u_j}{\partial x_i}\right) \tag{3.100}$$

By separating the isotropic and deviatoric parts of the viscous stress tensor, it can be rewritten as,

$$\underline{\boldsymbol{\tau}} = \left(\beta + \frac{2}{3}\mu\right)\left(\nabla \cdot \mathbf{u}\right) \underline{\mathbf{I}} + 2\mu \underline{\mathbf{S}} - \frac{2}{3}\mu \left(\nabla \cdot \mathbf{u}\right) \underline{\mathbf{I}} \tag{3.101}$$

The second coefficient of viscosity is evaluated using Stoke's hypothesis, where the bulk viscosity estimated by $\beta + \frac{2}{3}\mu = 0$. This assumption is valid *a priori* only for dilute mono-atomic gas and at low Mach number. In other situations, this can lead to incorrect results [26], as it was shown to have a significant impact on the shock induced vortex generation as well as on the smoothing of situations with complex shock interactions. On the other hand, it is a complex parameter to calculate accurately as it requires the use of the kinetic theory of gases [93]. Nonetheless, this assumption will be used throughout this work.

The viscous stress tensor is finally defined as,

$$\underline{\boldsymbol{\tau}} = -\frac{2}{3}\mu \left(\nabla \cdot \mathbf{u}\right) \underline{\mathbf{I}} + \mu \left(\nabla \mathbf{u} + \left(\nabla \mathbf{u}\right)^T\right) \tag{3.102}$$

Energy diffusion fluxes

Energy is dissipated through viscous stresses work, temperature diffusion and energy transport by molecular diffusion. These processes are as follows,

- Viscous fluxes work given by $\underline{\boldsymbol{\tau}} \cdot \mathbf{u}$
- Heat conduction modelled by Fourier's law

$$\mathbf{q}_c = -\lambda \nabla T \tag{3.103}$$

where λ is the heat conductivity of the mixture

- The molecular diffusion induced energy dissipation is estimated by (neglecting Dufour effect),

$$\mathbf{q}_d = \sum_{k=1}^{N} h_k \mathbf{J}_k \tag{3.104}$$

This last term is often neglected but Cook [68] highlights its importance in ensuring the consistency between mass and energy transport equations. It is therefore used in this work.

3.5.3 Transport properties for gaseous species

Transport properties have to be estimated for individual species. Mixture rules are then applied to obtain mixture properties. It can be noted that numerous mixing rules exist, and there is no clear choice about which one is best in a given situation. In this work, Wilke's mixing rule is considered [294].

Species dynamic viscosities are calculated at a given temperature using Sutherland's law,

$$\mu_k = \mu_{k_{ref}} \left(\frac{T}{T_{0_k}} \right)^{3/2} \frac{T_{0_k} + S_k}{T + S_k} \tag{3.105}$$

where T_{0_k} is the reference temperature (different for each species), $\mu_{k_{ref}}$ is the dynamic viscosity at the reference temperature and S_k is the Sutherland constant.

The mixture viscosity is estimated as,

$$\mu = \sum_{k=1}^{N} \frac{X_k \mu_k}{\sum_{j=1}^{N} X_j \Phi_{kj}} \tag{3.106}$$

where the inter-collisional parameter Φ_{kj} is given by,

$$\Phi_{kj} = \frac{1}{\sqrt{8}} \frac{1}{\sqrt{1 + \frac{W_k}{W_j}}} \left(1 + \sqrt{\frac{\mu_k}{\mu_j}} \left(\frac{W_j}{W_k} \right)^{1/4} \right)^2 \tag{3.107}$$

Similarly to species viscosities, species thermal conductivities could be estimated using kinetic theory [93], but this is much more complex and this level of accuracy is not needed for the considered applications. In this work, the mixture thermal conductivity is computed from the mixture dynamic viscosity using the assumption of a constant mixture Prandtl (Pr) number,

$$\lambda = \frac{\mu C_p}{Pr} \tag{3.108}$$

This assumption has been found to be valid in most air-flames due to the large amount of diluent (N_2) present.

The diffusion coefficient used in the Hirschfelder and Curtis [128] law, is an effective diffusion coefficient of species k in the mixture. The simplest way of evaluating it consists in deriving it from assumed species Lewis (Le_k) or Schmidt (Sc_k) numbers [106]. Smooke and Giovangigli [263] were the first to propose the constant Lewis strategy considered in this work. Since, $Sc_k = \frac{\mu}{\rho D_k} = \frac{\nu}{S_c} = Le_k Pr$, the effective diffusion coefficient can be estimated as,

$$D_k = \frac{\mu}{\rho Sc_k} = \frac{\nu}{Sc_k} \tag{3.109}$$

where Sc_k is an *a priori* specified constant Schmidt number.

3.5.4 Gaseous chemical kinetics

Chemical reactions are taken into account in the equations by adding a source term in both the mass and energy conservation equations. This last term depends on the form of the energy retained. Some authors use total chemical energy (sum of chemical, sensible and kinetic energy), and as such do not need an energy source term in the energy conservation equation. However, in this work, the total non-chemical energy has been used (sum of sensible and kinetic energy), and a source term accounting for the net heat release of chemical reactions is needed.

Mass fraction formulation

The chemical source term described in this section applies to the simulation of detailed chemistry effects accounting for N species reacting through M reactions. Chemical mechanisms can be written as,

$$\sum_{k=1}^{N} \nu'_{k_j} \mathcal{M}_k \rightleftarrows \sum_{k=1}^{N} \nu''_{k_j} \mathcal{M}_k \text{ for } j = 1, \cdots, M \tag{3.110}$$

where $\mathcal{M}_k$ denotes the name of species k, ν'_{k_j} and ν''_{k_j} are the stoichiometric coefficients of species k in reaction j. The mass conservation through chemical reactions enforces,

$$\sum_{k=1}^{N} \nu'_{k_j} W_k = \sum_{k=1}^{N} \nu''_{k_j} W_k \tag{3.111}$$

The rate of production/destruction of species k, $\dot{\omega}_k$ is the sum of the rates $\dot{\omega}_{k_j}$ produced by the M reactions,

$$\dot{\omega}_k = \sum_{j=1}^{M} \dot{\omega}_{k_j} = W_k \sum_{j=1}^{M} \left(\nu''_{k_j} - \nu'_{k_j} \right) \mathcal{Q}_j \tag{3.112}$$

where $\mathcal{Q}_j$ is the rate of progress of reaction j.

The rate of progress of reaction j is computed as follows,

$$\mathcal{Q}_j = K_{f_j} \prod_{k=1}^{N} [X_k]^{\nu'_{k_j}} - K_{r_j} \prod_{k=1}^{N} [X_k]^{\nu''_{k_j}} \tag{3.113}$$

where K_{f_j} and K_{r_j} are the forward and backward reactions rate constants of reaction j. The modelling of these two terms represents a central problem in combustion.

Some reactions require a third-body to proceed, an example of such reaction is,

$$H + OH + M \Rightarrow H_2O + M \tag{3.114}$$

In these reactions, the molar concentration of the third-body species is computed by,

$$[M] = \sum_{k=1}^{N} \alpha_{k_j} [X_k] \tag{3.115}$$

where the coefficients α_{k_j} are referred to as third-body efficiencies of species k in reaction j. Unless otherwise specified, a third-body efficiency is assumed to be unity.

Both reaction rate constants are related together through an equilibrium constant defined by,

$$K_{r_j} = K_{f_j} K_j^{eq} \tag{3.116}$$

and computed as,

$$K_j^{eq} = \exp\left(\frac{\Delta S_j^0}{\mathcal{R}_u} - \frac{\Delta H_j^0}{\mathcal{R}_u T}\right)\left(\frac{P_0}{\mathcal{R}_u T}\right)^{\sum_{k=1}^{N}\left(\nu''_{k_j} - \nu'_{k_j}\right)} \tag{3.117}$$

where $P_0 = 1\,[atm]$, ΔH_j^0 and ΔS_j^0 refer to the enthalpy (sum of sensible and chemical) and entropy changes during reaction j, and are given by,

$$\Delta H_j^0 = \sum_{k=1}^{N}\left(\nu''_{k_j} - \nu'_{k_j}\right) W_k \left(h_k\left(T\right) - \Delta h_{f_k}^0\right) \tag{3.118}$$

$$\Delta S_j^0 = \sum_{k=1}^{N}\left(\nu''_{k_j} - \nu'_{k_j}\right) s_k\left(T\right) \tag{3.119}$$

where s_k is the entropy of species k computed using JANAF tables [59].

In its simplest formulation, the forward rate constant is modelled by an empirical Arrhenius law given by,

$$K_{f_j} = A_{f_j} T^{\beta_j} \exp\left(-\frac{E_{a_j}}{RT}\right) \tag{3.120}$$

where A_{f_j} is the pre-exponential factor, β_j the temperature exponent and E_{a_j} the activation energy. Appendix B presents the chemical mechanisms used throughout this work.

The net heat release due to chemical reactions is simply computed as the sum of the production rate of each species times its formation enthalpy. It reads,

$$\dot{\omega}_T = \sum_{k=1}^{N} \Delta h_{f_k}^0 \dot{\omega}_k \tag{3.121}$$

Volume fraction formulations

Similarly to the analysis conducted in §. 3.5.1, the energy source term does not change from the FCMF formulation when using the QCVF or FCVF models. For the same reason, the volume fraction source term for the QCVF model reads,

$$\left(\dot{\omega}_k\right)^z = \frac{1}{\rho_k}\dot{\omega}_k \tag{3.122}$$

and, for the FCVF model we have,

$$\left(\dot{\omega}_k\right)^\rho = 0 \tag{3.123}$$

3.6 Full equation sets

The full equation sets for the four different approaches are now written in full, more details can be found in the previous sections.

The momentum and energy conservation equations are similar in all models and read,

$$\frac{\partial \rho \mathbf{u}}{\partial t} + \nabla \cdot \left(\rho \mathbf{u}\mathbf{u}\right) = -P\underline{\mathbf{I}} + \nabla \cdot \underline{\boldsymbol{\tau}} \tag{3.124}$$

$$\frac{\partial \rho E}{\partial t} + \nabla \cdot \left[\left(\rho E + P\right)\mathbf{u}\right] = \nabla \cdot \left(\underline{\boldsymbol{\tau}} \cdot \mathbf{u}\right) - \nabla \cdot \mathbf{q}_c - \nabla \cdot \mathbf{q}_d + \dot{\omega}_T \tag{3.125}$$

Species transport differs between models,

- *Quasi- and Fully-Conservative Mass Fraction* (QCMF and FCMF)

$$\frac{\partial \rho Y_k}{\partial t} + \nabla \cdot (\rho Y_k \mathbf{u}) = -\nabla \cdot \mathbf{J}_k + \dot{\omega}_k \tag{3.126}$$

- *Quasi-Conservative Volume Fraction* (QCVF)

$$\begin{cases} \dfrac{\partial \rho_k z_k}{\partial t} + \nabla \cdot (\rho_k z_k \mathbf{u}) = -\nabla \cdot \mathbf{J}_k + \dot{\omega}_k \\ \dfrac{\partial z_k}{\partial t} + \mathbf{u} \cdot \nabla z_k = -\dfrac{1}{\rho_k} \nabla \cdot \mathbf{J}_k + \dfrac{1}{\rho_k} \dot{\omega}_k \end{cases} \tag{3.127}$$

- *Fully-Conservative Volume Fraction* (FCVF)

$$\begin{cases} \dfrac{\partial \rho_k z_k}{\partial t} + \nabla \cdot (\rho_k z_k \mathbf{u}) = -\nabla \cdot \mathbf{J}_k + \dot{\omega}_k \\ \dfrac{\partial \rho_k}{\partial t} + \nabla \cdot (\rho_k \mathbf{u}) = 0 \end{cases} \tag{3.128}$$

3.7 Filtered equations for LES

This section aims at introducing the filtered equations solved by the code `FlAMEnCo3D` for reacting turbulent flows. Closures associated with the unclosed turbulent terms are also discussed.

The LES approach, as already pointed out, is based on the filtering of the governing equations separating the large (resolved) scales from the small (unresolved) ones which are smaller than the filter size $\bar{\Delta}$ and whose effects have to be modelled. A brief introduction to the filtering procedure is given before a presentation of the filtered equations and associated closures of the Subgrid Scale (SGS) terms.

3.7.1 Low-pass filtering procedure

The spatial filtering operation for a quantity φ is defined as,

$$\bar{\varphi}(\mathbf{x}) = \int_{-\infty}^{+\infty} \varphi(\mathbf{x}) \mathcal{F}(\mathbf{x} - \mathbf{x}^*) \, \mathrm{d}\mathbf{x}^* \tag{3.129}$$

where $\mathcal{F}$ is the LES filter. With this operator, one can define the Reynolds decomposition of φ into a sum of filtered and sub-filtered parts as follows,

$$\varphi = \bar{\varphi} + \varphi' \tag{3.130}$$

where φ' is the sub-filter part. To manipulate the Navier-Stokes equations, three properties are required for this procedure :

- *Consistency* : The filtering of a constant is the constant itself,

$$\bar{a} = a \Leftrightarrow \int_{-\infty}^{+\infty} \mathcal{F}(\mathbf{x} - \mathbf{x}^*) \, \mathrm{d}\mathbf{x}^* = 1 \tag{3.131}$$

- *Linearity* : $\overline{\varphi + \psi} = \bar{\varphi} + \bar{\psi}$
- *Commutation with differentiation* : Commute in both time and space with partial differentiation,

$$\overline{\frac{\partial \varphi}{\partial x}} = \frac{\partial \overline{\varphi}}{\partial x} \tag{3.132}$$

The most commonly used filters are the sharp cut-off filter in wavenumber space, and the Gaussian and top-hat filters in physical space. The Gaussian filter is defined by,

$$\mathcal{F}\left(\mathbf{x}-\mathbf{x}^{*}\right)=\left(\frac{6}{\pi\bar{\Delta}^{2}}\right)^{1/2}\exp\left(\frac{-6|x_{i}-x_{i}^{*}|^{2}}{\bar{\Delta}^{2}}\right) \tag{3.133}$$

where x_i and x_i^* are the coordinates of points $\mathbf{x}$ and $\mathbf{x}^*$. The top-hat filter is defined as,

$$\mathcal{F}\left(\mathbf{x}-\mathbf{x}^{*}\right)=\begin{cases}\dfrac{1}{\bar{\Delta}^{3}} & |x_{i}-x_{i}^{*}|\leqslant\dfrac{\bar{\Delta}}{2}\\[2ex] 0 & |x_{i}-x_{i}^{*}|\geqslant\dfrac{\bar{\Delta}}{2}\end{cases} \tag{3.134}$$

The most widely employed filtering in LES is the *implicit filtering*, in which the grid and discretisation operators are considered to be the filter, meaning that the filter width is taken as some multiple of the grid size and the effective subgrid model damps out solution content smaller than the filter size. In the *explicit filtering* approach, the filtering operation is separated from the grid and disretisation operators, in which case the filter size is completely determined by the user and independent of the mesh considered. As in most LES reported so far, an implicit filtering approach is considered in this work, with a filter size taken as $\bar{\Delta}=2\left(\Delta_{x}\Delta_{y}\Delta_{z}\right)^{1/3}$, where Δ_x, Δ_y and Δ_z are the cell dimensions in x, y and z directions respectively.

In the case of compressible equations, to avoid modelling the mass conservation equation SGS terms, a mass-weighted filtered procedure has been introduced by Favre, and is referred to as Favre filtering. It is defined by,

$$\bar{\rho}\tilde{\varphi}\left(\mathbf{x}\right)=\int_{-\infty}^{+\infty}\rho\varphi\left(\mathbf{x}\right)\mathcal{F}\left(\mathbf{x}-\mathbf{x}^{*}\right)\mathrm{d}\mathbf{x}^{*} \tag{3.135}$$

It can also be written as,

$$\tilde{\varphi}=\frac{\overline{\rho\varphi}}{\bar{\rho}} \tag{3.136}$$

This allows the filtered continuity equation to be closed exactly. The Favre decomposition into filtered and sub-filtered parts is given by,

$$\varphi=\tilde{\varphi}+\varphi'' \tag{3.137}$$

This operator is linear, but due to the presence of the density in the integral, it does not commute with partial derivatives, i.e.,

$$\widetilde{\frac{\partial\varphi}{\partial x}}\neq\frac{\partial\tilde{\varphi}}{\partial x} \tag{3.138}$$

The Favre-filtered equations are structurally similar to the unfiltered equations, with the notable exception of the SGS terms presence.

For compressible flows, the SGS terms are usually written as,

$$\overline{\rho\varphi\psi}=\bar{\rho}\widetilde{\varphi\psi}=\bar{\rho}\tilde{\varphi}\tilde{\psi}+\overline{\rho\varphi''\psi''} \tag{3.139}$$

$$=\bar{\rho}\tilde{\varphi}\tilde{\psi}+\underbrace{\bar{\rho}\left(\widetilde{\varphi\psi}-\tilde{\varphi}\tilde{\psi}\right)}_{\text{SGS term}} \tag{3.140}$$

The relevant quantities are thus filtered, Favre-filtered or evaluated in terms of filtered quantities to give, $\overline{\varphi}$, $\tilde{\varphi}$ and $\hat{\varphi}$ respectively.

3.7.2 Filtered momentum equation

The unfiltered momentum equation is given in Eq. 3.124 and when filtered, yields,

$$\frac{\partial \bar{\rho}\tilde{\mathbf{u}}}{\partial t} + \nabla \cdot (\bar{\rho}\tilde{\mathbf{u}}\tilde{\mathbf{u}}) = -\nabla \cdot \bar{P} + \nabla \cdot \hat{\underline{\boldsymbol{\tau}}} - \underbrace{\nabla \cdot \left[\bar{\rho}\left(\widetilde{\mathbf{u}\mathbf{u}} - \tilde{\mathbf{u}}\tilde{\mathbf{u}}\right)\right]}_{(\mathbf{I})} + \underbrace{\nabla \cdot \left(\bar{\underline{\boldsymbol{\tau}}} - \hat{\underline{\boldsymbol{\tau}}}\right)}_{(\mathbf{II})} \tag{3.141}$$

where $\bar{\rho}\left(\widetilde{\mathbf{u}\mathbf{u}} - \tilde{\mathbf{u}}\tilde{\mathbf{u}}\right) = \underline{\boldsymbol{\tau}}_t$ is the SGS stress tensor (also referred to as the Reynolds stresses).

3.7.3 Filtered mass fraction transport equation

The unfiltered conservation of the mass of each species is given by Eq. 3.126 and when filtered, reads,

$$\frac{\partial \bar{\rho}\tilde{Y}_k}{\partial t} + \nabla \cdot \left(\bar{\rho}\tilde{Y}_k\tilde{\mathbf{u}}\right) = -\nabla \cdot \hat{\mathbf{J}}_k - \underbrace{\nabla \cdot \left[\bar{\rho}\left(\widetilde{Y_k\mathbf{u}} - \tilde{Y}_k\tilde{\mathbf{u}}\right)\right]}_{(\mathbf{III})} + \underbrace{\bar{\dot{\omega}}_k}_{(\mathbf{IV})} \tag{3.142}$$

3.7.4 Filtered volume fraction transport equation

The filtering of the volume fraction transport equation, but also the species mass transport written with the new set of variable is not straightforward, and remains an open question. Furthermore, to the author's knowledge, such filtering of the volume fraction equations has not been presented in the literature before. The approach taken here represents a first approximation that still requires validation.

By following the idea behind the definition of the source and diffusion terms for the volume fraction (§. 3.5.1 and §. 3.5.4), where $\dot{\omega}^z = \frac{1}{\rho_k}\dot{\omega}_k$, the filtered volume fraction transport could be written as,

$$\frac{\partial \tilde{z}_k}{\partial t} + \tilde{u} \cdot \nabla \tilde{z}_k = -\frac{1}{\overline{\rho}_k}\nabla \cdot \hat{\mathbf{J}}_k + \frac{1}{\overline{\rho}_k}\overline{\dot{\omega}}_k - \frac{1}{\overline{\rho}_k}\underbrace{\nabla \cdot \left[\bar{\rho}\left(\widetilde{Y_k\mathbf{u}} - \tilde{Y}_k\tilde{\mathbf{u}}\right)\right]}_{(\mathbf{III})} \tag{3.143}$$

where,

$$\frac{\overline{\rho Y_k}}{\overline{\rho}} = \frac{\overline{\rho_k z_k}}{\overline{\rho}} \tag{3.144}$$

and where it is assumed that it can be re-written as,

$$\overline{\rho}\tilde{Y}_k = \overline{\rho}_k \tilde{z}_k \tag{3.145}$$

which is not entirely satisfactory, but is used as a first approximation nonetheless in the present work.

A different filtering approach might be needed to derive a filtered version of these equations in a more consistent way, and could be based on a volume weighted filter instead of the density-based Favre filtering technique. Additionally, it is worth highlighting that the closure proposed here for the volume fraction unclosed terms could only be validated correctly through a DNS simulation employing a similar equation set. This would allow an accurate measurement of the SGS terms and the derivation of a more consistent SGS model, if needed.

3.7.5 Filtered energy equation

The total non-chemical energy is defined in §. 3.2 and its transport equation is given in Eq. 3.125. The Favre averaging of the momentum and mass transport equations was relatively straightforward, but such

is not the case for the energy equation. Indeed, the application of the filtering operator to the energy definition would lead to,

$$\overline{\rho}\tilde{E} = \overline{\rho}\tilde{\varepsilon} + \frac{1}{2}\overline{\rho}\widetilde{\mathbf{u}\mathbf{u}} \tag{3.146}$$

which cannot be directly computed. Several techniques have been used to circumvent this problem by using a modified form of the energy taking into account the SGS kinetic energy, which implies that pressure and temperature calculations from the total energy have to be adapted to the new formulation. On the other hand, by keeping the EoS untouched, a change of variable could be applied to the pressure, but recovering the actual pressure would be made difficult [287].

Another solution have been proposed by Vreman *et al.* [287] and adopted in this work, where an equation is derived for a computable total non-chemical energy (Eq. 3.147) by adding the filtered kinetic-energy equation to the filtered equation for internal energy.

$$\widehat{\rho E} = \bar{\rho}\tilde{\varepsilon} + \frac{1}{2}\bar{\rho}\tilde{\mathbf{u}}\tilde{\mathbf{u}} \tag{3.147}$$

The filtered total non-chemical energy equation thus reads,

$$\begin{aligned}\frac{\partial \widehat{\rho E}}{\partial t} + \nabla \cdot \left[\left(\widehat{\rho E} + \bar{P}\right)\tilde{\mathbf{u}}\right] &= \nabla \cdot (\hat{\underline{\boldsymbol{\tau}}}\tilde{\mathbf{u}}) - \nabla \cdot \hat{\mathbf{q}}_c + \nabla \cdot \hat{\mathbf{q}}_d \\ &\quad - \mathcal{B}_1 - \mathcal{B}_2 - \mathcal{B}_3 + \mathcal{B}_4 + \mathcal{B}_5 + \mathcal{B}_6 - \mathcal{B}_7 + \bar{\dot{\omega}}_T\end{aligned} \tag{3.148}$$

where the $\mathcal{B}_i$ terms are defined as follows,

$$\textbf{(V)} \quad \bar{\dot{\omega}}_T = -\sum_{k=1}^{N} \Delta h^0_{f_k} \bar{\dot{\omega}}_k \tag{3.149}$$

$$\textbf{(VI)} \quad \mathcal{B}_1 = \nabla \cdot \left[\bar{\rho}\left(\widetilde{\varepsilon\mathbf{u}} - \tilde{\varepsilon}\tilde{\mathbf{u}}\right)\right] \tag{3.150}$$

$$\textbf{(VII)} \quad \mathcal{B}_2 = \overline{P\nabla \cdot \mathbf{u}} - \bar{P}\nabla \cdot \tilde{\mathbf{u}} \tag{3.151}$$

$$\textbf{(VIII)} \quad \mathcal{B}_3 = \nabla \cdot (\underline{\boldsymbol{\tau}}_t \cdot \tilde{\mathbf{u}}) \tag{3.152}$$

$$\textbf{(IX)} \quad \mathcal{B}_4 = \underline{\boldsymbol{\tau}}_t \cdot \nabla \cdot \tilde{\mathbf{u}} \tag{3.153}$$

$$\textbf{(X)} \quad \mathcal{B}_5 = \overline{\underline{\boldsymbol{\tau}} \cdot \nabla \cdot \mathbf{u}} - \bar{\underline{\boldsymbol{\tau}}} \cdot \nabla \cdot \tilde{\mathbf{u}} \tag{3.154}$$

$$\textbf{(XI)} \quad \mathcal{B}_6 = \nabla \cdot (\bar{\underline{\boldsymbol{\tau}}} \cdot \tilde{\mathbf{u}} - \hat{\underline{\boldsymbol{\tau}}} \cdot \tilde{\mathbf{u}}) \tag{3.155}$$

$$\textbf{(XII)} \quad \mathcal{B}_7 = \nabla \cdot (\bar{\mathbf{q}}_c - \hat{\mathbf{q}}_c) \tag{3.156}$$

3.7.6 Unclosed terms

A summary of the SGS terms, denoted in the previous paragraphs by **I** – **XII**, is given here. They represent the interaction between the resolved and unresolved scales, but also between unresolved scales. As such, they cannot be directly computed using the filtered flow variables and need to be modelled.

It is worth mentioning that fluctuations of the transport coefficients have been neglected in the filtered equations derivation, and it follows that these coefficients can directly be computed from filtered quantities (temperature, mass fractions, etc.).

The unclosed terms are as follows,

- (**I**) : Non-linearity of the convective terms, SGS viscous stresses (**Modelled**)
- (**II**) : Term due to the non-linearity of the viscous stresses and the non-commutation property of the Favre filtering procedure. Usually neglected under the assumption $\bar{\underline{\boldsymbol{\tau}}} - \hat{\underline{\boldsymbol{\tau}}} = 0$. *A priori* tests by Vreman *et al.* [287] show that it is a least an order of magnitude lower than (**I**) (*Neglected*)

- (**III**) : SGS flux of species mass fractions (**Modelled**)
- (**IV**) : Filtered reaction rate of the species (**Modelled**)
- (**V**) : Filtered energy source term, essentially depends on the model chosen for $\bar{\dot{\omega}}_k$ (**Modelled**)
- (**VI**) : SGS flux of internal energy (**Modelled**)
- (**VII**) : SGS pressure dilatation (pure compressible term) (**Modelled**)
- (**VIII**) : SGS viscous fluxes (transfer of kinetic energy from the resolved scales to the SGS) (**Modelled**)
- (**IX**) : SGS viscous fluxes (transfer of kinetic energy from the resolved scales to the SGS) (**Modelled**)
- (**X**) : SGS viscous dissipation (conversion of the SGS kinetic energy into internal energy) (*Neglected* [287])
- (**XI**) : Non-linearity of the viscous stresses, similar to (**II**) (*Neglected* [287])
- (**XII**) : Non-linearity of the heat fluxes, neglected under the assumption that the second order spatial derivative of temperature are much larger than the second order derivative of its fluctuations (*Neglected* [287])

3.7.7 Closure for SGS terms

Reynolds stresses terms

In this work, the novel reconstruction method proposed by Thornber *et al.* [275, 276] is employed to model **I**, **VIII** and **IX**. The numerical method employed does not conserve kinetic energy, rather the reconstruction is designed to give a leading order dissipation of the TKE proportional to the velocity increment at the cell interface $\left(\Delta u^3\right)$ as defined in Kolmogorov analysis. This new method also improves the behaviour of the Godunov method at high wave-numbers, and acts as an implicit subgrid model [86, 113], while retaining monotonicity. By further making the assumption that the implicit dissipation introduced by the numerical method is sufficient to model the dissipation of TKE, all the terms related to the Reynolds stresses can be neglected.

SGS scalar transport

These terms represent the transport of scalar quantities (internal energy and species mass fractions) by subgrid-scale turbulent motions. They are usually modelled using a gradient hypothesis coupled with *a priori* specified turbulent Schmidt (Sc_t) and Prandtl (Pr_t) numbers.

For the mass fraction equation, we have **III** modelled by,

$$\bar{\rho}\left(\widetilde{Y_k\mathbf{u}} - \tilde{Y}_k\tilde{\mathbf{u}}\right) = \hat{\mathbf{J}}_k^t = -\frac{\bar{\rho}\hat{\nu}_t}{Sc_t}\frac{W_k}{W}\nabla\tilde{X}_k \tag{3.157}$$

By regrouping the internal energy and pressure SGS dilatation, we find that the subgrid scalar quantity transported is the sensible enthalpy, and thus, the modelling of **VI** and **VII** is expressed as,

$$\nabla\cdot\left[\bar{\rho}\left(\widetilde{\varepsilon\mathbf{u}} - \tilde{\varepsilon}\tilde{\mathbf{u}}\right)\right] + \overline{P\nabla\cdot\mathbf{u}} - \bar{P}\nabla\cdot\tilde{\mathbf{u}} = -\nabla\cdot\left(\frac{\bar{\rho}\hat{\nu}_t\hat{C}_p}{Pr_t}\nabla\tilde{T}\right) \tag{3.158}$$

The turbulent diffusion coefficient has been modelled in this work using the Smagorinsky [261] model described by,

$$\hat{\nu}_t = \left(C_s\bar{\Delta}\right)^2\sqrt{2\hat{\underline{\mathbf{S}}}:\hat{\underline{\mathbf{S}}}} = \left(C_s\bar{\Delta}\right)^2|\hat{\mathbf{S}}| \tag{3.159}$$

where C_s is the Smagorinsky constant is usually found between 0.1 and 0.25. In general this model assumes that production and destruction of TKE are in equilibrium. Its main limitation resides in the *a priori* specification of the constant that varies under different flow conditions. Additionally, it does not have the correct limiting behaviour near walls, but it is a widely used model that gives reasonable results. Otherwise stated, $C_s = 0.16$ in this work.

3.7.8 Source term modelling

The heat release term is given by Eq. 3.121. Hence, it only depends on the modelling of the individual species reaction rates. The modelling of the turbulent reaction rate is discussed in §. 2.2.2 for the different modelling approaches and in §. 7.3.3 for an emphasis on the FSD in particular.

3.8 Conclusion

In this chapter, the different equations considered in this work to simulate compressible reacting multi-component flows have been presented in details.

Amongst the numerous modern models published to tackle the problem of spurious pressure oscillations appearance at species interfaces when using a shock-capturing model, a few have been extended to deal with thermal perfect gas effects and two only applied in reacting flows [6, 147, 270]. The selection of the models retained for this work is presented in §. 3.1.1, while numerous definitions of flow variables and thermodynamic coefficients for multi-component flows are given (§. 3.1.2).

The next sections present the hyperbolic operator of each equation sets retained for this work, namely the Euler equations (§. 3.2) and volume fraction based model of Allaire *et al.* [7] (§. 3.3.1 and §. 3.3.2). An in-depth description of the different equations of state and thermodynamic closures considered for this problem (§. 3.4) follows, namely the calorically perfect and thermally perfect gas models, the classical isothermal closure and the isobaric closure introduced by Allaire *et al.* [7] for the volume fraction formulation.

The definitions of viscous and reacting terms to augment the Euler equations to form the Navier-Stokes equations have been discussed in §. 3.5. At the same time, the new terms introduced by the author in the volume fraction transport equation sets to account for diffusion and reactions mechanisms are also derived and discussed. The computation of the different transport coefficients (viscosity, species diffusion, etc.) is then highlighted in addition to the different assumptions considered in this work (constant Pr number, constant but non-unity species Le number, etc.).

A brief summary of all equations sets is provided in §. 3.6 where it is highlighted that all models considered rely on similar momentum and energy conservation equations, but differ by the way species transport is accounted for (mass fraction, volume fraction, etc.).

Finally, the LES filtering operation is introduced and the different filtered governing equations are presented along with the new unclosed terms arising from the filtering (§. 3.7). A review of the different subgrid terms follows where it is explained whether they are neglected or modelled, in which case the corresponding model is discussed.

CHAPTER 4

Numerical methods

This chapters presents in details the numerical methods considered in this work to solve the governing equations presented in the previous chapter (Chapter 3). The main method used is the so-called finite-volume Godunov method presented by Godunov [109]. It constitutes one of the most widely considered approach for the solution calculation of numerous systems of hyperbolic equations. It is massively used thanks to its robustness and its low computational requirements.

One of the main advantage of such approach is its behaviour in the vicinity of discontinuities such as shock waves as it allows their capture without special treatments such as local diffusivity, etc. In fact, only methods based on the conservative variables are able to accurately predict a shock speed and its strength [278], which is further emphasized by the well known conclusions of Lax and Wendroff [174] stating that if a conservative method is convergent it does converge on the weak solution of the conservation laws. As this work is concerned with the simulation of compressible combustion, shock waves are one of the main features that need to be captured and accurately simulated, thus explaining the use of the Godunov method.

The first part of the chapter presents the coordinate transformation from the Cartesian based system to a curvilinear body-fitted system. A second part discusses the integration of the hyperbolic operator, while a third part details the integration of both the viscous and source terms. The time-stepping algorithms considered in this work will then be presented as well as the boundary conditions.

4.1 Generalised Curvilinear Coordinates

4.1.1 Definitions

The general approach used in this work to deal with non-Cartesian geometries consists in the application of a transformation from the physical Cartesian coordinates (x, y, z) to a body-fitted curvilinear frame of reference (also referred to as *computational frame of reference*, denoted by (ξ, η, ζ)).

The general transformation of coordinates can be expressed considering the invertible mapping Ξ transforming the physical $\mathbf{X}(x, y, z, t)$ to the computational $\mathbf{x}(\xi, \eta, \zeta, \tau)$ space,

$$\Xi : \mathbf{X} \mapsto \mathbf{x} \tag{4.1}$$

The transformation can thus be written as,

$$\begin{cases} \xi = \xi(x, y, z, t) \\ \eta = \eta(x, y, z, t) \\ \zeta = \zeta(x, y, z, t) \\ \tau = \tau(t) \end{cases} \tag{4.2}$$

Using the chain rule of differentiation, partial derivatives needed in the governing equations are expressed as,

$$\frac{\partial}{\partial x} = \frac{\partial}{\partial \xi}\frac{\partial \xi}{\partial x} + \frac{\partial}{\partial \eta}\frac{\partial \eta}{\partial x} + \frac{\partial}{\partial \zeta}\frac{\partial \zeta}{\partial x} \tag{4.3}$$

$$\frac{\partial}{\partial y} = \frac{\partial}{\partial \xi}\frac{\partial \xi}{\partial y} + \frac{\partial}{\partial \eta}\frac{\partial \eta}{\partial y} + \frac{\partial}{\partial \zeta}\frac{\partial \zeta}{\partial y} \tag{4.4}$$

$$\frac{\partial}{\partial z} = \frac{\partial}{\partial \xi}\frac{\partial \xi}{\partial z} + \frac{\partial}{\partial \eta}\frac{\partial \eta}{\partial z} + \frac{\partial}{\partial \zeta}\frac{\partial \zeta}{\partial z} \tag{4.5}$$

$$\frac{\partial}{\partial t} = \frac{\partial}{\partial \xi}\frac{\partial \xi}{\partial t} + \frac{\partial}{\partial \eta}\frac{\partial \eta}{\partial t} + \frac{\partial}{\partial \zeta}\frac{\partial \zeta}{\partial t} + \frac{\partial}{\partial \tau} \tag{4.6}$$

Considering that this work is solely concerned with non-moving grids, it follows,

$$\frac{\partial \xi}{\partial t} = \frac{\partial \eta}{\partial t} = \frac{\partial \zeta}{\partial t} = 0 \tag{4.7}$$

and the mapping between the computational and physical time is the identity, $t = \tau$.

The two coordinate systems are thus related by,

$$\begin{pmatrix} \mathrm{d}x \\ \mathrm{d}y \\ \mathrm{d}z \end{pmatrix} = \begin{pmatrix} \frac{\partial x}{\partial \xi} & \frac{\partial x}{\partial \eta} & \frac{\partial x}{\partial \zeta} \\ \frac{\partial y}{\partial \xi} & \frac{\partial y}{\partial \eta} & \frac{\partial y}{\partial \zeta} \\ \frac{\partial z}{\partial \xi} & \frac{\partial z}{\partial \eta} & \frac{\partial z}{\partial \zeta} \end{pmatrix} \begin{pmatrix} \mathrm{d}\xi \\ \mathrm{d}\eta \\ \mathrm{d}\zeta \end{pmatrix} = \begin{pmatrix} x_\xi & x_\eta & x_\zeta \\ y_\xi & y_\eta & y_\zeta \\ z_\xi & z_\eta & z_\zeta \end{pmatrix} \begin{pmatrix} \mathrm{d}\xi \\ \mathrm{d}\eta \\ \mathrm{d}\zeta \end{pmatrix} \tag{4.8}$$

where the tensor of the transformation is related to the tensor of the inverse transformation by,

$$\begin{pmatrix} x_\xi & x_\eta & x_\zeta \\ y_\xi & y_\eta & y_\zeta \\ z_\xi & z_\eta & z_\zeta \end{pmatrix}^{-1} = \begin{pmatrix} \xi_x & \xi_y & \xi_z \\ \eta_x & \eta_y & \eta_z \\ \zeta_x & \zeta_y & \zeta_z \end{pmatrix} \tag{4.9}$$

Using matrix algebra, the inverse of a matrix is calculated as $\underline{\mathbf{A}}^{-1} = \mathrm{adj}\,\underline{\mathbf{A}}/|\underline{\mathbf{A}}|$. Applying this rule to Eq. 4.9 yields,

$$\begin{pmatrix} \xi_x & \xi_y & \xi_z \\ \eta_x & \eta_y & \eta_z \\ \zeta_x & \zeta_y & \zeta_z \end{pmatrix} = \frac{1}{J} \begin{pmatrix} y_\eta z_\zeta - y_\zeta z_\eta & -(x_\eta z_\zeta - x_\zeta z_\eta) & x_\eta y_\zeta - x_\zeta y_\eta \\ -(y_\xi z_\zeta - y_\zeta z_\xi) & x_\xi z_\zeta - x_\zeta z_\xi & -(x_\xi y_\zeta - x_\zeta y_\xi) \\ y_\xi z_\eta - y_\eta z_\xi & -(x_\xi z_\eta - x_\eta z_\xi) & x_\xi y_\eta - x_\eta y_\xi \end{pmatrix} \tag{4.10}$$

where J is the jacobian of the transformation, calculated as the determinant of the matrix, given by,

$$J = x_\xi \left(y_\eta z_\zeta - y_\zeta z_\eta\right) + x_\eta \left(y_\zeta z_\xi - y_\xi z_\zeta\right) + x_\zeta \left(y_\xi z_\eta - y_\eta z_\xi\right) \tag{4.11}$$

The derivatives of the curvilinear coordinates (ξ, η, η) according to the Cartesian coordinates (x, y, z) can be approximated numerically in the cell centres and cell faces.

4.1.2 Governing equations in the Generalised Curvilinear Coordinates system

It is worth reminding the reader that the governing equations for all approaches can be written in a compact form, at the exception of the volume fraction transport for the QCVF model (Eq. 3.127). Without loss of generality, it is reminded below for the Navier-Stokes equations (also referred to as the FCMF or QCMF models in this work),

$$\frac{\partial \mathbf{U}}{\partial t} + \frac{\partial \mathbf{F_i}}{\partial x} + \frac{\partial \mathbf{G_i}}{\partial y} + \frac{\partial \mathbf{H_i}}{\partial z} = \frac{\partial \mathbf{F_v}}{\partial x} + \frac{\partial \mathbf{G_v}}{\partial y} + \frac{\partial \mathbf{H_v}}{\partial z} + \mathbf{S} \tag{4.12}$$

where the conservative variables are given by,

$$\mathbf{U} = [\rho Y_k,\ \rho u,\ \rho v,\ \rho w,\ \rho E]^T \tag{4.13}$$

the hyperbolic fluxes by,

$$\mathbf{F_i} = \left[\rho Y_k u,\ \rho u^2 + P,\ \rho uv,\ \rho uw,\ (\rho E + P)\, u\right]^T \tag{4.14}$$

$$\mathbf{G_i} = \left[\rho Y_k v,\ \rho uv,\ \rho v^2 + P,\ \rho vw,\ (\rho E + P)\, v\right]^T \tag{4.15}$$

$$\mathbf{H_i} = \left[\rho Y_k w,\ \rho uw,\ \rho vw,\ \rho w^2 + P,\ (\rho E + P)\, w\right]^T \tag{4.16}$$

the viscous fluxes as,

$$\mathbf{F_v} = [J_{k_x},\ \tau_{xx},\ \tau_{xy},\ \tau_{xz},\ u\tau_{xx} + v\tau_{xy} + w\tau_{xz} - q_{c_x} - q_{d_x}]^T \tag{4.17}$$

$$\mathbf{G_v} = \left[J_{k_y},\ \tau_{xy},\ \tau_{yy},\ \tau_{yz},\ u\tau_{xy} + v\tau_{yy} + w\tau_{yz} - q_{c_y} - q_{d_y}\right]^T \tag{4.18}$$

$$\mathbf{H_v} = [J_{k_z},\ \tau_{xz},\ \tau_{yz},\ \tau_{zz},\ u\tau_{xz} + v\tau_{yz} + w\tau_{zz} - q_{c_z} - q_{d_z}]^T \tag{4.19}$$

and finally the source term as,

$$\mathbf{S} = [\dot{\omega}_k,\ 0,\ 0,\ 0,\ \dot{\omega}_T]^T \tag{4.20}$$

where the vectors $\mathbf{J}_k$, $\mathbf{q}_c$ and $\mathbf{q}_d$, the matrix $\underline{\boldsymbol{\tau}}$ are all defined in §. 3.5.

By using the chain-rule on Eq. 4.12 and multiplying by the Jacobian we obtain,

$$\begin{aligned}
&J\frac{\partial \mathbf{U}}{\partial t} + J\xi_x\frac{\partial \mathbf{F_i}}{\partial \xi} + J\eta_x\frac{\partial \mathbf{F_i}}{\partial \eta} + J\zeta_x\frac{\partial \mathbf{F_i}}{\partial \zeta} \\
&\quad + J\xi_y\frac{\partial \mathbf{G_i}}{\partial \xi} + J\eta_y\frac{\partial \mathbf{G_i}}{\partial \eta} + J\zeta_y\frac{\partial \mathbf{G_i}}{\partial \zeta} \\
&\quad + J\xi_z\frac{\partial \mathbf{H_i}}{\partial \xi} + J\eta_z\frac{\partial \mathbf{H_i}}{\partial \eta} + J\zeta_z\frac{\partial \mathbf{H_i}}{\partial \zeta} = \quad J\xi_x\frac{\partial \mathbf{F_v}}{\partial \xi} + J\eta_x\frac{\partial \mathbf{F_v}}{\partial \eta} + J\zeta_x\frac{\partial \mathbf{F_v}}{\partial \zeta} \\
&\qquad\qquad + J\xi_y\frac{\partial \mathbf{G_v}}{\partial \xi} + J\eta_y\frac{\partial \mathbf{G_v}}{\partial \eta} + J\zeta_y\frac{\partial \mathbf{G_v}}{\partial \zeta} \\
&\qquad\qquad + J\xi_z\frac{\partial \mathbf{H_v}}{\partial \xi} + J\eta_z\frac{\partial \mathbf{H_v}}{\partial \eta} + J\zeta_z\frac{\partial \mathbf{H_v}}{\partial \zeta} \\
&\qquad\qquad + \ J\mathbf{S}
\end{aligned} \tag{4.21}$$

where all previous terms can be expanded as,

$$J\xi_x\frac{\partial \mathbf{F_i}}{\partial \xi} = \frac{\partial J\xi_x \mathbf{F_i}}{\partial \xi} - \mathbf{F_i}\frac{\partial J\xi_x}{\partial \xi} \tag{4.22}$$

Using this expansion and re-arranging the previous equation with all the terms on the left-hand side, one obtains,

$$\begin{aligned}
&J\frac{\partial \mathbf{U}}{\partial t} + \frac{\partial}{\partial \xi}\left(J\xi_x\mathbf{F_i} + J\xi_y\mathbf{G_i} + J\xi_z\mathbf{H_i} - J\xi_x\mathbf{F_v} - J\xi_y\mathbf{G_v} - J\xi_z\mathbf{H_v}\right) \\
&\quad + \frac{\partial}{\partial \eta}\left(J\eta_x\mathbf{F_i} + J\eta_y\mathbf{G_i} + J\eta_z\mathbf{H_i} - J\eta_x\mathbf{F_v} - J\eta_y\mathbf{G_v} - J\eta_z\mathbf{H_v}\right) \\
&\quad + \frac{\partial}{\partial \zeta}\left(J\zeta_x\mathbf{F_i} + J\zeta_y\mathbf{G_i} + J\zeta_z\mathbf{H_i} - J\zeta_x\mathbf{F_v} - J\zeta_y\mathbf{G_v} - J\zeta_z\mathbf{H_v}\right) \\
&\quad - \mathbf{F_i}\left(\frac{\partial J\xi_x}{\partial \xi} + \frac{\partial J\eta_x}{\partial \eta} + \frac{\partial J\zeta_x}{\partial \zeta}\right) + \mathbf{F_v}\left(\frac{\partial J\xi_x}{\partial \xi} + \frac{\partial J\eta_x}{\partial \eta} + \frac{\partial J\zeta_x}{\partial \zeta}\right) \\
&\quad - \mathbf{G_i}\left(\frac{\partial J\xi_y}{\partial \xi} + \frac{\partial J\eta_y}{\partial \eta} + \frac{\partial J\zeta_y}{\partial \zeta}\right) + \mathbf{G_v}\left(\frac{\partial J\xi_y}{\partial \xi} + \frac{\partial J\eta_y}{\partial \eta} + \frac{\partial J\zeta_y}{\partial \zeta}\right) \\
&\quad - \mathbf{H_i}\left(\frac{\partial J\xi_z}{\partial \xi} + \frac{\partial J\eta_z}{\partial \eta} + \frac{\partial J\zeta_z}{\partial \zeta}\right) + \mathbf{H_v}\left(\frac{\partial J\xi_z}{\partial \xi} + \frac{\partial J\eta_z}{\partial \eta} + \frac{\partial J\zeta_z}{\partial \zeta}\right) \\
&\quad - J\mathbf{S} = 0
\end{aligned} \tag{4.23}$$

By further accounting for the fact that,

$$\frac{\partial J\xi_x}{\partial \xi} + \frac{\partial J\eta_x}{\partial \eta} + \frac{\partial J\zeta_x}{\partial \zeta} = 0 \tag{4.24}$$

$$\frac{\partial J\xi_y}{\partial \xi} + \frac{\partial J\eta_y}{\partial \eta} + \frac{\partial J\zeta_y}{\partial \zeta} = 0 \tag{4.25}$$

$$\frac{\partial J\xi_z}{\partial \xi} + \frac{\partial J\eta_z}{\partial \eta} + \frac{\partial J\zeta_z}{\partial \zeta} = 0 \tag{4.26}$$

we can simplify the previous expression,

$$\begin{aligned} J\frac{\partial \mathbf{U}}{\partial t} &+ \frac{\partial}{\partial \xi}\left(J\xi_x\mathbf{F_i} + J\xi_y\mathbf{G_i} + J\xi_z\mathbf{H_i}\right) \\ &+ \frac{\partial}{\partial \eta}\left(J\eta_x\mathbf{F_i} + J\eta_y\mathbf{G_i} + J\eta_z\mathbf{H_i}\right) \\ &+ \frac{\partial}{\partial \zeta}\left(J\zeta_x\mathbf{F_i} + J\zeta_y\mathbf{G_i} + J\zeta_z\mathbf{H_i}\right) = \quad \frac{\partial}{\partial \xi}\left(J\xi_x\mathbf{F_v} + J\xi_y\mathbf{G_v} + J\xi_z\mathbf{H_v}\right) \\ &\qquad + \frac{\partial}{\partial \eta}\left(J\eta_x\mathbf{F_v} + J\eta_y\mathbf{G_v} + J\eta_z\mathbf{H_v}\right) \\ &\qquad + \frac{\partial}{\partial \zeta}\left(J\zeta_x\mathbf{F_v} + J\zeta_y\mathbf{G_v} + J\zeta_z\mathbf{H_v}\right) \\ &\qquad + J\mathbf{S} \end{aligned} \tag{4.27}$$

The careful reader would recognise here a form similar to Eq. 4.12 in a curvilinear coordinate system with,

$$\frac{\partial J\mathbf{U}}{\partial t} + \frac{\partial J\mathbf{F_i^\xi}}{\partial \xi} + \frac{\partial J\mathbf{G_i^\eta}}{\partial \eta} + \frac{\partial J\mathbf{H_i^\zeta}}{\partial \zeta} = \frac{\partial J\mathbf{F_v^\xi}}{\partial \xi} + \frac{\partial J\mathbf{G_v^\eta}}{\partial \eta} + \frac{\partial J\mathbf{H_v^\zeta}}{\partial \zeta} + J\mathbf{S} \tag{4.28}$$

where the curvilinear hyperbolic fluxes are,

$$\begin{cases} \mathbf{F_i^\xi} = \xi_x\mathbf{F_i} + \xi_y\mathbf{G_i} + \xi_z\mathbf{H_i} \\ \mathbf{G_i^\eta} = \eta_x\mathbf{F_i} + \eta_y\mathbf{G_i} + \eta_z\mathbf{H_i} \\ \mathbf{G_i^\zeta} = \zeta_x\mathbf{F_i} + \zeta_y\mathbf{G_i} + \zeta_z\mathbf{H_i} \end{cases} \tag{4.29}$$

the curvilinear viscous fluxes become,

$$\begin{cases} \mathbf{F_v^\xi} = \xi_x\mathbf{F_v} + \xi_y\mathbf{G_v} + \xi_z\mathbf{H_v} \\ \mathbf{G_v^\eta} = \eta_x\mathbf{F_v} + \eta_y\mathbf{G_v} + \eta_z\mathbf{H_v} \\ \mathbf{G_v^\zeta} = \zeta_x\mathbf{F_v} + \zeta_y\mathbf{G_v} + \zeta_z\mathbf{H_v} \end{cases} \tag{4.30}$$

The system of governing equations is thus similar in the computational reference frame, the only difference residing in the expression of the fluxes and vector of conserved variables, now corresponding to a combination of the different physical fluxes. The fully developed system of equations is given below.

- Vector of conserved variables $\mathbf{U}$,

$$\mathbf{U} = \begin{pmatrix} \rho Y_k \\ \rho u \\ \rho v \\ \rho w \\ \rho E \end{pmatrix} \tag{4.31}$$

- Vectors of hyperbolic fluxes $\mathbf{F}_{\mathbf{i}}^{\xi}$, $\mathbf{G}_{\mathbf{i}}^{\eta}$ and $\mathbf{H}_{\mathbf{i}}^{\zeta}$,

$$\mathbf{F}_{\mathbf{i}}^{\xi} = \begin{pmatrix} \rho Y_k \left(u\xi_x + v\xi_y + w\xi_z\right) \\ \rho u \left(u\xi_x + v\xi_y + w\xi_z\right) + P\xi_x \\ \rho v \left(u\xi_x + v\xi_y + w\xi_z\right) + P\xi_y \\ \rho w \left(u\xi_x + v\xi_y + w\xi_z\right) + P\xi_z \\ \left(\rho E + P\right)\left(u\xi_x + v\xi_y + w\xi_z\right) \end{pmatrix} \tag{4.32}$$

$$\mathbf{G}_{\mathbf{i}}^{\eta} = \begin{pmatrix} \rho Y_k \left(u\eta_x + v\eta_y + w\eta_z\right) \\ \rho u \left(u\eta_x + v\eta_y + w\eta_z\right) + P\eta_x \\ \rho v \left(u\eta_x + v\eta_y + w\eta_z\right) + P\eta_y \\ \rho w \left(u\eta_x + v\eta_y + w\eta_z\right) + P\eta_z \\ \left(\rho E + P\right)\left(u\eta_x + v\eta_y + w\eta_z\right) \end{pmatrix} \tag{4.33}$$

$$\mathbf{H}_{\mathbf{i}}^{\zeta} = \begin{pmatrix} \rho Y_k \left(u\zeta_x + v\zeta_y + w\zeta_z\right) \\ \rho u \left(u\zeta_x + v\zeta_y + w\zeta_z\right) + P\zeta_x \\ \rho v \left(u\zeta_x + v\zeta_y + w\zeta_z\right) + P\zeta_y \\ \rho w \left(u\zeta_x + v\zeta_y + w\zeta_z\right) + P\zeta_z \\ \left(\rho E + P\right)\left(u\zeta_x + v\zeta_y + w\zeta_z\right) \end{pmatrix} \tag{4.34}$$

- Vectors of viscous fluxes $\mathbf{F}_{\mathbf{v}}^{\xi}$, $\mathbf{G}_{\mathbf{v}}^{\eta}$ and $\mathbf{H}_{\mathbf{v}}^{\zeta}$,

$$\mathbf{F}_{\mathbf{v}}^{\xi} = \begin{pmatrix} J_{k_x}\xi_x + J_{k_y}\xi_y + J_{k_z}\xi_z \\ \tau_{xx}\xi_x + \tau_{xy}\xi_y + \tau xz\xi_z \\ \tau_{xy}\xi_x + \tau_{yy}\xi_y + \tau yz\xi_z \\ \tau_{zx}\xi_x + \tau_{zy}\xi_y + \tau zz\xi_z \\ \beta_x\xi_x + \beta_y\xi_y + \beta_z\xi_z \end{pmatrix} \tag{4.35}$$

$$\mathbf{G}_{\mathbf{v}}^{\eta} = \begin{pmatrix} J_{k_x}\eta_x + J_{k_y}\eta_y + J_{k_z}\eta_z \\ \tau_{xx}\eta_x + \tau_{xy}\eta_y + \tau xz\eta_z \\ \tau_{xy}\eta_x + \tau_{yy}\eta_y + \tau yz\eta_z \\ \tau_{zx}\eta_x + \tau_{zy}\eta_y + \tau zz\eta_z \\ \beta_x\eta_x + \beta_y\eta_y + \beta_z\eta_z \end{pmatrix} \tag{4.36}$$

$$\mathbf{H}_{\mathbf{v}}^{\zeta} = \begin{pmatrix} J_{k_x}\zeta_x + J_{k_y}\zeta_y + J_{k_z}\zeta_z \\ \tau_{xx}\zeta_x + \tau_{xy}\zeta_y + \tau xz\zeta_z \\ \tau_{xy}\zeta_x + \tau_{yy}\zeta_y + \tau yz\zeta_z \\ \tau_{zx}\zeta_x + \tau_{zy}\zeta_y + \tau zz\zeta_z \\ \beta_x\zeta_x + \beta_y\zeta_y + \beta_z\zeta_z \end{pmatrix} \tag{4.37}$$

  where the energy equation right-hand side is given by $\beta_i = \tau_{ij}u_j - q_{c_i} - q_{d_i}$ where Einstein summation is used.

- Source term vector $\mathbf{S}$

$$\mathbf{S} = \begin{pmatrix} \dot{\omega}_k \\ 0 \\ 0 \\ 0 \\ \dot{\omega}_T \end{pmatrix} \tag{4.38}$$

4.2 The Godunov-type method

The finite-volume Godunov method is employed in this work to compute the governing equations solutions. This method was developed by Godunov [109] as an answer to the problem of conservation of the CIR method of Courant, Isaacson and Rees [173] applied to non-linear systems of hyperbolic laws. The general framework of the method is described here with the presentation of the Initial Boundary-Value Problem (IBVP) before a slight variation of it named the *method of lines* employed in this work is discussed. The interested reader should refer to Toro [278] for more information.

4.2.1 Initial Boundary-Value Problem

The IBVP represents the most general formulation of the Godunov method, and is briefly presented here in a one dimensional formulation as an introduction to the methodology. It can readily be extended to further space dimensions. The general IBVP for a system of hyperbolic conservation laws in a domain $x \in [0\,;\,l]$ is described by,

$$\frac{\partial \mathbf{U}}{\partial t} + \frac{\partial \mathbf{F}\left(\mathbf{U}\right)}{\partial x} = 0 \tag{4.39}$$

where the initial value is given by $\mathbf{U}\left(x,0\right) = \mathbf{U}^0\left(x\right)$, and the boundary values by $\mathbf{U}\left(0,t\right) = \mathbf{U}_L\left(t\right)$ and $\mathbf{U}\left(l,t\right) = \mathbf{U}_R\left(t\right)$.

To account for the presence of discontinuities in the solution, such as shocks, the integral form of the equations is retained in a control volume defined by $[x_1\,;\,x_2] \times [t_1\,;\,t_2]$,

$$\int_{x_1}^{x_2} \mathbf{U}\left(x,t_2\right) \mathrm{d}x = \int_{x_1}^{x_2} \mathbf{U}\left(x,t_1\right) \mathrm{d}x + \int_{t_1}^{t_2} \mathbf{F}\left(x_1,t\right) \mathrm{d}t - \int_{t_1}^{t_2} \mathbf{F}\left(x_2,t\right) \mathrm{d}t \tag{4.40}$$

The Godunov method is usually a two-step method, where the first step is referred to as the *reconstruction step*, whilst the second one is the resolution of the Riemann problem.

In the first step, an appropriate distribution of initial data is assumed at a given time t^n and denoted $\mathbf{U}\left(x,t^n\right)$. The flow variables are initialised in the discretised domain assuming a cell average value in each finite volumes, as illustrated on Fig. 4.2 and estimated by,

$$\mathbf{U}_i^n = \frac{1}{\Delta x} \int_{x_{i-1/2}}^{x_{i+1/2}} \mathbf{U}\left(x,t^n\right) \mathrm{d}x \tag{4.41}$$

The next step is to solve the IBVP described by Eq. 4.39 assuming the piecewise distribution of Eq. 4.41. This approach leads to the definition of local Riemann problems at each inter-cell boundaries with the left and right boundary values given respectively by $\mathbf{U}_i^n$ and $\mathbf{U}_{i+1}^n$, and further denoted by $\mathbf{RP}\left(\mathbf{U}_i^n, \mathbf{U}_{i+1}^n\right)$. The formulation of the inter-cell Riemann problem is given by,

$$\frac{\partial \mathbf{U}}{\partial t} + \frac{\partial \mathbf{F}}{\partial x} = 0 \tag{4.42}$$

$$\mathbf{U}\left(x,t^n\right) = \begin{cases} \mathbf{U}_i^n & x < x_{i+1/2} \\ \mathbf{U}_{i+1}^n & x > x_{i+1/2} \end{cases} \tag{4.43}$$

The general solution of the Riemann problem is a similarity solution depending only on the ratio x/t, and the boundaries given by $\mathbf{U}_L$ and $\mathbf{U}_R$. A typical situation of two Riemann problems at the left and right of a given volume is presented in Fig. 4.1.

Assuming that the time-step is chosen to avoid interactions between the wave emerging from both sides of the cell, the global solution $\mathbf{U}(x,t)$, with $x \in [0\,;\,l]$ and $t \in \left[t^n\,;\,t^{n+1}\right]$ as a function of the Riemann solution gives,

$$\mathbf{U}(x,t) = \mathbf{U}^n_{i+1/2}(x,t)\,, \qquad x \in [x_i\,;\,x_{i+1}] \tag{4.44}$$

where $\mathbf{U}^n_{i+1/2}(x,t)$ is the solution of $\mathbf{RP}\left(\mathbf{U}^n_i, \mathbf{U}^n_{i+1}\right)$. The solution can then be advanced in time, which is directly performed by means of averaging $\mathbf{U}(x,t)$ at each cell as depicted in Fig. 4.1, following,

$$\mathbf{U}^{n+1}_i = \frac{1}{\Delta x}\int_{x_{i-1/2}}^{x_{i+1/2}} \mathbf{U}\left(x, t^{n+1}\right) \mathrm{d}x \tag{4.45}$$

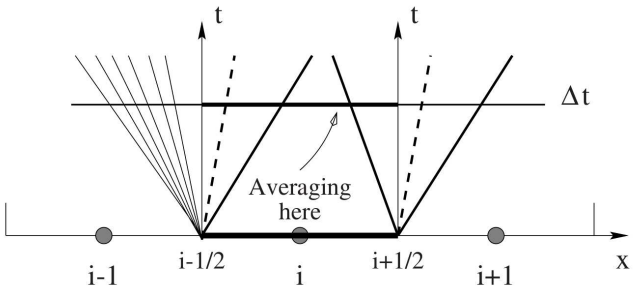

Figure 4.1: *Riemann problem wave pattern emerging at the boundaries of a given volume and averaging of the solution in* $x \in \left[x_{i-1/2}\,;\,x_{i+1/2}\right]$ *[278]*

The integration being a complex numerical operation since the exact expression of the local Riemann problem is required at each inter-cell position, the integral form of the equation is used,

$$\int_{x_{i-1/2}}^{x_{i+1/2}} \mathbf{U}\left(x,t^{n+1}\right)\mathrm{d}x = \int_{x_{i-1/2}}^{x_{i+1/2}} \mathbf{U}\left(x,t^{n}\right)\mathrm{d}x + \int_{t^n}^{t_{n+1}} \mathbf{F}\left(\mathbf{U}\left(x_{i-1/2},t\right)\right)\mathrm{d}t - \int_{t^n}^{t_{n+1}} \mathbf{F}\left(\mathbf{U}\left(x_{i+1/2},t\right)\right)\mathrm{d}t \tag{4.46}$$

where the left-hand side term and the first term on the right-hand side represent respectively the average values of the solution $\mathbf{U}(x,t)$ at time t^n and t^{n+1} as given in Eq. 4.41 and Eq. 4.45. Additionally, $\mathbf{U}\left(x_{i-1/2},t\right)$ and $\mathbf{U}\left(x_{i+1/2},t\right)$ represent the solutions of the Riemann problems on both sides of the control volume, along the respective inter-cell positions $x_{i-1/2}$ and $x_{i+1/2}$. By recalling the assumption that the time-step is small enough to avoid interactions between the different waves, these solutions correspond to the similarity solutions of the Riemann problems along their characteristic lines defined by $x/t = 0$. It can therefore be written,

$$\mathbf{F}\left(\mathbf{U}\left(x_{i-1/2},t\right)\right) = \mathbf{F}\left(\mathbf{U}^n_{i-1/2}\right) \tag{4.47}$$

$$\mathbf{F}\left(\mathbf{U}\left(x_{i+1/2},t\right)\right) = \mathbf{F}\left(\mathbf{U}^n_{i+1/2}\right) \tag{4.48}$$

where $\mathbf{U}^n_{i-1/2}$ and $\mathbf{U}^n_{i+1/2}$ represent the similarity solutions of $\mathbf{RP}\left(\mathbf{U}^n_{i-1}, \mathbf{U}^n_i\right)$ and $\mathbf{RP}\left(\mathbf{U}^n_i, \mathbf{U}^n_{i+1}\right)$ respectively along the intercell positions $x_{i-1/2}$ and $x_{i+1/2}$.

Thus, the Godunov formulation allowing the evolution of the solution in time from t^n to t^{n+1} is given by,

$$\mathbf{U}^{n+1}_i = \mathbf{U}^n_i + \frac{\Delta t}{\Delta x}\left(\mathbf{F}\left(\mathbf{U}^n_{i-1/2}\right) - \mathbf{F}\left(\mathbf{U}^n_{i+1/2}\right)\right) \tag{4.49}$$

and the whole process is depicted in Fig. 4.2. The standard form of the method presented here is linear and according to Godunov's theorem is first-order accurate.

4.2.2 The method of lines

The Godunov formulation presented in the previous section corresponds to the explicit, fully-discrete form of the method, where both spatial and temporal integrations are carried out simultaneously. The

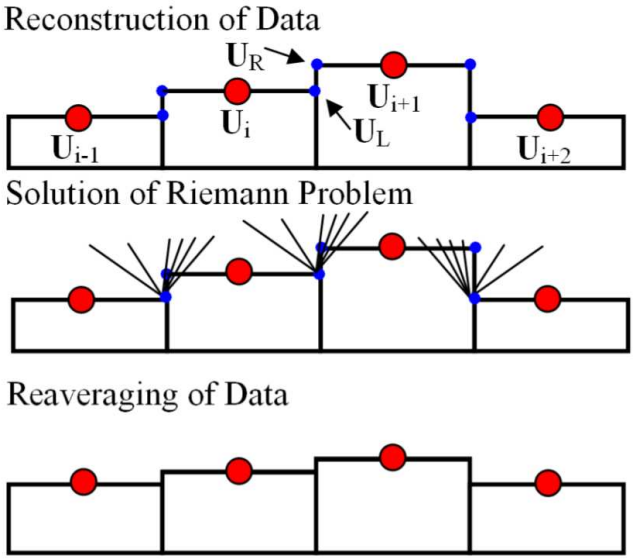

Figure 4.2: *Geometric interpretation of the first-order Godunov method [132]*

formulation used in the present work is slightly different and is known as the *method of lines* in which both integrations are decoupled.

We can rewrite the IBVP problem described by Eq. 4.39 by assuming a spatial discretisation and keeping the time continuous, resulting in an Ordinary Differential Equation (ODE) system,

$$\frac{\mathrm{d}\mathbf{U}(t)}{\mathrm{d}t} = \frac{1}{\Delta x}\left(\mathbf{F}_{i-1/2} - \mathbf{F}_{i+1/2}\right) \tag{4.50}$$

where the inter-cell fluxes are approximations of the true fluxes given by $\mathbf{F}(\mathbf{U}(x,t))$ at the corresponding interfaces and time instants. A direct choice for the estimation of the fluxes resides in the Godunov method discussed previously.

To advance the solution in time, the ODE given in Eq. 4.50 needs to be solved. There are numerous methodologies available to solve ODEs numerically, the simplest of all being the first-order explicit Euler time integration leading to the Godunov formulation presented in Eq. 4.49. Other approaches consist in using multi-step algorithms to increase both the stability range and order of accuracy. Several of these methods are regrouped in the class of so-called explicit *multi-step Runge-Kutta* methods.

Considering the system of governing equation in curvilinear coordinates derived in §. 4.1.2 and presented in Eqs. 4.28-4.38, the application of the method of lines results in,

$$\begin{aligned}\frac{\partial J\mathbf{U}}{\partial t} =& \frac{1}{\Delta\xi}\left(\Delta\mathbf{F}^{\xi}{}_{i-1/2,j,k} - \Delta\mathbf{F}^{\xi}{}_{i+1/2,j,k}\right)\\ &+\frac{1}{\Delta\eta}\left(\Delta\mathbf{G}^{\eta}{}_{i,j-1/2,k} - \Delta\mathbf{G}^{\eta}{}_{i,j+1/2,k}\right)\\ &+\frac{1}{\Delta\zeta}\left(\Delta\mathbf{H}^{\zeta}{}_{i,j,k-1/2} - \Delta\mathbf{H}^{\zeta}{}_{i,j,k+1/2}\right) + J\mathbf{S}_{i,j,k}\end{aligned} \tag{4.51}$$

where the notation $\Delta\mathbf{F}^{\xi}$ denotes the difference between hyperbolic and viscous fluxes as follows,

$$\Delta\mathbf{F}^{\xi}{}_{i-1/2,j,k} = \mathbf{F}^{\xi}_{\mathbf{i}}{}_{i-1/2,j,k} - \mathbf{F}^{\xi}_{\mathbf{v}}{}_{i-1/2,j,k} \tag{4.52}$$

Finally, it is common practice when using generalised curvilinear coordinates to normalise the com-

putation plane, and thus $\Delta\xi = \Delta\eta = \Delta\zeta = 1$, leading to the final expression of the method of lines,

$$\begin{aligned}\frac{\partial J\mathbf{U}}{\partial t} =& \Delta\mathbf{F}^{\xi}{}_{i-1/2,j,k} - \Delta\mathbf{F}^{\xi}{}_{i+1/2,j,k} \\ &+\Delta\mathbf{G}^{\eta}{}_{i,j-1/2,k} - \Delta\mathbf{G}^{\eta}{}_{i,j+1/2,k} \\ &+\Delta\mathbf{H}^{\zeta}{}_{i,j,k-1/2} - \Delta\mathbf{H}^{\zeta}{}_{i,j,k+1/2} + J\mathbf{S}_{i,j,k}\end{aligned} \tag{4.53}$$

§. 4.3.1 details the computation of the Godunov fluxes through the use of an approximate Riemann solver, while §. 4.4 presents the computation of the viscous fluxes and source terms. The time integration schemes used in this work are discussed in §. 4.5.

4.3 Computation of the hyperbolic fluxes

4.3.1 HLLC approximate Riemann solver

Choice of the HLLC

The fluxes needed by either the Godunov method or the method of lines are obtained through the solution of the inter-cell Riemann problem. Two types of Riemann solver could be used to this end, either exact or approximate solvers. The former are computing the exact solution of the Riemann problem at the expense of a large computational cost. On the other end, the class of approximate solvers relies on the approximation of the solution.

Within the class of approximate solvers, the Harten, Lax and Van Leer (HLL) solver [175] is one of the most popular accounting for its simplicity that relies on the assumption that the wave pattern emerging from the Riemann problem is constituted by two waves only (shock or rarefaction). An other popular choice is the so-called Roe solver [252] relying on the approximation of the Jacobian matrix of the problem defined as $\underline{\mathbf{A}} = \partial\mathbf{F}/\partial\mathbf{U}$.

The HLLC (Harten, Lax and Van Leer Contact) was introduced by Toro [278] as an extension of the HLL approximate solver. The approximation of the inter-cell fluxes relies on the assumption that the solution of the Riemann problem consists in three different waves generating four different states. The HLLC thus accounts for the missing contact wave (middle wave) neglected by the HLL solver. Because of this, it is slightly more expensive to use, but features an increased accuracy.

The present work is concerned with the simulation of compressible multi-component flows where contact surfaces are of particular relevance (e.g. mixing layers). As already pointed out in §. 2.3.2, the naive use of Godunov type methods leads to pressure and/or velocity oscillations at interfaces between different species. A great care in the choice of the Riemann solver is thus needed to ensure that these pressure oscillations will not occur. Abgrall [5], Abgrall and Karni [6] and Billet and Abgrall [25] showed that the double-flux method could alleviate these pressure oscillations with any schemes fulfilling the condition of perfectly preserving a stationary contact discontinuity. The HLL scheme does not fulfil this condition and neither does flux splitting schemes such as the Van Leer and Advection Upstream Splitting Method (AUSM) in general, at the exception of the class AUSM$^+$ thanks to the concept of common speed of sound [181, 182]. The HLLC approximate solver also perfectly conserves contact discontinuities thanks to the contact wave being explicitly accounted for in its formulation. The HLLC will thus be used throughout this work.

HLLC

The HLLC Riemann solver provides an approximate solution to the Riemann problem defined in Eqs. 4.42-4.43. The wave structure corresponding to the approximate solution given by the HLLC is pictured in

Fig. 4.3 and features three waves separating four different and constant states. The middle wave is always a contact discontinuity, while the left and right waves can be any combination of shock waves and rarefaction fans. The middle wave moves at a speed S_*, while the left and right wave at the respective speeds S_L and S_R.

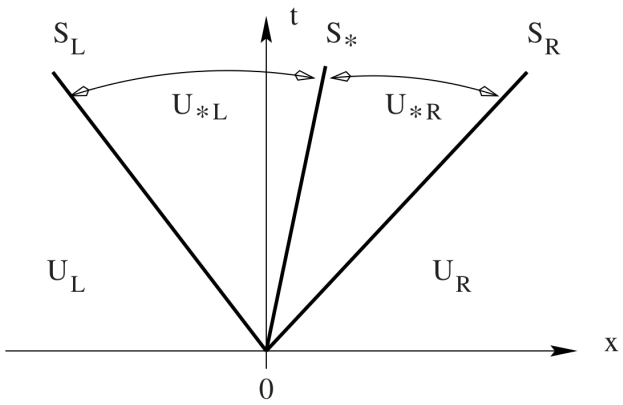

Figure 4.3: *Wave structure of the HLLC approximate Riemann solver [278]*

The solution of the Riemann solver given by the HLLC is thus [278],

$$\mathbf{U}(x,t) = \begin{cases} \mathbf{U}_L & x/t \leqslant S_L \\ \mathbf{U}_{*L} & S_L \leqslant x/t \leqslant S_* \\ \mathbf{U}_{*R} & S_* \leqslant x/t \leqslant S_R \\ \mathbf{U}_R & x/t \geqslant S_R \end{cases} \tag{4.54}$$

where $\mathbf{U}_{*L}$ and $\mathbf{U}_{*R}$ are the so-called *intermediate states* obtained through the accounting of the middle wave presence. The inter-cell fluxes defined by $\mathbf{F}_{HLLC} = \mathbf{F}(\mathbf{U}(x,0))$ are thus given by,

$$\mathbf{F}_{HLLC} = \begin{cases} \mathbf{F}_L & 0 \leqslant S_L \\ \mathbf{F}_{*L} & S_L \leqslant 0 \leqslant S_* \\ \mathbf{F}_{*R} & S_* \leqslant 0 \leqslant S_R \\ \mathbf{F}_R & 0 \geqslant S_R \end{cases} \tag{4.55}$$

The intermediate states fluxes are computed through the use of Rankine-Hugoniot jump-conditions across characteristics waves of respective speeds S_L and S_R (more details are provided in [278]),

$$\mathbf{F}_{*L} = \mathbf{F}_L + S_L(\mathbf{U}_{*L} - \mathbf{U}_L) \tag{4.56}$$

$$\mathbf{F}_{*R} = \mathbf{F}_R + S_R(\mathbf{U}_{*R} - \mathbf{U}_R) \tag{4.57}$$

The intermediate states are given (see [278] for more details) by,

$$\mathbf{U}_{*s} = \rho_s \left(\frac{S_s - u_s}{S_s - S_*}\right) \begin{pmatrix} Y_{k_s} \\ S_* \\ v_s \\ w_s \\ E_s + (S_* - u_s)\left(S_* + \dfrac{P_s}{\rho_s(S_s - u_s)}\right) \end{pmatrix} \tag{4.58}$$

where the subscript s refers to either the left or right interpolated state. Once the intermediate states are determined, their fluxes can be estimated using either Eq. 4.14, Eq. 4.59 or Eq. 4.57. Inter-cell fluxes

can then be computed using Eq. 4.55.

$$\mathbf{F}_{*s} = \begin{pmatrix} (\rho Y_k)_{*s}\, u_* \\ (\rho u)_{*s}\, u_* + P_* \\ (\rho v)_{*s}\, u_* \\ (\rho w)_{*s}\, u_* \\ ((\rho E)_{*s} + P_*)\, u_* \end{pmatrix} \tag{4.59}$$

The only remaining quantities to evaluate are the wave speeds S_L, S_R and S_*. Several approaches exist for this purpose, and the Approximative Noniterative Riemann Solver (ANRS) considered in this work is discussed below.

Approximative Noniterative Riemann Solver (ANRS)

The wave speeds estimation is carried out using the ANRS which is an approximate state Riemann solver. The aim of such an approach is to provide an estimate of the values in the intermediate regions by approximating them using information on the surrounding states and the waves separating them. Three solvers are considered within the ANRS algorithm, the first one providing a simple linearised estimation of intermediate values (PVRS), while the others are more specific, assuming either two shock waves (TSRS) or two rarefaction fans (TRRS).

The switching between the three solvers is depicted in Fig. 4.4 where $P_{max} = \max(P_L,\, P_R)$, and $P_{min} = \min(P_L,\, P_R)$. The switching parameter value Q measuring the flow smoothness has been set to 2 ($Q = 2$) according to Toro [278].

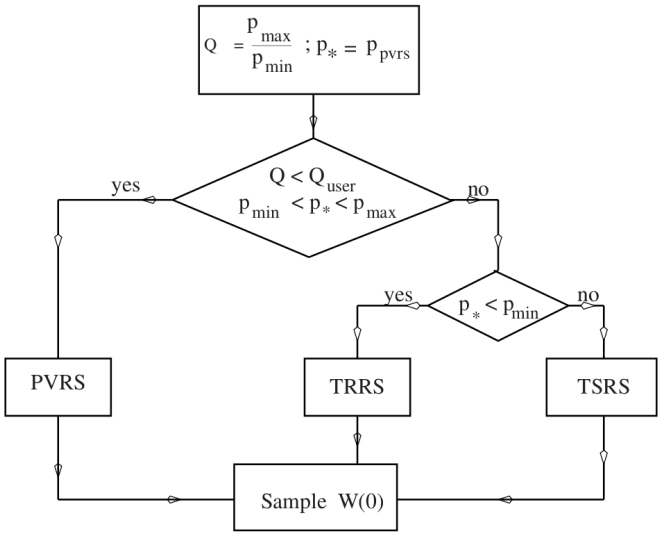

Figure 4.4: *Flow chart for the ANRS approximate Riemann solver [278]*

According to the ANRS algorithm, the left and right characteristic waves are estimated as follows,

$$S_L = \begin{cases} u_L - c_L & P_* \leqslant P_L \\ u_L - c_L\sqrt{1 + \dfrac{\gamma+1}{2\gamma}\left(\dfrac{P_*}{P_L} - 1\right)} & P_* > P_L \end{cases} \tag{4.60}$$

$$S_R = \begin{cases} u_R - c_R & P_* \leqslant P_R \\ u_R - c_R\sqrt{1 + \dfrac{\gamma+1}{2\gamma}\left(\dfrac{P_*}{P_R} - 1\right)} & P_* > P_R \end{cases} \tag{4.61}$$

where the intermediate pressure and wave speed are obtained as,

- PVRS solver ($Q \leqslant 2$ and $\min(P_L,\ P_R) \leqslant P_* \leqslant \max(P_L,\ P_R)$)

$$P_* = \frac{1}{2}(P_L + P_R) + \frac{1}{8}(u_L - u_R)(c_L + c_R)(\rho_L + \rho_R) \tag{4.62}$$

$$S_* = \frac{1}{2}(u_L + u_R) + \frac{2(P_L - P_R)}{(c_L + c_R)(\rho_L + \rho_R)} \tag{4.63}$$

- TRRS solver ($P_* < \min(P_L,\ P_R)$)

$$P_* = \frac{1}{2}\left[P_L\left(1 + \frac{\gamma - 1}{2c_L}(u_L - S_*)\right)^{\frac{2\gamma}{\gamma - 1}} + P_R\left(1 + \frac{\gamma - 1}{2c_R}(S_* - u_R)\right)^{\frac{2\gamma}{\gamma - 1}}\right] \tag{4.64}$$

$$S_* = \frac{P_{LR}^z \frac{u_L}{c_L} + \frac{u_R}{c_R} + \frac{2}{\gamma - 1}(P_{LR}^z - 1)}{P_{LR}^z \frac{1}{c_L} + \frac{1}{c_R}} \tag{4.65}$$

with $P_{LR}^z = \left(\frac{P_L}{P_R}\right)^{\frac{\gamma - 1}{2\gamma}}$

- TSRS solver ($\min(P_L,\ P_R) < P_*$)

$$P_* = \frac{\mathcal{A}_L + \mathcal{A}_R - (u_R - u_L)}{\frac{\mathcal{A}_L}{P_L} + \frac{\mathcal{A}_R}{P_R}} \tag{4.66}$$

$$S_* = \frac{1}{2}(u_L + u_R) + \frac{1}{2}\left[(P_* - P_R)\frac{\mathcal{A}_R}{P_R} - (P_* - P_L)\frac{\mathcal{A}_L}{P_L}\right] \tag{4.67}$$

with $\mathcal{A}_s = P_s\sqrt{\frac{2}{\rho_s((\gamma + 1)P_0 + (\gamma - 1)P_s)}}$ and $P_0 = \max(0,\ P_{*,PVRS})$

HLLC in curvilinear coordinates

In this work, the curvilinear coordinate system is adopted for multi-dimensional simulations. The HLLC solver therefore needs to be adapted to this new reference frame. The current implementation follows the derivation proposed by Bagadir and Drikakis [13]. The main steps of the HLLC remain similar to the procedure outlined above, but small variations need to be accounted for, in addition to the new formulation of the conservative variables and fluxes vectors.

Without loss of generality, the one-dimensional ξ direction is considered here. HLLC fluxes are still calculated using Eq. 4.55, where intermediate states (subsonic states) are defined by,

$$\mathbf{U}_{*s} = \begin{pmatrix} (\rho Y_k)_{*s} \\ (\rho u)_{*s} \\ (\rho v)_{*s} \\ (\rho w)_{*s} \\ (\rho E)_{*s} \end{pmatrix} = \frac{1}{S_s - S_*}\begin{pmatrix} (\rho Y_k)_s (S_s - \lambda_s) \\ \rho_s u_s (S_s - \lambda_s) + (P_{*s} - P_s)\hat{\xi}_x \\ \rho_s v_s (S_s - \lambda_s) + (P_{*s} - P_s)\hat{\xi}_y \\ \rho_s w_s (S_s - \lambda_s) + (P_{*s} - P_s)\hat{\xi}_z \\ (\rho E)_s (S_s - \lambda_s) + P_{*s}S_* - P_s\lambda_s \end{pmatrix} \tag{4.68}$$

where λ_s is the cell face normal velocity and is given by $\lambda_s = u_s\hat{\xi}_x + v_s\hat{\xi}_y + w_s\hat{\xi}_z$, while P_{*s} is given by $P_{*s} = \rho_s(\lambda_s - S_s)(\lambda_s - S_*) + P_s$ and the normalised metrics are computed as,

$$\hat{\xi}_i = \frac{\xi_i}{\mathcal{M}} \tag{4.69}$$

$$\mathcal{M} = \sqrt{\xi_x^2 + \xi_y^2 + \xi_z^2} = |\nabla\xi| \tag{4.70}$$

where $\mathcal{M}$ is the magnitude of the face normal vector.

Wave speeds are then computing using the ANRS solver presented above, but effectively replacing u_L and u_R by λ_L and λ_R respectively.

The intermediate fluxes are then expressed by,

$$\mathbf{F}_{*s} = \mathcal{M} \begin{pmatrix} (\rho Y_k)_{*s} S_* \\ (\rho u)_{*s} S_* + P_{*s}\hat{\xi}_x \\ (\rho v)_{*s} S_* + P_{*s}\hat{\xi}_y \\ (\rho w)_{*s} S_* + P_{*s}\hat{\xi}_z \\ ((\rho E)_{*s} + P_{*s}) S_* \end{pmatrix} \tag{4.71}$$

By further taking into account the fact that the Jacobian is constant at cells interfaces, we have,

$$J\mathbf{F}_{*s} = J\mathcal{M} \begin{pmatrix} (\rho Y_k)_{*s} S_* \\ (\rho u)_{*s} S_* + P_{*s}\hat{\xi}_x \\ (\rho v)_{*s} S_* + P_{*s}\hat{\xi}_y \\ (\rho w)_{*s} S_* + P_{*s}\hat{\xi}_z \\ ((\rho E)_{*s} + P_{*s}) S_* \end{pmatrix} \tag{4.72}$$

Furthermore, it can be seen that the intermediate wave speed (S_*) represents the flux speed normal to the inter-cell boundary, such that,

$$S_* = u_*\hat{\xi}_x + v_*\hat{\xi}_y + w_*\hat{\xi}_z = \frac{1}{\mathcal{M}}\left(u_*\xi_x + v_*\xi_y + w_*\xi_z\right) \tag{4.73}$$

and thus,

$$u_* = \mathcal{M}S_* \tag{4.74}$$

Finally, the normal vector magnitude can be rewritten as a function of the local Jacobian as follows,

$$\mathcal{M} = \frac{1}{|J|}\sqrt{\beta_{11}^2 + \beta_{12}^2 + \beta_{13}^2} = \frac{1}{|J|}\beta \tag{4.75}$$

where $\beta_{ij} = J\dfrac{\partial \xi_i}{\partial x_j}$ with $\xi_i = \xi,\ \eta,\ \zeta$ and $x_j = x,\ y,\ z$ are the components of the adjoint matrix defined in Eq. 4.10.

The final form of the intermediate HLLC fluxes in the generalised curvilinear coordinate system is thus,

$$J\mathbf{F}_{*s} = \frac{J}{|J|} \begin{pmatrix} (\rho Y_k)_{*s} S_*\beta \\ (\rho u)_{*s} S_*\beta + P_{*s}\beta_{11} \\ (\rho v)_{*s} S_*\beta + P_{*s}\beta_{12} \\ (\rho w)_{*s} S_*\beta + P_{*s}\beta_{13} \\ ((\rho E)_{*s} + P_{*s}) S_*\beta \end{pmatrix} \tag{4.76}$$

and the supersonic fluxes are given by,

$$J\mathbf{F}_{s} = \frac{J}{|J|} \begin{pmatrix} (\rho Y_k)_{s} \lambda_s\beta \\ (\rho u)_{s} \lambda_s\beta + P_s\beta_{11} \\ (\rho v)_{s} \lambda_s\beta + P_s\beta_{12} \\ (\rho w)_{s} \lambda_s\beta + P_s\beta_{13} \\ ((\rho E)_{s} + P_s) \lambda_s\beta \end{pmatrix} \tag{4.77}$$

4.3.2 Variable reconstruction and high-order schemes

Introduction

As already pointed out, the Godunov method presented earlier (§. 4.2) corresponds to a simple piecewise constant distribution of the data employed during the reconstruction step (Eq. 4.41, Fig. 4.2) which formally achieves a first order spatial accuracy.

However, Godunov versatile formulation allows the extension of the method to higher-order reconstructions, and thus greater spatial accuracy through the use of reconstruction methods. The underlying principle of these methods is the approximation of the initial data at the cell edges by using fitting functions. Two main class of methods are available in the literature, the *Monotone Upstream-centred Scheme for Conservation Laws* (MUSCL) [153,178,278,284] and the *Essentially Non-Oscillatory* (ENO) and *Weighted Non-Oscillatory* (WENO) [15]. Only the MUSCL class of schemes is considered in this work.

Achieving high-order spatial accuracy for hyperbolic conservation laws remains a challenge as discontinuities are allowed. As pointed out earlier, data need to be interpolated in both upwind and downwind directions. First order methods would not cause oscillations or create new extrema, but any sharp features of the solution would be smeared by numerical dissipation. Modern reconstruction methods use high-order interpolation in smooth regions of the flow and revert to low-order interpolation when sharp gradients are encountered.

Choice of the reconstructed variables

It is well known that the variables set (primitive, conservative, characteristics, etc.) to interpolate has a significant impact on the solution.

Interpolating conservative variables is sometimes noisy and can lead to pressure and temperature oscillations near material or contact surfaces, which is exactly what this work aims to avoid in multicomponent flows. For this reason, this approach will not be considered here, even though it is the solution associated with the smallest computational cost.

Interpolating primitive variables is efficient computationally (although less so that reconstructing the conservative ones), but is prone to produce small oscillations near shock waves, especially in the case of interacting shock waves such as the colliding shocks problem presented in §. 5.1.2. In this case, primitive variables are extracted from conservative variables, then limited. Eventually, the limited conserved variables used in the Riemann solver are recovered using the limited primitive variables.

The last solution, interpolating characteristics variables, is interesting in the vicinity of shocks as it reduces the oscillations amplitude observed with the primitive variable interpolation. However, the computational cost associated with this approach is a lot larger than limiting primitives variables. An additional issue arising when using this limiting technique is the appearance of small temperature spikes near contact waves, which is not acceptable when reacting problems are considered. This could be avoided by using a hybrid scheme switching between primitive variables reconstruction everywhere in the flow, and characteristics near shock waves, thus taking advantage of both methods.

Despite the advantages of the hybrid method, primitive variables will be limited in this work as it was found that this interpolation worked well in most encountered situations. The primitive variables used for the different schemes are as follows,

- QCVF : $\mathbf{V} = [u,\ v,\ w,\ P,\ z_k,\ \rho_k]^T$

- FCVF : $\mathbf{V} = [u,\ v,\ w,\ P,\ z_k,\ \rho_k]^T$
- QCMF : $\mathbf{V} = [u,\ v,\ w,\ P,\ T,\ Y_k]^T$
- FCMF : $\mathbf{V} = [u,\ v,\ w,\ P,\ \rho,\ Y_k]^T$

1^{st} order Upwind

The first order Upwind scheme corresponds simply to a piecewise constant reconstruction used in the standard Godunov method, yielding,

$$\mathbf{V}_L^n = \mathbf{V}_{i-1}^n \tag{4.78}$$
$$\mathbf{V}_R^n = \mathbf{V}_i^n \tag{4.79}$$

for the **RP** $\left(\mathbf{U}_{i-1}^n,\ \mathbf{U}_i^n\right)$. This scheme will be referred to as Upwind1 in the remainder of this report.

Second-order MUSCL reconstruction

To increase the order of accuracy obtained through the Upwind1 scheme, a piecewise linear distribution is considered within the cell, which results in a second-order accurate scheme. An example of such distribution is pictured in Fig. 4.5 and the data distribution within cell i follows,

$$\mathbf{V}(x) = \mathbf{V}_i + \frac{x - x_i}{\Delta x}\Delta_i, \qquad x \in \left[x_{i-1/2}\ ;\ x_{i+1/2}\right] \tag{4.80}$$

where $\mathbf{V}_i$ represents the cell averaged value of $\mathbf{V}$. From this distribution, values at the left and right inter-cell boundaries are expressed as,

$$\mathbf{V}_{i,L} = \mathbf{V}_i - \frac{1}{2}\Delta_i \tag{4.81}$$
$$\mathbf{V}_{i,R} = \mathbf{V}_i + \frac{1}{2}\Delta_i \tag{4.82}$$

where Δ_i is a suitably chosen slope. It can also be remarked that the mean integral value of Eq. 4.80 is still $\mathbf{V}_i$ independently of the slope choice Δ_i.

The Riemann problem presented in Eqs. 4.42-4.43 is thus slightly modified, and becomes,

$$\frac{\partial \mathbf{U}}{\partial t} + \frac{\partial \mathbf{F}}{\partial x} = 0 \tag{4.83}$$

$$\mathbf{V}(x, t^n) = \begin{cases} \mathbf{V}_{i+1/2,L} = \mathbf{V}_i^n + \dfrac{1}{2}\Delta_i & x < x_{i+1/2} \\ \mathbf{V}_{i+1/2,R}^n = \mathbf{V}_{i+1}^n - \dfrac{1}{2}\Delta_{i+1} & x > x_{i+1/2} \end{cases} \tag{4.84}$$

The determination of Δ_i is at the heart of the MUSCL reconstruction technique and there exists numerous approaches for its estimation, all sharing the common goal of enforcing a monotone character to avoid spurious oscillations near discontinuities. According to Godunov's theorem [109], *there are no linear monotone reconstruction schemes of order of accuracy higher than one.* The slope calculation therefore relies on non-linear monotone reconstruction to circumvent this culprit.

The slope calculation retained in the present work is the *MinMod* slope featuring a second-order accurate reconstruction. Two slopes are defined for each component V_i^j of the primitive variables vector $\mathbf{V}_i$,

$$\Delta_{i-1/2}^j = V_i^j - V_{i-1}^j \tag{4.85}$$
$$\Delta_{i+1/2}^j = V_{i+1}^j - V_i^j \tag{4.86}$$

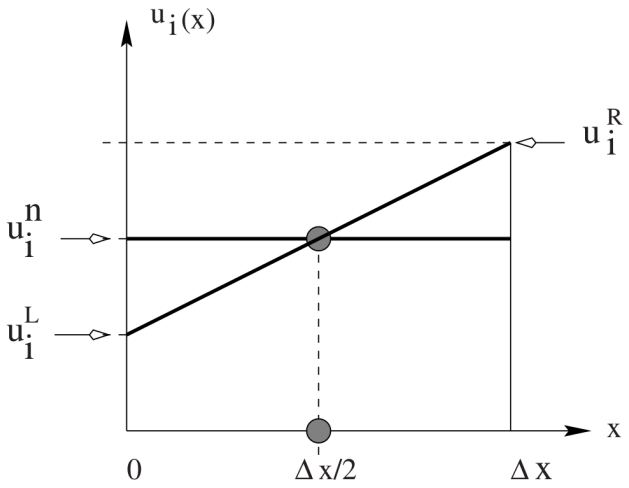

Figure 4.5: *Piecewise linear MUSCL reconstruction of the cell averaged data in a single cell*

Slopes Δ_i^j are then estimated as the minimum value of $\Delta_{i+1/2}^j$ and $\Delta_{i-1/2}^j$ provided that they have similar signs, and zero otherwise to avoid an oscillatory behaviour [178].

$$\Delta_i^j = \begin{cases} \Delta_{i-1/2}^j & \Delta_{i-1/2}^j < \Delta_{i+1/2}^j \ \& \ \Delta_{i-1/2}^j \times \Delta_{i+1/2}^j > 0 \\ \Delta_{i+1/2}^j & \Delta_{i-1/2}^j > \Delta_{i+1/2}^j \ \& \ \Delta_{i-1/2}^j \times \Delta_{i+1/2}^j > 0 \\ 0 & \Delta_{i-1/2}^j \times \Delta_{i+1/2}^j < 0 \end{cases} \tag{4.87}$$

The computed slope is obviously different for each component of the vector and the reconstructed boundary states $\mathbf{V}_L$ and $\mathbf{V}_R$ are described by each of their components,

$$V_L^j = V_i^j - \frac{1}{2}\Delta_i^j \tag{4.88}$$

$$V_R^j = V_i^j + \frac{1}{2}\Delta_i^j \tag{4.89}$$

A simplified formulation used in the present work features a slope limiter function Φ defined by,

$$\Phi = \max\left(0,\ \min\left(1,\ \frac{\Delta_{i+1/2}^j}{\Delta_{i-1/2}^j}\right)\right) \tag{4.90}$$

which has the advantage of accounting for the three different situations in a single expression. Reconstructed inter-cell values are thus given by,

$$V_L^j = V_i^j - \frac{1}{2}\Phi\Delta_{i-1/2}^j \tag{4.91}$$

$$V_R^j = V_i^j + \frac{1}{2}\Phi\Delta_{i-1/2}^j \tag{4.92}$$

This reconstruction scheme will be referred to as MinMod2 in the remainder of this work.

Fifth-order MUSCL reconstruction

A formulation similar to the MinMod2 is used for a fifth-order accurate MUSCL scheme. The piecewise linear reconstruction presented above is also used, but the slopes computation and their limiting is more complex. It has been presented by Kim and Kim [153], and successfully applied to numerous compressible flows by Thornber *et al.* [275, 276] where its increased resolution compared to the MinMod2 has been highlighted.

Similarly to Eq. 4.84, the initial conditions of the local Riemann problem at $x_{i+1/2}$ are now computed with,

$$\mathbf{V}_{i+1/2,L} = \mathbf{V}_i + \frac{1}{2}\Phi^{lim,L} r^{lim,L} \left(\mathbf{V}_i - \mathbf{V}_{i-1}\right) \tag{4.93}$$

$$\mathbf{V}_{i+1/2,R} = \mathbf{V}_{i+1} - \frac{1}{2}\Phi^{lim,R} r^{lim,R} \left(\mathbf{V}_{i+2} - \mathbf{V}_{i+1}\right) \tag{4.94}$$

The monotonicity is enforced by limiting the linear extrapolation through the left and right limiters $\Phi^{lim,s}$ which are defined by,

$$\Phi^{lim,s} = \max\left(0,\ \min\left(2,\ 2r_i^{lim,s},\ \phi^s\right)\right) \tag{4.95}$$

where the terms ϕ^s are given by,

$$\phi^L = \frac{-\dfrac{2}{r_{i-1}^{lim,L}} + 11 + 24 r_i^{lim,L} - 3 r_i^{lim,L} r_{i+1}^{lim,L}}{30} \tag{4.96}$$

$$\phi^R = \frac{-\dfrac{2}{r_{i+2}^{lim,R}} + 11 + 24 r_{i+1}^{lim,R} - 3 r_{i+1}^{lim,R} r_i^{lim,R}}{30} \tag{4.97}$$

and the slope ratios are estimated as follows,

$$r_i^{lim,L} = \frac{\mathbf{V}_{i+1} - \mathbf{V}_i}{\mathbf{V}_i - \mathbf{V}_{i-1}} \tag{4.98}$$

$$r_i^{lim,R} = \frac{\mathbf{V}_i - \mathbf{V}_{i-1}}{\mathbf{V}_{i+1} - \mathbf{V}_i} \tag{4.99}$$

4.3.3 Low-Mach number adjustment

One of the main issues of the finite volume Godunov method is its large numerical dissipation at low Mach number making them hardly suitable for LES or DNS calculations. Thornber *et al.* [276] showed that the inviscid fluxes computation using a standard Godunov method produced a leading order kinetic energy dissipation rate proportional to the speed of sound, which smears all features at low-Mach numbers. A simple and very effective technique for reducing this induced dissipation was derived by Thornber *et al.* [276] by modifying the velocity jump at the inter-cell boundaries. The velocity is altered by a blending function behaving like an upwind scheme for large Mach numbers and like a fully centred scheme towards low-Mach numbers. The modified dissipation is not a function of the speed of sound any more, but follows the four-fifth law of Kolmogorov [165]. This simple modification has been shown to work very well in compressible mixing problems, and produces the proper decay of turbulent kinetic energy in homogeneous decaying turbulence [86, 276].

The corrected velocities are expressed by,

$$\mathbf{u}_L^c = \frac{\mathbf{u}_L + \mathbf{u}_R}{2} + z\frac{\mathbf{u}_L - \mathbf{u}_R}{2} \tag{4.100}$$

$$\mathbf{u}_R^c = \frac{\mathbf{u}_L + \mathbf{u}_R}{2} + z\frac{\mathbf{u}_L - \mathbf{u}_R}{2} \tag{4.101}$$

where the blending function z is defined by,

$$\begin{aligned} z &= \min\left(\max\left(M_L,\ M_R\right),\ 1\right) \\ &= \min\left(\max\left(\frac{\sqrt{u_L^2}}{c_L},\ \frac{\sqrt{u_R^2}}{c_R}\right),\ 1\right) \end{aligned} \tag{4.102}$$

where $\mathbf{u}_s$ are the original limited left and right velocity vectors, and $\mathbf{u}_s^c$ are the low-Mach adjusted limited velocities. This adjustment is only applied to the velocity component as it was shown in [276] that applying it to pressure and density would result in increased diffusion in contact surfaces which is not desirable.

Its effect can be observed in Fig. 4.6 where a single mode rolling vortex development is shown computed with the MUSCL5 with and without Low-Mach adjustment. The large dissipation of the Godunov method at low Mach number is here clearly identified.

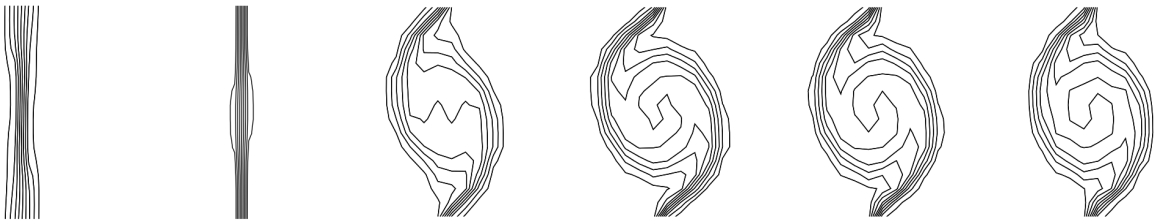

(a) *Without LMC (left)* $M = 0.02$ *and (right)* $M = 0.002$

(b) *With LMC (left)* $M = 0.2$*, (center left)* $M = 0.02$*, (center right)* $M = 0.002$ *and (right)* $M = 0.0002$

Figure 4.6: *Effect of the low-Mach correction on a single rolling vortex development computed (a) without and (b) with LMC at different Mach number [273]*

4.3.4 Double-Flux model

The QCMF was developed initially by Abgrall and Karni [6] for calorically perfect gases and extended to thermally perfect gases by Billet and Abgrall [25] and solves the Navier-Stokes equations in a different way than the usual Godunov method. The main idea behind the special treatment of the governing equations is to locally reduce the problem to behave similarly as a single-fluid flow which has been shown to be solved without pressure oscillations by Godunov-like methods in §. 2.3.2. The classical Godunov method expresses the inter-cell fluxes as a function of the limited variables on both sides of the inter-cell boundary.

$$\mathbf{F}_{i+1/2} = \mathbf{F}\left(\mathbf{U}_{i+1/2,L},\, \mathbf{U}_{i+1/2,R}\right) \tag{4.103}$$

As pointed out in §. 3.4.5, Billet and Abgrall [25] showed that when using the calorically-like formulation of energy derived in Eq. 3.82, if both γ and ρh_0^m were frozen in each cell for the entire time-step, pressure and velocity are conserved across a material interface. The gas mixture in each cell is thus treated as its own constant thermal properties single-component gas. To achieve this, two interface fluxes are computed for each inter-cell boundary. The first one, $\mathbf{F}_{i+1/2,L} = \mathbf{F}\left(\mathbf{U}_{i+1/2,L},\, \mathbf{U}_{i+1/2,R},\, \gamma_{i+1/2,L}\right)$ where fluids in both cells i and $i+1$ are assumed to be $\gamma_{i+1/2}$ fluids. The second flux, $\mathbf{F}_{i+1/2,R} = \mathbf{F}\left(\mathbf{U}_{i+1/2,L},\, \mathbf{U}_{i+1/2,R},\, \gamma_{i+1/2,R}\right)$ assumes that fluids in both i and $i+1$ cells are $\gamma_{i+1/2,R}$ fluids.

This definition is equivalent to freeze γ and ρh_0^m on each finite hyper-volume defined by $[i-1/2,\, i+1/2]\times \left[t^n,\, t^{n+1}\right]$, and we have $\gamma_{i+1/2,L} = \gamma_{i-1/2,R} = \gamma_i$. By applying the method of lines in the cartesian reference frame in cell i on this new formulation, we get,

$$\frac{\partial \mathbf{U}}{\partial t} = \frac{1}{\Delta x}\left(\mathbf{F}_L\left(\mathbf{U}_{i+1/2,L},\, \mathbf{U}_{i+1/2,R},\, \gamma_i\right) - \mathbf{F}_R\left(\mathbf{U}_{i-1/2,L},\, \mathbf{U}_{i-1/2,R},\, \gamma_i\right)\right) \tag{4.104}$$

It shall be remarked that since ρh_0^m is frozen in time, its associated flux $\rho h_0^m u$ is not added to the energy fluxes.

The first step of the procedure is thus referred as the energy projection step and consists in obtaining the thermal properties approximation as piecewise linear functions of temperature to obtain the energy in a single-fluid like form (value of ρh_0^m and γ are obtained in each cell of the domain). It further consists in integrating the governing equations in time to obtain the new values of momentum and mass fractions,

as well as the quasi-conservative energy. The second step, the thermal properties correction step involves the update of the different thermodynamic quantities using a temperature extracted from the double-flux pressure calculated from the quasi-conservative energy. The relaxed total energy is finally obtained.

The algorithm for integrating the governing equations from t^n to t^{n+1} using a multi-stage explicit integration scheme is illustrated as follows for the RK2-SSP scheme,

1. Compute ρh_0^m and γ in all cells of the domain
2. Interpolate primitive variables $\mathbf{V} = [\mathbf{u},\, P,\, Y_k,\, T]^T$ to the cell edges
3. Compute the predictor values ($\widetilde{\mathbf{U}}$) based on the conservation laws, double-flux model and time integration scheme,

$$\begin{pmatrix} \widetilde{\rho Y_k} \\ \widetilde{\rho \mathbf{u}} \\ \widetilde{\rho E} \end{pmatrix}_i = \mathbf{U}_i^n - \frac{\Delta t}{3\Delta x}\left(\mathbf{F}_L\left(\mathbf{U}_{i+1/2,L}^n,\, \mathbf{U}_{i+1/2,R}^n,\, \gamma_i^n\right) - \mathbf{F}_R\left(\mathbf{U}_{i-1/2,L}^n,\, \mathbf{U}_{i-1/2,R}^n,\, \gamma_i^n\right)\right) \tag{4.105}$$

4. Update primitive variables at cell i, $\widetilde{\mathbf{V}}_i$,

$$\widetilde{Y_k} = \frac{\widetilde{\rho Y_k}}{\sum_{k=1}^{N} \widetilde{\rho Y_k}} \tag{4.106}$$

$$\widetilde{\mathbf{u}} = \frac{\widetilde{\rho \mathbf{u}}}{\sum_{k=1}^{N} \widetilde{\rho Y_k}} \tag{4.107}$$

$$\widetilde{P_{df}} = (\gamma_i^n - 1)\left(\widetilde{\rho E} - (\rho h_0^m)^n - \frac{1}{2}\widetilde{\rho}\widetilde{\mathbf{u}}\widetilde{\mathbf{u}}\right)_i \tag{4.108}$$

$$\widetilde{T} = \frac{\widetilde{P_{df}}}{\mathcal{R}\sum_{k=1}^{N} \frac{\widetilde{\rho Y_k}}{\mathcal{M}_k}} \tag{4.109}$$

5. Repeat $2-4$ for each stage of the time marching algorithm selected
6. At the final stage, corrected values are obtained from the predicted ones. In the case of the RK2-SSP, this would lead to,

$$\begin{pmatrix} (\rho Y_k)^{n+1} \\ (\rho \mathbf{u})^{n+1} \\ (\rho E)^{*} \end{pmatrix}_i = \frac{1}{4}\mathbf{U}_i^n + \frac{3}{4}\widetilde{\mathbf{U}}_i - \frac{\Delta t}{4\Delta x}\left(\mathbf{F}_L\left(\widetilde{\mathbf{U}}_{i+1/2,L},\, \widetilde{\mathbf{U}}_{i+1/2,R},\, \gamma_i^n\right) - \mathbf{F}_R\left(\widetilde{\mathbf{U}}i_{-1/2,L},\, \widetilde{\mathbf{U}}_{i-1/2,R},\, \gamma_i^n\right)\right) \tag{4.110}$$

7. At the end of the final stage, use the primitive variables new values to update γ^{n+1} and $(\rho h_0^m)^{n+1}$,

$$P_{df}^{n+1} = (\gamma_i^n - 1)\left((\rho E)^{*} - (\rho h_0^m)^n - \frac{1}{2}\left(\rho \mathbf{u}^2\right)^{n+1}\right)_i \tag{4.111}$$

$$T^{n+1} = \frac{P_{df}^{n+1}}{\mathcal{R}\sum_{k=1}^{N} \frac{(\rho Y_k)^{n+1}}{\mathcal{M}_k}} \tag{4.112}$$

$$\gamma^{n+1} = \gamma\left(Y_k^{n+1},\, T^{n+1}\right) \tag{4.113}$$

$$(h_0^m)^{n+1} = h_0^m\left(Y_k^{n+1},\, T^{n+1}\right) \tag{4.114}$$

8. The relaxed total energy is finally updated to give,

$$(\rho E)^{n+1} = \frac{P_{df}^{n+1}}{\gamma^{n+1}-1} + (\rho h_0^m)^{n+1} + \frac{1}{2}\left(\rho \mathbf{u}^2\right)^{n+1} \tag{4.115}$$

4.3.5 Transport of volume fraction for the QCVF model

Volume fraction transport is governed by an advection equation which is not conservative. Therefore, the Riemann solver can not be directly applied to compute the fluxes and update the solution in time. It is not clear on how the approximate HLLC Riemann solver can be adapted consistently with the Euler equations augmented with an advection equation. The HLL and Roe solvers have been previously adapted to an advection equation [5, 260]. Following the modification proposed by Johnsen and Colonius [143], the volume fraction equation can be rewritten in semi-discrete form,

$$\left(\frac{\mathrm{d}\overline{z}_k}{\mathrm{d}t}\right)_i = -\frac{u_i}{\Delta x}\begin{cases} \left((z_k)_{L,i+1/2} - (z_k)_{L,i-1/2}\right) & u_i \geqslant 0 \\ \left((z_k)_{R,i+1/2} - (z_k)_{R,i-1/2}\right) & u_i \leqslant 0 \end{cases} \tag{4.116}$$

where $\overline{z}_k$ denotes a cell averaged value.

It can be verified that it satisfies the oscillation-free behaviour for an isolated contact surface, and that it also propagates shocks properly. However, if the pressure varies strongly in a field of non-constant volume fraction, the wave speed u_i of the advection equation is not consistent any more with the middle wave speed of the HLLC solver S_*.

To overcome the inconsistency between the different speeds, the chain rule is applied to the advection equation leading to,

$$\frac{\partial z_k}{\partial t} + \frac{\partial z_k u}{\partial x} - z_k \frac{\partial u}{\partial x} = 0 \tag{4.117}$$

where the second term is written as a conservative flux, and the third term is treated as a source term allowing the adjustment of the velocity. By further integrating Eq. 4.117 over a computational cell, we obtain a form similar to Eq. 4.50 with the addition of a source term,

$$\left(\frac{\mathrm{d}\overline{z}_k}{\mathrm{d}t}\right)_i = -\frac{1}{\Delta x}\left((z_k u)_{i+1/2} - (z_k u)_{i-1/2}\right) + \frac{1}{\Delta x}\int_{x_{i-1/2}}^{x_{i+1/2}} z_k \frac{\partial u}{\partial x}\,\mathrm{d}x \tag{4.118}$$

which is an exact equation. By approximating the cell integral value of z_k by $\overline{z}_k$ as done in the finite volume framework (Eq. 4.41), it yields,

$$\left(\frac{\mathrm{d}\overline{z}_k}{\mathrm{d}t}\right)_i = -\frac{1}{\Delta x}\left((z_k u)_{i+1/2} - (z_k u)_{i-1/2}\right) + \frac{1}{\Delta x}\overline{z}_k\left(u_{i+1/2}^{HLLC} - u_{i-1/2}^{HLLC}\right) \tag{4.119}$$

and where u^{HLLC} corresponds to the speed given by the HLLC solver for the conservative form of the equation, i.e. either u_L, u_R or S_*, thus ensuring the consistency between the different terms. This equation is exact far from interfaces, and is evaluated using a central difference scheme thus formally achieving a second-order accuracy. This does not deteriorate the solution accuracy as shock-capturing schemes are at most first-order at discontinuities [178]. However, when using the MUSCL5 scheme, 5^{th} order limited variables are used, thus making differences between a formally fifth-order scheme and a second-order one using fifth-order reconstructed data very small.

The fluxes at interfaces are thus given by,

$$F_{i+1/2}(z_k) = \begin{cases} \left(z_{k,L,i+1/2} - z_{k,i}\right) u_{L,i+1/2} & 0 \leqslant S_{L,i+1/2} \\ \left(z_{k,L,i+1/2} - z_{k,i}\right) S_{*,i+1/2} & S_{L,i+1/2} \leqslant 0 \;;\; 0 \leqslant S_{R,i+1/2}, S_{*,i+1/2} \\ \left(z_{k,R,i+1/2} - z_{k,i}\right) S_{*,i+1/2} & S_{L,i+1/2}, S_{*,i+1/2} \leqslant 0 \;;\; 0 \leqslant S_{R,i+1/2} \\ \left(z_{k,R,i+1/2} - z_{k,i}\right) u_{R,i+1/2} & S_{R,i} \leqslant 0 \end{cases} \tag{4.120}$$

$$F_{i-1/2}\left(z_k\right) = \begin{cases} \left(z_{k,L,i-1/2} - z_{k,i}\right) u_{L,i-1/2} & 0 \leqslant S_{L,i-1/2} \\ \left(z_{k,L,i-1/2} - z_{k,i}\right) S_{*,i-1/2} & S_{L,i-1/2} \leqslant 0 \ ; \ 0 \leqslant S_{R,i-1/2}, S_{*,i-1/2} \\ \left(z_{k,R,i-1/2} - z_{k,i}\right) S_{*,i-1/2} & S_{L,i-1/2}, S_{*,i-1/2} \leqslant 0 \ ; \ 0 \leqslant S_{R,i-1/2} \\ \left(z_{k,R,i-1/2} - z_{k,i}\right) u_{R,i-1/2} & S_{R,i-1/2} \leqslant 0 \end{cases} \tag{4.121}$$

and the difference of fluxes in a cell reads,

$$\begin{aligned} \frac{\partial F_i}{\partial x} &= \frac{1}{\Delta x}\left(F_{i+1/2} - F_{i-1/2}\right) \\ &= \frac{1}{\Delta x}\left(\left(z_{k,i+1/2} - z_{k,i}\right) u_{i+1/2} - \left(z_{k,i-1/2} - z_{k,i}\right) u_{i-1/2}\right) \\ &= \frac{1}{\Delta x}\left(z_{k,i+1/2} u_{i+1/2} - z_{k,i-1/2} u_{i-1/2} - z_{k,i}\left(u_{i+1/2} - u_{i-1/2}\right)\right) \end{aligned} \tag{4.122}$$

4.4 Computation of the viscous fluxes and source terms

4.4.1 Viscous fluxes and source terms

The governing equations in curvilinear coordinates have been presented at the beginning of the chapter in §. 4.1.2. They now need to be discretised within the finite volume framework where data are stored at cell centres and grid points at nodes. It can be reminded, that the chain rule of differentiation is used to compute spatial derivatives in physical space such as the following example for temperature,

$$T_x = \xi_x T_\xi + \eta_x T_\eta + \zeta_x T_\zeta \tag{4.123}$$

where variables derivatives in curvilinear space are estimated using central differencing at cell faces. A similar discretisation is used for metric derivatives. It can be further noted that the Jacobian appears only once in the implementation as,

$$T_x = \frac{1}{J}\left(\beta_{11} T_\xi + \beta_{21} T_\eta + \beta_{31} T_\zeta\right) \tag{4.124}$$

and the terms appearing in the fluxes computations are of the form $J\xi_x T_x$ leading to,

$$J\xi_x T_x = J\frac{1}{J}\beta_{11}\frac{1}{J}\left(\beta_{11} T_\xi + \beta_{21} T_\eta + \beta_{31} T_\zeta\right) \tag{4.125}$$

$$= \frac{1}{J}\beta_{11}\left(\beta_{11} T_\xi + \beta_{21} T_\eta + \beta_{31} T_\zeta\right) \tag{4.126}$$

Transport coefficients are centrally averaged at cell faces as well to obtain $\mu_{i+1/2}$, $\lambda_{i+1/2}$, $h_{k_{i+1/2}}$, etc. These centrally averaged values are then used to obtain the inter-cell boundary diffusion coefficients $D_{k_{i+1/2}}$.

Source terms are directly computed at cell centres using the cell-centred values available. It shall be noted that derivatives at cell centres (e.g. u'_Δ, ν_t, $|\underline{\mathbf{S}}|$) are computed using the previous relations but using cell-centred metrics, Jacobian values and central differencing.

4.4.2 Remarks on the QCVF

Recalling the species diffusion and source terms as derived for the QCVF in §. 3.5, one could remark that they are non-conservative for volume fractions. They have been derived to enforce mass conservation such that by summing diffusion fluxes or source terms across all species the results would be zero. However, they are not enforcing volume conservation, indicating that volume fractions are not conserved but merely transported. The novel extension of the QCVF to reacting and viscous flows presented in this work thus creates new challenges highlighted in this paragraph, as well as the solutions retained to

address them.

This can be illustrated by considering two species diffusing into each other at thermodynamic equilibrium (similar pressure and temperature). By assuming that one species is two times heavier than the other, mass conservation tells that the lighter fluid will diffuse twice as fast as the heavy fluid such that mass is conserved. This implies in turn that for every mole of dense fluid diffusing, two moles of the light must do as well. Under a pressure-temperature equilibrium each mole of gas takes up a similar volume, this then means that twice as much volume of the light gas will diffuse to ensure mass conservation, and the volume is not conserved.

This now poses a problem in the sense that the thermodynamic closure relies on volume fractions summing to unity. The novel solution derived, applied and validated in this work (§. 5.4.1) is to apply a correction to volume fractions when the departure from unity of their sum becomes too large (taken to be 10^{-13} in the code). The relaxation procedure works by modifying all species volume fractions in a cell to recover the pressure equilibrium with the additional constraints that each species mass and the total mass must be conserved as well as total energy. To do so an iterative isentropic compression or expansion is applied to all species following $PV^{\gamma} = cst$. This correction is applied in all cells where the departure from unity appears too large. In terms of volume fraction, this leads to,

$$\left(\frac{z_k^{m+1}}{z_k^m}\right)^{\gamma_k} = \left(\frac{P^{m+1}}{P^m}\right) \tag{4.127}$$

where m denotes the current iteration and $m+1$ the next one. At the end of the iterative process, we should have,

$$\sum_{k=1}^{N} z_k = 1 \tag{4.128}$$

$$\mathcal{C}^m \sum_{k=1}^{N} \left(\frac{P^{m-1}}{P^m}\right)^{\frac{1}{\gamma_k^{m-1}}} z_k^m - 1 = 0 \tag{4.129}$$

where,

$$\mathcal{C}^m = \left(\sum_{k=1}^{N} \left(\frac{P^{m-1}}{P^m}\right)^{\frac{1}{\gamma_k^{m-1}}} z_k^{m-1}\right)^{-1} \tag{4.130}$$

The iterative process thus unfolds as follows,

1. Estimate the two first values of pressure P^0 and P^1 using for P^0 the procedure outlined in Appendix A.1, while P^1 is computed with the assumption that $\gamma_k = \gamma_{mix}$
2. The first iteration looks like

$$\mathcal{C}^1 = \left(\sum_{k=1}^{N} \left(\frac{P^0}{P^1}\right)^{\frac{1}{\gamma_k^0}} z_k^0\right)^{-1} \tag{4.131}$$

3. From $\mathcal{C}^m$ a new set of species volume fraction can be computed using,

$$z_k^m = \mathcal{C}^m \sum_{k=1}^{N} \left(\frac{P^{m-1}}{P^m}\right)^{\frac{1}{\gamma_k}^{m-1}} z_k^{m-1} \tag{4.132}$$

4. A new value of P^m can then be estimated using Appendix A.1, as well as γ_k^m using $\rho\varepsilon$ and z_k^m
5. This is iterated until a certain tolerance is obtained for $\dfrac{P^m - P^{m-1}}{P^m}$ which is set to 10^{-10} in the present work.

A second question arising when using the QCVF is the definition of the species density when a species is not initially present in the cell. In reacting flows, at the first time-step when a species will be produced in a cell, its density is undefined given that its volume fraction is zero, according to Allaire *et al.* [7]. The choice taken in this work is to use the mixture temperature and pressure, and compute the species density at those given conditions, which means that both diffusion and species creation happen at the mixture conditions.

Finally, the question of the enthalpy fluxes is posed. The QCVF models allows each species to have its own temperature during diffusion. The approach taken here is to keep the individual species temperature constant during diffusion.

4.5 Time integration

4.5.1 Time-stepping schemes

Once all the fluxes (viscous and inviscid) and source terms have been computed, time integration of Eq. 4.53 can be carried out. Several solutions exist to this end, the most direct of them being the explicit Euler scheme which is first-order accurate.

Higher-order accuracy in time can be achieved with multi-step methods, the so-called *Runge-Kutta* methods. Time integration is performed in multiple explicit stages. For each stage, fluxes and source terms are computed separately using the solution obtained at the previous stage as the new initial condition.

By considering again the curvilinear ODE obtained by the application of the method of lines to the governing equations and written in Eq. 4.53, one can see that all right-hand side terms have now been computed, leaving only a differential form on the left hand side. The different time integration schemes presented below are used to advance this ODE in time.

First-order explicit Euler

The first-order forward discretisation of the time derivative leads to,

$$\frac{(J\mathbf{U})_{i,j,k}^{n+1} - (J\mathbf{U})_{i,j,k}^{n}}{\Delta t} = \mathrm{RHS}\left(\mathbf{U}^n,\, t^n\right) \tag{4.133}$$

where the operator RHS indicates the explicit computation of the right-hand side of Eq. 4.53 using $\mathbf{U}^n$ at time t^n. As already pointed out, computations presented in this work have all been obtained on stationary grids, which implies $J_{i,j,k}^n = J_{i,j,k}^0$. By regrouping all terms corresponding to the current time on the right-hand side of the equation, we obtain,

$$\mathbf{U}_{i,j,k}^{n+1} = \mathbf{U}_{i,j,k}^{n} + \frac{\Delta t}{J_{i,j,k}} \left(\mathrm{RHS}\left(\mathbf{U}^n,\, t^n\right)\right) \tag{4.134}$$

where the time-step size Δt discussed in §. 4.5.2 satisfies the stability constraints of explicit schemes.

Two-stage second-order Runge-Kutta method

This scheme has been derived by Ruuth and Spiteri [255] and is described as being an optimal two-stage, second-order explicit strong stability preserving Runge-Kutta scheme. The integration is performed in a predictor and a corrector stage,

- *Predictor stage* : An intermediate solution $\mathbf{U}^1$ is computed using a first-order Euler scheme

$$\mathbf{U}^1_{i,j,k} = \mathbf{U}^n_{i,j,k} + \frac{\Delta t}{J_{i,j,k}} \left(\mathrm{RHS}\left(\mathbf{U}^n,\, t^n\right)\right) \tag{4.135}$$

- *Corrector stage* : The solution at time t^{n+1} is obtained using the following expression,

$$\mathbf{U}^{n+1} = \frac{1}{2}\left(\mathbf{U}^1 + \mathbf{U}^n + \frac{\Delta t}{J_{i,j,k}} \left(\mathrm{RHS}\left(\mathbf{U}^1,\, t^1\right)\right)\right) \tag{4.136}$$

The estimation of a stable time-step size is discussed in §. 4.5.2.

Two-stage second-order strong stability preserving Runge-Kutta method

Similarly to the two-stage scheme, the four-stage second-order strong stability preserving Runge-Kutta scheme (RK2-SSP) of Ruuth and Spiteri [255] is considered in this work. This scheme feature three predictor stages allowing the computation of three intermediate solutions, and a fourth stage behaving as a corrector step. However, the scheme is second-order as only a single intermediate solution is required in the corrector step.

- *Predictor stage 1*

$$\mathbf{U}^1_{i,j,k} = \mathbf{U}^n_{i,j,k} + \frac{\Delta t}{3J_{i,j,k}} \left(\mathrm{RHS}\left(\mathbf{U}^n,\, t^n\right)\right) \tag{4.137}$$

- *Predictor stage 2*

$$\mathbf{U}^2_{i,j,k} = \mathbf{U}^1_{i,j,k} + \frac{\Delta t}{3J_{i,j,k}} \left(\mathrm{RHS}\left(\mathbf{U}^1,\, t^1\right)\right) \tag{4.138}$$

- *Predictor stage 3*

$$\mathbf{U}^3_{i,j,k} = \mathbf{U}^2_{i,j,k} + \frac{\Delta t}{3J_{i,j,k}} \left(\mathrm{RHS}\left(\mathbf{U}^2,\, t^2\right)\right) \tag{4.139}$$

- *Corrector stage*

$$\mathbf{U}^{n+1}_{i,j,k} = \frac{1}{4}\mathbf{U}^n_{i,j,k} + \frac{3}{4}\mathbf{U}^3_{i,j,k} + \frac{\Delta t}{4J_{i,j,k}} \left(\mathrm{RHS}\left(\mathbf{U}^3,\, t^3\right)\right) \tag{4.140}$$

The estimation of a stable time-step size is presented below.

4.5.2 Stability constraints and definition of the time-step size

The choice of a time-step size for the different explicit integration schemes presented above is critical and must satisfy stability constraints. For the compressible Navier-Stokes equations, but also for the others models (QCMF, QCVF and FCVF), these stability constraints are given by two conditions, the first one on the inviscid fluxes, and the second one on the viscous fluxes. One could also add a constraint on the source terms.

The inviscid constraint results from the fact that waves emanating from both sides of the cells at the local Riemann solver must not interact with each other during the time-step. Indeed, their interactions are highly non-linear phenomena that cannot be accounted for during the averaging process. Therefore, the time-step is limited to avoid this,

$$\Delta t^i_{\min} = \mathrm{CFL}\,\frac{\min\left(\Delta\xi_i\right)}{\max\left(\lambda_i\right)} \tag{4.141}$$

where $\xi_i = \xi, \eta, \zeta$ and the λ_i are the system eigenvalues, which for a three-dimensional domain are $\lambda_0 = u^*$, $\lambda_1 = \lambda_0 - c$ and $\lambda_2 = \lambda_0 - c$ where u^* is the cell face normal velocity.

The CFL parameter is the well known *Courant-Friedrichs-Lewy* number and provides some control on the time-step size. The largest this coefficient is, the largest the time-step size is, and therefore the more efficient the time integration becomes. However, one must take care to keep its value within some limits such that time integration remains stable. Stability limits for the three implemented schemes are given below,

- *Explicit Euler* : $0 < \mathrm{CFL} < 1$
- *RK2* : $0 < \mathrm{CFL} < 1$
- *RK2-SSP* : $0 < \mathrm{CFL} < 3$

The second limitation on the time-step size stems from viscous phenomena present in the flow, and especially on the limitation of the cell Reynolds number or Peclet number. The viscous time-step size is thus limited by either viscous diffusion (viscosity), thermal diffusion (heat conductivity and mixture heat capacity) or species diffusion (Schmidt number),

$$\Delta t^\mu_{\min} = \mathrm{CFL}\,\frac{\rho \min\left(\Delta\xi_i\right)^2}{2\mu} \tag{4.142}$$

$$\Delta t^\lambda_{\min} = \mathrm{CFL}\,\frac{\rho C_v \min\left(\Delta\xi_i\right)^2}{2\lambda} \tag{4.143}$$

$$\Delta t^{Sc}_{\min} = \mathrm{CFL}\,\frac{\rho \min\left(Sc_k\right) \min\left(\Delta\xi_i\right)^2}{2\mu} \tag{4.144}$$

During the computation, each of these restrictions is computed in every cells, and the smallest value is taken as the time-step size for the current time-step, yielding,

$$\Delta t = \min\left(\Delta t^i_{\min},\ \Delta t^\mu_{\min},\ \Delta t^\lambda_{\min},\ \Delta t^{Sc}_{\min}\right) \tag{4.145}$$

4.6 Boundary conditions

Although boundary conditions are often seen as a small and non-critical part of simulations, it has been shown that deriving adequate boundary conditions for multi-species compressible reacting flows is a critical issue in many codes. This is particularly relevant in codes using high-order methods (low dissipation methods), such as LES and DNS. The periodic boundary conditions often seen in DNS simulations, represents the only case where an exact closure of the problem can be given at the boundary. It works by folding the domain onto itself thus alleviating the need for boundary conditions. However, this limits considerably the methods range of applications, as inlets and outlets are essential in a number of relevant combustion applications such as combustors, etc. [238].

Additionally, unsteady simulations of the compressible Navier-Stokes equations require an accurate control of waves reflections at the computational domain boundaries, where they have to be eliminated to avoid interacting with the solution. Within the RANS framework, the numerical dissipation is usually

high enough to eliminate acoustic waves, but as LES strives to reduce numerical viscosity, it is often found that waves amplitudes are not attenuated within the computational domain, therefore requiring non-reflecting or absorbing boundary conditions.

This section presents the implementation of the different types of boundary conditions considered in this work, where both Navier-Stokes Characteristic (NSCBC) and simple boundary conditions are considered. The NSCBC implementation is presented first, with an highlight on the novel derivation for the QCVF model, while simpler formulations of the boundary conditions are considered next. Details about the derivation of the NSCBC can be found in Appendix D.

4.6.1 Navier-Stokes Characteristic Boundary Conditions (NSCBC)

To achieve such a non-reflecting or absorbing behaviour, a new technique for the boundaries treatment based on the inviscid characteristic theory was introduced for the Euler equations [271, 272], which was further extended to the Navier-Stokes equations by Poinsot and Lele [237]. However the formulation proposed by Poinsot and Lele was derived for perfect gases with constant and homogeneous thermodynamic properties. An extension of their method to tackle multi-species reacting flows with complex thermodynamic properties has been presented by Baum *et al.* [18]. This is a field of constant improvement, and work is still carried out to improve the different formulations considered. The reader is directed towards [224, 268, 299] for a more comprehensive presentation.

The technique shared by these methods is based on the idea that any hyperbolic system of conservation laws can be decomposed into a corresponding system of propagating waves, where at the boundaries some are leaving the domain, while others are penetrating it. Outgoing waves are completely determined by the solution inside the computational domain, while incoming wave can not be fully determined without some additional informations provided by the user, given under the form of boundary conditions. To determine the waves corresponding to the problem at hand, a transformation between the current conservative system and a primitive system where propagation directions and amplitudes can be calculated is needed. This transformation can take numerous forms depending on the set of equations, primitive and conservative variables used to derive it.

The principle of the method is thus to infer incoming waves amplitudes from the outgoing waves and some appropriate LODI (Local One Dimensional Inviscid) relations. The derivation of the LODI relations is presented in Appendix D.

More details about the transformation applied to the governing equations are given in Appendix D where the choice of the set of primitive variables used ($\mathbf{V} = [u, P, \rho Y_k]^T$ for mass fraction models and $\mathbf{V} = [u, P, \rho_k z_k, z_k]^T$ for volume fraction models) is discussed and where derivations of the wave structures for the different models are presented.

4.6.2 Implementation of the NSCBC

Derivations presented in Appendix D have allowed to replace convective derivatives (flux terms) in the primitive system by equal values expressed in terms of characteristic waves of the system (Eq. D.44 and Eq. D.89 for the mass and volume fraction models respectively). The conservative system was also replaced by a system where fluxes have been replaced by characteristic waves of the system (Eq. D.53 and Eq. D.98 for the mass and volume fraction models respectively).

The next step is to determine the waves whose values will change at boundaries depending on the chosen boundary conditions. This is achieved by assuming that in the case of the full Navier-Stokes equations, the waves amplitudes are similar to the case of a local inviscid one-dimensional problem, defined by the so-called LODI relations. These are used to provide the "compatibility" relations between

incoming and outgoing waves in conjunction with the physical boundary conditions selected. The LODI relations for the velocity, pressure, species mass fractions and temperature are presented below,

$$\frac{\partial u}{\partial t} + \frac{1}{2}\left(\mathcal{L}_1 - \mathcal{L}_2\right) = 0 \tag{4.146}$$

$$\frac{\partial P}{\partial t} + \frac{\rho c}{2}\left(\mathcal{L}_1 + \mathcal{L}_2\right) = 0 \tag{4.147}$$

$$\frac{\partial \rho Y_k}{\partial t} + \frac{\rho Y_k}{2c}\left(\mathcal{L}_1 + \mathcal{L}_2\right) + \mathcal{L}_{2+k} = 0 \tag{4.148}$$

$$\frac{\partial \rho}{\partial t} + \frac{\rho}{2c}\left(\mathcal{L}_1 + \mathcal{L}_2\right) + \mathcal{L}_S = 0 \tag{4.149}$$

$$\frac{\partial Y_k}{\partial t} + \frac{1}{\rho}\left(\mathcal{L}_{2+k} - Y_k \mathcal{L}_S\right) = 0 \tag{4.150}$$

$$\frac{\partial T}{\partial t} + \frac{(\gamma - 1)\, T}{2c}\left(\mathcal{L}_1 + \mathcal{L}_2\right) - \frac{T}{\rho \mathcal{R}} \sum_{k=1}^{N} \mathcal{R}_k \mathcal{L}_{2+k} = 0 \tag{4.151}$$

where the wave strengths are given by Eqs. D.39-D.40 for the mass fraction models and Eqs. D.83-D.84 for the volume fraction models. These relations are used to infer the $\mathcal{L}_i$'s correct values at boundaries, so that they are compatible with the chosen conditions.

The whole procedure followed for the boundary treatment can be summarised as,

1. Time integration is done as described in the previous sections inside the computational domain.
2. At each boundary, eigenvalues signs are computed ($\lambda_+ = u + c$, $\lambda_- = u - c$, $\lambda_k = u$), and the $\mathcal{L}_i$'s associated with waves leaving the domain are determined from the inside solution by using one-sided derivatives.
3. Using the LODI relations, the $\mathcal{L}_i$'s associated with incoming waves are estimated by taking into account the user inputs as presented in the next section.
4. When all the $\mathcal{L}_i$'s are known, their values are used to compute the normal term vector $\mathbf{d}$ (Eq. D.45 for mass fraction and Eq. D.90 for volume fraction models) which is fed back into the system (Eq. D.53 for mass fraction and Eq. D.98 for volume fraction models) to advance the solution in time. The viscous, diffusive and reacting terms are also computed using one-sided derivatives and the interior points and added to the inviscid systems.

4.6.3 Subsonic inlet

Once the LODI relations are known, it is straightforward using the technique presented by Poinsot and Lele [237]. Many different inlet conditions can be chosen, where different quantities, gradients, etc. are imposed. In the present work however, a soft inlet has been implemented (perfectly non-reflecting inlet) and another case where the velocity, mixture composition, temperature and pressure are imposed as time varying quantities.

It shall be noted that a supersonic inflow features no leaving wave, and thus characteristic boundary conditions are not justified in this case.

Perfectly non-reflecting inlet

For non-reflecting inlets, all waves enter the domain except the one associated with the eigenvalue $u - c$. In theory, to obtain a perfectly non-reflecting inlet, all waves amplitudes entering the domain need to be zero, while $\mathcal{L}_-$ is computed using the domain information. In practice doing so often leads to an

ill-posed problem, and a possible drift of inlet values leading to an erroneous mass flow. To circumvent this, incoming waves are often relaxed towards the imposed inlet state such that,

$$\mathcal{L}_+ = -\mathcal{B}_+ \left(u - u_{in}\right) \tag{4.152}$$
$$\mathcal{L}_k = -\mathcal{B}_k \left(Y_k - Y_{k_{in}}\right) \tag{4.153}$$

where $\mathcal{B}_+$ and $\mathcal{B}_k$ are relaxation coefficients and u_{in} and $Y_{k_{in}}$ are the imposed inlet quantities.

Controlled inflow

In the case of a controlled inflow, some quantities are specified at the inlet and can vary in time. This type of inflow is one of the most used at is allows to control the amount of turbulence provided by the inlet, or to control the mixture composition, temperature, velocity as functions of what happens inside the domain. It is used in this work for the control of a laminar flame position in the domain by adapting the inlet velocity to the flame movements.

In this inflow, the wave $\mathcal{L}_-$ ($\mathcal{L}_2$) associated with the eigenvalue $\lambda_- = u - c$ is the only one leaving the domain, and as such is fully determined by the domain data. From Eq. 4.146, we have,

$$\mathcal{L}_1 = \mathcal{L}_2 - 2\left(\frac{\partial u}{\partial t}\right)^t \tag{4.154}$$

where quantities denoted $()^t$ are target quantities to impose at the boundary. Similarly, using Eq. 4.150, the wave $\mathcal{L}_{2+k}$ becomes,

$$\mathcal{L}_{2+k} = Y_k \mathcal{L}_S - \rho\left(\frac{\partial Y_k}{\partial t}\right)^t \tag{4.155}$$

The problem is now to express the entropy wave as a function of the other known waves amplitudes. The temperature LODI can be rewritten as,

$$\sum_{k=1}^{N} \mathcal{R}_k \mathcal{L}_{2+k} = \left(\frac{\partial T}{\partial t}\right)^t \frac{\rho \mathcal{R}}{T} + \left(\mathcal{L}_1 + \mathcal{L}_2\right) \frac{\left(\gamma - 1\right)}{2c} \frac{\rho T \mathcal{R}}{T} \tag{4.156}$$

By multiplying Eq. 4.150 by $\mathcal{R}_k$, we obtain,

$$\frac{\partial \mathcal{R}_k Y_k}{\partial t} + \frac{\mathcal{R}_k}{\rho}\left(\mathcal{L}_{2+k} - Y_k \mathcal{L}_S\right) = 0 \tag{4.157}$$

By summing the previous relation for all species, it yields,

$$\frac{\partial \mathcal{R}}{\partial t} + \frac{1}{\rho}\sum_{k=1}^{N} \mathcal{R}_k \mathcal{L}_{2+k} - \frac{\mathcal{R}\mathcal{L}_S}{\rho} = 0 \tag{4.158}$$

By isolating $\mathcal{L}_S$, it reads,

$$\mathcal{L}_S = \frac{\rho}{\mathcal{R}} \frac{\partial \mathcal{R}}{\partial t} + \frac{1}{\mathcal{R}} \sum_{k=1}^{N} \mathcal{R}_k \mathcal{L}_{2+k} \tag{4.159}$$

By inserting Eq. 4.156 and replacing $\mathcal{L}_1$ by its value given by Eq. 4.154, the entropy wave is finally given by,

$$\mathcal{L}_S = \frac{\rho}{\mathcal{R}} \sum_{k=1}^{N} \left(\mathcal{R}_k \left(\frac{\partial Y_k}{\partial t}\right)^t\right) + \frac{\rho}{T}\left(\frac{\partial T}{\partial t}\right)^t + \frac{\rho\left(\gamma - 1\right)}{c}\left(\mathcal{L}_2 - \left(\frac{\partial u}{\partial t}\right)^t\right) \tag{4.160}$$

4.6.4 Subsonic outlet

Similarly to the inlet boundary condition, there are many different possible choices for the outlet of the domain. Forced responses can be chosen to simulate specific flows, but the most widely used outlet conditions are either the perfectly non-reflecting or partially non-reflecting outflows. The first one does not necessarily lead to a well-posed problem as if the pressure is not specified by the inlet, the flow has no mean to know what would the mean pressure be. Physically the mean pressure is conveyed by pressure waves reflecting on regions far from the computational domain where the static pressure is fixed back to the inside of the boundaries. Additionally, if perfectly non-reflecting outlet is used, a drift in the mean value of pressure is usually observed. For these reasons, only the partially non-reflecting outflow is used in this work.

At the outflow, the only wave entering the domain is the wave with the eigenvalue $u-c$, which is $\mathcal{L}_-$ or $\mathcal{L}_2$. Only the pressure need to be fixed at the outlet, the other quantities will fluctuate to accommodate pressure changes. Therefore, only Eq. 4.147 is needed and for an outlet with a constant static pressure, this yields,

$$\mathcal{L}_2 = -\mathcal{L}_1 \tag{4.161}$$

However, this generates reflecting waves as one inviscid condition is enforced [237]. Only "soft" boundary conditions are able to lead to both a well-posed problem and control the outlet pressure without imposing it. This leads to,

$$\mathcal{L}_2 = \mathcal{B}_2 \left(P - P_\infty\right) \tag{4.162}$$

where $\mathcal{B}_2 = \sigma \left(1 - M^2\right) c/L$ where σ is an adjustable constant, L is the dimension of the domain and M denotes the maximum Mach number in the flow.

4.6.5 Slip wall / Symmetry

Adiabatic slip walls or symmetry boundary conditions are very useful in numerous computations. They are characterised by a single inviscid condition, the normal velocity is zero. As the normal velocity is zero, it immediately yields that $\mathcal{L}_{2+k}$ is zero. The wave associated with the eigenvalue $u - c$ is leaving the domain while the one associated with $u + c$ is entering the domain. Eq. 4.146 suggests that,

$$\mathcal{L}_1 = \mathcal{L}_2 \tag{4.163}$$

4.6.6 Non characteristic boundary conditions

In two and three-dimensional situations, NSCBC can become quite difficult to use, especially in presence of walls, corners, and common boundary cells shared by outflow and wall for example. Such corners cells present a challenge for the method, as an outflow would have its pressure value imposed, while it is supposed to be left completely free for the wall and the question of what would be the best treatment of such cells still remains an open question. Additionally, edges have to be treated by considering a second set of NSCBC conditions related to the second direction of the surface to be treated. As pointed out previously, supersonic inflow and outflow boundary conditions to not require special treatments and as no complex subsonic inflow is used in this work, NSCBC are not used in multi-dimensional simulations. Instead, simple boundary conditions are considered usually involving a zero gradient condition.

Symmetry

Symmetry conditions or slip walls are quite easy to treat, as they only require to enforce a zero normal velocity, while mixture composition, pressure and temperature are left floating. As no flux must cross the inter-cell boundaries, symmetry condition is enforced by copying cell values across the boundary, while taking care of recalculating the velocity components such that the velocity vector in the boundary cells has the same magnitude but an opposite direction as the one in the domain. This generates a symmetric Riemann solver with no flux across the inter-cell boundary.

Viscous wall

On a viscous wall, the same procedure as the symmetry condition is applied, but this time, all velocity components are reversed in boundary cells, such that both tangential and normal velocities are zero. Temperature, pressure and mixture composition are left floating.

Supersonic inflow/outflow

In supersonic inflow/outflow, the boundary treatment is very simple. In the case of an inflow, boundary cells are initialised with the correct values and left untouched during the whole simulation. As no information can propagate upstream, they will not be modified by the flow. For outflows, boundary cells are filled by copying value emanating from the last cell of the domain. As no information can travel upstream, these boundary conditions simply correspond to a zero gradient condition.

Subsonic outflow

This case is slightly more involved, as it would require a proper wave control to obtain the correct solution. In our case, the pressure is held fixed at the value decided by the user, velocities are just copied in boundary cells with the hypothesis of a Von Neumann boundary (zero gradient). The energy is thus recalculated, as well as the density. Two additional measures are taken to minimize pressure reflections in the domain. The first one consists in using as much as possible a damping domain where pressure waves and discontinuities are getting smoother such that the zero gradient hypothesis remains valid. Secondly, the hyperbolic operator is solved with a reduced order of accuracy (Upwind1) to smooth even more any discontinuities in the flow, thereby reducing even more the possible reflections.

4.7 Conclusion

The two numerical techniques (double-flux and classical Godunov scheme) used in this work with the two formulations (mass and volume fractions) have been presented in this section. The Godunov method (§. 4.2) was introduced in a curvilinear coordinate system (§. 4.1), while the approximate HLLC Riemann solver used throughout this work was also presented (§. 4.3.1). The different variable reconstruction schemes (§. 4.3.2), time-stepping algorithms (§. 4.5) and stable time-step size estimation (§. 4.5.2) are also detailed.

The evaluation of the hyperbolic fluxes for the double-flux (QCMF) method was shown (§. 4.3.4) following the original derivation presented in [6, 25]. The computation of the advective fluxes for the novel quasi-conservative volume fraction (QCVF) was also introduced (§. 4.3.5) using both the HLLC solver for the equations written in conservation form, and an extension of the HLLC to tackle the outstanding issue of the remaining non-conservative equations for the transport of volume fraction. Thus a unified framework build around the HLLC solver and high-order MUSCL reconstruction methods is able to accurately solve the QCMF, FCMF, FCVF and QCVF equation sets.

The implementation of viscous and source terms was also briefly highlighted (§. 4.4), but remains much simpler than the hyperbolic fluxes calculation. To counteract the non-conservation of volume fraction during diffusive and reactive processes, a pressure equilibrium technique has been introduced (§. 4.4.2) to enforce the pressure equilibrium in cells where the sum of the volume fractions would depart too much from unity.

Finally, the implementation of characteristic boundary conditions (NSCBC) for the mass fractions equation is presented (§. 4.6) based on the previous published work, and a novel implementation of characteristic boundary conditions for the volume fraction (Volume Fraction Characteristic Boundary Conditions) system of equations is discussed. The mathematical details and validation of this new derivation

on classical acoustic and entropy waves propagation are discussed in Appendix D.

In the next chapters, the following models and techniques will be used,

- Quasi-Conservative Volume Fraction (5-equation model of Allaire *et al.* [7] augmented by the author to solve viscous and reacting flows)
- Fully-Conservative Volume Fraction (author's reformulation of the 5-equation model)
- Quasi-Conservative Mass Fraction (double-flux model of Abgrall and Karni [6] and Billet [25])
- Fully-Conservative Mass Fraction (Navier-Stokes equations)

PART II

Validation and verification of the proposed algorithms

CHAPTER 5

One-dimensional validation and verification tests

The numerical methods presented in Chapter 4 used to solve the governing equations presented in Chapter 3 have been implemented in a new code referred to as `FlAMEnCo1D` written from scratch by the author. The code solves the presented equations using the discussed numerical methods in a one-dimensional domain discretised by a mesh composed of Nx equidistant cells on a single CPU.

This chapter provides detailed information on many of the verification problems that were used to ensure that the implemented methods worked properly, gain confidence on their use and knowledge about their respective limits, strengths and weaknesses. Results were compared against analytical solutions (when available), literature values (when available) or the internationally accepted `Cantera` [110] code for combustion problems.

The first section details the validation of the implementation of the Riemann solver, time marching algorithms and variable reconstruction at cell interfaces on a simple problem (§. 5.1). A second section details the behaviour of the hyperbolic operators of the different equation sets presented above that are compared on problems of increasing complexity (§. 5.2). Next, diffusion effects are added and tested (§. 5.3). Finally, chemical reactions are accounted for, and the different approaches are tested on complex viscous reacting compressible problems (§. 5.4). All validation tests and the governing equations operators tested are summarised in Table 5.1.

Test cases	Advection		Diffusion	Reaction
	Sub.	Sup.		
Inviscid test cases (§. 5.2)				
Stationary contact surface	✓			
Moving material surface	✓	✓		
Moving contact surface	✓	✓		
Multi-species shock-tube	✓	✓		
Shock-bubble interaction	✓	✓		
Diffusive test cases (§. 5.3)				
Pure diffusion			✓	
Advection diffusion	✓	✓	✓	
Reactive test cases (§. 5.4)				
0D Constant Volume Reactor				✓
1D laminar flame	✓		✓	✓
1D detonations	✓	✓	✓	✓

Table 5.1: *Summary of one-dimensional validation test problems - Sub. stands for "Subsonic" and Sup. for "Supersonic", ✓ means that this part of the governing equations was tested*

As one of the key characteristic of methods addressing the pressure oscillations issue is their quasi-conservative behaviour, it is important to measure these errors such that the performance of each model can be assessed. It shall be noted that these are quite difficult to compare between different authors as they are quite sensitive to the implementation of the different schemes, but similar trends can be obtained. Similarly to Billet and Abgrall [25], conservation errors at time-step n are computed as follows,

$$\mathcal{E}_{\mathbf{W}}^{n} = \left| \frac{\displaystyle\int_0^L \left(\mathbf{W}^n(x) - \mathbf{W}^0(x)\right) \mathrm{d}x}{\displaystyle\int_0^L \mathbf{W}^0(x)\, \mathrm{d}x} \right| \tag{5.1}$$

where $\mathbf{W}^n$ is the vector of conserved variables $[\rho Y_k,\ \rho u,\ \rho E]^T$ at time n, and $x \in [0\,;\ L]$ is the computational domain.

Throughout the whole chapter, the four different approaches implemented to simulate reacting compressible mixtures of perfect gases are referred to as **QCVF** for the 5-equation model of Allaire *et al.* [7] extended to viscous and reacting flows, **FCVF** for the 5-equation model of Allaire *et al.* [7] written in strong conservation form, **FCMF** for the Navier-Stokes equations solved with classical Godunov scheme, and **QCMF** for the double-flux model of Abgrall and Karni [6] and Billet and Abgrall [25].

5.1 Time-stepping, reconstruction schemes and Riemann solver validation

5.1.1 Time-stepping and reconstruction validation

The different time-stepping schemes, as well as the different reconstruction methods are validated on the simple gaseous bubble advection test.

Test case

Initial conditions for this problem are defined with a bubble of high temperature helium (He) being carried by a nitrogen (N_2) coflow. The helium temperature is $T_{He} = 2000\,[K]$, while the nitrogen temperature is $T_{N_2} = 1000\,[K]$, pressure is constant everywhere in the flow field with $P = 101325\,[Pa]$. The bubble is $D = 0.2\,[m]$ wide and initially sits at $x_0 = 0.5\,[m]$. The flow speed is set at $U = 100\,[m/s]$ towards the positive x. The computation is carried out for a full displacement cycle, until the bubble comes back to its original position, or $t_f = 10^{-2}\,[s]$.

The domain is discretised by $Nx = 200$ cells while the interface values are computed using the MUSCL5 scheme. The calorically perfect EoS is considered, while the QCVF model is used. Periodic boundary conditions are applied on both sides of the domain, while the time marching algorithm is RK2-SSP with $CFL = 0.3$.

Results for the time-marching algorithms

A comparison between the different time marching algorithm is presented in Fig. 5.1 where almost no difference can be seen between the different algorithms implemented. The slight differences observed between the RK2(-SSP) schemes and the Euler are mostly due to the fact that at $CFL = 0.3$, the Euler scheme is closer to its stability limit than the two others.

This is further visible in Fig. 5.2 where solutions obtained for different time-marching schemes are presented for several CFL values. For smooth problems the theoretical limits are $CFL < 1$ for Euler and

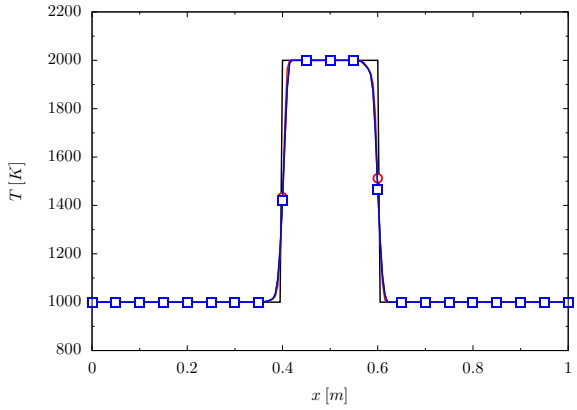

Figure 5.1: *Comparison between implemented time-stepping schemes with* $CFL = 0.3$ - — *Ref,* ○ *Euler,* ⬠ *RK2,* □ *RK2-SSP*

RK2 and $CFL < 3$ for RK2-SSP, while here, Euler becomes unstable for $CFL > 0.3$, and RK2-SSP for $CFL > 1.5$. RK2 is the only scheme where both theoretical and practical limits seem to match.

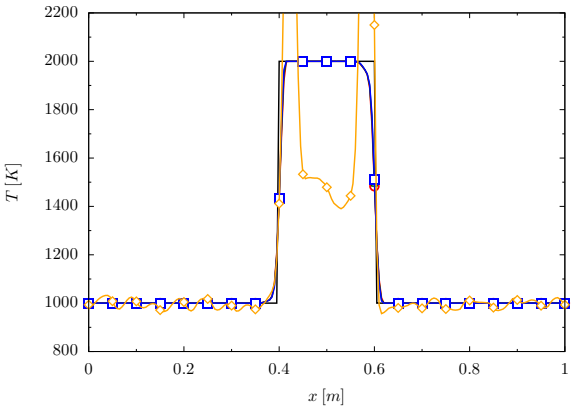

(a) *Euler scheme* - — *Ref,* ○ $CFL = 0.1$, ⬠ $CFL = 0.2$, □ $CFL = 0.3$, ◇ $CFL = 0.4$

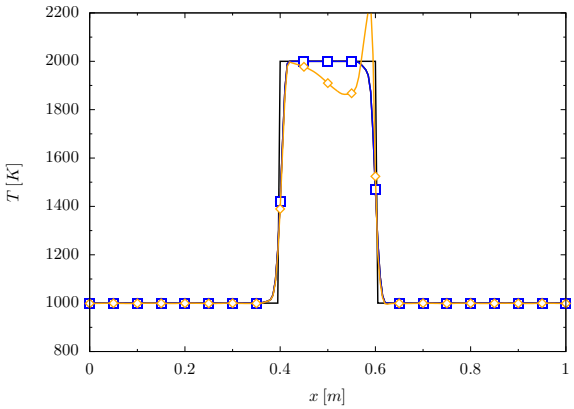

(b) *RK2 scheme* - — *Ref,* ○ $CFL = 0.3$, ⬠ $CFL = 0.5$, □ $CFL = 0.95$, ◇ $CFL = 1.1$

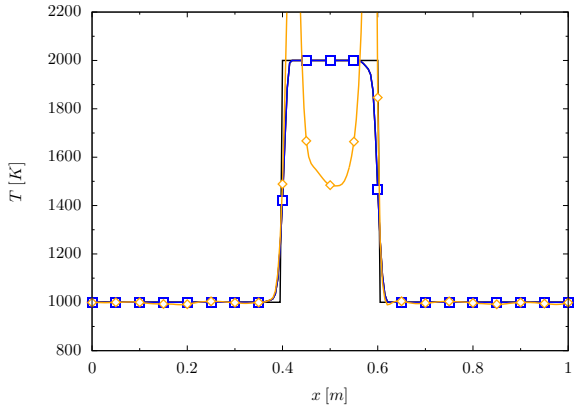

(c) *RK2-SSP scheme* - — *Ref,* ○ $CFL = 0.3$, ⬠ $CFL = 0.9$, □ $CFL = 1.5$, ◇ $CFL = 2.0$

Figure 5.2: *Comparison of the sensitivity to the CFL for the implemented time-marching algorithms*

Results for the reconstruction order of accuracy

Results obtained with the different reconstruction methods are presented in Fig. 5.3 where grids of $Nx = 100$ and $Nx = 500$ cells have been considered. The results are as expected with a significantly smeared contact surface obtained with the Upwind1 reconstruction, less so for the MinMod2 and sharply resolved for the MUSCL5. It can be noted that the MUSCL5 used on $Nx = 100$ cells still gives better results than the Upwind1 with $Nx = 500$ cells. Additionally, a grid convergence is observed with all reconstruction schemes, indicating that the current implementation seems correct.

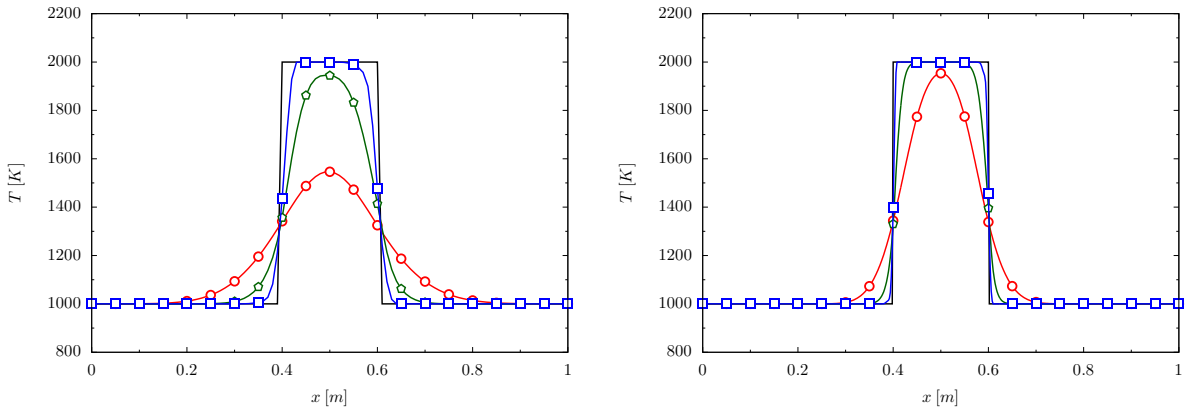

(a) $Nx = 100$ **(b)** $Nx = 500$

Figure 5.3: *Comparison between the different reconstruction methods and effect of grid refinement -* — *Ref,* ○ *Upwind1,* ⬠ *MinMod2,* □ *MUSCL5*

5.1.2 Riemann solver validation

Due to its unique properties, shock tube benchmark problems have been widely used for numerical algorithms validations resulting in a large amount of data in the literature. Exact solutions can also be computed when considering calorically perfect gases, and iterative procedures can be derived to obtain approximate solutions in the thermally perfect case [140].

In a typical shock tube experiment, three waves develop, namely a contact wave, a shock wave and a rarefaction wave. The currently employed Riemann approximate solver (HLLC) features the capability of capturing accurately the three type of waves. This test case tests the correct implementation of the Riemann solver in a single case. It shall be noted that in this case, only a single species is considered, which makes this problem different than the multi-species shock tube experiment presented later.

As presented in §. 4.3.2 primitive variables are limited at cell interfaces, and the two test cases discussed here will help shed some light on the relevance of this choice.

Test cases

The test cases considered for the Riemann solver validation are defined by setting $\mathbf{Q} = [P,\ T,\ U]^T$ to the left and right of a diaphragm positioned initially at $x_0 = 0.5\ [m]$.

- Shock tube problem initially defined by,

$$\mathbf{Q_L} = [10\ [atm],\ 300\ [K],\ 0\ [m/s]]^T$$
$$\mathbf{Q_R} = [1\ [atm],\ 300\ [K],\ 0\ [m/s]]^T$$

- Colliding shock problem initialised as,

$$\mathbf{Q_L} = [1\ [atm],\ 262.5\ [K],\ 500\ [m/s]]^T$$
$$\mathbf{Q_R} = [1\ [atm],\ 262.5\ [K],\ -500\ [m/s]]^T$$

The gas considered for this study is nitrogen (N_2) using the calorically perfect EoS. Both problems are computed on a meter long domain using walls on both sides as boundary conditions. The computational domain is discretised with $Nx = 500$ cells, while the solution is marched in time using the RK2-SSP scheme and a CFL number of $CFL = 0.5$. The variables are limited at the cell interface using the MUSCL5 reconstruction method. The FCMF formulation is used for this problem.

Results

The analytical solution of the Riemann problem is used as the reference solution for the shock tube problem, while for the colliding shocks, a computation using the Upwind1 limiting method and $Nx = 5000$ cells is being used.

Shock tube results are depicted in Fig. 5.4 and Fig. 5.5 for $t = 8 \times 10^{-4}\ [s]$, while the colliding shocks ones are visible in Fig. 5.6 for $t = 4 \times 10^{-4}\ [s]$.

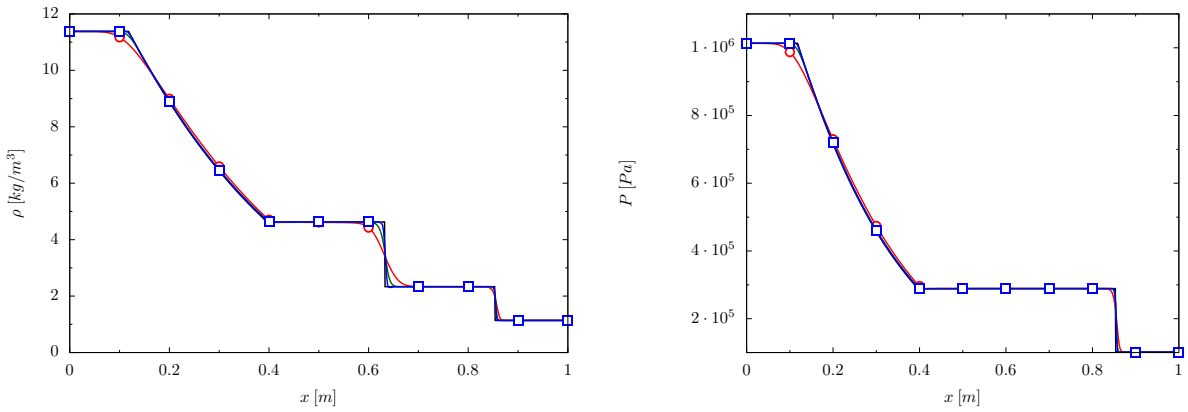

(a) *Density* **(b)** *Pressure*

Figure 5.4: *Comparison of the reconstruction methods on the single species shock tube problem at* $t = 8 \times 10^{-4}\ [s]$ *using* $Nx = 500$ *cells -* — *Ref,* ○ *Upwind1,* ⬠ *MinMod2,* □ *MUSCL5*

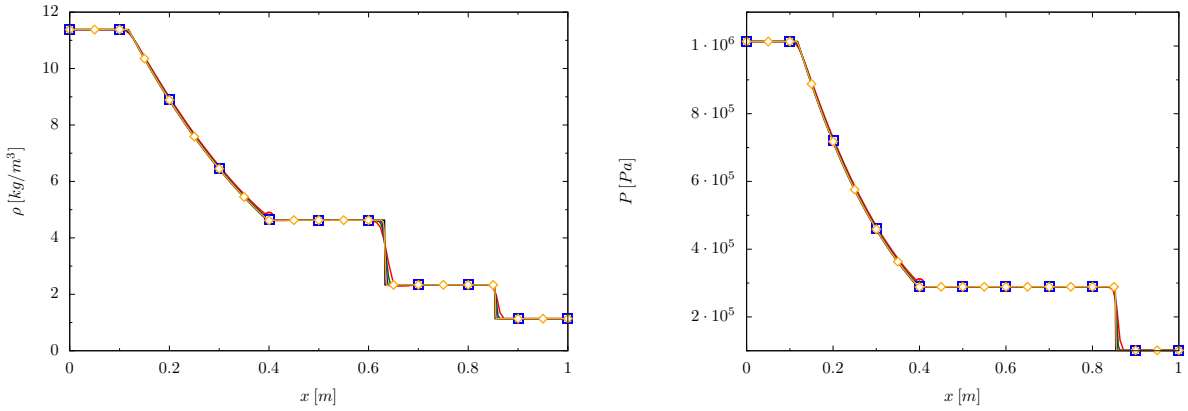

(a) *Density* **(b)** *Pressure*

Figure 5.5: *Grid convergence on the single species shock tube problem at* $t = 8 \times 10^{-4}\ [s]$ *with MUSCL5 reconstruction -* — *Ref,* ○ $Nx = 125$, ⬠ $Nx = 250$, □ $Nx = 500$, ◇ $Nx = 1000$

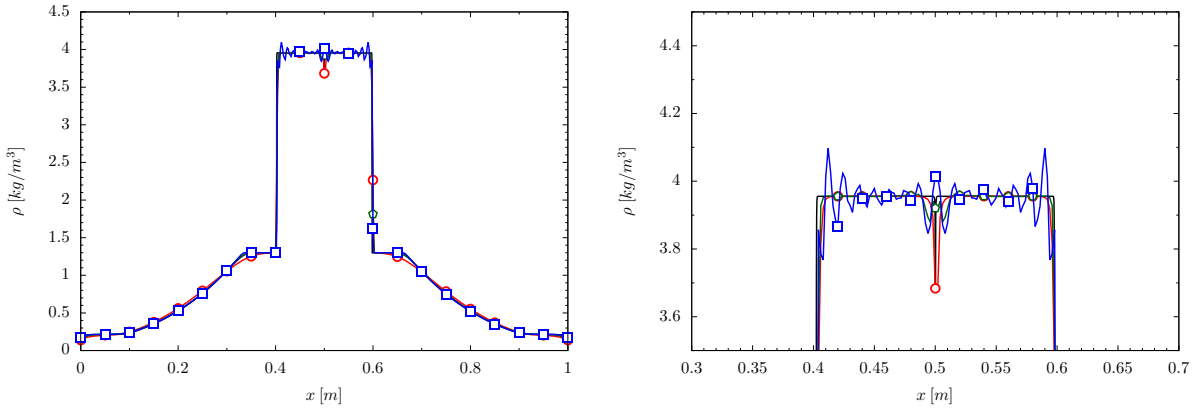

(a) *Density* **(b)** *Zoom on collision*

Figure 5.6: *Comparison of the reconstruction methods on the single species colliding shocks problem at* $t = 4 \times 10^{-4}\ [s]$ *with* $Nx = 500$ *cells - — Ref, Upwind1, MinMod2, MUSCL5*

The first remark is that calculations agree very well with reference solutions, thereby indicating a correct implementation of the Riemann solver. On the shock tube problem, all reconstruction methods seem to capture the shock front quite accurately, but the contact surface is significantly smeared by the Upwind1 limiting. Grid convergence shows that using the MUSCL5 limiting technique allows an accurate capture of all types of waves even on coarse grids.

The colliding shocks problem highlights clearly the short wavelength oscillations generated at a shock front by limiting primitive variables when using high-order methods. As already pointed out, characteristic variables could be limited at the shock thus reducing the oscillations amplitude, but these usually only occurs in extreme situations. Moreover, it can be seen that the MinMod2 limiter features a solution which is oscillation free without a noticeable decrease in the accuracy.

It shall also be noted that all reconstruction schemes exhibit a small temperature spike (and density dip) at the location where the two shocks collide. This effect does not seem to disappear with grid refinement, as even the reference solution depicts it.

5.1.3 Conclusion

This section has presented the HLLC Riemann solver implementation validation, as well as the different reconstruction schemes and time-marching algorithms. The results presented are pointing towards a correct implementation of all these components as results compare very well with analytical (or reference) solutions available.

Given that the time-marching algorithm does have a negligible impact on the results, and given that the RK2-SSP method features the largest stability range of the three methods implemented, unless otherwise mentioned, it will be use throughout this work.

Taking into account the accurate results provided by the MUSCL5 scheme over a range of problems, unless otherwise mentioned, this scheme will be used throughout the rest of the work. However, the reader shall keep in mind, that in some cases, this limiter definition coupled with primitive variable reconstruction might lead to short wavelength oscillations near shocks.

5.2 Inviscid test cases

In this section, the hyperbolic operator of the different equation sets presented in Chapter 3 will be tested in a variety of configurations of increasing complexity, from a stationary contact surface to a multi-species shock tube experiment using thermally perfect gases.

A particular emphasis will be put in this section on conservation errors generated by the different schemes, such that more information on their respective behaviour can be gathered.

5.2.1 Stationary contact interface

This simple test case is used to check whether the implemented methods are stable in presence of stationary discontinuities. It shall be reminded that the double-flux method works only with Riemann solvers perfectly preserving stationary contact waves, and this problem helps highlighting this feature of the HLLC Riemann solver. The capability of the HLLC approximate solver to account correctly for the presence of the contact discontinuity is also tested.

Test case

The initial set-up is similar to the one presented in §. 5.1.1 at the exception, that this time the velocity is set to zero everywhere in the domain. The domain is discretised with $Nx = 500$ cells, and $CFL = 0.5$ is considered for the time marching. Both EoS are considered in this case. The final time of the computation has been chosen as $t_f = 10^{-1}\,[s]$, thus leaving the time to any (if any) instability to develop. The expected behaviour of such a test case is for the solution at any time to be strictly similar to the initial conditions.

Results

Results obtained with the thermally perfect EoS are depicted in Fig. 5.7 for the different primitive variables. Similar results are obtained with the calorically perfect EoS. The observed behaviour is as expected, where the different quantities remain constant over time without generating spurious oscillations despite the almost 5×10^5 iterations it took to reach the final time. The HLLC capability of capturing stationary contact interfaces, and keeping them stationary without generating spurious oscillations has thus been demonstrated.

Conservation errors are depicted in Fig. 5.8. It can be remarked that both FCVF and QCVF do conserve mass and energy perfectly (to machine precision), while an extremely small imbalance can be observed for the FCMF and QCMF approaches. Interestingly, the imbalance observed here seems to plateau for the FCMF, but keep growing very slowly for the QCMF (5×10^5 iterations lead to a change in errors of 10^3).

5.2.2 Moving material interface

Test case

A material interface as defined by Johnsen *et al.* [144] is a discontinuity in mixture composition (i.e. between two fluids) in an otherwise uniform flow field. A bubble of helium (He) is carried by a nitrogen (N_2) coflow in a uniform temperature ($T = 750\,[K]$) and pressure ($P = 101325\,[Pa]$) flow. The speed of both the coflow and bubble is initially set at $U = 100\,[m/s]$ in the increasing x-direction. The bubble size is set to $D = 0.2\,[m]$. The computation is also carried out for a full cycle, i.e. $t_f = 10^{-2}\,[s]$.

The meter long domain is discretised with $Nx = 500$ cells, $CFL = 0.5$ is used for the time-marching and the thermally perfect EoS is considered. Periodic boundary conditions are applied on both sides of

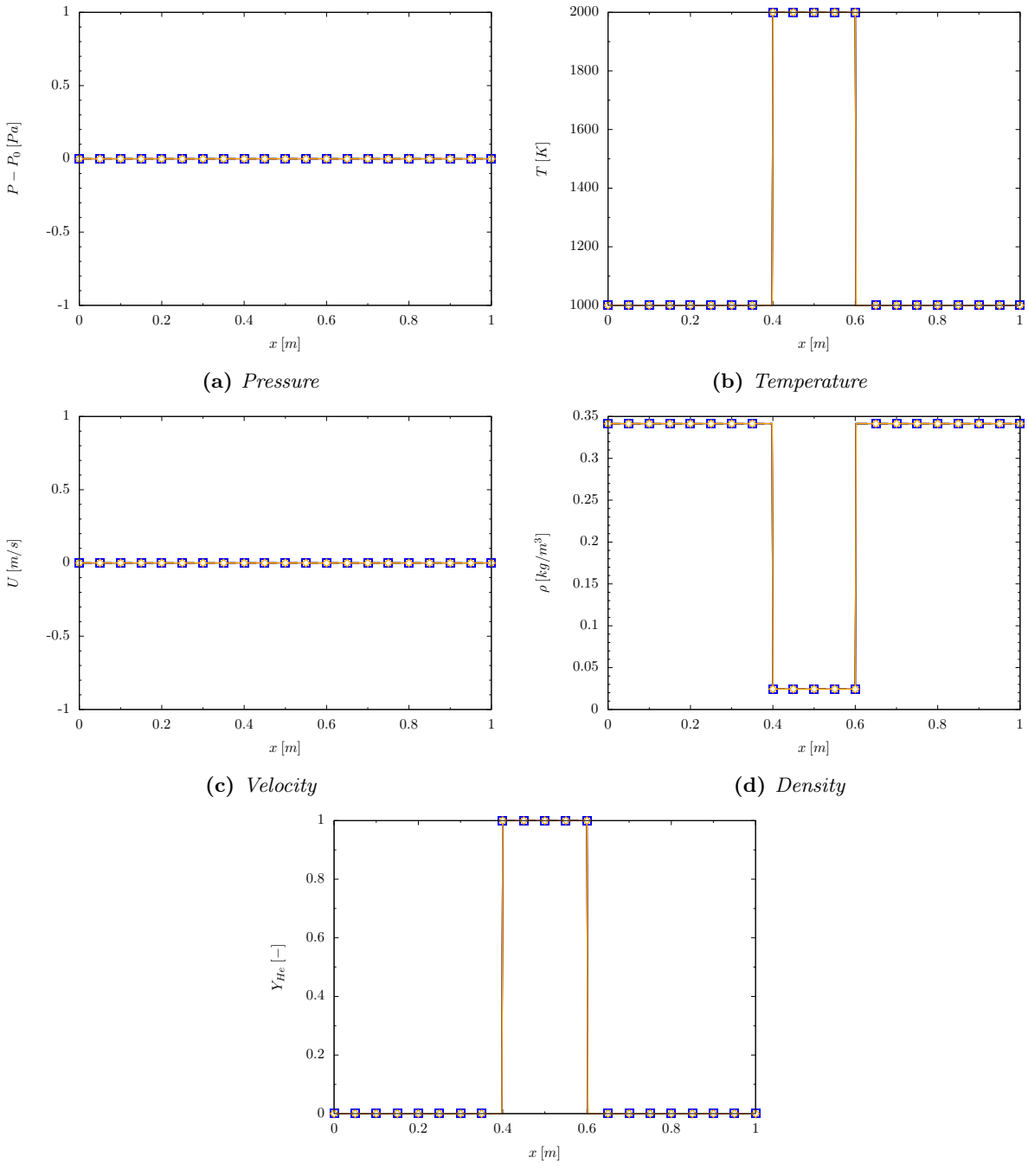

(a) *Pressure* **(b)** *Temperature*

(c) *Velocity* **(d)** *Density*

(e) Y_{He}

Figure 5.7: *Primitive variables for the stationary contact surface computed with the thermally perfect EoS at* $t = 10^{-1}$ *[s] -* — *Ref,* ○ *QCVF,* ⬠ *FCVF,* □ *QCMF,* ◇ *FCMF*

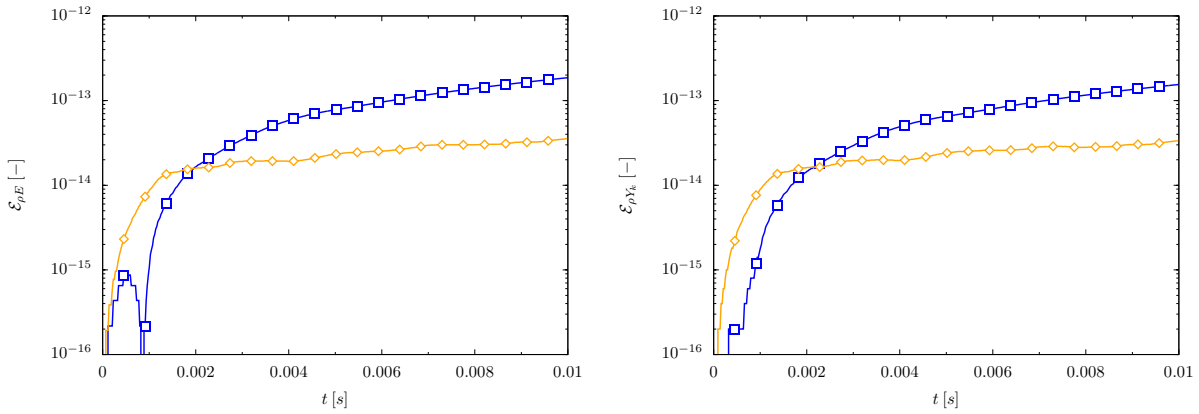

(a) *Total Energy* **(b)** *Total Mass*

Figure 5.8: *Conservation errors for the stationary contact surface computed with the thermally perfect EoS -* ○ *QCVF,* ⬠ *FCVF,* □ *QCMF,* ◇ *FCMF*

the domain.

Results

The reference solution used here is analytical and simply corresponds to the initial condition.

Fig. 5.9 depicts results obtained with the thermally perfect EoS, although it shall be noted that similar results are obtained with the calorically perfect EoS. No FCVF results are visible here, as temperature spikes at the interface prevented the simulation from running after $t = 1 \times 10^{-4}$ $[s]$. The failure of the classical Godunov method (FCMF) applied to the resolution of multi-species flows with different heat capacity ratios is here clearly illustrated. High wave-number pressure oscillations are observed with a rather large magnitude ($\Delta P \approx 300[Pa]$), while the velocity field is also contaminated through the pressure gradient term in the momentum equations. Finally, large temperature spikes ($\Delta T \approx 1200\,[K]$) are visible on both sides of the He bubble. It can also be pointed out that pressure oscillations in a one dimensional domain would trigger Kelvin-Helmoltz instabilities in two- and three-dimensional simulations, thereby increasing artificially any mixing rate. Both of these effects (temperature spikes and pressure oscillations) are clearly unacceptable in any type of simulation.

Both quasi-conservative methods (QCVF and QCMF) are performing well, and the pressure field is maintained perfectly uniform throughout the simulation, as are the velocity and temperature fields. The He mass fraction plot (Fig. 5.9) indicates that the QCMF seems to be the most diffusive method while the QCVF seems to be the least. Regarding the QCMF, this could be due to the fact that the Riemann problem is solved twice at the interface, and as such the amount of numerical diffusion would be increased compared to the FCMF. A possible explanation for the QCVF sharp resolution of the contact wave could be its second-order formulation (i.e. without numerical diffusion) for the volume fraction transport equation, thus reducing the overall diffusion added to the solution.

The test case has also been repeated using supersonic speed (i.e. $U = 1000\,[m/s]$) to test whether this would make a difference, but the results remain remarkably similar albeit featuring larger pressure and temperature departures from the analytical solution.

Conservation plots for the momentum, energy and mass are presented in Fig. 5.10. Both QCVF and FCMF model seem to conserve perfectly all conserved quantities, as conservation errors do stabilise around $\mathcal{E} \approx 10^{-14}$ after an initial growth, which correspond roughly to machine precision. On the other hand, QCMF conservation errors although extremely small as well ($\mathcal{E} < 10^{-12}$) do not seem to be bounded

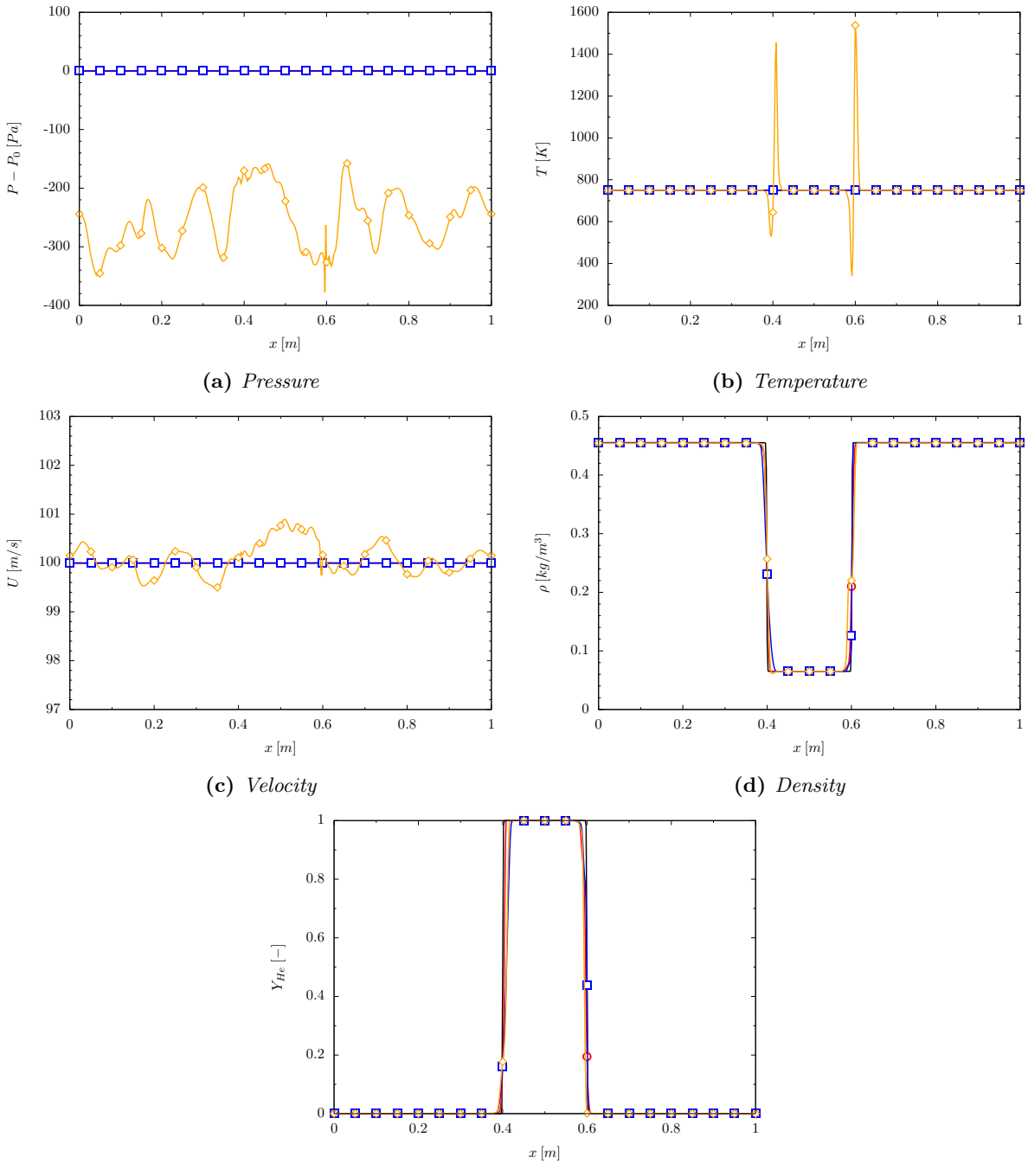

(a) *Pressure* **(b)** *Temperature*

(c) *Velocity* **(d)** *Density*

(e) Y_{He}

Figure 5.9: *Primitive variables for the moving material discontinuity computed with the thermally perfect EoS at* $t = 10^{-2}$ $[s]$ - — *Ref,* ○ *QCVF,* ⬠ *FCVF,* □ *QCMF,* ◇ *FCMF*

and are continuously increasing. Results presented by Houim and Kuo [133] and Billet and Abgrall [25] seems to agree with this, despite featuring more oscillating error profiles.

It is worth highlighting here that the comparison of conservation errors between authors is a challenging problem as this type of error is extremely dependent on the implementation, compiler options and hardware used for the simulations. Nonetheless, orders of magnitude comparisons are feasible, and so far the present work compares very well with the published data.

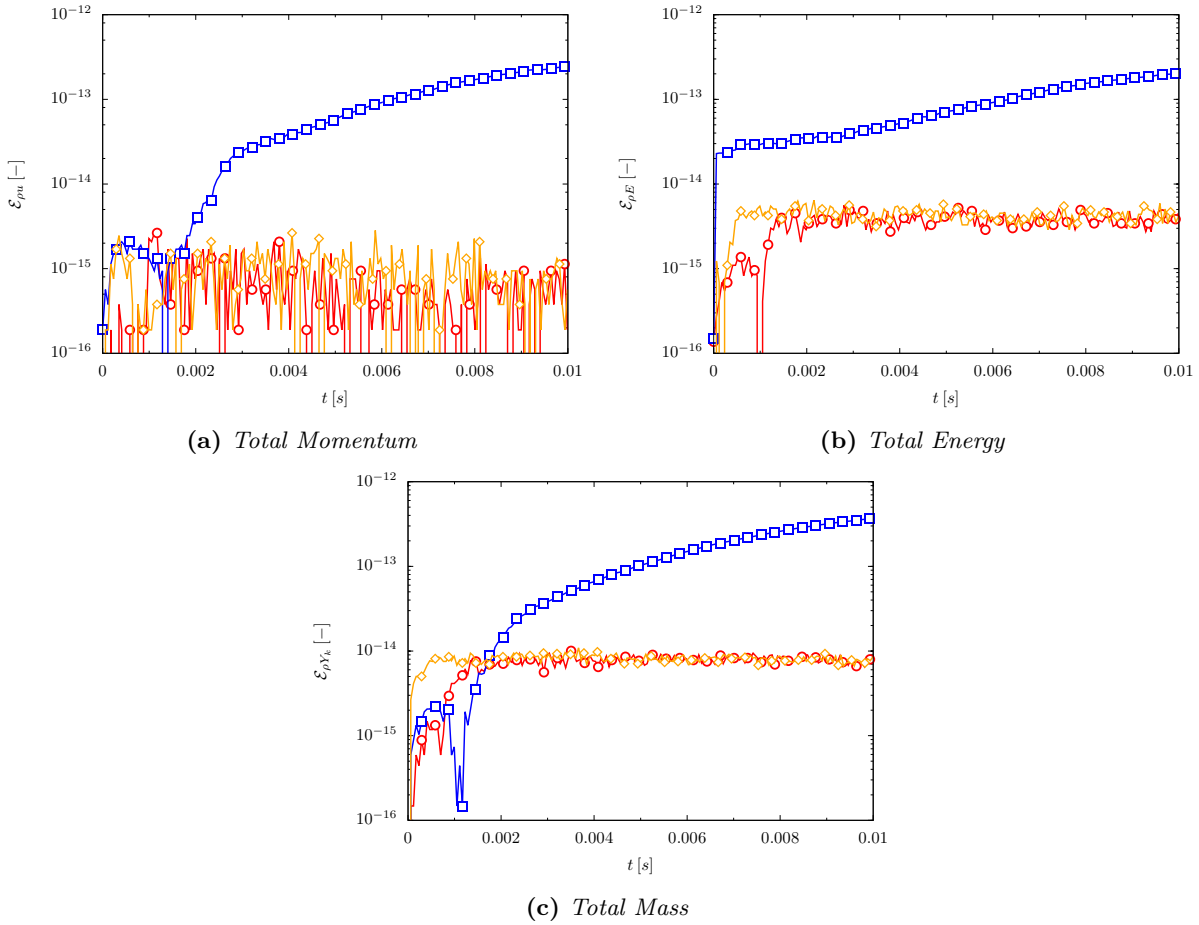

(a) *Total Momentum*

(b) *Total Energy*

(c) *Total Mass*

Figure 5.10: *Conservation errors for the moving material discontinuity computed with the thermally perfect EoS -* ○ *QCVF,* ⬠ *FCVF,* □ *QCMF,* ◇ *FCMF*

5.2.3 Moving contact interface

Test case

This test case is similar to the one used for the time-marching algorithms and reconstruction schemes validations (§. 5.1.1) and is dubbed as a moving contact surface, using here the definition of Johnsen *et al.* [144], i.e. a discontinuity across which both composition and temperature are different, but the pressure and velocity remain uniform.

The domain is discretised with $Nx = 500$ cells, while $CFL = 0.5$ is used for advancing the solution in time until $t_f = 10^{-2}$ $[s]$. Periodic boundary conditions are used on both sides.

Results

Plots of relevant variables are displayed on Fig. 5.11, while conservation errors are pictured on Fig. 5.12. Similarly to the material wave test case, the most striking feature is the failure of the conservative schemes to advect a contact surface without pressure oscillations. The oscillations magnitude is even larger in the present case compared to the material interface, they are nearly twice as large ($\Delta P \approx 800\,[Pa]$), while the velocity high wavenumber oscillations are also larger ($\Delta U \approx 6\,[m/s]$). This is believed to be due to the temperature discontinuity. A slight density undershoot can also be observed for the FCMF at the left interface, which could potentially cause negative mass fractions.

Interestingly, the FCVF method features a rather clean temperature field ($\Delta T \approx 5\,[K]$) even if both the pressure and velocity fields are contaminated with oscillations. On the other hand, both quasi-conservative methods conserve perfectly pressure and velocity. The temperature field is also correctly reproduced, and once again it can be seen that the QCMF seems slightly more diffusive than the QCVF model.

Although leading to vastly erroneous results, both fully-conservative schemes do conserve all conserved quantities very well almost to machine precision. The QCVF also does a very good job at featuring both an oscillation free solution and very low conservation errors which are comparable to the fully-conservative schemes. On the contrary, the main weakness of the QCMF is highlighted with this test case. Although conserving both mass and momentum very well (less so than the other schemes), it does not do so for total energy with a final error of $\mathcal{E}_{\rho E} \approx 0.4\%$, comparable to the results presented by Houim [133] for a similar test case. However such errors have to be tolerated since classical fully-conservative methods are unable to compute such a problem.

5.2.4 Multi-species shock tube

Test cases

The capability of the HLLC solver and the different approaches to deal with multi-species variable γ shock problems is tested in this section by using three test cases of increasing complexity. Similarly to the single species shock tube presented in §. 5.1.2, the left and right states are defined in terms of $\mathbf{Q} = [P,\, T,\, U,\, Y_k]^T$ and the initial position of the interface is given by x_0. The test cases are as follows,

- N_2/He shock tube with $x_0 = 0.4\,[m]$ and,

$$\mathbf{Q_L} = [10\,[atm],\, 300\,[K],\, 0\,[m/s],\, Y_{He} = 1,\, Y_{N_2} = 0]^T$$
$$\mathbf{Q_R} = [1\,[atm],\, 300\,[K],\, 0\,[m/s],\, Y_{He} = 0,\, Y_{N_2} = 1]^T$$

- H_2/O_2 shock tube with $x_0 = 0.5\,[m]$ and,

$$\mathbf{Q_L} = [10\,[atm],\, 750\,[K],\, 0\,[m/s],\, Y_{H_2} = 1,\, Y_{O_2} = 0]^T$$
$$\mathbf{Q_R} = [1\,[atm],\, 750\,[K],\, 0\,[m/s],\, Y_{H_2} = 0,\, Y_{O_2} = 1]^T$$

- H_2/O_2 shock tube with $x_0 = 0.5\,[m]$ and,

$$\mathbf{Q_L} = [50\,[atm],\, 750\,[K],\, 0\,[m/s],\, Y_{H_2} = 1,\, Y_{O_2} = 0]^T$$
$$\mathbf{Q_R} = [1\,[atm],\, 750\,[K],\, 0\,[m/s],\, Y_{H_2} = 0,\, Y_{O_2} = 1]^T$$

The first problem is rather simple as γ_{He} is constant across the whole temperature range and the shock is sufficiently weak such that γ_{N_2} changes occurring at the shock are rather small. The second problem increases the level of complexity with two species featuring a variable γ with larger changes than N_2. Finally, the last problem increases even further the pressure jump between the left and right states

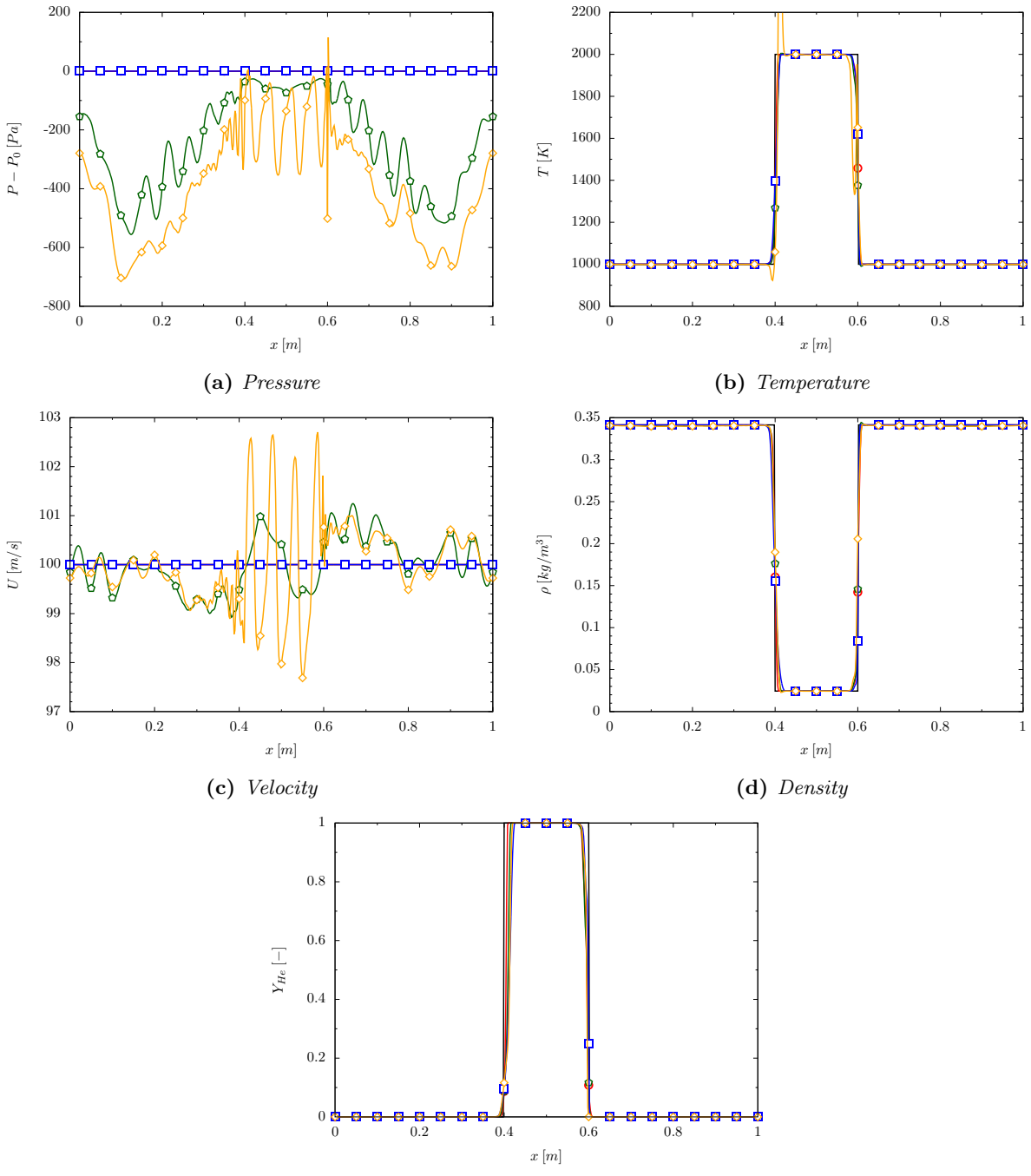

(a) *Pressure*

(b) *Temperature*

(c) *Velocity*

(d) *Density*

(e) Y_{He}

Figure 5.11: *Primitive variables for the moving contact wave computed with the thermally perfect EoS at* $t = 10^{-2}\ [s]$ - — *Ref,* ○ *QCVF,* ⬠ *FCVF,* □ *QCMF,* ◇ *FCMF*

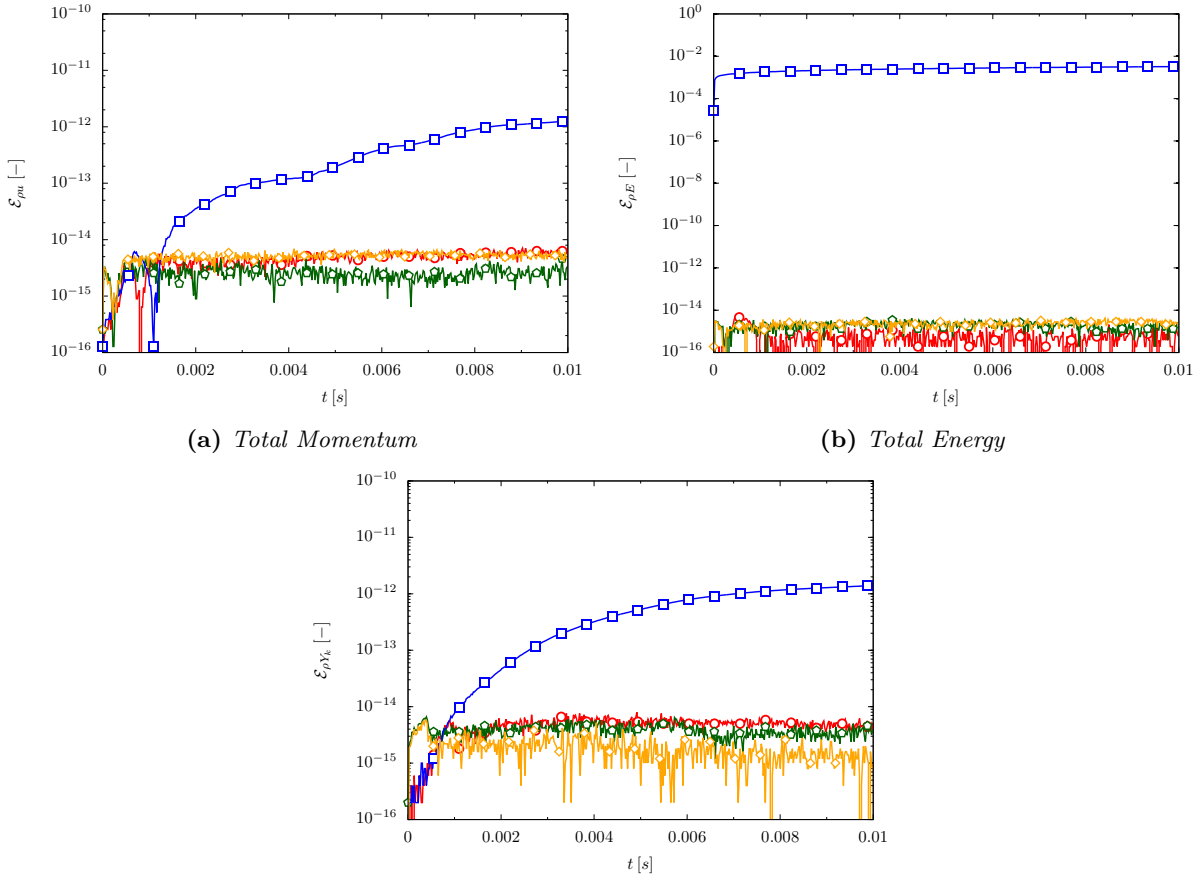

(a) *Total Momentum*

(b) *Total Energy*

(c) *Total Mass*

Figure 5.12: *Conservation errors for the moving contact wave computed with the thermally perfect EoS -* ○ *QCVF,* ⬠ *FCVF,* □ *QCMF,* ◇ *FCMF*

to test the shock capturing capabilities of the quasi-conservative methods at large Mach number. This is indeed a known deficiency that can potentially occur with quasi-conservative methods where shock position and speed are not well predicted.

The meter long computational domain is discretised with $Nx = 1000$ cells, while $CFL = 0.3$ is used for the time marching. Both boundary conditions are walls, but the solution is stopped before either the rarefaction or shock waves reach them. The first problem is thus computed up to $t_f = 3 \times 10^{-4}\,[s]$, while the two O_2/H_2 problems are simulated up $t_f = 2 \times 10^{-4}\,[s]$.

Results

Analytical solutions in the shocked region for the first problem have been calculated using the iterative procedure highlighted in John [140] and are compared in Table 5.2 with the results obtained with the different models. Results for the He/N_2 shock problem are presented in Fig. 5.13 for the variables of interest and Fig. 5.14 for the conservation errors.

The first observation regards the complete failure of the FCVF system of equations to tackle shock wave problems. Not a single variable is predicted correctly showing that this method can not be applied in the simulation of multi-species flows. This complete failure does remind of the results presented by Lv and Ihme [188] for the FCMF scheme. From this point, the FCVF scheme will not be considered any more for simulations.

All remaining schemes (FCMF, QCVF, QCMF) behave correctly and capture accurately the three waves of the problem. The slight undershoot of pressure (resp. overshoot of velocity) at the tail of the expansion wave for the QCVF model is a remnant of the initial discontinuity and is not considered to be indicative of any particular weakness of the model. The QCMF also features such an undershoot (resp. overshoot), albeit of a significantly smaller magnitude. The FCMF suffers from a non-physical jump of velocity across the contact surface which is analogous to the results obtained by Karni [147] who showed that the rate of convergence of this error as mesh resolution increases is extremely slow. It can also be noted that errors between analytical and computed results are quite small for all schemes except the FCVF, and just slightly above 1% on the temperature and density values, and as such can be tolerated.

Variables	Computed				Exact	Difference (%)			
	QCVF	FCVF	FCMF	QCMF		QCVF	FCVF	FCMF	QCMF
$V_{shock}\ [m.s^{-1}]$	709.5	-	710	710	**712**	0.351	-	0.281	0.281
$P\ [MPa]$	0.4609	-	0.4614	0.4609	**0.4617**	0.173	-	0.065	0.173
$\rho\ [kg.m^{-3}]$	3.062	-	3.063	3.063	**3.03**	1.056	-	1.089	1.089
$T\ [K]$	507.1	-	507.4	507	**513.1**	1.150	-	1.092	1.170
$U\ [m.s^{-1}]$	445.6	-	446	445.6	**444.7**	0.202	-	0.292	0.202

Table 5.2: *Comparison between analytical and computed shocked values for the multi-species He/N_2 shock-tube problem computed with the thermally perfect EoS*

Energy and mass are both perfectly conserved by both fully-conservative schemes and the QCVF model. Once more, the QCMF suffers from a poor conservation of energy with a final error of roughly 0.2 % which is lower than the reported value in Houim and Kuo [133]. The mass conservation of the QCMF appears to be better in our case ($\mathcal{E}_{\rho Y_k} \approx 10^{-14}$), while Houim and Kuo reported about 7×10^{-4}. However, despite these conservation errors, the multi-species Riemann problem is calculated with a high degree of accuracy by the QCMF approach.

Regarding the two other test cases, upwind solutions have also been obtained with $Nx = 5000$ cells and the QCMF model and will be used as reference data. The increased complexity of the problems is that γ now varies in both the shock and rarefaction regions, while on the previous test case, it did not vary in the rarefaction. Results for both pressure ratios ($P_L/P_R = 10$ and $P_L/P_R = 50$) are presented in Fig. 5.15 and Fig. 5.16 respectively. Variations of γ in the domain for both test cases are visible in Fig. 5.17, while conservation errors are depicted in Fig. 5.18.

The agreement between reference and computed solutions is once again very good for all models. The FCMF model features large spikes in pressure, velocity and temperature at the contact surface, while temperature was not impacted in the previous test case. These temperature spikes are also visible on the values of γ in Fig. 5.17. The relative magnitude of these spikes seems relatively independent of the pressure ratio initially applied.

The most significant difference between the results obtained for both O_2/H_2 shock problems and the He/N_2 is visible in Fig. 5.18 for the QCMF model. The mass conservation error is not negligible any more, reaching $\mathcal{E}_{\rho Y_k} \approx 10^{-4}$ %, but is independent of the shock strength. The energy error is smaller than in the He/N_2 shock and is found to decrease with the shock strength. Both the FCMF and QCVF feature similar conservation errors in all cases.

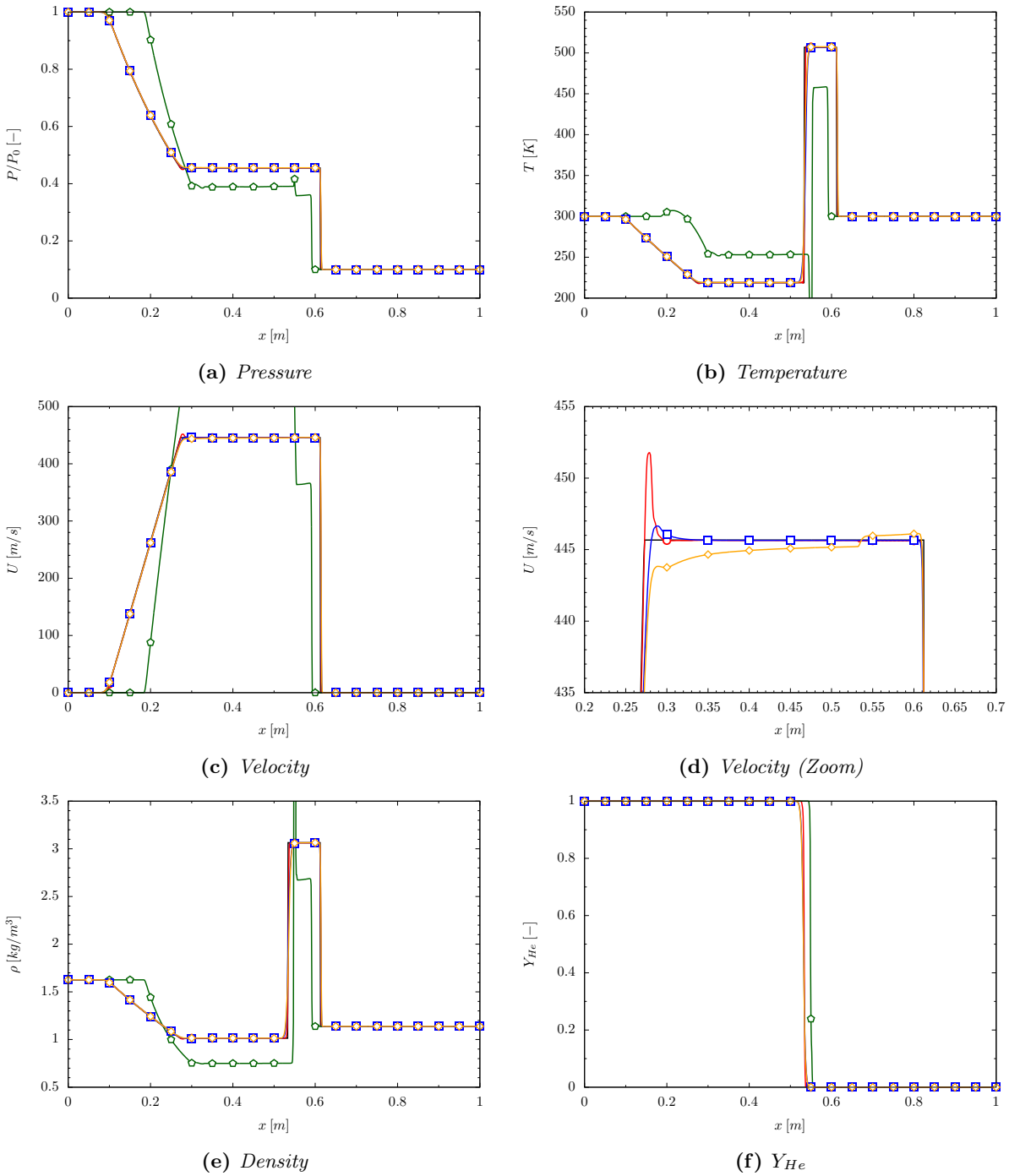

(a) *Pressure* **(b)** *Temperature*

(c) *Velocity* **(d)** *Velocity (Zoom)*

(e) *Density* **(f)** Y_{He}

Figure 5.13: *Primitive variables for the He/N_2 multi-species shock-tube computed with the thermally perfect EoS at $t = 3 \times 10^{-4}$ [s] - — Ref, ○ QCVF, ⬠ FCVF, □ QCMF, ◇ FCMF*

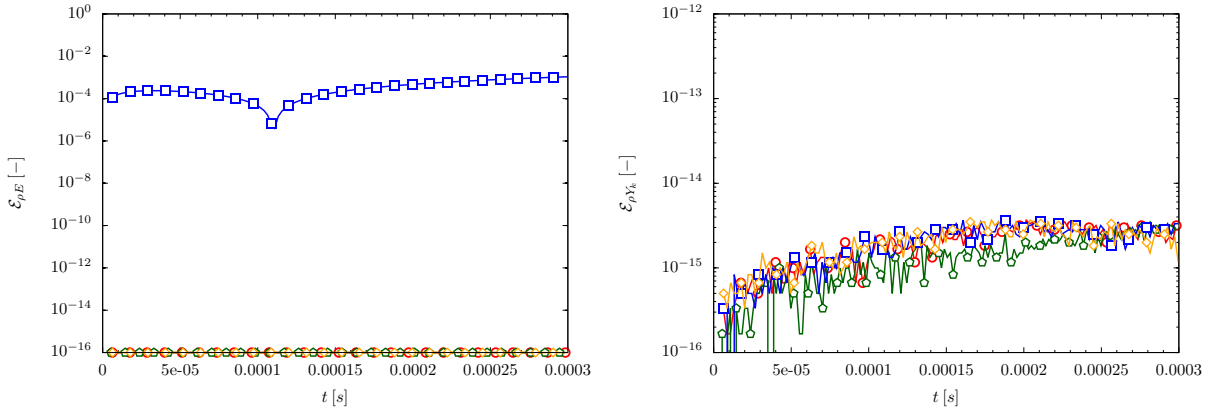

(a) *Total Energy* **(b)** *Total Mass*

Figure 5.14: *Conservation errors for the He/N_2 multi-species shock-tube computed with the thermally perfect EoS - ○ QCVF, ⬠ FCVF, □ QCMF, ◇ FCMF*

5.2.5 Shock-bubble interaction

Test case

This problem is a right-facing shock wave travelling in air and passing through an helium slab thus producing a complex series of transmitted and reflected shock waves inside the slab. This problem is more complex albeit more representative of numerous scenarios of practical interest such as shock-bubble interactions and Richtmyer-Meshkov instabilities. The problem is the one-dimensional version of the classical helium shock-bubble interaction problem presented experimentally by Haas and Sturtevant [122] and numerically by [13, 143, 198, 250, 259, 270]. The two-dimensional version problem is discussed at length in §. 6.2.

The domain has a length of $L = 0.325\,[m]$ which corresponds to $6.5D$, where $D = 5\,[cm]$ is the bubble diameter and spans $-2.5 \leqslant x/D \leqslant 4$. The upstream edge of the bubble is situated at $x/D = 0$, and the shock is initially positioned at $x/D = -1$ and is initialised as a perfect discontinuity over a single cell. It travels for one diameter before impacting the bubble thus leaving some time for the numerical start-up errors (pair of low-frequency/low-amplitude waves moving upstream with the contact discontinuity speed) to disappear [129]. The shock is travelling at $M_s = 1.22$ in air. The helium slab and surrounding air are initially in thermal and mechanical equilibriums. According to the literature, the helium is not pure in the slab, but contaminated with 28 % of air by mass. The different states can be defined by their different vectors $\mathbf{Q} = [P/P_{air},\ \rho/\rho_{air},\ U/c_{air},\ \gamma/\gamma_{air},\ Y_{air},\ Y_{He}]^T$,

- *Post-shock air* $(x/D \in [-2.5, -1.0])$ and is characterised by,

$$\mathbf{Q_{shock}} = [1.5698,\ 1.3764,\ 0.3336,\ 1.0,\ 1.0,\ 0.0]^T$$

- *Bubble* $(x/D \in [0, 1])$ defined as,

$$\mathbf{Q_b} = [1.0,\ 0.1829,\ 0.0,\ 1.18,\ 0.28,\ 0.72]^T$$

- *Pre-shock air* $(x/D \in [-1.0, 0] \bigcup [1, 4])$ and is defined by,

$$\mathbf{Q_{air}} = [1.0,\ 1.0,\ 0.0,\ 1.0,\ 1.0,\ 0.0]^T$$

where $D = 50\,[mm]$, $\rho_{air} = 1.29\,[kg/m^3]$, $P_{air} = 101325\,[Pa]$, $\gamma_{air} = 1.4$ and $c_{air} = 331.6\,[m/s]$. Details on the shock wave properties estimation for both calorically and thermally perfect EoS are given in Appendix C.

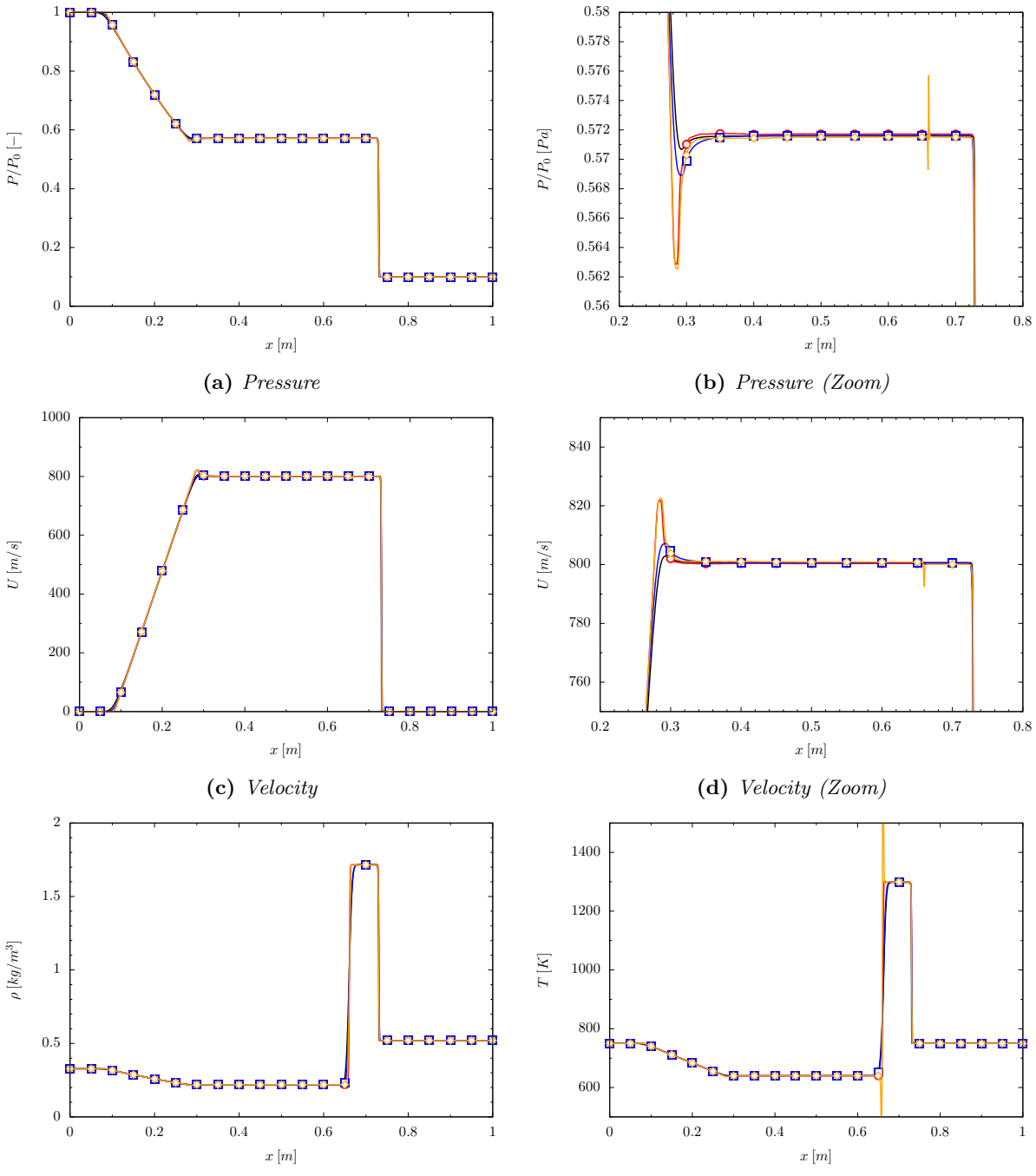

(a) *Pressure* **(b)** *Pressure (Zoom)*

(c) *Velocity* **(d)** *Velocity (Zoom)*

(e) *Density* **(f)** *Temperature*

Figure 5.15: *Primitive variables for the O_2/H_2 - $P_L/P_R = 10$ multi-species shock-tube computed with the thermally perfect EoS at $t = 2 \times 10^{-4}$ [s] - — Ref, ○ QCVF, □ QCMF, ◇ FCMF*

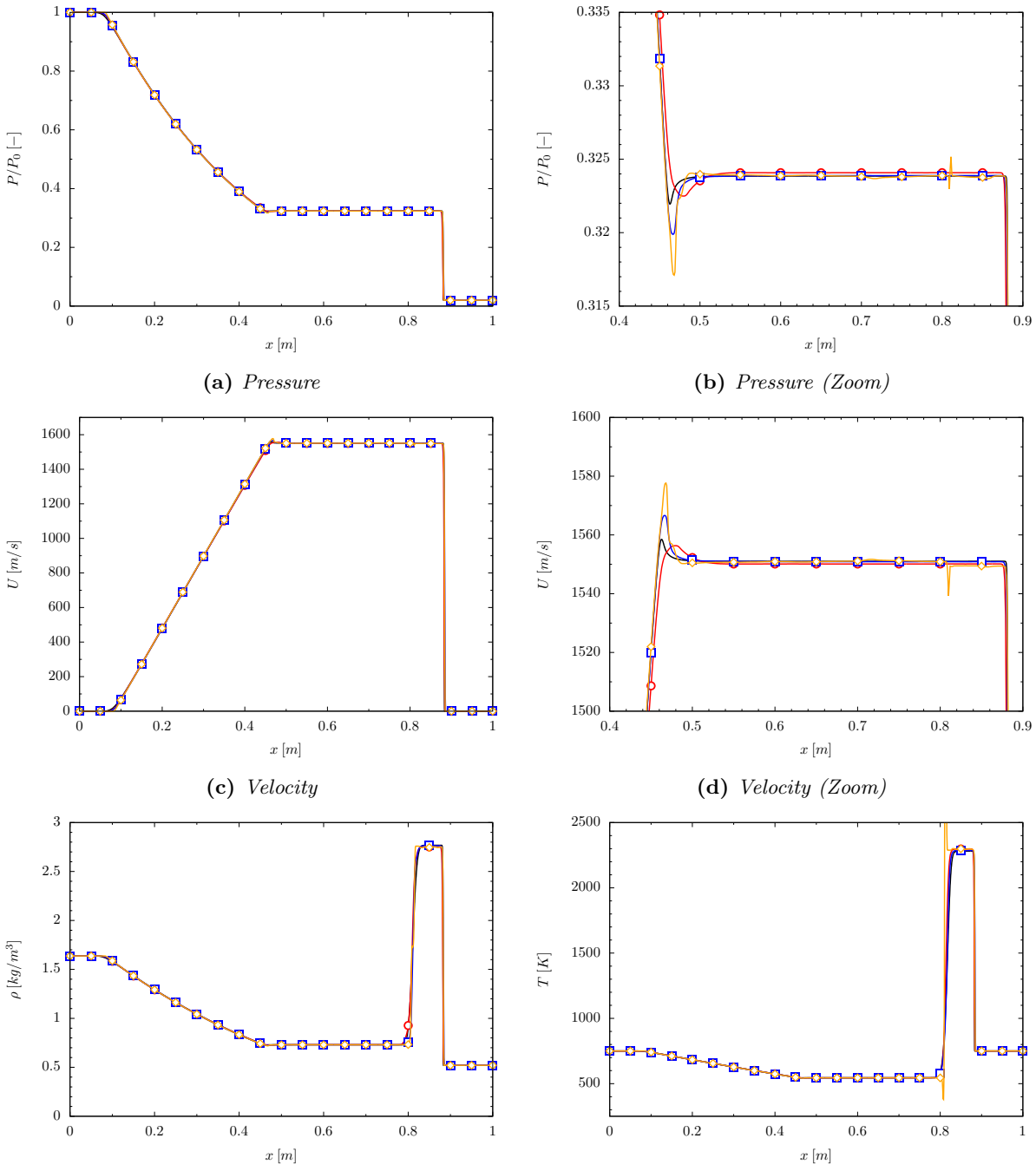

(a) *Pressure*

(b) *Pressure (Zoom)*

(c) *Velocity*

(d) *Velocity (Zoom)*

(e) *Density*

(f) *Temperature*

Figure 5.16: *Primitive variables for the O_2/H_2 - $P_L/P_R = 50$ multi-species shock-tube computed with the thermally perfect EoS at $t = 2 \times 10^{-4}$ [s] - — Ref, ○ QCVF, □ QCMF, ◇ FCMF*

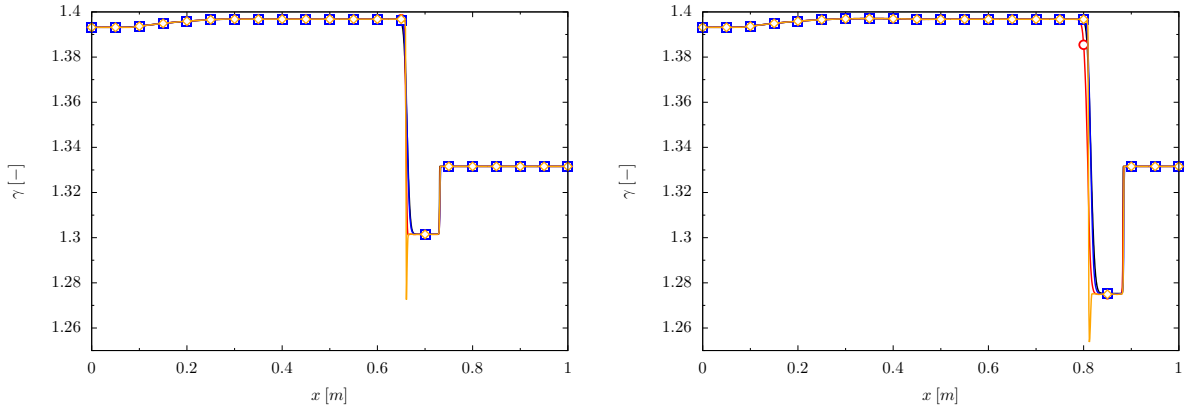

(a) $P_L/P_R = 10$ **(b)** $P_L/P_R = 50$

Figure 5.17: *γ variations for the O_2/H_2 - $P_L/P_R = 50$ multi-species shock-tube computed with the thermally perfect EoS at $t = 2 \times 10^{-4}$ [s] - — Ref, ○ QCVF, □ QCMF, ◇ FCMF*

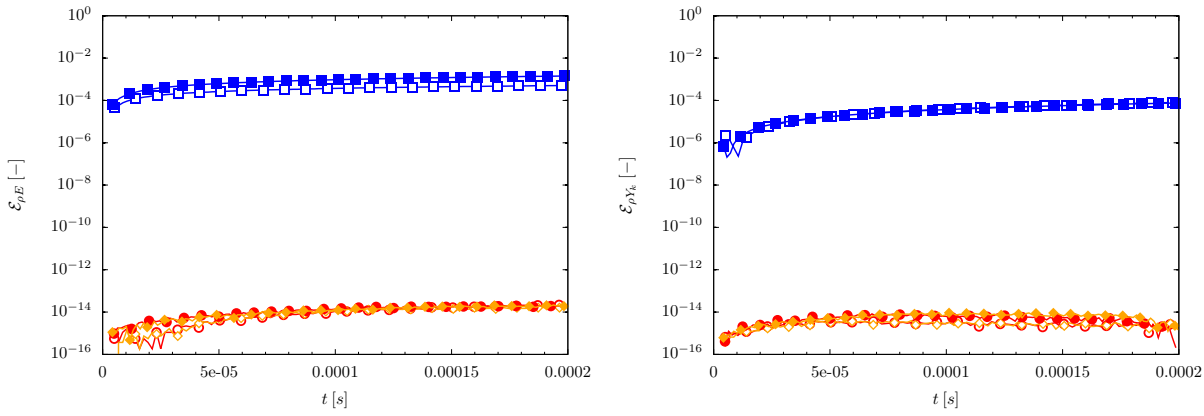

(a) *Total Energy* **(b)** *Total Mass*

Figure 5.18: *Conservation errors for the O_2/H_2 multi-species shock-tube computed with the thermally perfect EoS - filled symbol for $P_L/P_R = 50$ and empty symbols for $P_L/P_R = 10$ - ○ QCVF, □ QCMF, ◇ FCMF*

Computations are run on a grid composed of $Nx = 1300$ cells, with a cell size corresponding to $\Delta x/D = 0.005$, or $\Delta x = 2.5 \times 10^{-4}$ [m]. Similarly to published results, the calorically perfect EoS is considered for the study, and $CFL = 0.5$ for the time marching. The final time has been chosen as $t_f = 5 \times 10^{-4}$ [s] to let some time to the different shocks to propagate.

Results

The results are presented in Fig. 5.19, where the complex system of shocks and expansion waves can be seen. The main shock is at the right of the domain after having been transmitted through the helium slab. A rarefaction wave at the left is propagating towards the left and results from the initial interaction between the shock and the slab. Numerous other shocks can be seen, resulting from several reflections/transmissions within the moving slab.

The three different methods employed here (QCMF, QCVF and FCMF) seem to converge towards a single solution, which is a good indication of the correctness of the different approaches considered. The most noticeable feature indicating the failure of the FCMF in this type of problem are the two large spikes of temperature forming on both sides of the slab. Temperature is roughly bounded by $270\,[K] \leqslant T \leqslant 330\,[K]$ without the spikes, and roughly between $250\,[K] \leqslant T \leqslant 500\,[K]$ in the case of the

FCMF. This clearly cannot be tolerated if any temperature dependent processes have to be accounted for.

Fig. 5.20 depicts the pressure oscillations and temperature spikes obtained for different grid resolutions. According to Karni [147], the rate of convergence of these pressure oscillations is extremely slow. This can be observed here, where a ratio of 16 exists between the coarsest and finest grids, and oscillations can still be observed at the finest level. A more worrisome observation is the increase of the temperature spikes magnitude as the mesh is being refined.

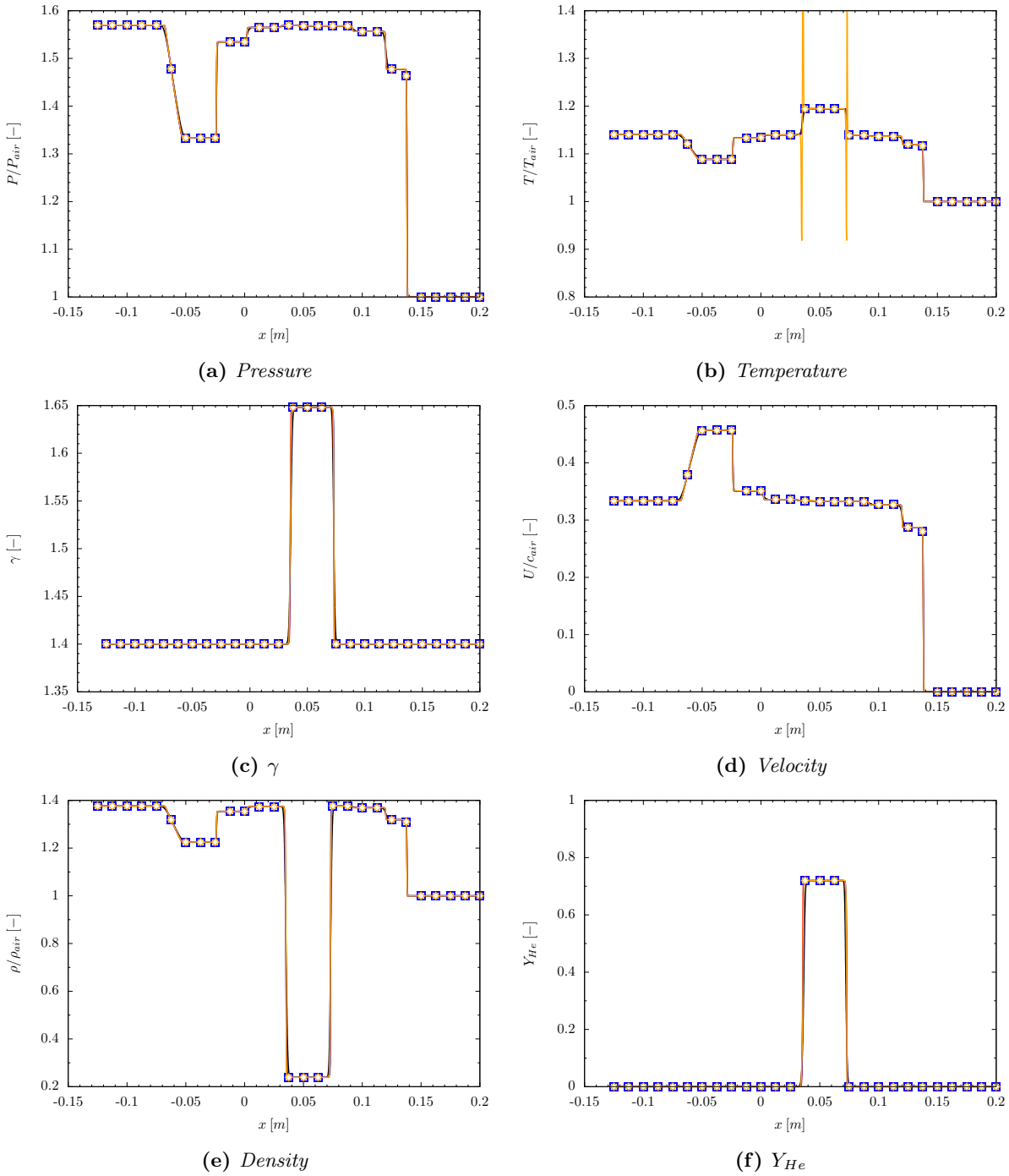

(a) *Pressure* **(b)** *Temperature*

(c) γ **(d)** *Velocity*

(e) *Density* **(f)** Y_{He}

Figure 5.19: *Primitive variables for the shock-bubble interaction computed with the calorically perfect EoS at* $t = 4 \times 10^{-4}$ $[s]$ - — *Ref,* ○ *QCVF,* □ *QCMF,* ◇ *FCMF*

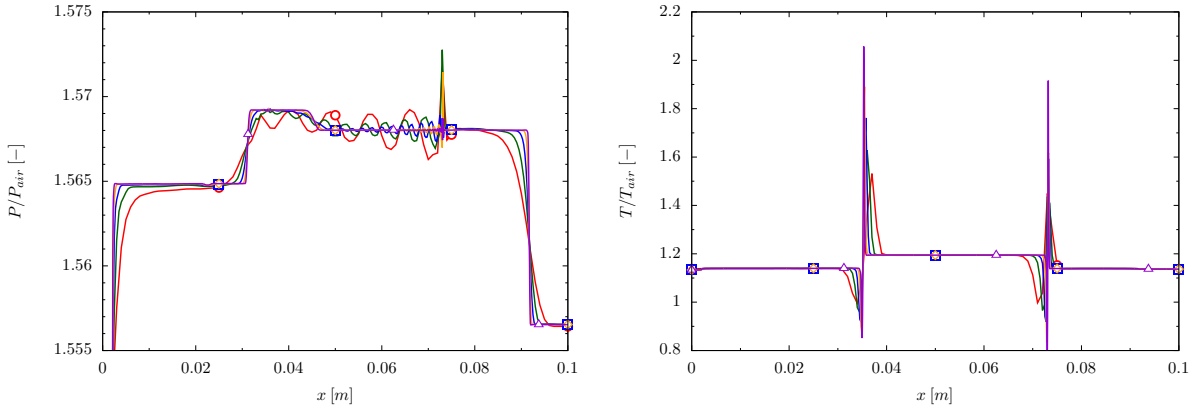

(a) *Pressure (Zoom)* **(b)** *Temperature (Zoom)*

Figure 5.20: *Grid convergence for the shock-bubble interaction computed with the calorically perfect EoS and FCMF model at* $t = 4 \times 10^{-4}$ $[s]$ - $Nx = 325$, $Nx = 650$, $Nx = 1300$, $Nx = 2600$, $Nx = 5200$

5.2.6 Discussion

Several observations can be made about the multi-component models tested. The FCMF generates significant oscillations of pressure and velocity at material interfaces as well as temperature spikes, due essentially to the numerical method employed. The FCVF is both unstable and unreliable in the simulation of multi-components flows. Furthermore, it does not capture shock-waves correctly. This model is thus discarded for the rest of the work. Both the QCMF and QCVF model eliminate pressure oscillations.

The QCMF is generally more dissipative than the QCVF, which can be potentially explained by the numerical methods used to solve both sets of equations. On the other hand, the QCVF does conserve mass, momentum and energy a lot better than the QCMF which features the largest energy errors. Based on the test cases of this section, both the QCMF and QCVF models will be used for the validation of the diffusive fluxes presented below.

Finally, a remark on the rather poor energy conservation featured by the QCMF model can be made. It can be shown that most of the energy conservation errors occurring are due to the freezing of both γ and h_0^m when the hyperbolic integration step artificially mixes species at sharp contact surfaces [6, 133]. Abgrall and Karni [6] further estimated that energy conservation errors could be related to the maximum variation of γ between two consecutive cells. This implies that an initially smeared profile would feature smaller conservation errors. This is illustrated in Fig. 5.21, where the moving contact wave has been initialised with different smeared profiles of temperature and mass fractions following,

$$\varphi_i = \frac{\varphi_{in} + \varphi_{out}}{2} - \frac{\varphi_{out} - \varphi_{in}}{2} \tanh\left(C_s\left(\frac{D}{2} - |x_i - x_0|\right)\right) \tag{5.2}$$

where φ_{in} is the value inside the bubble, conversely φ_{out} is the value outside, D is the bubble diameter and x_0 the position of its centre. It can be seen that as C_s decreases and the smearing increases, conservation errors reduce up to $\mathcal{E}_{\rho E} \approx 10^{-5}$ for $C_s = 50$. A slight smearing will therefore be initially applied in the simulations presented in the next sections to reduce conservation errors.

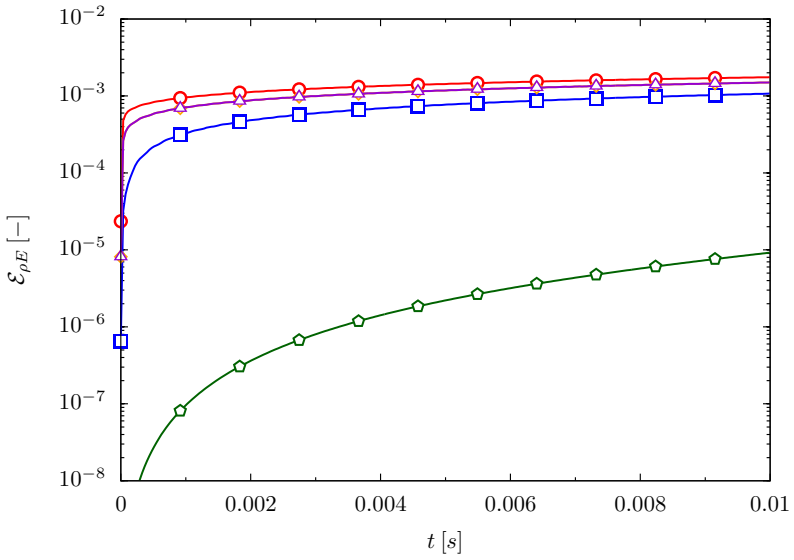

Figure 5.21: *QCMF energy conservation error as a function of the initial smearing of the interface for the moving contact wave problem computed with the thermally perfect EoS -* ○ *Sharp profile,* ⬠ $C_s = 50$, □ $C_s = 500$, ◇ $C_s = 5000$, △ $C_s = 50000$

5.3 Viscous test cases

In this section, the integration of the parabolic terms in the different equation sets is discussed. Two different test cases are presented, a pure diffusion problem where parabolic terms are the only ones relevant, and a second where diffusion and advection are coupled. For both these problems, analytical solutions are available to evaluate the computed results and the software implementation.

5.3.1 Constant property diffusion

Test case

This problem tests the diffusion of a front of two different gases with identical thermo-physical properties. If the initial pressure, temperature and velocity are initially uniform in the domain, they should remain so during the diffusion process.

The gases considered are both H_2. The domain is initially at atmospheric pressure and $T = 300\,[K]$ within a zero velocity flow. The mass fraction is initially set at $Y_1 = 0$ everywhere for the first species and $Y_2 = 1$ for the second species. The viscosity value is fixed at $\mu = 10^{-5}\,[Pa.s]$, while the Schmidt number is being varied to obtain the selected values of the diffusion coefficient. The values considered are $Sc = 1.22116$, 1.22116×10^{-1}, 1.22116×10^{-2} corresponding respectively to $D = 10^{-4}$, 10^{-3}, 10^{-2}.

The parabolic part of the equations is integrated using a classical second-order central difference scheme. The domain is $L = 9\,[mm]$ long and discretised with cells of size $\Delta x = 15\,[\mu m]$ or $Nx = 600$ cells. The solution is advanced in time with $CFL = 0.5$, and an outflow boundary conditions is used on the right of the domain. The left boundary condition is modified such that mass fractions are kept constant at $Y_1 = 1$ and $Y_2 = 0$, so that Y_1 diffuses inside the domain and Y_2 outside, and the thermally perfect EoS is considered.

Analytical solution

Under the assumptions above mentioned (uniform pressure, temperature), no velocity, similar thermo-physical properties for both species and transmissive boundary conditions, the Navier-Stokes equations can be simplified to give,

$$\begin{cases} \dfrac{\partial \rho}{\partial t} = 0 \\ \dfrac{\partial u}{\partial t} = 0 \\ \dfrac{\partial T}{\partial t} = 0 \\ \dfrac{\partial Y_k}{\partial t} = D \dfrac{\partial^2 Y_k}{\partial x^2} \end{cases} \tag{5.3}$$

and the boundary conditions are given by,

$$\begin{cases} Y_1\,(x,\,0) = Y_i \\ Y_1\,(0,\,t) = Y_0 \\ \dfrac{\partial Y_k}{\partial x}\,(\infty,\,t) = 0 \\ Y_2\,(x,\,t) = 1 - Y_1\,(x,\,t) \end{cases} \tag{5.4}$$

It can be shown that the analytical solution for the mass fractions distributions is given by,

$$Y_1(x,\,t) = Y_i + (Y_0 - Y_i)\,\mathcal{A}(x,\,t) \tag{5.5}$$

$$\mathcal{A}(x,\,t) = \operatorname{erf}\left(\frac{x}{2\sqrt{Dt}}\right) \tag{5.6}$$

where $\operatorname{erf}(x)$ is the complementary error function defined as,

$$\operatorname{erf}(x) = \frac{2}{\sqrt{\pi}}\int_x^\infty \mathrm{e}^{-t^2}\,\mathrm{d}t \tag{5.7}$$

Results

Mass fractions and pressure profiles during diffusion are plotted in Fig. 5.22 at different times. It is clear that calculated results agree very well with the analytical solution for all values of the diffusion coefficient. The pressure remains uniform during diffusion showing the stability of the implementation. It can be noted that the results obtained for all schemes (QCMF, FCMF, QCVF) do match almost perfectly between each others which is a strong indication of their respective accuracy.

5.3.2 Constant property advection and diffusion

Test case

This problem tests the advection of a diffusive front thereby coupling the hyperbolic and parabolic operators. The gases considered have similar thermo-physical properties, and similarly to the pure diffusion problem, if the pressure, temperature and velocity are initially uniform, they should remain so during coupled diffusion and advection.

The gases considered are both H_2. The domain is initially at atmospheric pressure and $T = 300\,[K]$ with a varying velocity as indicated in Table 5.3. The diffusive front is initially positioned at $x_0 = 1.5[mm]$ in a $L = 9\,[mm]$ long domain. The viscosity value is fixed at $\mu = 2 \times 10^{-5}\,[Pa.s]$, while the Schmidt number varies to match selected values of the diffusion coefficient. The species Lewis number was taken similar to the H_2 Lewis in a stoichiometric mixture with air at atmospheric temperature, i.e. $Le = 0.33$, yielding $S_c = 0.2244$ if $Pr = 0.68$.

The parabolic part of the equations is integrated using a classical second-order central difference scheme, while the hyperbolic is integrated with the MUSCL5. The domain is discretised with cells of size $\Delta x = 15\,[\mu m]$ or $Nx = 600$ cells. The solution is advanced in time with $CFL = 0.5$. An inflow boundary condition has been applied to the left of the domain while an outflow boundary condition is used on the right. The thermally perfect EoS is considered.

Different velocities have been considered to cover a large range of cell Peclet number ($Pe = u\Delta x/D$) as shown in Table 5.3. Mach number values have been computed using γ values at the flow temperature.

Variables	$Pe = 0.1$	$Pe = 1$	$Pe = 10$	$Pe = 100$
Sc	0.2244	0.2244	0.2244	0.2244
$\Delta x\,[\mu m]$	15	15	15	15
$U\,[m/s]$	7.25587	72.5587	725.587	7255.87
M	0.00494	0.0494	0.494	4.94

Table 5.3: *Test cases for the advection-diffusion problem*

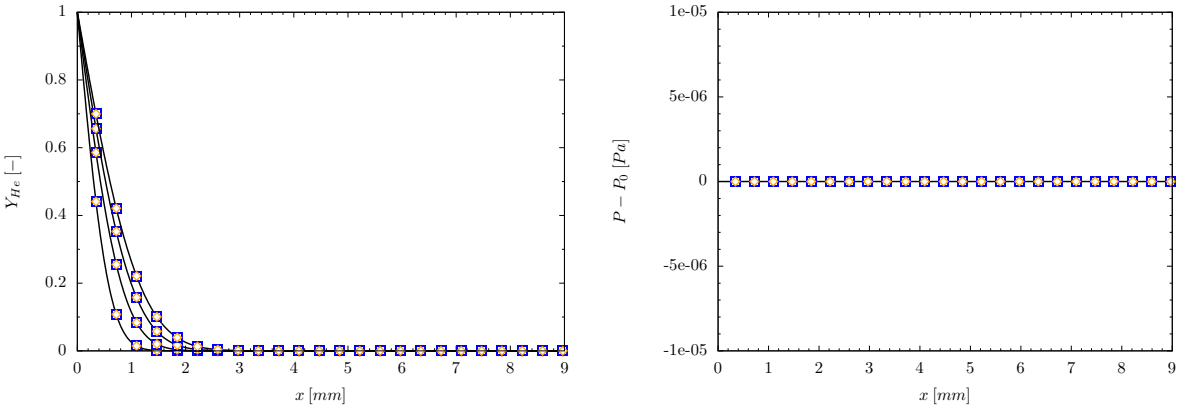

(a) $D = 10^{-4}$ – $t = 1,\ 2,\ 3,\ 4 \times 10^{-3}$ $[s]$

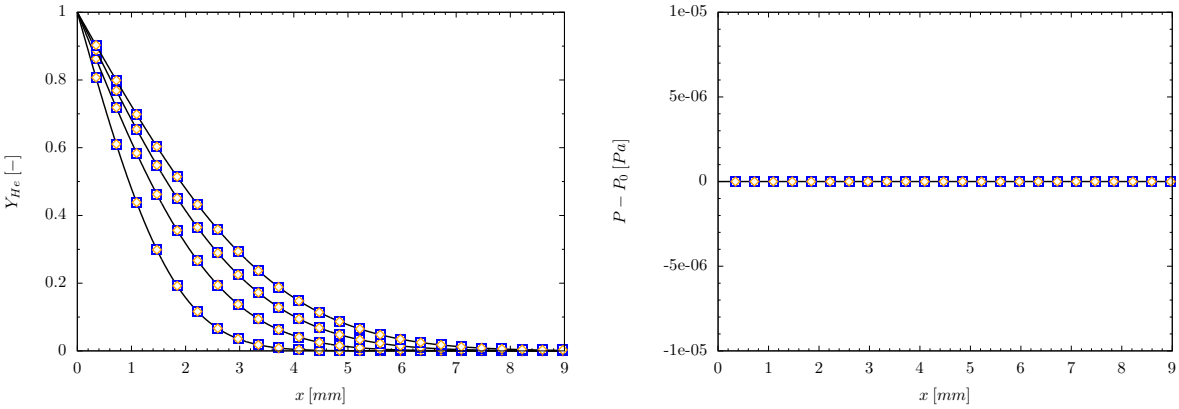

(b) $D = 10^{-3}$ – $t = 2.5,\ 11,\ 25,\ 44 \times 10^{-4}$ $[s]$

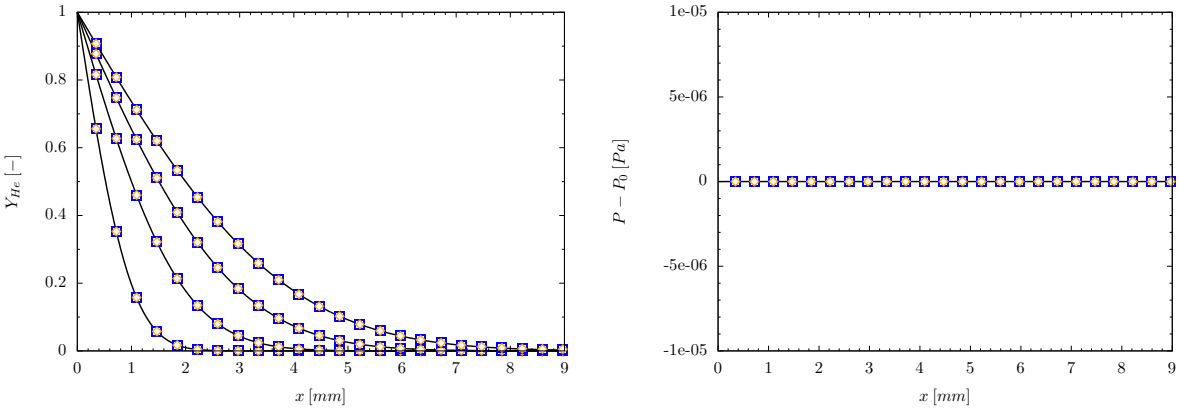

(c) $D = 10^{-2}$ – $t = 3,\ 11,\ 25,\ 44 \times 10^{-5}$ $[s]$

Figure 5.22: *Comparison between analytical and computed solutions for the mass fraction (left) and pressure (right) distributions for the pure diffusion problem - — Ref, ○ QCVF, □ QCMF, ◇ FCMF*

Analytical solution

Under the problem conditions, the full Navier-Stokes equations can be reduced to,

$$\begin{cases} \dfrac{\partial \rho}{\partial t} = 0 \\ \dfrac{\partial u}{\partial t} = 0 \\ \dfrac{\partial T}{\partial t} = 0 \\ \dfrac{\partial Y_k}{\partial t} = -u\dfrac{\partial Y_k}{\partial x} + D\dfrac{\partial^2 Y_k}{\partial x^2} \end{cases} \tag{5.8}$$

If the initial conditions are given by,

$$Y_1\left(x,\, 0\right) = \begin{cases} 1 & x \leqslant x_i \\ 0 & x > x_i \end{cases} \tag{5.9}$$

$$Y_2\left(x,\, t\right) = 1 - Y_1\left(x,\, t\right) \tag{5.10}$$

it can be shown that the analytical solution for the mass fractions distributions is given by,

$$Y_1\left(x,\, t\right) = \frac{1}{2}\left[1 - \operatorname{erf}\left(\frac{x - x_i - ut}{2\sqrt{Dt}}\right)\right] \tag{5.11}$$

Results

Figs. 5.23 to 5.24 depicts both mass fractions and pressure distributions for the different Peclet numbers investigated, at several front positions. The overall agreement between analytical and computed solutions is excellent, and this is observed for all models. The different models feature nearly indistinguishable results, showing once more the consistency between them. Pressure remains perfectly uniform as well, which indicates a good stability of the different algorithms.

At low Peclet number, the agreement is excellent everywhere along the front, but when it increases, some numerical rounding of the sharp fronts is observed and is due to the numerical diffusion added to the solution by the hyperbolic operator. However this addition remains small for high-order schemes, but becomes quite severe and decreases the solution quality for third-order schemes or lower (Fig. 5.25).

5.3.3 Discussion

The validation of the parabolic (diffusion fluxes) and hyperbolic operators has been tested on two benchmark problems and compared with analytical solutions. Excellent agreements were obtained for all models considered and all test cases considered. This does not allow any choice between the QCMF and QCVF as for now. The next section introduces source terms and presents the validation of the three operators in strongly coupled test problems.

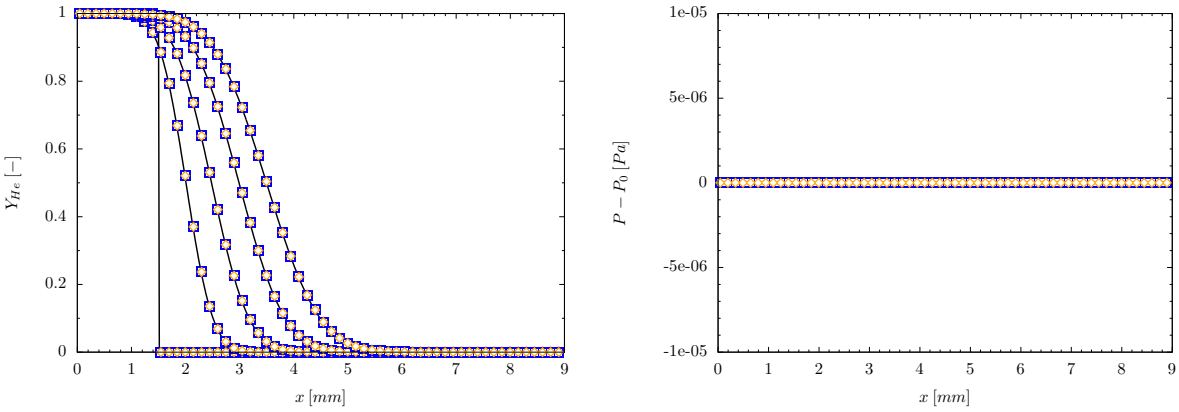

(a) $Pe = 10^{-1}$

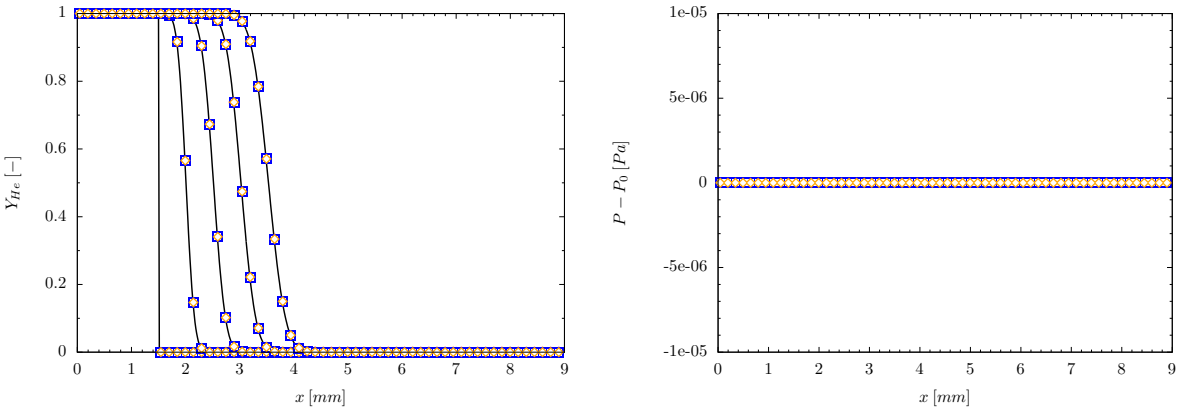

(b) $Pe = 10^{0}$

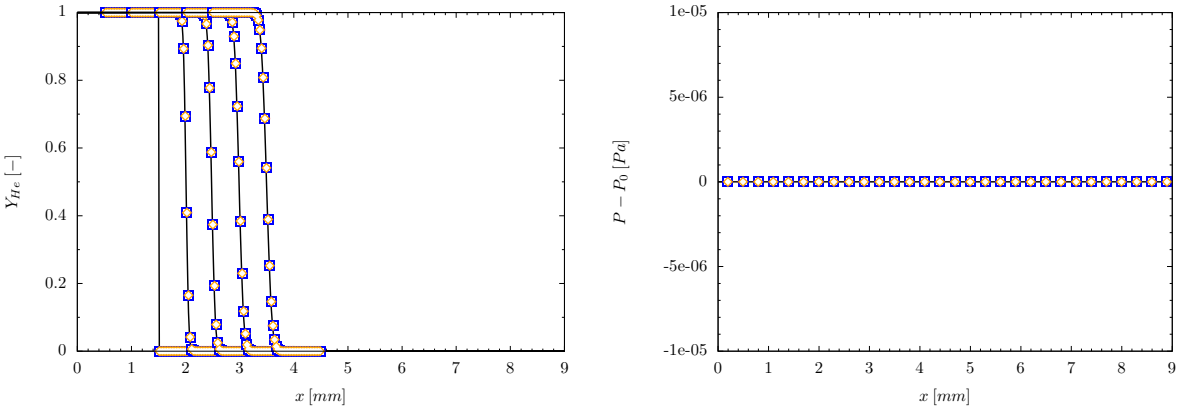

(c) $Pe = 10^{1}$

Figure 5.23: *Comparison between analytical and computed solution for the mass fraction (left) and pressure (right) distributions for the advection-diffusion problem after the front has moved by a distance* $\delta = 0.5,\ 1,\ 1.5,\ 2\ [mm]$ - — *Ref,* ○ *QCVF,* □ *QCMF,* ◇ *FCMF*

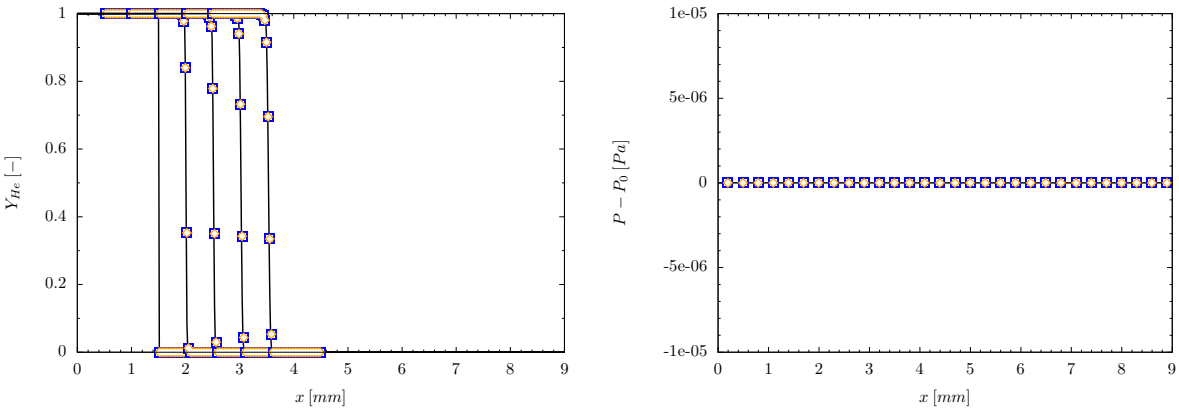

(a) $Pe = 10^2$

Figure 5.24: *(cont) Comparison between analytical and computed solutions for the mass fraction (left) and pressure (right) distributions for the advection-diffusion problem after the front has moved by a distance* $\delta = 0.5,\ 1,\ 1.5,\ 2\ [mm]$ *- — Ref, ○ QCVF, □ QCMF, ◇ FCMF*

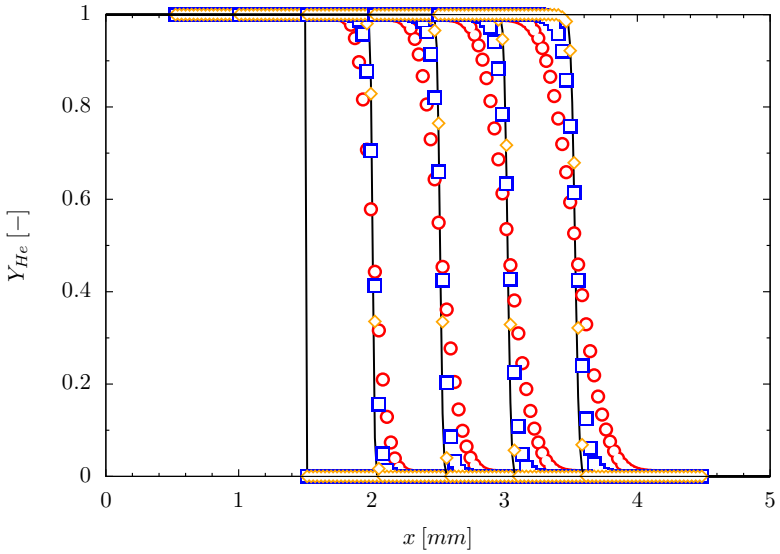

Figure 5.25: *Effect of the reconstruction order of accuracy on the advection of a diffusive front at* $Pe = 10^2$ *after the front has moved by a distance* $\delta = 0.5,\ 1,\ 1.5,\ 2\ [mm]$ *- — Ref, ○ Upwind1, □ MinMod2, ◇ MUSCL5*

5.4 Reacting test cases

In this last section, the implementation of the chemical source terms and thermodynamic relations is reviewed through the adiabatic constant reactor volume problem (§. 5.4.1). All the modules presented above (advection, viscous fluxes and source terms) are then brought together in two complex test cases, the first one being a slow freely propagating laminar flame (§. 5.4.2), while the second is a detonation (§. 5.4.3). Both of these test cases are extremely challenging for the current methods, the first one due to the very low-Mach number and the very delicate interplay between diffusion, advection and reaction, and the second for the large discontinuities present in the flow.

5.4.1 Adiabatic constant volume reactor

Test case

This problem aims at testing the source term integrator and the thermodynamic properties evaluation. The reaction mechanisms considered in this study are presented in Appendix B, and are of increasing size both in terms of number of species, but also in terms of number of reactions.

The problem is a constant volume adiabatic combustion (CVR or Constant Volume Reactor). A domain composed of two cells is uniformly initialised with a burnable mixture at a temperature higher than the auto-ignition temperature of the considered mixture ($T_0 = 1200\,[K]$ has been selected in this work) and at atmospheric pressure. The mixture compositions considered are summarised in Table 5.4, while the EoS considered is thermally perfect.

Species	CERFACS $2s\_CM2$	ONERA	Westbrook
Fuel	0.04734	0.02643	0.02643
O_2	0.18886	0.20977	0.20977
N_2	0.76380	0.76380	0.76380

Table 5.4: *Initial conditions for the adiabatic constant volume reactor problem*

The uniformity of the initial distribution (or the computation of the solution on a single cell) ensures that there is no inter-cell fluxes. This also implies that the source term is the only part of the equations being significant in this test case, along with the thermodynamic properties evaluation. The solution is advanced in time using the RK2-SSP algorithm and a constant time-step size of $\Delta t = 5 \times 10^{-9}\,[s]$ to capture fast reactions and short lived radicals. Temperature, pressure and species mass fractions are recorded during the simulations.

Results

Computed solutions are compared with results obtained with the internationally accepted code `Cantera` [110] which solves an ODE system to provide very accurate solutions.

Results for the $2s\_CM2$ methane mechanism are shown in Fig. 5.26, those for the ONERA H_2/air are depicted on Fig. 5.27 and data obtained from the Westbrook H_2/air mechanism are presented in Fig. 5.29. The overall agreement for these three mechanisms of increasing complexity is very good with errors smaller than 0.5 % for the final values of pressure, temperature and mass fractions (Fig. 5.28). Peaks observed at $t \approx 5 \times 10^{-5}\,[s]$ are explained by the very small delay between values computed with `FlAMEnCo1D` and `Cantera`. These errors are well within the acceptability limit and could be further reduced by decreasing the time-step size (Fig. 5.30). It can also be noted, that when the time-step increases above a certain limit, reaction rates become too large, and oscillations in the mass fractions start to appear which could eventually lead to negative values for intermediate species.

RMS errors values are presented in Table 5.5 for the ONERA mechanism further illustrating the very small errors featured by the different approaches considered here.

Variables		`Cantera`	RMS Errors QCVF	FCMF	QCMF
T	[K]	2.9117×10^{3}	1.63×10^{0}	7.15×10^{-1}	4.61×10^{0}
P	[Pa]	2.2154×10^{5}	1.40×10^{2}	5.23×10^{-1}	4.00×10^{2}
Y_{O_2}	[-]	2.0742×10^{-2}	1.26×10^{-4}	1.20×10^{-4}	2.68×10^{-4}
Y_{H_2}	[-]	3.7396×10^{-3}	1.71×10^{-5}	1.58×10^{-5}	3.60×10^{-5}
Y_{H_2O}	[-]	1.8521×10^{-1}	1.49×10^{-4}	1.08×10^{-4}	3.56×10^{-4}
Y_H	[-]	7.1226×10^{-4}	4.84×10^{-5}	4.07×10^{-6}	1.07×10^{-5}
Y_O	[-]	4.6450×10^{-3}	2.31×10^{-5}	1.53×10^{-5}	6.07×10^{-5}
Y_{OH}	[-]	2.1152×10^{-2}	4.88×10^{-5}	1.36×10^{-5}	1.39×10^{-4}

Table 5.5: *RMS errors for the QCVF, QCMF and FCMF schemes compared to* `Cantera` *for the constant volume reactor problem computed with the ONERA chemical mechanism*

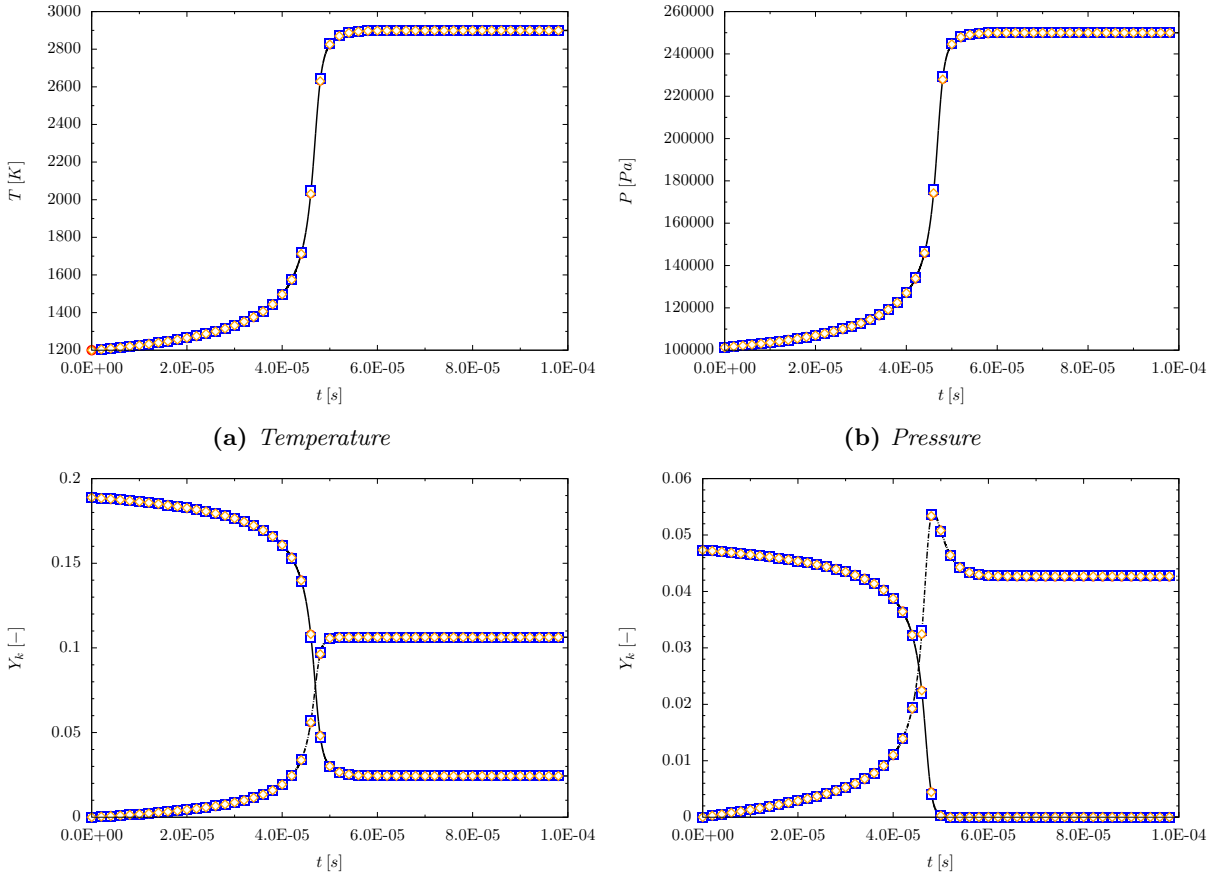

(a) *Temperature* **(b)** *Pressure*

(c) — O_2, -·- H_2O **(d)** — CH_4, -·- CO

Figure 5.26: *Time evolution of different quantities for the constant volume reactor problem computed with the CERFACS 2s_CM2 methane chemical mechanism -* —/-·- `Cantera`, ○ *QCVF,* □ *QCMF,* ◇ *FCMF*

Remarks on the QCVF model

As pointed out in §. 4.4.2, the QCVF model does not ensure volume conservation through diffusion and reactions. This is illustrated in Fig. 5.31, where the temperature evolution computed is compared with

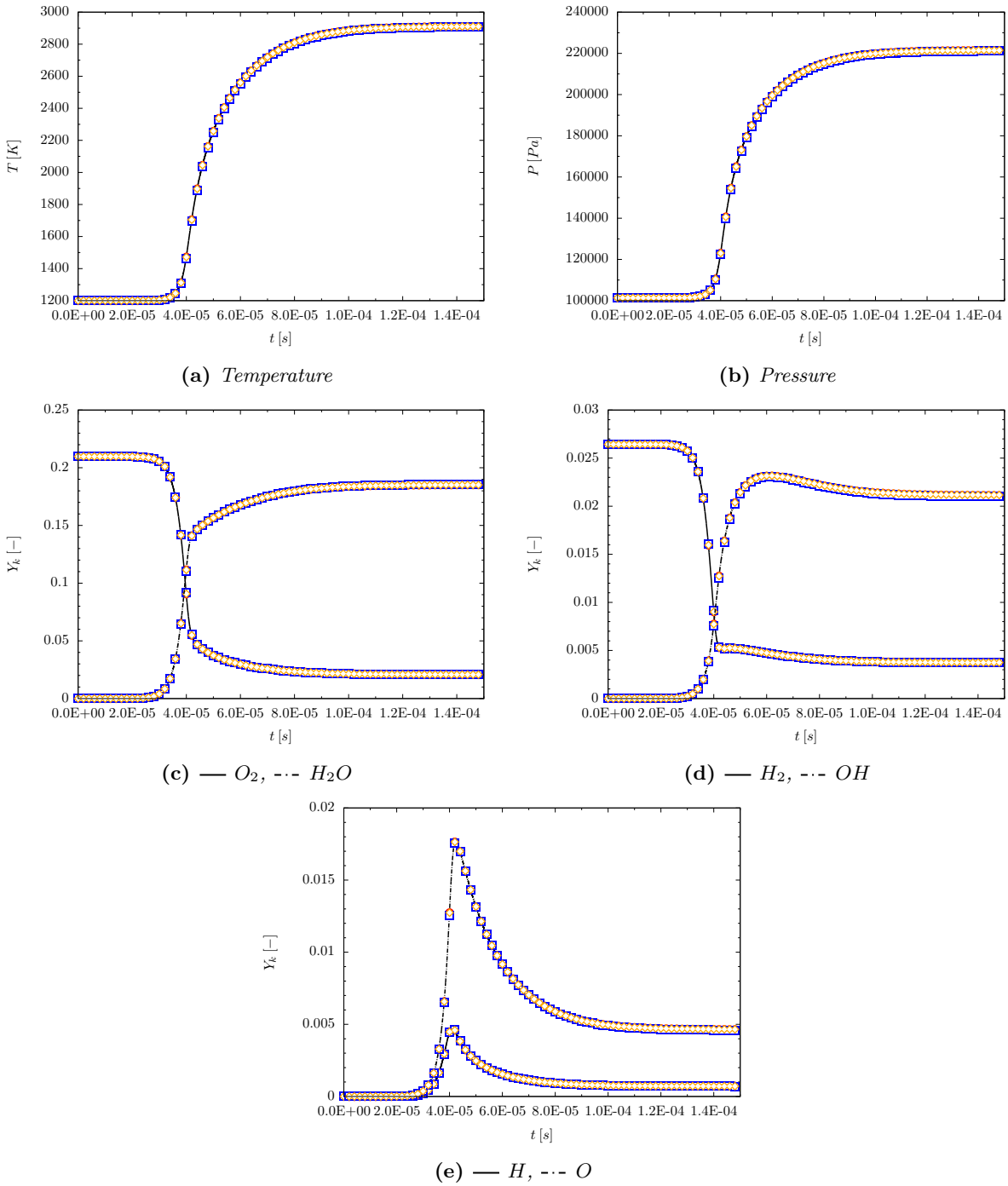

(a) *Temperature*

(b) *Pressure*

(c) — O_2, -·- H_2O

(d) — H_2, -·- OH

(e) — H, -·- O

Figure 5.27: *Time evolution of different quantities for the constant volume reactor problem computed with the ONERA H_2 chemical mechanism -* —/-·- `Cantera`, ○ *QCVF*, □ *QCMF*, ◇ *FCMF*

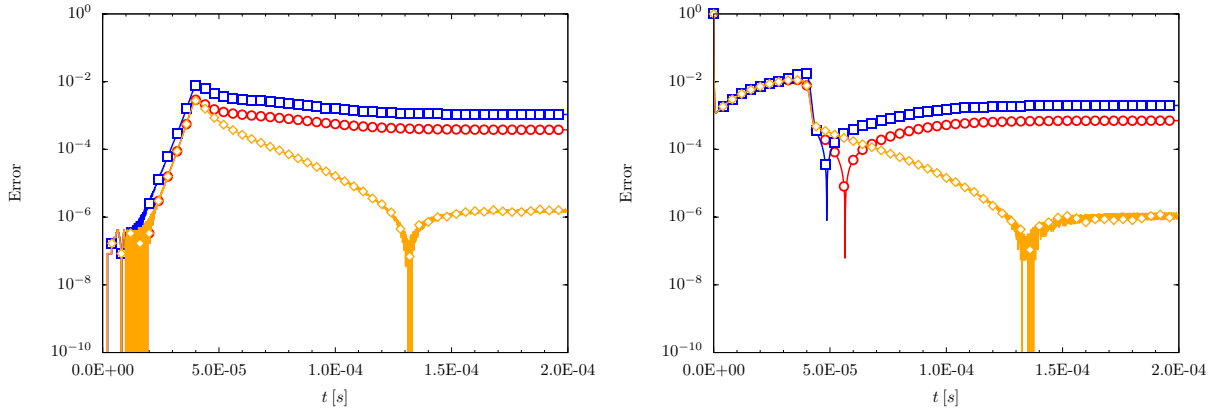

(a) *Temperature* **(b)** H_2O

Figure 5.28: *Time evolution of the error between* `Cantera` *and* `FlAMEnCo1D` *results for the constant volume reactor problem computed with the ONERA H_2 mechanism - ○ QCVF, □ QCMF, ◇ FCMF*

`Cantera` reference solution when enabling or disabling the pressure relaxation presented in §. 4.4.2.

It can be seen that if at early times, the sum of species volume fractions is unity, it does not remains so when reactions start. The pressure correction is thus applied every time the departure is too large, while conserving each species mass and total energy (each species individual energy is not necessarily conserved).

The absence of pressure relaxation does lead to erroneous results of all variables (only temperature is displayed here). Simultaneously, errors are consistently larger than 2 %, which while remaining relatively small still represents an increase of an order of magnitude compared to the results where pressure relaxation is enabled.

Total mass conservation is also improved when enabling the pressure relaxation step, thus showing that it constitutes an acceptable solution for the QCVF model.

Remarks on the thermodynamic properties

As mentioned earlier, results obtained in this section have all been obtained using the thermally perfect EoS thereby matching `Cantera` results. In the case where the QCMF or QCVF approaches are not available, which is the main part of the literature available, a compromise has to be found. It has been shown in §. 5.2 that the classical FCMF approach does not allow multiple γ values in the same domain. The solution usually retained consists in selecting *a priori* a value of γ that is shared by all species, at the cost of introducing errors in the computation of temperature.

This is illustrated in Fig. 5.32 where results using three different values of γ are displayed and compared to the reference solution obtained with the thermally perfect EoS.

Species γ are imposed by specifying C_{p_k} for each species as follows,

$$C_{p_k} = \frac{\gamma_t R_k}{\gamma_t - 1} \tag{5.12}$$

where γ_t is the target specific heat ratio specified by the user.

In this particular instance, three values have been selected, the one corresponding to the non-reacted mixture ($\gamma_u = 1.3342$), the one corresponding to the final mixture ($\gamma_b = 1.2509$, 6 % less than γ_u) and

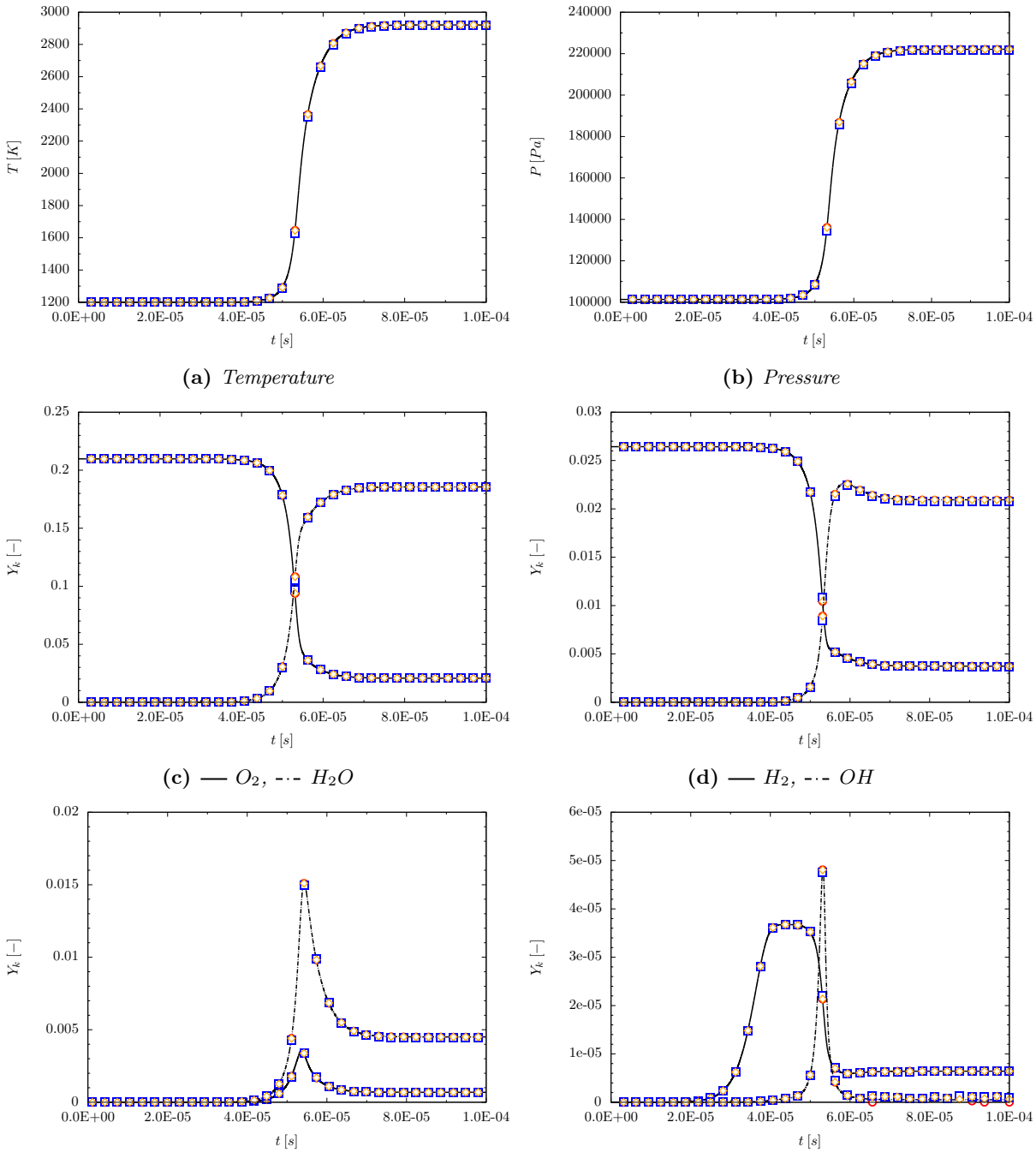

(a) *Temperature* **(b)** *Pressure*

(c) — O_2, -·- H_2O **(d)** — H_2, -·- OH

(e) — H, -·- O **(f)** — HO_2, -·- H_2O_2

Figure 5.29: *Time evolution of different quantities for the constant volume reactor problem computed with the Westbrook H_2 chemical mechanism -* —/-·- `Cantera`, ○ *QCVF,* □ *QCMF,* ◇ *FCMF*

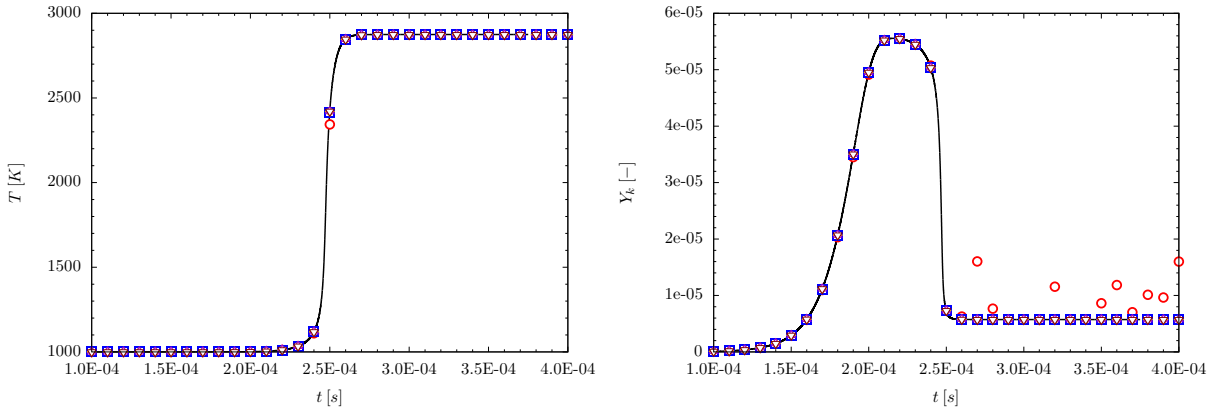

(a) *Temperature* **(b)** H_2O_2

Figure 5.30: *Effect of the time-step size on the constant volume reactor problem computed with the Westbrook H_2 chemical mechanism -* —— `Cantera`, $\Delta t = 5 \times 10^{-8}$ $[s]$, $\Delta t = 1 \times 10^{-8}$ $[s]$, $\Delta t = 5 \times 10^{-9}$ $[s]$, $\Delta t = 1 \times 10^{-9}$ $[s]$, $\Delta t = 5 \times 10^{-10}$ $[s]$, $\Delta t = 1 \times 10^{-10}$ $[s]$

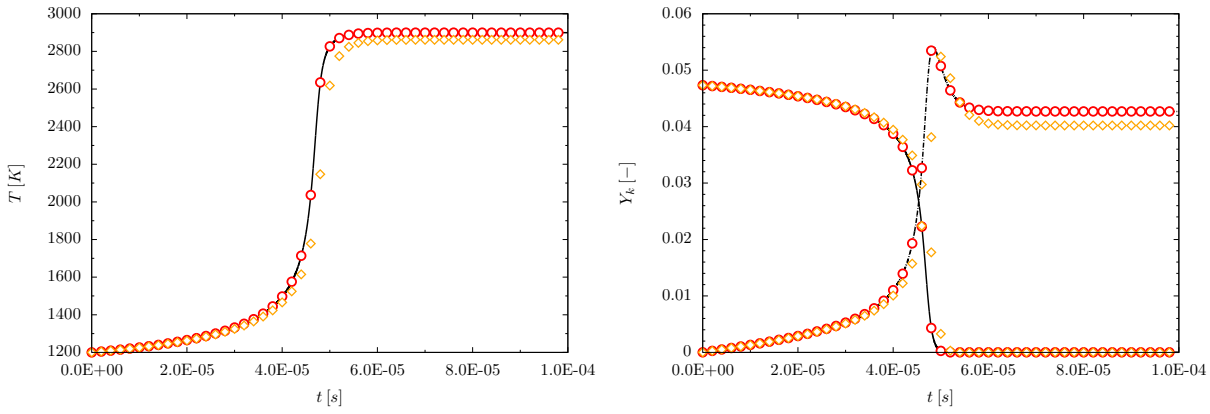

(a) *Temperature* **(b)** —— CH_4, -·- CO

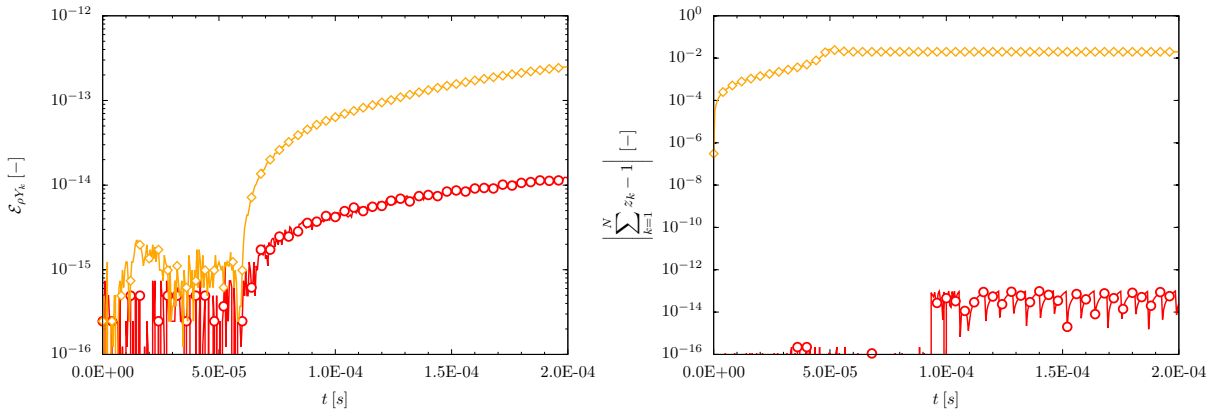

(c) *Mass conservation error* **(d)** *Departure from unity of the volume fraction sum*

Figure 5.31: *Effect of the pressure relaxation step on the constant volume reactor test case using the CERFACS $2s\_CM2$ chemical mechanism and the QCVF approach -* ——/-·- `Cantera`, ***With*** *pressure correction,* ***Without*** *pressure correction*

the average of both previous values ($\gamma_{mid} = \frac{1}{2}(\gamma_u + \gamma_b) = 1.2925$). Both burnt and unburnt values of γ are provided by the reference solution of `Cantera`.

Results displayed here are encouraging (Fig. 5.32), as they show that by selecting γ based on the burnt mixture value, it is possible to solve this test case with a good accuracy, albeit with a slight delay in time. However, using the value from the unburnt mixture results in large temperature differences $\Delta T \approx 200\,[K]$, which are also visible in other variables, and especially the production of a lot more OH and consequently significantly less H_2O. Differences in temperature between the two extreme cases is about 6 % of the reference value, which corresponds to the difference in γ between the two cases.

5.4.2 Laminar freely propagating premixed flame

The implementation and time integration of the source term have been verified in the previous paragraph. Previous sections have demonstrated the correct implementation of both hyperbolic and parabolic operators. The present test case brings all of these modules together in a very challenging test case for an unsteady compressible reacting code due to both the very low Mach number of the flow (at most $M = 0.05$), and the very delicate interplay between highly non-linear diffusion, advection and reactions that need to be accounted for precisely.

Test case

The problem consists in the calculation of the speed at which a planar laminar flame propagates in a burnable fuel/air mixture, and in the species distributions over the flame front.

The approach taken in this work to simulate a freely propagating laminar flame was to hold the flame stationary in a small domain by controlling the inlet velocity and using non-reflecting boundary conditions on both sides of the domain. More details on the non-reflecting boundary conditions derivation and implementation are given in §. 4.6 and Appendix D. The left half of the domain is initialised with the specified conditions of mixture composition, inlet temperature and pressure, while the right half is initialised with flame equilibrium conditions. The flame thus propagates towards the left of the domain, but is held in a specified position by varying the inlet velocity, until both the flame position and speed do not change any more, thus indicating a steady-state solution. The flame speed corresponds then simply to the inlet velocity.

The flame position in the domain is measured as the distance between the left boundary and the flame front and is given by,

$$\delta = \frac{\int_0^L \rho Y_F \, \mathrm{d}x}{\rho_0 Y_F^{in}} \tag{5.13}$$

where ρ_0 is the fresh gas density and Y_F^{in} denotes the inlet fuel mass fraction.

The position of the flame is controlled by specifying the inlet velocity using the simple control strategy devised by Bell *et al.* [19], where the next time-step velocity is obtained using,

$$u^{n+1} = u^n + t\frac{\Delta u}{\tau} \tag{5.14}$$

and the velocity increment is estimated as,

$$\Delta u = 2\frac{\delta_0 - \delta - \tau\,(u^n - s_{est})}{\tau} \tag{5.15}$$

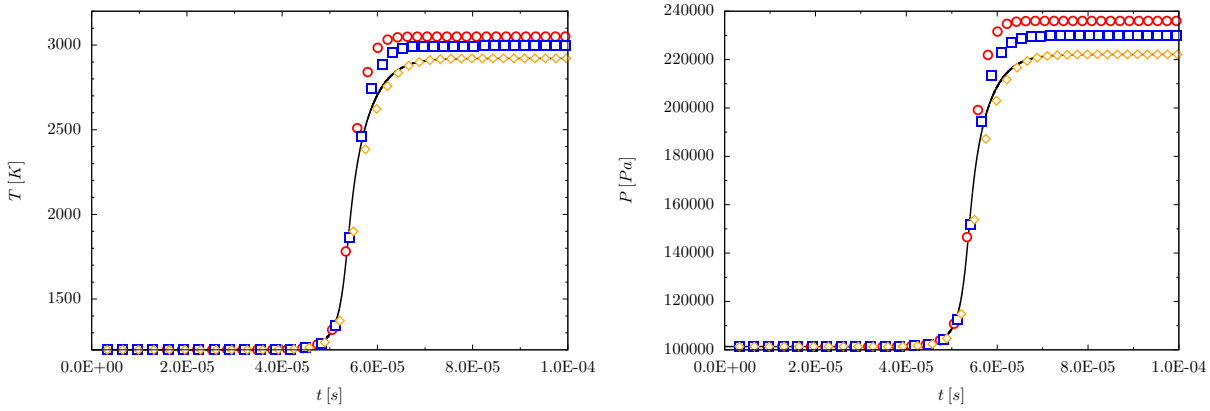

(a) *Temperature* **(b)** *Pressure*

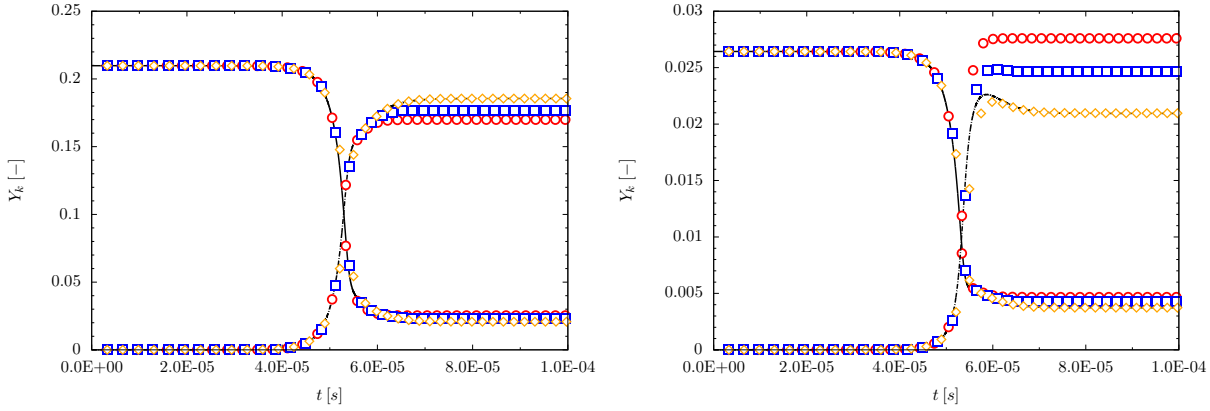

(c) — O_2, -·- H_2O **(d)** — H_2, -·- OH

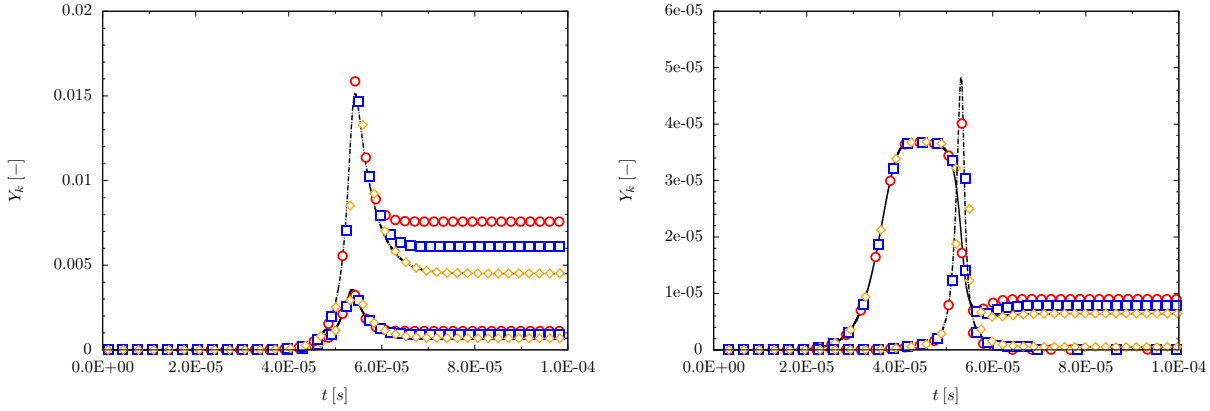

(e) — H, -·- O **(f)** — HO_2, -·- H_2O_2

Figure 5.32: *Time evolution of different quantities for the constant volume reactor problem computed with the Westbrook H_2 chemical mechanism, the calorically perfect EoS and the QCMF approach for several values of γ - —/-·- `Cantera` (thermally perfect EoS), ○ $\gamma = \gamma_u$, □ $\gamma = \frac{1}{2}(\gamma_u + \gamma_b)$, ◇ $\gamma = \gamma_b$*

where τ is a period upon which δ reaches δ_0, and s_{est} is an estimation of the flame speed given simply by,

$$s_{est} = \frac{\delta^n - \delta^{n-1}}{\Delta t} \tag{5.16}$$

To ensure a robust control strategy, the velocity change over a single time-step is limited by,

$$\Delta u = \min\left(\Delta u,\ \beta \max\left(u^n, 0\right)\right) \tag{5.17}$$

where β is a relaxation factor of the order of 0.2 in general and τ is taken as $\tau = 10\Delta t$.

Two mechanisms have been used for the present study, both the simple CERFACS $2s\_CM2$ methane and the more complex Westbrook H_2. The inlet temperature was taken as $T_{in} = 300\,[K]$ and the stoichiometric ratio as unity. The diffusion coefficients are estimated using a constant flow Prandtl number of $Pr = 0.68$, while the individual Schmidt numbers are presented in Table 5.6 with values taken in [258] for the methane and [106] for the hydrogen. The inlet mixture compositions are also given in the same table.

Westbrook	H_2	O_2	O	OH	H_2O	H	HO_2	H_2O_2	N_2
Sc	0.82	0.22	0.53	0.54	0.60	0.14	0.82	0.82	0.92
Le	0.33	1.20	0.78	0.79	0.88	0.20	1.20	1.21	1.35
Y_{in}	0.029	0.226	0.000	0.000	0.000	0.000	0.000	0.000	0.745
2s_CM2	CH_4	CO_2	CO	O_2	H_2O	N_2			
Sc	0.68	0.98	0.76	0.76	0.60	0.75			
Le	1.00	1.44	1.12	1.12	0.88	1.10			
Y_{in}	0.055	0.000	0.000	0.220	0.000	0.725			

Table 5.6: *Schmidt and Lewis number considered for the one-dimensional freely propagating laminar premixed flame computation*

The domain length is $L = 5\,[mm]$ for the methane mechanism and $L = 1\,[cm]$ for the hydrogen case due to the higher hydrogen flame speed. The cell size is taken as $\Delta x = 20\,[\mu m]$ for the methane ($Nx = 250$) and $\Delta x = 25\,[\mu m]$ for the hydrogen ($Nx = 400$). The computations are carried with the MUSCL5 reconstruction, RK2-SSP time-marching algorithm and $CFL = 1$. The thermally perfect EoS is considered here to compute accurately the different thermodynamic quantities.

Results

Exact solutions cannot be obtained for this problem due to its non-linearity. In place of the exact solution, results obtained in this work are compared with those of `Cantera` [110]. It shall be noted that in `Cantera`, two ways of computing diffusion coefficients are used, both of them relying on the kinetic theory, but one uses a mixture-averaged formulation of diffusion coefficients and is dubbed *Mixture-Averaged*, while the second is more expensive and solves the full $N \times N$ system of equations and is thus dubbed *Full-Diffusion* in the following.

For the methane flame, whose results are presented in Fig. 5.33, the agreement is very good between `Cantera` and both the QCVF and QCMF approaches. The flame speed also agree quite well, as s_l^0 (QCVF) $= 0.383\,[m/s]$, while s_l^0 (QCMF) $= 0.384\,[m/s]$, and the reference solution lies between s_l^0 (Cantera Mixture) $= 0.3672\,[m/s]$ and s_l^0 (Cantera Full) $= 0.3848\,[m/s]$. Species profiles are also well captured, even the short life species such as CO. It can be noted that this agreement is partially due to the use of adjusted Schmidt numbers presented in the literature [258], and thus allows a quite precise calculation.

The hydrogen flame on the other hand is a more complex flame which is more sensitive to diffusion, especially the short life species such as HO_2 and H_2O_2, and the mono-atomic extremely diffusive hydrogen (H). Computed results are compared with `Cantera` in Fig. 5.34. The agreement is reasonable but not overly good. The QCVF predicts well the flame structure, while the QCMF tends to over-predict most of the intermediate species mass fractions. The temperature obtained with the QCVF and QCMF also over predict `Cantera` solution by respectively $\Delta T = 23\,[K]$ and $\Delta T = 84\,[K]$. Similarly, computed flame speed differ between the two models with s_l^0 (QCVF) $= 1.67\,[m/s]$ and s_l^0 (QCMF) $= 1.785\,[m/s]$ compared to s_l^0 (Cantera Mixture) $= 1.81\,[m/s]$ and s_l^0 (Cantera Full) $= 1.78\,[m/s]$. Discrepancies between `Cantera` and computed results is at most 7% for the laminar flame speed, which is still reasonable given the simplified diffusion approach considered here. Furthermore, diffusion coefficients considered in this work have been extracted directly from the literature and not adjusted to the current chemical mechanism and thus results are error prone.

The main point highlighted here is the difference between the QCMF and QCVF for complex chemical mechanisms. One possible explanation for this behaviour could be found in the increased numerical diffusion observed for the QCMF in the inviscid test cases. This would have the effect of slightly enhancing diffusion through the flame front and increasing both the flame speed and flame temperature. The thermodynamic properties have been tested in Fig. 5.29 and can therefore be ruled out as a potential source of error. However, a grid convergence test has been conducted, and the QCVF features results closer to `Cantera` reference in terms of both speed and temperature ($s_l^0 = 1.69[m/s]$ and $\Delta T = 15[K]$), but the QCMF does not show any improvement in the temperature distribution and a marginal improvement in flame speed ($s_l^0 = 1.79\,[m/s]$).

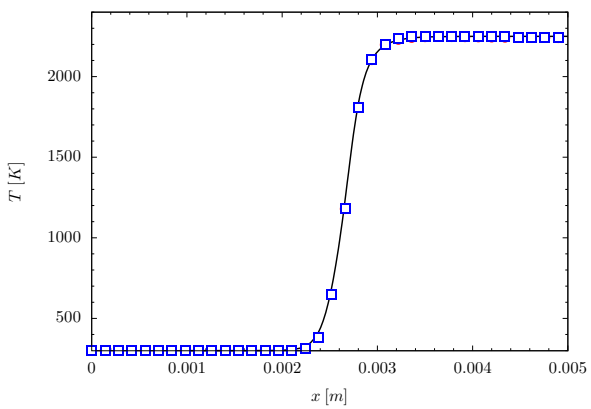

(a) *Temperature*

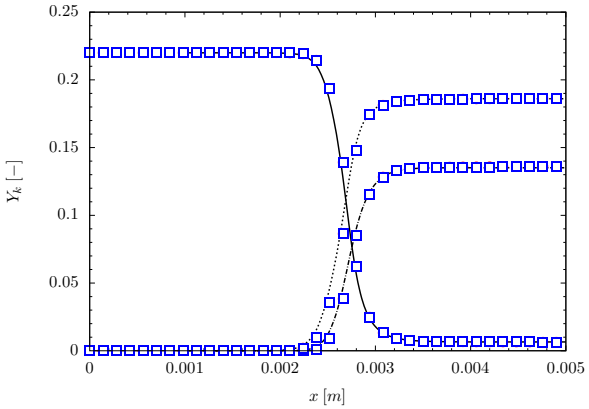

(b) — O_2, -·- CO_2, - - $1.5 \times H_2O$

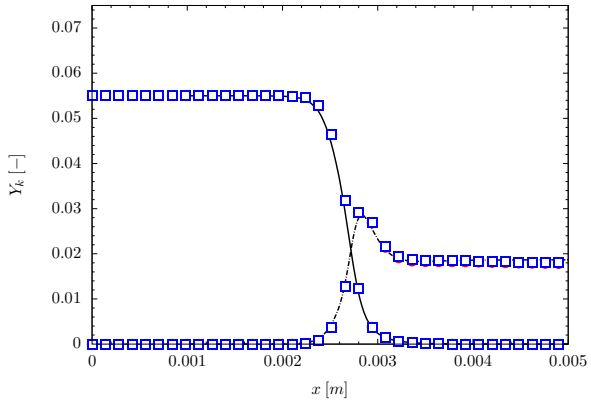

(c) — CH_4, -·- CO

Figure 5.33: *Premixed laminar flame structure computed with the CERFACS 2s_CM2 mechanism with* $T_{in} = 300\,[K]$, $\phi = 1.0$ - —/-·- `Cantera`, ○ *QCVF*, □ *QCMF*

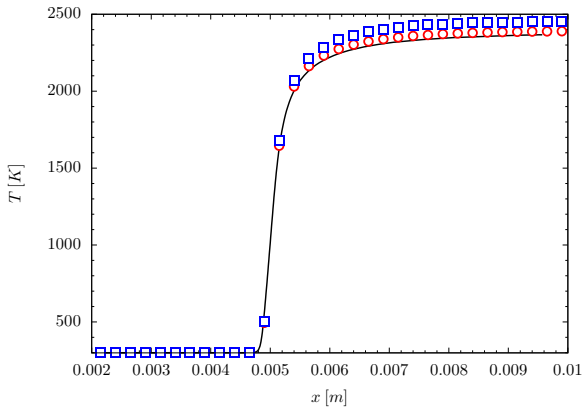

(a) *Temperature*

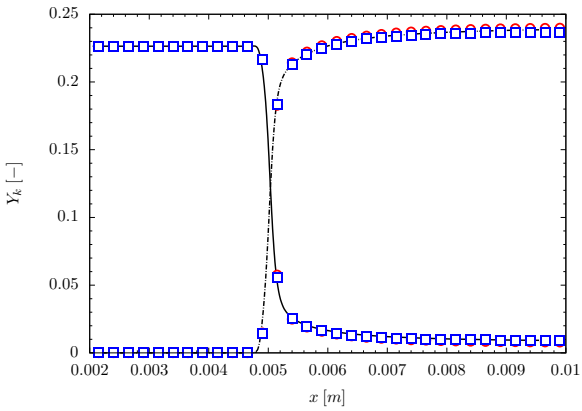

(b) — O_2, -·- H_2O

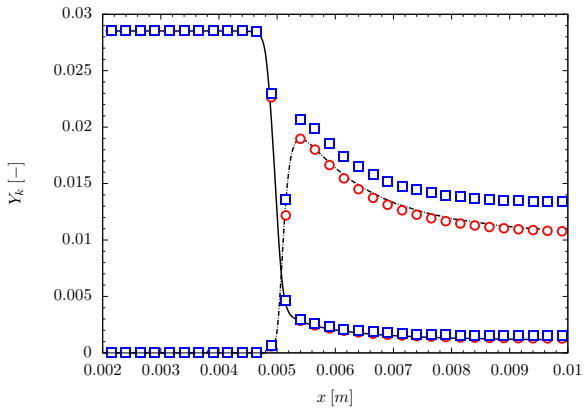

(c) — H_2, -·- $2.0 \times OH$

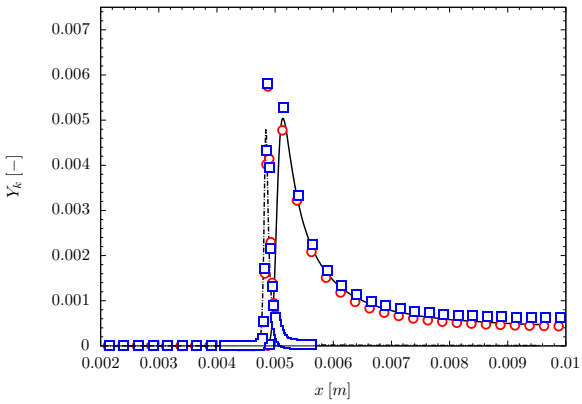

(d) — O, -·- $9.0 \times HO_2$

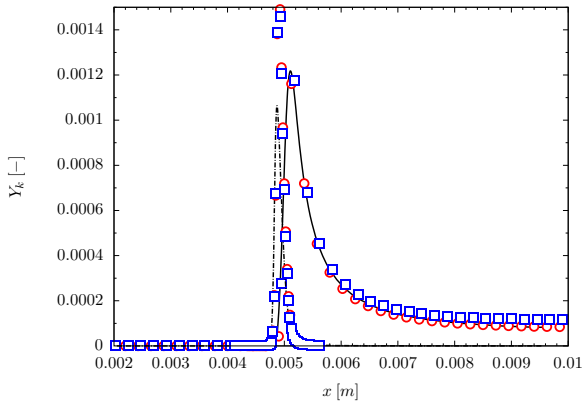

(e) — H, -·- $2.0 \times H_2O_2$

Figure 5.34: *Premixed laminar flame structure computed with the Westbrook H_2/Air mechanism with $T_{in} = 300$ [K], $\phi = 1.0$ - —/-·- `Cantera`, ○ QCVF, □ QCMF*

Effect of the equivalence ratio

The influence of the equivalence ratio on the flame structure, speed and burnt temperature is displayed in Fig. 5.35 and Fig. 5.36 for the methane and hydrogen mechanisms respectively. The inlet temperature is kept at $T_{in} = 300\,[K]$, but the mixture composition is changed. Due to the very close results obtained between the QCMF and QCVF for the methane mechanism, only the results obtained with the QCMF are shown in Fig. 5.35. The agreement with the reference solution is very good, with both temperature and speed trends correctly predicted. The temperature distribution is also correctly predicted for the different stoichiometric ratios considered.

The same hybrid conclusion as previously mentioned can be drawn for the hydrogen flame. The flame structure is correctly predicted by the QCVF while the flame speed estimation given by the QCMF is better. However, both models follow closely the trends of temperature and flame speed given by `Cantera`. The increasing difference between the QCVF flame speed and `Cantera`'s estimation as the stoichiometric ratio increases is attributed to the fact that diffusion coefficients considered in this study have been given by Giacomazzi [106] for stoichiometric mixtures, and any deviation from this ratio should result in a change of Schmidt numbers which is not reproduced here.

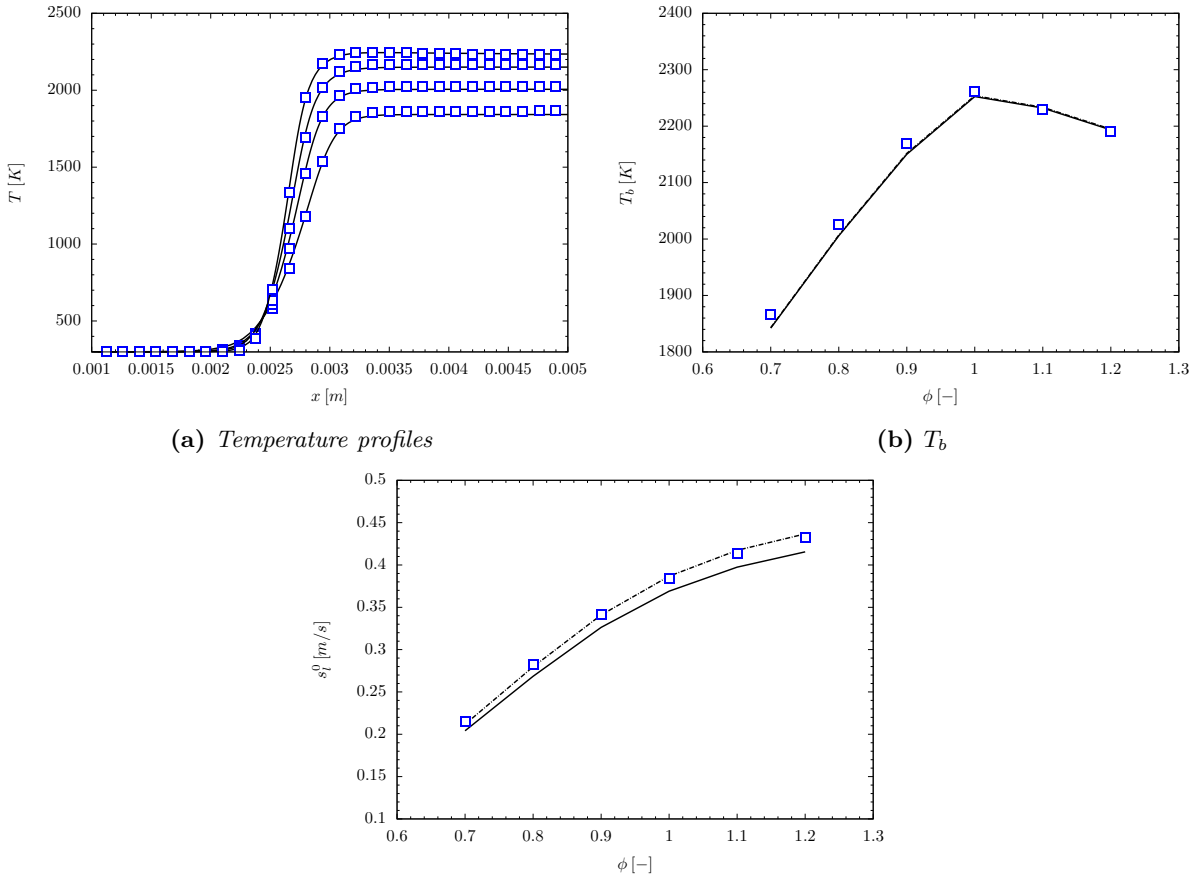

(a) *Temperature profiles* **(b)** T_b

(c) s_l^0

Figure 5.35: *Influence of the equivalence ratio on the flame structure, speed and burnt temperature using the CERFACS 2s_CM2 mechanism with* $T_{in} = 300\,[K]$ - — `Cantera` *Mixture Averaged,* -·- `Cantera` *Full Diffusion,* ◻ *QCMF*

Effect of the inlet temperature

Contrary to the previous paragraph, the inlet temperature is here varied while the mixture composition remains constant with $\phi = 1.0$. Results for both the methane and hydrogen mechanisms are presented

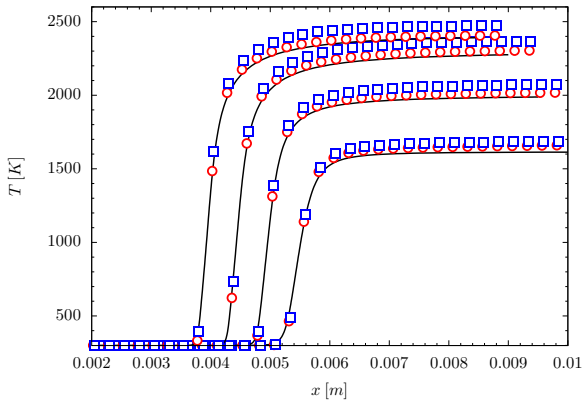

(a) *Temperature profiles (curves are shifted for clarity)*

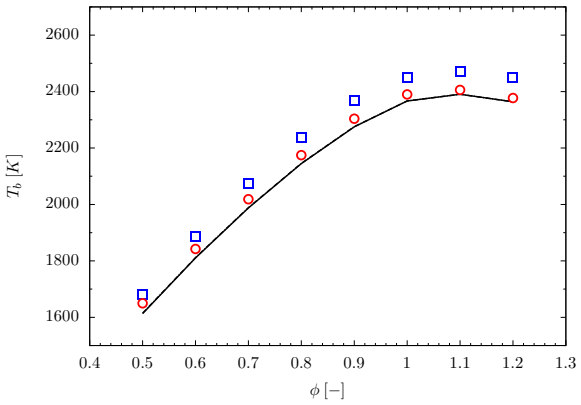

(b) T_b

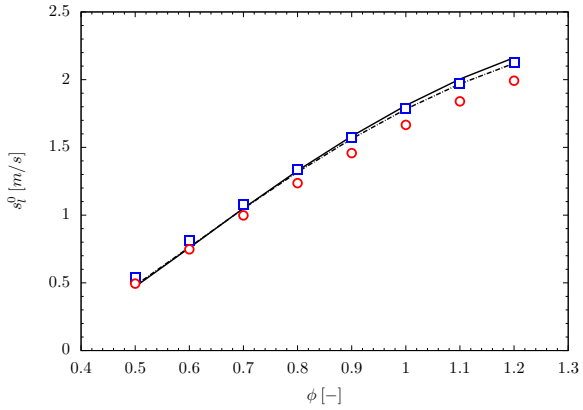

(c) s_l^0

Figure 5.36: *Influence of the equivalence ratio on the flame structure, speed and burnt temperature using the Westbrook H_2/Air mechanism with $T_{in} = 300\,[K]$ - —— `Cantera` Mixture Averaged, -·- `Cantera` Full Diffusion, ○ QCVF, □ QCMF*

in Fig. 5.37 and Fig. 5.38 respectively. Once again, results obtained for both QCMF and QCVF on the methane flame are extremely close to `Cantera`'s predictions. The burnt temperature and flame speed are correctly captured, but a slight divergence of the flame speed at high inlet temperature can be observed. This is most probably due to an unaccounted change in the diffusion coefficients. Nonetheless, the overall agreement is very good.

The hydrogen flame results feature the same dual conclusion has previously outlined, with a very good estimation of the flame speed by the QCMF and of the flame structure by the QCVF. At large inlet temperature ($T_{in} = 800\,[K]$), the flame structure computed with the QCVF is extremely close to the reference results with errors in temperature smaller than $\Delta T = 10\,[K]$, while the error featured by the QCMF remains roughly constant at $\Delta T \approx 80\,[K]$, which in relative error is quite small (at most 3.33 %) but remains noticeable nonetheless. The velocity estimation seems closer this time between QCMF and QCVF, and the error becomes noticeable only at large speed values (and high inlet temperature).

Remarks on the thermodynamic properties

Results for the freely propagating laminar flames have been presented up to now using the thermally perfect EoS, and thus cannot be obtained with the FCMF approach. Similarly to the constant volume reactor, the capability of a single value of γ to represent the flow field is discussed. In this case, three values of γ have been considered, the reactant's ($\gamma_u = 1.4003$), the product's ($\gamma_b = 1.248$) and the average

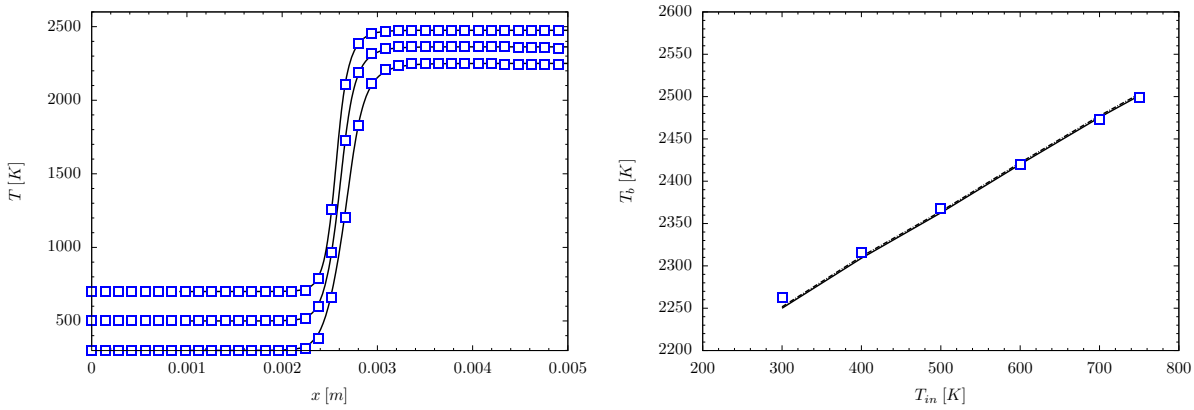

(a) *Temperature profiles* **(b)** T_b

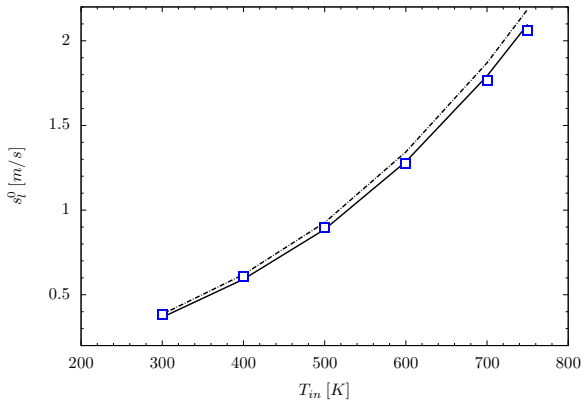

(c) s_l^0

Figure 5.37: *Influence of the reacting mixture temperature on the flame structure, speed and burnt temperature using the CERFACS* $2s\_CM2$ *mechanism with* $\phi = 1.0$ - — `Cantera` *Mixture Averaged,* -·- `Cantera` *Full Diffusion,* ◻ *QCMF*

between both values ($\gamma_{mid} = \frac{1}{2}(\gamma_u + \gamma_b) = 1.3242$).

Computed results are presented in Fig. 5.39, where contrary to the constant volume reactor, it can be seen, that no single value of γ would lead to an accurate solution. This could be explained by the highly non-linear behaviour of such a problem with both large and small length and time scales. The flame characteristics obtained with these values of γ are presented in Table 5.7. It clearly shows that both products temperature and flame speed are not well predicted by a constant γ simulation without a careful adjustment of the specific heat ratio. A closer look at these results tells us that it would be impossible to find a value of γ satisfying both the flame temperature and propagating speed, as in this case, a correct speed would be achieved for $\gamma_{mid} \leqslant \gamma \leqslant \gamma_u$, and a correct burnt temperature for $\gamma_b \leqslant \gamma \leqslant \gamma_{mid}$ which is incompatible.

	`Cantera`	γ_u	γ_{mid}	γ_b
$T_b\,[K]$	2350	2657	2515	2250
$s_l^0\,[m/s]$	1.81	1.99	1.57	1.06

Table 5.7: *Stoichiometric freely propagating laminar premixed hydrogen flame characteristics when computed using the QCVF and calorically perfect EoS for different values of* γ

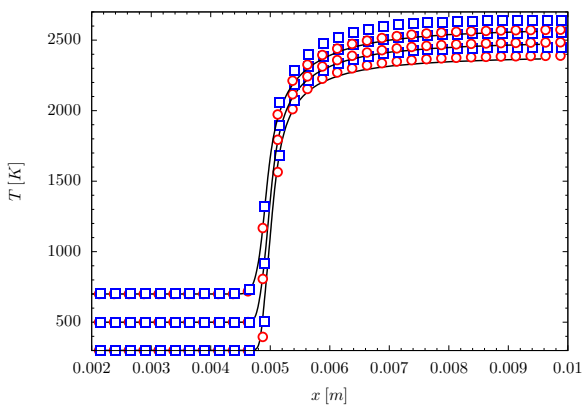

(a) *Temperature profiles*

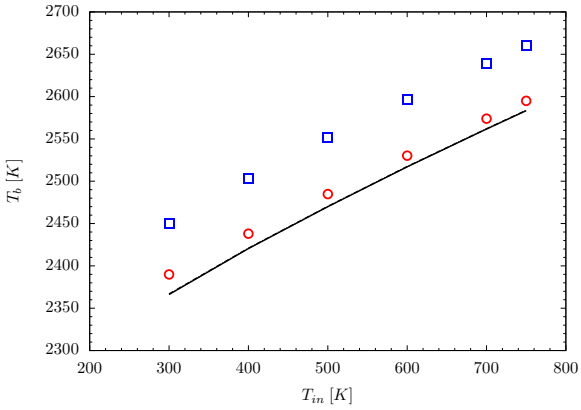

(b) T_b

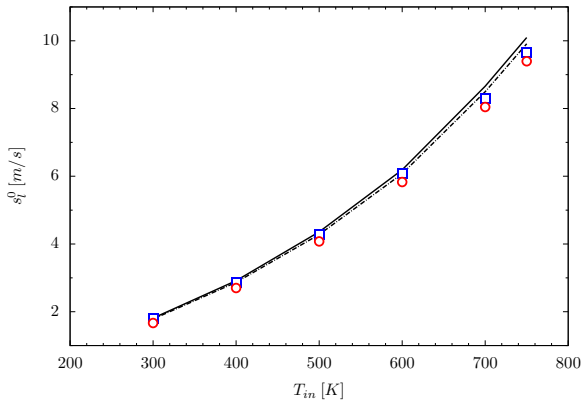

(c) s_l^0

Figure 5.38: *Influence of the reacting mixture temperature on the flame structure, speed and burnt temperature using the Westbrook H_2/Air mechanism with $\phi = 1.0$ - — `Cantera` Mixture Averaged, -·- `Cantera` Full Diffusion, ○ QCVF, □ QCMF*

5.4.3 Detonations

The last reacting test case is even more challenging, as to the laminar flame complexity of calculating accurately source terms and diffusion coefficients, as well as the hyperbolic fluxes at a very low Mach number, a shock travelling into a flammable mixture is added. The reactions start in the overheated mixture resulting from the shock compression. The delay between the shock deposition of energy and the initial temperature increase due to chemical reactions causes the pressure and temperature to be constant in a small zone, called the Von Neumann zone which is less than 2 $[mm]$ long, but where most chemical reactions occur. The Von Neumann zone is a direct consequence of the chemical mechanism ignition delay at the post-shock temperature and is a complex flow feature to capture properly. The flame thus follows the shock with a small buffer zone and features a supersonic speed with respect to the reactants speed of sound.

This problem has been studied extensively by Oran *et al.* [101–104, 221] and Deiterding [73] using both reduced and complex chemical mechanisms as well as simplified thermodynamic (single constant γ in the whole domain). As exact solutions cannot be computed, Deiterding's results presented in [73] will be used as the reference for comparing values obtained in the Von Neumann zone as well as the leading discontinuity velocity with the computed data.

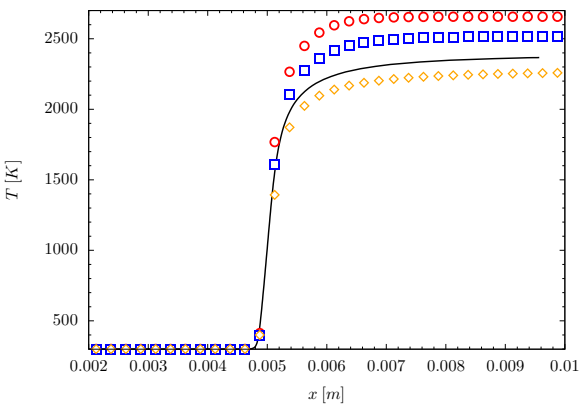

(a) *Temperature*

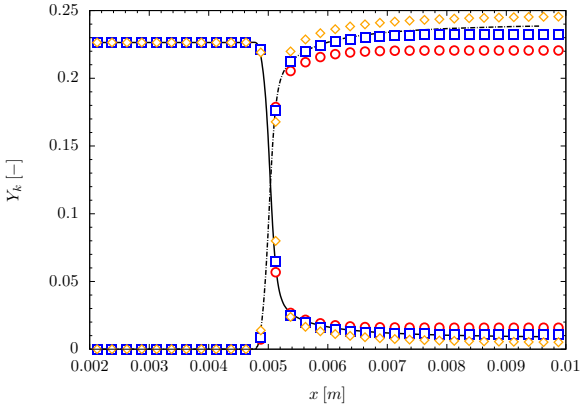

(b) — O_2, -·- H_2O

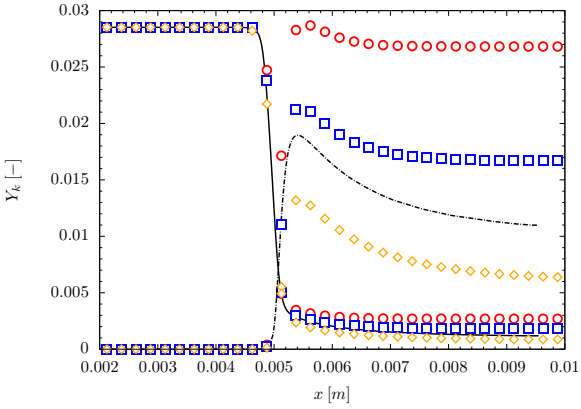

(c) — H_2, -·- $2.0 \times OH$

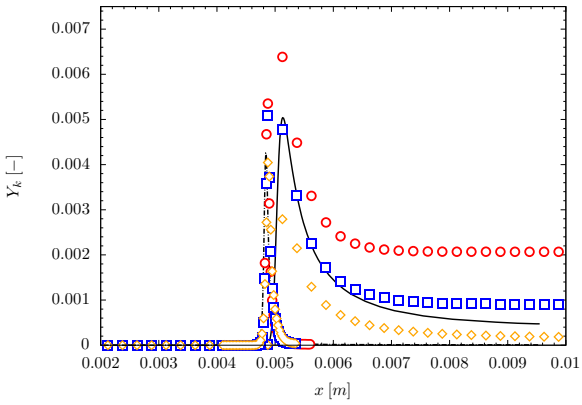

(d) — O, -·- $9.0 \times HO_2$

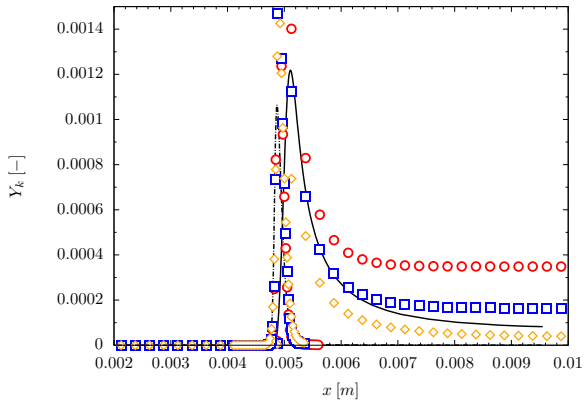

(e) — H, -·- $2.0 \times H_2O_2$

Figure 5.39: *Stoichiometric freely propagating laminar premixed hydrogen flame computed with the Westbrook H_2/Air mechanism and the QCVF using the calorically perfect EoS for different values of γ -* —/-·- `Cantera`, ○ γ_u, □ $\gamma_{mid} = \frac{1}{2}(\gamma_u + \gamma_b)$, ◇ γ_b

Test case

The detonation in this problem is initiated by propagating a shock wave at the speed of $S_s = 1650\,[m/s]$ initially placed at $x_0 = 3\,[cm]$ into the reactants. The chemical mechanism considered here is the Westbrook mechanism [290] detailed in Appendix B. The diluent gas considered is Argon (Ar) as it has been shown experimentally to lead to clean detonation waves. The initial molar ratios of $O_2/H_2/Ar$ is 1/2/7 with an initial pressure of $P = 6.67\,[kPa]$ and an initial temperature of $T = 298\,[K]$. The initial shock wave is strong enough to trigger the formation of a detonation, but not too strong so that the resulting detonation is not over-driven. The post-shock properties were calculated using the iterative procedure of John [140] needed when the thermally perfect EoS is considered and are presented in Table 5.8.

	Ratio	Pre-Shock	Post-Shock
$\rho\,[kg/m^3]$	4.135	0.08497	0.3514
$P\,[kPa]$	27.3	6.67	182.1
$U\,[m/s]$	–	0.0	1251
$T\,[K]$	6.60	298	1967

Table 5.8: *$H_2/O_2/Ar$ Chapman-Jouget detonation shock properties with $S_s = 1650\,[m/s]$*

The domain is $L = 1.5\,[m]$ long and discretised with $Nx = 12000$, $Nx = 24000$, $Nx = 48000$ and $Nx = 96000$ cells, leading to cell sizes of respectively $\Delta x = 125\,[\mu m]$, $\Delta x = 62.5\,[\mu m]$, $\Delta x = 31.25\,[\mu m]$ and $\Delta x = 15.625\,[\mu m]$. The boundary conditions considered are reflecting at the left (wall or symmetry), while the right boundary conditions is an outflow. In theory, the right boundary conditions does not really matter, as the simulation is stopped before the leading shock wave reaches it. The MUSCL5 and RK2-SSP are used respectively for the reconstruction and time-marching and the CFL value has been adjusted to ensure that the time-step was kept sufficiently small for the chemical reactions to be precisely integrated, i.e. $\Delta t_{max} = 5 \times 10^{-9}\,[s]$. The solution was advanced in time until the leading shock velocity relative to the upstream gas velocity reached a steady value, which usually took around $700\,[\mu s]$.

Results

Exact solutions for this problem cannot be obtained, and although reference values are available for the Von Neumann region, there is no reference solution for the flow field around the shock. The reference solution used in this work has thus been obtained using the QCMF model on a very fine grid with $\Delta x = 15.625\,[\mu m]$. For the sake of clarity, all results presented for the detonation problem have been shifted such that the leading shock position coincides with $x_0 \approx 0$.

The detonation propagation with time is shown in Fig. 5.40, where early transients are visible as well as the progressive convergence of the lead shock towards a pseudo steady-state solution. The shock position with time is also depicted, and a convergence can also be observed.

A comparison between detonation structures computed with the different models on the coarse grid ($\Delta x = 125\,[\mu m]$) is presented in Fig. 5.41. The first observation is that the QCVF does not seem to give the correct solution. It seems that the shock speed is not accurately predicted, which is a known deficiency of quasi-conservative schemes, but did not seem to be relevant for the QCVF, as was demonstrated in the test cases of §. 5.2.4. By refining the grid, to investigate this error, it has been found that the QCVF computations were not able to run more than $100\,[\mu s]$ as they were stopped by a divergence of the pressure computation. The QCVF thus appears to be less stable for strong shock waves (pressure ratio of 25 here) than the QCMF model. This could also be related to the way the pressure is computed using a polynomial function of P that requires the computation of P^5 (which is very large) and multiply it by m_5 which is extremely small (10^{-14} at most) thus leading to a potential numerical instability (cf. Appendix A.1).

It has been argued by Deiterding [73] that in detonation problems, the multiple γ problem was not

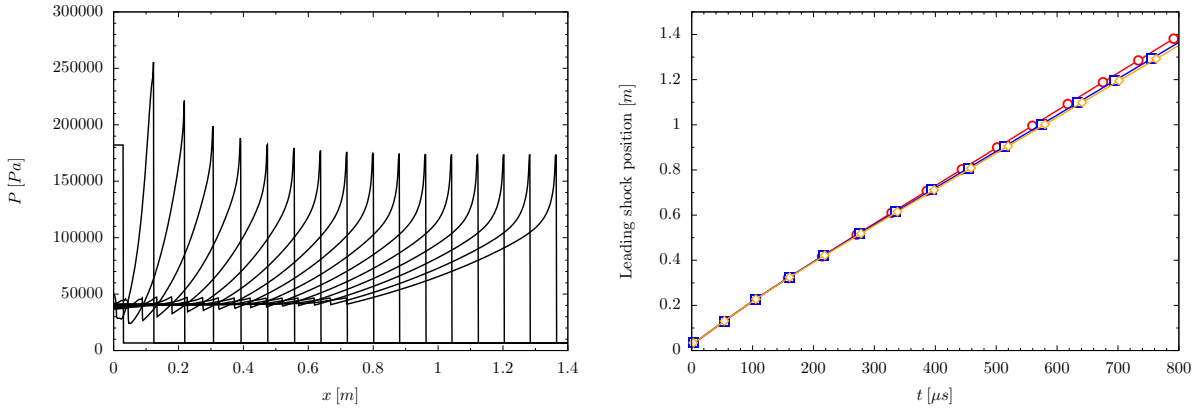

(a) *Pressure profiles* **(b)** *Shock position*

Figure 5.40: *$H_2/O_2/Ar$ Chapman-Jouget detonation convergence on the $Nx = 24000$ grid (pressure profile and leading shock position) computed with the thermally perfect EoS - —/-·- Ref, ○ QCVF, □ QCMF, ◇ FCMF*

relevant as no contact wave existed within the flow. This is verified here, showing that computations with the FCMF led to a fair agreement with the reference solution, partly due to the coarseness of the grid employed. The QCMF on the other hand features a very good agreement with the flame structure used as a reference. The Von Neumann zone is correctly captured by both of these approaches as are species distributions in the post-shock region. Overall the qualitative agreement with data presented by Deiterding [73] is good, except for the QCVF model.

Table 5.9 shows a quantitative comparison between the current results and reference values. The correct results obtained with the QCMF can be mentioned with an error in pressure of 3.7 $[kPa]$ and 2.8 $[m/s]$ and 11 $[m/s]$ for the detonation and Von Neumann speeds respectively. The temperature prediction is slightly less precise with an error of roughly 40 $[K]$. The error is a bit larger for the FCMF which could indicate that although no pressure oscillations have been observed, there is still an error being produced due to the conservative behaviour of the algorithm. Finally, errors are very large for the QCVF confirming that it is apparently unable to capture this type of flow features.

	Deiterding [73]	Houim [133]	QCMF	QCVF	FCMF
P_{vn} $[kPa]$	177.3	173.9	173.6	185.0	169.1
T_{vn} $[K]$	1921.7	1915.2	1881.5	1995.0	1852.5
U_{vn} $[m/s]$	1231.4	–	1220.0	1261.1	1201.0
S_{det} $[m/s]$	1626.9	1619.8	1624.1	1673.1	1605.2

Table 5.9: *$H_2/O_2/Ar$ Chapman-Jouget detonation characteristics computed with the different approaches using $\Delta x = 125$ $[\mu m]$*

Grid Convergence

A grid convergence has been performed using the QCMF model, and the results are presented in Fig. 5.42 for the flow structure and in Table 5.10 for the different variables in the Von Neumann spike. The mesh size does not seem to have an significant effect on the solution obtained. The Von Neumann spike is better resolved, but no notable improvement can be otherwise noted. The very reactive intermediate H_2O_2 species is already quite well resolved using the coarsest mesh, and the finest one does not seem to bring significant improvements.

The quantitative prediction of Von Neumann properties gets closer to reference values with mesh

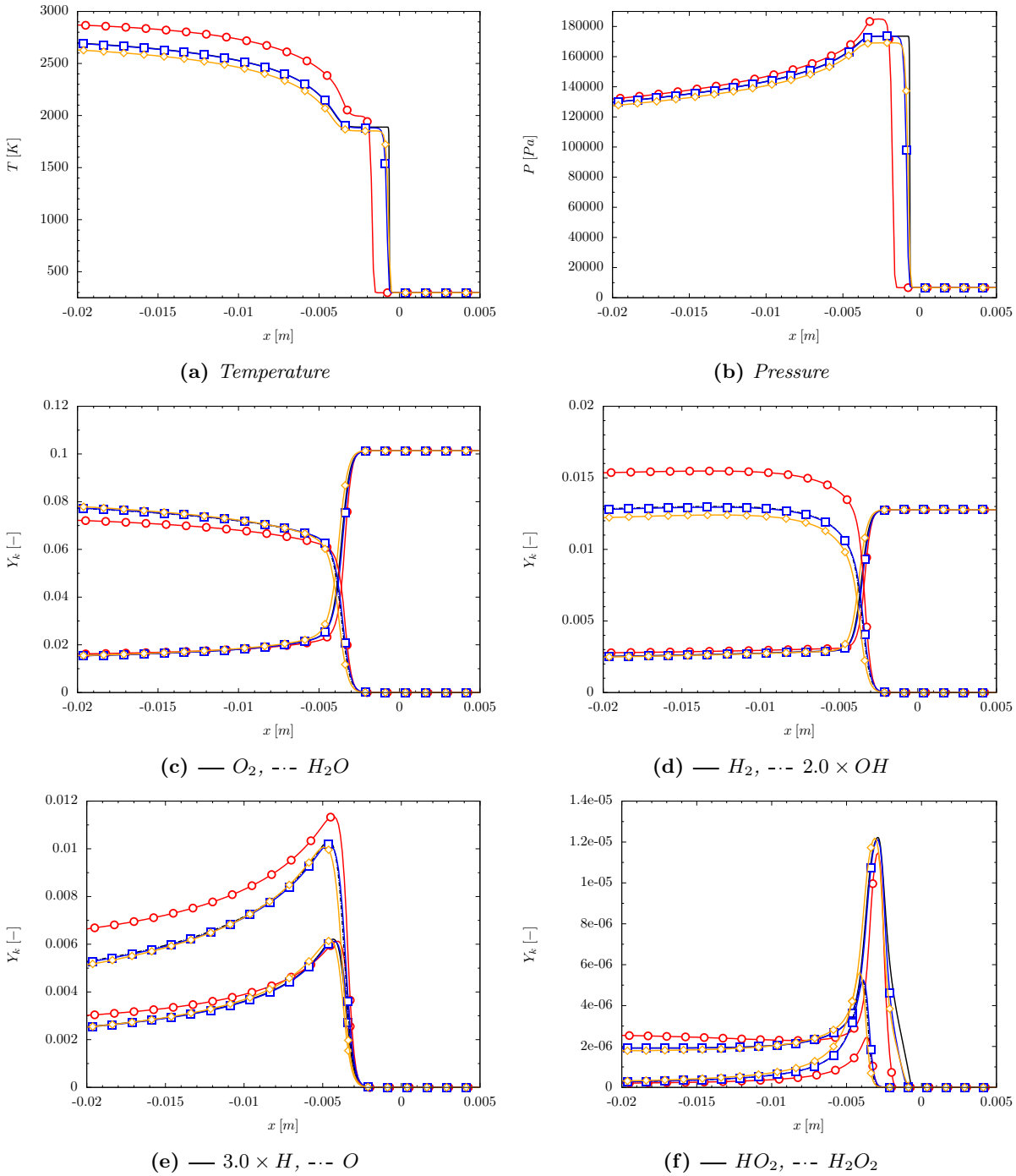

(a) *Temperature*

(b) *Pressure*

(c) — O_2, -·- H_2O

(d) — H_2, -·- $2.0 \times OH$

(e) — $3.0 \times H$, -·- O

(f) — HO_2, -·- H_2O_2

Figure 5.41: *$H_2/O_2/Ar$ Chapman-Jouget detonation wave structure computed with the Westbrook H_2/Air mechanism on the $Nx = 12000$ cells grid with the thermally perfect EoS - —/-·- Ref, ○ QCVF, □ QCMF, ◇ FCMF*

refinement. The error in temperature drops to about 30 $[K]$, while the error in pressure remains the same. Both velocity estimations are also better, with respective errors of 0.6 $[m/s]$ and 10 $[m/s]$ for the detonation and Von Neumann speeds. The method therefore performs quite well for all grids considered, thereby indicating its robustness.

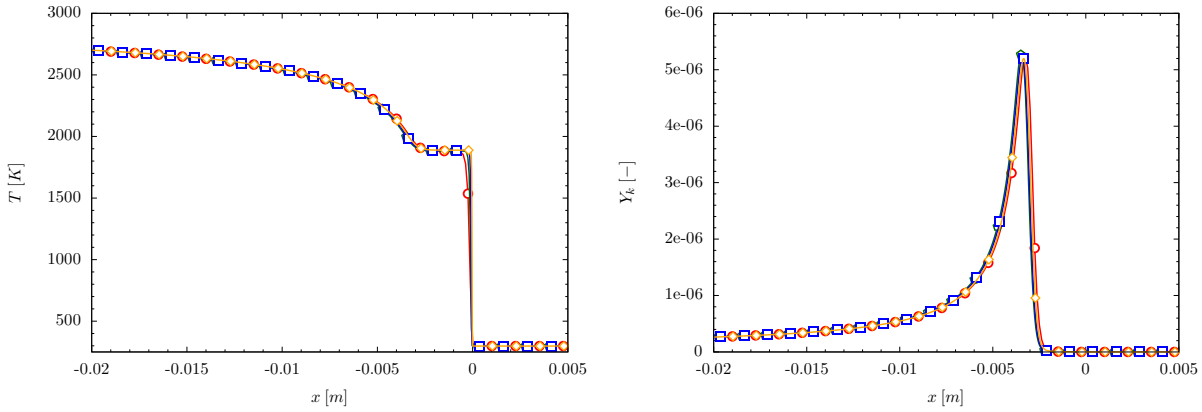

(a) *Temperature* **(b)** H_2O_2

Figure 5.42: *Grid convergence of the $H_2/O_2/Ar$ Chapman-Jouget detonation wave computed with the QCMF approach and the thermally perfect EoS -* —/-·- *Ref,* ○ $Nx = 12000$, ⬠ $Nx = 24000$, □ $Nx = 48000$, ◇ $Nx = 96000$

	Deiterding [73]	Houim [133]	125 $[\mu m]$	62.5 $[\mu m]$	31.25 $[\mu m]$	15.625 $[\mu m]$
P_{vn} $[kPa]$	177.3	173.9	173.6	173.5	173.6	173.6
T_{vn} $[K]$	1921.7	1915.2	1881.5	1884.0	1887.2	1889.3
U_{vn} $[m/s]$	1231.4	–	1220.0	1220.5	1220.5	1221.2
S_{det} $[m/s]$	1626.9	1619.8	1624.1	1624.4	1625.1	1627.5

Table 5.10: *$H_2/O_2/Ar$ Chapman-Jouget detonation characteristics using cell size ranging from $\Delta x = 125$ $[\mu m]$ to $\Delta x = 15.625$ $[\mu m]$ computed with the QCMF*

Influence of diffusion

All computations presented thus far for the detonation case have been computed using only the hyperbolic part of the equations. No species diffusion or heat conduction was accounted for. It has been shown in [73] that diffusion did not have a significant impact on the solution, and this is the case here as shown in Fig. 5.43 and Table 5.11.

Unfortunately, the additional diffusion added by the parabolic operator to the solution did not improve the QCVF approach stability which was still unable to obtain a converged solution.

The QCMF method on the other hand confirms that diffusion has a negligible impact on the results obtained, except maybe on the detonation speed. The difference observed in the other quantities is not large enough to see the influence of diffusion on the solution.

Remarks on the thermodynamic properties

Similarly to what has been presented for the constant volume reactor and laminar flame speed, the specific heat ratio influence on the simulation of a detonation is investigated here. γ values considered here have been taken in the unburnt ($\gamma_u = 1.556$) and burnt mixtures ($\gamma_b = 1.432$), and in the Von Neumann spike ($\gamma_{vn} = 1.49$), which corresponds almost exactly to the average between the reactants and products values.

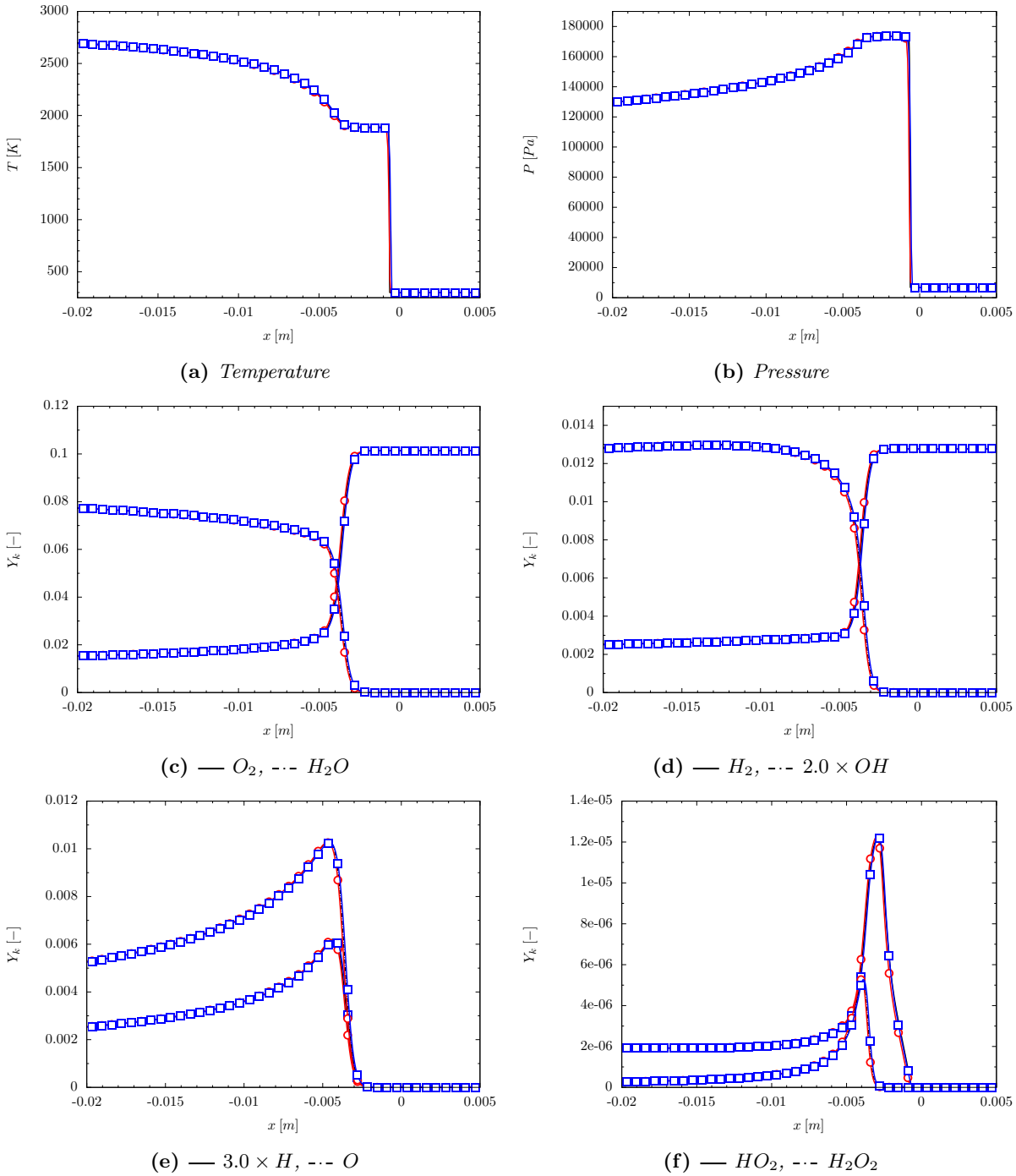

(a) *Temperature*

(b) *Pressure*

(c) — O_2, -·- H_2O

(d) — H_2, -·- $2.0 \times OH$

(e) — $3.0 \times H$, -·- O

(f) — HO_2, -·- H_2O_2

Figure 5.43: *Influence of diffusion on the $H_2/O_2/Ar$ Chapman-Jouget detonation wave structure computed with the QCMF and the thermally perfect EoS on the $Nx = 24000$ grid - —/-·- Ref, ○ Diffusion OFF, □ Diffusion ON*

	Deiterding [73]	Houim [133]	Diffusion OFF	Diffusion ON
$P_{vn}\ [kPa]$	177.3	173.9	173.6	173.7
$T_{vn}\ [K]$	1921.7	1915.2	1887.0	1887.5
$U_{vn}\ [m/s]$	1231.4	–	1220.5	1221.0
$S_{det}\ [m/s]$	1626.9	1619.8	1625.1	1630.5

Table 5.11: *$H_2/O_2/Ar$ Chapman-Jouget detonation characteristics with and without diffusion fluxes using $\Delta x = 31.25\ [\mu m]$ and computed using the QCMF*

The detonation structures obtained for these different γ values are visible in Fig. 5.44, while the estimation of the different quantities in the Von Neumann spike are presented in Table 5.12.

The main flow features seems to be predicted by all γ values, given that a Von Neumann spike can be observed for all γ considered with values of pressure relatively close to the reference solution. The main difference between the three cases lies in the prediction of the Von Neumann and burnt temperatures, the larger (resp. the lower) the γ value is, the larger (resp. the lower) the Von Neumann temperature, and consequently the faster (resp. the slower) the leading shock front moves. Additionally, the spike size also depends strongly on the temperature, as it is basically directly linked with the mixture ignition delay at the given temperature and pressure. This implies that low values of γ leading to smaller Von Neumann temperature values also lead to longer Von Neumann spikes.

It appears that a detonation can be accurately determined with a single γ value corresponding to the value found in the Von Neumann zone ($\gamma = \gamma_{vn}$). The detonation structure is correctly reproduced in terms of species distribution, but also of pressure and temperature. The leading shock speed is also accurately captured. However, as shown in the laminar flame calculation, the acceleration phase of the flame can not be properly captured by a single γ value, which explains why a compromise has to be found on the γ value when simulating deflagration-to-detonation transition [101–104, 221].

	Deiterding [73]	Houim [133]	$\gamma = \gamma(Y_k, T)$	$\gamma_u = 1.556$	$\gamma_{vn} = 1.49$	$\gamma_b = 1.432$
$P_{vn}\ [kPa]$	177.3	173.9	173.5	169.5	176.6	174.6
$T_{vn}\ [K]$	1921.7	1915.2	1884.0	1631.1	1835.1	1997.1
$U_{vn}\ [m/s]$	1231.4	–	1220.5	1225.5	1221.9	1229.5
$S_{det}\ [m/s]$	1626.9	1619.8	1624.4	1580.9	1622.3	1648.2

Table 5.12: *$H_2/O_2/Ar$ Chapman-Jouget detonation characteristics computed with the QCMF for different values of γ using the calorically perfect EoS and $\Delta x = 62.5\ [\mu m]$*

5.4.4 Discussion

Three type of problems of increasing complexity (constant volume reactor, laminar flame and detonation) have been computed using the two quasi-conservative methods presented in the previous chapters.

All models featured a very good agreement with the reference solution for the constant volume reactor problem using either simple or complex chemical mechanisms. Errors of at most 0.2 % for the temperature, pressure and species mass fractions were measured.

The next problem, a laminar freely propagating premixed flame, was a very challenging test for fully compressible unsteady algorithms as a very delicate balance had to be computed between the non-linear diffusion, advection and source terms, and this at a very low Mach number, of the order of 0.05. Both methods (QCMF and QCVF) performed very well for the simple $2s\_CM2$ chemical mechanism in a large

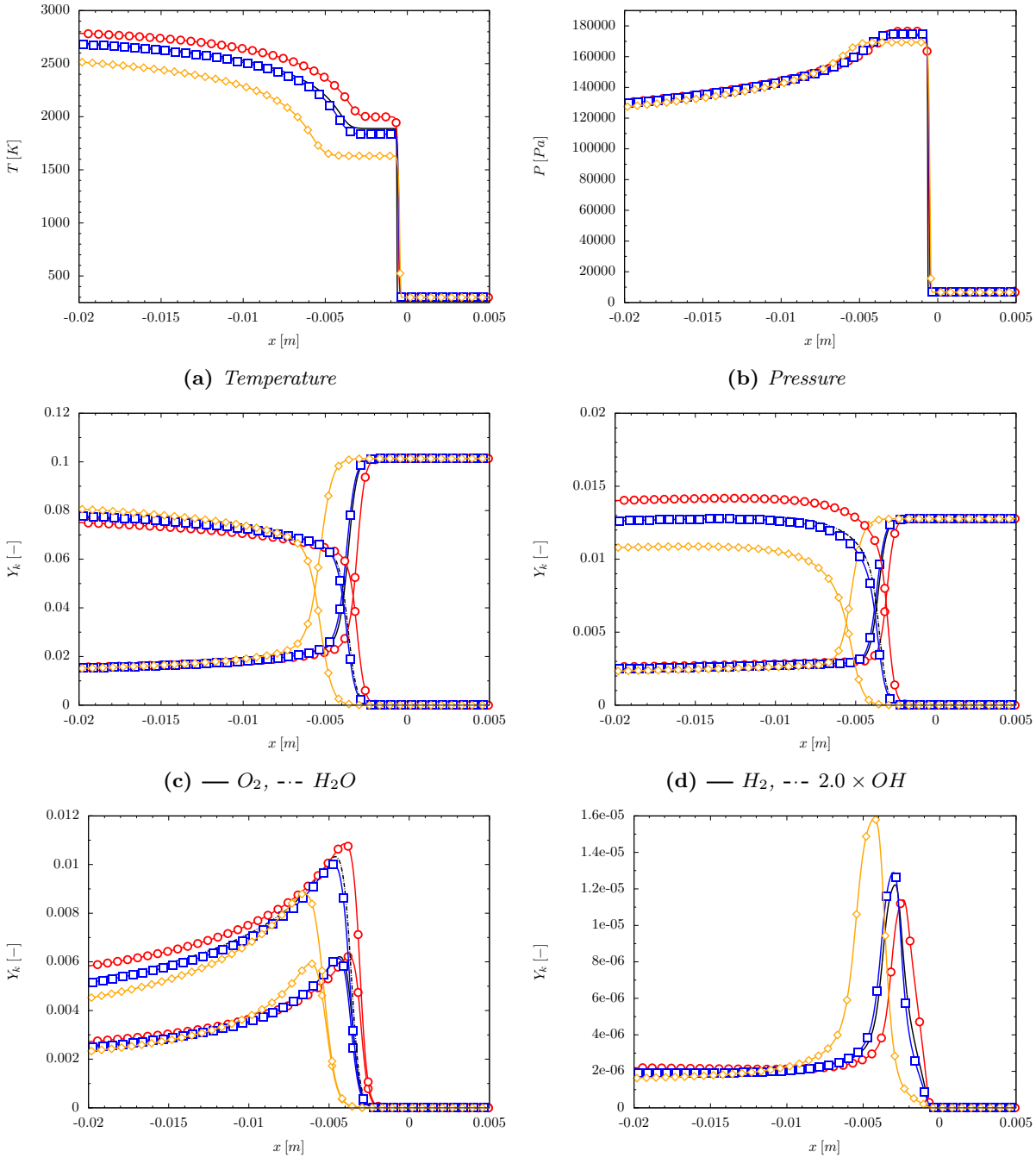

(a) *Temperature*

(b) *Pressure*

(c) — O_2, -·- H_2O

(d) — H_2, -·- $2.0 \times OH$

(e) — $3.0 \times H$, -·- O

(f) — HO_2

Figure 5.44: *$H_2/O_2/Ar$ Chapman-Jouget detonation wave computed with the QCMF on the $Nx = 24000$ grid with the calorically perfect EoS using different values of γ - —/-·- Ref, ○ γ_u, □ γ_{vn}, ◇ γ_b*

range of stoichiometric ratios and inlet temperatures. The flame speed and internal structure were both well predicted. On the more complex mechanism, the conclusion is a bit more ambiguous as the QCVF predicted a correct flame structure but a slower flame than the reference calculation (`Cantera`), while the QCMF featured a good estimation of the flame speed, but an overestimation of the products temperature. The main reason behind these discrepancies has been identified as the diffusion coefficient calculation. Indeed, a simple approximation has been employed here with constant (but non-unity) Lewis numbers, which is known to be less precise, especially in hydrogen flames. Additionally, the larger numerical diffusion observed in inviscid test cases for the QCMF compared with the QCVF could explain the slightly more energetic combustion observed with this model (larger flame speed and products temperature). Nonetheless, the overall performance of both algorithms remains good.

On the last test case, the hydrogen detonation, it was found that the QCVF was not able to obtain a solution on another grid than the coarsest due to instabilities in the pressure calculation. This was partially attributed (but not limited) to a numerical instability resulting from the multiplication of very small numbers by very large ones. This could also be due to the hypothesis made in the model, such as the creation of species at the mixture conditions, which could maybe be replaced by Ton's [277] way of doing. Ton considers that combustion and/or diffusion is occurring at the temperature of the dominant species in the cell if its mass fraction is larger than 0.5 and the mixture temperature otherwise. On the other hand, the QCMF behaves properly and good qualitative and quantitative agreements were found with reference data [73, 133].

5.5 Conclusion

This chapter presented the validation and verification of four different methods used to compute compressible multi-component flows. Two fully conservative, and two quasi-conservative methods were tested on inviscid, viscous and reacting test cases.

The implementation was first checked in terms of time-stepping, variable reconstruction and Riemann solver in three simple test cases. The first one consisted in the advection of a slab of helium in a nitrogen coflow, the second was the classical single species shock-tube problem and the third was a shock colliding test. The time-stepping was validated and found to have almost no effect on the solution, except of course outside of its stability bounds. The Riemann solver performed as excepted, capturing properly contact, expansion and shock waves, and the variable reconstruction showed a reduction of the numerical dissipation added to the solution with the increase of the order of accuracy.

The different approaches were then tested on inviscid problems such as the advection of an helium slab in a nitrogen coflow (with and without initially uniform temperature field), and multi-species shock-tube problems with several pressure ratios and species. It was found that both fully-conservative schemes featured pressure and velocity oscillations at the contact surface due to their inability to conserve a pressure equilibrium between two species. These were so dramatic for the FCVF that it was not used for the viscous and reacting test cases. Both quasi-conservative methods displayed the expected results which consisted in a uniform pressure field after the advection of the slab. The conservation errors of the QCMF were found to be larger than the QCVF especially in shock-tube problems where the energy conservation error was 0.2 % for the QCMF and 10^{-12} % for the QCVF. The mass conservation error was 10^{-4} for the QCMF and 10^{-14} for the QCVF in shock-tube problems. Additionally, the QCMF was found to be more diffusive than the QCVF.

Diffusive tests were also presented showing a perfect agreement with the analytical solution, and this for both the QCMF and QCVF models. Further tests coupling both the advection and diffusion featured a near perfect agreement with the analytical solution at the exception of a slight rounding off of initially sharp diffusive moving fronts at high Peclet numbers. However, this rounding-off is a normal effect and was similar for all models.

Finally, the different models were tested in reacting test cases, first by checking only the source term integration on simple methane and complex hydrogen mechanisms, then by coupling the inviscid and viscous operators with the source term in the simulation of premixed laminar flames and detonations. The source term integration showed that both quasi-conservative methods correctly predicted the evolution of temperature, pressure and mixture composition in an adiabatic constant volume reactor. It was also shown that a constant γ value (corresponding to the products value) could lead to accurate results. Methane laminar flame structures and speeds computed with the QCMF and QCVF models were in good agreement with the reference results from `Cantera`. The hydrogen flame structure was correctly predicted by the QCVF, but the QCMF over-predicted the products temperature. The laminar flame speed was, on the other hand, correctly estimated by the QCMF and under-estimated by the QCVF. This was attributed to the simple diffusion approach retained in this work and to the larger numerical diffusion of the QCMF. It was also shown that no single γ value could be used to predict both the flame speed and temperature of a laminar flame. Eventually, it was shown that detonation waves were correctly predicted by the QCMF model, but that the QCVF was not able to properly capture the strong shock wave which eventually led to a divergence of the method. A single γ value (corresponding to the value found in the Von Neumann spike) was shown to be able to resolve properly most of the detonation wave features.

A summary of results obtained for each models on the different test cases is presented in Table 5.13.

Test cases	QCVF	FCVF	QCMF	FCMF
Inviscid test cases (§. 5.2)				
Stationary contact surface	✓	✓	✓	✓
Moving material surface	✓	×	✓	×
Moving contact surface	✓	×	✓	×
Multi-species shock-tube	✓	×	✓	×
Shock-bubble interaction	✓	×	✓	×
Diffusive test cases (§. 5.3)				
Pure diffusion	✓	NA	✓	✓
Advection diffusion	✓	NA	✓	✓
Reactive test cases (§. 5.4)				
0D Constant Volume Reactor	✓	NA	✓	✓
1D laminar flame	✓	NA	✓	✓
1D detonation	×	NA	✓	×

Table 5.13: *Summary of one-dimensional validation results of the QCVF, FCVF, QCMF, FCMF schemes - ✓ means test successful (computed and reference/analytical solutions agree, no crash of the computation, etc.) × means test failed (crash of the computation, pressure oscillations, temperature spikes, etc.) and NA means Non Applicable (has not been tested)*

No strong argument in favour of the QCMF or QCVF emerges from these validation tests. Lower conservation errors are obtained with the QCVF at the expense of an increased sensitivity to strong shock problems. Both schemes are further compared on multiple dimensions problems such as reacting and non-reacting shock-bubble interactions.

CHAPTER 6

Multi-dimensional validation and verification tests

One dimensional validation and verification problems have been presented in the previous chapter. The different methods developed have been thoroughly tested against test cases of increasing complexity, including an increasing number of physical phenomena such as diffusion and chemical reactions. The three selected algorithms, QCVF, QCMF and FCMF have been implemented in a new parallel curvilinear block-structured code referred to as `FlAMEnCo3D` written by the author based on the data structure provided by Shapiro and presented in [105].

This chapter presents the application of these algorithms on multi-dimensional problems, mostly in two space dimensions. Benchmark cases similar to those presented in the previous chapter are computed here for the validation of the hyperbolic and parabolic parts of the equations, and to assess the behaviour of the QCVF approach in multidimensional flows. Moving contact surfaces (§. 6.1.1), cylindrical and spherical shock tube experiments (§. 6.1.2) are presented in a first part along with a diffusion case (§. 6.1.3). These problems also aims at ensuring the absence of directional bias in the resolution of the equations.

Once the quality of the solution has been established and the absence of directional bias assessed, the three previously mentioned algorithms are used to compute more complex flow fields such as an inert (§. 6.2) and a reacting (§. 6.3) shock-bubble interaction problems. The first one corresponds to the well-known experiment of Haas and Sturtevant [122], while the reacting test is taken from the numerical experiment of Billet *et al.* [26]. Given the failure of the QCVF model to simulate strong detonations waves (§. 5.4.3), but given its good performance in the simulation of laminar premixed flames (even fast ones), the reacting shock-bubble is used to asses the possibility of using the QCVF model in reacting flows in the absence of strong shock waves. The influence of the algorithm employed to compute the solution and of the thermodynamic considered are also investigated.

6.1 Inviscid and viscous validation test cases

Simple inviscid and viscous test cases are discussed in this section, as a mean to establish the correct behaviour of the different algorithms in several space dimensions, and to validate the multi-dimensional implementation.

It shall be noted, that although the code is implemented in a curvilinear framework, all the results presented here have been obtained on Cartesian grids. However, the curvilinear implementation has also been validated on similar cases with skewed grids but this is out of the scope of this work.

6.1.1 Moving contact surface

A two-dimensional bubble of hot helium in a colder nitrogen coflow is initialised in a square periodic domain with a side length of $L = 1\ [m]$. The bubble diameter is set to $D = 0.2\ [m]$. The helium

temperature is $T_{He} = 2000\,[K]$, while the coflow temperature is $T_{N_2} = 1000\,[K]$. The whole domain is at atmospheric pressure and a uniform flow field of magnitude $U = 100\,[m/s]$ is imposed. To avoid a too particular study (advection along grid lines), the velocity vectors are oriented with an angle of $\alpha = 25\,[deg]$ with the horizontal axis, yielding velocity components $u = 90.63\,[m/s]$ and $v = 42.26\,[m/s]$. The initial interface is not smeared thus representing the hardest case possible to all algorithms (sharp discontinuity). The domain is discretised by a 100×100 cells grid, thus having $\Delta x = \Delta y = 0.01\,[m]$. Both MUSCL5 and RK2-SSP schemes have been used for the spatial discretisation and time-marching respectively, with $CFL = 0.5$. The bubble centre is initially placed at $(x_0,\, y_0) = (0.5,\, 0.25)\,[m]$, and the simulation is run until the bubble comes back to its original horizontal position, i.e. after being advected $l = 1.103\,[m]$.

Fig. 6.1 presents a one-dimensional cut through the bubble parallel to the velocity vector at the final time of the simulation. The behaviour of the different algorithms is similar to what has already been pointed out in the previous chapter, with the fully conservative model creating pressure and velocity oscillations leading to a significant deformation of the bubble shape as visible in Fig. 6.2. Both quasi-conservative schemes preserve perfectly both pressure and velocity as expected, and the bubble shape is well conserved after the advection on this coarse grid. A slightly greater numerical diffusion is featured by the QCMF model at the tail of the bubble as visible on both Fig. 6.1 and Fig. 6.2 compared to the QCVF results. Similar results are obtained in other velocity directions and planes.

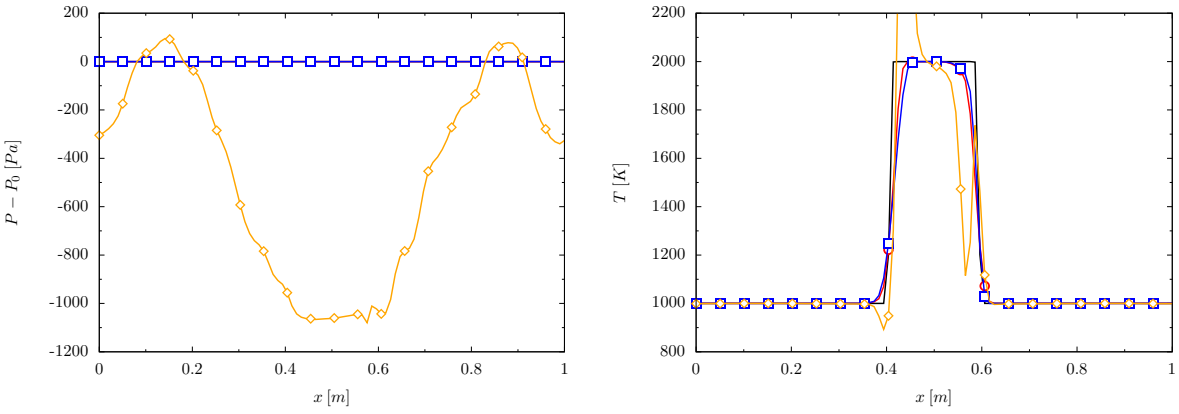

(a) *Pressure*

(b) *Temperature*

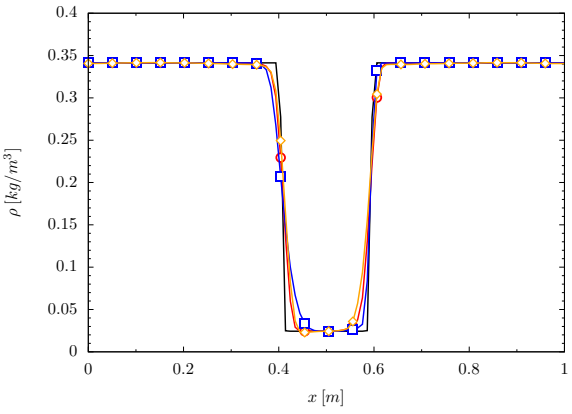

(c) *Density*

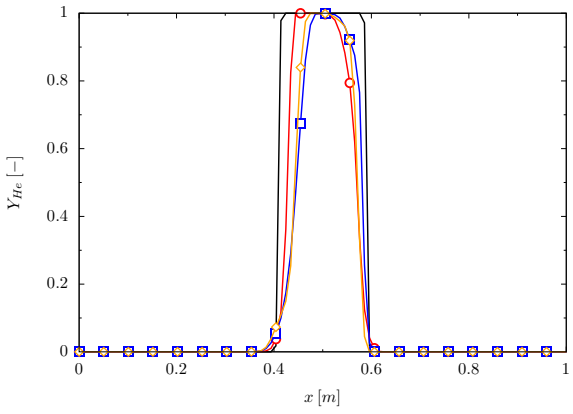

(d) Y_{He}

Figure 6.1: *Moving contact surface profiles obtained on a slice parallel to the velocity vector passing through the bubble centre at the final bubble position, $t = 1.103 \times 10^{-2}\,[s]$ on a 100×100 grid with the different models and the thermally perfect EoS - — Ref, ○ QCVF, □ QCMF, ◇ FCMF*

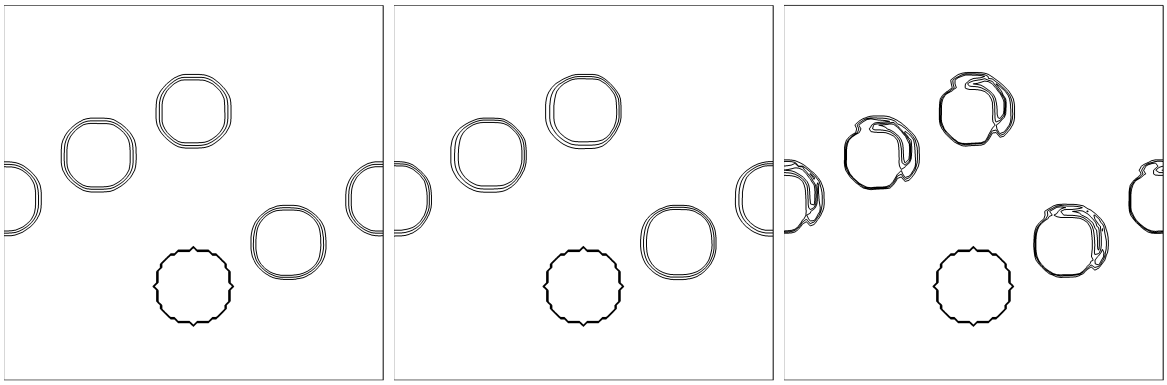

(a) *QCVF* **(b)** *QCMF* **(c)** *FCMF*

Figure 6.2: *Temperature isopleths for the two dimensional moving contact surface computed with the QCVF, QCMF and FCMF using the thermally perfect EoS on a* 100×100 *grid at* $t = 0,\ 0.25t_{final},\ 0.5t_{final},\ 0.75t_{final},\ t_{final}$ *- Isopleths at* $1100,\ 1500,\ 1900\ [K]$

6.1.2 Multi-species shock-tube

In this section, a similar shock-tube experiment as presented in §. 5.2.4 is presented in multi-dimensions, as the so-called cylindrical and spherical sod-shock problems. The exact same set-up is used at the exception that instead of initialising the left and right states, a cylindrical (resp. spherical) bubble of pressurised helium has been initialised with a diameter of $D = 0.8\,[m]$ at the centre of a $L = 2\,[m]$ square (resp. cubic) domain. The domain is discretised by 400^2 (resp. 400^3) cells, yielding, $\Delta x = \Delta y = \Delta z = 5 \times 10^{-3}\ [m]$. The MUSCL5 and RK2-SSP have been used respectively for the variable reconstruction and time integration with $CFL = 0.5$, while the thermally perfect EoS was considered.

Contrary to the one-dimensional test case, there is no exact solution for this test case in multiple dimensions. However, Toro [278] shows that the addition of a geometric source term to the Euler equations allows to obtain solutions for the cylindrical and spherical problems, yielding the following system of equations,

$$\frac{\partial \mathbf{U}}{\partial t} + \frac{\partial \mathbf{F}\left(\mathbf{U}\right)}{\partial x} = \mathbf{S}_{geom} \tag{6.1}$$

where the geometric source term is defined by,

$$\mathbf{S}_{geom} = -\frac{\alpha}{r}\begin{pmatrix} \rho u Y_k \\ \rho u^2 \\ \left(\rho E + P\right) u \end{pmatrix} \tag{6.2}$$

where $\alpha = 1$ for cylindrical problems and $\alpha = 2$ for spherical ones. These terms have been implemented in `FlAMEnCo1D` in order to give a reference solution for the computations. Reference solutions have been obtained on $Nx = 1000$ cells, but also on $Nx = 200$ cells to compare directly the results with those obtained with the multi-dimensional code in several radial directions.

Fig. 6.3 and Fig. 6.4 respectively feature results obtained in two dimensions for the cylindrical shock tube and in three dimensions for the spherical one. The multi-dimensional profiles compare very well with reference solutions obtained using the geometric source term presented above. The three algorithms performs very similarly at the exception of the temperature spike obtained with the FCMF at the species interface, which was expected.

Fig. 6.5 presents some samples of temperature taken at different angles in cylindrical and spherical Riemann problems thus evaluating the directional biases influence on the solution. In both problems

it can be seen that any directional bias in the calculation is very weak, as the agreement between the different directions shows.

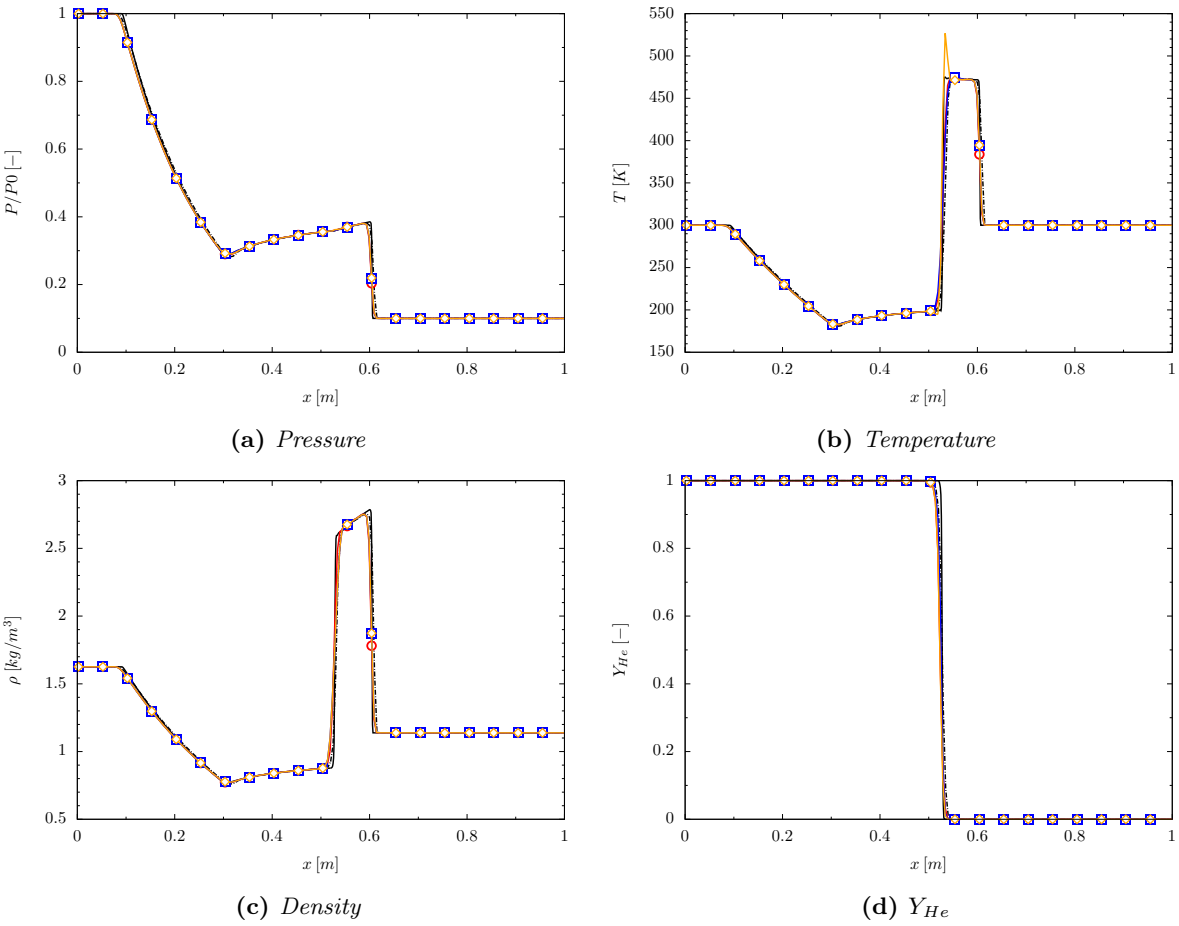

(a) *Pressure* **(b)** *Temperature*

(c) *Density* **(d)** Y_{He}

Figure 6.3: *Pressure, temperature, density and mass fraction profiles for the cylindrical Riemann problem computed with the thermally perfect EoS on a* 400×400 *grid (half the domain is shown here) - —/-·- Ref,* ○ *QCVF,* □ *QCMF,* ◇ *FCMF*

6.1.3 Viscous test cases

The hyperbolic operator in multiple space dimensions has been presented above, where it was shown that a very weak rotational bias was introduced by numerical methods, which is expected when computing solutions at different angles compared to the grid lines. The viscous fluxes implementation is now verified in a simple test case similar to the pure diffusion problem presented in §. 5.3.1. The case is similar here but in two dimensions to check the presence of directional bias in the computation of the viscous fluxes.

The constant property diffusion case is here computed on a square mesh of side length $L = 18\,[mm]$ and discretised with a grid of 600×600 cells, yielding $\Delta x = \Delta y = 30\,[\mu m]$. A patch of diameter $D = 9\,[mm]$ is initialised at the centre of the domain and let to diffuse with a diffusion coefficient set to $D = 5 \times 10^{-3}\,[m^2/s]$. The computation is run with the MUSCL5 and RK2-SSP schemes with $CFL = 0.5$ and is stopped after $t = 1\,[ms]$. As previously considered, hydrogen is used as the gas for these simulations.

Fig. 6.6 shows the excellent agreement gained between the analytical and computed solutions. No difference can be observed between the different models, similarly to what was observed in one-dimensional test cases. Additionally, it can be seen on Fig. 6.7 that the rotational bias is once again very weak thus validating the current implementation.

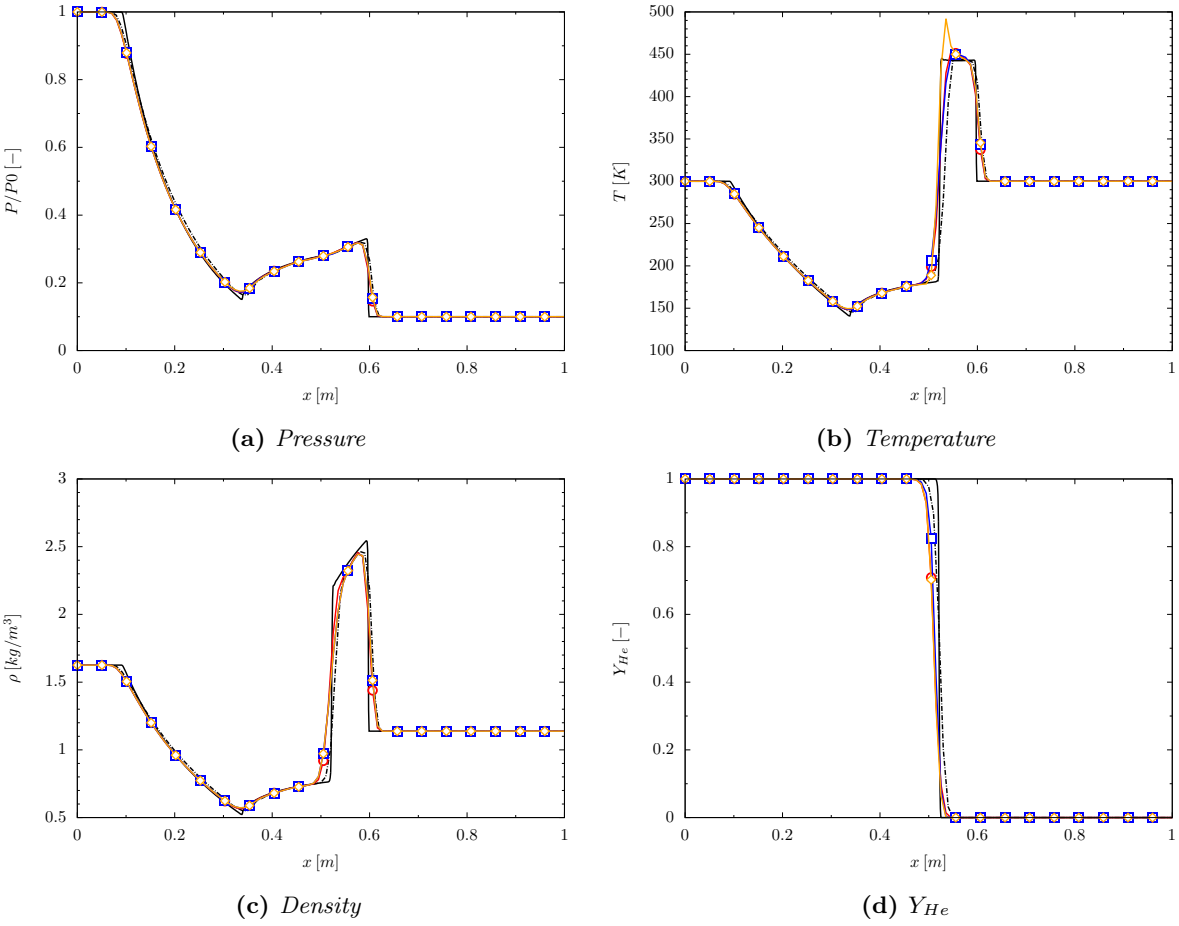

(a) *Pressure* **(b)** *Temperature*

(c) *Density* **(d)** Y_{He}

Figure 6.4: *Pressure, temperature, density and mass fraction profiles for the spherical Riemann problem computed with the thermally perfect EoS on a* $400 \times 400 \times 400$ *grid (quarter of the domain shown here) - —/-·- Ref,* ○ *QCVF,* □ *QCMF,* ◇ *FCMF*

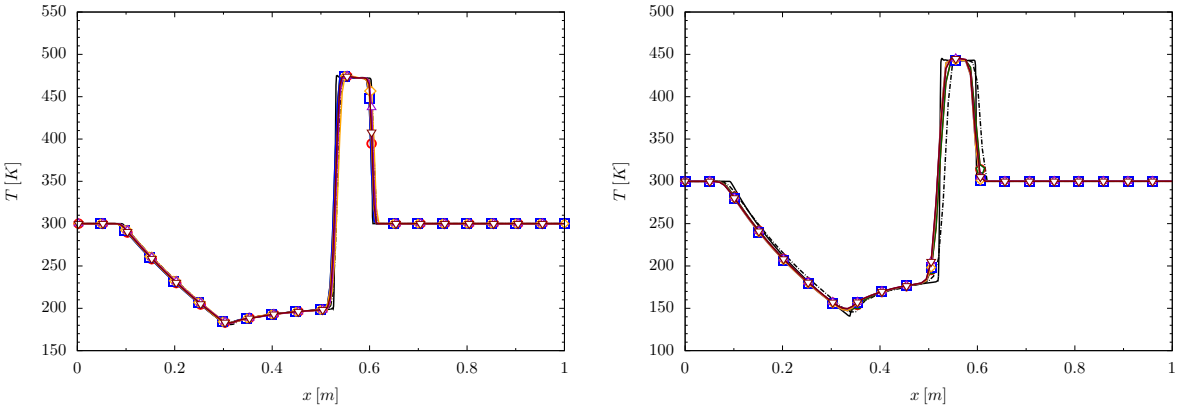

(a) *Cylindrical problem - —/-·- Ref,* ○ $\theta = 0$, ⬠ $\theta = 30$, □ $\theta = 60$, ◇ $\theta = 90$, △ $\theta = 120$, ▽ $\theta = 150$

(b) *Spherical problem - —/-·- Ref,* ○ $\theta = 30,\ \phi = 30$, ⬠ $\theta = 30,\ \phi = 60$, □ $\theta = 60,\ \phi = 60$, ◇ $\theta = 60,\ \phi = 60$, △ $\theta = 90, \phi = 30$, ▽ $\theta = 90,\ \phi = 60$

Figure 6.5: *Rotational invariance for the cylindrical and spherical Riemann problems computed with the thermally perfect EoS*

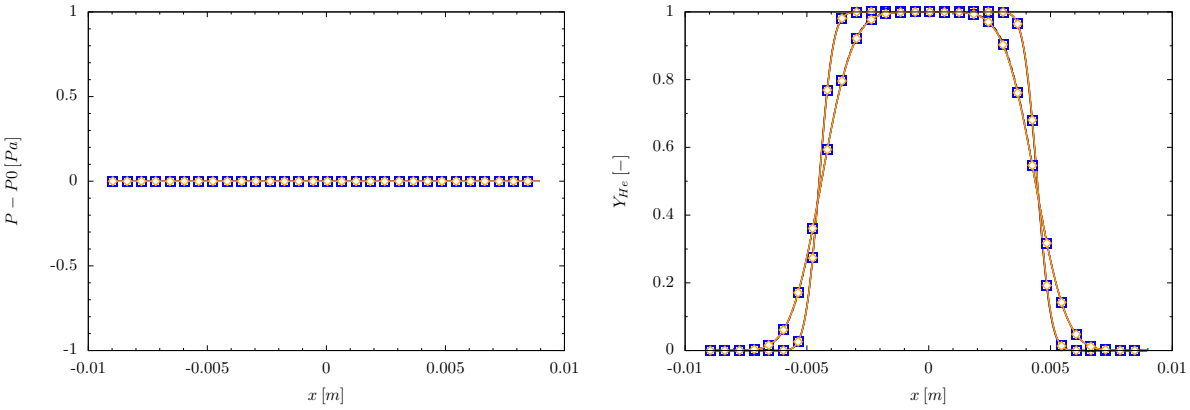

(a) *Pressure* **(b)** Y_{He}

Figure 6.6: *Pressure and mass fraction profiles for the two-dimensional diffusion problem computed with the thermally perfect EoS on a* 600×600 *grid at* $t = 2 \times 10^{-4}$ $[s]$ *and* $t = 1 \times 10^{-3}$ $[s]$ *- —/-·- Ref, ○ QCVF, □ QCMF, ◇ FCMF*

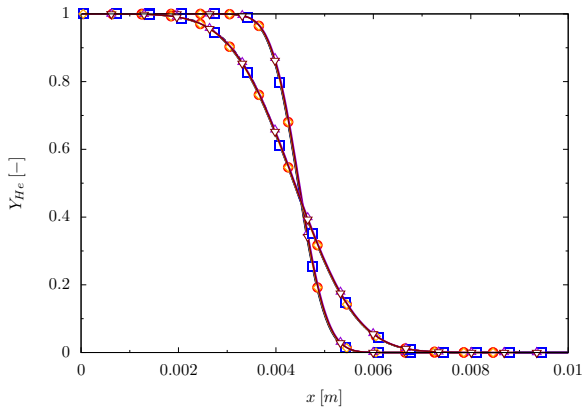

Figure 6.7: *Rotational invariance for the diffusion problem computed with the thermally perfect EoS at* $t = 2 \times 10^{-4}$ $[s]$ *and* $t = 1 \times 10^{-3}$ $[s]$ *- —/-·- Ref, ○* $\theta = 0$, *⬠* $\theta = 30$, *□* $\theta = 60$, *◇* $\theta = 90$, *△* $\theta = 120$, *▽* $\theta = 150$

6.1.4 Discussion

The previous section has verified on three different problems the implementation of the three algorithms QCVF, QCMF and FCMF on the block-structured curvilinear code `FlAMEnCo3D`. The advection of a gaseous bubble showed that the initial circular shape was adequately preserved using quasi-conservative schemes, thus avoiding pressure oscillations, while using a fully-conservative model resulted in a dramatic change of the initial shape. Furthermore, cylindrical and spherical shock tube tests validated the Riemann solver in all directions for the three types of waves encountered in compressible flows. As expected, the FCMF featured temperature spikes at interfaces between species while quasi-conservative schemes did not. The rotational bias introduced by the considered numerical methods when solving flows whose velocity vectors are not aligned with grid lines was found very weak and therefore negligible. Finally, the diffusion test case compared extremely well for all models against the analytical solution available, while the rotational bias was also found extremely weak and thus neglected.

6.2 Inert Shock-bubble interaction

6.2.1 Introduction

The investigation of the shock-bubble interaction dynamics relies on the numerical reproduction of the experiments performed by Haas & Sturtevant [122]. Namely, the interaction of a planar shock wave propagating through air and impacting a cylindrical bubble filled with helium. Helium being lighter than air, the interface acts as a divergent acoustic lens, spreading the shock, while in the experiment involving R22 refrigerant, the interface behaves as a convergent acoustic lens, leading to a very different flow behaviour.

In the experiment, the bubble was produced by inflating a cylindrical former whose walls were made from a thin layer of nitrocellulose, thus, a very good control over the shape of the bubble was exercised, yielding an almost two-dimensional flow. Therefore, two-dimensional calculations are expected to give very similar results compared to experimental data gathered for both bubble compositions. This test case is one of several well known problems used to test compressible multi-component flow solvers capabilities and thus a significant amount of data is available in the literature [13, 143, 198, 250, 259, 270] allowing a direct comparison with the results obtained with the current algorithms.

6.2.2 Test case

Domain

The computational set-up is presented in Fig. 6.8. In the current analysis, we have assumed that the flow was symmetrical about the shock axis, and therefore, only the domain upper half has been computed. The boundary conditions applied were as follows,

- Symmetry on the top wall and axis
- Supersonic Inflow/Outflow on the sides (i.e. extrapolation with zero gradient on all conserved variables)

The computational domain is $6.5D$ long, and spans $-2.5 \leqslant x/D \leqslant 4.0$, and $0 \leqslant y/D \leqslant 0.89$, where D is the helium/R22 bubble diameter. The position $x/D = 0$ corresponds to the left side of the cylinder.

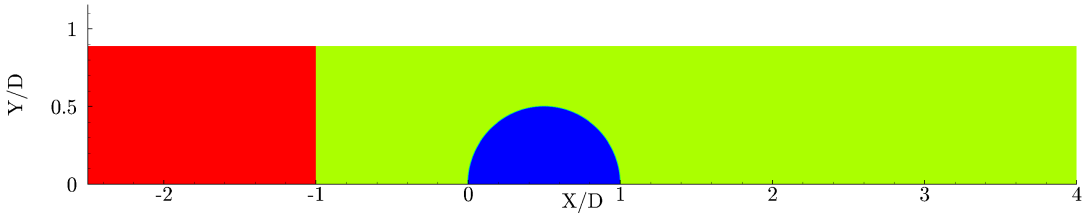

Figure 6.8: *Initial density profile for the computation of the shock-bubble interaction*

Initial Conditions

Initially, a Mach 1.22 normal shock wave is imposed at $x/D = -1$, which leaves the time for the shock to smear to its numerically stable profile from the exact discontinuity initially specified, thus avoiding the so-called "start-up errors" [129]. Start-up errors, taking the form of a pair of low-frequency/low-amplitude waves moving with the contact characteristic speed, are thus prevented from interfering with the interaction process. Shock properties are estimated following the methodology presented in Appendix C.

The bubble and the surrounding air are assumed to be initially in thermal and mechanical equilibriums, similarly to what has been done in all previous computations presented in the literature. According to the experimental data available, the bubble is not filled with pure helium, but rather with helium

contaminated with about 28 [%] of air, thus changing the thermodynamic properties of the bubble. In the case of the refrigerant R22, it has been estimated that the contamination was about 3.4 [%], and thus neglected in the computational studies.

Table 6.1 presents the initial flow conditions in all zones of the domain, in both dimensional and non-dimensional forms.

	Helium bubble		R22 bubble	
	$[SI]$	$[-]$	$[SI]$	$[-]$
I - Shocked Air				
$P\,[Pa]$	159059	1.5698	159059	1.5698
$\rho\,[kg/m^3]$	1.7755	1.3764	1.7755	1.3764
$u\,[m/s]$	110.63	0.3336	110.63	0.3336
$\gamma\,[-]$	1.4000	1.0000	1.4000	1.0000
II - Unshocked Air				
$P\,[Pa]$	101325	1.0000	101325	1.0000
$\rho\,[kg/m^3]$	1.2900	1.0000	1.2900	1.0000
$u\,[m/s]$	0.0000	0.0000	0.0000	0.0000
$\gamma\,[-]$	1.4000	1.0000	1.4000	1.0000
III - Bubble (Helium + 28% Air / R22)				
$P\,[Pa]$	101325	1.0000	101325	1.0000
$\rho\,[kg/m^3]$	0.2359	0.1829	3.6069	2.7960
$u\,[m/s]$	0.0000	0.0000	0.0000	0.0000
$\gamma\,[-]$	1.6480	1.1800	1.2490	0.8921

Table 6.1: *Dimensional ([SI]) and non-dimensional ([-]) initial flow conditions for both bubble compositions considering a calorically perfect gas - Dimensionless quantities computed with* $D = 50\,[mm]$, $\rho_{air} = 1.29\,[kg/m^3]$, $P_{air} = 101325\,[Pa]$, $\gamma_{air} = 1.4$ *and* $a_{air} = 331.6\,[m/s]$

A smooth initial interface has been used for the simulations to avoid the growth of artificial instabilities triggered by a sharp interface. The function used to this end is the following,

$$Y_k = \frac{Y_{k,in} + Y_{k,out}}{2} - \frac{Y_{k,in} - Y_{k,out}}{2} \tanh\left(\frac{r - r_0}{\Delta_x}\right) \tag{6.3}$$

where r_0 is the bubble radius and Δ_x is the cell size. This allows the interface to be spread initially on a similar number of cells for each case independently of the grid resolution.

Five different resolution levels have been used and are presented in Table 6.2.

	Δ_x/D	Δ_y/D	$\Delta_x\,[m]$	$\Delta_y\,[m]$	N_{cells}
2I	0.02	0.02	1.00×10^{-3}	1.00×10^{-3}	$325 \times 45 = 14,625$
2II	0.01	0.01	5.00×10^{-4}	5.00×10^{-4}	$650 \times 89 = 57,850$
2III	0.005	0.005	2.50×10^{-4}	2.50×10^{-4}	$1,300 \times 178 = 231,400$
2IV	0.0025	0.0025	1.25×10^{-4}	1.25×10^{-4}	$2,600 \times 356 = 925,600$
2V	0.00125	0.00125	6.25×10^{-5}	6.25×10^{-5}	$5,200 \times 712 = 3,702,400$

Table 6.2: *Grid resolution and number of cells for two-dimensional computations*

Considering the weakness of the shock and the low initial temperature ($T < 300\,[K]$), the gas thermal imperfection does not significantly impacts the initial flow field. It only results in a very small difference

in shocked pressure ($\sim 20\,[Pa]$), temperature ($\sim 1\,[K]$) and shocked γ.

Calculations are carried out using the MUSCL5 reconstruction, along with the RK2-SSP time integration scheme with $CFL = 0.75$. The EoS considered is the calorically perfect following the results available in the literature [13, 143, 198, 250, 259, 270].

6.2.3 Grid convergence results

The five grids presented in Table 6.2 are used to compute the time evolution of the shock-bubble interaction. Results are presented at two different time instants in Fig. 6.9 and Fig. 6.10 where the bubble shape obtained on all grids is pictured.

The effect of the grid resolution of the bubble dynamics is presented in Fig. 6.10, where the QCVF model has been used for all computations. It clearly shows that refined solutions are converging towards a solution comparable to published results, which is a good indication of the present results quality. The main and transmitted shocks positions are clearly grid independent even for a very coarse grid with $\Delta x = 1\,[mm]$, which is similar to the downstream interface behaviour (where the Kelvin-Helmoltz influence is less critical as it appears at later times). On the other hand, the upstream and air-jet positions are more sensitive to grid resolution due to the mixing occurring along them.

6.2.4 Results for the Helium cylinder

Qualitative description of the flow - flow visualisations

In this section, the time evolution of the shock-cylinder interaction is presented using the QCVF model and 2IV grid. During the interaction evolution, it can clearly be seen that no spurious pressure oscillations are generated, and this is also valid for the other flow quantities such as temperature and velocity. Fig. 6.11 depicts the time evolution using a non-linear function of the density gradient magnitude to highlight the complex flow structure.

The key stages of the interaction are clearly visible in Fig. 6.11, and unfold as follows,

- $t = 0\,[\mu s]$: The incident shock hits the bubble from the left.
- $t = 37\,[\mu s]$: The incident shock divergence due to its faster speed in the bubble is clearly visible, while the reflected wave is a rarefaction due to the higher acoustic impedance (ρc_{air}) of the surrounding air. The quadruple shock configuration moving upward at the top of the bubble is also clearly visible. It is forming between the incident, reflected and transmitted shocks. The transmitted shock internal reflection is barely visible, but forms a small cusp at the bubble interface.
- $t = 77\,[\mu s]$: The transmitted shock has reached the right interface and has been transmitted to the surrounding air, while the shock within the bubble hit the centreline and is redirected towards the inside of the bubble forming a small oval (the upper half is visible here), while parts of it are also transmitted through the right interface forming a complex pattern of shocks. The reflected shock has almost reached the top of the experimental section, as well as the quadruple shock. The upstream interface of the bubble is flattening.
- $t = 117\,[\mu s]$: The bubble starts to appear slightly perturbed by the successive accelerations due to the numerous waves and its left side is now almost flat. Seeds of a Kelvin-Helmoltz instability developing on the left side are also visible. The quadruple shock configuration has been reflected at the top wall and is now accelerating in the shocked-air. Its reflection also created a strong wave that will impact the cylinder top.
- $t = 277\,[\mu s]$: The numerous shocks resulting from different reflections on the top wall, on the interface, and the different transmissions are observable, as well as the large vorticity generation at the upstream interface, where a jet is forming leading the cylinder to adopt a kidney-like shape.

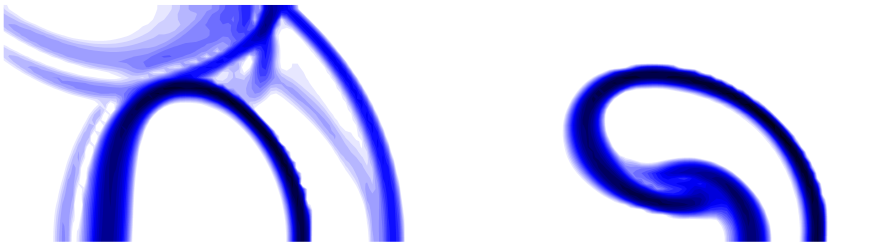

(a) $\Delta x/D = \Delta y/D = 0.02$

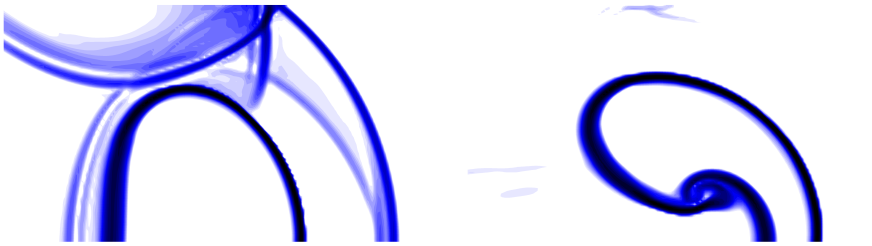

(b) $\Delta x/D = \Delta y/D = 0.01$

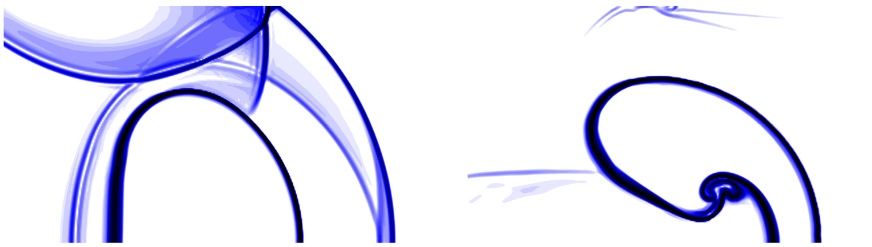

(c) $\Delta x/D = \Delta y/D = 0.005$

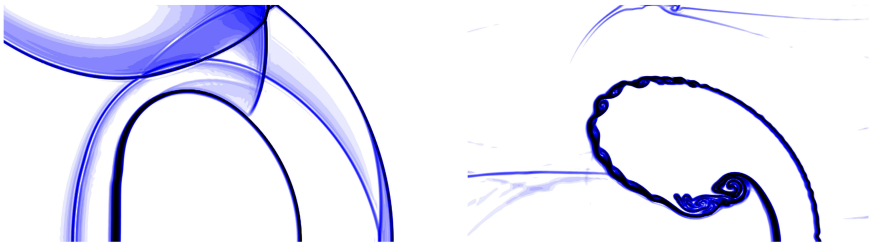

(d) $\Delta x/D = \Delta y/D = 0.0025$

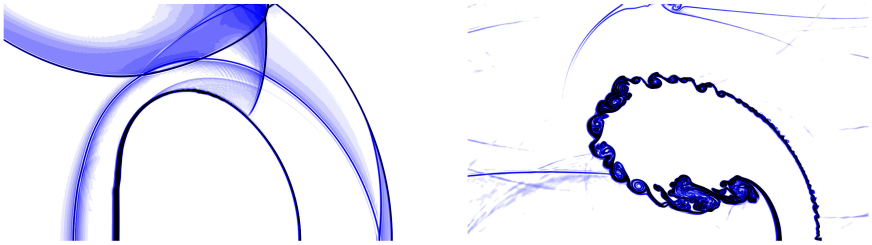

(e) $\Delta x/D = \Delta y/D = 0.00125$

Figure 6.9: *Snapshots of helium shock-cylinder interaction on different grids using the QCVF model and* $\gamma = \gamma(Y_k)$ *at* $t = 117\ \mu s$ *(left) and* $t = 477\ \mu s$ *(right) - Non-linear function of the density gradient magnitude* $(\Phi = log_{10}(|\nabla\rho| + 1.0))$*, with contours from* $\Phi = 1.0$ *to* $\Phi = 3.0$

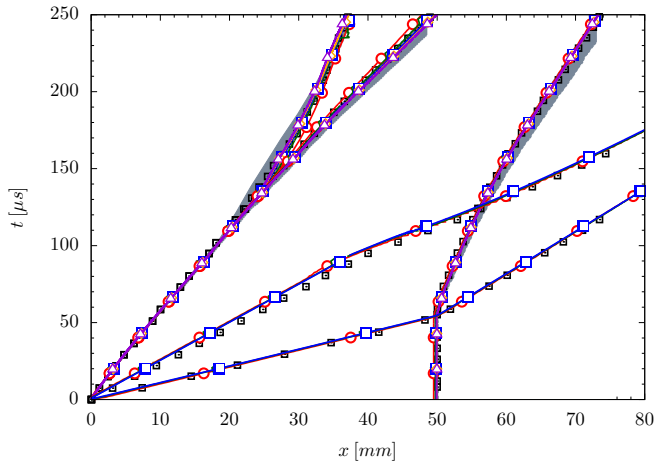

Figure 6.10: *Time evolution of the interaction with the refinement of the grid using the QCVF model and* $\gamma = \gamma(Y_k)$ *-* *Quirk and Karni [250],* *Range of published data,* $\Delta x/D = 0.02$, $\Delta x/D = 0.01$, $\Delta x/D = 0.005$, $\Delta x/D = 0.0025$, $\Delta x/D = 0.00125$

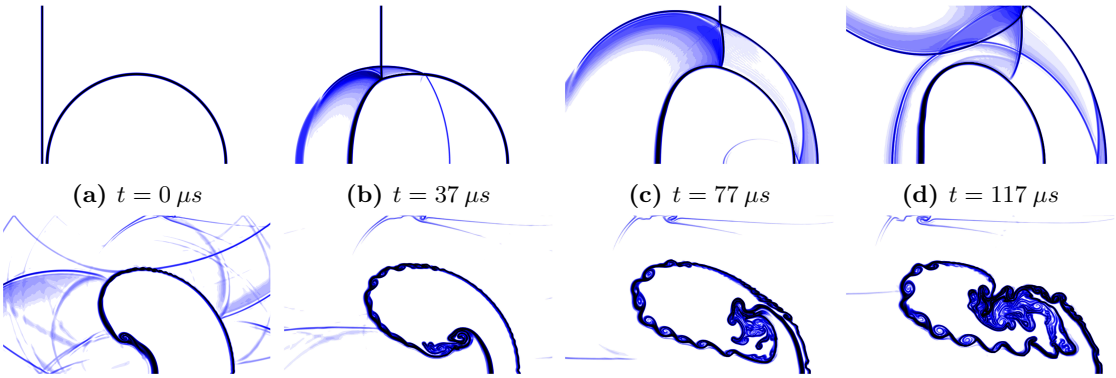

(a) $t = 0\ \mu s$ **(b)** $t = 37\ \mu s$ **(c)** $t = 77\ \mu s$ **(d)** $t = 117\ \mu s$

(e) $t = 277\ \mu s$ **(f)** $t = 477\ \mu s$ **(g)** $t = 677\ \mu s$ **(h)** $t = 877\ \mu s$

Figure 6.11: *Time-series snapshots of helium shock-cylinder interaction on grid* 2IV *using the QCVF model and* $\gamma = \gamma(Y_k)$ *- Non-linear function of the density gradient magnitude* ($\Phi = log_{10}(|\nabla\rho| + 1.0)$)*, with contours from* $\Phi = 1.0$ *to* $\Phi = 3.0$

- $t = 477\,[\mu s]$: The jet becomes clearly visible, and vorticity generation has also increased significantly along the whole interface.
- $t = 677\ [\mu s]$: The cylinder is now spreading following the impact of the jet-air head on the downstream interface, while turbulent mixing is now widespread along the whole interface. The large vortical structure resulting from the air acceleration at the centreline is also clearly visible.
- $t = 877\ [\mu s]$: One can observe that the top and bottom (not shown) vortical structures are now almost fully separated, and are only linked by a thin string of helium. A clear vortex structure induced by the numerous Kelvin-Helmoltz instabilities is also visible.

These results are in good qualitative agreement with computations presented by Marquina and Mulet [198], Terashima and Tryggvason [270], Quirk and Karni [250] amongst others.

Quantitative description of the flow - Space-Time diagrams

Up to now, results clearly indicate a good qualitative agreement with experimental and numerical results presented in the literature. However, to obtain a serious validation, quantitative results are also needed.

This section presents measurements of the position and velocity of several prominent features of the flow, amongst which, the following are tracked,

- Most upstream position of the cylinder
- Position of the air-jet (most upstream position of the cylinder along the centreline), which coincides with the upstream position until the formation of the air-jet
- Position of the downstream interface of the bubble (along the centreline)
- Position of the incoming shock (tracked along the top wall)
- Position of the reflected and then transmitted shock along the centreline (coincides with the upstream shock position until the interaction with the cylinder)

Interfaces positions are found by using an interpolation to find the position at which the helium mass fraction is $(Y_{He})_{bubble}/2 = 0.36$, which implies that the position error is a most one cell size. Shocks are found by looking for a large pressure difference, and by looking on both sides find the maximum and minimum pressure values, which are then used to estimate the pressure value at the shock centre. It is then used to find the position at which this pressure is obtained. The shock position error is then roughly one cell size as well, the reader is invited to refer to Table 6.2 to find the different cell sizes considered in this work.

Fig. 6.12 presents a selection of numerical results obtained by aforementioned authors while Fig. 6.13 features a comparison with a computed solution obtained with the QCVF model on grid 2III. It shows the spread obtained on the data immediately after being hit by the shock for the downstream interface, and at the end of the flattening/beginning of the roll-up for the upstream interface. The reference data used in the literature are usually taken from Quirk and Karni [250], and a similar reference is taken in this work.

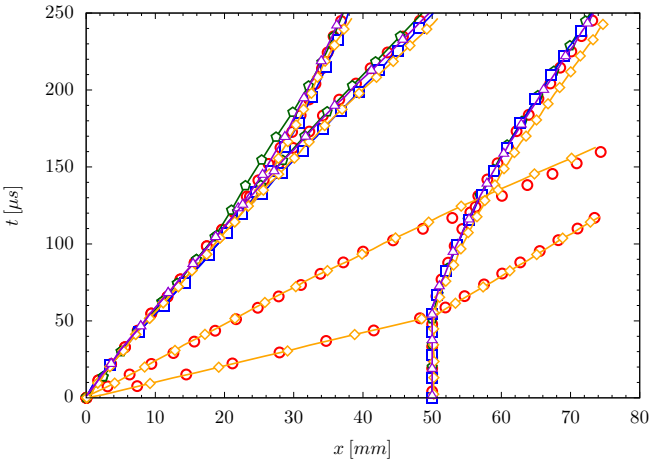

Figure 6.12: *Numerical results available in the literature for the helium shock-cylinder interaction - ○ Quirk and Karni [250], ⬠ Terashima and Tryggvason [270], □ Bagadir and Drikakis [13], ◇ Marquina and Mulet [198] and △ Shankar et al. [259]*

Some authors have also ran the simulation for a longer time, up to $t = 800[\mu s]$ in the case of Terashima and Tryggvason [270]. A comparison with these results is presented in Fig. 6.14, where data from Quirk and Karni are used for the early times behaviour comparison, and data of Terashima and Tryggvason for later times. The agreement is once again deemed good, only a small difference is observed in the prediction of the upstream interface position, which has been shown to disappear when using finer grids.

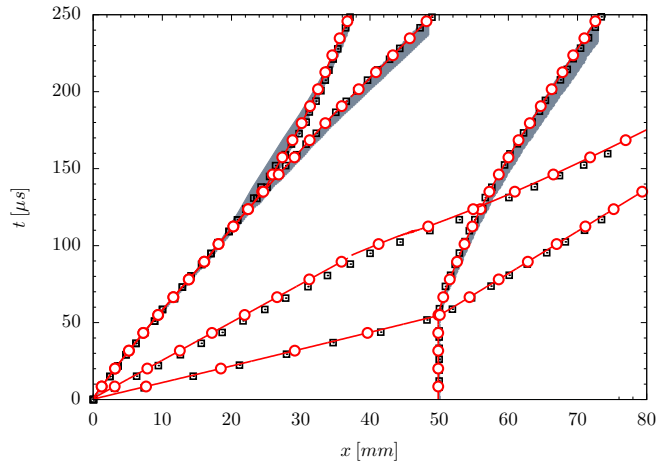

Figure 6.13: *Space-Time diagram of the bubble motion computed in grid* 2III *with the caloric EoS -* ◘ *Quirk and Karni [250],* ■ *Range of published data,* ○ *QCVF*

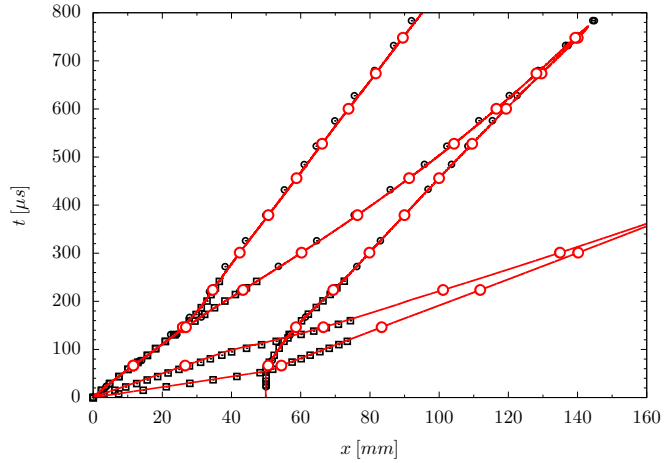

Figure 6.14: *Space-Time diagram of the bubble motion computed on grid* 2III *with* $\gamma = \gamma\,(Y_k)$ *-* ◘ *Quirk and Karni [250],* ○ *Terashima and Tryggvason [270],* ○ *QCVF*

Velocities measurements

The previous paragraph showed the good agreement obtained between published and current data. Both early and late stages of the interaction are properly captured both qualitatively and quantitatively. The current section aims at comparing the different features (interfaces, shocks, etc.) velocities. Table 6.3 presents a comparison of the current results with experimental data [122], and the numerical results of Quirk and Karni [250] and Marquina and Mulet [198]. Velocities measurements have been done using a simple linear fit to the $x - t$ diagrams in intervals specified in the table. Experimental measurements have an estimated error or 11% [122], while computed results feature a much smaller error.

The good agreement between the results of both Quirk and Karni [250] and Marquina and Mulet [198] can be noted, as well as with the experimental data of Haas and Sturtevant [122], where all the results are within the error bounds. The main difference lies in the incident shock velocity where discrepancies are mostly due to a slightly different temperature used, a non-negligible error can also be noted on the downstream interface. This last discrepancy can be partly explained by looking closely at Fig. 6.16 on which the downstream interface trajectory appears positively curved after being hit by the refracted shock. This suggests an acceleration of the interface, with an initial velocity being about $V_{Do} \approx 90\ [m/s]$ at $t = 55\ [\mu s]$, before a constant velocity is reached with $V_{Do} \approx 148\ [m/s]$. Therefore, we could have

		Haas / Sturtevant		Quirk / Karni		Marquina / Mulet	
	Vel $[m/s]$	Vel	*Error* [%]	Vel	*Error* [%]	Vel	*Error* [%]
Incident shock	405	410	*−1.2*	422	*−4.0*	414	*−2.2*
Refracted shock	920	900	*2.2*	943	*−2.4*	943	*−2.4*
Transmitted shock	366	393	*−6.9*	377	*−2.9*	373	*−1.9*
Upstream (early)	177	170	*4.1*	178	*−0.06*	176	*0.06*
Upstream (late)	111	113	*−1.8*	–	–	111	*0.00*
Downstream	141	145	*−2.8*	146	*−3.4*	153	*−7.8*
Air Jet	225	230	*−2.2*	227	*−0.08*	229	*−1.7*

Table 6.3: *Main features velocity - Intervals used for the measurements are* $V_{IS} = [0\,;\,60]$, $V_{RS} = [0\,;\,52]$, $V_{TS} = [52\,;\,240]$, $V_{U1} = [10\,;\,52]$, $V_{U2} = [140\,;\,240]$, $V_{Do} = [140\,;\,240]$, $V_{AJ} = [140\,;\,240][\mu s]$

obtained any mean value in this interval for the downstream velocity depending on the fitting interval, but by fitting data over the whole range, we obtain the intermediate value of $V_{Do} = 141\,[m/s]$.

The fact that the incident shock speed measured in this set of computation appears to be slightly smaller than other numerical data, would explain the underestimation of most of the other velocities, as the impulse on the interface will be slightly weaker, and thus vorticity generation, which finally impacts the accelerations of both the air jet and downstream interface.

Additionally, the rather large differences observed for the refracted and transmitted shock speeds with Haas and Sturtevant's measurements [122], is also visible in the data of Quirk and Karni and Marquina and Mulet. These discrepancies might be explained by the assumption made in all numerical simulations of a uniform bubble contamination by air, which is most certainly not the case. By looking at the data, it would seem that the air concentration should be higher close to the membrane and rapidly decreasing towards the centre of the cylinder. By running different contamination profiles on a coarse grid, it might be possible to test many configurations and chose the one that would lead to the best agreement with experimental results. Such approach has not been considered in this work.

6.2.5 Effect of the model used on the solution

Results obtained with the different models are presented in Fig. 6.15 for the flow field and Fig. 6.16 for the space-time diagram, where it can be seen that they all provide nearly identical results. This can partly be explained by the short time scale on which the interaction actually happens, therefore diminishing the pressure oscillations influence at early times for the FCMF model. These oscillations do not have the time to impact significantly the bubble shock governed dynamics, captured properly by the FCMF model. However, temperature spikes are present in the flow as visible on Fig. 6.17, thus rendering the method unusable for the computation of any temperature dependant phenomena (mass, energy and momentum diffusion, combustion, etc.). The temperature obtained with both quasi-conservative method is bounded by roughly $T_{min} = 270\,[K]$ and $T_{max} = 340\,[K]$ (Fig. 6.18), while the FCMF features temperatures between $T_{min} = 210\,[K]$ and $T_{max} = 570\,[K]$. However, both quasi-conservative models (QCMF, QCVF) give a very good agreement with published data.

6.2.6 Effect of the Low-Mach correction on the results

The Low Mach number correction (LMC) has been applied to evaluate its effect on the solution. It has been designed to significantly reduce Godunov schemes numerical dissipation at low Mach number. This is the case of the bubble turbulent mixing, which is moving relatively slowly relative to the local flow velocity. Therefore, it is expected that the Low-Mach adjustment will have a non-negligible effect on the

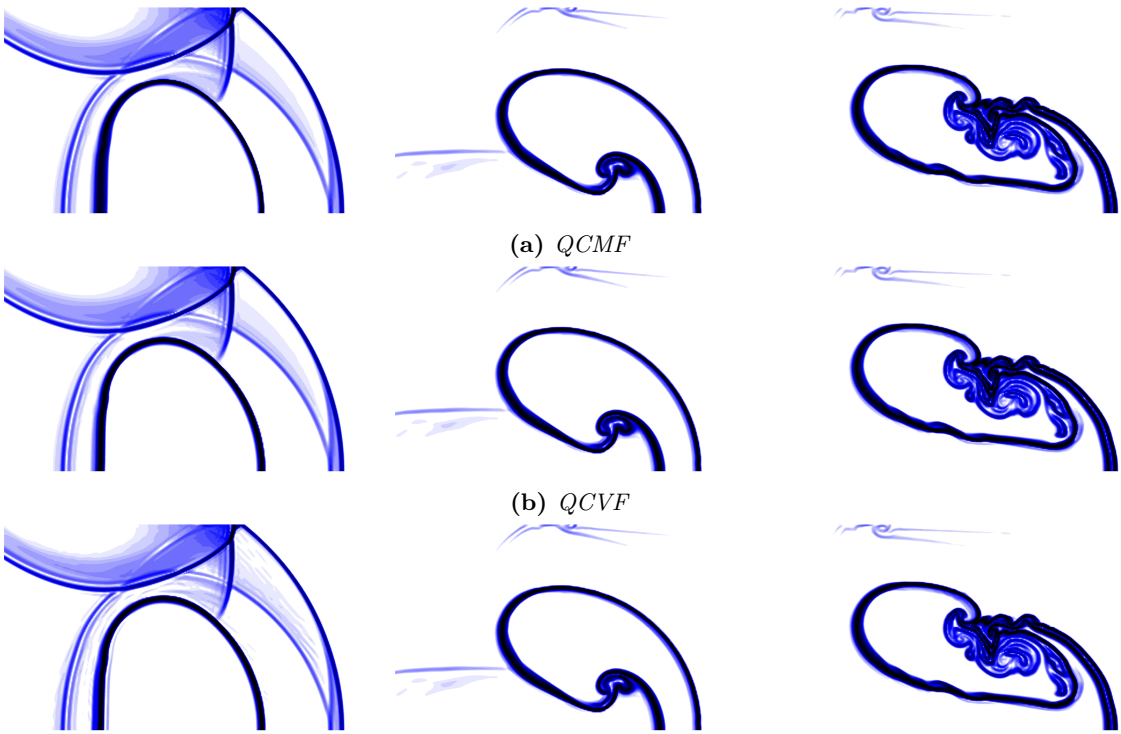

(a) *QCMF*

(b) *QCVF*

(c) *FCMF*

Figure 6.15: *Snapshots of helium shock-cylinder interaction obtained with different models on grid* 2III *and using* $\gamma = \gamma(Y_k)$ *at* $t = 117\ \mu s$ *(left),* $t = 477\ \mu s$ *(center) and* $t = 877\ \mu s$ *(right) - Non-linear function of the density gradient magnitude* ($\Phi = log_{10}(|\nabla\rho| + 1.0)$)*, with contours from* $\Phi = 1.0$ *to* $\Phi = 3.0$

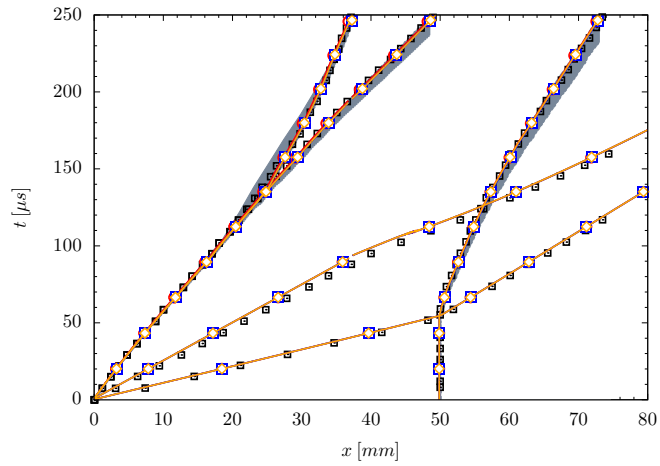

Figure 6.16: *Space-Time diagram of the bubble motion computed with the different models (QCMF, QCVF, FCMF) using* $\gamma = \gamma(Y_k)$ *on grid* 2III - *Quirk and Karni [250],* *Range of published data,* *QCVF,* *QCMF,* *FCMF*

mixing of the interface (enhancing it), if not on its propagation.

Fig. 6.19 presents the flow visualisation obtained with and without LMC on grid 2III with the QCVF model, while Fig. 6.20 presents the space-diagram comparing the dynamics of the interaction in both cases.

As expected, LMC effects seem to be rather small on the global shock-cylinder interaction, the different velocities being only very slightly affected by the decreased numerical dissipation, it is the most notable

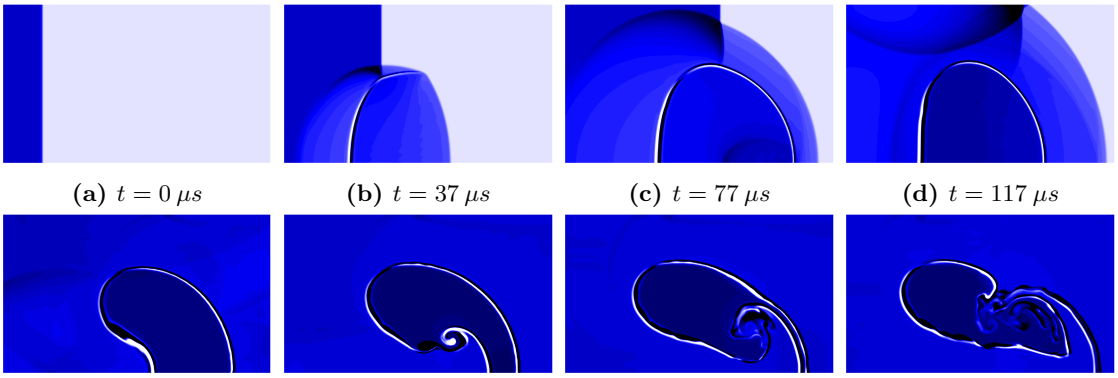

(a) $t = 0\ \mu s$ **(b)** $t = 37\ \mu s$ **(c)** $t = 77\ \mu s$ **(d)** $t = 117\ \mu s$

(e) $t = 277\ \mu s$ **(f)** $t = 477\ \mu s$ **(g)** $t = 677\ \mu s$ **(h)** $t = 877\ \mu s$

Figure 6.17: *Snapshots of helium shock-cylinder interaction computed with the FCMF on grid* 2III *and using* $\gamma = \gamma(Y_k)$ *- Temperature field with contours clipped between* $T = 270\ K$ *(white) and* $T = 340\ K$ *(black)*

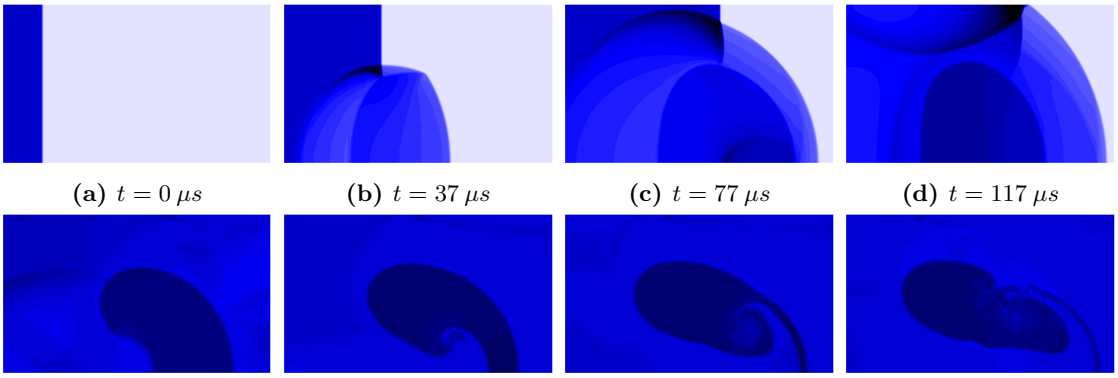

(a) $t = 0\ \mu s$ **(b)** $t = 37\ \mu s$ **(c)** $t = 77\ \mu s$ **(d)** $t = 117\ \mu s$

(e) $t = 277\ \mu s$ **(f)** $t = 477\ \mu s$ **(g)** $t = 677\ \mu s$ **(h)** $t = 877\ \mu s$

Figure 6.18: *Snapshots of helium shock-cylinder interaction computed with the QCVF on grid* 2III *and using* $\gamma = \gamma(Y_k)$ *- Temperature field with contours clipped between* $T = 270\ K$ *(white) and* $T = 340\ K$ *(black)*

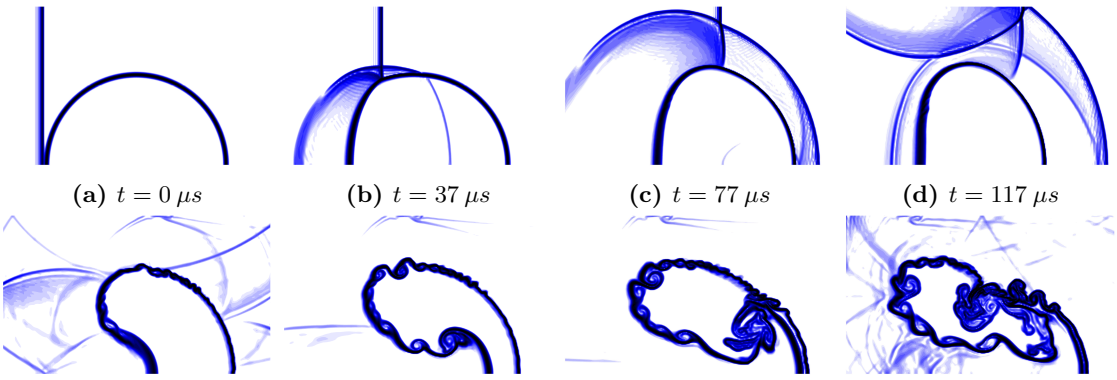

(a) $t = 0\ \mu s$ **(b)** $t = 37\ \mu s$ **(c)** $t = 77\ \mu s$ **(d)** $t = 117\ \mu s$

(e) $t = 277\ \mu s$ **(f)** $t = 477\ \mu s$ **(g)** $t = 677\ \mu s$ **(h)** $t = 877\ \mu s$

Figure 6.19: *Snapshots of helium shock-cylinder interaction computed with the QCVF on grid* 2III *with Low-Mach adjustment and* $\gamma = \gamma(Y_k)$ *- Non-linear function of the density gradient magnitude* $(\Phi = log_{10}(|\nabla\rho| + 1.0))$*, with contours from* $\Phi = 1.0$ *to* $\Phi = 3.0$

on the upstream interface. However, turbulent mixing along the interface is a lot stronger when using the LMC which acts as an anti-diffusive term. It is particularly visible at late times ($t \geqslant 117\,[\mu s]$), when the upstream interface already started to mix with the surrounding air which is also visible in Fig. 6.20, while it only happens later when the LMC is off. The shock pattern is not affected, but one can remark small density oscillations behind the shock due to the anti-diffusive behaviour of the LMC. The shock

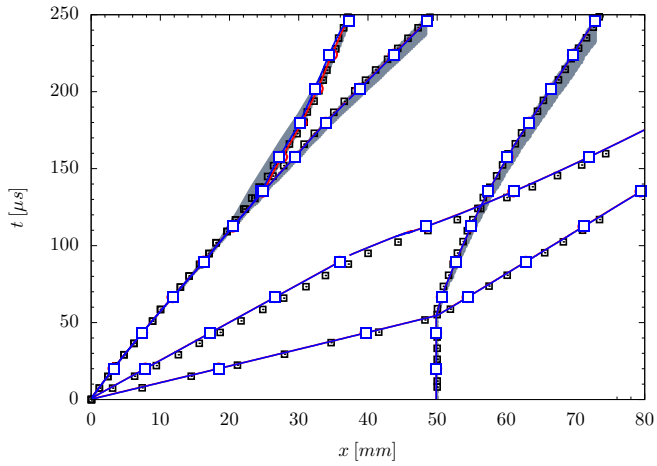

Figure 6.20: *Space-Time diagram of the bubble motion computed on grid* 2III *with* $\gamma = \gamma(Y_k)$ *and the QCVF model with and without Low-Mach adjustment -* ◘ *Quirk and Karni [250],* ○ *Terashima and Tryggvason [270],* ○ *QCVF* ***without*** *LMC,* ◘ *QCVF* ***with*** *LMC*

pattern remains quite similar, up until the increased mixing affects it, as it can be seen at $t = 877\ [\mu s]$.

6.2.7 Remarks on the thermodynamic properties

For a single species code, only the case of constant γ through the entire domain is possible, unless using some artificial viscosity, diffusion, or special formulations removes pressure and/or temperature oscillations generated (Fig. 6.17). In this rather simplified inviscid computation (i.e. no temperature/species diffusion, and no viscosity), it is interesting to know what would be the simulated behaviour of the bubble should the user be unable to use stable multi-component methods. In this case, the value of γ is held constant throughout the domain at the selected value of $\gamma = \gamma_{air} = 1.4$, such that the shock speed remains similar to the variable γ case upon impacting the bubble. This also ensures that the momentum transferred by the shock to the bubble remains identical to the baseline case and thus allows a direct comparison.

Fig. 6.21 presents flow snapshots, in a similar manner as previous sections, while Fig. 6.22 presents the space-time diagram of the interaction when using different or similar γ for each species.

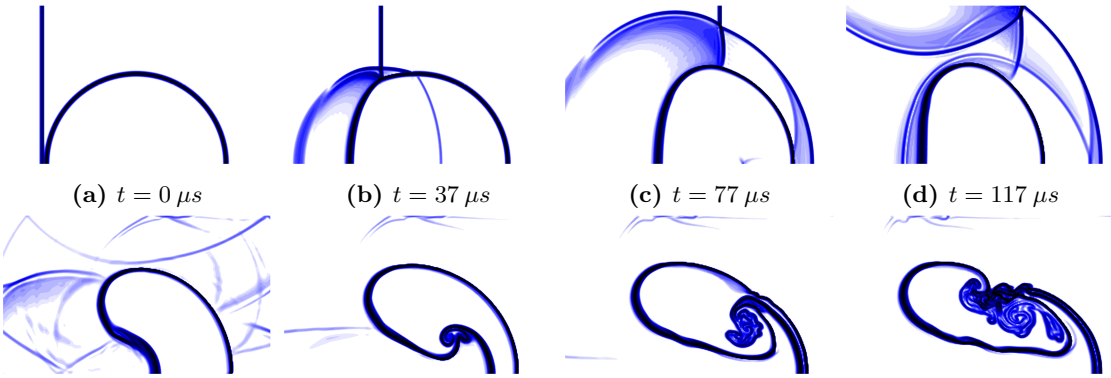

(a) $t = 0\ \mu s$ **(b)** $t = 37\ \mu s$ **(c)** $t = 77\ \mu s$ **(d)** $t = 117\ \mu s$

(e) $t = 277\ \mu s$ **(f)** $t = 477\ \mu s$ **(g)** $t = 677\ \mu s$ **(h)** $t = 877\ \mu s$

Figure 6.21: *Snapshots of helium shock-cylinder interaction computed with the QCVF on grid* 2III *and* $\gamma = \gamma_{air} = 1.4$ *- Non-linear function of the density gradient magnitude* ($\Phi = log_{10}(|\nabla\rho| + 1.0)$)*, with contours from* $\Phi = 1.0$ *to* $\Phi = 3.0$

Flow visualisations show that heat capacity ratio changes do not have a significant impact on the in-

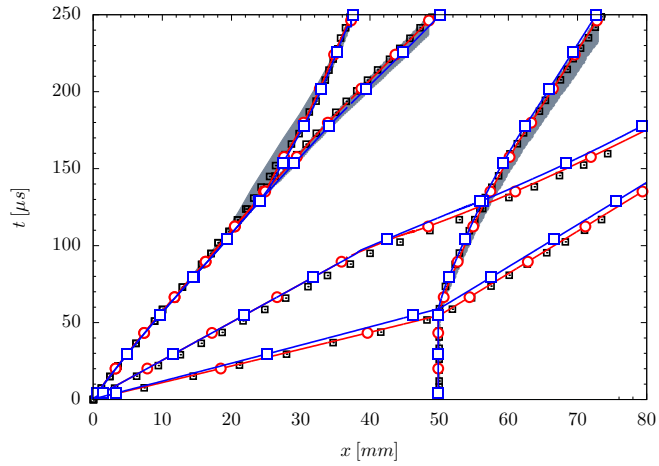

Figure 6.22: *Space-Time diagram of the bubble motion computed on grid* 2III *with* $\gamma = \gamma(Y_k)$ *and the QCVF model with and without Low-Mach adjustment -* ◘ *Quirk and Karni [250],* ○ *Terashima and Tryggvason [270],* ○ *QCVF with* $\gamma = \gamma(Y_k)$, ◘ *QCVF with* $\gamma = \gamma_{air} = 1.4$

teraction, however a slight delay estimated at roughly $\Delta t \approx 10\,[\mu s]$ can be observed between the reference solution and the constant γ solution. This can be mainly attributed to the change of the speed of sound in the bubble, which by having $\mathcal{R}_{He} = 2077.27\,[J/kg.K]$ and $T_{bubble} = 273.63\,[K]$, gives $c_{bubble} \approx 968\,[m/s]$ for $\gamma_{bubble} = 1.648$, and $c_{bubble} \approx 892\,[m/s]$ with $\gamma_{bubble} = 1.4$, which represent roughly a change of 10%.

Mixing profiles also remain quite similar for both computations as both impulses on the bubble are similar, only the shock/reschock pattern within the bubble is affected. The conclusion would be that changes in γ values in this particular case are not too significant during the early stages of the interaction, but more so at late times when the small difference in the impulse has had the time to cause larger departures from the experiment. Changes would be more significant for a temperature dependant simulation, as the bubble is being heated by the shocks in the case of $\gamma_{bubble} = 1.648$, with a temperature of $T_{bubble} \approx 325\,[K]$, or $T_{bubble}/T_{bubble,init} \approx 1.2$, while in the case of $\gamma_{bubble} = 1.4$, we have $T_{bubble} \approx 310\,[K]$, or $T_{bubble}/T_{bubble,init} \approx 1.13$, meaning a difference of roughly 6%. This could prove critical for combustion simulations due to the exponential dependency of reaction rates on temperature.

6.2.8 Results for the R22 ($CHClF_2$) cylinder

Qualitative description of the flow - flow visualisations

In this section, the time evolution of the R22 shock-cylinder interaction is presented. Results have been obtained using the QCMF model on grid 2III using the calorically perfect EoS. As presented earlier, the helium bubble due to its lower density acts as a divergent acoustic lens for the incident shock, while the R22 cylinder, due to its higher density behaves as a convergent lens, thus focusing the shock within the bubble. This leads to a dramatically different flow configuration.

Fig. 6.23 presents the time evolution of the R22 shock-cylinder interaction using a logarithmic function of the density gradient, thus highlighting weak features, that would be otherwise hidden by the strength of the incident shock.

The first interesting remark on these results is on their agreement with reference data (both experimental from Haas and Sturtevant [122] and numerical by Quirk and Karni [250]). Salient shock-bubble interaction features are all clearly accounted for. The results shall now be described in more details.

The first picture shows the bubble 57 $[\mu s]$ after it has been first hit by the incident shock, and a

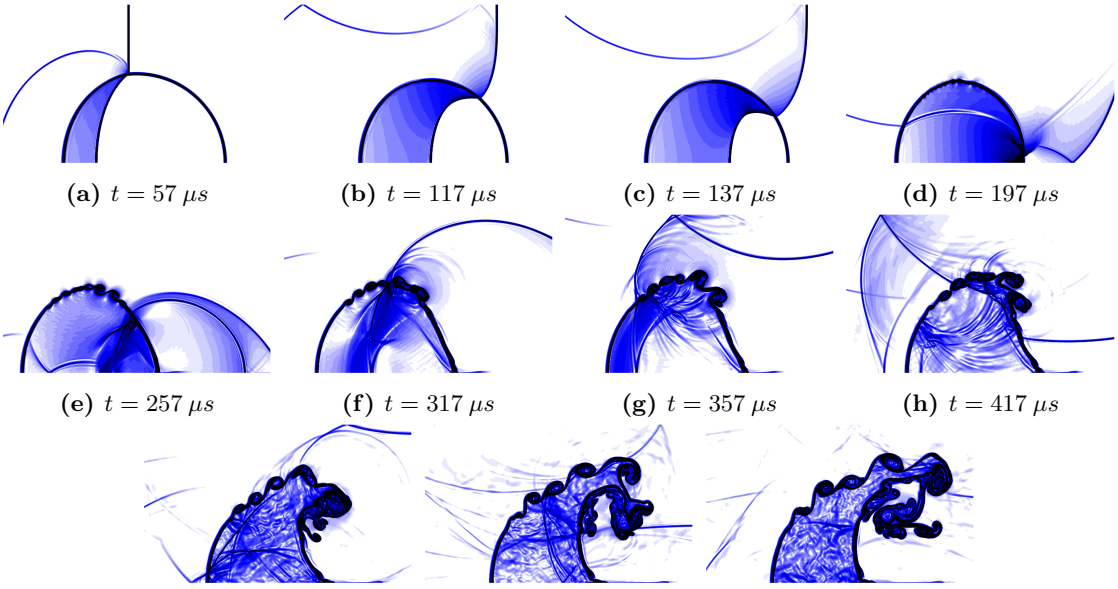

(a) $t = 57\ \mu s$ **(b)** $t = 117\ \mu s$ **(c)** $t = 137\ \mu s$ **(d)** $t = 197\ \mu s$

(e) $t = 257\ \mu s$ **(f)** $t = 317\ \mu s$ **(g)** $t = 357\ \mu s$ **(h)** $t = 417\ \mu s$

(i) $t = 577\ \mu s$ **(j)** $t = 737\ \mu s$ **(k)** $t = 877\ \mu s$

Figure 6.23: *Snapshots of R22 shock-cylinder interaction computed with the QCMF on grid* 2III *and* $\gamma = \gamma(Y_k)$ *- Non-linear function of the density gradient magnitude* ($\Phi = log_{10}(|\nabla\rho| + 1.0)$)*, with contours from* $\Phi = 1.0$ *to* $\Phi = 3.0$

slight deformation is already visible. The incident shock is visible between the top of the domain and the bubble, and is linked to a slower curved refracted shock due to the bubble lower speed of sound ($c_{bubble} \approx 182\,[m/s]$). A slight thickening of the shock can be observed close to the interface, as observed on experimental visualisations, and is explained by Quirk and Karni as the result of a compression system matching the pressure jumps between the weak and strong parts of the refracted shock.

As time advances, the difference between the shock speeds inside and outside the bubble becomes more pronounced, and by $t = 117\,[\mu s]$, the refracted shock has folded into two parts, running almost normal to each other. The compression ramp system turning the shock $90\,[deg]$ is also quite visible. The shock has begun to fold after travelling roughly a bubble radius, and a perturbation is almost visible on the bubble interface due to the vorticity generated. By $t = 137\,[\mu s]$, the compression ramp has clearly steepened and the central part of the shock is still running horizontally (as does the incident shock), while the second side of the refracted shock is moving almost vertically. The shock system is thus converging towards the most downstream point of the bubble. At $t = 197\,[\mu s]$, both parts of the shock have been focused to almost a point. The shock is then partially transmitted to the ambient air through the interface and partially reflected inside the bubble. The interface is now quite perturbed and a roll-up at the top can already be observed.

As time reaches $t = 257\,[\mu s]$, a complex system of shocks and contact surfaces is visible both inside and outside the bubble resulting from the shocks refractions/transmissions and reflections. A strong transmitted shock can be seen lagging behind the incident shock, but running faster until they eventually merge. A thin feature is visible downstream of the bubble, and is also visible in the experimental shadowgraph, and has been unduly exaggerated in Quirk and Karni simulations for an unknown reason. This thin jet of fluid has been shot forward by the focusing of the refracted shock on the interface. By $357\,[\mu s]$, the bubble has moved substantially from its original position and has began to elongate. A backward moving shock is also visible within the bubble leading to yet other reflections/transmissions of shocks. The surface of the bubble is now quite corrugated due to the numerous roll ups taking place. The backward moving shock eventually emerges from the bubble as a backscattered wave ($t = 417\,[\mu s]$), promoting the production of vorticity in the process. The bubble continues to elongate until it evolves in a large vortex pair (only the top part is shown here) at much later times. The agreement is still quite

good at these late times, even though we have conducted an inviscid computation here.

Quantitative description of the flow - Space-Time diagrams

The R22 cylinder dynamics after its interaction with the incident shock is described in Fig. 6.24 for the early stages and Fig. 6.25 for the overall motion. As it can be seen, the agreement is very good with the experimental data of Haas and Sturtevant [122], but also with previous numerical simulations of Quirk and Karni [250]. Early times agreement is very good for the main features tracked (main shock and its transmission, the second shock emanating from the convergence of the transmitted shock at the downstream interface, the upstream and downstream interface), but a small deviation can be observed at late times for the downstream interface position compared to the experimental value gathered by Haas and Sturtevant [122]. It also appears that the bubble is moving slightly faster in these results than in the experiment, and no reason has been found to explain this fact, other than potential experimental errors or imprecise measurements leading to a small difference in the initial conditions (R22 contamination with air, incident shock speed, etc.).

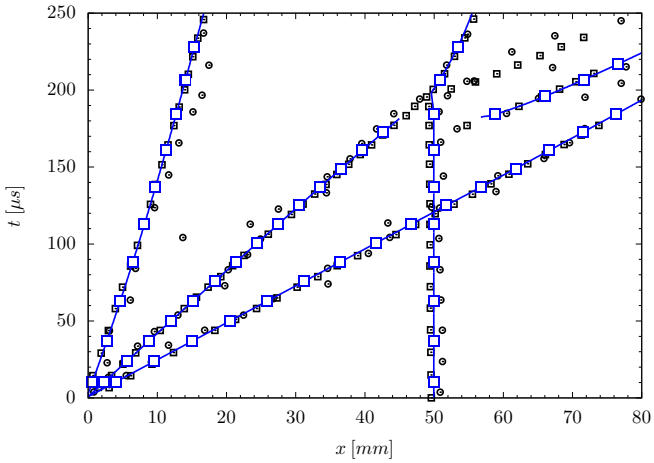

Figure 6.24: *Space-Time diagram of the bubble motion computed in grid* 2III *with the QCMF model and the caloric EoS -* ◘ *Quirk and Karni [250],* ○ *Haas and Sturtevant [122],* ◘ *QCMF*

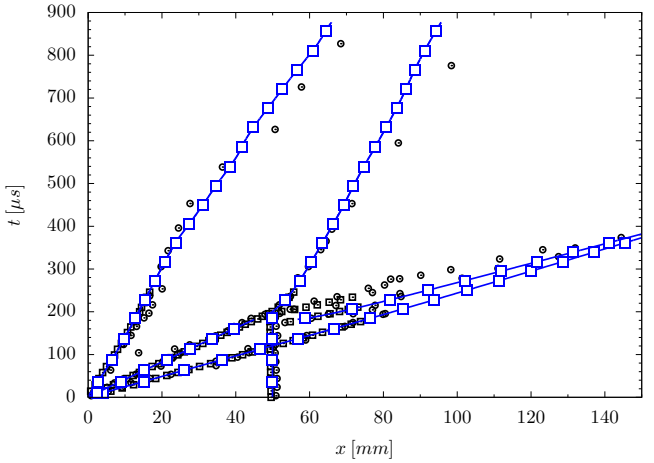

Figure 6.25: *Space-Time diagram of the bubble motion computed on grid* 2III *with* $\gamma = \gamma\,(Y_k)$ *and the QCMF model -* ◘ *Quirk and Karni [250],* ○ *Haas and Sturtevant [122],* ◘ *QCMF*

6.3 Reacting shock-bubble interaction

6.3.1 Test case

The reacting shock-bubble interaction problem computed by Billet *et al.* [26] was reproduced here, to assess the different algorithms capabilities to capture complex flow features involving shocks, contact surfaces, etc. It shall be mentioned that no experimental data exist for this test case, and as such results obtained in the present work will be qualitatively compared with results presented by Billet *et al.* [26]. However, this quantitative comparison will only shed light on the differences between computations, not on which one would agree best with a potential experiment, and as such not on which algorithm perform best.

The two-dimensional flow consists in a hydrogen cylinder surrounded by an air coflow and interacting with a Mach two shock wave. The hydrogen bubble diameter is set to $D = 5.6\,[mm]$, and initially placed at $x_0 = 4\,[mm]$. To shorten the computational domain, a stationary shock is initialised at $x_s = 7\,[mm]$ and the H_2 bubble travels through the shock. The bubble is initialised using Eq. 5.2 where $C_s = 33000$ yielding an initial interface thickness of approximately $\delta \approx 0.25\,[mm]$ thus stabilising it by suppressing the seeds of various instabilities such as Richtmyer-Meshkov or Rayleigh-Taylor. The schematic of the initial conditions is provided in Fig. 6.26, while Table 6.4 presents the initial values in the three regions of the domain. The shock conditions presented in this table have been computed using the method described in Appendix C to account for the change of γ through the shock. The chemical mechanism used is the Westbrook H_2/air mechanism (Appendix B), while diffusion coefficients are computed using the Schmidt number presented in Table 5.6. The EoS considered for the problem is the thermally perfect one.

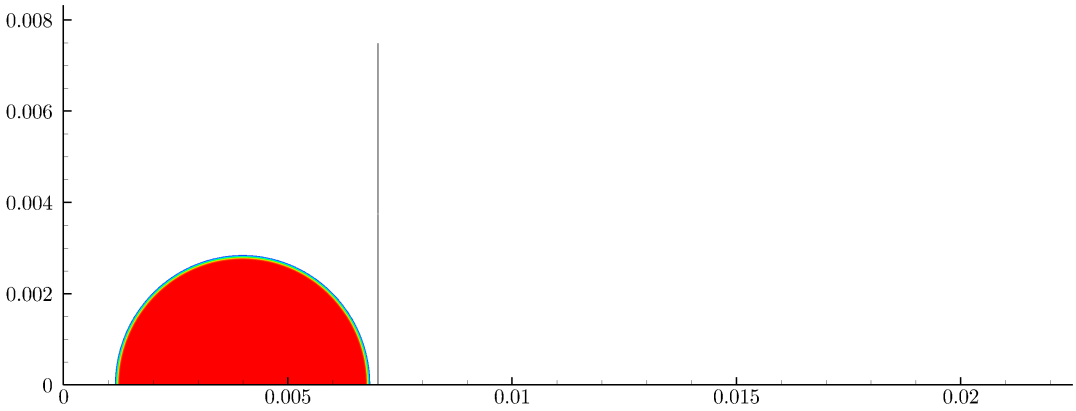

Figure 6.26: *Schematic of initial flow-field and computational domain for the H_2 shock-bubble interaction*

	I - Shocked Air	II - Unshocked Air	III - H_2 bubble
$P\,[Pa]$	452520	101325	101325
$\rho\,[kg/m^3]$	1.0019	0.3515	0.0246
$T\,[K]$	1567.0	1000.0	1000.0
$u\,[m/s]$	435.27	1240.6	1240.6
$v\,[m/s]$	0.0000	0.0000	0.0000
$\gamma\,[-]$	1.3077	1.3349	1.3801
$M\,[-]$	0.5664	2.0000	0.5203
$Y_{O_2}\,[-]$	0.2320	0.2320	0.0000
$Y_{H_2}\,[-]$	0.0000	0.0000	1.0000
$Y_{N_2}\,[-]$	0.7680	0.7680	0.0000

Table 6.4: *Initial flow conditions for the H_2 shock-bubble interaction considering thermally perfect gases*

Similarly to the inert shock-bubble interaction case, only the upper part of the domain is simulated here, with a height of the computation domain taken as $h = 7.5\,[mm]$ with a length of $L = 22.5\,[mm]$. The domain is discretised using regular Cartesian grids defined in Table 6.5.

	$\Delta_x\,[m]$	$\Delta_y\,[m]$	N_{cells}
2I	50.0×10^{-6}	50.0×10^{-6}	$450 \times 150 = 67500$
2II	25.0×10^{-6}	25.0×10^{-6}	$900 \times 300 = 270000$
2III	12.5×10^{-6}	12.5×10^{-6}	$1800 \times 600 = 1080000$

Table 6.5: *Grids used for the two-dimensional computations of the H_2 shock-bubble interaction*

Computations are carried out using the MUSCL5 reconstruction coupled with the RK2-SSP time integration scheme. It shall also be noted that given the operator un-split time integration considered in the current implementation, the global time-step size is limited by chemistry, and as such has been limited to about $\Delta t \approx 10^{-9}\,[s]$ for all computations, which corresponds to $CFL \approx 0.1$ on grid 2III. The Low-Mach adjustment has also been applied for all computations. The boundary conditions applied are symmetry on the top and bottom of the domain, while a supersonic inflow is applied on the left and a supersonic outflow on the right.

Before presenting results, it is worth highlighting the differences between the reference computations of Billet *et al.* [26] and the current results and remind the reader that these computations are used to assess whether the considered algorithms are able to cope with such complex flow fields involving a wide range of time and length scales. First of all, the chemical mechanism considered is different, the Westbrook H_2/air consisting of 9 species and 34 irreversible reactions is used, while Billet *et al.* [26] uses the Miller *et al.* [207], consisting of 9 species and 19 reversible reactions. Secondly, the estimation of the diffusion coefficients in the current work relies on the constant Schmidt number (constant but non-unity Lewis number) assumption and the Hirschfelder and Curtis [128] approximation, while Billet *et al.* [26] solve the full diffusion matrix using the EGLIB library [92]. In our computations, viscosity is estimated using the Sutherland's law for individual species, Wilke's mixing law for the mixture, and a constant Prandtl approach is considered for the heat diffusivity, while the EGLIB is used to obtain all these coefficients in Billet *et al.* [26] computations. Last but not least, the current code assumes that the volume viscosity is zero, despite it not being verified for non mono-atomic species and compressible flows, while Billet *et al.* do consider it. Finally, considering that hydrogen flames are highly sensitive to diffusion, especially in the presence of high curvature fronts (thermo-diffusive instability), it is expected that the present results will differ from the reference data to a certain point. What will be compared is the general flow behaviour and bubble motion.

6.3.2 Grid convergence results

Results obtained on the three grids retained for the study are presented in Fig. 6.27 where the H_2 mass fraction is pictured at different times. Grid resolution effects are clearly visible in the increased resolution of the secondary vortices. The main vortex is properly captured at all grid levels, but the turbulent mixing level in the bubble increases with grid resolution showing that more and more vortical structures are resolved. However, since the problem involves fluid instabilities, no grid converged solution can be achieved unless the grid size is further reduced to be significantly smaller than the Kolmogorov scale (estimated to be $\eta_k \approx 2.5\,[\mu m]$ in this case) which is clearly impractical.

6.3.3 Flow behaviour

The temporal evolution of the bubble shape and position is presented in Fig. 6.28 where pressure isopleths and H_2 mass fraction are displayed in a similar fashion as Billet *et al.* [26] for direct comparison. Computed results obtained in this work agree well with Billet *et al.* results, showing similar development of the H_2 bubble and pressure fields. However, differences in the vortical structures and temperature

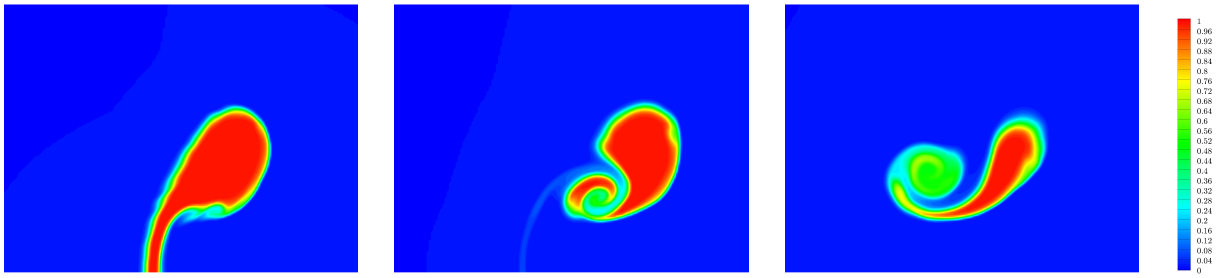

(a) $\Delta x = \Delta y = 50\ \mu m$

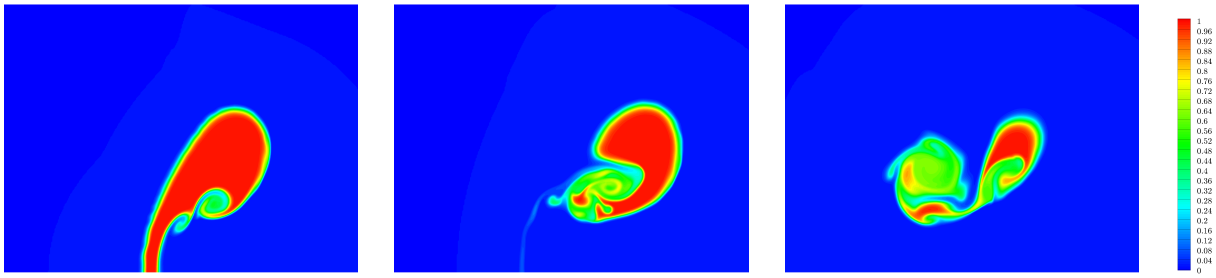

(b) $\Delta x = \Delta y = 25\ \mu m$

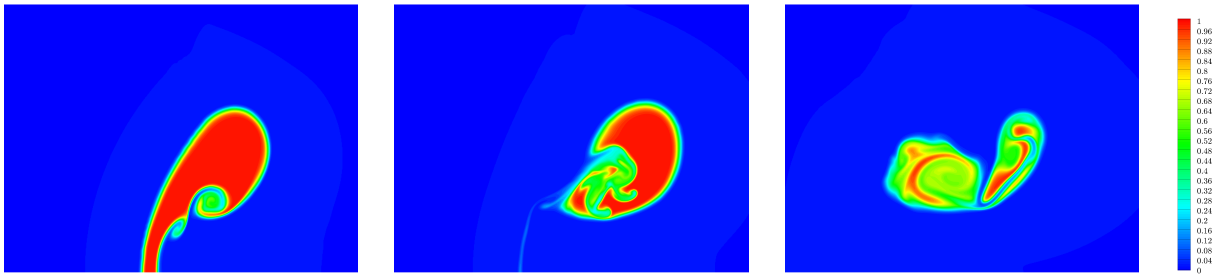

(c) $\Delta x = \Delta y = 12.5\ \mu m$

Figure 6.27: *Snapshots of reacting shock-cylinder interaction on different grids using the QCMF model and the thermally perfect EoS at $t = 6\ \mu s$ (left), $t = 9\ \mu s$ (center) and $t = 14\ \mu s$ (right) - H_2 mass fraction*

levels are observed.

At $t = 1\,[\mu s]$, the bubble has already collided with the denser hot air, and both a refracted wave propagating towards the right, and a reflected wave towards the left are visible. An expansion wave following the reflected shock can also be noticed. A transmitted wave connected tangentially to the refracted wave through the bubble interface also propagates towards the left of the domain. The propagation of these various waves can be followed between $t = 1\,[\mu s]$ to $t = 3\,[\mu s]$. The formation of a focusing wave is observed at the right of the left interface of the bubble propagating towards the axis of symmetry at $t = 2\,[\mu s]$, while its strengthening is visible at later times. The refracted wave leaves the bubble at about $t \approx 2\,[\mu s]$ and becomes the second transmitted wave, while a internal reflected wave propagates to the right. Baroclinic vorticity accumulates at the compressed interface thanks to the large pressure and density gradients, and to the small hydrogen density. At $t = 4\,[\mu s]$, a vortex begins to form at the shocked interface due to the negative vorticity accumulated, and is observed slightly earlier in our results than in Billet *et al.* [26] due to the absence of volume viscosity smoothing the interface. A secondary vortex can also be seen forming under the primary vortex, rotating in the same direction following the large negative values of vorticity. Simultaneously, the main reflected shock travels upward and is followed by a rather strong circular shock emerging from the bubble. By a similar mechanism as the right interface, positive vorticity is being stored in the left interface of the bubble. Up to $t \approx 7\,[\mu s]$, H_2 mass fraction variations can be attributed to turbulent mixing, and not yet to combustion.

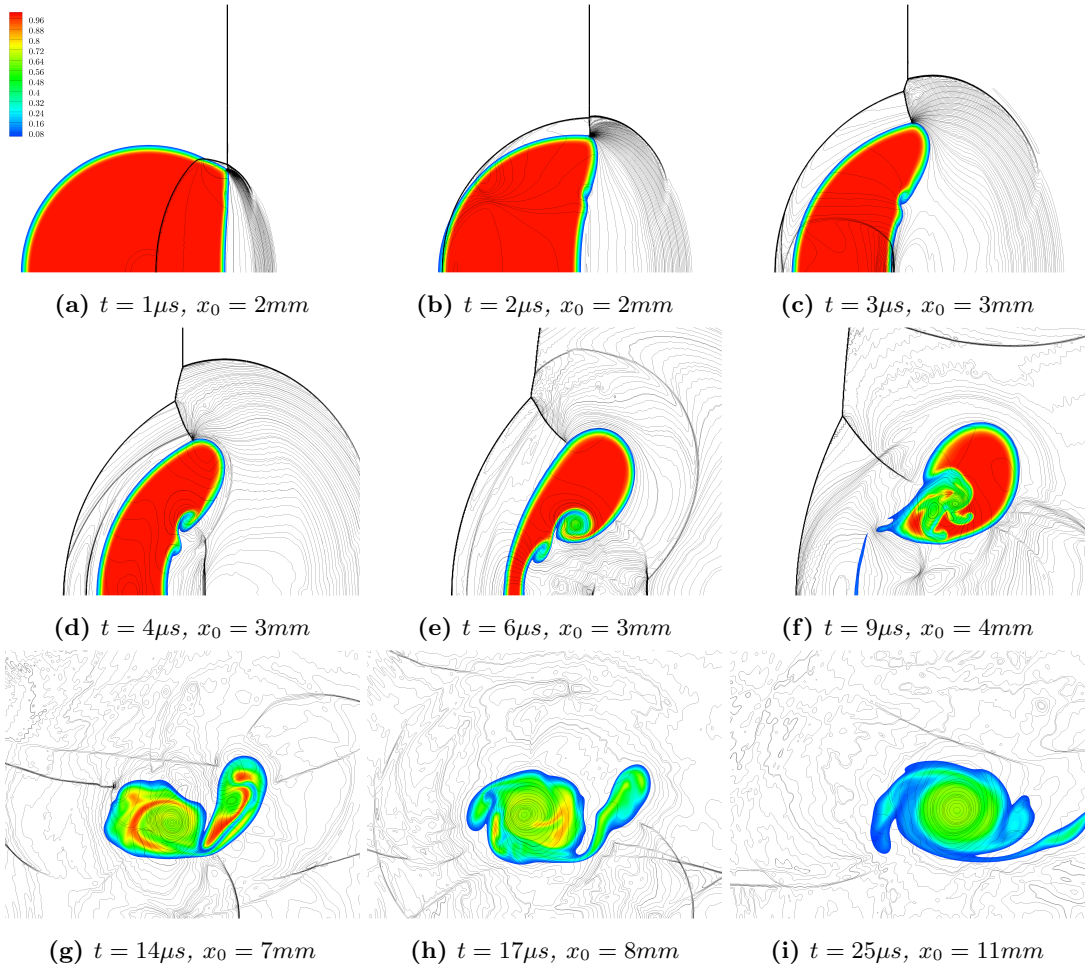

(a) $t = 1\mu s,\ x_0 = 2mm$ **(b)** $t = 2\mu s,\ x_0 = 2mm$ **(c)** $t = 3\mu s,\ x_0 = 3mm$

(d) $t = 4\mu s,\ x_0 = 3mm$ **(e)** $t = 6\mu s,\ x_0 = 3mm$ **(f)** $t = 9\mu s,\ x_0 = 4mm$

(g) $t = 14\mu s,\ x_0 = 7mm$ **(h)** $t = 17\mu s,\ x_0 = 8mm$ **(i)** $t = 25\mu s,\ x_0 = 11mm$

Figure 6.28: *Snapshots of reacting shock-cylinder interaction obtained on grid* 2III *and using the thermally perfect EoS at different times - Contours of* Y_{H_2} *clipped below* $Y_{H_2} = 0.05$ *and isopleths of pressure with 100 lines between* $P = 1$ *bar and* $P = 8$ *bar,* x_0 *indicates the position of the left of the picture, each image representing a domain of size* 8×6 *mm*

At $t \approx 8\,[\mu s]$, the main vortex has started to pull the remaining of the bubble towards the centreline. The hydrogen filament at the left of the bubble get thinner and thinner due to the large negative vorticity at its right, and the positive vorticity at its left. Additionally, the flow decelerates at the right due to the numerous shocks, while the left is still relatively fast, thus accelerating further the thinning of the filament. At $t \approx 9\,[\mu s]$, the filament has been burned away by diffusion flames originating from both sides. A jet of denser fluid is being shot at the centre of the resulting pocket of hydrogen. The positive vorticity stored earlier at the left interface has been converted into a positive vortex at the left, while the negative vorticity at the right initiated a negative vortex at the right. The fuel is then gradually burned as the pure hydrogen region is being rolled around the main vortex.

The main differences observed between current results and Billet *et al.* [26] can be explained by the absence of volume viscosity in the present simulation, as well as the use of the Low-Mach adjustment, both contributing to increase turbulent mixing. This triggers chemical reactions earlier than in reference results, which can be observed in the early burning of the hydrogen filament. Additionally, slightly higher temperatures are observed in the mixing regions due to the enhanced mixing and possibly the different chemical mechanism considered. It could also be noticed that the higher temperatures obtained in these simulations could be linked to the same problem already highlighted in the one-dimensional laminar flame calculations (§. 5.4.2). Following this, diffusion of the light species such as the atomic H and O could be responsible, but this cannot be evaluated at the time.

Several variables are plotted in Fig. 6.29 at $t = 14\,[\mu s]$ allowing a direct comparison with the data obtained by Billet *et al.* [26]. The first observation is that a good overall agreement is obtained, where the main features are captured with the correct order of magnitude. However, several differences are worth pointing out. Mixing profiles in both left and right vortices are different. On the bubble left hand side, reference data depict Kelvin-Helmoltz instabilities growing along the inner interface while there are none here. The separation of both vortices by a jet of dense air is less pronounced in the current results than in the reference and does not feature the same structure. Additionally, it can be seen that temperatures obtained here are somewhat higher than in the reference data when at $t = 14\,[\mu s]$, the maximum temperature is $T_{\max} \approx 2300\,[K]$ while in the current results we obtained values upward of $T_{\max} \approx 2900\,[K]$. This is explained by an earlier start of the combustion process, where $T_{\max} \approx 2000\,[K]$ in the filament at $t \approx 9\,[\mu s]$ in the reference data and $T_{\max} \approx 2700\,[K]$ at the same time in the computed results presented here. These higher temperatures thus lead to a different flame structure due to the impact of heat release on the flow field. However, numerical Schlieren visualisations feature a very good agreement with the reference solution, but also with Houim and Kuo data [133].

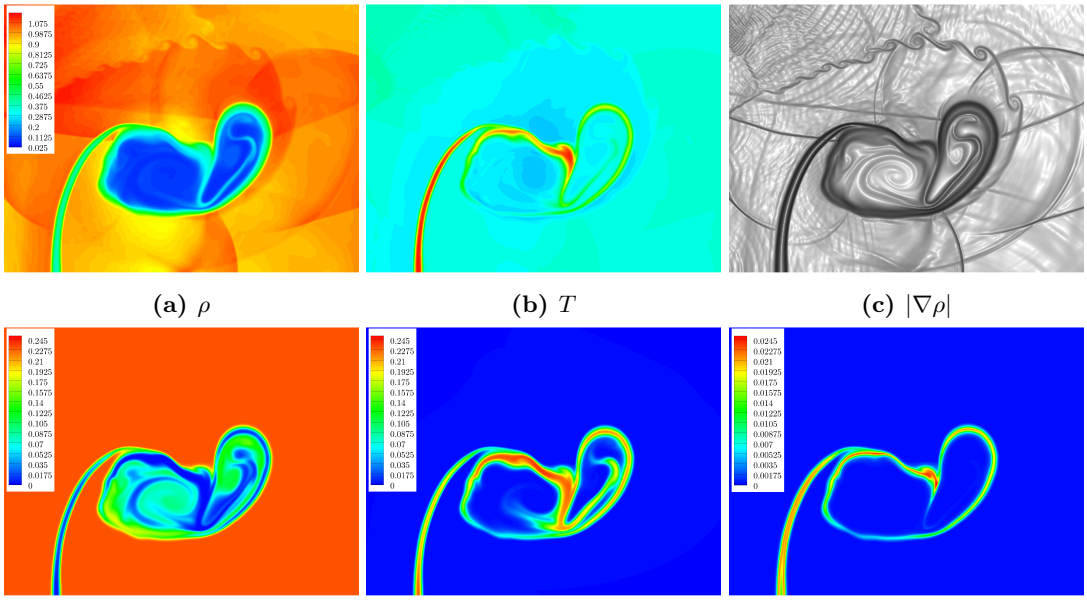

(a) ρ **(b)** T **(c)** $|\nabla\rho|$

(d) O_2 **(e)** H_2O **(f)** OH

Figure 6.29: *Computed results for the shocked H_2-cylinder interaction obtained on grid* 2III*, using the thermally perfect EoS and QCMF model at $t = 14\,\mu s$ - $x_0 = 7\,[mm]$ and the size of each frame is $8 \times 6\,mm$*

6.3.4 Influence of the model

Computations have been run with both the QCVF and FCMF models. Computations using the FCMF were found to be crashing relatively shortly after the shock impact on the bubble due to the very large temperature spikes at the interfaces. Thus, its inability to compute multi-dimensional flow fields is verified. On the other hand, calculations with the QCVF did not encounter any troubles during the early stages of the calculations, however, at later times $t \approx 30\,[\mu s]$, simulations were found to be repeatedly stopping due to a divergence of the pressure calculation using the Newton-Raphson procedure highlighted in Appendix A.1. This instability of the algorithm has already been encountered in one-dimensional detonations calculations and seems to be purely numerical.

Nevertheless, results obtained with both quasi-conservative algorithms are compared in Fig. 6.30 where an early time agreement is visible, while late time behaviours appear different. This can be related to the combustion process starting earlier for the QCVF model, which apparently seems related to higher temperature values as can be seen in Fig. 6.31 where at $t = 9\,[\mu s]$, the H_2 filament temperature is higher

by about $\Delta T = 100\,[K]$ for the QCVF. The combustion then propagates towards the main vortex and reaches it earlier than the QCMF. As a results, the denser jet between the two vortices rotates negatively for the QCVF which is similar to the reference solution, whereas it rotates positively for the QCMF. By looking closely at the pressure fields, this can also be related to a stronger vortex in the case of the QCVF model.

In the absence of experimental data, considering the different hypothesis between the reference solution and current approaches and finally considering that the reference solution also employs the QCMF approach [26, 133], it is difficult to assess whether one model performs better than the other. The main conclusion is that current results are not completely identical which, similarly to the one-dimensional laminar flames and detonations calculations could be explained by the different responses of the models to diffusion. This behaviour difference appears related to the different numerical dissipation amounts that each model introduces into the solution. Finally, the instability of the QCVF model appearing when computing such cases must be kept in mind and further investigated.

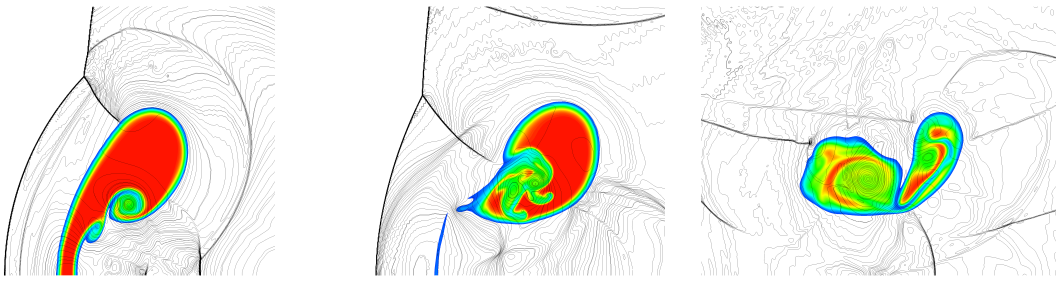

(a) *QCMF*

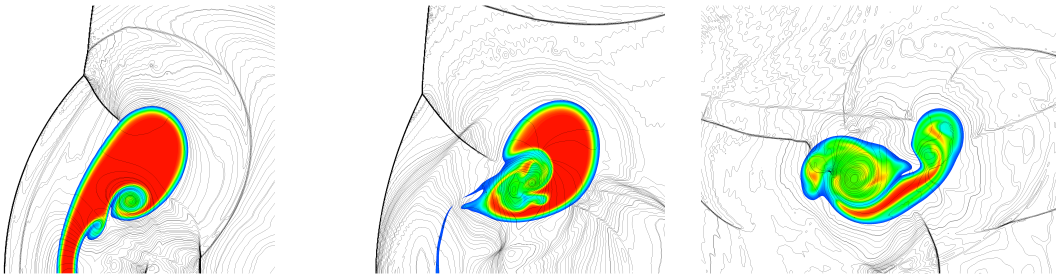

(b) *QCVF*

Figure 6.30: *Snapshots of reacting H_2 shock-cylinder interaction obtained on grid* 2III *with the thermally perfect EoS and different models at $t = 6\,\mu s$ (left), $t = 9\,\mu s$ (center) and $t = 14\,\mu s$ (right) - Contours of Y_{H_2} clipped below $Y_{H_2} = 0.05$ and isopleths of pressure with 100 lines between $P = 1$ bar and $P = 8$ bar*

6.3.5 Remarks on the thermodynamic properties

A final computation has been run using the QCMF model but altering thermodynamic quantities. Each species heat capacity ratio was fixed to a defined value and the impact of such a change on the flow field was studied. In order to keep the similarity between the variable and constant γ simulations, it was decided to set $\gamma = \gamma_{air}$, where γ_{air} corresponds to the un-shocked state with $\gamma_{air} = 1.3349$. By using this value, shock properties remain roughly constant (small changes in the shocked state with $\Delta T \approx 17\,[K]$ and $\Delta P \approx -4000\,[Pa]$), thus maintaining constant the momentum exchange from the shock to the bubble. The results obtained are visible in Fig. 6.32, where some differences between the computations can be observed.

The most striking difference resides in the bubble temperature, which is approximately $100\,[K]$ higher for the constant γ case. This has an effect on the ignition delay of the current chemical mechanism, and as expected, combustion starts earlier for this case and propagates faster along the mixing line. Given this higher temperature, the burning rate is higher in the constant γ case and the bubble is be-

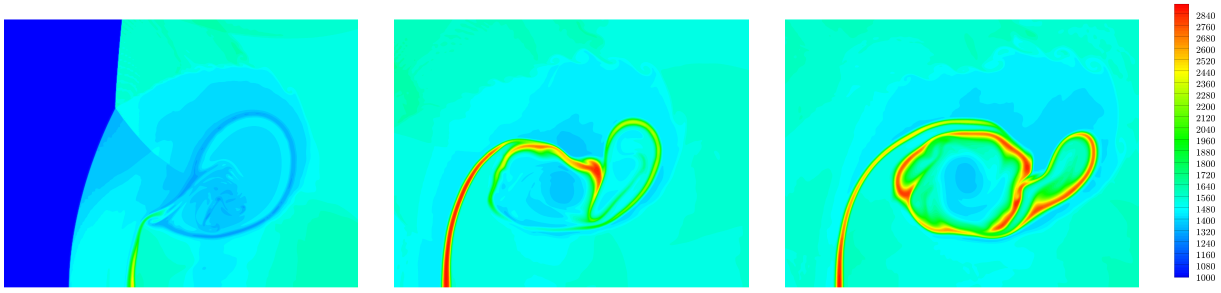

(a) *QCMF*

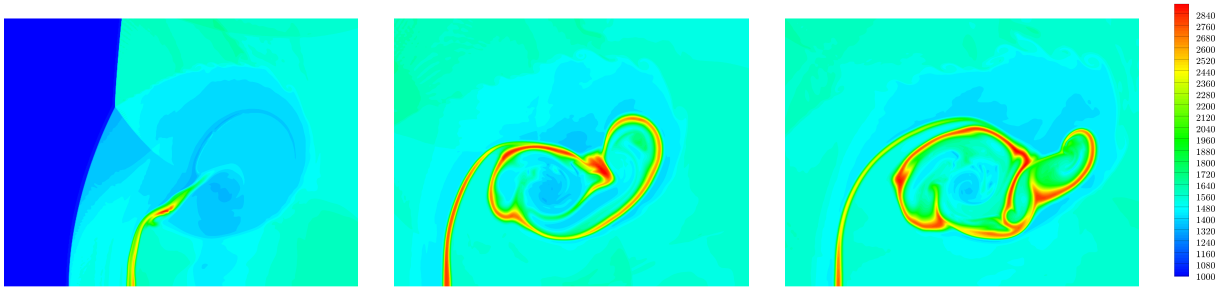

(b) *QCVF*

Figure 6.31: *Snapshots of reacting H_2 shock-cylinder interaction obtained on grid* 2III *with the thermally perfect EoS and different models at $t = 9\ \mu s$ (left), $t = 14\ \mu s$ (centre) and $t = 18\ \mu s$ (right) - Contours of temperature*

ing consumed slightly faster. However, it seems that species diffusion is limiting the burning speed, as at late times both burning speed appear similar even though the constant γ features higher temperatures.

A conclusion similar to the different test cases presented in Chapter 5 appears in this problem, where the constant γ simulation yields very similar flow structures but different magnitudes of temperature, pressure and velocity.

6.4 Conclusion

This chapter presented the validation of the different algorithms (QCVF, QCMF and FCMF) implementation in a multi-dimensional framework. The implementation has been tested on multi-dimensional inviscid and viscous problems (§. 6.1) from which an analytical solution was known, such as a moving contact wave and multi-dimensional shock-tube problem. A pure diffusion test problem was also computed successfully to validate the viscous fluxes implementation. The absence of directional bias was also verified for all test cases. The curvilinear implementation of the different operators (hyperbolic and parabolic operators) within the curvilinear framework was then considered validated.

In a second section, the well-known shock-bubble interaction experiment of Haas and Sturtevant [122] was replicated numerically and results compared with other similar computational studies. The agreement between the present results and both experimental and other numerical data was found very good both qualitatively and quantitatively (measurements of the different flow features speeds) for both bubble compositions (helium or R22). The numerical technique impact on this problem was also investigated, and it was found that both QCMF and QCVF models yielded almost perfectly identical results, which were virtually indistinguishable. Results obtained with the FCMF albeit featuring very similar flow features were found to present large temperature spikes along the whole bubble/ambient air interface. As the simulation was purely inviscid, this did not impact results, but this would be problematic in the case of temperature dependent problems. The low-Mach correction influence was also discussed, and although

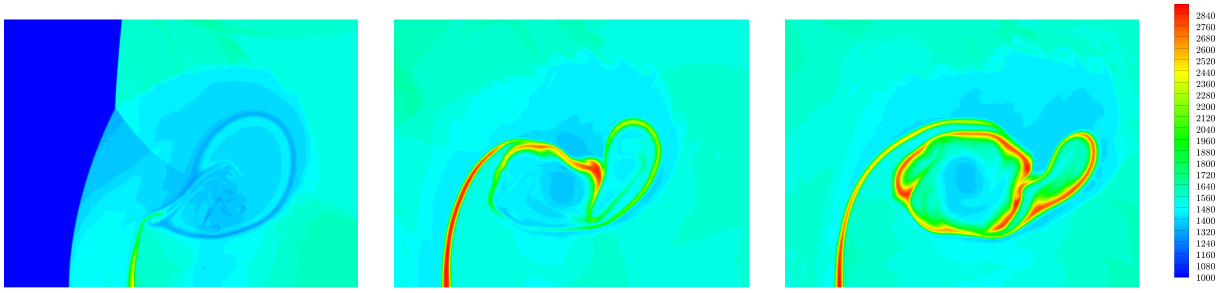

(a) $\gamma = \gamma\,(Y_k,\, T)$

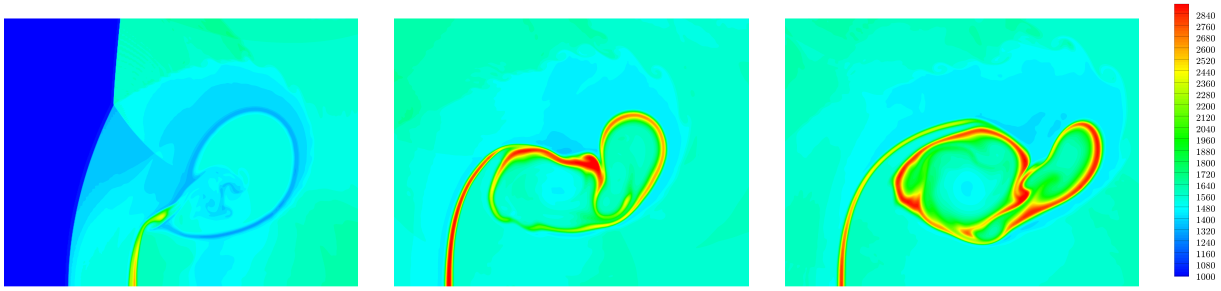

(b) $\gamma = 1.3349$

Figure 6.32: *Snapshots of reacting shock-cylinder interaction obtained on grid* 2III *with the different EoS and the QCMF model at* $t = 9\ \mu s$ *(left),* $t = 14\ \mu s$ *(centre) and* $t = 18\ \mu s$ *(right) - Contours of temperature*

the flow field was visually different when applying the correction due to the enhanced mixing occurring along the material interface, the bubble position and overall shape were not affected. The adiabatic index impact was finally investigated, and it was found that while keeping the shock impulse on the bubble constant, changing the adiabatic index of the bubble had an immediate effect on shocks within the bubble. Early times results were found to agree well with reference solutions, but a late time divergence can be speculated as the different features positions obtained with the single γ value start to increasingly deviate from the reference solution ($\gamma_{bubble} \neq \gamma_{air}$). Finally, similar conclusions were drawn on the R22 shock-bubble test, which presented a very good agreement with both experimental and computational data.

The last section is concerned with the computation of a similar problem but accounting for both diffusive and reactive effects. As no experimental results are available for this case, our results are qualitatively compared with the reference computations presented by Billet *et al.* [26]. An hydrogen bubble is impacted by a shock-wave and following the temperature increase due to the compression of the bubble, chemical reactions are initiated and propagate along the interface between the cold hydrogen and hot air similarly to a diffusion flame. A strong mixing, not unlike the one observed for the helium bubble then takes place and mixes the hydrogen with air, thus triggering chemical reactions within the bubble. Accounting for the simplifying assumptions applied in this work and not in the reference solution (constant but non-unity Lewis number, no volume viscosity, etc.), a correct qualitative agreement was found with the reference data both in terms of temperature values, salient flow features and species mass fractions when using either the QCMF or QCVF model. The bubble deformation and subsequent chemical reactions were properly reproduced. Additionally QCVF results (model found to fail in one-dimensional detonations) featured some differences with the QCMF results but a close agreement with reference data nonetheless. It also displayed a small numerical instability causing some simulations to stop at late times due to a divergence in the pressure calculation. The FCMF model was found to be crashing at very early times due to large temperature spikes along the reacting interface. In the absence of experimental data, there is no possibility of assessing which model (QCMF or QCVF) behave better, but both have been shown to work properly in such a challenging test case.

PART III

Application to the semi-confined hydrogen explosion case

CHAPTER 7

Semi-confined explosions theory and modelling

This chapter presents the relevant theoretical and numerical tools needed to provide a good understanding of explosions and their modelling. The key mechanisms driving flame acceleration are reviewed in a first section (§. 7.1.1). The different phases of the flame structure development in classical semi-confined explosions and their impact on the overall process are then highlighted (§. 7.1.2).

A extensive review of experimental results obtained during the last decades on large, medium and small-scale semi-confined explosions is presented in §. 7.2. The relevance of the different tests on explosion safety analysis is outlined and a survey of the corresponding numerical studies is provided. The choice of the test case used in this research work, namely the Sydney University combustion chamber is explained and a brief review of the experimental set-up, results and bias is given in §. 7.2.4.

Finally, the issue of compressible combustion modelling is addressed by presenting the model retained in this work. The Flame Surface Density approach is discussed, before the introduction of the filtered progress variable equation. A quick review of the main concepts is presented (§. 7.3.3). Finally, a detailed discussion on the flame wrinkling factors modelling considered in this research is provided (§. 7.3.4).

7.1 Semi-confined explosions phenomenology

During the flame propagation in a semi-confined or confined geometry, common key mechanisms can be identified as having significant impacts on flame propagation characteristics, but also on the pressure generated, and as such the damage to the surrounding structures in the case of industrial accidents. The present section briefly highlights different mechanisms responsible for flame acceleration in semi-confined geometries, but also the different propagation modes observed in such cases.

7.1.1 Flame acceleration mechanisms

Semi-confined explosions occurring during combustion of an inflammable cloud in an initially quiescent flow usually feature flames travelling at moderate speeds of roughly $2-6\,[m/s]$ which is slightly higher than the laminar flame speed as they are pushed outwards by expanding hot gases. In the particular case of completely unobstructed or unconfined combustion, flame speeds remain moderate as does the generated overpressure, except in the particular case where the cloud detonates due to a strong ignition, in which case a massive overpressure is generated potentially reaching pressures upwards of $P = 20\,[bar]$. However, in practice such configurations are not encountered and local areas can be partly confined and thus change the flame behaviour by accelerating it [28].

Two main mechanisms for flame acceleration are the thermo-diffusive instability most often encountered in hydrogen (or hydrogen-enriched) flames, and turbulence either self-generated during propagation or already present in the flow due to an external mechanism (stirring, pistons, etc.). Self-generated turbulence is most often found in confined and semi-confined explosions and often leads to the most devastating

results (Buncefield plant explosions in December 2005 where turbulence generated by surrounding bushes accelerated the flame and led to a transition to detonation [186, 187]). The relevance of this acceleration mechanism is the reason why semi-confined explosions are always studied as combustion starting in an initially stagnant flow, such that turbulence generation mechanisms can be fully integrated within simulations. Flame acceleration in such configurations is therefore very dependant on the obstacle nature (shape, size, number, position).

Fig. 7.1 depicts different mechanisms of turbulence generation in a semi-confined explosion problem, where turbulence is concentrated in the obstacle wakes. During the flame propagation due to both reactants consumption and hot gas expansion (dilatation by a factor $5-10$ similarly to the density ratio between products and reactants) pushing the fresh mixture towards the vent. The reactants velocity increases and generates turbulence near obstacles upstream of the flame. Instead of propagating in a stagnant flow, the flame now interacts with a turbulent flow.

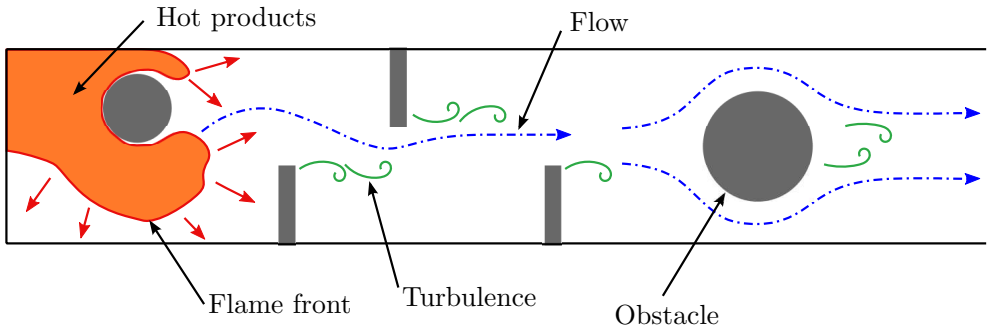

Figure 7.1: *Turbulence generation mechanisms in a semi-confined explosion*

When the flame interacts with turbulent wakes, it get wrinkled and stretched thus increasing its surface and increasing significantly the volumetric reaction rate. By a feedback mechanism, its speed increases noticeably as well, which increases further the wakes turbulence intensity, thus enhancing even more its speed due to a more pronounced wrinkling, and so on and so forth. This positive feedback loop is the main mechanism behind flame acceleration is semi-confined explosions and is responsible for the large overpressures observed in such flows. When the blockage ratio due to obstacles traps a non-negligible amount of gas (either reactants or products), the pressure builds up even more, similarly to what happens in a piston engine.

7.1.2 Propagation modes and flame development

Experimental and computational studies of semi-confined explosions led to the definition of five characteristic flame development phases. These have been described for explosions happening in initially stagnant flows. It shall be noted that phases described below are not always found in semi-confined explosions, and depending on the obstacles configuration, fuel and mixture stoichiometric ratio, pressure, etc. can vary widely in magnitude and duration. Fig. 7.2 depicts a schematic of the different phases.

- *Ignition* : The combustion process is started by an energy deposition coming from a spark, another explosion, laser focusing, etc. Energy is transferred from the source to the inflammable mixture through creation of plasma, etc. until an autonomous kernel starts to propagate without external feeding.
- *Laminar spherical propagation* : The flame kernel expands outwardly as it grows spherically or hemi-spherically if the ignition happens close to a wall. The flame propagates at its laminar speed multiplied by the expansion factor estimated as the density ratio between reactants and products, yielding $s_a = s_l^0 \dfrac{\rho_u}{\rho_b}$. The flame speed during this phase is very sensitive to the thermo-diffusive

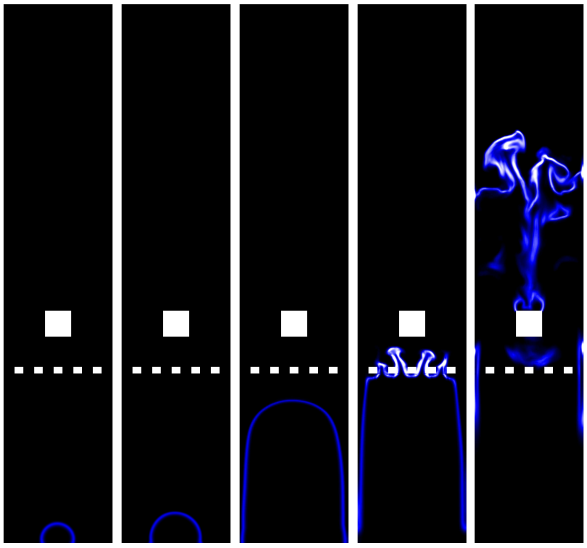

Figure 7.2: *View of the different propagation phases of a flame in a semi-confined explosion problem with (a) Ignition, (b) Spherical laminar propagation, (c) Finger-shaped laminar propagation, (d) Flame/obstacle interaction, (e) Turbulent flame - Results obtained with the QCMF model and FurebyM wrinkling factor*

instability (e.g. cellular burning for low Lewis number) and curvature effects as curvature is initially very large and decreases with time when the kernel radius increases.

- *Finger shape laminar structure* : The flame elongates following the main chamber direction, and eventually gets close to the walls. This geometrical change of the flame front has been described analytically by Bychkov *et al.* [42] and first described by Clanet and Searby [64]. Far from the walls during the early stages of the spherical growth, reactants are pushed normally to and away from the flame front by hot expanding gases. However, when the flame gets closer to the walls, the flow induced by the spherical kernel interacts with them. The streamlines initially purely radial slowly get skewed along the main chamber direction. Later on, reactants get trapped between the walls and the flame front therefore decreasing the flame speed down to its laminar value, as expansion effects become negligible. The flame thus propagates faster along the chamber direction than towards walls, creating a very distinctive finger-shape. Additionally, it was shown analytically by Bychkov *et al.* [42] that this configuration led to an exponential increase of the flame tip speed as long as the flame is not in contact with walls. Given the large surge in flame speed, it is critical to capture this propagation phase accurately.

- *Flame/obstacle interaction* : When the flame speed remains moderate, interactions with obstacles has for main effect to distort the flame front with a weak wrinkling. The flame structure remains laminar. Large curvatures effects are expected in these zones similarly to the early spherical growth of the kernel.

- *Turbulent flame* : Once a certain flame speed is reached, the interaction between the obstacle wakes and the flame front becomes significant and the flame starts to transition towards a turbulent burning regime as it gets more and more wrinkled. Once a turbulent regime is established, the flame accelerates even more rapidly until very large speeds are obtained, up to several hundreds of meter per second.

One could add two additional phases representing respectively the ultimate stage of the turbulent propagation when the flame front couples with a shock wave which leads to a detonation with flame speeds of several thousands meters per second, or on the other hand when the flame reaches low turbulence zones, a re-laminarisation of the front can be observed where flame speed decreases down to its laminar value.

To obtain an accurate simulation of semi-confined explosions, each of these phases (at the notable exception of the ignition) have to be properly captured as an error on one of these could potentially have a very large impact on the followings. For example, if the initial flame acceleration is not properly reproduced, the flame could remain in a fast laminar propagation mode instead of transitioning towards a fully turbulent one.

7.2 Experimental and numerical studies

7.2.1 Introduction

In order to validate and assess the different combustion modelling approaches performance, and in particular those presented in this work, it is necessary to find a suitable experimentally investigated test case. These have been long used for the main purpose of establishing flame speed correlations or other empirical laws to estimate explosions consequences on surrounding structures. However, they have also been used to validate numerical techniques. It appears obvious that real scale tests can not be conducted given the danger and cost associated. The only experimental data available on real configurations have been obtained during accidents using witnesses recollections, investigation of structural damages, potential data recorded by on-site instrumentations (tanks pressure sensors during the Buncefield accident [186, 187]).

Precise and detailed experimental data for such cases can only be gathered on precisely designed and instrumented experimental rigs using high-speed cameras, pressure sensors. They are usually composed of a closed box with several obstacles. The usual experimental set-up [123] requires the chamber filling with an inflammable homogeneous mixture left to rest for a long enough time to suppress all turbulence and approximate the flow field as being initially stagnant. The explosion is then triggered using either a spark plug or focusing laser beams in a small region of space. The flame propagates following the phases highlighted earlier and data are recorded. In the case of an initially turbulent flow field, laminar propagation phases would not be observed, and the flame speed would reach much higher values. This type of configuration reproduces a real accident where ignition occurs a long time after the accidental leak that produced the burnable mixture, assuming that the mixture is homogeneous. The flame wrinkling due to the numerous obstacles of a real case, as well as the confinement are well accounted for in these experiments yielding valuable data for safety analysis.

Experiments can be grouped into two categories, the very large ones with chambers volumes being several cubic meters, and the small ones where the total volume can be measured in litres, i.e. small scale and large scale experiments.

7.2.2 Medium and large scale experiments and numerical studies

Due to the apparatus size, large scale experiments are usually limited to overpressure measurements at several different locations. Flame visualisations are indeed extremely difficult to obtain for these configurations that do not always have the necessary optical accesses, or are even too large for the camera field of view thus requiring the camera to be some 30 $[m]$ away from the rig. The parametrisation of these experiments involves mixture composition, ignition position, number of obstacles, etc. Rigs dimensions vary from $V = 0.14\,[m^3]$ up to $V = 550\,[m^3]$ for [130, 131] with intermediate sizes of roughly $V = 10 - 35\,[m^3]$ [28, 225, 292]. Most of these experiments have been run with either ethylene of propane which are amongst the most used fuels. Large scale experiments involving hydrogen are less common due to the very large pressures and flame speeds reached with such fuel. Nevertheless, one can note the experiment of Groethe in a 72.5 $[m]$ long tunnel [114], or the Texas A&M University chamber [226] as well as the Whiteshell Laboratories explosions in Canada [292].

Numerical studies of these large scale geometries have usually been conducted using URANS [10, 16, 28, 195, 228], while a few employed a phenomenological approach [248] which will not be discussed here.

The large scale test cases simulated using URANS usually feature a large range of geometric details, the smallest being no more than a centimetre long. These fine structures are not explicitly represented on the computational grid but are usually accounted for using porosity models or PDR (Porosity Distributed Resistance) modelling their blockage ratio and turbulence generation. Several codes using such approaches exist and one can cite COBRA (Mantis Numerics Ltd), EXSIM (Tel-Tek), FLACS (CMR/GexCon), etc. in which numerous parameters are used to adjust the flame behaviour given the configuration. The turbulent flame speed is a modelled parameter for which models varies widely in their complexity, ranging from the constant value imposed by the user, time delay controlling the transition between laminar and turbulent propagations, to the more advanced correlations used by FLACS depending on the turbulent fluctuations. All of these models leave the heavy responsibility of defining the numerous constants to the user, knowing that each of these can potentially have a large effect on the solution. A benchmark comparison between different codes have been presented by the *HySafe* network on several explosions cases [16, 195] showing reasonable *a posteriori* agreement with experimental data.

The inherent limitations of URANS regarding turbulence modelling clearly indicate that these models are not adapted to the transition between laminar and turbulent propagation modes computation, which limits its accuracy in the case of deflagrations starting in stagnant flows. Accounting for the regular increase in computational power, the LES is becoming an attractive tool for the simulation of such explosions on massively parallel computers [249]. The combustion community in its majority recognises it as the future solution for the simulation of reacting turbulent flows, be it in industrial or academic applications. The flow unsteady features are finely captured, allowing an accurate prediction of the flame transient behaviour. However, this comes at the cost of very fine grids, limiting its use for very large scale explosions. Results obtained by Molkov and Makarov [193,209] on a $6.5\,m^3$ configuration using a dynamic grid around the flame front with cells of 35 $[mm]$ showed promises for the overpressure prediction, but calculations carried out on a 550 $[m^3]$ geometry (SOLVEX) using cells of 0.8 $[m]$ clearly illustrated the LES limitations.

Promising results have been obtained very recently using the TFLES approach on 6.1 $[m]$ and 1.5 $[m]$ long chambers by Quillatre [249]. Both flame position and overpressure were correctly reproduced using meshes of 20×10^6 cells of respective size 12 $[mm]$ and 3 $[mm]$. This represents one of the first successful example of LES upscaling for semi-confined explosions.

7.2.3 Small scale experiments and numerical studies

Smaller experimental tests allow for simpler use and more comprehensive parametric studies (fuel, obstacles shapes, sizes, positions, etc.), although it shall be kept in mind that these are less representative of the real cases in terms of scales (both spatial and temporal) involved. Indeed, conclusions found for small scale problems do not necessarily apply to large scale ones. The flow parameters are not modified in a similar way during the scale up. Gas quantity and large scale structures increase with the chamber dimensions, while the Kolmogorov scale tends to decrease as the Reynolds number increases, and the laminar flame speed remains constant.

However, thanks to their limited sizes, flow visualisations can be captured in addition to the usual pressure measurements. This enables a fine study of the flame speed, position but also of its structure and geometry during the different propagation phases.

Three research centres are publishing the bulk of small scale experimental studies. These are Loughborough University, Sydney University and Istituto di Ricerche sulla Combustione (IRC, Combustion Research Institute) in Italy. Loughborough University explosions are using propane and methane as fuels and feature three different chambers of respective volumes 0.056 $[m^3]$ [94], 0.011 $[m^3]$ [138] and 0.0033 $[m^3]$ [185]. Parametric studies involve the number and shape of obstacles. The Italian Combustion Institute studies explosions in a chamber 0.005 $[m^3]$ with either methane or hydrogen-enriched methane [44]. The experiment focuses on the initial turbulence level impact on the flame propagation

and overpressure. Finally, the University of Sydney mainly employed two different chambers. The first one features a volume of 0.02 $[m^3]$ filled with propane and investigated the obstacle shape influence on flame characteristics [199], while the second chamber occupies 0.0006 $[m^3]$ and presents the widest range of parameters studied amongst the aforementioned studies [123, 151, 200]. Three fuels were considered, namely the methane, propane and hydrogen allowing a direct comparison of their effects on the overpressure and flame propagation. Additionally, the obstacles shapes, number and position effects were investigated, leading to 17 different geometrical configurations, each tested with the three different fuels thus providing 51 different sets of experimental data. In all of them the flame speed and position were recorded, as well as the overpressure in two different locations.

These experiments have been mostly designed to be reproduced in computational studies and to allow a good understanding of the underlying mechanisms of pressure generation and flame acceleration. Historically, URANS methods have been used to simulate such geometries, improving the comprehension of such phenomena over the experimental and phenomenological studies available at the time. It has been shown that URANS could predict rather correctly the overpressure generated by semi-confined explosions, but the same authors also highlighted the difficulties associated with the determination of the numerous constants of RANS combustion models [227, 240]. Since about 2005, several LES studies have shown that LES could prove an invaluable tool for the prediction of explosions, as this method allows an accurate simulation of all fine features driving both the flame speed and overpressure (acceleration/deceleration near obstacles, transition from laminar to turbulent propagation, wrinkling of the flame, pockets formation of products or reactants, etc.) [77, 115].

The recent numerous experimental measurements of Loughborough University, Sydney University and IRC although primarily designed for safety analysis have proven themselves extremely useful in the validation of several combustion sub-models, thanks to their very well defined experimental set-up (initially stagnant flow, boundary conditions, geometry, etc.). Building upon the experimental data published, numerous publications from the same organisations (Loughborough [76–80], Sydney [115–118, 123, 136, 137, 156, 200] and IRC [75]) have compared LES and experimental results using a large range of computations methods. The majority of these works have been focused on turbulent combustion models while also reproducing the parametric studies based on the geometry changes. Di Sarli *et al.* [79, 80] highlighted that the Flame Surface Density framework was well suited for these simulations and provided accurate results, but pointed out that the predictions quality was highly dependent on the combustion model considered. Most of these results have been obtained for methane and propane, but to date almost no LES simulations have reproduced the Sydney hydrogen deflagrations at the exception of Quillatre *et al.* [249] using TFLES modelling and Abdel-Raheem *et al.* [3] using DFSD (Dynamic FSD).

7.2.4 Selected test case, Masri deflagration chamber

Experimental Set-Up

As pointed out in the previous paragraphs, the Sydney experiment features the largest database of experimental results obtained for numerous combinations of geometries and fuels. It is also a typical example of the small scale explosion rigs used to study phenomena driving semi-confined explosions. Numerous similar configurations exist, but this particular geometry presents four advantages, the first being its small size which makes it an ideal candidate for LES simulations that are inherently costly. Secondly, the amount of experimental data and configurations is very large and allows the testing of combustion models in a wide range of operating conditions. Third, several computational studies considering the Liquefied Petroleum Gas (LPG, usually approximated with propane) and the Compressed Natural Gas (CNG usually approximated with methane) [115–118] have been published but none regarding the hydrogen except Abdel-Raheem *et al.* [3] who studied the influence of the ignition radius on the solution and simulated three different geometries. Finally, a collaboration with Prof. Masri from Sydney University allowed us to have a direct access to the pressure measurements and flame visualisations recorded during experimental campaigns such that we could post-process and use them in any way deemed necessary for this work.

Fig. 7.3 pictures the chamber geometry. It features a square cross section of side length $l = 50\,[mm]$ and a height of $L = 250\,[mm]$, thus leading to a total volume of $0.625\,[L]$ and an aspect ratio of $L/l = 5$. The chamber is built with transparent Perspex allowing a optical access from one side. Three removable baffle plates (interchangeably called grids or obstacles) may be placed in the chamber at respective height of $19\,[mm]$ (Grid 1), $42\,[mm]$ (Grid 2) and $79\,[mm]$ (Grid 3) from the chamber closed end. These consists in five strips that are $4\,[mm]$ wide and evenly separated by six gaps of $5\,[mm]$ yielding an overall blockage ratio of 0.4, with a thickness of $3\,[mm]$. Downstream of the baffle plates an obstacle of square cross-section may be positioned such that its base is placed $96\,[mm]$ above the bottom of the chamber. Two different sizes have been studied experimentally, the first being $12\,[mm]$ for a blockage ratio of 0.24 and a second measuring $25\,[mm]$ for a blockage ratio of 0.5. In the current study, only the smallest obstacle is simulated and Fig. 7.4 depicts all geometries considered. Given the large number of geometries, Masri's notation is kept here, where 0 means that there is nothing at the position, B stands for baffles and S for the small obstacle, e.g. $0B0S$ means only the second grid and small obstacle.

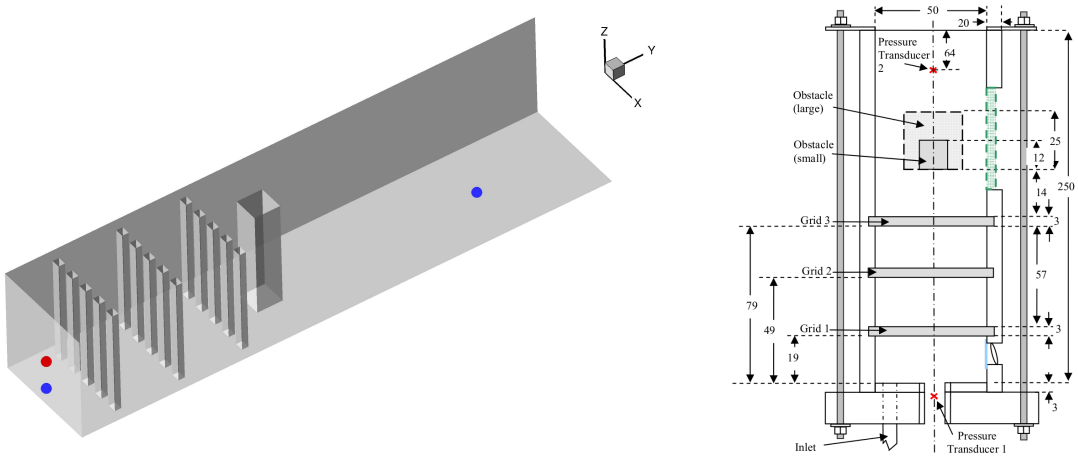

Figure 7.3: *Configuration of the Masri combustion chamber oriented vertically during the experiment - (Left) Base is on the left and the open vent on the right, blue dots denotes pressure probes and the red dot indicates the ignition point, (Right) Detailed geometry*

Three fuel mixtures have been experimentally considered, while only the hydrogen one is simulated here,

- LPG ($95\%C_3H_8$, $4\%C_4H_10$ and 1% of other hydrocarbons) with $\phi = 1.0$
- CNG ($88.8\%CH_4$, $7.8\%C_2H_4$, $1.9\%CO_2$ and $1.2\%N_2$ while the 0.3% remaining are a mixture of propane, propene, butane and pentane) with $\phi = 1.0$
- H_2 with $\phi = 0.7$

Experiment were conducted using the following sequence that was repeated over fifty times for each configurations to estimate the results sensitivity to random external perturbations (external temperature, humidity, mixture stoichiometric ratio, etc.),

1. Seven times the chamber volume is injected into the cavity between each runs to purge it through a valve located in its base
2. A lid is positioned at the top to keep the mixture inside
3. The mixture is let to rest for $15\,[s]$ (CNG), $10\,[s]$ (LPG) and $5\,[s]$ (H_2) which is deemed long enough to damp any velocity fluctuations
4. The lid is removed $1\,[s]$ before ignition which is produced by focusing Nd:YAG infra-red laser beams $2\,[mm]$ above the chamber base

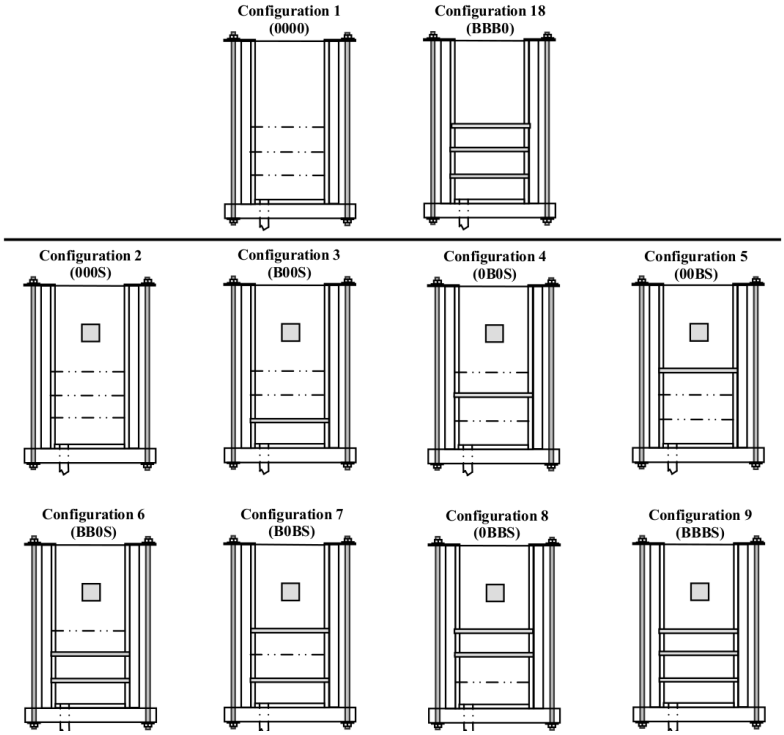

Figure 7.4: *Families of configurations for the Masri combustion chamber*

Experimental results

Explosion analysis relies on the study of critical criteria that need to be investigated experimentally, such that the ability of the different numerical approaches to reproduce them can be evaluated.

The first parameters needed to validate the selected LES modelling approach upon comparison with experimental results are the flame position and its front structure as it propagates into the chamber. Experimental pictures using the LIF-OH method have been obtained for all fuels with a frequency of 5 $[kHz]$ as pictured in Fig. 7.5 for the BB0S hydrogen deflagration. The amount of OH is measured and used as a tracker for the flame position. The structure of the flame is clearly visible and this helps to understand the driving mechanisms behind explosions. It shall be noted however that small scale structures can not be viewed on these images as they represent an averaging of the flame over the width of the chamber thus blurring all fine details.

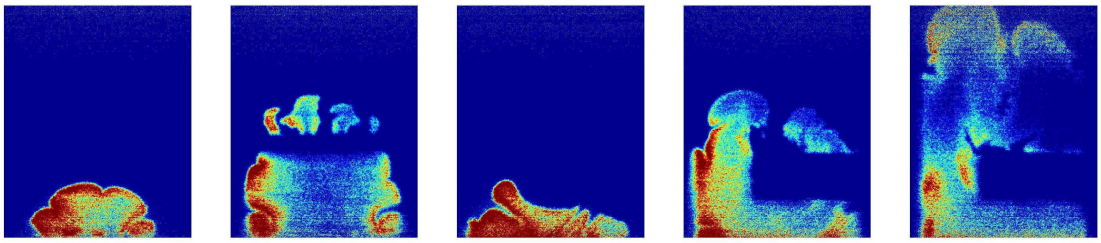

(a) **(b)** **(c)** **(d)** **(e)**

Figure 7.5: *LIF-OH experimental visualisation of an hydrogen flame in the BB0S configuration, (a) and (b) show the first (bottom) and second (center) baffles, while (c), (d) and (e) show the obstacle*

The second set of parameters are the flame speed and position, the former being extracted from the latter. The flame position, defined as the height above the chamber bottom is measured on the experimental images at the highest flame front position. The flame speed is then obtained by computing the

position time derivative. These are some of the main parameters that need to be reproduced correctly by the LES approach, as well as their variations when the geometry changes.

Finally, the most important parameter is the maximal overpressure reached in the domain during the flame propagation. In safety studies and accident scenario, it is the only parameter that allows the dimensioning of the facilities structures such that they can withstand an explosion. Two piezo-electric sensors have been positioned in the chamber, one at the base and the other in the axis of the main obstacle further downstream. Measurements have been gathered during two different campaigns, the first one took place in May 2010 and consisted of 30 runs, while the second took place in June 2011 and witnessed 20 more runs for a total of 50 experimental measurements. A set of measurements is provided as an example in Fig. 7.6 for the BBBS configuration.

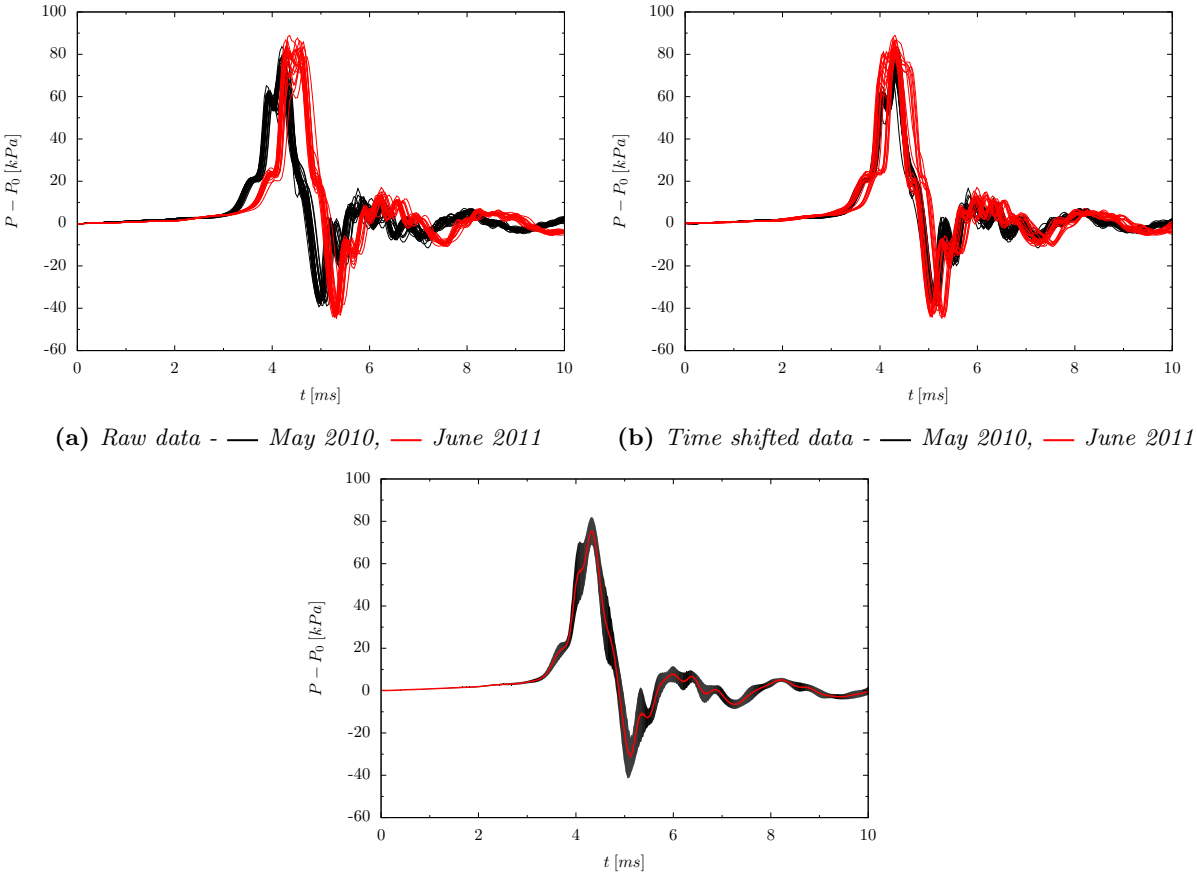

(a) *Raw data -* — *May 2010,* — *June 2011*

(b) *Time shifted data -* — *May 2010,* — *June 2011*

(c) *Mean and std. dev. -* ■ *Std. dev.,* — *Mean*

Figure 7.6: *Experimental overpressure profiles in the Masri BBBS configurations*

An important factor in the experimental data is the variability of pressure measurements. Table 7.1 presents the spread in maximum overpressure values and the time to peak. It is interesting to note that the pressure variability within a single experimental campaign is quite large with up to 5% of standard deviation for the second campaign, thus highlighting the chaotic aspects of this experiment. Contrary to CNG and LPG flames, hydrogen flames time to peak features very small standard deviations. However, differences in pressure peaks between campaigns appears quite large with about 12% of standard deviation. This indicates the high sensitivity of these semi-confined explosions, and can potentially be explained by a slight difference in the initial energy deposition, different atmospheric conditions (humidity, temperature, etc.). Following the approach of Prof. Masri, the different pressure measurements are time-shifted such that they all peak at the same time, and then a mean and standard deviation can be defined as shown in Fig. 7.6. Following Prof. Masri, the hydrogen peak time is not considered as a reliable parameter for assessing the numerical results quality.

	May 2010	June 2011	Global Statistics
Wall Overpressure [kPa]			
Mean	72.5	90.7	79.5
Std. dev. / Mean [%]	2.8	5.2	12.2
Time to peak [ms]			
Mean	4.22	4.57	4.36
Std. dev. / Mean [%]	0.9	1.2	4.1

Table 7.1: *Experimental variability in wall overpressure and time to peak for the BBBS configuration*

7.3 Compressible turbulent combustion modelling

7.3.1 Introduction

Large Eddy Simulation is now a widely acknowledged method for the simulation of turbulent reacting flows. The turbulent combustion model considered in this work needs to be able to simulate both laminar and turbulent propagation modes of the flame in a semi-confined environment but also to be of relative ease of implementation and to feature a reasonable cost. The Thickened Flame model (ATF, TFLES) and the FSD approaches have both been considered in the literature for the simulation of such cases [80, 117, 249]. Despite its limitations in accounting for curvature and preferential diffusion effects, the FSD approach is used in this work using an algebraic closure of the source term.

Due to the very high flame speeds reached at the open end of the chamber with the hydrogen in combination with the large overpressure recorded, a compressible code is deemed necessary to fully account for these phenomena. Additionally, the aim of this work is to investigate the possibilities of the developed algorithms (QCMF, QCVF) to accurately capture the early stages of the flame acceleration which could potentially lead to a detonation for larger geometries or blockage ratios. To this end, a fully compressible shock-capturing scheme is required. However, it has now been established that classical fully compressible shock-capturing methods would not be able to cope with a moving interface without generating pressure oscillations and temperature spikes, therefore, algorithms presented and validated in the previous chapters are coupled with the FSD approach to simulate these slow and fast deflagrations.

Within the FSD framework, species transport and combustion are accounted for by the progress variable (c) transport equation which is similar in nature to the species transport equations §. 7.3.2. Two formulations could be used when considering the progress variable transport, the first being to transport c using an unsymmetrical formulation (Eq. 2.58) where the density would be explicitly computed using the continuity equation, or a second symmetrical formulation (Eq. 2.57) where c and $1-c$ would be transported as two progress variables with different thermodynamic properties. This is the choice retained here as the symmetric formulation has been employed in the previous chapters for the validation of the algorithms.

7.3.2 Progress variable definition and transport equation for the progress variable

In premixed combustion, flames are very thin with $\delta_0^l = 0.1-1[mm]$ which is significantly smaller than the filter size $\bar{\Delta}$. In the LES context, one approach is to ignore for the most part the internal flame structure by using a progress variable varying between $c = 0$ in reactants and $c = 1$ in products. The chemical status of the mixture is then addressed by assuming a single step irreversible reaction between reactants and products. Several definitions of the progress variable could be used based on the temperature, fuel mass fraction, products mass fraction, etc. In this work, the dimensionless H_2 mass fraction is used

following,

$$c = 1 - \frac{Y_{H_2}}{Y^u_{H_2}} \tag{7.1}$$

where Y_{H_2} is the hydrogen mass fraction and $Y^u_{H_2}$ its value in the reactants.

The unfiltered progress variable transport equation is recalled here and reads,

$$\frac{\partial \rho c}{\partial t} + \frac{\partial}{\partial x_i}\left(\rho u_i c\right) = \frac{\partial}{\partial x_j}\left(\rho D_c \frac{\partial c}{\partial x_j}\right) + \dot{\omega}_c \tag{7.2}$$

where D_c is the progress variable diffusivity estimated as $D_c = \dfrac{\nu}{Sc}$.

The Favre filtered transport equation reads,

$$\frac{\partial \overline{\rho}\tilde{c}}{\partial t} + \frac{\partial}{\partial x_i}\left(\overline{\rho}\tilde{c}\tilde{u}_i\right) = \overline{\dot{\omega}}_c + \frac{\partial}{\partial x_i}\left(\bar{\rho}\frac{\bar{\nu}}{S_c}\frac{\partial \tilde{c}}{\partial x_i}\right) - \frac{\partial}{\partial x_i}\left[\bar{\rho}\left(\widetilde{u_i c} - \tilde{u}_i\tilde{c}\right)\right] \tag{7.3}$$

The energy and momentum equations remain as presented in §. 3.7.5 and §. 3.7.2 respectively, where it should be noted that buoyancy terms are not added due to the short residence time of the flame within the combustion chamber (at most 9 $[ms]$). The source term and sub-grid scalar transport still need to be closed as presented below for the turbulent transport and in §. 7.3.3 for the source term.

The modelling of the unresolved scalar transport is quite challenging owing to the highly non-linear nature of this term. It also features an anisotropic behaviour which further increases the complexity of its modelling. In turbulent premixed combustion in particular, this could be made even more complex due to the large pressure gradients (and associated density variation) which could potentially cause counter-gradient diffusion. However, it has been shown by Boger and Veynante [30] that in LES a large portion of the gradient fluxes was resolved, and that a simple gradient approach for the subgrid term would be able to recover the counter-gradient diffusion. The subgrid scalar transport thus reads,

$$\frac{\partial}{\partial x_i}\left[\bar{\rho}\left(\widetilde{uc} - \tilde{u}\tilde{c}\right)\right] = -\frac{\partial}{\partial x_i}\left(\overline{\rho}\overline{D}_t\frac{\partial \tilde{c}}{\partial x_i}\right) \tag{7.4}$$

where D_t is the turbulent diffusion coefficient of the progress variable estimated by $D_t = \dfrac{\nu_t}{Sc_t}$ and Sc_t is the turbulent Schmidt number.

7.3.3 Flame Surface Density modelling

The concepts of FSD proposed in the LES framework are very similar to their RANS counterparts and can also be derived from flamelets equations. The flame front is viewed as a collection of thin wrinkled propagating interfaces between the products and reactants. Within the limit of high Damköhler number, they can be assumed to propagate at the local laminar flame speed, and thus are considered as laminar flamelets.

The flame front wrinkling can thus be described by the mean flame surface area per unit volume, or flame surface density. Assuming that individual flamelets are propagating with their laminar flame speed, the mean reaction rate can therefore be expressed as,

$$\bar{\dot{\omega}}_c\Sigma = \rho_0 s_l^0 \Sigma \tag{7.5}$$

where s_l^0 is the laminar flame speed and ρ_0 is the fresh gases density.

The FSD Σ can be modelled using either a transport equations such as the one presented by Hawkes and Cant [124], or alternatively using an algebraic model considering the balance between the production

and destruction of FSD, as done by Boger *et al.* [29] based on an extensive DNS database. His model is very similar to the BML approach in the context of RANS, and has been used with success by several authors for the simulation of premixed flames [118, 156] and reads,

$$\Sigma = 4\frac{\tilde{c}\,(1-\tilde{c})}{L_\Sigma} \tag{7.6}$$

where $\tilde{c}$ is the filtered reaction progress variable, and L_Σ is the flame wrinkling scale also calculated as $\bar{\Delta}/\beta$. The model coefficient β being either a constant or modelled based on a SGS wrinkling factor. Several models for the SGS wrinkling factor have been proposed following either the BML or EBU approaches by Charlette *et al.* [58], the SGS RMS fluctuations by Angelberger *et al.* [9], or more complex dynamics formulations as presented by Knikker *et al.* [161].

In the present work, algebraic formulations only are considered following the analysis of Boger *et al.* [30] where FSD models take a similar form as the BML model in the RANS framework,

$$\Sigma = 4\beta\frac{\tilde{c}\,(1-\tilde{c})}{\bar{\Delta}} \tag{7.7}$$

where the parameter β takes the value $\sqrt{\frac{6}{\pi}}\Xi_\Delta$ for infinitely thin flame front, or large enough values of $\bar{\Delta}/\delta_l^0$, where Ξ_Δ is the flame wrinkling factor (directly linked to the subgrid flame surface lost in the filtering process). It is defined by,

$$\Xi_\Delta = \frac{\overline{|\nabla c|}}{|\nabla \overline{c}|} \tag{7.8}$$

where recalling the generalised FSD definition presented in §. 2.2.4, it can be re-written as,

$$\Sigma = \overline{|\nabla c|} = \Xi_\Delta |\nabla \overline{c}| \tag{7.9}$$

Comparing the previous equations, it can be seen that Boger *et al.* [30] proposes in fact an algebraic equation for $|\nabla \overline{c}|$,

$$|\nabla \overline{c}| \approx 4\sqrt{\frac{6}{\pi}}\frac{\tilde{c}\,(1-\tilde{c})}{\bar{\Delta}} \tag{7.10}$$

The model coefficient β is not universal, and is known to depend on the grid resolution, fuel, turbulence levels, etc. From the literature, values between $\beta = 1$ and $\beta = 2.6$ has been used. However, using a constant value for this coefficient is similar to the EBU approach which is inappropriate and known to lead to β dependant results. To avoid such issue, several methods can be used,

- Choosing a constant value of β based on parametric studies on the filter width, wrinkling factor, etc. or iterating/tuning to match experimental results.
- Use a dynamic of self-scalable model for the coefficient Ξ_Δ using local flame and flow characteristics to recover some of the unresolved FSD contributions

7.3.4 Modelling Ξ_Δ and the fractal dimension

Fractal flame model

The flame wrinkling factor is defined by Knikker *et al.* [162] as the ratio of FSD and its projection in the direction normal to the flame propagation. By identifying the flame surface as a fractal surface, it can be estimated as,

$$\Xi_\Delta = \left(\frac{\bar{\Delta}}{\delta_c}\right)^{D-2} \tag{7.11}$$

where $\bar{\Delta}$ is the filter width usually considered as the outer cut-off scale in LES, δ_c is the inner cut-off (smallest scale for the interaction of the turbulent eddies with the flame front), and D the fractal dimension of the flame. The main assumption behind such a model for the flame wrinkling factor is that vortices of all sizes between the inner and outer cut-off scales are contributing to the overall wrinkling of the flame surface.

Cut-off scales

In general the outer cut-off is represented by the integral length scale which is also the size of the largest eddies in the flow, but in LES, the filter size $\bar{\Delta}$ is generally used [161,162]. The selection of the inner cut-off scale is much more debatable, as many different scales can be thought of. There are several possibilities based on either physical or intuitive arguments. Amongst the available length scales, the predominantly used are the Gibson scale (Gouldin [112]), the Kolmogorov scale (Peters [229]) and the laminar flame thickness (Knikker *et al.* [161,162], Wang *et al.* [288]). Other computations have been presented using the inverse of surface averaged curvature of the flame (Fureby [98]). However, from experimental data, Knikker *et al.* [161,162] have identified that $\delta_c = 3\delta_l^0$ gave good results, and as such, this length scale is used in this work.

Fractal dimension

The last item to discuss here is the choice of the fractal dimension. In a true fractal model, this parameter would be held constant at the flame fractal dimension, however, in the current application, it may vary both in time and location in the flow depending on local conditions. Since the introduction of the fractal theory by Mandelbrot, it has been widely used for various applications, and the analysis of turbulence and combustion in particular. The underlying principle of fractal models is to identify the flame surface as a fractal surface, which can not be described by any other means. Kobayashi *et al.* [163] have shown that there exists a wide range of self-similar shapes and forms between the inner and outer cut-off scales in lean premixed flames. The range of fractal dimensions found by experimental means ($D = 2.37$, Gouldin [112], $D = 2.35 - 2.41$ Sreenevasan and Meneveau [266]), mathematical analysis (Hentschel and Procaccia [127]), and dynamic similarity approach ($D = 2.37$, Kerstein [152]) shows the non-uniqueness of such dimension.

Examination of experimental flames in the late 1980's (rod stabilised V-flame [71], rim stabilised conical flames [216], edge stabilised oblique flames [119], wall stabilised oblique flames [62] and pulsed-flames flow reactor [220]) by North and Santavicca [220] led to the conclusion that the fractal dimension was increasing with turbulence intensity and inversely to the laminar flame speed (the flame is more wrinkled). This was explained by the distortions of the flame front occurring at a rate proportional to the turbulent velocity fluctuations u', and the competing smoothing of the flame front at a rate proportional to the laminar flame speed s_l^0. Through these combined effects, they derived an algebraic relation automatically limiting the fractal dimension between its laminar (D_l) and turbulent (D_t) values,

$$D = \frac{D_l}{\frac{u'}{s_l^0} + 1} + \frac{D_t}{\frac{s_l^0}{u'} + 1} \tag{7.12}$$

This model has also been successfully applied within the LES framework by Fureby [98] modelling propane/air flames, and replacing u' by the SGS velocity fluctuations u'_Δ (Eq. 7.14),

$$D = \frac{D_l}{\frac{u'_\Delta}{s_l^0} + 1} + \frac{D_t}{\frac{s_l^0}{u'_\Delta} + 1} \tag{7.13}$$

It shall be noted that laminar and turbulent values are not uniquely defined, and are dependent on the fuel and flow configuration. A rather wide range of values for the fractal dimension of hydrogen premixed

flames on one hand, and of freely propagating premixed flames on the other can be found in the literature.

Chatakonda *et al.* [60] extracted the fractal dimension from two DNS databases of high Reynolds number, low Damköhler hydrogen flames, where a lower value is found at $D \approx 2.1$ and an upper value at $D \approx 2.7$ for the highest Reynolds case. Similarity arguments showed that at high Reynolds number, the low Damköhler limit of the fractal dimension is 8/3 and not 7/3 as previously considered.

Kwon *et al.* [169] measured and simulated spherically growing hydrogen flames in turbulent flows, where fractal dimensions were found between $D = 2.0$ (laminar value) and $D \approx 2.15$, which is lower than the theoretical value. This has been attributed to the limited size of the experimental apparatus thus limiting the flame growth time. Similar experiments of outwardly propagating C_3H_8/air and $H_2/O_2/N_2$ spherical flames have been conducted by Kwon *et al.* [168] that were found to be accelerating with fractal dimensions measured between $D = 2.20$ and $D = 2.25$.

Very interesting results have been obtained by Bradley *et al.* [34] who found that freely propagating premixed turbulent flames had a fractal dimension of $D \approx 2.33$ which is in good agreement with the theoretical value of 7/3. Similar values have also been found by Gostintsev *et al.* [111] on self turbulising freely-propagating flames where fractal dimension were found in the range $D \approx 2.2 - 2.33$. Numerical investigations by Molkov *et al.* [194, 210] led to the conclusion that $D = 2.33$ might be an overestimation of the fractal dimension of the resolved field, and a lower value should be considered and suggested $D \approx 2.22$ was suggested which is still the range proposed by Gostintsev *et al.* [111] for large-scale unconfined explosions.

Following these results, it has been decided for the present work to use $D = 2.33$ for the case where the fractal dimension is supposed constant (Boger model in Table 7.2), and $D_l = 2.1$, $D_t = 2.33$ for both the BogerM and FurebyM models (Table 7.2), since $D = 2.1$ corresponds to the lowest value of the DNS simulations at high Reynolds number, and $D = 2.33$ corresponds to the theoretical limit of freely propagating premixed turbulent flames.

7.3.5 Other algebraic models of Ξ_Δ

Numerous algebraic models have been proposed in the literature, some of them being listed in Table 7.2, and most of them requiring an approximation of the SGS velocity fluctuations u'_Δ, estimated here using the Smagorinsky model,

$$u'_\Delta = \frac{\nu_t}{C_s\bar{\Delta}} = \left(C_s\bar{\Delta}\right)^2 |\hat{\mathbf{S}}| \tag{7.14}$$

The main drawback of this formulation of the SGS fluctuations is its sensitivity to thermal expansion across the flame front. To remedy this, Colin *et al.* [66] proposed a model for u'_Δ as a function of vorticity, arguing that the obtained fluctuations will be unaffected by heat release. However, Ma *et al.* [191] also argue that heat release affects vorticity transport through dilatation and baroclinic torque, thus modifying the resolved vorticity. Additionally, one could obtain the fluctuations by solving a transport equation for k_{sgs}, the SGS turbulent kinetic energy, but this would require extra modelling, which would further complicate the combustion modelling. Therefore, the simplest solution is retained here in the form of the Smagorinsky model.

Some models also require an efficiency function, usually referred to as Γ, which accounts for the limited ability of small vortices (of size smaller than $\bar{\Delta}$) to wrinkle the flame front. The most common are,

- *Angelberger et al.* [9]

$$\Gamma_n = 0.75 \exp\left[-\frac{1.2}{\left(u'_\Delta/s_l^0\right)^{0.3}}\right]\left(\frac{\bar{\Delta}}{\delta_l^0}\right)^{2/3} \tag{7.15}$$

- *Charlette et al.* [56]

$$\Gamma_\Delta = \left\{ \left[\left(f_u^{-a_1} + f_\Delta^{-a_1} \right)^{-1/a_1} \right]^{-b_1} + f_{Re}^{-b_1} \right\}^{-1/b_1} \tag{7.16}$$

$$f_u = 4 \left(\frac{27}{110} C_k \right)^{1/2} \left(\frac{18}{55} C_k \right) \left(\frac{u'_\Delta}{s_l^0} \right)^2 \quad , \; C_k = 1.5 \tag{7.17}$$

$$f_\Delta = \left\{ \frac{27}{110} C_k \pi^{3/4} \left[\left(\frac{\bar{\Delta}}{\delta_l^0} \right)^{4/3} - 1 \right] \right\}^{1/2} \tag{7.18}$$

$$f_{Re} = Re_\Delta^{1/2} \left[\left(\frac{9}{55} \right) \exp \left(-\frac{3}{2} C_k \pi^{3/4} Re_\Delta^{-1} \right) \right]^{1/2} \quad , \; Re_\Delta = \frac{u'_\Delta \bar{\Delta}}{\nu} \approx 4 \left(\frac{u'_\Delta}{s_l^0} \right) \left(\frac{\bar{\Delta}}{\delta_l^0} \right) \tag{7.19}$$

$$a_1 = 0.60 + 0.20 \exp \left[-0.1 \left(\frac{u'_\Delta}{s_l^0} \right) \right] - 0.20 \exp \left[-0.01 \left(\frac{\bar{\Delta}}{\delta_l^0} \right) \right] \quad , b_1 = 1.4 \tag{7.20}$$

Adjustable constants are also used in several models, and these values are difficult to determine *a priori*. User-defined constants are considered in several models, notably in the model of Boger *et al.* [29, 30], Colin *et al.* [66], Angelberger *et al.* [9]. These last two authors as well as Charlette *et al.* [56] derived their model based on flame stretch study from DNS simulations of a flame vortex pair interaction [204], and express Ξ_Δ as,

$$\Xi_\Delta = 1 + a \Gamma_n \frac{u'_\Delta}{s_l^0} \tag{7.21}$$

where for Angelberger *et al.* [9], $a = 1$, which may lead to excessively high reaction rates. Thus, it needs to be adjusted on a simulation basis. Colin *et al.* [66] model a as a function of the turbulent Reynolds number defined as $Re_t = 4 \left(\frac{u'}{s_l^0} \right) \left(\frac{L}{\delta_l^0} \right)$ which helps recovering $\Xi_\Delta \approx 1 + u'_\Delta / s_l^0$ when all vortices (from L to η_k) wrinkle the flame front as follows from Damköhler theory [70]. In practice, the estimation of a global Re_t in a LES simulation remains problematic as local values of integral length scale and RMS fluctuations are unknown. Charlette *et al.* [56], on the other hand use a model that requires only two parameters (u'_Δ / s_l^0 and Δ / δ_l^0) by formulating their efficiency function, referred to as Γ_Δ in terms of the energy spectrum in homogeneous turbulence using the same dataset as Colin *et al.* [66], and improving at the same time the limiting behaviour.

Other authors use different correlations, but remain in spirit close to the aforementioned models (Fureby [98], Zimont [303] where s_T is approximated as a function of u'_Δ and Da_Δ, Gülder [120] derived from a simplified transport equation for Ξ_Δ and an equilibrium assumption, etc.).

Finally, Hawkes' model is the most recent considered in this work. It has been presented in [126] and aims at addressing the main shortcomings associated with other FSD models, namely their dependency to the filter size even in the absence of changes in the resolved to unresolved scale physics (regime change). Hawkes argues that the inner cut-off scale and fractal dimension should not depend on the filter size but as much as possible on the physics. This models is designed with the assumption of large turbulent intensity (large Ka number) and high-Reynolds number in mind, but also aims at asymptotically satisfy the laminar regime and $\Xi_\Delta = 1$ in the limit of small filter size (DNS limit). The inner cut-off and fractal dimension are both expressed as function of the Obukhov-Corrsin and Gibson length scales, while the fractal dimension ranges $D = 2.33 - 2.66$ or $D = 7/3 - 8/3$ [60]. It has been validated *a posteriori* against DNS results of a hydrogen shear-flames.

To summarise, the simplest closure considered in this work is a constant inner cut-off scale, as well as a constant fractal dimension model. It is known to be too coarse to represent properly the range of flame speeds and turbulence levels encountered in real flame accelerations [288], but constitutes a correct first order approximation. The effect of a finer modelling of the combustion source term will then be investigated in §. 8.5.5.

Model name	Reference	Wrinkling factor Ξ_Δ
Boger	[29, 30]	$\Xi_\Delta = \left(\frac{\bar{\Delta}}{3\delta_l^0}\right)^{D_f-2}$
BogerM	[29, 30, 98]	$\Xi_\Delta = \left(\frac{\bar{\Delta}}{3\delta_l^0}\right)^{D_f-2}$ $D_f = \frac{D_l}{\frac{u'_\Delta}{s_l^0}+1} + \frac{D_t}{\frac{s_l^0}{u'_\Delta}+1}$
Angelberger	[9]	$\Xi_\Delta = 1 + a\Gamma_n\left(\frac{u'_\Delta}{s_l^0}\right)$, $a = 1$
Charlette	[56]	$\Xi_\Delta = 1 + \min\left[\frac{\bar{\Delta}}{\delta_l^0}, \Gamma_\Delta\left(\frac{u'_\Delta}{s_l^0}\right)\right]^{0.5}$
Colin	[66]	$\Xi_\Delta = 1 + \alpha\Gamma_n\left(\frac{u'_\Delta}{s_l^0}\right)$ $\alpha = \frac{2\ln(2)}{3c_{ms}\left(Re_t^{1/2}-1\right)}$, $c_{ms} = 0.28$
FurebyM	[98, 191]	$\Xi_\Delta = 1 + \Gamma_n\left(\frac{u'_\Delta}{s_l^0}\right)^{D_f-2}$ $D_f = \frac{D_l}{\frac{u'_\Delta}{s_l^0}+1} + \frac{D_t}{\frac{s_l^0}{u'_\Delta}+1}$
Zimont	[303]	$\Xi_\Delta = 1 + 0.51\left(\frac{u'_\Delta}{s_l^0}\right)^{3/4}\left(\frac{\bar{\Delta}}{\delta_l^0}\right)^{1/4}$
Gülder	[120]	$\Xi_\Delta = 1 + 0.62\left(\frac{u'_\Delta\eta_k}{\nu}\right)\sqrt{\frac{u'_\Delta}{s_l^0}}$
Hawkes	[126]	$\Xi_\Delta = \left(1+\frac{\bar{\Delta}}{\eta_i}\right)^{D_f-2}$ $D_f - 2 = \frac{1}{3} + \frac{1}{3}\frac{L_{OC}^4}{L_G^4+L_{OC}^4}$ $\eta_i = \left(L_{OC}^4 + L_G^4\right)^{1/4}$ $L_G = 0.2\left(\frac{s_l^0}{u'_\Delta}\right)^3$ $L_{OC} = 5.5\left(\frac{D_c^3}{\varepsilon_\Delta}\right)^{1/4} = 5.5\left(\frac{(\nu/Sc_c)^3}{u'^3_\Delta/\bar{\Delta}}\right)^{1/4}$

Table 7.2: *List of selected algebraic flame wrinkling factor Ξ_Δ for the Flame Surface Density approach*

CHAPTER 8

Semi-confined explosions results

Since the 2000's, the use of LES solvers on massively parallel computers considerably increased the prediction capabilities of CFD, allowing the reproduction of transient reacting flows such as semi-confined explosions [76–80, 115–118, 123, 136, 137, 156, 200, 249]. Computational studies highlighted the increased accuracy of the LES approach over the URANS modelling by capturing the flow fine structures governing the explosions dynamics (acceleration and deceleration when the flame is interacting with obstacles, laminar to turbulent propagation mode transition, flame wrinkling, formation of pockets, etc.) which are necessary for an accurate prediction of the flame speed and generated overpressure.

The results presented in this chapter are building upon these previous studies. The Sydney combustion chamber [151] is here studied using a fully-compressible low-dissipation shock-capturing LES solver relying on the Flame Surface Density formalism for modelling the flame/turbulence interaction.

- In a first section, a short theoretical and one-dimensional analysis of the different wrinkling factor models considered in this work is presented. This helps extracting trends that are used later to explain the flame behaviour (§. 8.2.1).
- The application of these models to the simulation of the full three-dimensional geometry of the combustion chamber is then presented, with an emphasis on the LES validation with direct comparison with available experimental data, and on the understanding of the processes governing such flows. The quality of the presented simulations is also evaluated (§. 8.3).
- A study of the influence of several parameters on the flame behaviour and results reliability is discussed (§. 8.5), while the geometry effects on the flame characteristics are also presented (§. 8.6).

8.1 Numerical set-up

This section outlines the different numerical parameters, grids, sub-models employed for the LES computations of the Sydney test case in three dimensions.

8.1.1 Computational domain and grids

The computational domain is constituted by the combustion chamber of dimension $50 \times 50 \times 250\,[mm]$ and was extended in all directions by $250\,[mm]$ to create a plenum chamber designed to avoid pressure reflections at the boundaries. The mesh is coarsened in this region to increase the damping effect on the pressure as visible in Fig. 8.1.

The calculations presented in the next sections have been mainly carried out on a fine grid of roughly 7×10^6 cells with a characteristic size of $\Delta_x = \Delta_y = \Delta_z = 0.5\,[mm]$ in the chamber and then expanded with a ratio of approximately 1.1 in all directions in the plenum. A longitudinal cut of the mesh for the configuration BBB0 is presented in Fig. 8.1. In order to investigate the effect of grid resolution, two other

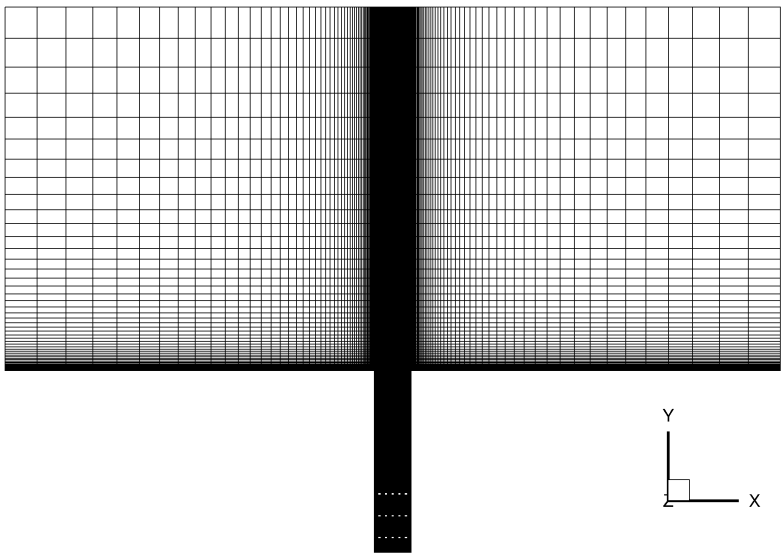

(a) *Mesh with damping plenum*

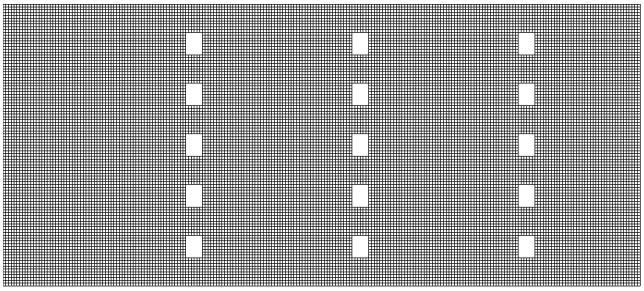

(b) *Zoom on the obstacles of the combustion chamber*

Figure 8.1: *Longitudinal cut through the fine computational grid used for the simulation of the Masri BBB0 configuration*

grids have been build, with cell sizes of respectively $\Delta_x = \Delta_y = \Delta_z = 1\ [mm]$ and $\Delta_x = \Delta_y = \Delta_z \approx 1.5\ [mm]$ and with a total number of cells of respectively 1.2×10^6 and 6×10^5 cells.

8.1.2 Numerical and physical parameters

The LES solver employed in this study is the in-house code referred to as `FlAMEnCo3D` and validated in the previous chapters, resolving the compressible Navier-Stokes equations in a fully-compressible manner on block-structured curvilinear grids presented in Fig. 8.1. The governing equations are integrated on the computational grid using the MUSCL5 variable reconstruction scheme and the RK2-SSP time integration scheme. The Low-Mach number correction is also applied in order to finely resolve the small scale turbulent structures and helps in maintaining the stability of the computations when large cells are used.

Diffusion coefficients for these calculations have been taken as $Sc = 0.7$ and $Pr = 0.7$ yielding a unity Lewis number. Turbulent parameters have also been selected at $Sc_t = 0.7$ and $Pr_t = 0.7$ following the

settings of Di Sarli *et al.* [77,78]. The Smagorinsky constant has been set to $C_s = 0.16$.

The laminar flame properties for an hydrogen flame, i.e. its laminar flame speed and thermal thickness also have to be specified as they represent the most critical parameters for the wrinkling factor modelling. The choice of these values presents a certain complexity given the wide range of values available in the literature. This is highlighted in §. 8.5.3. The baseline values used in this work have been extracted using the Westbrook H_2/air mechanism presented in previous chapters with a stoichiometric ratio of $\phi = 0.7$ and $T_{in} = 300\,[K]$, yielding $s_l^0 = 1.02\,[m/s]$ and $\delta_l^0 = 0.35\,[mm]$.

In this work, hydrogen flames are considered, and the following one-step irreversible equation using 4 species (H_2, O_2, N_2, H_2O) is assumed to represent the overall reaction,

$$2H_2 + O_2 + 3.76N_2 \rightarrow 2H_2O + 3.76N_2 \tag{8.1}$$

As the considered mixture is lean ($\phi = 0.7$), there is some oxygen left in the products mixture, and the nitrogen is considered inert. In the FSD framework, species mass fractions are not given by solving a species transport equation, but are derived based on the above reaction equation and the progress variable definition, and yields,

$$Y_{H_2} = (1-c)\,Y_{H_2}^u \tag{8.2}$$

$$Y_{H_2O} = cY_{H_2}^u \frac{W_{H_2O}}{W_{H_2}} \tag{8.3}$$

$$Y_{N_2} = 1 - Y_{O_2}^u - Y_{H_2}^u = Y_{N_2}^u \tag{8.4}$$

$$Y_{O_2} = 1 - Y_{N_2} - Y_{O_2} - Y_{H_2} = Y_{O_2}^u - cY_{H_2}^u \frac{W_{O_2}}{2W_{H_2}} \tag{8.5}$$

Using the species mass fractions given by these relations, the mixture viscosity, molar mass and other thermodynamic properties can be determined.

8.1.3 Initial and boundary conditions

Boundary conditions

As pointed during the computational grid presentation, the explosion chamber surrounding air is accounted for using a plenum in the LES calculations. At the boundaries of the plenum, outflow boundary conditions are applied. It shall be noted that given the complexity of NSCBC boundary conditions in multi-dimensional domains, and especially in corner regions, coupling of different boundary types (wall and outflow, etc.), etc. they have not been implemented `FlAMEnCo3D`. Therefore, only simple zero gradient boundary conditions are considered for the multi-dimensional simulations presented in this chapter, hence, the outflow conditions considered here are the ones presented in §. 4.6.6.

The walls of the chamber, as well as the obstacles have been simulated using adiabatic non-slip wall conditions which constitutes a similar settings as the other semi-confined LES analysis presented in the literature [79,117] using similar mesh sizes. Note that this does not allow the resolution of the boundary layers ($y^+ \approx 20-80$). It shall also be noted that no wall functions have been used to account for boundary layers effects. The momentum equation turbulence modelling is purely implicit as highlighted in §. 3.7, and the Reynolds stress tensor terms are modelled solely by the numerical diffusion of the algorithm (ILES approach). This implies that the flow modelling close to the walls might not be optimal. Indeed, it has been shown that ILES could successfully simulate wall-bounded flows when the boundary layer was fully resolved ($y^+ \approx 1-5$) [86,99,302], but little is known on its capability of simulating wall-bounded flows with non-resolved boundary layers and this question still leads to *unresolvable controversies amongst LES practitioners* [33]. It can be estimated that an increased dissipation near walls will result from such a modelling, which could increase pressure losses in the chamber.

To improve the wall modelling, several options are available. The most natural would be to use a model that takes into account local flow conditions, such as a dynamic Smagorinsky formulation, or the WALE turbulent viscosity [90]. However, this option do have the negative effect of adding a viscous dissipation of turbulent kinetic energy in the whole flow field. It would thus render the ILES computations too dissipative as the current algorithms numerical dissipation has been designed to represent the natural turbulent kinetic energy decay. However, it would improve the progress variable turbulent diffusion that is modelled with a constant Smagorinsky model. A second option would be to resolve boundary layers with a mesh refinement, but this would prove to be overly expensive. A third option would be to consider that momentum dissipation is modelled with the correct order of magnitude by the ILES approach, but that progress variable turbulent diffusion is too strong close to the walls due to the static Smagorinsky modelling. To counteract that, one could set $C_s = 0$ in the cells directly in contact with walls to account for flame quenching due to heat losses.

Initial conditions

The initial mixture initialised in the domain is similar to the experiment, and is a hydrogen/air mixture with $\phi = 0.7$, yielding an initial composition given by,

$$Y^u_{H_2} = \frac{1}{1 + \frac{s}{\phi}\left(1 + 3.76\frac{W_{N_2}}{W_{O_2}}\right)} \tag{8.6}$$

$$Y^u_{O_2} = \frac{s}{\phi} Y^u_{H_2} \tag{8.7}$$

$$Y^u_{N_2} = 1 - Y^u_{H_2} - Y^u_{O_2} \tag{8.8}$$

and $Y^u_{H_2} = 0.02014$, $Y^u_{O_2} = 0.2283$ and $Y_{N_2} = 0.75156$.

During the experiments, the mixture is put to rest for a given time such that most turbulent structures are damped by viscosity. A quiescent velocity field is thus used in the majority of the LES simulations of the Sydney explosion chamber presented in the literature. However, in this research work, a turbulent background velocity has been used with velocity fluctuations $u' \approx 0.1 s^0_l$ and $l_t \approx 5\,[mm]$ or 10% of the combustion chamber width as experimentally determined by Masri *et al.* [201]. Kempf *et al.* [150] methodology has been used for the turbulent generation and is highlighted in Appendix C. This value of turbulent velocity has been shown to have no effect on the flame propagation (§. 8.5.2) but is strong enough to let the problem inherent symmetry be broken by a physical mechanism (non-symmetric flow field) rather than by accumulated numerical errors.

Finally, the ignition process is not simulated as it involves numerous highly complex physical phenomena (plasma formation, energy transfer between a plasma and a gas, shock waves generation, transfer of energy between the laser beams and a gas, etc.). In order to avoid this complex modelling, and following a similar procedure as Di Sarli *et al.* [79], Gubba *et al.* [117], and Quillatre [249], a small sphere of radius $5\,[mm]$ is initialised with a unity progress variable. It has been found that this hemisphere held enough energy to initiate the flame propagation in the chamber. This coarse modelling is not problematic for the current simulations as it only impacts the combustion timing (§. 8.5.2) but as the experimental time to peak is not reliable (§. 7.2.4), it is of little relevance.

8.2 One-dimensional preliminary results

The one-dimensional analysis of the different wrinkling factor models considered in this work consists of two parts. The first one (§. 8.2.1) evaluates the theoretical behaviour of the different models when subjected to several turbulence intensity levels. The second part (§. 8.2.2) focuses on the flame speed obtained with these models. It shall be noted however that this one-dimensional analysis only gives an illustration of the different models behaviours and can only be used to assess some trends. As the current analysis is simplified, the presented results may not apply to the general case.

8.2.1 Theoretical behaviour of the different models for Ξ_Δ

This section is interested in looking at the different models responses to turbulent fluctuations changes in the flow field. The different wrinkling factors are plotted as functions of the normalised turbulent intensity (u'_Δ/s_l^0). The laminar flame quantities are taken to be similar to the values used in the main LES study and presented in §. 8.1 while the cell size is $\Delta x = 0.5\,[mm]$. When needed, the kinematic viscosity has been approximated by the kinematic viscosity of air at $T = 300\,[K]$, a Kolmogorov scale of $\eta_k = 10^{-5}\,[m]$ has been assumed, and following the experimentally measured value, $l_t = 5\,[mm]$ [201]. For the Colin model, the turbulent Reynolds number is calculated as $Re_t = \dfrac{4u'l_t}{s_l^0\delta_l^0}$, where it is assumed that $u' \approx u'_\Delta$.

Fig. 8.2 depicts the variation of Ξ_Δ with u'_Δ/s_l^0, this could also be plotted as a function of the Karlovitz number. Indeed, by making the assumption that the laminar flame speed and thickness are independent of the temperature and pressure (which is what has been used in the this work), the Karlovitz number is solely a function of the turbulent intensity. Thus, it represents the main parameter of such a simulation, and flame wrinkling factor is expected to increase from $\Xi_\Delta = 1$ at $Ka = 0$ ($u'_\Delta = 0\,[m/s]$) to values that are model dependent when Ka increases.

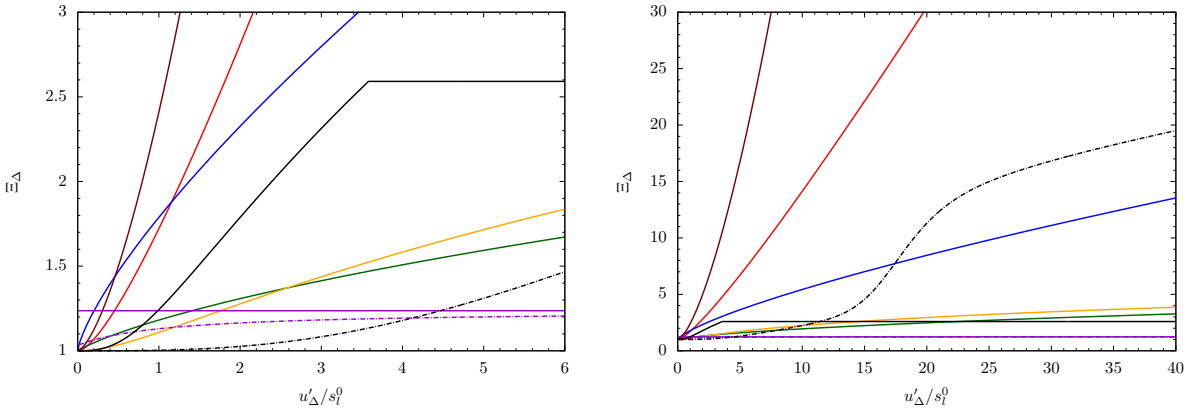

Figure 8.2: *Flame wrinkling factor Ξ_Δ as a function of the normalised turbulent intensity u'_Δ/s_l^0 for the different SGS models - — Charlette, -·- Hawkes, — Angelberger, — Colin, — Zimont, — FurebyM, — Boger, -·- BogerM, — Gulder*

Peters [231] shows that Ξ_Δ increases linearly at low u'_Δ/s_l^0 based on experimental data of Abdel-Gayed and Bradley [2]. As turbulence intensity increases, what is referred to as a "bending effect" by Ma *et al.* [191] is observed, until Ξ_Δ eventually becomes insensitive to the increasing u'_Δ/s_l^0. From models presented earlier, most of them follow the proposed trend, at the exception of Angelberger [9], Charlette [56], Fureby [98] and Gülder [121]. As presented in Ma *et al.* [191], it was found in *a priori* studies that many of these models tend to over-predict FSD in the *thin reaction zone* regime, as they share a common assumption of equilibrium between the generation and destruction of FSD, and the estimation of $s_d = s_l^0$. This latter assumption can prove inaccurate for the higher flame curvature encountered in the *TRZ*. For this reason, the Angelberger model features an ever-increasing wrinkling factor for increasing turbulence intensities, and no bending effect is observed. The limiting behaviour of the Charlette model at high u'_Δ/s_l^0 is clearly visible, as the wrinkling factor get clipped such that the inner cut-off scale is limited to the laminar flame thickness. For the Fureby model, the limiting behaviour is build into the fractal dimension so that the curve looks somewhat similar to the expected one. It can be seen that three models (Angelberger, Zimont and Gulder) feature a sharp increase of the wrinkling factor at low turbulence intensity, which could pose problems in the simulation of accelerating flames, as almost no laminar propagation would be allowed with these models.

Fig. 8.3 presents a glimpse at some models behaviours when changing parameters values, namely the Hawkes, Angelberger and Charlette models. Charlette and Hawkes models have wrinkling factor that

depends on the kinematic viscosity. Hawkes model appears quite sensitive to the viscosity value, and as temperature increases (and the viscosity with it, following Sutherland's law), the wrinkling factor value decreases noticeably (wrinkling factor decreases by 50% when the temperature increases by 500%, i.e. a change of viscosity of 2200%). This would cause the flame computed with Hawkes model to have shallower progress variable gradient at the tail, as for a given turbulence intensity, the reaction rate will decrease in the higher temperature regions. Similarly, for Charlette's model, the saturation limit is reached faster at lower temperatures and lower wrinkling factors are found at high temperatures. Finally, following the suggestion of Ma *et al.* [191], the constant of the Angelberger model in front of the efficiency function is reduced from unity to $a = 0.2$ such that comparable magnitudes in Ξ_Δ values with the other models are observed. However, this does not change the ever-increasing behaviour of the model.

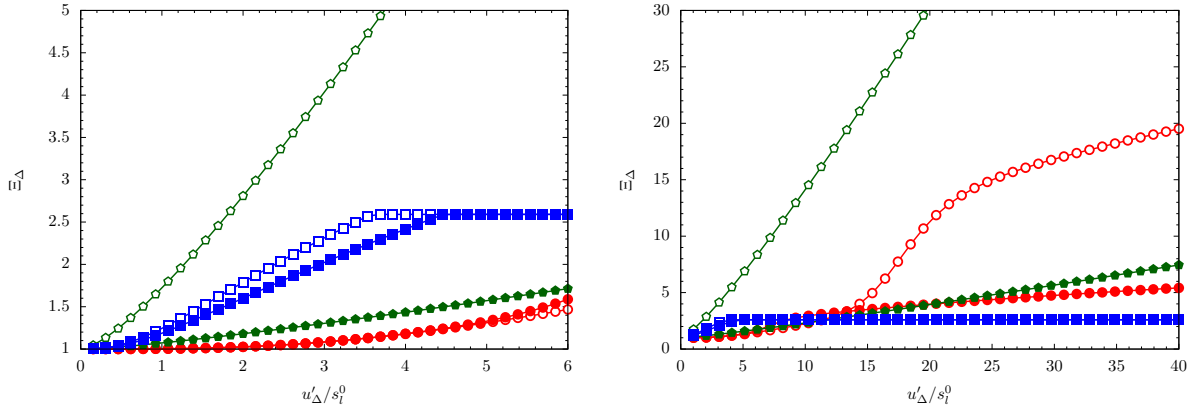

Figure 8.3: *Variation of the flame wrinkling factor Ξ_Δ as a function of the normalised turbulent intensity u'_Δ/s^0_l for the different SGS models -* ○ *Hawkes $\nu = \nu\,(300\,[K])$,* ● *Hawkes $\nu = \nu\,(1500\,[K])$,* □ *Charlette $\nu = \nu\,(300\,[K])$,* ■ *Charlette $\nu = \nu\,(1500\,[K])$,* ⬠ *Angelberger $a = 1$,* ⬟ *Angelbeger $a = 0.2$*

Considering the Masri test case which features long laminar growths and laminar interactions with obstacles, the need to have a SGS model that predicts moderate wrinkling values ($\Xi_\Delta < 4$) at moderate Karlovitz number ($Ka_\Delta \approx 10$) encountered during the early flame/obstacles interactions is clear. From the theoretical analysis, it can be inferred that both Zimont and Gülder models would predict too large wrinkling factors values and would be unable to capture the different laminar propagation phases. On a similar test case but computed with the TFLES approach [249], Charlette's model was found to yield flame speeds that were too large compared to Colin model predictions and experimental measurements. Even though the fuel and thus the laminar flame quantities were different, this would mean that all models predicting larger wrinkling factors than the Charlette's model at moderate Karlovitz number would be over-predicting the wrinkling factor needed in the Masri test case. It was thus decided to discard both the Zimont and Gülder models in the remaining of the analysis, however the modified Angelberger ($a = 0.2$) model is kept.

8.2.2 Turbulent flame speeds

Numerical set-up

In order to measure the flame speed obtained with these different models, one-dimensional flames are computed. The set-up of this case is similar to the one considered for the one-dimensional laminar flame calculations presented in §. 5.4.2 and uses the same code, i.e. `FlAMEnCo1D`. The flame propagates into a burnable mixture of hydrogen/air with $\phi = 0.7$, and is held in a constant position by means of a varying inlet velocity controlled by the algorithm outlined in §. 5.4.2 using the newly developed NSCBC conditions for the QCVF model (more details in Appendix D and §. 4.6). The numerical parameters and models are the one presented in §. 8.1 for the different transport coefficients, laminar flame quantities, etc.

The study assumes $u' \approx u'_\Delta$ in the whole domain, and using Eq. 7.14, the turbulent viscosity value

is $\nu_t = C_s \bar{\Delta} u'_\Delta$ is imposed throughout the domain. This means that the flame propagates into a frozen turbulent field, where the turbulence intensity is independent of both space and time. As pointed out earlier this constitutes and oversimplification of the actual three-dimensional results where the turbulent diffusivity varies in the flame front and is far from constant in the domain.

The domain is $L = 12\,[cm]$ long and discretised with $Nx = 240$ cells, yielding $\Delta_x = 0.5\,[mm]$, while the solution is computed with the QCVF method coupled with the MUSCL5 variable reconstruction scheme and the time is integrated with the RK2-SSP technique with $CFL = 0.5$.

Findings

The computed flame speeds for the different models at the different turbulent intensities are presented in Fig. 8.4. The results presented concur with the findings discussed in the previous section. At low turbulence intensity, all models except the Boger's model lead to $s_T \approx s_l^0$. Charlette's model yields consistently larger wrinkling factor than any other models up to $u'_\Delta/s_l^0 \approx 10$ and thus the largest flame speed, while Hawkes' model yields the maximum flame speeds at very high turbulence levels, which can be explained in part by the larger fractal dimension considered ($D \approx 8/3$). The flame speed computed with the Hawkes' model also becomes the largest for intensity larger than $u'_\Delta/s_l^0 \approx 10$, which is in good agreement with the theoretical predictions. Except at low turbulence intensity ($u'_\Delta/s_l^0 < 5$), both the Boger and BogerM models yield very similar results, which indicates that not much difference should be observed for the three-dimensional simulations when using these models.

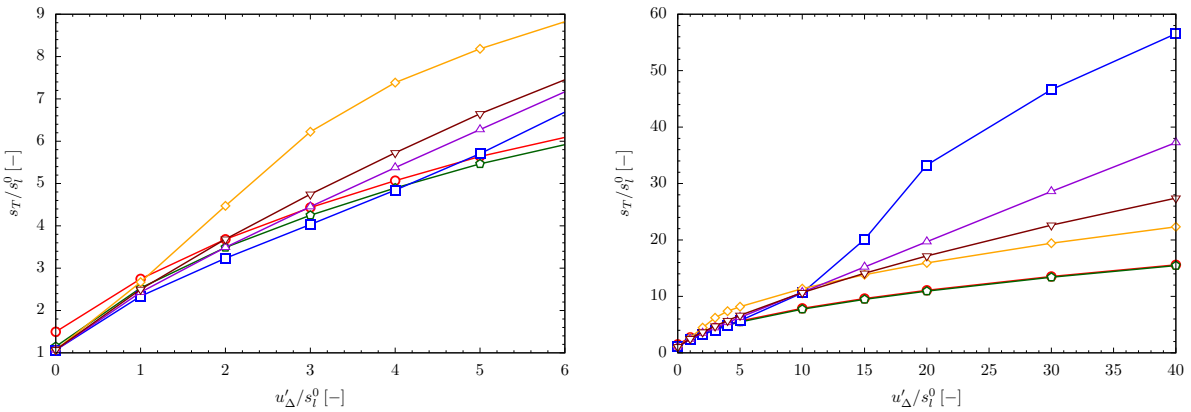

Figure 8.4: *Turbulent flame speed (s_T/s_l^0) as a function of the turbulence intensity (u'_Δ/s_l^0) for different Ξ_Δ models computed with the QCVF model and the thermally perfect EoS - Boger, BogerM, Hawkes, Charlette, Angelberger, FurebyM*

An example of progress variable profile is depicted in Fig. 8.5, where Hawkes' model has been used. Flame profiles get thicker as the turbulence intensity increases, which is expected behaviour. Indeed, the progress variable turbulent diffusivity increases linearly with the turbulent intensity, while the increase is slower for the reaction rate, leading to a thickening of the flame. It can also be remarked that as predicted in the previous section the progress variable gradients are shallower on the products side when using the Hawkes' model due to the reduced value of the wrinkling factor at high temperatures.

8.3 LES validation and quality

The results presented in this section aim at validating qualitatively and as much as possible quantitatively the current LES approach applied to explosion studies through three main criteria,

- Estimating characteristic explosions phenomena (overpressure, flame speed, flame shape)
- Reproducing geometry modifications effects on the flame propagation

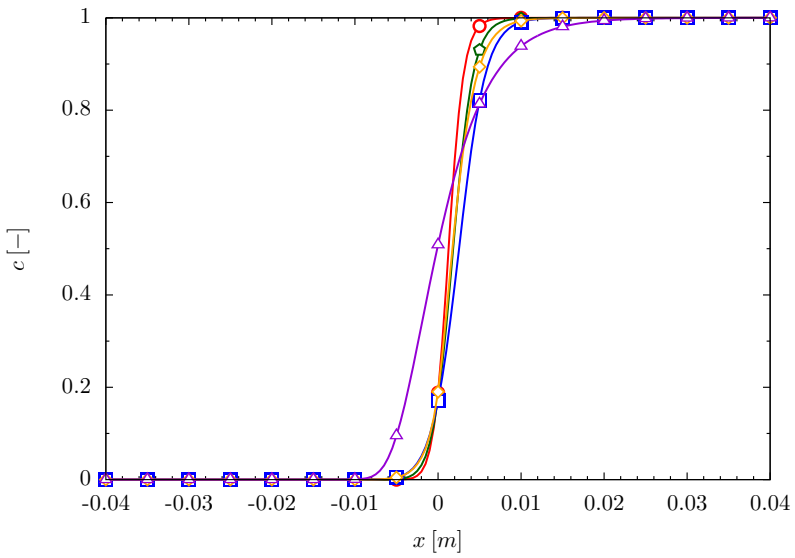

Figure 8.5: *Turbulent flame progress variable profile as a function of the turbulence intensity (u'_Δ/s_l^0) for the Hawkes model computed using the QCVF approach and the thermally perfect EoS -* ○ $u'_\Delta/s_l^0 = 1$, ⬠ $u'_\Delta/s_l^0 = 2$, □ $u'_\Delta/s_l^0 = 5$, ◇ $u'_\Delta/s_l^0 = 10$, △ $u'_\Delta/s_l^0 = 20$

- Quantifying the LES quality

8.3.1 Characteristics of semi-confined explosions

The objective of this section is to extract and analyse the characteristic parameters and behaviour of the simulated flames and compare it with available experimental data. To this end, results obtained on the BBB0 configuration with the QCMF model will be analysed qualitatively in terms of flame shape and quantitatively in terms of the flame speed and overpressure generated. The combustion model considered in this section is the Boger model with a constant fractal dimension of $D = 2.33$ which, as already pointed out, would give a coarse approximation of the different quantities. Thus the results presented in this section are mainly indicative of the capabilities of the current LES framework and aims at validating its behaviour. The accuracy of the results will be discussed when evaluating the performance of the different combustion models in §. 8.5.5.

Flame shape

Fig. 8.6 (left) shows the flame propagation for the BBB0 configuration as obtained experimentally using the LIF-OH imaging technique [123]. The obstacles have been added in post-processing by the author to help the understanding. The corresponding LES results are shown in Fig. 8.6 (right) for similar flame positions, where a good agreement is observed between the two sets.

During the first propagation steps, the laminar flame propagates with an hemispheric shape (not shown here). This long initial growth controls the flame strength and shape upon interaction with the first baffle. It can be noted that due to the small distance between the first baffle and the ignition point, the flame still features an hemispherical shape when hitting the grid, as it did not have the time to elongate in a finger shape.

When interacting with the first grid (noted *g1*), fingers are created through the two central obstacles, followed quickly by two other fingers through the lateral intervals. The four fingers thus created merge while propagating downstream towards the second baffle. The flame structure is still laminar at this point, but starts to get slightly wrinkled due to the low turbulence levels encountered. Small pockets

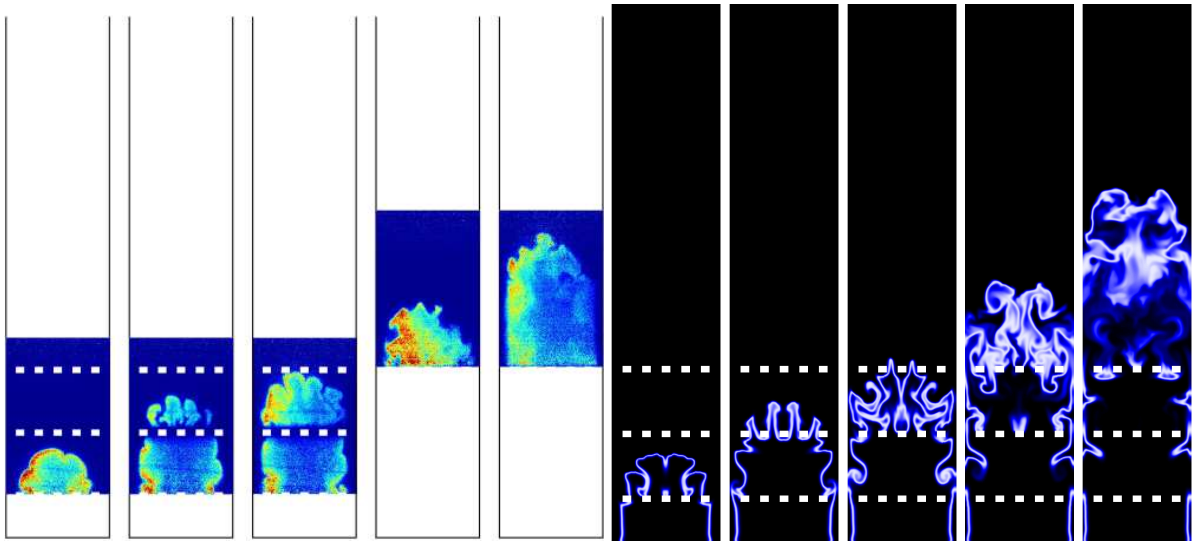

(a) *Experimental data* **(b)** **(c)** **(d)** **(e)** **(f)**

Figure 8.6: *Flame propagation in the BBB0 configuration - (a) Experimental LIF-OH images, (b)-(f) LES reaction rate computed with the QCMF approach, Boger model ($D = 2.33$) and the thermally perfect EoS - Time intervals are similar between the LES and experimental visualisations, t_0, $t_0 + 0.4\,ms$, $t_0 + 0.8\,ms$, $t_0 + 1\,ms$ and $t_0 + 1.2\,ms$*

of fresh reactants can potentially form behind the obstacles, but unlike the LPG and CNG fuels where these pockets take a long time to consume, the faster hydrogen flame consumes them relatively quickly. The qualitative agreement between the experimental and computational results up to this point is quite good as the different fingers and their merging are quite well reproduced by the LES.

When interacting with the second grid (noted *g2*), four fingers are created almost simultaneously through the central strips of the grid, and due to the higher turbulence levels get quickly wrinkled. Due to fastest flame speeds, the fingers do not have the time to completely merge before their interaction with the third baffle plate (noted *g3*) in the LES, but seems to do so in the experimental results. It seems that the LES is predicting larger flame speeds at this time, as the flame shooting through *g2* expands to occupy the full width of the channel while experimental results show that it remains relatively far from the side walls.

The flame, which has now transitioned to a turbulent propagation mode, accelerates even more and impacts strongly the top grid generating a large amount of turbulence in the process. The fingers generated through the six intervals do not have the time to develop and merge due to the intense turbulence. The resulting flame front then propagates at high speed towards the exhaust of the chamber, where the pocket of reactants pushed outside the chamber by the expanding products will be consumed.

From these visualisations, it can be seen that the different propagation phases of a flame in a semi-confined explosion are qualitatively well reproduced, even if some differences can be observed with experimental measurements.

Speed and position of the flame

The position and speed of the flame for the BBB0 configuration predicted by the LES simulations are compared with the experimental values in Fig. 8.7. The position of the flame is measured in the sim-

ulations following a process similar to the experiment, i.e. the point defined by $\tilde{c} = 0.5$ positioned the furthest from the ignition point is taken as the flame front position. The speed is then simply determined using first-order derivative calculations.

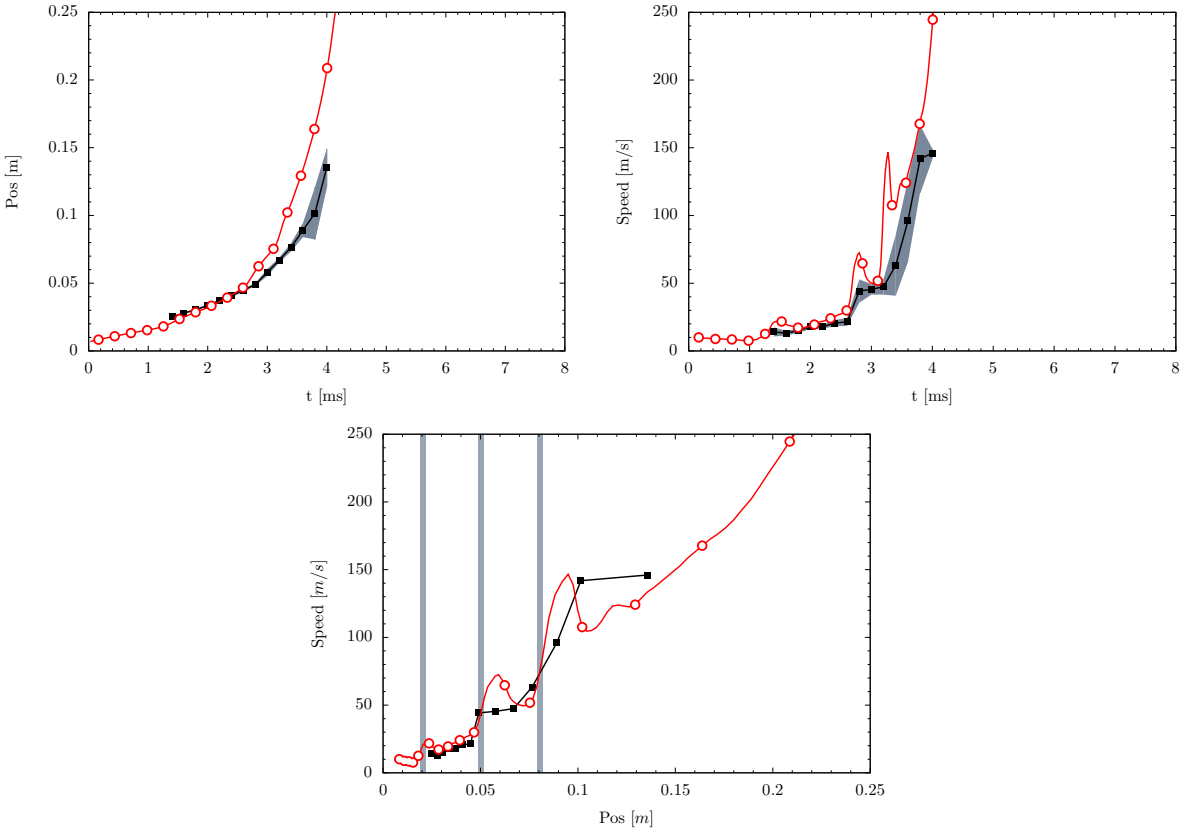

Figure 8.7: *Comparison between the experimental and computed flame speed and position for the BBB0 configuration with Boger model ($D = 2.33$) and the thermally perfect EoS - ■ Experimental values, ○ QCMF - Greyed areas depict obstacles*

Before the first obstacle, the flame propagates at an average speed of $7.5\,[m/s]$ which is slightly higher than the speed of the spherical flame as expressed by Poinsot and Veynante [238] and given by $s_a = \frac{\rho_u}{\rho_b} s_l^0$, which in our case would give $s_a \approx 6.3\,[m/s]$. This higher value is easily explained by the fact that even though the flame is in a laminar propagation mode, the combustion model employed here (Boger) does not degenerate correctly to a unity wrinkling factor at low turbulence intensity due to the constant fractal dimension assumption. This means that even though the flame should be laminar, the reaction rate given by Boger's model corresponds to a weakly turbulent flame, and is approximately 23% higher which corresponds almost exactly to the flame speed over-prediction. This flame would be, and actually is found slower for the other models that degenerate correctly to the wrinkling factor laminar value, e.g. when using Hawkes' model, a speed of $6.5\,[m/s]$ is found.

At the first grid, the flame acceleration is primarily due to the flow restriction caused by the strips, but also to the weak wrinkling that increases its surface. The burning rate remains laminar in the whole front but is applied on a larger reacting surface, thus leading to an increased overall reaction rate, and to a increase of the propagation velocity. The flame then slows down noticeably when expanding between grids *g1* and *g2* due to expansion hydrodynamics effects.

A second acceleration is observed when the flame interacts with the second grid, but as the flame is faster when impacting the obstacle ($s_t \approx 30\,[m/s]$ instead of $s_t \approx 10\,[m/s]$), the flame speed increase resulting from the restriction is larger ($\Delta s_t \approx 20\,[m/s]$ compared to $\Delta s_t \approx 10\,[m/s]$). It shall also

be noted that the flame speed roughly doubles every time it passes through a grid. The wakes turbulence intensity keeps increasing and the total flame surface area also keeps increasing thus leading to a flame speed increase and strong wrinkling. Using a model sensitive to turbulence (Angelberger, Hawkes, BogerM, etc.) would also result in an increase of the wrinkling factor, as some of the flame wrinkling is not resolved any more and needs to be modelled. The speed obtained after the second obstacle already reaches $s_t = 70\,[m/s]$ compared to the $s_t \approx 25\,[m/s]$ found after the first obstacle (almost multiplied by 3), and $s_t \approx 25\,[m/s]$ found by Quillatre [249] for the C_3H_8 stoichiometric mixture.

The interaction between the flame and *g3* is even stronger than with *g2* as the speed of the flame now reaches almost $s_t \approx 150\,[m/s]$ after the obstacle. A very strong turbulence is also created, which without a static combustion model (constant fractal dimension) could create an even larger acceleration due to an increase of the local reaction rate. The deceleration after the grid is also noticeable as the flame reaches the final volume of the chamber where it can expand without any obstruction. After this, the flame occupies the whole chamber width and pushes the fresh gases ahead at an ever increasing speed up to the exhaust plane, where the speed reaches $s_t \approx 250\,[m/s]$.

The departure from the experimental curves are explained by the large flame speeds reached after grid *g2*. Indeed, considering that the acquisition frequency of the imaging system is $f = 5\,[kHz]$, meaning that an image is obtained every $2 \times 10^{-4}\,[s]$, a flame propagating at $s_t \approx 70\,[m/s]$ (which is a low estimate reached after $2.3\,[ms]$) would have travelled $d = 1.4\,[cm]$ between two acquisitions which is too much for a precise estimation of its speed. This is clearly visible in the last section of the domain, where the experimental measurements do not capture the flame deceleration after the third baffle, while a stabilisation of the flame speed has been captured after both *g1* and *g2*.

Overpressure

As already pointed out, a semi-confined explosion generates a strong overpressure, which is the critical parameter in the case of safety analysis. Fig. 8.8 presents the comparison between the measured and computed overpressure values at the two sensor positions. The numerical results are compared with the experimental results and the standard mean deviation after 50 experimental runs as explained in §. 7.2.4. For both sensors, the overpressure is under predicted by the LES computation, although the timing is correctly reproduced. The wall sensor positioned after the grids features an under-prediction of the overpressure by almost 50% compared to the experimental value, while the base value is under-estimated by 25%. The difference between the two values indicates that the current calculation predicted significantly more pressure losses due to the obstacles than the experiment ($-10\,[kPa]$ for the LES and $0\,[kPa]$ experimentally between the base and wall peak overpressures).

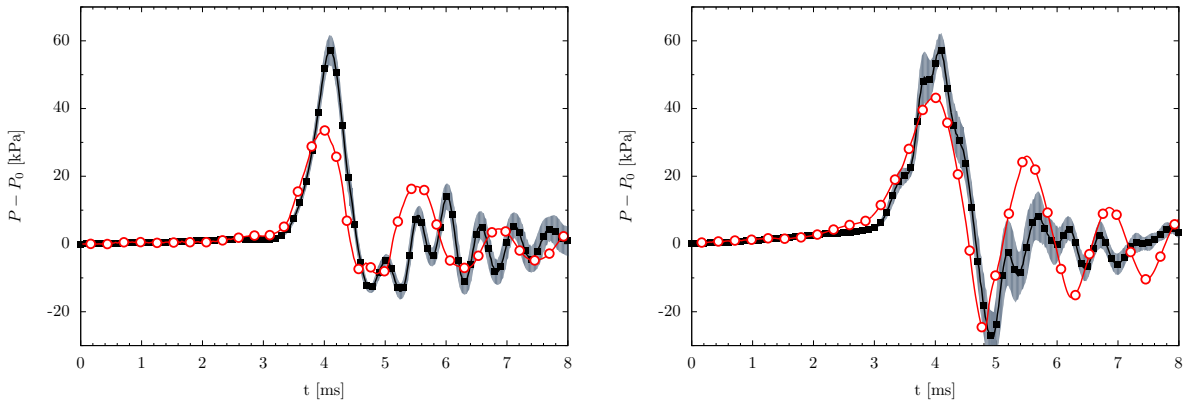

(a) *Wall sensor* **(b)** *Base sensor*

Figure 8.8: *Comparison between the experimental and computed overpressure for the BBB0 configuration - ■ Experimental values, ○ QCMF LES results with Boger model ($D = 2.33$) and thermally perfect EoS*

This increased losses can be related in part to what has been pointed out regarding the turbulence modelling choices of this work, especially in the near-wall regions. It was inferred that under-resolved walls computed with ILES would lead to two effects, the first one being an over-prediction of the dissipation of turbulent kinetic energy near walls due to a boundary layer being too thick. This in turns leads to increased pressure losses as the flame propagates towards the exhaust. A second effect, would be that as boundary layers thickness are over-predicted, the actual blockage ratio experienced by the flame is higher than what it should be, and this would lead to both an increase of the flame speed at the flame shoots through grids *g1* to *g3* (which is observed and leads to a large expansion of the flame between *g2* and *g3*) and to an further increase of pressure losses. However, it can be noted that this only constitutes an educated guess, and only precise measurements of the current ILES technique behaviour in non-reacting wall-bounded flows could answer accurately to this question.

The acoustic reflections (pressure oscillations) observed experimentally after the initial peak of pressure are not very well reproduced in the current calculation, both in amplitude and frequency. This does not represent a major parameter of the simulation, but still constitutes an interesting phenomena to capture. Several reasons could explain this, the first one being the different geometry, where in the CFD domain a plenum has been attached to the top of the chamber, while in the experiment, the pressure waves can also expands downward at the exhaust around the experimental rig. In our case, this is not possible. A second reason could be linked to the plenum size too small to properly damp pressure waves, or even to the computation which does not deal correctly with the reactants combustion outside of the chamber, where it has been pushed by the hot expanding products. The final reason could be associated with the domain boundaries where a zero-gradient is applied, which is known to cause pressure reflections when the actual gradients are non negligible.

As explained in both Di Sarli *et al.* [78] and investigated by Quillatre [249] using a 0D code, the pressure increase inside the chamber is due to two competing mechanisms, the combustion rate ($\mathcal{V}_{comb}$) and the venting rate ($\mathcal{V}_{vent}$). The combustion leads to an increase in pressure due to the conversion of the dense reactants into light hot expanding products and their subsequent accumulation. On the other hand, the fresh mixture escaping the chamber through the exhaust contributes to a decrease in pressure by through a venting mechanism.

Following Quillatre [249], a precise volumetric analysis can be done to investigate the overpressure origins. The venting rate is simply defined as the flow rate exiting the chamber through the exhaust and reads,

$$\mathcal{V}_{vent} = \int_{Exhaust} v \, \mathrm{d}S \tag{8.9}$$

where v is the velocity component normal to the exhaust section, corresponding to the y-direction in our computations. By considering that reactants with a density ρ_u have been replaced by products with a density ρ_b and were occupying a volume $V_u = \dfrac{\rho_b}{\rho_u} V_b$, the volumetric combustion rate can be written as the temporal variation of the volume of gas created by the combustion within the chamber. This is expressed as the temporal variation of the difference between the products and reactants volumes, or,

$$\mathcal{V}_{comb} = \frac{\partial}{\partial t}\left(V_b - V_u\right) = \frac{\partial V_b}{\partial t}\left(1 - \frac{\rho_b}{\rho_u}\right) \tag{8.10}$$

The volume of burned gas variation can be simply linked to the reaction rate of H_2O following,

$$\frac{\partial V_b}{\partial t} = \frac{1}{\rho_b} \int_{\mathbb{V}} \dot{\omega}_c \, \mathrm{d}v \tag{8.11}$$

where $\mathbb{V}$ is the chamber volume.

Based on these relations, it can be inferred that when $\mathcal{V}_{comb} > \mathcal{V}_{vent}$, the pressure increases in the chamber, and vice versa. Fig. 8.9 depicts for the BBB0 geometry both flow rates and the overpressure

at the base of the chamber. The first three vertical lines indicate the times at which the flame reaches the different grids. It is very interesting to note the coincidence between the overpressure peak and the change of sign of $\mathcal{V}_{comb} - \mathcal{V}_{vent}$ (first dashed vertical line). After the initial pressure peak, the acoustic oscillations are well predicted by the competition between venting and combustion rates, indicating that the boundary conditions, or the computational domain might not be responsible for the discrepancies observed with the experimental measurements, but the combustion model might be. These oscillations are basically the mechanism by which the pressure in the chamber comes back to its equilibrium value which is the far-field or atmospheric pressure. When the combustion is stronger than the venting, pressure increases which is followed by a time during which venting rates are higher and the pressure decreases. Oscillations amplitude thus decreases with time until $P_{chamber} \approx P_0$.

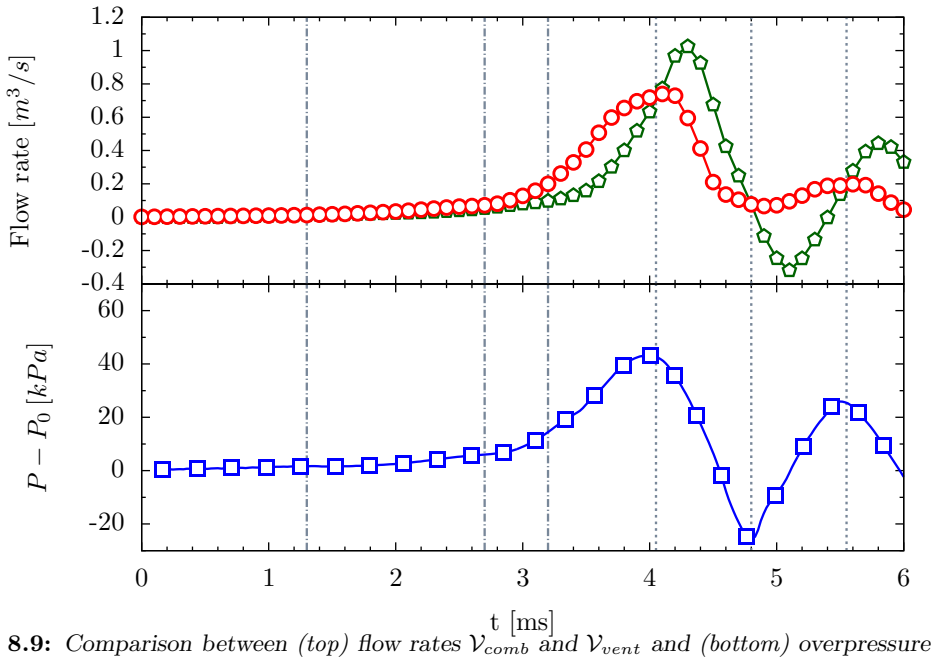

Figure 8.9: *Comparison between (top) flow rates $\mathcal{V}_{comb}$ and $\mathcal{V}_{vent}$ and (bottom) overpressure at the base of the chamber BBB0 configuration* - -·- *Grids g1, g2, g3,* - - $\mathcal{V}_{comb} - \mathcal{V}_{vent} = 0$, $\mathcal{V}_{comb}$, $\mathcal{V}_{vent}$, *Base overpressure*

The overpressure in the chamber can thus be explained as follows,

- Initially, with a relatively slow flame and a laminar structure, the generated volumes of gas are evacuated properly through the exhaust and almost no pressure accumulation is observed
- The reaction rate increases dramatically when the flame reaches the obstacles (increase of flame surface, and in general of wrinkling factor as well), while they also block the increased generated volumes from being evacuated at the exhaust thus increasing the overpressure
- The time elapsed between these two phenomena explains the large overpressure generated mostly when after the flame has reached the final obstruction and that a large amount of gas was trapped
- Acoustic reflections then bring the system back to an equilibrium state ($P_{chamber} = P_0$) alternating the dominated combustion and venting instances

8.3.2 Geometry modification effects

In the experimental rig designed by Prof. Masri [151], the different grids and obstacles can be removed and added at will, such that numerous different geometrical configurations could be studied, e.g. the impact of removing and adding grids, their position with respect to the ignition point, etc. In this case,

only the addition of the additional obstacle on top of the three grids is considered, as a more detailed investigation of geometrical effects is presented in §. 8.6.

Fig. 8.10 depicts the flow behaviour of both flames at similar times, while their respective positions and speeds are presented in Fig. 8.11, as well as the overpressure at both sensors locations in Fig. 8.12.

One can remark almost identical flame developments up until the interaction with the third baffle. A difference occurs at this point due to the presence of the obstacle. Contrary to the BBB0 case where the four fingers emerging from the last grid ($g3$) almost instantaneously merged under the intense turbulence influence, the obstacle splits the emerging fingers in two larger fingers on each sides leaving in the process a rather large pocket of reactants trapped under it. The turbulence intensity in the wake of the main obstruction generates two contra-rotating vortices bringing the two larger fingers together into a single fully turbulent flame front which resumes its propagation towards the exhaust at a very high-speed. These vortices also help in mixing hot products with the reactants positioned at the top of the obstacle, thus accelerating a burning that would otherwise take longer as the flame can not directly reach this region. The burning under the obstacle and in its wake lasts after the flame has left the chamber for about 0.5 $[ms]$ thus influencing the acoustic reflections observed later. However, the flame speed and position seem rather similar between the two geometries despite the presence of the additional large obstruction.

This is further observed in the comparison of the computed flame velocity and position for both geometries (Fig. 8.11 and Fig. 8.12). The two propagations are very similar as predicted by the experiment, although the reasons behind the large delay between the two experimental datasets for a flame behaviour that should be very similar are not clear and appear larger than what random chaotic perturbations would give. The two computed results feature similar accelerations at the obstacles, at the exception of the sharp peak of velocity due to the presence of the main obstruction observed for the BBBS, where a velocity of $s_t \approx 170\,[m/s]$ is attained. The flame then slows down dramatically when reaching the unobstructed part of the chamber and the BBB0 and BBBS resume a similar propagation. It shall be noted, and this is verified here, that the obstacle main impact is not an increase in turbulence intensity (although it also contributes to the overall turbulence), but rather to delay the venting of the fresh gas mixture by trapping some of it thus increasing dramatically the overpressure measured experimentally in the chamber from $P_{\max} = 57\,[kPa]$ for BBB0 to $P_{\max} = 75\,[kPa]$ for the BBBS configuration.

However, this increased overpressure due to the main obstruction is not captured by the current combustion model, as the pressure predicted for both BBB0 and BBBS configurations by the LES computations are almost similar. This can be explained by the fact that the total flame surface (Eq. 8.12) is growing similarly in both cases as shown in Fig. 8.13 and that the reaction rate per unit surface is similar and equal to $\rho_0 s_l^0$ therefore leading to very similar volumetric production rates (Fig. 8.14). The BBBS still features a slightly larger total flame surface corresponding to the slight increase in overpressure observed in the LES results. It shall be noted, that when using a combustion model able to adapt to the local turbulence intensity, a larger difference between the two computations would be observed as the combustion volumetric production rate would then be different as it would be driven both by the flame propagation increasing its surface, but also the increase in the wrinkling factor accounting for the unresolved contribution of the FSD.

$$\Sigma_{tot} = \int_{\mathbb{V}} \Xi_\Delta |\nabla \widetilde{c}|\, \mathrm{dv} = \int_{\mathbb{V}} 4\Xi_\Delta \sqrt{\frac{6}{\pi}} \frac{\tilde{c}\,(1-\tilde{c})}{\bar{\Delta}}\, \mathrm{dv} \tag{8.12}$$

8.3.3 LES quality

Pope quality criterion definition

As pointed out earlier, all simulations presented in this chapter and in the previous section in particular have been carried out using using similar grids with $\Delta_x = \Delta_y = \Delta_z = 0.5\,[mm]$ and cubical cells.

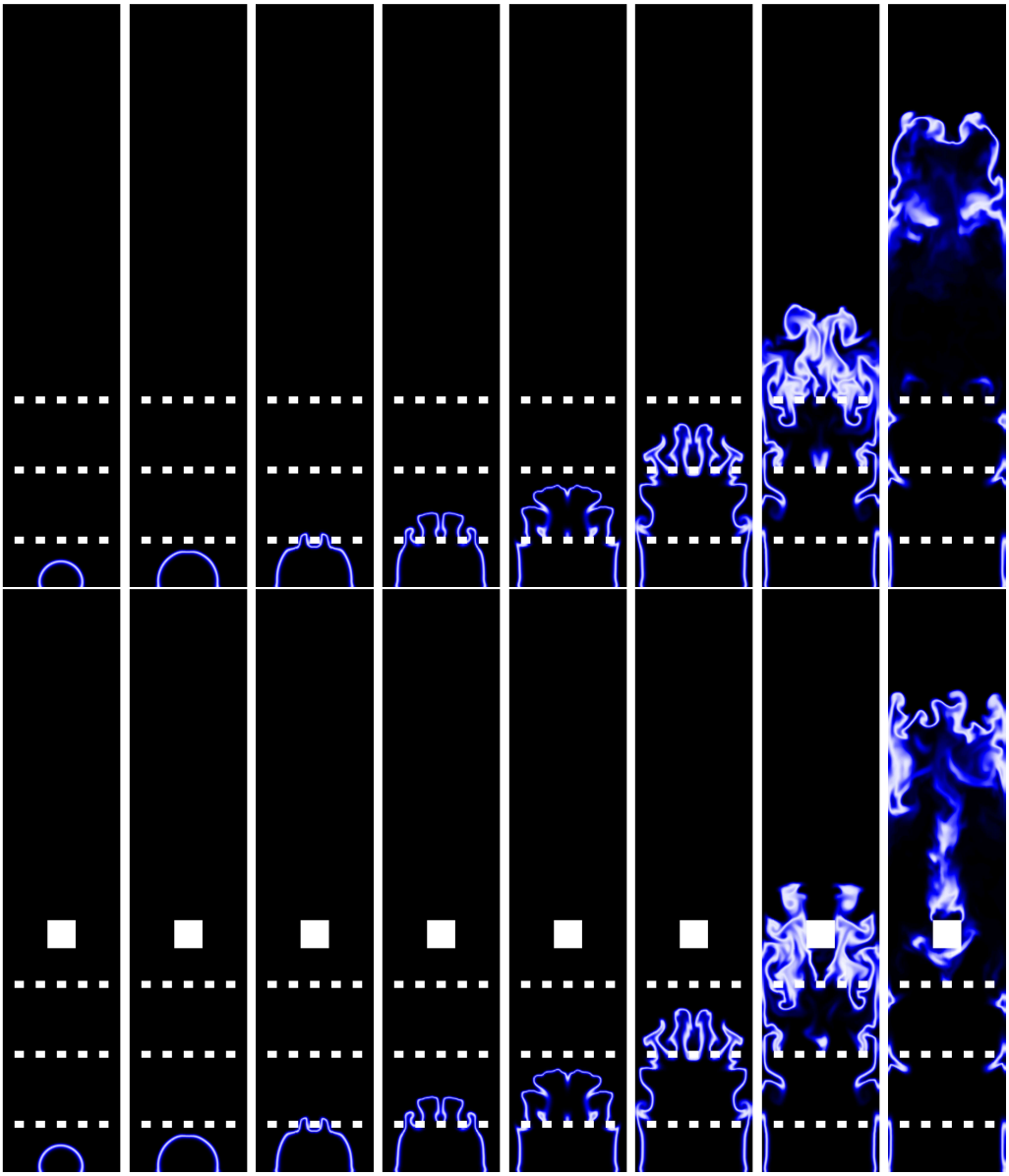

Figure 8.10: *Comparison between the flame structures for the (top) BBB0 and (bottom) BBBS configurations showing the reaction rate computed with the QCMF approach, Boger model ($D = 2.33$) and the thermally perfect EoS*

Before drawing conclusions based on the results presented in the next section, it is of prime importance to evaluate the results quality, and especially to estimate if the current grids are fine enough to resolve most flow features. This can be done using different criteria, such as the Pope criterion which requires that the resolved turbulent kinetic energy (TKE) represents between 70% and 80% of the total TKE content of the flow. Other quality criteria applied to LES have been presented by Celik *et al.* [51] based on the ratio of total diffusivity over turbulent one, or on the relation between the mesh resolution and the Kolmogorov scale.

As pointed out, the most widely used criterion for estimating an LES calculation quality consists in measuring the amount of resolved TKE compared to the total TKE content of the flow. In an LES calculation, reminding the velocity decomposition presented in Eq. 2.24, the instantaneous velocity field

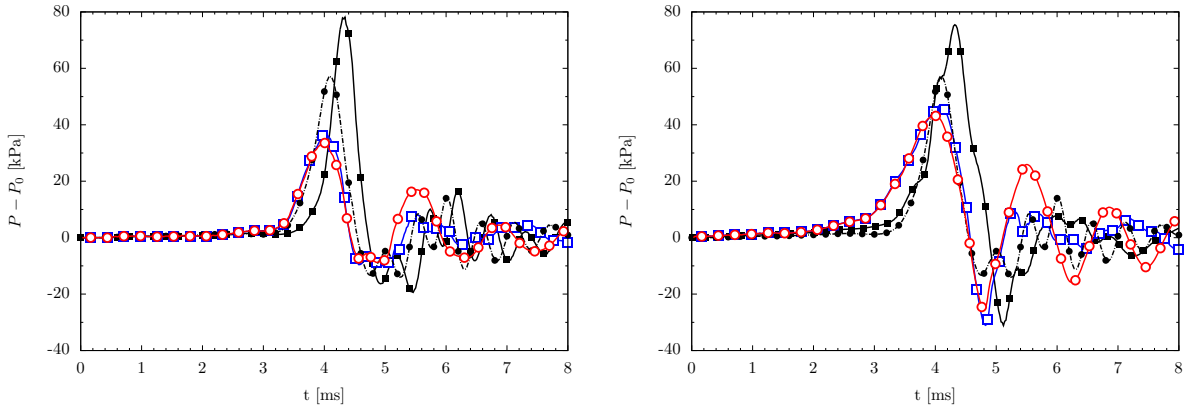

(a) *Wall sensor* **(b)** *Base sensor*

Figure 8.11: *Comparison between the experimental and computed (QCMF LES results with Boger model ($D = 2.33$) and thermally perfect EoS) overpressure for the BBBS configuration - ● Experimental BBB0, ■ Experimental BBBS, ○ Computed BBB0, □ Computed BBBS*

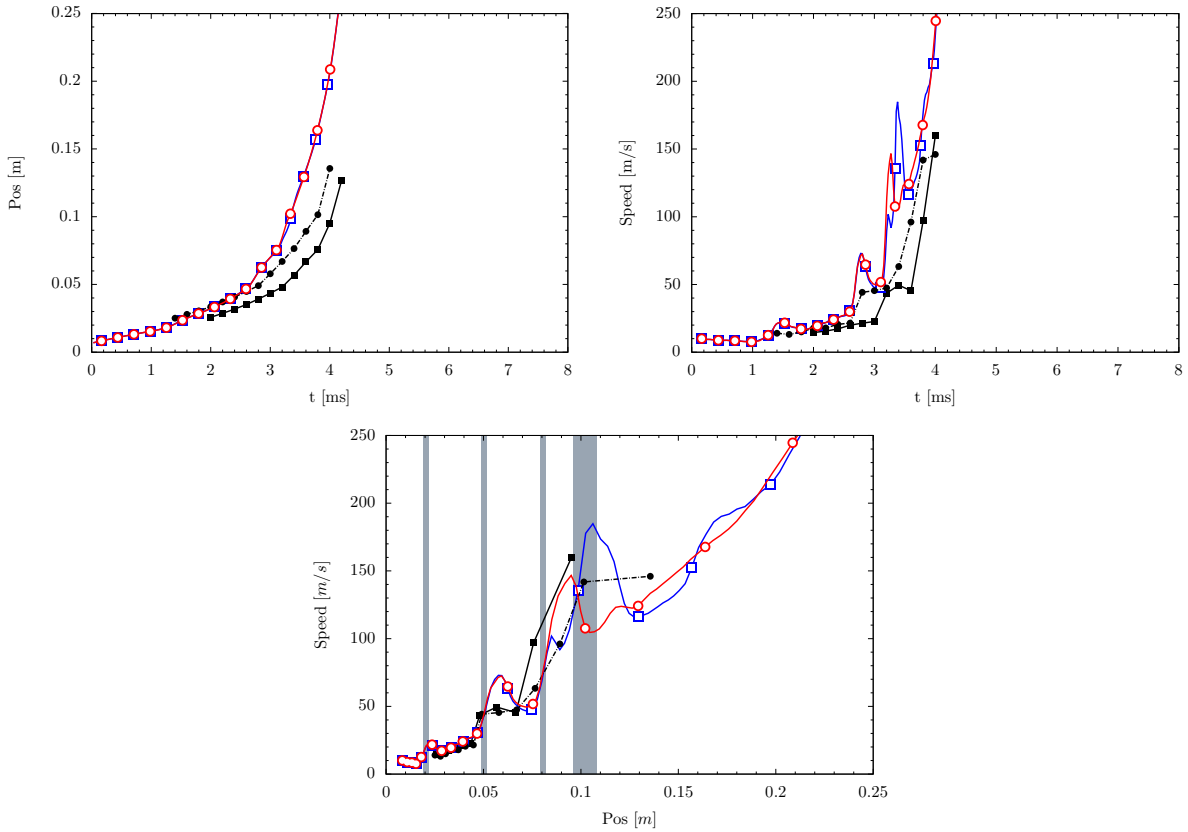

Figure 8.12: *Comparison between the experimental and computed (QCMF LES results with Boger model ($D = 2.33$) and thermally perfect EoS) flame speed and position for the BBBS configuration - ● Experimental BBB0, ■ Experimental BBBS, ○ Computed BBB0, □ Computed BBBS*

$\mathbf{U}$ can be decomposed following,

$$\mathbf{U} = \tilde{\mathbf{U}} + \mathbf{u}''(t) = \langle \tilde{U} \rangle + \widetilde{\mathbf{U}'} + \mathbf{u}''(t) \tag{8.13}$$

where $\tilde{\mathbf{U}}$ is the resolved instantaneous velocity that can be decomposed into a statistical mean $\langle \tilde{U} \rangle$ and large scale resolved fluctuations $\widetilde{\mathbf{U}'}$, while $\mathbf{u}''(t)$ denotes the unresolved velocity fluctuations. The resolved

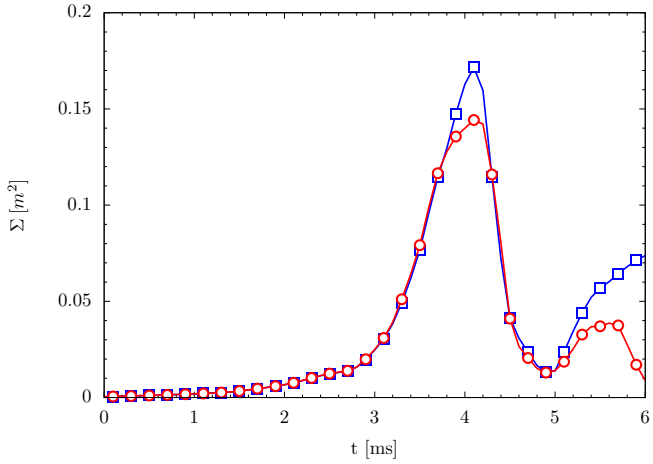

Figure 8.13: *Comparison between the total flame surface computed in the BBB0 and BBBS configurations using the QCMF and Boger model ($D = 2.33$) with the thermally perfect EoS -* ○ *Computed BBB0,* □ *Computed BBBS*

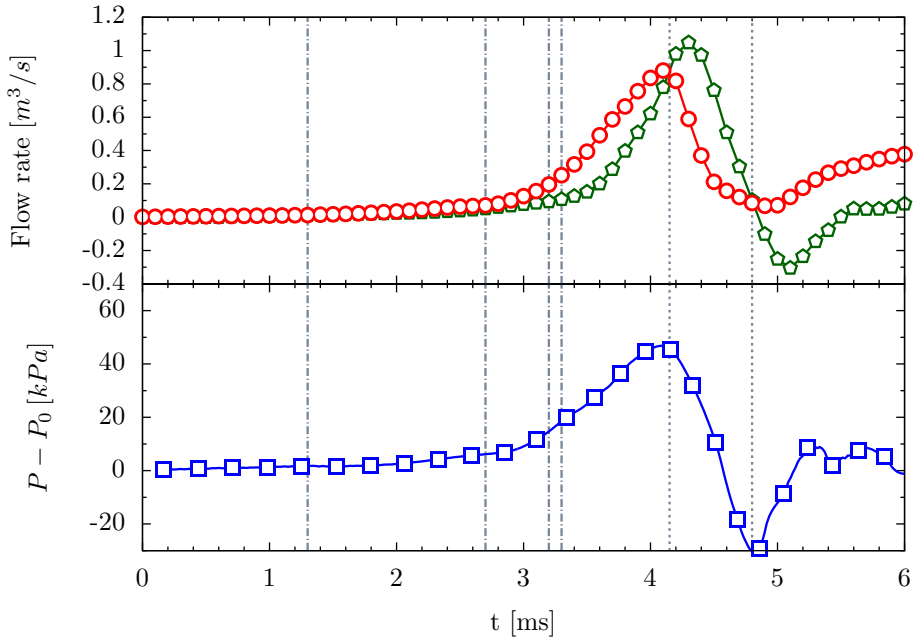

Figure 8.14: *Comparison between (top) flow rates $\mathcal{V}_{comb}$ and $\mathcal{V}_{vent}$ and (bottom) overpressure at the base of the chamber BBBS configuration -* - · - *Grids g1, g2, g3 and obstacle,* - - $\mathcal{V}_{comb} - \mathcal{V}_{vent} = 0$, ○ $\mathcal{V}_{comb}$, ⬠ $\mathcal{V}_{vent}$, □ *Base overpressure*

and unresolved TKEs are then computed by,

$$k_{res} = \frac{1}{2}\widetilde{\mathbf{U}'}^2 \tag{8.14}$$

$$k_{sgs} = \frac{1}{2}\mathbf{u}''^2 \tag{8.15}$$

The Pope quality criterion is thus expressed as,

$$\mathcal{H}_k = \frac{k_{res}}{k_{tot}} = \frac{k_{res}}{k_{sgs} + k_{res}} \tag{8.16}$$

Estimation of the resolved turbulent kinetic energy

In a statistically stationary flow, the estimation of the resolved TKE is a rather simple task as, in this case, a statistical mean corresponds simply to a temporal mean ($\langle . \rangle_t$), which is easily obtained by averaging the solution at numerous time instants. The resolved turbulent fluctuations $\widetilde{\mathbf{U}'}$ are then easily extracted using their RMS value, extracting the mean from the resolved flow field such as,

$$\sqrt{\langle \widetilde{\mathbf{U}'}^2 \rangle_t} = \sqrt{\langle \widetilde{\mathbf{U}}^2 \rangle_t - \langle \widetilde{\mathbf{U}} \rangle_t^2} \tag{8.17}$$

The challenging issue occurring in problems such as the one investigated here, is that no statistical mean (or temporal mean) can be defined, as it varies with time. To remedy this, Di Sarli *et al.* [80] applied a different procedure consisting in calculating a statistical average on a small time interval noted $\hat{t}$ defined such that it is small enough compared to the flame propagation time, but such that it is also large enough compared to the turbulent fluctuations characteristic time. The RMS of the resolved velocity turbulent fluctuations is thus,

$$\sqrt{\langle \widetilde{\mathbf{U}'}^2 \rangle_{\hat{t}}} = \sqrt{\langle \widetilde{\mathbf{U}}^2 \rangle_{\hat{t}} - \langle \widetilde{\mathbf{U}} \rangle_{\hat{t}}^2} \tag{8.18}$$

Hence, it appears that in transient flows, defining a statistical mean is both more involved and less soundly based than in a statistically stationary flow. However, it allows to obtain an estimation of k_{res} order of magnitude. When applying this technique to a methane-air propagating premixed turbulent flame, a bin size of $\hat{t} = 0.1\,[ms]$ has been used such that enough samples could be used for the averaging. In this work, a similar interval has been employed over which 100 equidistant solutions have been averaged. It would seem that such an interval fulfil the conditions stated previously, although it has to be pointed out that as the hydrogen flame is much faster, this averaging window might still be too large. Hall *et al.* considered the window of $\hat{t} \approx 0.25\,[ms]$ to post-process hydrogen experimental measurements [123].

Estimation of the SGS turbulent kinetic energy

The unresolved TKE is simply estimated using the Smagorinsky model such that [80],

$$k_{sgs} = \frac{1}{\left(C_s \bar{\Delta}\right)^2} \nu_{sgs}^2 = C_s^2 \bar{\Delta}^2 |\tilde{S}|^2 \tag{8.19}$$

Results

Fig. 8.15 presents the different TKEs (both resolved and unresolved), as well as the Pope criterion at the time where the flame is fully turbulent and propagating upwards. The large TKE regions, be it resolved or unresolved are mostly similar which is as expected, especially near the top of the chamber where most of the turbulence is located. It can be noted that in the strongly turbulent zones, the unresolved TKE is five times smaller than the resolved one. The high level of unresolved TKE close to the walls and grids can be noted and is due to the absence of wall functions close to the walls. The ILES approach then applies a non-negligible quantity of subgrid viscosity.

However, it can be observed that the simulation quality in critical zones (around the flame and in the obstacles wakes) is globally correct with a quality criterion greater than 0.95. Close to the walls, the quality criteria is quite low, but it does not constitute a problem as the resolved levels of TKE are very low anyway. At the bottom of the chamber, the flow is still laminar, and as such its TKE content is extremely low.

A last remark can be made on the plot of the resolved TKE which appears relatively blurred. This could be explained by a averaging window ($\hat{t}$) which is too large considering the high speed of the flame at this time. Reducing the window could lead to lower values of resolved kinetic energy as the overall

motion of the flame (which happens at $s_t \approx 250\,[m/s]$) would not be taken into account. Despite this potential small reduction, the quality of the LES is overall correct, even if small zones do locally feature lower quality index values.

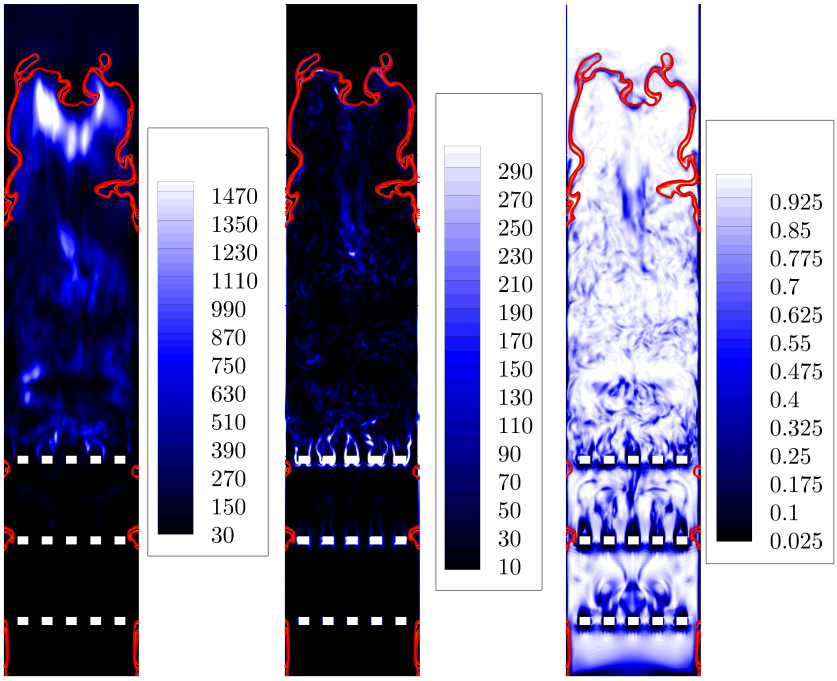

(a) *Resolved TKE* (m^2/s^2) **(b)** *Unresolved TKE* (m^2/s^2) **(c)** $\mathcal{H}_k$

Figure 8.15: *Resolved, Unresolved turbulent kinetic energy and Pope quality criteria for the BBB0 configuration computed with the QCMF approach, Boger model ($D = 2.33$) and the thermally perfect EoS - The flame front is indicated by red isopleths*

8.3.4 Conclusion

In this section, the current LES framework capabilities were investigated in the case of a small-scale explosion chamber experimentally studied at Sydney University. This study has confirmed that the LES is a promising tool for predicting small-scale explosions, and could be used in safety studies.

The flame speed propagation, as well as the flame position have been correctly estimated. Although the present approach using Boger's model ($D = 2.33$) which is the simplest of the available models does not allow the flame to propagate at its laminar speed in a laminar flow due to the constant fractal dimension applied, the laminar propagation, as well as the transition towards a turbulent burning mode have been qualitatively well reproduced but less so quantitatively. The flame speed at early time was found to be slightly too large owing to the coarse approximation employed with the Boger's model, but the overall agreement is encouraging.

However, computed overpressures were not quantitatively well predicted, although the timing of the flame and the overall overpressure profiles are in fair agreement with the experimental values. Underpredictions of about 25% and 40% have been found for the base and wall sensors respectively in the BBB0 configurations and about 40% and 55% for the base and pressure sensors respectively in the BBBS configuration. These large differences have been attributed to the inability of the current combustion model (Boger with constant fractal dimension) to account for a local increases of the turbulent intensity, and therefore of the unresolved flame surface and subsequent increase in reaction rate. It shall also be noted that pressure losses due to an inaccurate wall modelling approach are also responsible for these underestimations.

Finally, it is worth highlighting the importance of accurately capturing the early laminar flame propagation such that turbulence generated by the reactants being pushed out of the chamber has the correct intensity. It also has a significant effect when the flame front interacts with the first grid, as this first velocity increase drives the transition from a laminar to a turbulent propagation mode. Hence, the relevance of the long initial laminar flame can not be under-estimated as it plays a very important role in controlling the flame behaviour and generated overpressure. This is why a SGS wrinkling factor model accounting for the laminar flame propagation is of paramount importance for the simulation of such flows.

8.4 Influence of the equation set and thermodynamic properties

In this section, the results obtained with the different flow models developed and validated in the previous chapters (QCVF and QCMF) will be briefly presented, before a discussion of the effects of the specific heat ratio on the explosion behaviour is presented. It shall be noted that computations presented in this section have all been run on the fine grid and using the Boger's wrinkling model with $D = 2.33$. The numerical parameters are similar to those presented in §. 8.1, only the flow model (§. 8.4.1) or the EoS (§. 8.4.2) considered changes.

8.4.1 Effect of the model (QCMF, QCVF)

The baseline case (BBB0 with Boger model, $D = 2.33$ and the thermally perfect EoS) has been computed using both the QCVF and QCMF approaches in order to assess the modelling approach influence. Results obtained with the two models in terms of flame structure, speed, position and overpressure are depicted in Figs. 8.16 to 8.18.

Differences obtained between the two models are extremely subtle and seem to result from the long-time accumulation of small differences. Indeed, it is not before the flame has almost reached the third baffle that slight differences between the QCVF and QCMF predictions become visible. The QCVF appears marginally faster by about 2% which does not represent a significant difference. This agrees well with one-dimensional FSD results where the QCVF was found very marginally faster than the QCMF ($s_t\,(QCVF) = 1.54\,[m/s]$ and $s_t\,(QCMF) = 1.53\,[m/s]$). Similarly, peak overpressures observed are extremely similar both in magnitude and timing, the only difference residing in the late time acoustic reflections where the QCVF predicts a larger amplitude which is in agreement with the slightly faster flame observed leading to a larger venting rate, and thus a larger pressure drop when the combustion venting rate decreases.

Both models have been shown to provide a good agreement with experimental results, but more importantly between themselves thus showing the consistency of the new approach derived in this research. This also indicates that the assumptions made in §. 3.7.4 do not seem to have a negative impact on the solution and constitute an acceptable first-order solution. This would of course require further validation in different flame configurations (jet flames, etc.).

8.4.2 Influence of the specific heat ratio

Similarly to the previous chapters, the impact of using a value of γ constant in both space and time such that a FCMF-type approach could be used is discussed in this section. It has previously been shown that in the case of laminar flames, a constant γ value could not accurately predict both the flame speed and temperature, but in the case of FSD models, the laminar flame speed is controlled by the user, so it appears *a priori*, that finding the value of γ matching the correct flame temperature would be sufficient to correctly capture the flame dynamics.

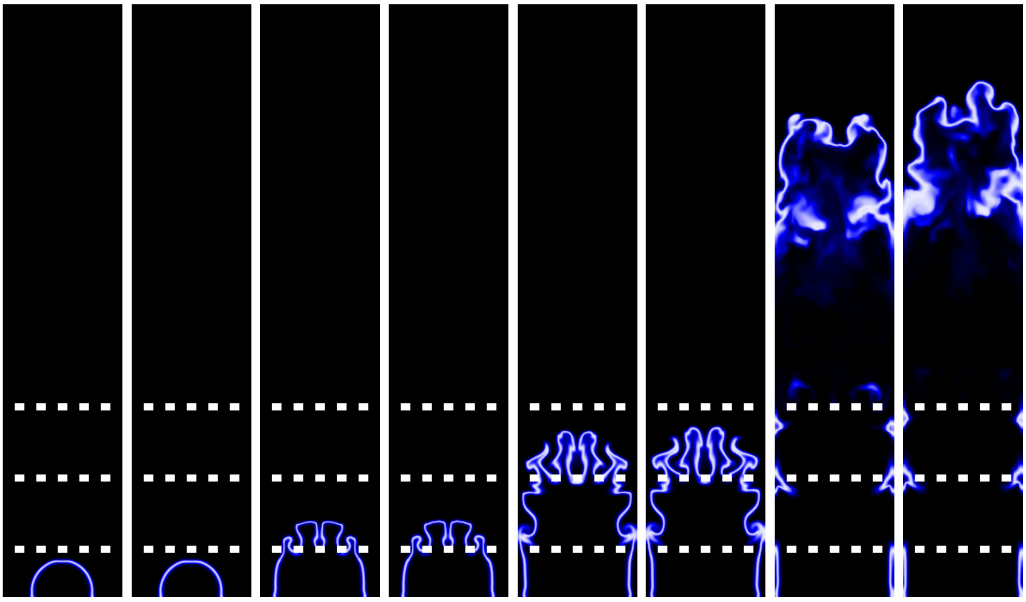

(a) $t = 1.0\,ms$ **(b)** $t = 2.0\,ms$ **(c)** $t = 3.0\,ms$ **(d)** $t = 4.0\,ms$

Figure 8.16: *Comparison between the flame structures for the (left) QCMF and (right) QCVF models for the BBB0 configurations showing the reaction rate computed with the Boger model ($D = 2.33$) and the thermally perfect EoS*

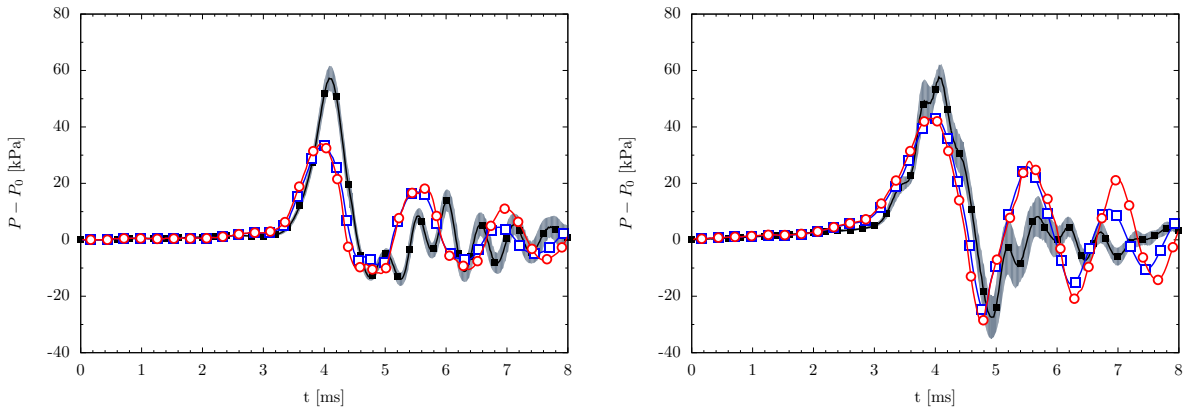

(a) *Wall sensor* **(b)** *Base sensor*

Figure 8.17: *Comparison between the experimental, QCMF and QCVF (LES results with Boger model ($D = 2.33$) and thermally perfect EoS) overpressure for the BBB0 configuration - ■ Experimental BBB0, ○ QCVF, □ QCMF*

The products temperature can be simply estimated by considering that combustion is a constant total-enthalpy process, and thus,

$$h_b + \Delta h_b^0 = h_u + \Delta h_u^0 \tag{8.20}$$

where $h_u = C_{p_u} T_u$ and $h_b = C_{p_b} T_b$. By remembering that to enforce a specified γ value for each species, the heat capacities at constant pressure are computed as,

$$C_{p_k} = \frac{\gamma_t \mathcal{R}_k}{\gamma_t - 1} \tag{8.21}$$

where γ_t is the target value defined by the user. From this, and having $\gamma_u = \gamma_b = \gamma$, the products

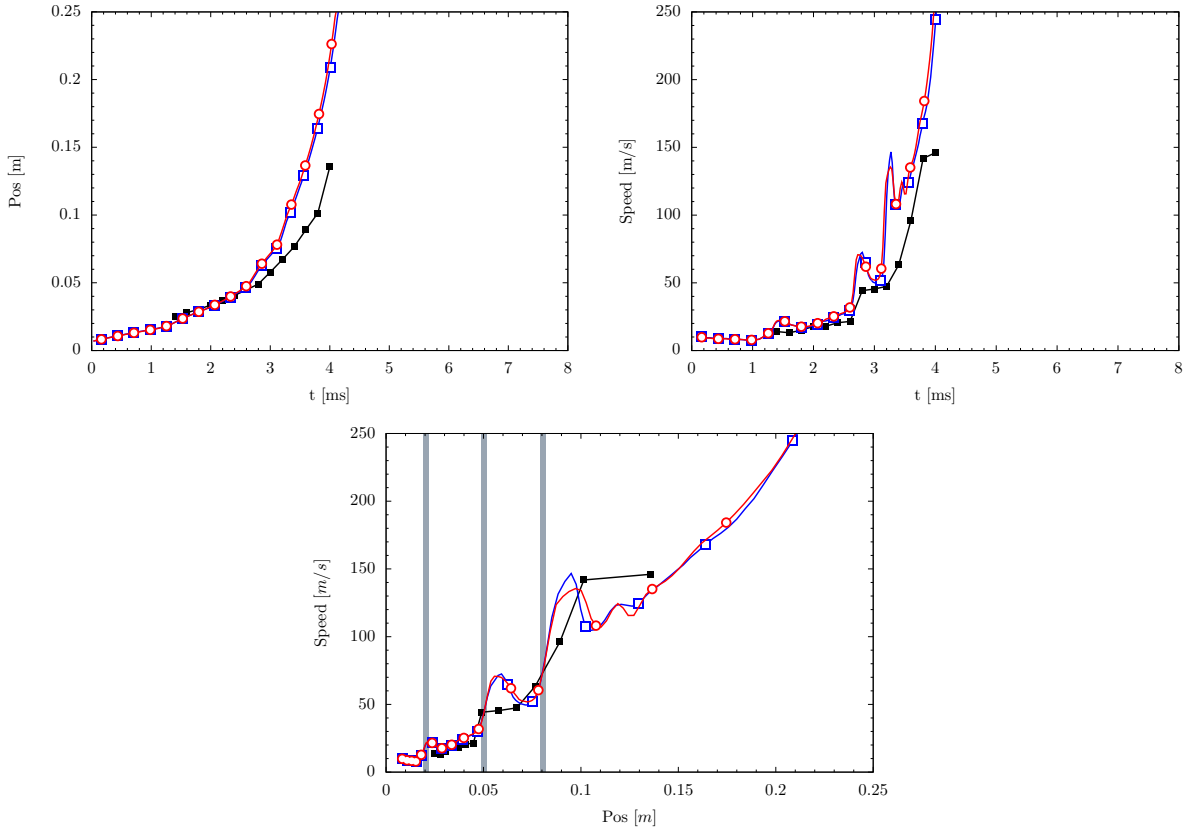

Figure 8.18: *Comparison between the experimental, QCMF and QCVF (LES results with Boger model ($D = 2.33$) and thermally perfect EoS) flame position and speed for the BBB0 configuration - ■ Experimental BBB0, ○ QCVF, □ QCMF*

temperature is expressed as,

$$T_b = \frac{\mathcal{R}_u}{\mathcal{R}_b} T_u + \left(\Delta h_u^0 - \Delta h_b^0\right) \frac{\gamma - 1}{\gamma \mathcal{R}_b} \tag{8.22}$$

which, using the properties of both reactant and product mixtures for an hydrogen flame at $\phi = 0.7$ leads to the results depicted in Fig. 8.19.

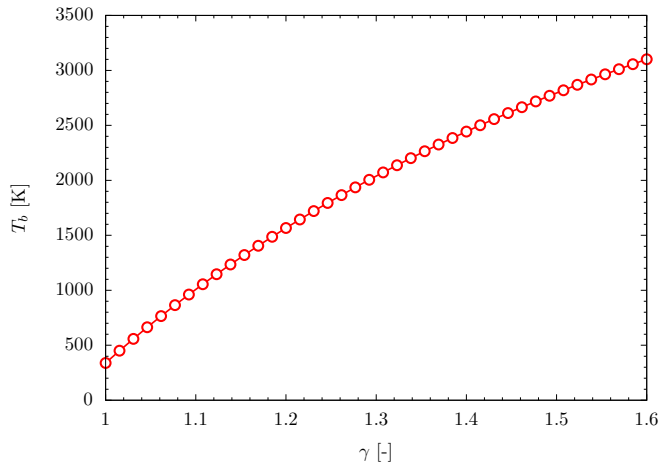

Figure 8.19: *Product temperature as a function of the specific heat ratio for an hydrogen mixture with $\phi = 0.7$*

For thermally perfect simulations, we have respectively $\gamma_u = 1.40$ and $\gamma_b = 1.26$ and $T_b = 2036\,[K]$ corresponding to the adiabatic flame temperature of an hydrogen flame under this stoichiometric ratio. To cover a wide range of possibilities, four values have been selected for this investigation, namely $\gamma_1 = 1.3$, $\gamma_2 = \dfrac{\gamma_u + \gamma_b}{2} = 1.33$, $\gamma_3 = 1.35$ and $\gamma_4 = 1.4$.

Fig. 8.20 depicts the results obtained using different values of γ at similar times compared to the base sensor time-to-peak. The first observation is that all flame structures look very similar especially at $t = t_{peak} - 1\,[ms]$ which is still within the laminar propagation. At later times, the different flame structures start to diverge due to the turbulent background, but also the different speeds reached. The second observation matches the expected behaviour, which is that flames at low value of γ have a low temperature, while higher γ leads to higher temperatures. By looking at the flame behaviour in Fig. 8.21, it can be seen that higher flame temperatures lead to higher flame speeds. This could appear surprising as temperature does not directly affect the reaction rate within the FSD framework, and the reaction source term remains constant for all computations. However, by recalling the propagation speed of an spherical flame definition, it can be seen that when the products temperature increases, and their density decreases, the expansion ratio (ρ_u/ρ_b) increases leading to higher flame propagation speed at early stages. This over-estimation during the early stages of the propagation as already been highlighted as one of the key parameter controlling the overall flame dynamics. It can also be observed the pressure time-to-peak time is monotonically decreasing with the increase of γ.

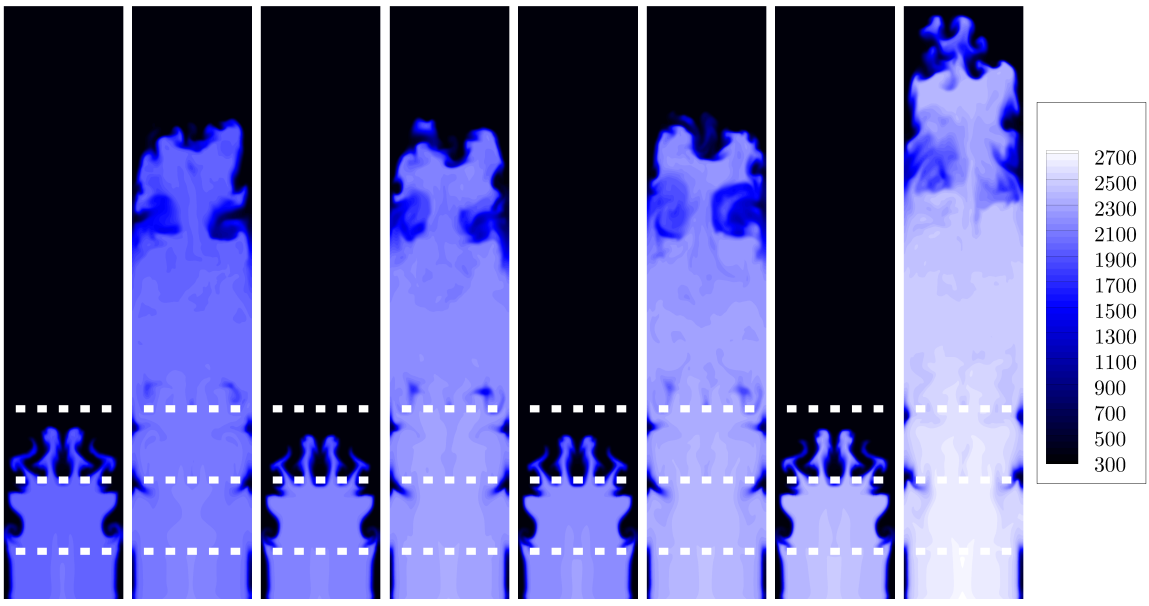

(a) $\gamma = 1.3$ $(t_{peak} = 4.3\,ms)$ **(b)** $\gamma = 1.33$ $(t_{peak} = 4.0\,ms)$ **(c)** $\gamma = 1.35$ $(t_{peak} = 3.9\,ms)$ **(d)** $\gamma = 1.4$ $(t_{peak} = 3.7\,ms)$

Figure 8.20: *Comparison between the flame structures for different γ values with (left) $t = t_{Peak} - 1\,ms$ and (right) $t_{Peak} = t\,(P = P_{\max})\,ms$ showing the temperature contours for configurations BBB0 computed with the Boger model ($D = 2.33$) - Time in brackets refer to the peak time*

Further looking at the volumetric reaction rate definition (which governs the flame overpressure), it can be seen that it appears inversely proportional to the hot products density. Thus, a temperature increase implies a larger volumetric reaction rate and a larger expansion of the hot gases, thereby increasing the flame speed. This is illustrated in Fig. 8.22, where a decrease of the γ value by 8% leads to a reduction of the maximum combustion rate of roughly $0.4\,[m^3/s]$, or approximately 35 % of its value.

A decrease in the value of γ by 8% leads to a delay in peak pressure of $\Delta t = 0.8\,[ms]$ (or 20 % of its value) which is rather large and indicates a lower flame velocity, but also induces a 40% reduction of the maximum overpressure. This is far larger than the experimental uncertainty of 12% measured

for the full dataset and indicates that accurately predicting the flame kinematic (laminar flame speed s_l^0 and turbulent flame speed) is not enough and that a good prediction of the products thermodynamic properties is also extremely important. In this perfectly premixed case, the error is already quite large, but it could become even larger in partial premixing (e.g. explosion occurring during a gas leak), where reactants and products properties would also change depending on the level of premixing.

It can eventually be noted that when employing a value of γ corresponding approximately to the arithmetic mean between the reactants and products values, a reasonable agreement with the thermally perfect case can be obtained with an over-prediction of the peak pressure of approximately 4 $[kPa]$ (less than 10 %) which is within the experimental variability limit. This is rather reassuring as it shows that by careful adjusting the value of γ, accurate results would still be obtained when using FCMF-type approaches. However, the predicting capabilities for shocks and detonations would be degraded.

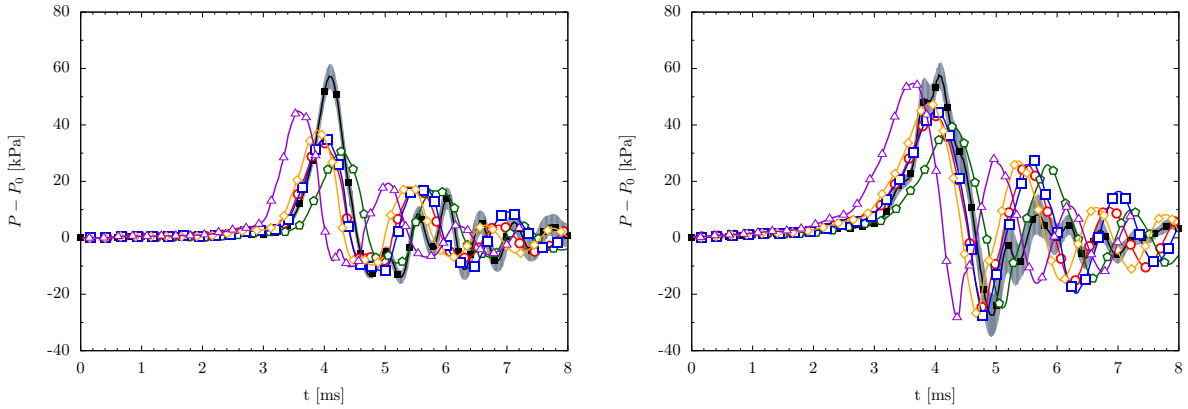

(a) *Wall sensor* **(b)** *Base sensor*

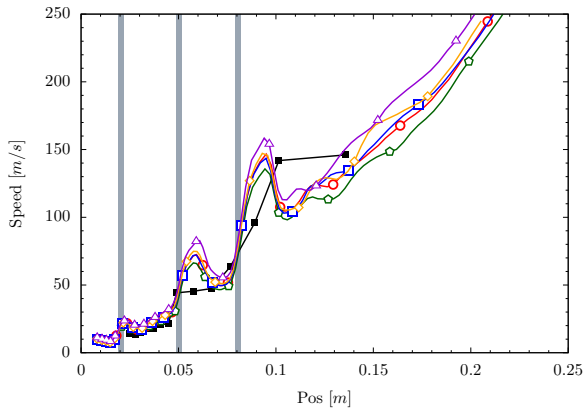

(c) *Position and speed*

Figure 8.21: *Flame properties as a function of the heat capacity ratio computed with the QCMF (LES results with Boger model ($D = 2.33$) and calorically perfect EoS) for the BBB0 configuration -* ■ *Experimental BBB0,* ○ $\gamma = \gamma(c,\, T)$, ⬠ $\gamma = 1.3$, □ $\gamma = 1.33$, ◇ $\gamma = 1.35$, △ $\gamma = 1.4$

8.5 LES uncertainty sources

The overpressure prediction for safety applications without knowledge about the results accuracy and reliability would be rather useless and quite dangerous. It is therefore important to investigate the different source of uncertainty in the input parameters and to evaluate their impact on the numerical results. The influence of several parameters on the flame propagation characteristics computed on the BBB0 geometry are presented in this section. The numerical parameters are presented first (reconstruction scheme), followed by the initial conditions (initial kernel radius and turbulent background), input

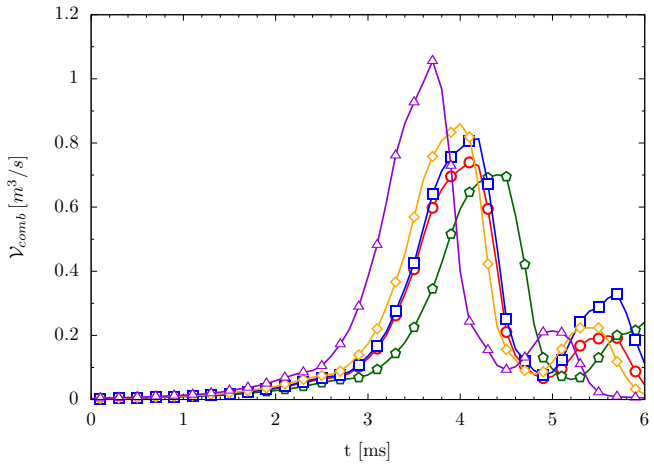

Figure 8.22: *Volume created by the combustion process as a function of the specific heat ratio for the BBB0 configuration computed with the LES QCMF with Boger model ($D = 2.33$) and the calorically perfect EoS -* ○ $\gamma = \gamma\,(c,\,T)$, ⬠ $\gamma = 1.3$, □ $\gamma = 1.33$, ◇ $\gamma = 1.35$, △ $\gamma = 1.4$

parameters (laminar flame speed and Smagorinsky constant), and finally the wrinkling factor models.

8.5.1 Influence of the numerical schemes

Three reconstruction schemes are implemented in `FlAMEnCo3D`, with the MUSCL5 featuring a 5^{th} order accurate reconstruction of the variables at cell edges which is the one that has been used up to now, a second-order scheme, MinMod2 with degraded diffusive properties and finally a first-order scheme which strongly smears any discontinuities. The numerical scheme influence on the solution is depicted in Fig. 8.23 where both the MUSCL5 and MinMod have been considered, the Upwind1 being too diffusive to lead to any meaningful results.

Reducing the scheme order of accuracy is known to increase the amount of numerical diffusion which directly impacts the results. If the flame speed estimation does not vary significantly, especially during the final phase of the propagation, the velocity increase during the interaction with the obstacle *g2* is greater with MinMod2 by about 20 $[m/s]$. This is compatible with observations made during the one-dimensional FSD analysis, where lowering the scheme order of accuracy resulted in a higher flame speeds. This is mainly explained Eq. 2.4 where it is clear that flame speed is proportional to the actual diffusion (physical plus numerical) coefficient, and thus increases when numerical diffusion increases. The time to peak thus reduces when employing lower-order schemes by about 0.5 $[ms]$ (or 12.5 % which is about ten times greater than the experimental variability). Besides, the added dissipation of the MinMod2 scheme clearly reduces the peak overpressure magnitude by about 16% which is larger than the experimental error, and thus not acceptable. The overall pressure losses are greater for low-order schemes, but pressure losses occurring between *g1* and *g3* do not seems to increase compared to results obtained with the MUSCL5. Indeed, both MinMod2 peaks (base and wall) underestimate the MUSCL5 predictions by about 16 , showing that additional losses are due mainly to pressure waves being smeared during their propagation, and not to additional dissipation stemming from walls. This highlights the relevance of using low-dissipation high-order schemes.

Finally, it can be noted that results dependency to the numerical scheme considered depends strongly on the grid considered. A finer grid would results in smaller differences between the different schemes as the overall numerical dissipation would be reduced.

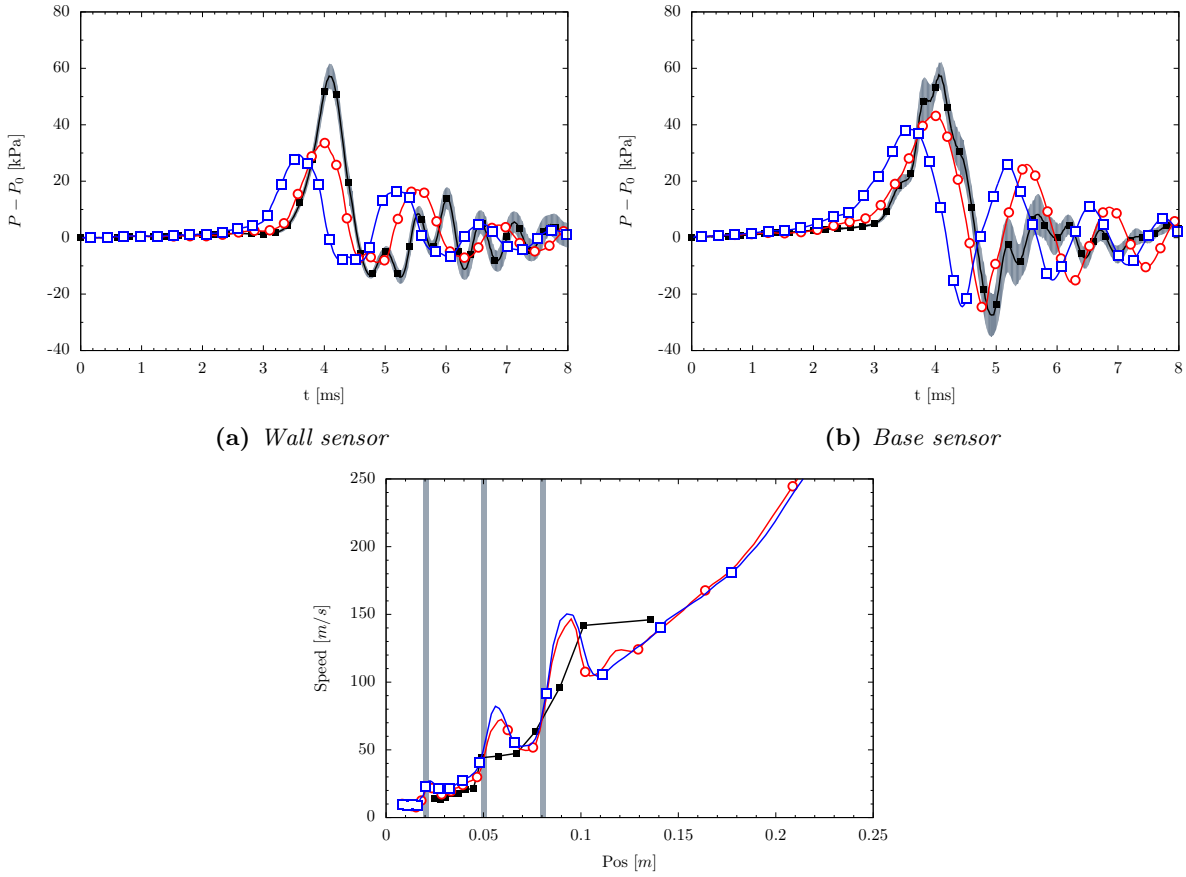

(a) *Wall sensor* **(b)** *Base sensor*

(c) *Position and speed*

Figure 8.23: *Influence of the numerical schemes employed (QCMF LES results with Boger model ($D = 2.33$) and thermally perfect EoS) on the flame characteristics for the BBB0 configuration - ■ Experimental BBB0, ○ MUSCL5, □ MinMod2*

8.5.2 Influence of the initial conditions

One potential source of errors when reproducing numerically experimental results is the slight differences existing between the computational and experimental initial conditions. Two key parameters have been identified here that are the initial turbulent intensity and initial kernel radius. Indeed, even though a delay is experimentally applied between the filling of the chamber and the ignition, non-quantified turbulence could still remain and influence the flame propagation. Secondly, the actual ignition process is a highly multi-scale multi-physics phenomenon including energy transfer between laser beams and gases, plasma formation and subsequent transfer of its energy to the surrounding flow, etc. As the modelling of such phenomena is beyond the current analysis, an initial patch of hot products was initialised and let to develop. The way ignition is modelled here could have a large impact of the solution.

Several turbulent intensities have been considered using an initial turbulent velocity field generated using the method presented in Appendix C with an integral length scale of $l_t = 5\,[mm]$ according to the experimental values of Hall [123] and u'/s_l^0 ranging from 0 to 0.16. Flame propagations resulting from these perturbed flow fields are visible in Fig. 8.24. The clear conclusion coming from these results is the absence of effect of the initial turbulence on the solution (overpressure changes by 0.05%), at least within the range of fluctuating velocities investigated. This also confirms that the flame transition to a turbulent burning regime actually comes from a self-generated turbulence and not due to a pre-existing one. One reason behind the negligible effect of the initial turbulence could be explained by both the damping effect of travelling pressure waves into a perturbed velocity field, and the time required for the

flame to initially propagate into the decaying turbulent field.

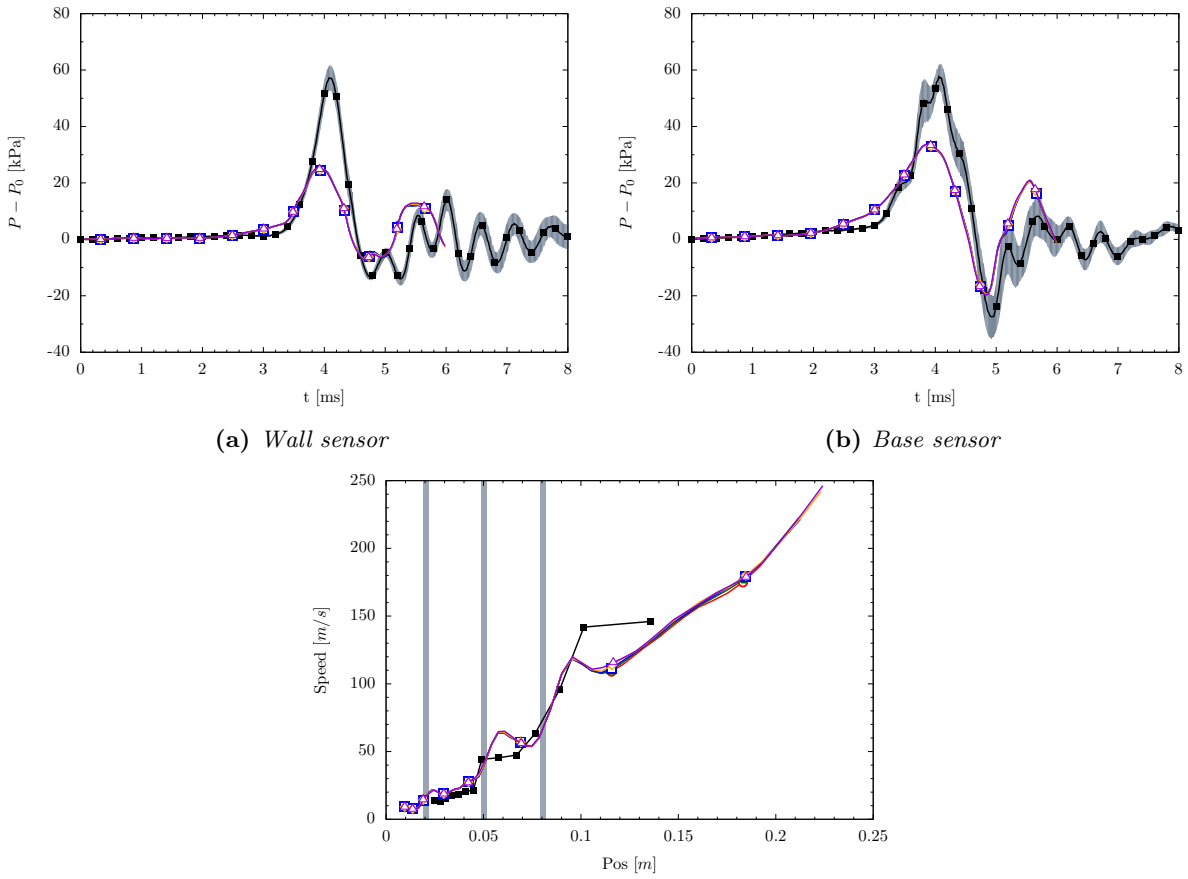

(a) *Wall sensor* **(b)** *Base sensor*

(c) *Position and speed*

Figure 8.24: *Influence of the initial turbulence intensity (QCMF LES results with Boger model ($D = 2.33$) and thermally perfect EoS) on the flame characteristics for the BBB0 configuration - ■ Experimental BBB0, ○ $u' = 0\,m/s$, ⬠ $u' = 0.02 s_l^0$, □ $u' = 0.04 s_l^0$, ◇ $u' = 0.08 s_l^0$, △ $u' = 0.16 s_l^0$*

Three initial radius have been simulated, with $R = 4,\ 5,\ 6\ [mm]$ and the results are depicted in Fig. 8.25. The impact of the initial kernel size is clearly visible here, but only affects the timing of the propagation, as the delay between two consecutive peaks is about $\Delta t \approx 0.16\ [m/s]$ corresponding to the time taken by a spherical flame propagating at $s_t \approx 7.5\ [m/s]$ to burn over a distance of $1\ [mm]$. As the flame is initially laminar, the initial size of the kernel is not relevant, and the overpressure peak remains constant. Other authors studied the influence of initialising the patch with different shapes [3] and arrived to similar conclusions. The initial size thus only affects the timing of the explosion, highlighting even further how weakly relevant the time-to-peak parameter is in this type of calculations, where changing the initial size could be enough to match experimental results.

8.5.3 Influence of the laminar flame speed

The laminar flame speed, even for well referenced fuels is only known with a non-negligible error margin, as shown in Glassman and Yetter [108] where the hydrogen flame speed for a stoichiometric ratio of $\phi = 0.7$ is given between $1.02\ [m/s]$ and $1.22\ [m/s]$ thus featuring a 20% spread, while hydrogen is a very well documented compound.

In this case, it has been decided to use an additional wrinkling model in addition to the Boger one where an increase of the laminar flame speed simply results in an increase of the source term by a sim-

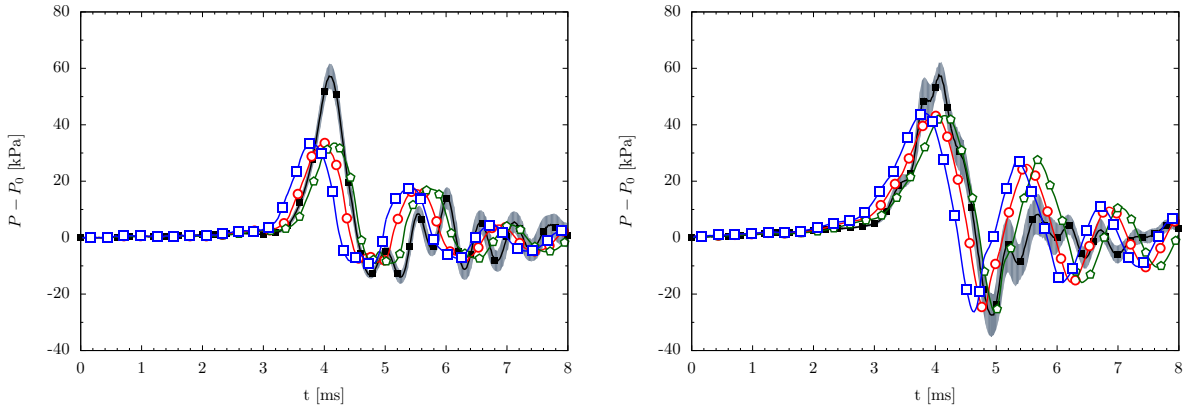

(a) *Wall sensor*

(b) *Base sensor*

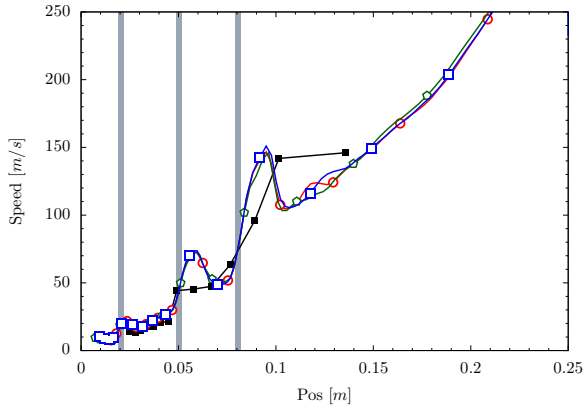

(c) *Position and speed*

Figure 8.25: *Influence of the initial kernel radius (QCMF LES results with Boger model ($D = 2.33$) and thermally perfect EoS) on the flame characteristics for the BBB0 configuration - ■ Experimental BBB0, ⬠ $R = 4\,mm$, ○ $R = 5\,mm$, □ $R = 6\,mm$*

ilar amount. Instead, a model where the laminar flame speed is explicitly needed in the evaluation of the wrinkling coefficients presents a more interesting test as it varies non-linearly with laminar speed changes. For this reason, Hawkes' model has also been considered as the laminar flame speed is needed in the estimation of both the inner cut-off and reduced fractal dimension.

The extrema of the laminar flame speed range presented by Glassman and Yetter [108] are considered here. The results obtained for both laminar flame speed values are visible in Fig. 8.26, and feature the expected trend. When the laminar flame speed increases, the overall flame propagation speed increases, the flame residence time decreases and the overpressure peak magnitude also becomes larger. If the time-shift is neglected, both Hawkes and Boger's models using $s_l^0 = 1.22\,[m/s]$ give errors compared to experimental measurements that are smaller than the experimental variability. The base pressure increase is 6 $[kPa]$ with Hawkes model ($\approx 10\%$) and 8 $[kPa]$ with Boger model ($\approx 15\%$) compared to results obtained with $s_l^0 = 1.02\,[m/s]$. Flame speeds feature similar increases with $\Delta s_t = 10\,[m/s]$ when interacting with grid *g1* and $\Delta s_t = 15\,[m/s]$ with grid *g2* between the smallest and largest laminar flame speed cases.

This sensitivity to the laminar flame speed value is worrying as contrary to model uncertainties (which can be addressed with better models, etc.), numerical scheme uncertainties (e.g. variables reconstruction), and initial conditions differences (appeared negligible in this case), this uncertainty seems difficult to reduce or even estimate. This is further emphasised by the fact that it still remains a challenge nowadays to obtain accurate and consistent measurements of laminar flame speed values even for well defined mixtures. Additionally, characterising the exact mixture that is going to explode in an accident

scenario is impossible, and as such a correct estimation of its laminar flame speed is also impossible. A sensitivity analysis is therefore required on this parameter whenever evaluating the actual safety bounds of infrastructures to ensure that worst case scenarios are accounted for.

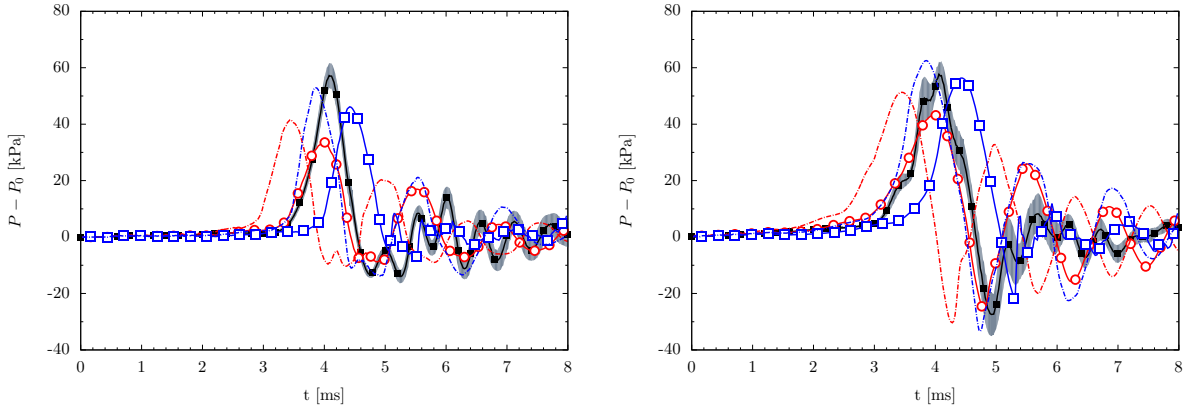

(a) *Wall sensor* **(b)** *Base sensor*

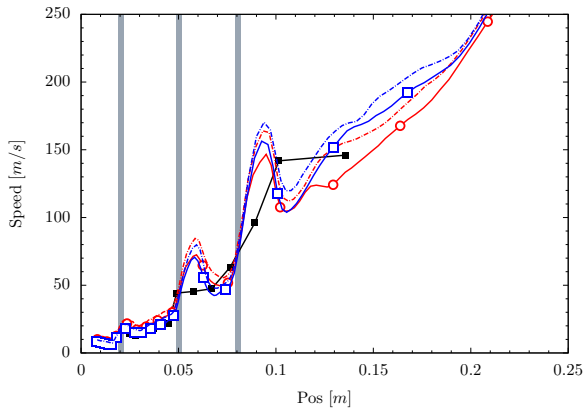

(c) *Position and speed*

Figure 8.26: *Influence of the laminar flame speed value (QCMF LES results with Hawkes model and thermally perfect EoS) on the flame characteristics for the BBB0 configuration -* ■ *Experimental BBB0,* ○ *Boger* $s_l^0 = 1.02\ m/s$, -·- *Boger* $s_l^0 = 1.22\ m/s$, □ *Hawkes* $s_l^0 = 1.02\ m/s$, -·- *Hawkes* $s_l^0 = 1.22\ m/s$

8.5.4 Influence of the turbulence modelling

Three parameters have been used in this work to account for turbulence effects on the flow field, with respectively the turbulent Schmidt number, the turbulent Prandtl number and the Smagorinsky constant considered uniform in both space and time. The influence of the two first parameters is not discussed here as they are similar to what was used in numerous other publications of semi-confined explosions [3,79,116] for both methane and hydrogen flames. On the other hand, the Smagorinsky constant is far from being uniquely defined, and its value depends on the grid size, distance to the walls, type of flow, etc. which are usually accounted for by using a Germano-like methodology to estimate it locally (dynamic approach), which has not been considered in this work.

However, results obtained in this section should not be over-interpreted. The Smagorinsky model describes the sub-grid scalar diffusion and features a linear dependence to C_s values, while Ξ_Δ will usually feature a non-linear dependency on C_s through the definition of u'_Δ (Eq. 7.14). Changing the value of C_s can thus significantly alter results, and the use of a dynamic model further complicates things as C_s becomes a local value. Other models for u'_Δ also lead to different predictions, and it is known that using a transport equation for k_{sgs} usually results in lower values of u'_Δ [98]. Additionally, the constant C_s is responsible for the determination of both the turbulent diffusion and reaction term (except in the

case of Boger's model, where the source term value is independent of the local turbulence intensity). By doubling the constant, the sub-grid fluctuations magnitude also doubles while the turbulent viscosity (and diffusivity) quadruples which is very large, meaning that the simulation will be highly sensitive to the value of this parameter.

For reasons similar to what as pointed out in the laminar flame speed influence study, the Hawkes' model is considered here in addition to the Boger's one. Apart from the baseline value of $C_s = 0.16$, both bounds of the range usually encountered for this constant are considered here, i.e. $C_s = 0.1$ and $C_s = 0.2$, although values as low as $C_s = 0.05$ have been used [191]. The results obtained for Boger's model are presented in Fig. 8.27 and in Fig. 8.28 for the Hawkes' model. The large impact of C_s values on the results is clearly visible here. However, different scenarios are observed for both Hawkes and Boger's models.

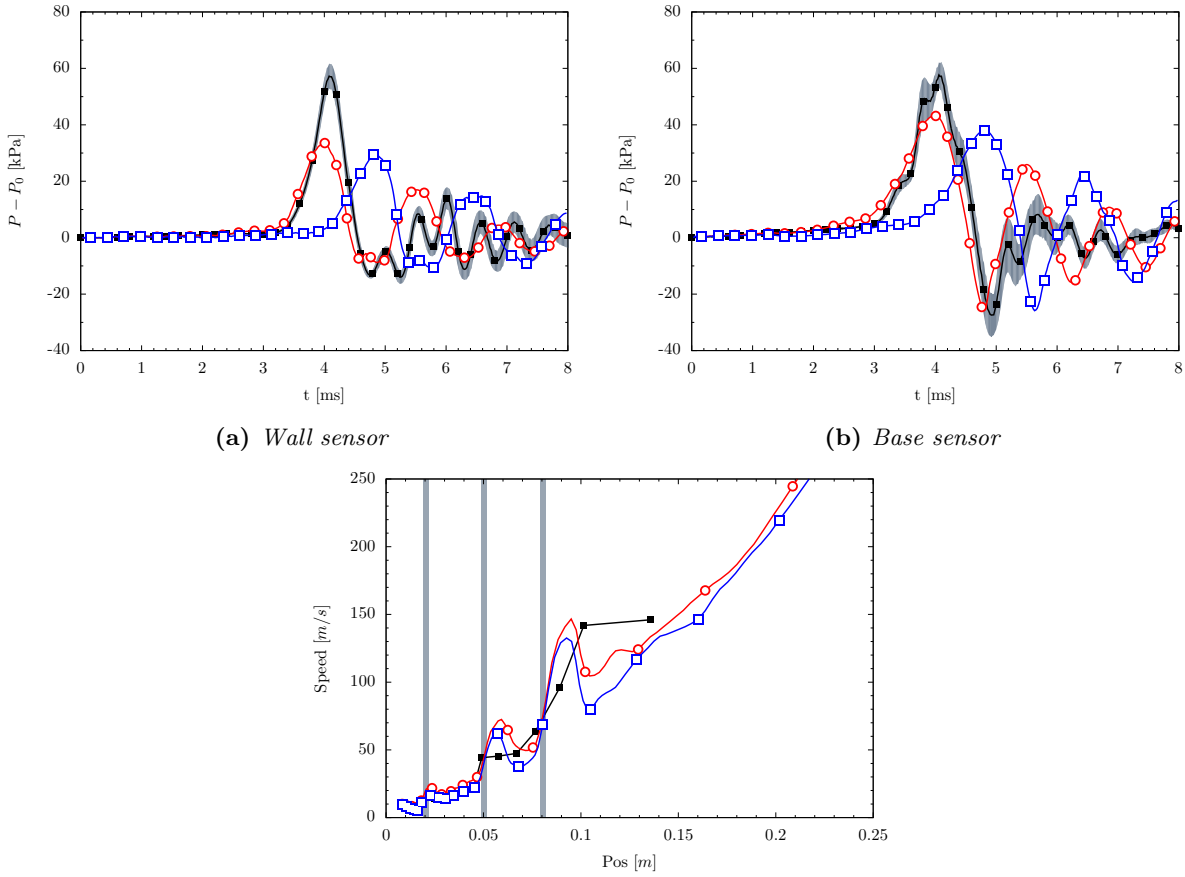

(a) *Wall sensor*

(b) *Base sensor*

(c) *Position and speed*

Figure 8.27: *Influence of the Smagorinsky constant value (QCMF LES results with Boger model ($D = 2.33$) and thermally perfect EoS) on the flame characteristics for the BBB0 configuration - ■ Experimental BBB0, □ $C_s = 0.10$, ○ $C_s = 0.16$*

In the case of Boger's model, the diffusion only is impacted by a change in turbulence intensity, and its level is (very) low at early times. The laminar phase is quite properly captured for both values of the coefficient, with a longer laminar zone in the case of the smaller value (about 1 $[ms]$ longer or 25 % of time-to-peak). When the flame transitions to a turbulent propagation mode, turbulence intensity levels increase and the turbulent diffusivity with it, but at this point, the main driver to the flame speed is the action of the hot expanding products pushing the flame downstream, in addition to the flame surface increase due to its wrinkling around obstacles. Changes in turbulent diffusivity are thus less significant leading to a relatively limited difference of $5\,[kPa]$ (about 15 %) between the two overpressure peaks. The smaller turbulent diffusion coefficient obtained with the small C_s value also leads to a slower flame, as diffusion remains the main mechanism driving premixed flame propagation.

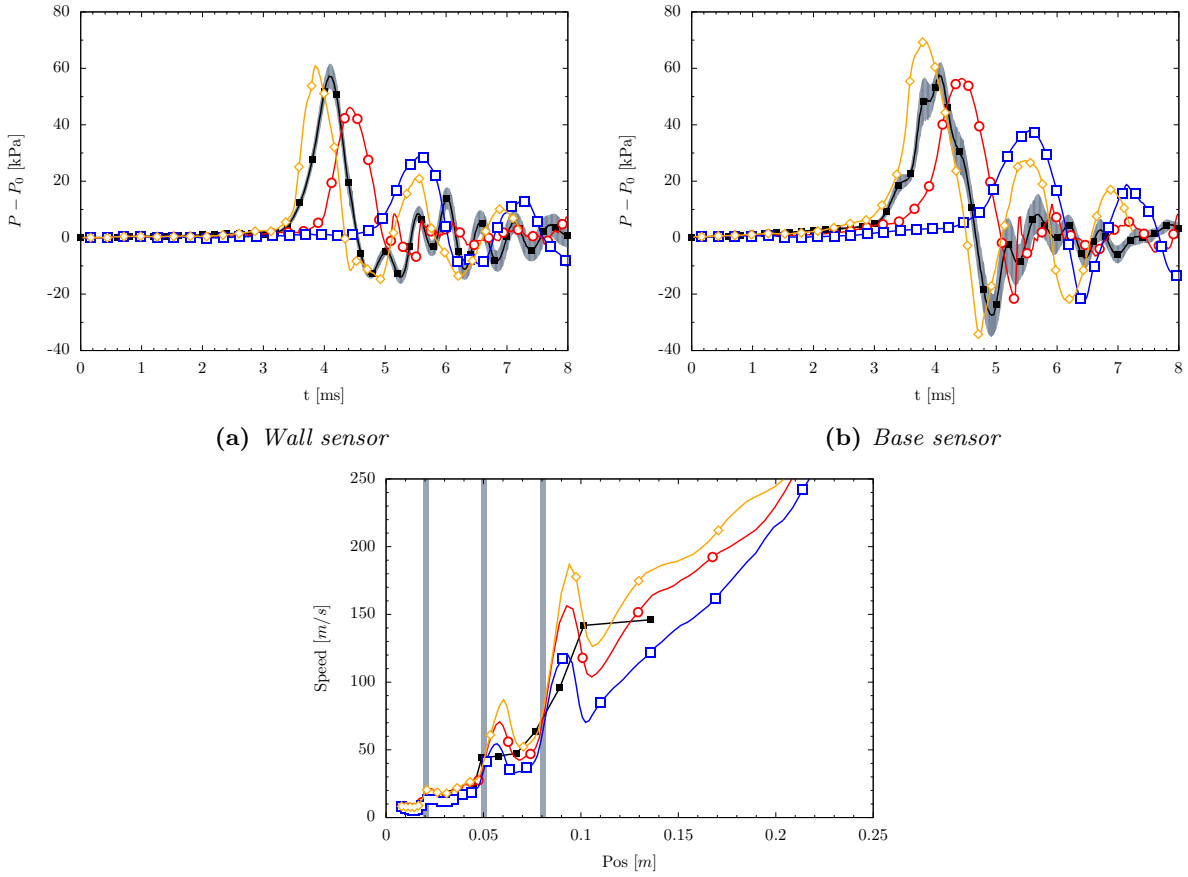

(a) *Wall sensor* **(b)** *Base sensor*

(c) *Position and speed*

Figure 8.28: *Influence of the Smagorinsky constant value (QCMF LES results with Hawkes model and thermally perfect EoS) on the flame characteristics for the BBB0 configuration -* ■ *Experimental BBB0,* □ $C_s = 0.10$, ○ $C_s = 0.16$, ◇ $C_s = 0.2$

Hawkes' model on the other hand features much larger solution changes when the value of the constant evolves. Apart from the diffusivity changes, by referring to Fig. 8.2 it can be seen that either an overestimation or an underestimation of the turbulence intensity by a fourfold factor have dramatic consequences on the value of Ξ_Δ and consequently on the flame speed predicted. This is especially true in the case of Hawkes' model giving low values of Ξ_Δ up to $u'_\Delta / s_l^0 \approx 10$, thus featuring the largest laminar propagation region of all models considered. The peak time increases by roughly $2\,[ms]$ (50 % of the time-to-peak) between the lowest and highest values of the constant, indicating a prolonged laminar burning mode when the constant is small, similarly to what was observed with Boger's model, and much more intense burning when the constant increases. Consequently, overpressures predicted nearly double when the Smagorinsky constant doubles as well. This sensitivity of the model to the Smagorinsky constant needs to be accounted for when defining the constant to be used. A potential solution to this problem resides in its dynamic calculation. This also raises additional issues such as the averaging volume, test filtering size, etc.

8.5.5 Influence of the wrinkling factor modelling

The different wrinkling models presented in Table 7.2 are used for the computation of the BBB0 case in order to test their influence on the solution. According to the theoretical analysis presented at the beginning of the chapter (§. 8.2.1), some differences should be visible. It can be speculated that Charlette's

model will lead to the fastest flame as it features the steepest slope of s_T/s_l^0 as a function of Ξ_Δ. On the other hand, Hawkes' model should initially be the slowest but once a certain turbulence level is reached, it should accelerate faster than the others.

The flame characteristics computed with the different models are presented in Fig. 8.29, while reaction rates contours are presented at four different time instants for each model, during the interaction with the first baffle (Fig. 8.30), during the interaction with the second baffle (Fig. 8.31), during the interaction with the third one (Fig. 8.32) and finally when the flame has reached halfway the distance between the last baffle and the chamber exhaust (Fig. 8.33).

The first observation from the evolution curves, is that even though a large spread is found between the different models predictions, the delay between the peak overpressures obtained for the fastest model (Charlette) and the slowest (Hawkes) is rather large, of the order of $\Delta t = 1.2\,[ms]$ (or approximately 30 % of the time-to-peak), but comparable with the effect of doubling the Smagorinsky constant from $C_s = 0.1$ to $C_s = 0.2$ (Fig. 8.27). The overpressure peaks magnitude as well as the first pressure acoustic reflection are well captured by the Angelberger, Charlette, FurebyM and Hawkes' model, i.e. all the models featuring a large range of turbulent flame speed. A rapid look at the reaction rate distributions for the different models highlights the striking similarity between the different flame structures (Figs. 8.30 to 8.33). It seems that no matter what the reaction rate is, the flame will feature the same structure, albeit at different times. Late times behaviours are not completely similar, as the formation of reactants pockets trapped by obstacles differ slightly from one model to the other. Angelberger and Hawkes' solutions both feature a "three-head" flame front at late times, with two small structures close to the walls and one large at the center, while the other model appear to have a more usual structure with a main flame front at the centre of the channel. This could be explained by a larger flame speed when interacting with *g2* leading to a larger expansion and folding of the flame front between *g2* and *g3*, and the formation of fingers close to the wall that do not have the time to merge with the main front.

The observations are thus as follows,

- Charlette's model predicts the fastest flame with a base time-to-peak of about $3.2\,[ms]$ while the experiment predicts about $4\,[ms]$. However, the overpressure is well predicted with an over-prediction of the pressure by only $8\,[kPa]$, which is smaller than the experimental variability. The reasons behind this are visible on Fig. 8.30 where it can be seen that the reaction rate predicted by this model is already behaving similarly to a turbulent flow with high wrinkling factor values in the fingertips, while other models still predict wrinkled laminar flame elements. At the second baffle plate, most of the flame front is not laminar any more. This indicates that the transition to the turbulent propagation regime is not well predicted by this model, but thanks to the clipping of the wrinkling factor at high turbulent intensities, the flame propagation speed does not increases too much.

- The two Boger's models (Boger and BogerM) do predict very similar overpressures and base time-to-peak as well as overpressure peaks with respectively $43\,[kPa]$ at $4\,[ms]$ and $42\,[kPa]$ at $4.2\,[ms]$. It seems normal for the BogerM to yield a delayed peak that is also slightly weaker, as contrary to the Boger's model, a laminar phase is accounted for. Nevertheless, the under-prediction of the pressure is about $15\,[kPa]$ which put these models predictions outside of the experimental variability range.

- Angelberger, Hawkes and FurebyM lead to very similar peak pressures with respectively $57\,[kPa]$, $56\,[kPa]$ and $57\,[kPa]$ which is well within the experimental variability. The reasons behind these correct predictions are made clear when looking at the reaction rate fields. The flame structure remains laminar with small reaction rate (comparable to laminar value) up until the flame reaches *g2*. It is only when the flame reaches the second baffle that reaction rates are increasing under turbulence influence. At the third baffle, fully turbulent fingers are observed for the three models while the flame structure at the bottom remains laminar at it get closer to the walls. When the flame finally reaches the unobstructed end of the chamber, its flame front is fully turbulent and regions of high activity can be observed.

From these observations, it is clear that all the models are able to capture to some extent all phases of the flame propagation, from the short spherical growth to the elongation in fingers through grids. The merging of the different fingers also seems to happen in a similar fashion for all models given the very similar flame structure observed during the final flame acceleration. It shall also be stressed that the observed performance of the different models results from a combined interaction of several sub-models (FSD, SGS scalar fluxes, ILES estimated SGS stresses, etc.) and it may not be possible to identify the sole performance of the FSD model. For these reasons, great care should be taken when generalising the current results.

8.6 Influence of the geometry on the explosions characteristics

Following the classification established by Gubba *et al.* [117], the different investigated geometries can be sorted in four families,

- Family 1 (00BS, 0BBS, BBBS) : The number of baffles increases progressively from the main obstacle
- Family 2 (BBBS, BB0S, B00S) : The number of baffles increases closer from the ignition end
- Family 3 (0BBS, B0BS, BB0S) : Two baffles positioned at different positions in the chamber
- Family 4 (00BS, 0B0S, B00S) : Only one baffle is positioned in the chamber at different positions

All of these configurations have been computed with the Hawkes' model, and some with the FurebyM model, which have been found to lead to the best results in the previous section.

The overall agreement is generally good, with a tendency of the Hawkes' model to always under-predict the overpressure. The largest under-prediction occurs for configuration with long laminar flame indicating that the Hawkes' model might not transition fast enough to turbulent burning regimes. Indeed, in the cases with numerous obstacles (BBBS, BB0S, B00S) especially placed close to the ignition, the model gives good predictions.

This behaviour is clearly illustrated in the Family 1 (Fig. 8.34) where obstacles are progressively approaching the ignition zone leading to prediction that get better and better. Similarly, Family 2 with always an obstacle close to ignition performs very well.

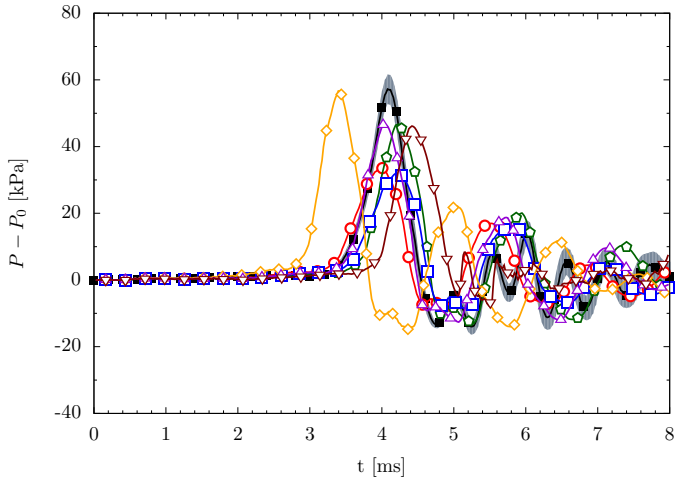

(a) *Wall sensor*

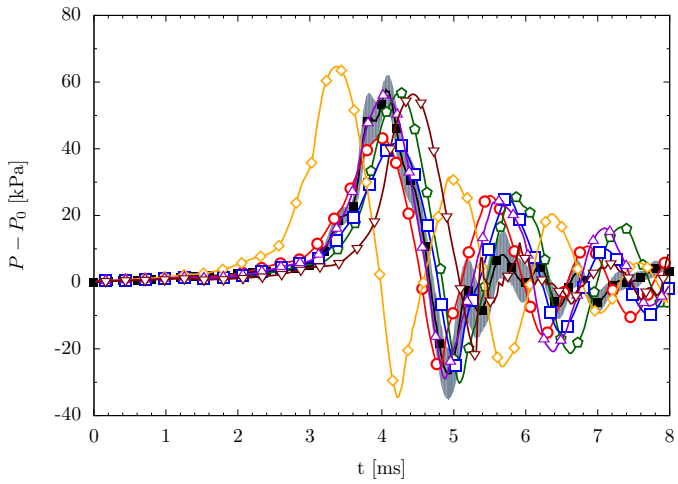

(b) *Base sensor*

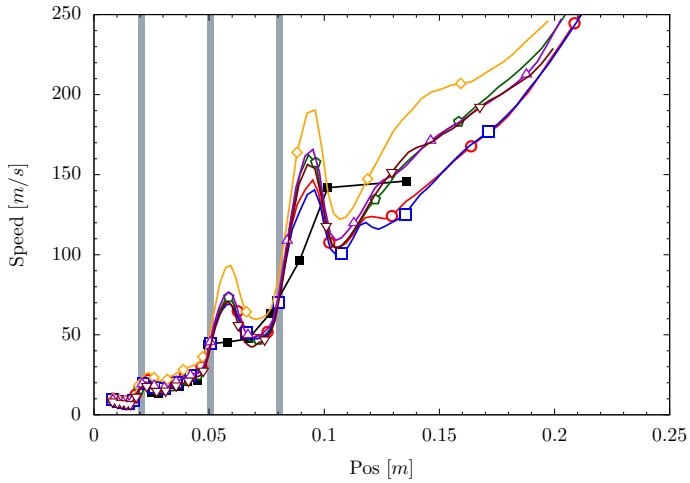

(c) *Position and speed*

Figure 8.29: *Influence of the subgrid model (QCMF LES results with thermally perfect EoS) on the flame characteristics for the BBB0 configuration -* ■ *Experimental BBB0,* ○ *Boger,* ⬠ *Angelberger,* □ *BogerM,* ◇ *Charlette,* △ *FurebyM,* ▽ *Hawkes*

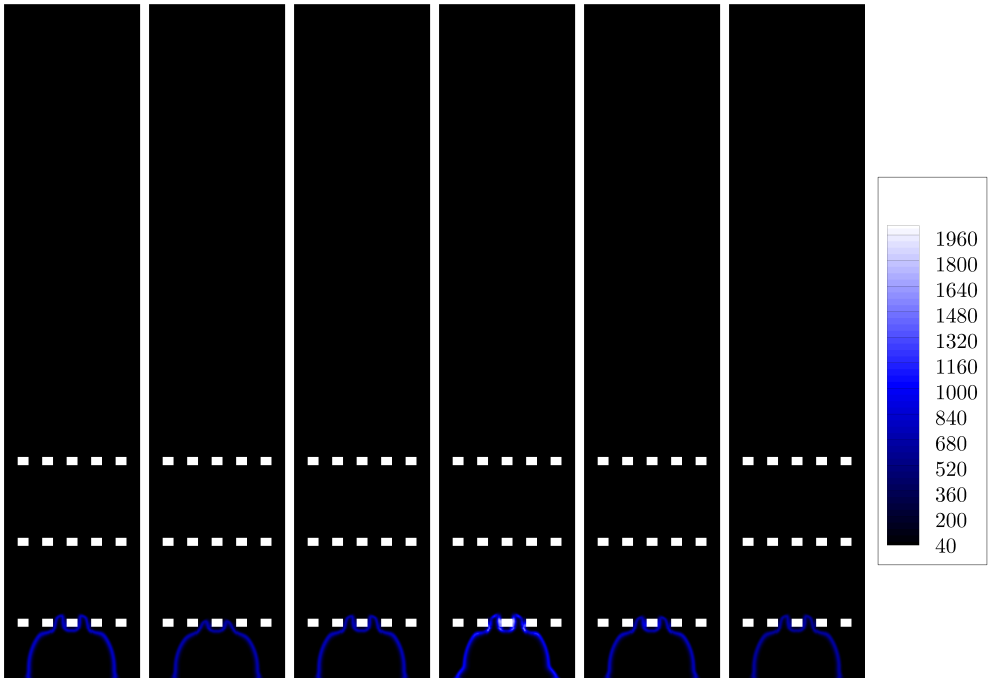

($t = 1.5\ ms$) (1.6) (1.6) (1.4) (1.6) (1.8)

Figure 8.30: *Comparison between the flame structures for the different wrinkling models on the BBB0 configurations showing the reaction rate computed with the QCMF approach and the thermally perfect EoS at the time of the interaction with the first baffle - Real time in ms indicated in brackets - (left) to (right) Boger, Angelberger, BogerM, Charlette, FurebyM and Hawkes*

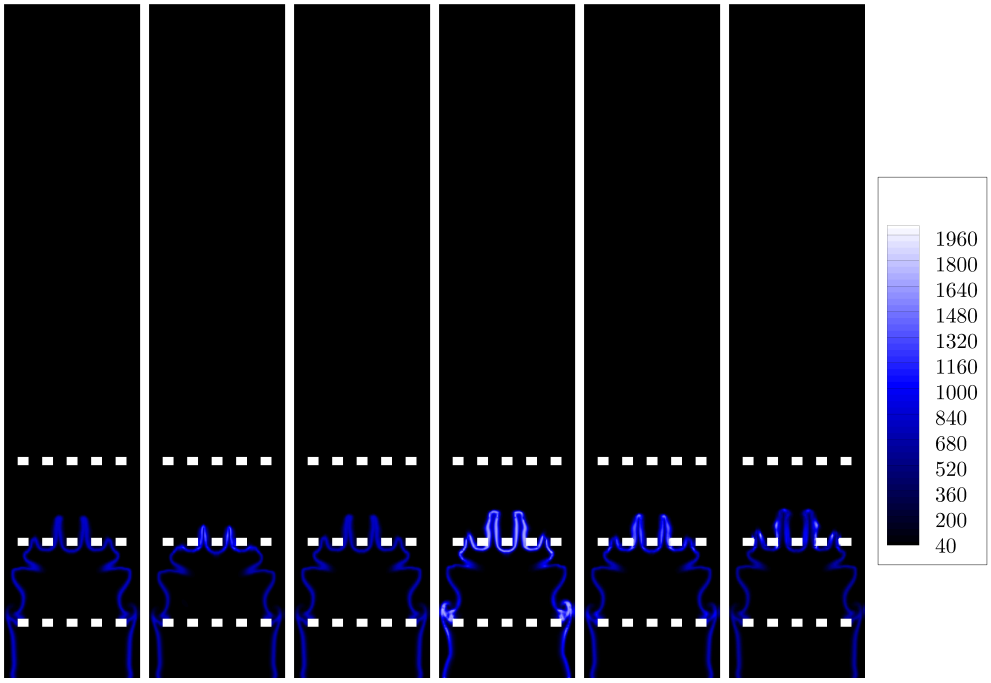

(2.8) (3.1) (3.0) (2.5) (3.0) (3.4)

Figure 8.31: *Comparison between the flame structures for the different wrinkling models on the BBB0 configurations showing the reaction rate computed with the QCMF approach and the thermally perfect EoS at the time of the interaction with the second baffle - Real time in ms indicated in brackets - (left) to (right) Boger, Angelberger, BogerM, Charlette, FurebyM and Hawkes*

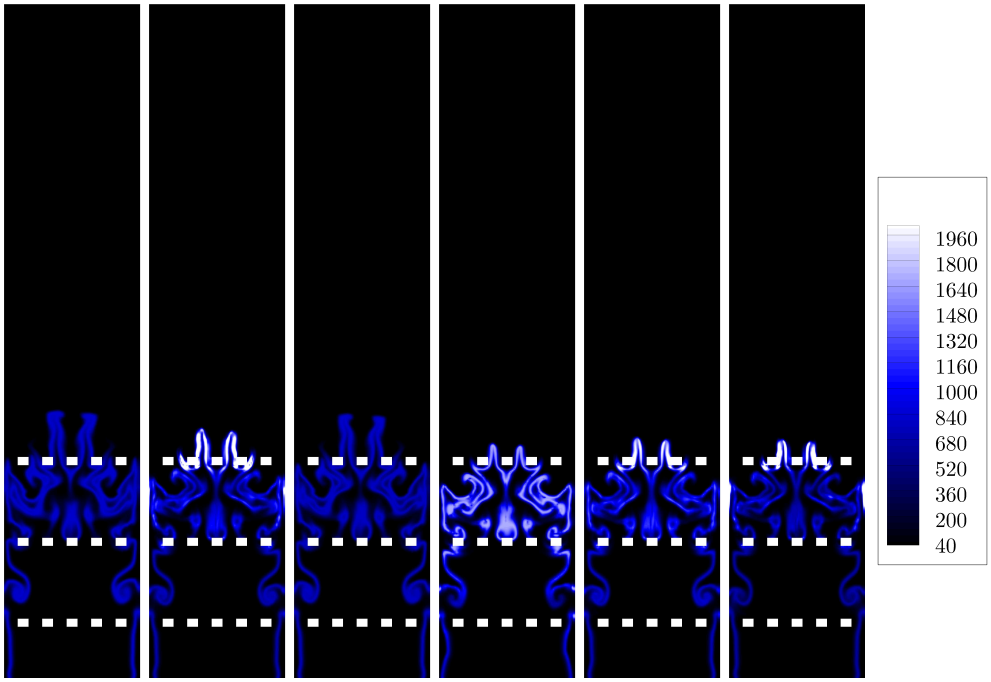

(3.3) (3.6) (3.5) (2.8) (3.4) (3.8)

Figure 8.32: *Comparison between the flame structures for the different wrinkling models on the BBB0 configurations showing the reaction rate computed with the QCMF approach and the thermally perfect EoS at the time of the interaction with the third baffle - Real time in ms indicated in brackets - (left) to (right) Boger, Angelberger, BogerM, Charlette, FurebyM and Hawkes*

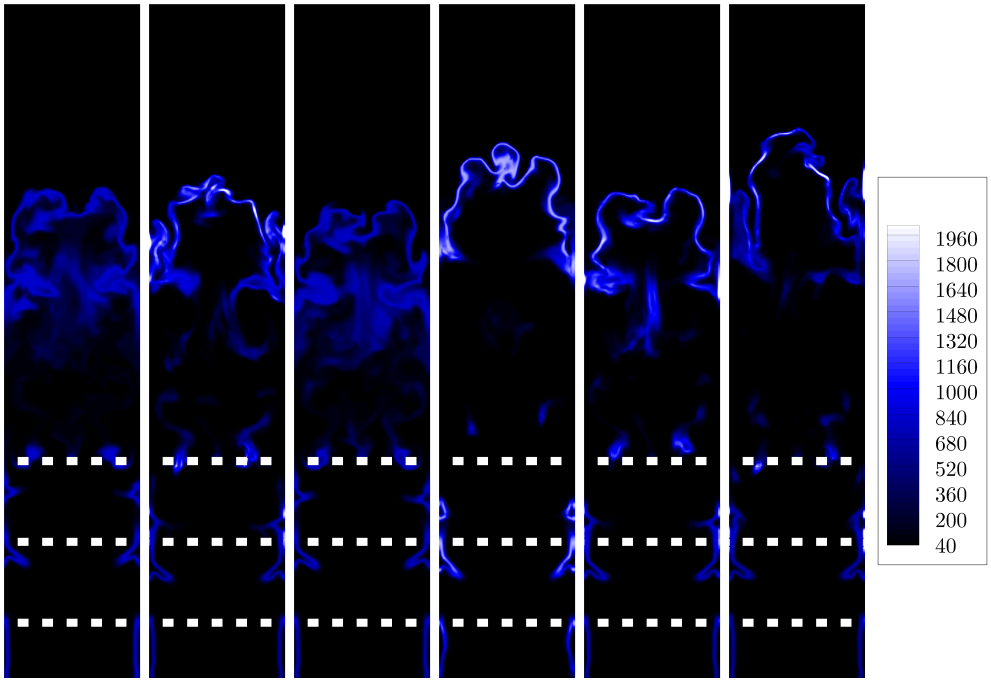

(3.9) (4.2) (4.1) (3.4) (4.0) (4.5)

Figure 8.33: *Comparison between the flame structures for the different wrinkling models on the BBB0 configurations showing the reaction rate computed with the QCMF approach and the thermally perfect EoS after interaction with all grids - Real time in ms indicated in brackets - (left) to (right) Boger, Angelberger, BogerM, Charlette, FurebyM and Hawkes*

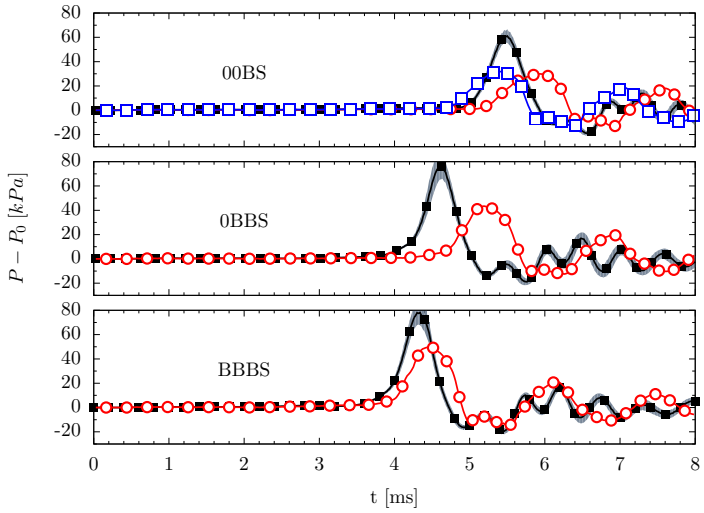

(a) *Wall sensor*

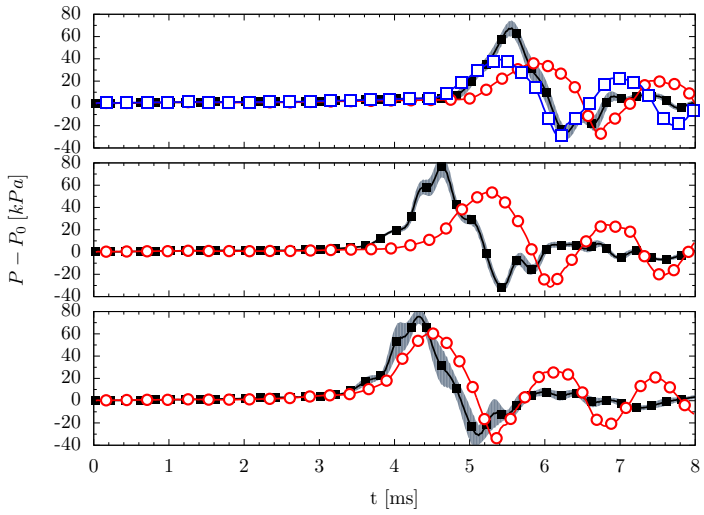

(b) *Base sensor*

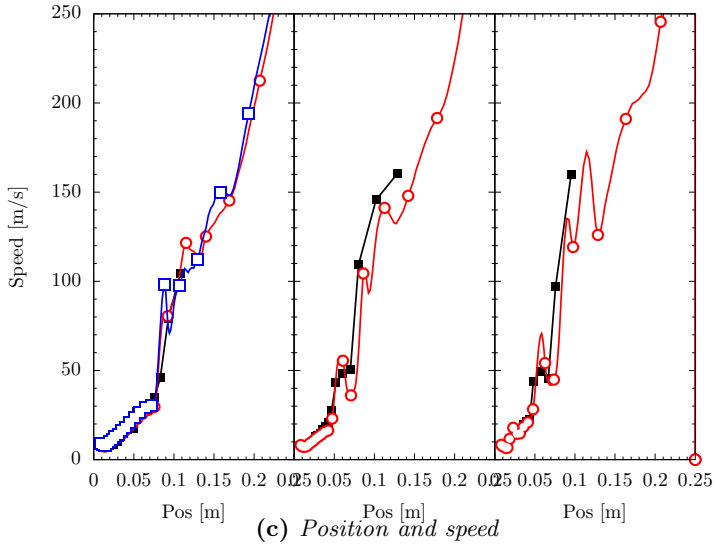

(c) *Position and speed*

Figure 8.34: *Influence of the geometry (QCMF LES results with thermally perfect EoS) on the flame characteristics for the Family 1 -* ■ *Experimental,* ○ *Hawkes,* □ *FurebyM*

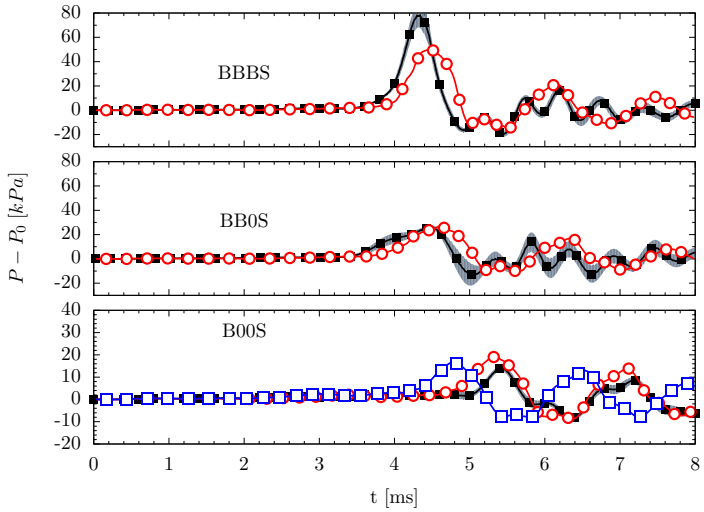

(a) *Wall sensor*

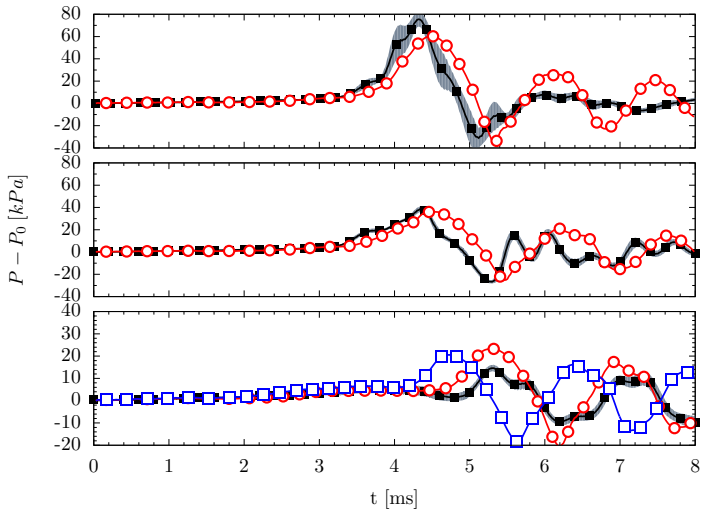

(b) *Base sensor*

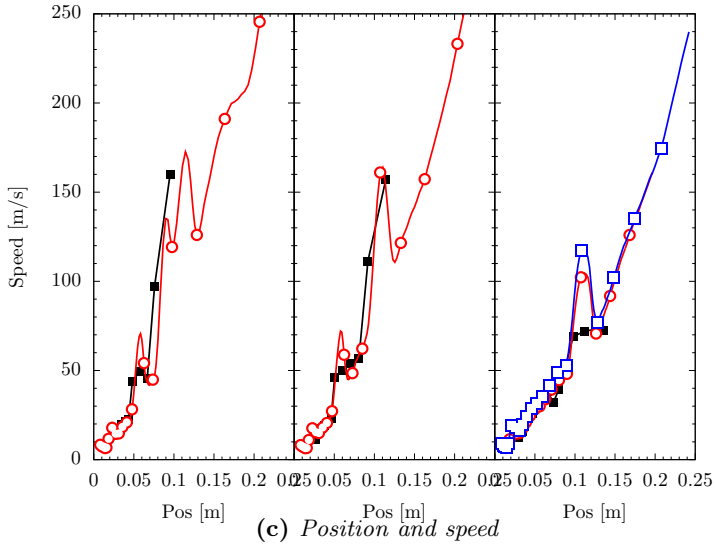

(c) *Position and speed*

Figure 8.35: *Influence of the geometry (QCMF LES results with thermally perfect EoS) on the flame characteristics for the Family 2 -* ■ *Experimental,* ○ *Hawkes,* □ *FurebyM*

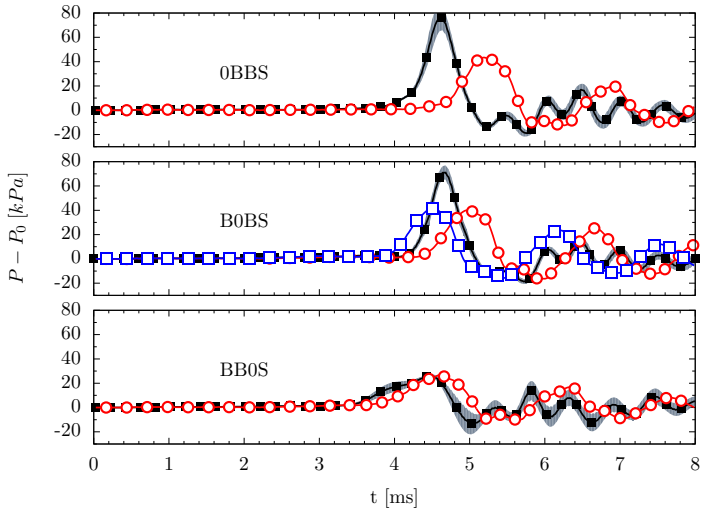

(a) *Wall sensor*

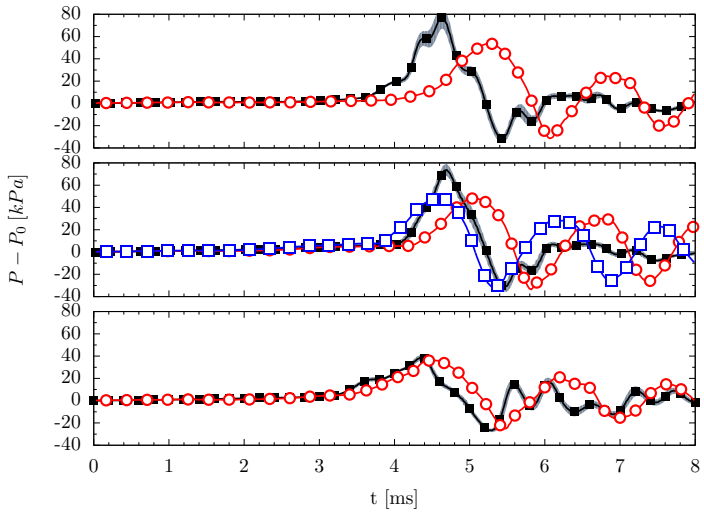

(b) *Base sensor*

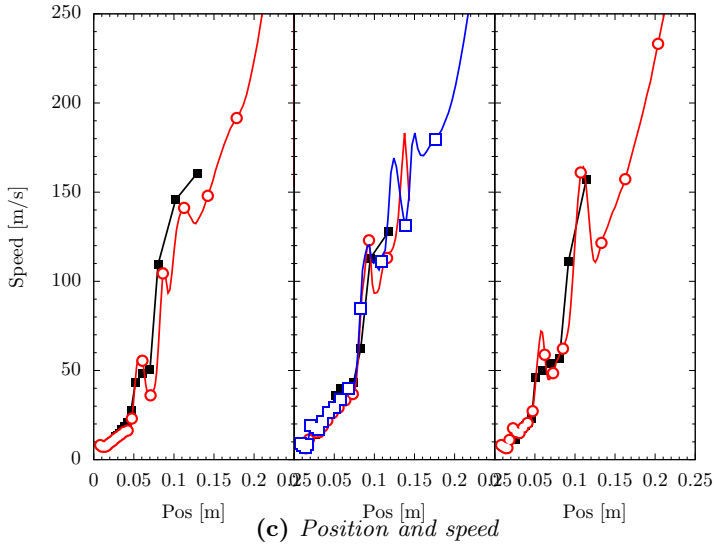

(c) *Position and speed*

Figure 8.36: *Influence of the geometry (QCMF LES results with thermally perfect EoS) on the flame characteristics for the Family 3 -* ■ *Experimental,* ○ *Hawkes,* □ *FurebyM*

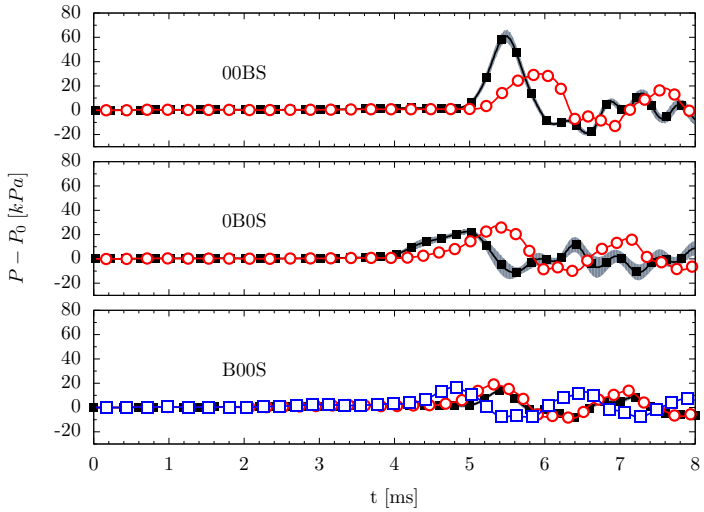

(a) *Wall sensor*

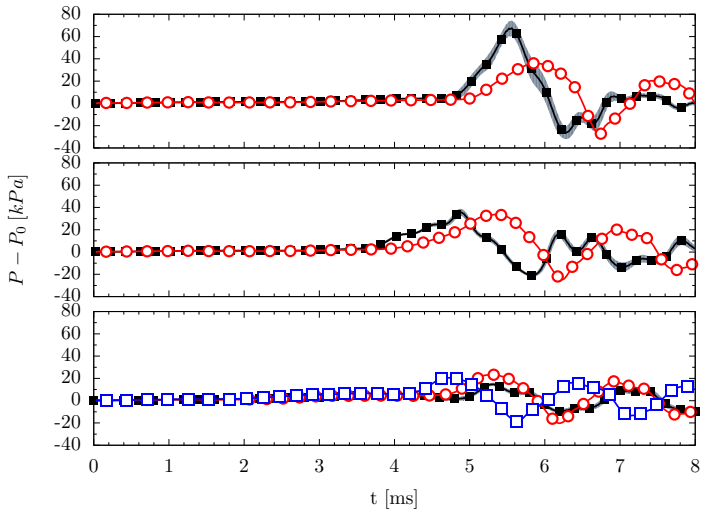

(b) *Base sensor*

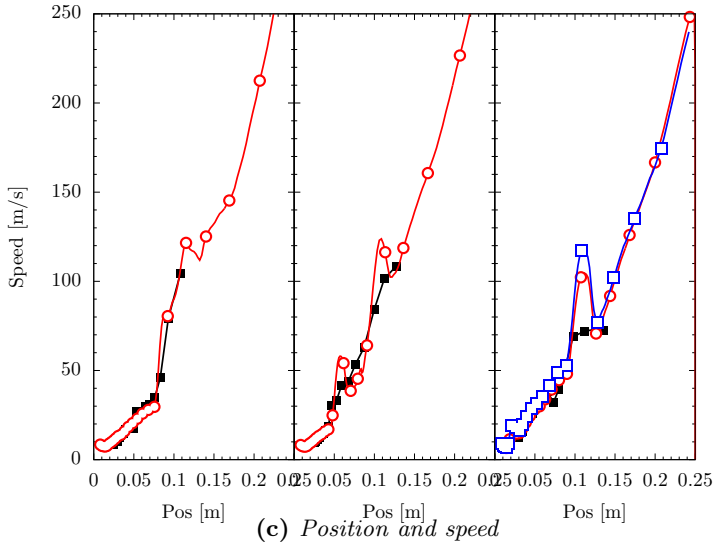

(c) *Position and speed*

Figure 8.37: *Influence of the geometry (QCMF LES results with thermally perfect EoS) on the flame characteristics for the Family 4 -* ■ *Experimental,* ○ *Hawkes,* □ *FurebyM*

8.7 Conclusion

A theoretical review of the different flame wrinkling models considered in this work has been presented, highlighting their responses under the influence of turbulence. It was found that all models except the constant fractal dimension one (Boger) were correctly recovering a unity wrinkling factor for negligible turbulence intensity levels. As it increases, it was found that Charlette's model would predict the fastest transition towards a fully turbulent burning mode, albeit limited by a clipping of the wrinkling factor value at high turbulent intensities, while the constant fractal dimension model would not present any response to the changes in turbulence intensities. On the other hand, Hawkes' model was found to have the shallowest increase of wrinkling factor at low turbulence intensity, but the largest values at high intensities due to the upper fractal dimension value of 8/3 compared to the usually considered 7/3. The other models were found between these two extremes. These considerations were validated using one-dimensional simulations where the flame speed were measured for flames propagating in frozen turbulence. The model response to a change of the physical coefficient (laminar viscosity value) was also presented, as some of them rely on the value of viscosity which changes sixfold between the reactants and products. It was found that at high temperatures, the transition from laminar to turbulent propagation mode of the flame would occur at larger intensities that in cold flows, but also that the value of the wrinkling factor would be dramatically reduced in the Hawkes' model, by a factor or approximately 4.

The constant fractal dimension model (Boger) was then used to assess the quality and validity of the LES simulations. The agreement between the experimental visualisations and LES results for the propagating flame in the obstacle filled chamber was found to be very good, with a qualitatively correct prediction of all the characteristic propagation modes, such as an initial spherical laminar propagation, elongation of the laminar flame front as it passes through the obstacles, merging of the fingers thus created, and subsequent wrinkling of the flame front under the influence of turbulence, before a transition to a fully turbulent flame front. The speed and position of the flame were also measured numerically and compared with experimentally obtained data where a correct agreement was found. The flame accelerations as it passes through the obstacles were well reproduced and the final speed of the flame was found to match fairly well with experimental measurements. However, due to the very fast flames (final speeds close to 300 $[m/s]$, experimental measurements of flame speed and positions suffer from quite large inaccuracies. The pressure was also measured in similar locations as the two experimental pressure sensors, and the results compared. The timing of the explosion was correctly reproduced, while an under-prediction of the computed overpressure peaks of respectively 25% and 50% at the base and wall sensors locations was found. Additionally, the late time acoustic reflections were not well predicted, albeit the equilibrium pressure value was correctly recovered. The quality of the LES was then assessed using Pope criterion to measure the amount of resolved TKE. It was found that more than 70% of it was being resolved highlighting that the resolution of the grid was enough.

Both QCMF and QCVF results were compared and found almost similar, while the effect of the specific heat ratio on the solution was evaluated. It was found that changing the value of the adiabatic index led to changes in the products temperature. As in the FSD framework, the reaction rate does not explicitly account for temperature effects, it could be guessed that changing the value of γ would not necessarily affect significantly the flame propagation. However, a very large effect was found, highlighting the need for a careful computation of this term, thus justifying the use of quasi-conservative methods. Increasing the value of γ was found to also accelerate the flame due solely to expansion effects. Indeed, the early stage propagation velocity (spherical growth) is directly function of the density ratio between the products and reactants, and thus the product temperature.

An analysis of the response of the LES computations to parameters changes was then presented by changing the numerical scheme, initial kernel radius, initial turbulent intensity, laminar flame speed, Smagorinsky constant and finally the wrinkling factor. The initial turbulent intensity was found to have no effect on the solution, while the radius only changes the peak time but not the flame propagation structure. The numerical scheme was found to accelerate the flame and reduce the overpressure magnitude which was as expected due to the numerical diffusion increase, while the laminar flame speed increase was

found to increase the overpressure magnitude and the flame speed leading to a earlier peak of pressure. This was also as expected, although when using complicated expressions for the reaction rate (estimation of the wrinkling factor Ξ_Δ), there are no simple relations linking changes in laminar flame speed with overpressures magnitude and overall flame speed changes. The Smagorinsky constant was found to have a very large impact on the solution as both turbulent diffusivity and wrinkling factor depend on it. An increase of the Smagorinsky constant was found to lead to a major increase in both flame speed and overpressure. Finally, the influence of the wrinkling factor was found moderate, as most models predict an overpressure between -25% and $+10\%$ of the experimental value. The major difference resides in the peak time, with more or less prolonged laminar propagation predicted by the different models. The flame structures were also found very similar between all models.

Finally, Hawkes' model was employed across a wide range of geometries and demonstrated the approach capabilities in the simulation of fast hydrogen explosions. Overpressure and flame speed and position were most of the time in agreement with the experimental measurements, thereby highlighting the potential of LES to accurately simulate small-scale explosions. Further tests would be needed to assess the capabilities and limitations of Hawkes' wrinkling factor model.

CHAPTER 9

Conclusion and recommendations

9.1 Conclusion

The recent attention focused on alternative fuels and reduction of pollutant emissions led to an increased interest in hydrogen as a fuel carrier, or as an energy source (nuclear fusion in facilities such as ITER and Wendelstein 7-X). The challenges associated with a widespread use of such a compound are well known and are twofold, being able to produce, transport and consume it with minimal environmental impact, but also enforce the safety and security of the different infrastructures involved in its life-cycle (production, extraction, consumption, etc.). The low-ignition energy, low detonation initiation energy combined with a high laminar flame speed and a wide flammability range make hydrogen a fuel that is particularly prone to produce large explosions and potentially detonations, which would in turn induce very large overpressures and extensive damages to the surrounding buildings and people [1]. This is further shown by the fact that hydrogen is often stored in pressurised tanks (700 $[bar]$), which, if leaking, could create very easily large inflammable clouds.

Explosions studies is now an established field of research and numerous lives have been saved by our increased knowledge of explosions and how to mitigate their impacts. Early risk preventions decisions were based on empirical correlations allowing a rough estimation of the potential damages caused by an explosion to a building or surrounding infrastructures. However, such approaches have inherent limitations such as a narrow range of applicability limited to configurations similar to the ones from which correlations have been extracted. Phenomenological approaches were then developed to improve the predictions accuracy by solving a set of differential equations for critical parameters such as the overpressure generated by explosions. Despite some noticeable improvements, these were unable to fully account for the geometry, and the turbulence modelling is usually based on empirical correlations.

Computational Fluid Dynamics (and more precisely Safety CFD or SCFD) has had a very positive role in the past 30 to 35 years in further improving both our understanding and prediction capabilities of such accidental events. Early studies realised with URANS methods in which the small structures of the studied configurations are accounted for using porosity models have shown encouraging results, especially on the simulation of very large explosions. However, these methods still rely on numerous model coefficients that need to be adjusted in each case, and the modelling of turbulence suffers from the statistical mean hypothesis (fully developed turbulence). These models have been shown to be unable to represent correctly the laminar flame speed but also the transition between the two flame propagation modes, laminar and turbulent, which have been both identified as key parameters in the prediction of explosions generated overpressures. Despite these limitations, URANS remains the workhorse of industrial studies, of explosions in particular thanks to its relatively affordable cost, and can still be used successfully in a risk reduction approach.

More recently, numerous LES studies carried out on massively parallel computers considerably increased our capabilities of simulating turbulent combustion in complex geometries. Building upon computational studies of small-scale experiments [76–80,115–118,123,136,137,156,200,249] studying hydrocar-

bon explosions, this research work focused on the simulation of hydrogen explosions on similar geometries.

In the particular case of hydrogen studies, and accounting for its high laminar flame speed added to its detonation properties, it is necessary to employ compressible LES solvers to accurately capture both low and high-speed deflagrations, but also shock waves. One such popular method is the finite-volume based Godunov method which has been shown to work well at all speeds and have positive shock-capturing capability [278]. Furthermore, in the presence of shocks or large temperature differences in the computational domain (the latter being always verified in combustion, and the former potentially in hydrogen studies), it is also of primary importance to finely account for the thermodynamic properties of the chemical mixture considered. One such key parameter is the heat capacity ratio variation as a function of temperature and mixture composition such that both shock speeds and temperatures can be accurately estimated. However, it has been shown that Godunov methods fail in the simulation of such multi-component/multi-species flows with complex thermodynamics and generates large pressure oscillations and temperature spikes at material interfaces. This has been attributed to the failure of conserving pressure equilibrium in presence of numerical diffusion [4, 5, 147, 170].

Recent literature developments have brought forward the double-flux method [6, 26] allowing the use of Godunov type methods in such flows while accounting for complex thermodynamics at the cost of a loss of energy conservation and an increased computational expense. The present work proposes a novel numerical approach designed to address the failure of Godunov scheme, while featuring better conservation properties and reduced computational cost (but increased memory usage) compared to the double-flux approach.

After a comprehensive review of the existing techniques (§. 2.3), the choice was made to extend the quasi-conservative 5-equation model of Allaire *et al.* [7] to reactive and viscous flows and to use the double-flux method as a benchmark model for comparison. The details of this extension of the 5-equation model to the case of viscous and reacting flows is presented in details in Chapter 3, where a second model consisting in the transformation of the quasi-conservative set of equations of the 5-equation model to a conservative set of equations is also considered. The governing equations, equation of states (calorically and thermally perfect gases approximations) and thermodynamic closures (isothermal and isobaric) of all methods considered in this work are discussed in details. A combination of two equation sets based respectively on volume and mass fraction along with quasi- and fully-conservative formulations are thus used for comparison,

- Quasi-Conservative Volume Fraction (QCVF) : 5-equation model of Allaire *et al.* [7] extended to viscous and reacting flows
- Fully-Conservative Volume Fraction (FCVF) : 5-equation model of Allaire *et al.* [7] extended to viscous and reacting flows and rewritten in conservation form
- Quasi-Conservative Mass Fraction (QCMF) : Fully-compressible viscous reacting Navier-Stokes equations solved with a quasi-conservative numerical scheme based on the Godunov method
- Fully-Conservative Mass Fraction (FCMF) : Fully-compressible viscous reacting Navier-Stokes equations solved with the classical Godunov scheme, and used here to highlight the different strengths and weaknesses of Godunov schemes in different test cases

The filtered forms of selected equation sets are presented for application to the LES framework, and a review of the closure of the sub-grid terms is provided (§. 3.7).

A detailed presentation of the numerical methods used to solve the different equation sets in the generalised curvilinear coordinate system is provided in Chapter 4 with notably the discussion of the Godunov method and approximate HLLC Riemann solver, variable reconstruction, time-integration schemes and viscous term discretisation. A particular attention has been given to the quasi-conservative treatment of the Navier-Stokes equations in the case of the QCMF model, and to the extension of the widely used

HLLC solver to the treatment of an advection equation in the case of the QCVF equation set based on an original idea of Johnsen and Colonius [143]. Finally, a novel formulation of the Navier-Stokes Characteristic Boundary Conditions have been derived for the QCVF equation set (§. 4.6, Appendix D), as well as a procedure for enforcing the pressure equilibrium in the case of diffusive and reactive flows.

Using a one-dimensional code written by the author, an extensive and comprehensive validation of the presented algorithms is then provided in Chapter 5, where the performance of the different algorithms are compared and evaluated in numerous test cases of increasing complexity. The findings are summarised in Table 9.1 and are as follows,

- Fully conservative methods feature large pressure (and consequently velocity) oscillations ($\approx 400[Pa]$) and temperature spikes ($\approx 1000\,[K]$) at material interfaces in moving contact and material waves as expected. In shock-tube experiments, pressure oscillations are also observed as species interfaces, as well as temperature spikes of large magnitudes ($\approx 1000\,[K]$) for the FCMF while correctly predicting the post-shock quantities, and a complete failure (wrong shock speed and post-shock pressure) for the FCVF model. Shock-bubble interaction test cases led to similar conclusions for the FCMF, and grid refinement analysis showed that pressure oscillations amplitudes were reduced with cell size (albeit at a very slow rate) but temperature spikes were increasing. Following its failure in shock-tube experiments, the FCVF was not considered for further testing, while the FCMF was kept as benchmark solution. It performed very well in viscous and constant volume reacting test cases due to the absence of moving contact surfaces, leading to accurate results. In one-dimensional flame simulations, it led to rapid halt of the computations due to out-of-bound temperature values. Surprisingly, it has been found to perform very well in detonation test problems which is attributed to the absence of contact waves in the simulation. As the shock travels through the mixture, no interface is created except the leading discontinuity.
- Both quasi-conservative schemes performed as expected for all inviscid test cases with an accurate prediction of the advection of a bubble while the conservation of the pressure equilibrium appeared excellent. The conservation qualities of the QCVF were found to be consistently better than the QCMF especially regarding the energy with respective errors of 10^{-13} and 10^{-3}. Shock-bubble interaction problems were also computed accurately, and it was found that the QCMF method was slightly more diffusive at contact and material interfaces than the QCVF, which was attributed to the interface-tracking flavour the QCVF model (advection equation for the volume fraction). Viscous test cases showed perfect agreement of both methods with analytical solution, at both low and high value of diffusion coefficients, and low and high Peclet number advection-diffusion problems. Constant reactor volume test cases also showed a very good agreement with the reference data of `Cantera`. One-dimensional flame speed calculations showed a good agreement with reference solutions as well, with an over-prediction of the temperature by the QCMF and an under-prediction of the flame speed by the QCVF. Detonation results with the QCMF were also in good agreement with the solution of Deiterding [73] in the Von-Neumann region, while the QCVF was unable to capture the strong leading discontinuity speed properly which was subsequently attributed to both its quasi-conservative character and a small instability of the scheme due to the procedure used to compute the pressure value.

The influence of the specific heat ratio index was also evaluated by running simulations using the FCMF with a single value of γ constant in both space and time to determine in which case the more complex QCMF/QCVF approaches could be replaced by a classical FMCF one. It was found that in constant volume reactors, a value of γ corresponding to the burnt value would give a reasonable agreement at the cost of slight delay in the ignition, but for laminar flame simulations, no single value of γ was found to predict both the correct temperature and flame speed (highlighting the relevance of estimating the complex thermodynamics in combustion). In detonation, a value of γ corresponding to the Von-Neumann value was found to predict approximately all the wave features.

Multi-dimensional validation cases presented at the beginning of Chapter 6 showed the correct implementation of the different algorithms in a multi-dimensional curvilinear framework. Two-dimensional inert and reacting shock-bubble test cases where also computed and their results compared with available

Test case	Advection		Diffusion	Reaction	QCVF	FCVF	QCMF	FCMF
	Sub.	Sup.						
Inviscid test cases (§. 5.2)								
Stationary contact surface	✓				✓	✓	✓	✓
Moving material surface	✓	✓			✓	×	✓	×
Moving contact surface	✓	✓			✓	×	✓	×
Multi-species shock-tube	✓	✓			✓	×	✓	×
Shock-Bubble interaction	✓	✓			✓	×	✓	×
Diffusive test cases (§. 5.3)								
Pure diffusion			✓		✓	NA	✓	✓
Advection diffusion	✓	✓	✓		✓	*NA*	✓	✓
Reactive test cases (§. 5.4)								
0D Constant Volume Reactor				✓	✓	NA	✓	✓
1D laminar flame	✓		✓	✓	✓	*NA*	✓	×
1D detonations	✓	✓	✓	✓	×	*NA*	✓	✓

Table 9.1: *Summary of one-dimensional validation of QCVF, FCVF, QCMF, FCMF schemes - Sub. stands for "Subsonic" and Sup. for "Supersonic", ✓ means (left) Governing equations terms tested (right) Solution agrees with analytical or reference solution, and no crash of the computation, × means test failed (crash of the computation, pressure oscillations, temperature spikes, etc.) and NA means Non Applicable (has not been tested)*

experimental and/or computational results published. In the inert case, it was found that both QCMF and QCVF captured accurately the bubble deformation and dynamics as well as the interface mixing, while the FCMF captured with similar accuracy the different flow features, but also presented large temperature spikes along the whole interface, which in the case of accounting for temperature-dependant phenomena would not be acceptable. The reacting shock-bubble results with both QCMF and QCVF algorithms showed a correct qualitative agreement with the published results, while a quantitative comparison could not be made due to the lack of published data. It shall be noted that the QCVF was able to compute this test case as accurately as the QCMF, even though it failed in the one-dimensional detonation problem. However, the small instability observed on the one-dimensional detonations problem was observed here as well with late time halts of computations highlighting the weaker stability of the QCVF algorithm over the QCMF.

The QCVF has thus been shown to feature better conservation of all conservative variables than the QCMF, with conservation errors comparable to the FCMF. In terms of computational cost, the difference between the two methods depends on a number of parameters such as the number of species simulated, if reaction and diffusion are accounted for (then the pressure equilibrium technique becomes necessary for the QCVF and it is relatively costly) and on what portion of the domain, etc. For inert cases, the cost of solving one additional equation per species (which includes the cost of reconstructing additional variables at the cell edges) is lower than the cost of solving the Riemann solver twice at each interface in the case of the QCMF approach when the number of species is limited. In the case of reaction/diffusion problems, the pressure equilibrium procedure of the QCVF is quite costly, and so the balance between the two approaches will depend on the amount of diffusing/reacting cells in the flow. Detailed investigations of the different algorithms execution times and memory usage are required to better understand they respective costs.

The present algorithms were then applied to the simulation of hydrogen explosion problems in the small-scale chamber of Sydney University [151]. The turbulent combustion model used in this work uses the Flame Surface Density formalism where an algebraic closure of the source term was considered. Several closures for the sub-grid flame wrinkling factor have been considered from the constant

fractal dimension approach of Boger [30] to the more involved efficiency functions of Angelberger [8, 9], Charlette [56, 57] or Hawkes [126]. The response of the different models to the turbulence intensity was theoretically investigated, where it was found that all models except the constant fractal dimension one were correctly recovering a unity wrinkling factor when the turbulence intensity was negligible, and a wrinkling factor increasing with turbulent intensity.

The constant fractal dimension model was then used to assess the quality and validity of the LES simulations carried on the Sydney explosion chamber. The agreement between the experimental visualisations and LES results for the propagating flame in the obstacle filled chamber was found to be very good, with a qualitatively correct prediction of all the characteristic propagation modes of a flame in a semi-confined explosion. The speed and position of the flame were also measured numerically and compared with the experimental data where a correct agreement was found. The pressure was also measured in similar locations as the two experimental pressure sensors, and the results compared. The timing of the explosion was correctly reproduced, while an under-prediction of the computed pressure of respectively 25% and 50% at the base and wall sensors locations was found and attributed to the coarse modelling of the combustion used in these tests. Finally, the model was found to account moderately well for the changes in geometry. The quality of the LES was then assessed and found correct with more than 70% of the turbulent kinetic energy resolved.

Both QCMF and QCVF results were compared and found almost similar, while the effect of the specific heat ratio on the solution was evaluated. It was found that even if this parameter is not taken into account explicitly by the reaction rate, as it influences the products temperature, it does have a large effect on the flame propagation characteristics through the expansion ratio that governs the early spherical growth of the flame kernel. This highlighted the need for a proper modelling of γ and through this, reinforced the choice of using the approaches presented in this work to simulate such a case.

The evaluation of the LES simulations responses to different models can be highlighted, where a large sensitivity to the sub-grid diffusion was found, but moderate for the sub-grid reaction rate models. The laminar flame speed being a not well defined parameters even for well-defined fuels, it has been shown that its influence on the overpressure estimation was moderate, and that its impact was more pronounced on the estimation of the peak time.

Finally, it has been found that LES was a powerful and accurate tool for the prediction of small-scale explosions. The fine structures of the flow were accurately predicted, such as the laminar propagation of the flame, interaction with the obstacles, wrinkling under turbulence influence, laminar to turbulent propagation mode transition, formation of hot products pockets, etc. allowing a precise estimation of the both the flame speed and overpressure. This highlights the increased predictive capabilities of LES over RANS, albeit at the cost of an increased computational cost, which can be tackled by using massively parallel computers. Fast deflagrations with high-order methods for hydrogen explosions have thus been presented and investigated.

9.2 Future work

Future work would involve investigating several points in terms of numerical modelling,

- Further validation of QCVF/QCMF approaches on multi-dimensional test cases
- Precise evaluations of the computational cost of each method (CPU time and memory)
- Investigation of the pressure instability of the QCVF approach

and on the combustion modelling,

- Dynamic modelling for FSD, and especially looking at the dynamic formulation of Hawkes model [126]

- Simulation of deflagration to detonation transition with Flame Surface Density following the idea of Vaagsaether and Bjerketvedt
- As hydrogen features a pronounced thermo-diffusive instability, taking the Lewis effects into account in the FSD simulations could improve the prediction of the overpressure, but also of the flame speed
- Large curvature of the flame front are usually encountered in flame/obstacles interactions and accounting for stretch effects could also improve the accuracy of the computations

Bibliography

[1] **Abdel-Aal, H., Sadik, M., Bassyouni, M., and Shalabi, M.** "A New Approach To Utilize Hydrogen As A Safe Fuel". *International Journal of Hydrogen Energy*, 2005:30:pp. 1511–1514.

[2] **Abdel-Gayed, R., Bradley, D., Hamid, M., and Lawes, M.** "Lewis Number Effects On Turbulent Burning Velocity". *Proceedings of the Combustion Institute*, 1984:20:pp. 505–512.

[3] **Abdel-Raheem, M., Ibrahim, S., Malalasekera, W., and Masri, A.** "LES Of Hydrogen Air Premixed Flames In A Small Scale Combustion Chamber". *International Journal of Hydrogen Energy*, 2015:40:pp. 3098–3109.

[4] **Abgrall, R.** "Generalisation Of The ROE Scheme For The Computation Of Mixture Of Perfect Gases". *Recherche Aerospatiale*, 1988:6:pp. 31–43.

[5] **Abgrall, R.** "How to Prevent Pressure Oscillations in Multi-Component Flow Calculations : A Quasi-Conservative Approach". *Journal of Computational Physics*, 1996:125:p. 150.

[6] **Abgrall, R. and Karni, S.** "Computations of Compressible Multifluids". *Journal of Computational Physics*, 2001:169(2):pp. 594–623.

[7] **Allaire, G., Clerc, S., and Kokh, S.** "A Five-Equation Model for the Simulation of Interfaces Between Compressible Fluids". *Journal of Computational Physics*, 2002:18:pp. 577–616.

[8] **Angelberger, C., Egolfopoulos, F., and Veynante, D.** "LES of Chemical And Acoustic Forcing Of A Premixed Dump Combustior". *Flow, Turbulence and Combustion*, 2000:65:pp. 205–222.

[9] **Angelberger, C., Veynante, D., Egolfopoulos, F., and Poinsot, T.** "LES Of Combustion Instabilities In Premixed Flames". *Proceedings of the summer program 1998*, NASA Ames / Stanford University - Center For Turbulent Research, 1998.

[10] **Arntzen, B.** "Modelling Of Turbulence And Combustion For Simulation Of Gas Explosions In Complex Geometries". Ph.D. thesis, Norwegian University Of Science And Technology, 1998.

[11] **Aspden, A., Day, M., and Bell, J.** "Turbulence-Flame Interactions In Lean Premixed Hydrogen : Transition To The Distributed Burning Regime". *Journal of Fluid Mechanics*, 2011:680:pp. 287–320.

[12] **Ayache, S. and Mastorakos, E.** "Conditional Moment Closure / Large Eddy Simulation of the Delft III Natural Gas Non-Premixed Jet Flame". *Flow, Turbulence and Combustion*, 2012:88:pp. 207–231.

[13] **Bagadir, A. and Drikakis, D.** "Numerical Experiments Using High-Resolution Schemes for Unsteady, Inviscid, Compressible Flows". *Computer Methods in Applied Mechanics and Engineering*, 2004:193:pp. 4675–4705.

[14] **Baldwin, B. and Lomax, H.** "Thin-Layer Approximation and Algebraic Model for Separated Turbulent Flows". In *AIAA, 16th Aerospace Sciences Meeting*. NASA, Ames Research Center, Huntsville, United States, January, 16-18 1978: p. 9.

[15] **Balsara, D. and Shu, C.W.** "Monotonicity Preserving Weighted Essentially Non-Oscillatory Schemes With Increasingly High-Order Accuracy". *Journal of Computational Physics*, 2000: 160(2):pp. 405–452.

[16] **Baraldi, D., Kotchourko, A., Lelyakin, A., Yanez, J., Middha, P., Hansen, O., Gavrikov, A., Efimenko, A., Verbecke, F., Makarov, D., and Molkov, V.** "An Inter-Comparison Exercise On CFD Model Capabilities To Simulate Hydrogen Deflagrations In A Tunnel". *International Journal of Hydrogen Energy*, 2009:34(18):pp. 7862–7872.

[17] **Bates, K., Nikiforakis, N., and Holder, D.** "Richtmyer-Meshkov Instability Induced By The Interaction Of A Shock Wave With A Block Of SF_6". *Physics of Fluids*, 2007:19:pp. 1–16.

[18] **Baum, M., Poinsot, T., and Thevenin, D.** "Accurate Boundary Conditions For Multi-Component Reactive Flows". *Journal of Computational Physics*, 1994:116:pp. 247–261.

[19] **Bell, J., Day, M., Grcar, J., and Lijewski, J.** "Active Control For Statistically Stationary Turbulent Premixed Flames Simulations". *Communications in Applied Mathematics And Computational Science*, 2006:1(1):pp. 29–51.

[20] **Bilger, R.** "Conditional Moment Closure for Turbulent Reacting Flow". *Physics of Fluids*, February 1993:5(2):pp. 436–444.

[21] **Bilger, R.** "Future Progress In Turbulent Combustion Research". *Progress in Energy and Combustion Science*, 2000:26:pp. 367–380.

[22] **Bilger, R.** "Bedstead - A Simple Three-Part PDF". Private Communication, 30th July 2010.

[23] **Bilger, R., Pope, S., Bray, K., and Driscoll, J.** "Paradigms in Turbulent Combustion Research". In *Proceedings of the Combustion Institute*, vol. 30, 2005: pp. 21–42.

[24] **Billet, G.** "Improvement of Convective Concentration Fluxes in a One-Step Reactive Flow Solver". *Journal of Computational Physics*, 2005:204(1):pp. 319–352.

[25] **Billet, G. and Abgrall, R.** "An Adaptive Shock-Capturing Algorithm for Solving Unsteady Reactive Flows". *Computers and Fluids*, 2003:32:pp. 1473–1495.

[26] **Billet, G., Giovangigli, V., and Gassowski, G.** "Impact Of Volume Viscosity On A Shock-Hydrogen-Bubble Interaction". *Combustion Theory and Modelling*, 2008:12(2):pp. 221–248.

[27] **Billet, G. and Ryan, J.** "A Runge-Kutta Discontinuous Garlerkin Approach To Solve Reactive Flows : The Hyperbolic Operator". *Journal of Computational Physics*, 2011:230:pp. 1064–1083.

[28] **Bjerketvedt, D., Bakke, J., and Van Wingerden, K.** "Gas Explosion Handbook". *Journal of Hazardous Material*, 1997:52:pp. 1–150.

[29] **Boger, M.** "Modelisation De Sous-Maille Pour La Simulation Aux Grandes Echelles De La Combustion Turbulente Premielangee". Ph.D. thesis, Ecole Centrale Paris, 2000.

[30] **Boger, M. and Veynante, D.** "Large Eddy Simulation of a Turbulent Premixed V-shape Flame". In *Advances in Turbulence VIII*. CIMNE, Barcelona, Spain, 2000: pp. 449–452.

[31] **Boger, M., Veynante, D., Boughanem, H., and Trouve, A.** "Direct Numerical Simulation Analysis of Flame Surface Density Concept for Large-Eddy Simulation of Turbulent Premixed Combustion". In *Proceedings of the Combustion Institute*, vol. 27, 1998: pp. 917–925.

[32] **Borghi, R.** "Turbulent Combustion Modelling". *Progress in Energy and Combustion Science*, 1988:14:p. 245.

[33] **Bouffanais, R.** "Advances and Challenges of Applied LES". *Computers and Fluids*, 2010:39:pp. 735–738.

[34] **Bradley, D.** "Instabilities And Flame Speeds In Large-Scale Gaseous Premixed Explosions". *Philosophic Transactions of the Royal Society Of London*, 1999:A(3567):p. 1.

[35] **Bray, K.** "Turbulent Transport in Flames". In *Proceedings of the Royal Society A*, vol. 451 of *Mathematical, Physical & Engineering Sciences*. London, October 1995: pp. 231–256.

[36] **Bray, K., Champion, M., and Libby, P.** *Turbulent Reacting Flows, Lecture Notes in Engineering*, chap. The Interaction between Turbulence and Chemistry in Premixed Turbulent Flames, pp. 541–563. Springer, Verlag, 1989:.

[37] **Bray, K., Libby, P., Masuya, G., and Moss, J.** "Turbulence Production in Premixed Turbulent Flames". *Combustion Science & Technology*, 1981:25(3-4):pp. 127–140.

[38] **Bray, K., Libby, P., and Moss, J.** "Unified Modelling Approach for Premixed Turbulent Combustion - Part I : General Formulation". *Combustion and Flame*, July 1985:61(1):pp. 87–102.

[39] **Bray, K. and Moss, J.** "A Unified Statistical Model of the Premixed Turbulent Flame". *Acta Aeronautica*, 1977:4:pp. 291–319.

[40] **Bush, W. and Fendell, F.** "Asymptotic analysis of laminar flame propagation for general Lewis numbers". *Combustion Science & Technology*, 1970:1:p. 421.

[41] **Butler, T. and O'Rourke, P.** "A Numerical Method for Two-Dimensionnal Unsteady Reacting Flows". In *16th Symposium International On Combustion*. The Combustion Institute, 1977: pp. 1503–1515.

[42] **Bychkov, V., Akkerman, V., Fru, G., Petchenko, A., and Eriksson, L.E.** "Flame Acceleration In The Early Stages Of Burning In Tubes". *Combustion and Flame*, 2007:150:pp. 263–276.

[43] **Cael, G., Ng, H., Bates, K., Nikiforakis, N., and Short, M.** "Numerical Simulation Of Detonation Structures Using A Thermodynamically Consistent And Fully Conservative Reactive Flow Model For Multi-Component Computations". In *Proceedings Of The Royal Society A*, 0371, 2009: pp. 1–19.

[44] **Cammarota, F., Di Benedetto, A., Di Sarli, V., Salzano, E., and Russo, G.** "Combined Effects Of Initial Pressure And Turbulence On Explosion Of Hydrogen-Enriched Methane/Air Mixtures". *Journal of Loss Prevention In The Process Industries*, 2009:22:pp. 607–613.

[45] **Candel, S. and Poinsot, T.** "Flame Stretch And The Balance Equation For The Flame Surface Area". *Combustion Science & Technology*, 1990:70(1-3):pp. 1–15.

[46] **Candel, S., Veynante, D., Lacas, F., Darabiha, N., and Rolon, C.** "Current Progress and Future Trends in Turbulent Combustion". *Combustion Science & Technology*, 1994:98(4-6):pp. 245–264.

[47] **Candel, S., Maistret, E., Darabiha, N., Poinsot, T., Veynante, D., and Lacas, F.** "Experimental and Numerical Studies of Turbulent Ducted Flames". In *Proceedings of the Marble Symposium*. CalTech, Pasadena, August 1988: .

[48] **Cant, R., Pope, S., and Bray, K.** "Modelling of Flamelet Surface to Volume Ratio in Turbulent Premixed Combustion". In *23rd Symposium International on Combustion*. The Combustion Institute, Pittsburgh, Orleans, 1990: pp. 809–815.

[49] **Cant, S.** "RANS and LES Modelling of Premixed Turbulent Combustion". *Fluid Mechanics and Its Applications*, 2001:95:pp. 63–90.

[50] **Cebeci, T. and Smith, A.** "Analysis of Turbulent Boundary Layers", 1974.

[51] **Celik, I., Cehreli, Z., and Yavuz, I.** "Index Of Resolution Quality For LES". *Journal of Fluid Engineering*, 2005:127(5):pp. 949–958.

[52] **Cha, C., Kosaly, G., and Pitsch, H.** "Modeling Extinction and Reignition in Turbulent Nonpremixed Combustion Using a Doubly-Conditioned Moment Closure Approach". *Physics of Fluids*, 2001:13(12):pp. 3824–3834.

[53] **Chakravarthy, S., Anderson, D., and Salas, M.** "The Splitting Coefficient Matrix Method For Hyperbolic Systems Of Gas Dynamics". In *18th AIAA Aerospace Sciences Meeting*, AIAA-80-0268, 1980: .

[54] **Chargy, D., Abgrall, R., Fezoui, L., and Larrouturou, B.** "Comparison Of Several Upwind Schemes For Multi-Component One Dimensional Inviscid Flows". *Rapport de recherche no. 1253*, INRIA, 1990.

[55] **Chargy, D., Abgrall, R., Fezoui, L., and Larrouturou, B.** "Conservative Numerical Schemes For Multi-Component Inviscid Flows". *Recherche Aerospatiale*, 1992:2:p. 61.

[56] **Charlette, F., Meneveau, C., and Veynante, D.** "A Power-Law Flame Wrinkling Model for LES of Premixed Turbulent Combustion Part I : Non-Dynamic Formulation and Initial Tests". *Combustion and Flame*, October 2002:131(1-2):pp. 159–180.

[57] **Charlette, F., Meneveau, C., and Veynante, D.** "A Power-Law Flame Wrinkling Model for LES of Premixed Turbulent Combustion Part II : Dynamic Formulation". *Combustion and Flame*, October 2002:131(1-2):pp. 181–197.

[58] **Charlette, F., Trouve, A., Boger, M., and Veynante, D.** "A Flame Surface Density Model For LES Of Turbulent Premixed Flames". In *The Combustion Institute Joint Meeting Of The British, German And French Sections*, 1999: .

[59] **Chase, M., Curnutt, J., Downey, J., McDonald, R., Syverud, A., and Valenzuela, E.** "JANAF Thermochemical Tables". *Journal of Physical Chemistry*, 1982:11(3):pp. 695–941.

[60] **Chatakonda, O., Hawkes, E., Aspden, A., Kerstein, A., Kolla, H., and Chen, J.** "On The Fractal Characteristics Of Low Damkohler Number Flames". *Combustion and Flame*, 2013: 160:pp. 2422–2433.

[61] **Chen, Y. and Bilger, R.** "Experimental Investigation Of Three-Dimensional Flame-Front Structure In Premixed Turbulent Combustion : I - Lean Hydrogen/Air Bunsen Flames". *Combustion and Flame*, 2004:138(1):pp. 155–174.

[62] **Cho, P., Law, C., Hertzberg, J., and Chen, R.** "Structure And Propagation Of Turbulent Premixed Flames Astabilized In A Stagnation Flow". *Proceedings of the Combustion Institute*, 1988:21(1):pp. 1493–1499.

[63] **Chung, S. and Law, C.** "An Invariant Derivation Of Flame Stretch". *Combustion and Flame*, 1984:55:pp. 123–125.

[64] **Clanet, C. and Searby, G.** "On The "Tulip Flame" Phenomenon". *Combustion and Flame*, 1996:105:pp. 225–238.

[65] **Colin, O.** "Simulation aux Grandes Echelles de la Combustion Turbulente Premelangee dans les Statoreacteurs". Ph.D. thesis, Institut National Polytechnique de Toulouse, CERFACS - Toulouse, May 2000.

[66] **Colin, O., Ducros, F., Veynante, D., and Poinsot, T.** "A Thickened Flame Model for Large Eddy Simulation of Turbulent Premixed Combustion". *Physics of Fluids*, July 2000:12(7):pp. 1843–1863.

[67] **Collela, P., Ferguson, R., and Glaz, H.** "Multifluid algorithms for Eulerian finite difference methods", 1989.

[68] **Cook, A.** "Enthalpy Diffusion In Multi-Component Flows". *Physics of Fluids*, 2009:21:pp. 1–16.

[69] **Cook, A. and Riley, J.** "A Subgrid Model For Equilibrium Chemistry In Turbulent Flows". *Physics of Fluids*, 1994:6(8):p. 2868.

[70] **Damköhler, G.** "Der Einfluss Der Turbulenz Auf Die Flammengeschwindigkeit in Gasgemischen". *Z. Electrochemie und angewandte Physikalische Chemie*, 1947:46(NACA TM No. 1112):pp. 601–652.

[71] **Dandekar, K. and Gouldin, F.** "Temperature And Velocity Measurements In Premixed Turbulent Flames". In *Aerospace Science Meeting AIAA*, 1981: .

[72] **Davis, S.** "An Interface Tracking Method For Hyperbolic Systems Of Conservation Laws". *Applied Numerical Mathematics*, 1992:10:p. 447.

[73] **Deiterding, R.** "Parallel Adaptive Simulation Of Multi-Dimensional Detonation Structures". Ph.D. thesis, Brandenburgischen Technischen Universitat Cottbus, 2003.

[74] **Desjardins, O., Moureau, V., and Pitsch, H.** "An Accurate Conservative Level-Set/Ghost Fluid Method For Simulating Turbulent Atomization". *Journal of Computational Physics*, 2008: 227:pp. 8395–8416.

[75] **Di Benedetto, A., Di Sarli, V., Cammarota, F., and Russo, G.** "Explosion Behaviour Of CH4/O2/N2/CO2 and H2/O2/N2/CO2 Mixtures". *International Journal of Hydrogen Energy*, 2009:34:pp. 6970–6978.

[76] **Di Sarli, V. and Di Benedetto, A.** "Sensitivity To The Presence Of The Combustion Submodel For LES Of Transient Premixed Flame-Vortex Interactions". *Industrial & Engineering Chemistry Research*, 2012:51(22):pp. 7704–7712.

[77] **Di Sarli, V., Di Benedetto, A., and Russo, G.** "Large Eddy Simulation and PIV Measurements of Unsteady Premixed Flames Accelerated by Obstacles". *Flow, Turbulence and Combustion*, 2009:83:pp. 227–250.

[78] **Di Sarli, V., Di Benedetto, A., and Russo, G.** "Using Large Eddy Simulation for Understanding Vented Gas Explosions in the Presence of Obstacles". *Journal of Hazardous Material*, 2009:169:pp. 435–442.

[79] **Di Sarli, V., Di Benedetto, A., and Russo, G.** "Sub-Grid Scale Combustion Models for Large Eddy Simulation of Unsteady Premixed Flames Propagating around Obstacles". *Journal of Hazardous Material*, 2010:180:pp. 71–78.

[80] **Di Sarli, V., Di Benedetto, A., and Russo, G.** "LES Of Transient Premixed Flame-Vortex Interactions In Gas Explosions". *Chemical Engineering Science*, 2012:71:pp. 539–551.

[81] **Donat, R. and Marquina, A.** "Capturing Shock Reflections : An Improved Flux Formula". *Journal of Computational Physics*, 1996:125:pp. 42–58.

[82] **Dorofeev, S.** "Flame Acceleration And DDT In Gas Explosions". *Journal de Physique IV France*, 2002:12:p. 1.

[83] **Dorofeev, S., Bezmelnitsin, A., and Sidorov, V.** "Transition To Detonation In Vented Hydrogen-Air Explosions". *Combustion and Flame*, 1995:103:pp. 243–246.

[84] **Dorofeev, S., Sidorov, V., Dvoinishnikov, A., and Breitung, W.** "Deflagration-To-Detonation Transition In Large Confined Volume Of Lean Hydrogen-Air Mixtures". *Combustion and Flame*, 1996:104:pp. 95–110.

[85] **Dorofeev, S., Sidorov, V., Kuznetsov, M., Matsukov, I., and Alekseev, V.** "Effect Of Scale On The Onset Of Detonations". *Shock Waves*, 2000:10:pp. 137–149.

[86] **Drikakis, D., Hahn, M., Mosedale, A., and Thornber, B.** "Large Eddy Simulation Using High-Resolution and High-Order Methods". *Philosophical Transactions of the Royal Society A*, 2009:367:pp. 2985–2997.

[87] **Duchamp de Lageneste, L. and Pitsch, H.** "Progress In Large Eddy Simulation of Premixed and Partially Premixed Turbulent Combustion". *Annual Research Briefs 20020314 067*, NASA Ames / Stanford University - Center For Turbulent Research, December 2001.

[88] **Duchamp de Lageneste, L. and Pitsch, H.** "A Numerical Scheme for the Large Eddy Simulation of Turbulent Combustion Using a Level-Set Approach". *Annual Research Briefs 20030328 482*, NASA Ames / Stanford University - Center For Turbulent Research, December 2002.

[89] **Duclos, J., Veynante, D., and Poinsot, T.** "A Comparison of Flamelet Models for Turbulent Premixed Combustion". *Combustion and Flame*, 1993:95(1-2):pp. 101–118.

[90] **Ducros, F., Nicoud, F., and Poinsot, T.** "Wall-adapting local eddy-viscosity models for simulations in complex geometries 1998". In *Proceedings of 6th ICFD Conference on Numerical Methods for Fluid Dynamics*, 1998: pp. 293–300.

[91] **Echekki, T. and Mastorakos, E.** *Turbulent Combustion Modeling.* Springer, 2011.

[92] **Ern, A. and Giovangigli, V.** "EGlib Server and User Manual http://www.cmap.polytechnique.fr/www.eglib/home.html".

[93] **Ern, A. and Giovangigli, V.** *Multicomponent Transport Algorithms.* Springer-Verlag, 1994.

[94] **Fairweather, M., Hargrave, G., Ibrahim, S., and Walker, D.** "Studies Of Premixed Flame Propagation In Explosion Tubes". *Combustion and Flame*, 1999:116(4):pp. 504–518.

[95] **Fedkiw, R., Aslam, T., Merriman, B., and Osher, S.** "A Non-Oscillatory Eulerian Approach To Interfaces In Multi-material Flows (The Ghost-Fluid Method)". *Journal of Computational Physics*, 1999:152:p. 457.

[96] **Fedkiw, R., Aslam, T., and Xu, S.** "The Ghost-Fluid Method For Deflagration and Detonation Discontinuities". *Journal of Computational Physics*, 1999:154:pp. 393–427.

[97] **Floyd, J., Kempf, A., Kronenburg, A., and Ram, R.** "A Simple Model for the Filtered Density Function for Passive Scalar Combustion LES". *Combustion Theory and Modelling*, 2009: 13(4):pp. 559–588.

[98] **Fureby, C.** "A Fractal Flame-Wrinkling Large Eddy Simulation Model for Premixed Turbulent Combustion". In *Proc. Combust. Inst.*, vol. 30, 2005: pp. 593–601.

[99] **Fureby, C.** "ILES and LES of Complex Engineering Turbulent Flows". *ASME Journal of Fluid Engineering*, 2007:129:pp. 1514–1523.

[100] **Fureby, C. and Lofstrom, C.** "Large-Eddy Simulation Of Bluff-Body Stabilized Flames". *Proceedings of the Combustion Institute*, 1994:25:pp. 1257–1264.

[101] **Gamezo, V., Ogawa, T., and Oran, E.** "Deflagration-To-Detonation Transition In Premixed H2-Air In Channels With Obstacles". In *45th AIAA Sciences Meeting And Exhibit*, AIAA 2007-1172, 2007: .

[102] **Gamezo, V., Ogawa, T., and Oran, E.** "Numerical Simulations On Flame Propagation And DDT In Obstructed Channels Filled With Hydrogen-Air Mixture". *Proceedings of the Combustion Institute*, 2007:31:pp. 2463–2471.

[103] **Gamezo, V., Ogawa, T., and Oran, E.** "Flame Acceleration and DDT In Channels With Obstacles : Effect Of Obstacle Spacing". *Combustion and Flame*, 2008:155:pp. 302–315.

[104] **Gamezo, V., Ogawa, T., and Oran, E.** "Deflagration-To-Detonation In H2-Air Mixtures : Effect Of Blockage Ratio". In *47th Aerospace Sciences Meeting*, AIAA 2009-440, 2009: .

[105] **Garcia-Uceda, A., Raimo, A., Shapiro, E., and Thornber, B.** "Steady Turbulent Flow Computations Using A Low-Mach Fully Compressible Scheme". *AIAA Journal*, 2014:52(11):pp. 2559–2575.

[106] **Giacomazzi, E., Picchia, F., and Arcidiacono, N.** "A Review Of Chemical Diffusion : Criticism And Limits Of Simplified Methods For Diffusion Coefficient Calculation". *Combustion Theory and Modelling*, 2007:12(1):pp. 135–158.

[107] **Giovangigli, V.** "Multicomponent Flow Modeling. Modeling And Simulation In Science, Engineering And Technology", 1999.

[108] **Glassman, I. and Yetter, R.** *Combustion*. Academic Press, 4th ed., 2008.

[109] **Godunov, S.** "A Difference Method For Numerical Calculation Of Discontinuous Solutions Of The Equations Of Hydrodynamics". *Matematicheskii Sbornik*, 1959:47(3):pp. 271–306.

[110] **Goodwin, D.G., Moffat, H.K., and Speth, R.L.** "Cantera: An Object-oriented Software Toolkit for Chemical Kinetics, Thermodynamics, and Transport Processes". http://www.cantera.org, 2014. Version 2.1.2.

[111] **Gostintsev, Y., Istratov, A., Kidin, N., and Fortov, V.** "Autoturbulization Of Gas Flames - Theoretical Treatment". *High Temperature Physics (Teplofizika Vysokih Temperatur)*, 1999:37(4):p. 633.

[112] **Gouldin, F.** "An Application Of Fractals To Modeling Premixed Turbulent Flames". *Combustion and Flame*, 1987:68(3):pp. 249–266.

[113] **Grinstein, F., Margolin, L., and Rider, W.** *Implicit Large Eddy Simulation : Computing Turbulent Fluid Dynamics*. Cambridge University Press, 2007.

[114] **Groethe, M., Merilo, E., Colton, J., Chiba, S., Sato, Y., and Iwabuchi, S.** "Large Scale Hydrogen Deflagrations And Detonations". In *Proceedings of the First International Conference on Hydrogen Safety*, 120105, 2005: .

[115] **Gubba, S., Ibrahim, S., and Malalasekera, W.** "LES Study Of Influence Of Obstacles On Turbulent Premixed Flames In A Small Scale Vented Chamber". In *6th Mediterranean Combustion Symposium*, 2009: .

[116] **Gubba, S., Ibrahim, S., Malalasekera, W., and Masri, A.** "LES Modeling Of Premixed Deflagrating Flames In A Small-Scale Vented Explosion Chamber With A Series Of Solid Obstructions". *Combustion Science & Technology*, 2008:180(10):pp. 1936–1955.

[117] **Gubba, S., Ibrahim, S., Malalasekera, W., and Masri, A.** "Measurements And LES Calculations Of Turbulent Premixed Flame Propagation Past Repeated Obstacles". *Combustion and Flame*, 2011:158(2):pp. 2465–2481.

[118] **Gubba, S., Ibrahim, S., Malalasekera, W., and Masri, A.** "An Assessment of LES of premixed flames propagating past obstacles". *Combustion Theory and Modelling*, 2009:13(3):pp. 513–540.

[119] **Gulati, A. and Driscoll, J.** "Velocity-Density Correlations And Favre Averages Measured In A Turbulent Premixed Flame". *Combustion Science & Technology*, 1986:48(5):pp. 285–307.

[120] **Gulder, O.** "Turbulent Premixed Combustion Modelling Using Fractal Geometry". In *23rd International Symposium on Combustion, The Combustion Institute*, 1990: pp. 835–842.

[121] **Gulder, O.** "Turbulent Premixed Flame Propagation Models for Different Combustion Regimes". In *23rd International Symposium on Combustion, The Combustion Institute*. Pittsburgh, 1990: pp. 743–835.

[122] **Haas, J. and Sturtevant, B.** "Interaction Of Weak Shock-Waves With Cylindrical And Spherical Gas Inhomogeneities". *Journal of Fluid Mechanics*, 1987:181:pp. 41–76.

[123] **Hall, R., Masri, A., Yaroshchyk, P., and Ibrahim, S.** "Effects of Position and Frequency of Obstacles in Turbulent Premixed Propagating Flames". *Combustion and Flame*, 2009:156:pp. 439–446.

[124] **Hawkes, E. and Cant, R.** "Implications Of A Flame Surface Density Approach to LESOf Premixed Turbulent Combustion". *Combustion and Flame*, 2001:126:pp. 1617–1629.

[125] **Hawkes, E. and Cant, R.** "A Flame Surface Density Approach to Large Eddy Simulation of Premixed Turbulent Combustion". *Proceedings of the Combustion Institute*, 2000:28:pp. 51–58.

[126] **Hawkes, E., Chatakonda, O., Kolla, H., Kerstein, A., and Chen, J.** "A Petascale Direct Numerical Simulation Study of the Modelling of Flame Wrinkling for Large-Eddy Simulation in Intense Turbulence". *Combustion and Flame*, 2012:159:pp. 2690–2703.

[127] **Hentschel, H. and Procaccia, I.** "Relative Diffusion In Turbulent Media. The Fractal Dimension Of Clouds". *Physical Review A*, 1984:29:pp. 1461–1470.

[128] **Hierschfelder, J. and Curtis, C.** *Molecular Theory Of Gases And Liquid*. John Wiley & Sons, 1954.

[129] **Hillier, R.** "Computation Of Shock Wave Diffraction At A Ninety Degree Convex Edge". *Shock Waves*, 1991:1:pp. 89–98.

[130] **Hjertager, B., Bjoerkhaug, M., and Fuhre, K.** "Explosion Propagation Of Non-Homogeneous Methane-Air Clouds Inside An Obstructed 50m3 Vented Vessel". *Journal of Hazardous Material*, 1988:19(2):pp. 139–153.

[131] **Hjertager, B., Fuhre, K., and Bjoerkhaug, M.** "Gas Explosion Experiments In 1:33 and 1:5 Scale Offshore Separator And Compressor Modules Using Stoichiometric Homogeneous Fuel/Air Clouds". *Journal of Loss Prevention In The Process Industries*, 1988:1(4):pp. 197–205.

[132] **Houim, R.** "Modelling The Influence Of Shock Waves On The Combustion Of Aluminium Droplets". Ph.D. thesis, Pennsylvania State University, December 2011.

[133] **Houim, R.W. and Kuo, K.K.** "A Low-Dissipation and Time-Accurate Method for Compressible Multi-Component Flow with Variable Specific Heat Ratios". *Journal of Computational Physics*, 2011:230:pp. 8527–8553.

[134] **Housman, J., Kiris, C., and Hafez, M.** "Time-Derivative Preconditionning Methods for Multi-Component Flows. Part I : Riemann Problems". *Journal of Applied Mechanics*, 2009:76:pp. 1–12.

[135] **Housman, J., Kiris, C., and Hafez, M.** "Time-Derivative Preconditionning Methods for Multi-Component Flows. Part II : Two-Dimensional Applications". *Journal of Applied Mechanics*, 2009: 76:pp. 1–12.

[136] **Ibrahim, S., Gubba, S., Masri, A., and Malalasekera, W.** "Calculations Of Explosion Deflagrating Flames Using A Dynamic FSD Model". *Journal of Loss Prevention In The Process Industries*, 2009:22(3):pp. 258–264.

[137] **Ibrahim, S. and Masri, A.** "The Effects Of Obstructions On Overpressure Resulting From Premixed Flame Deflagration". *Journal of Loss Prevention In The Process Industries*, 2001:14(3):pp. 213–221.

[138] **Jarvis, S., Hargrave, G., and Ibrahim, S.** "An Experimental Investigation Of Flame Deflagration Over Single And Multiple Solid Obstacles". In *Proceedings Of The Eighteenth International Colloqium On The Dynamics Of Explosions And Reactive Systems*, 2001: .

[139] **Jenny, P., Mueller, B., and Thomann, H.** "Correction Of Conservative Euler Solvers For Gas Mixtures". *Journal of Computational Physics*, 1997:132:p. 91.

[140] **John, J.E.** *Gas Dynamics*. Allyn And Bacon, 2nd ed., 1984.

[141] **Johnsen, E.** "Spurious Oscillations And Conservation Errors In Interface-Capturing Schemes". *Annual research briefs*, NASA Ames / Stanford University - Center For Turbulent Research, 2008.

[142] **Johnsen, E.** "On The Treatment Of Contact Discontinuities Using WENO Schemes". *Journal of Computational Physics*, 2011:230:p. 8665.

[143] **Johnsen, E. and Colonius, T.** "Implementation Of WENO Schemes In Compressible Multi-Component Flows". *Journal of Computational Physics*, 2006:219:p. 715.

[144] **Johnsen, E. and Ham, F.** "Preventing Numerical Errors Generated By Interface-Capturing Schemes In Compressible Multi-material Flows". *Journal of Computational Physics*, 2012:231:pp. 5705–5717.

[145] **Karaca, M., Lardjane, N., and Fedioun, I.** "ILES of High-Speed Non-Reacting and Reacting Air/H2 Jets With A 5th Order WENO scheme". *Computers and Fluids*, 2012:62:pp. 25–44.

[146] **Karni, S.** "Viscous Shock Profiles And Primitive Formulations". *SIAM Journal of Numerical Analysis*, 1992:29:pp. 1592–1609.

[147] **Karni, S.** "Multi-Component Flow Calculations by a Consistent Primitive Algorithm". *Journal of Computational Physics*, 1994:112:p. 31.

[148] **Karni, S.** "Hybrid MultiFluid Algorithms". *SIAM Journal of Scientific Computing*, 1996:17:p. 1019.

[149] **Kawai, S. and Terashima, H.** "A High-Resolution Scheme for Compressible Multi-Component Flows with Shock Waves". *International Journal of Numerical Methods in Fluids*, 2011:66(10):pp. 1207–1225.

[150] **Kempf, A., Klein, M., and Janicka, J.** "Efficient Generation Of Initial- And Inflow-Conditions For Transient Turbulent Flows In Arbitrary Geometries". *Flow, Turbulence and Combustion*, 2005: 74:pp. 67–84.

[151] **Kent, J., Masri, A., Starner, S., and Ibrahim, S.** "A New Chamber To Study Premixed Flame Propagation Past Repeated Obstacles". In *5th Asia-Pacific Conference On Combustion*, 2005: .

[152] **Kerstein, A.** "Fractal Dimension Of Turbulent Premixed Flames". *Combustion Science & Technology*, 1988:60(4):pp. 441–445.

[153] **Kim, K. and Kim, C.** "Accurate, Efficient and Monotonic Numerical Methods for Multi-Dimensional, Compressible Flows, Part II : Multi-Dimensional Limiting Process". *Journal of Computational Physics*, 2005:208:pp. 570–615.

[154] **Kim, S., Choi, C., and Huh, K.** "Second-Order Conditional Moment Closure Modeling of a Turbulent CH4/H2/N2 Jet Diffusion Flame". *Proceedings of the Combustion Institute*, 2005:30:pp. 735–742.

[155] **Kim, S., Huh, K., and Bilger, R.** "Second-Order Conditional Moment Closure Modeling of Local Extinction and Reignition in Turbulent Non-Premixed Hydrocarbon Flames". *Proceedings of the Combustion Institute*, 2002:29:pp. 2131–2137.

[156] **Kirkpatrick, M., Armfield, S., Masri, A., and Ibrahim, S.** "Large Eddy Simulation of a Propagating Turbulent Premixed Flame". *Flow, Turbulence and Combustion*, 2003:70:pp. 1–19.

[157] **Klein, M., Sadiki, A., and Janicka, J.** "A Digital Filter Based Generation Of Inflow Data For Spatially Developing DNS or LES". *Journal of Computational Physics*, 2002:186:pp. 652–665.

[158] **Klimenko, A.** "Multi-Component Diffusion of Various Admixtures in Turbulent Flow". *Fluid Dynamics*, 1990:25:p. 327.

[159] **Klimenko, A.** "Note on the Conditional Moment Closure in Turbulent Shear Flows". *Physics of Fluids*, 1995:7:pp. 446–448.

[160] **Klimenko, A. and Bilger, R.** "Comditional Moment Closure for Turbulent Combustion". *Progress in Energy and Combustion Science*, 1999:25:pp. 595–687.

[161] **Knikker, R., Veynante, D., and Meneveau, C.** "A Priori Testing of a Similarity Model for Large Eddy Simulation of Turbulent Premixed Combustion". *Proceedings of the Combustion Institute*, 2002:29:pp. 2105–2111.

[162] **Knikker, R., Veynante, D., and Meneveau, C.** "A Dynamic Flame Surface Density Model for Large Eddy Simulation of Turbulent Premixed Combustion". *Physics of Fluids*, November 2004: 16(11):pp. 91–94.

[163] **Kobayashi, H., Tamura, T., Maruta, K., and Niioka, T.** "Burning Velocities Of Turbulent Premixed Flames In A High-Pressure Environment". *Proceedings of the Combustion Institute*, 1996: 26:pp. 389–396.

[164] **Kolmogorov, A.** "A Refinement of Previous Hypotheses Concerning the Local Structure of Turbulence in a Viscous Incompressible Fluid at High-Reynolds Number". *Journal of Fluid Mechanics*, 1962:13:pp. 82–85.

[165] **Kolmogorov, A.** "Dissipation Of Energy In The Locally Isotropic Turbulence". In *Proceedings : Mathematical And Physical Sciences*, vol. 434, 1991: pp. 15–17.

[166] **Kronenburg, A.** "Double Conditioning of Reactive Scalar Transport Equations in Turbulent Nonpremixed Flames". *Physics of Fluids*, 2004:16(7):pp. 2640–2648.

[167] **Kronenburg, A., Bilger, R., and Kent, J.** "Second-Order Conditional Moment Closure For Turbulent Jet Diffusion Flame". In *Twenty-Seventh International Symposium on Combustion, The Combustion Institute*, 1998: pp. 1097–1104.

[168] **Kwon, O., Rozenchan, G., and Law, C.** "Cellular Instabilities And Self-Acceleration Of Outwardly Propagating Spherical Flames". *Proceedings of the Combustion Institute*, 2002:29:pp. 1775–1783.

[169] **Kwon, S., Wu, M.S., Driscoll, J., and Faeth, G.** "Flame Surface Properties of Premixed Flames In Isotropic Turbulence : Measurements And Numerical Simulations". *Combustion and Flame*, 1992:88:pp. 221–238.

[170] **Larrouturou, B.** "How To Preserve The Mass Fraction Positive When Computing Compressible Multi-Component Flows". *Journal of Computational Physics*, 1991:95:p. 59.

[171] **Launder, B., Morse, A., Ridi, W., and Spalding, D.** "Prediction of Free Shear Flows - A Comparison of the Performance of Six Turbulence Models". *Proceedings Conference on Free Turbulent Shear Flows*, July 20-21 1972:1.

[172] **Law, C.** *Combustion Physics*. Cambridge University Press, 2006.

[173] **Lax, P., Courant, S., and Rees, M.** "On The solution Of Non-Linear Hyperbolic Differential Equations By Finite Differences". *Communications in Pure Applied Mathematics*, 1952:5:pp. 243–255.

[174] **Lax, P. and Wendroff, B.** "Systems Of Conservation Laws". *Communications in Pure Applied Mathematics*, 1990:13:pp. 217–237.

[175] **Lax, P., Harten, A., and Van Leer, B.** "On Upstream Differencing And Godunov-Type Schemes For Hyperbolic Conservation Laws". *SIAM Review*, 1983:25(1):pp. 35–61.

[176] **Lea, C. and Ledin, H.** "A Review Of The State-Of-The-Art In Gas Explosion Modelling". *Tech. rep.*, Health And Safety Laboratory, 2002.

[177] **Lee, S., Lele, S., and Moin, P.** "Simulation of Spatially Evolving Compressible Turbulence And Application of Taylors Hypothesis". *Physics of Fluids A4*, 1992:4:pp. 1521–1530.

[178] **LeVeque, R.** *Finite Volume Method For Hyperbolic Problems*. Cambridge, 2002.

[179] **Libby, P. and Bray, K.** "Countergradient Diffusion in Premixed Turbulent Flames". *AIAA Journal*, February 1981:19(2):pp. 205–213.

[180] **Libby, P. and Williams, F.** *Turbulent Reacting Flows*. Topics in Applied Physics. Springer, Berlin, 1st ed., 1980.

[181] **Liou, M.** "A Sequel To AUSM : AUSM+". *Journal of Computational Physics*, 1996:129:pp. 364–382.

[182] **Liou, M.** "Ten Years In The Making - AUSM Family". In *15th AIAA Computational Fluid Dynamics Conference*, 2001-2521, 2001: pp. 1–15.

[183] **Liu, T., Khoo, B., and Yeo, K.** "Ghost-Fluid Method For Strong Shock Impacting On Material Interfaces". *Journal of Computational Physics*, 2003:190(2):pp. 651–681.

[184] **Liu, X., Osher, S., and Chan, T.** "Weighted Essentially Non Oscillatory Schemes". *Journal of Computational Physics*, 1994:115:pp. 200–212.

[185] **Long, E., Hargrave, G., Jarvis, S., Justham, T., and Halliwell, N.** "Characterisation Of The Interaction Between Toroidal Vortex Structures And Flame Front Propagation". In *Journal Of Physics : Conference Series*, vol. 45, p. 104. IOP Publishing, 2006:.

[186] **Lord Newton of Braintree**. "The Buncefield Incident 11 December 2005: The final report of the Major Incident Investigation Board". *Tech. Rep. 1*, Major Incident Investigation Board, 2008.

[187] **Lord Newton of Braintree**. "The Buncefield Incident 11 December 2005: The final report of the Major Incident Investigation Board". *Tech. Rep. 2*, Major Incident Investigation Board, 2008.

[188] **Lv, Y. and Ihme, M.** "Development of Discontinuous Garlerkin Method For Detonation And Supersonic Combustion". In *51st AIAA Aerospace Sciences Meeting*, AIAA 2013-0688. AIAA, Grapevine, US, 07-10 January 2013: pp. 1–12.

[189] **Lv, Y. and Ihme, M.** "Discontinuous Garlerkin Method For Compressible Viscous Reacting Flow". In *21st AIAA Computational Fluid Dynamics Conference*, AIAA 2013-3067. AIAA, San Diego, US, 24-27 June 2013: pp. 1–18.

[190] **Lv, Y. and Ihme, M.** "Discontinuous Garlerkin Method For Multi-Component Chemically Reacting Flows And Combustion". *Journal of Computational Physics*, 2014:270:pp. 105–137.

[191] **Ma, R., Stein, T., Chakraborty, N., and Kempf, A.** "A Priori Testing Of Algebraic FSD Models For LES". *Combustion Theory and Modelling*, 2013:17(3):pp. 431–482.

[192] **Magnussen, B. and Hjertager, B.** "On Mathematical Modelling of Turbulent Combustion with Special Emphasis on Soot Formation and Combustion". *Proceedings of the Combustion Institute*, 1976:16:pp. 719–729.

[193] **Makarov, D. and Molkov, V.** "Modeling And LES Of Deflagration Dynamics In A Closed Vessel". *Combustion, Explosion And Shock Waves*, 2004:40(2):pp. 136–144.

[194] **Makarov, D., Molkov, V., and Gostintsev, Y.** "Comparison Between RNG And Fractal Combustion Models For LES Of Unconfined Explosions". *Combustion Science & Technology*, 2007: 179(1-2):pp. 401–416.

[195] **Makarov, D., Verbecke, F., Molkov, V., Kotchourko, A., Lelyakin, A., Yanez, J., Baraldi, D., Heitsch, M., Efimenko, A., and Gavrikov, A.** "An Inter-Comparison Of CFD Models To Predict Lean And Non-Uniform Hydrogen Mixture Explosions". *International Journal of Hydrogen Energy*, 2010:35(11):pp. 5754–5762.

[196] **Mantel, T. and Borghi, R.** "A New Model of Premixed Wrinkled Flame Propagation Based on a Scalar Dissipation Equation". *Combustion and Flame*, 1994:96(4):pp. 443–457.

[197] **Marble, F. and Broadwell, J.** "Technical Report TRW-9-PV". *Tech. rep.*, Purdue University, Project Squid Headquarters, 1977.

[198] **Marquina, A. and Mulet, P.** "A Flux-Split Algorithm Applied To Conservative Models For Multi-Component Compressible Flows". *Journal of Computational Physics*, 2003:185:pp. 120–138.

[199] **Masri, A., Ibrahim, S., Nehzat, N., and Green, A.** "Experimental Study Of Premixed Flame Propagation Over Various Solid Obstructions". *Experimental Thermal and Fluid Science*, 2000: 21(1-3):pp. 109–116.

[200] **Masri, A., AlHarbi, A., Meares, S., and Ibrahim, S.** "A Comparative Study of Turbulent Premixed Flames Propagating Past Repeated Obstacles". *Industrial & Engineering Chemistry Research*, 2012:71:pp. 7690–7703.

[201] **Masri, A., Ibrahim, S., and Cadwallader, B.** "Measurements and Large Eddy Simulation of a Propagating Turbulent Premixed Flame". *Experimental Thermal and Fluid Science*, 2006:30:pp. 687–702.

[202] **Mastorakos, E. and Bilger, R.** "Second-Order Conditional Moment Closure for the Autoignition of Turbulent Flows". *Physics of Fluids*, June 1998:10(6):pp. 1246–1248.

[203] **Matalon, M. and Matkowsky, B.** "Flame As Gas Dynamic Discontinuities". *Journal of Fluid Mechanics*, 1982:124:p. 239.

[204] **Meneveau, C. and Poinsot, T.** "Stretching And Quenching Of Flamelets In Premixed Turbulent Combustion". *Combustion and Flame*, 1991:86:pp. 311–322.

[205] **Menter, F.** "Zonal Two-Equations k-ω Turbulence Models for Aerodynamic Flows". *AIAA Journal*, 1993:93-2906:pp. 1–24.

[206] **Miller, G. and Puckett, E.** "A High-Order Godunov Method For Multiple Condensed Phases". *Journal of Computational Physics*, 1996:128:pp. 134–164.

[207] **Miller, S., Mitchell, R., Smooke, M., and Kee, R.** "Towards A Comprehensive Chemical Kinetic Mechanism For The Oxidation Of Acetylene : Comparison Of Model Predictions With Results From Flame And Shock Tube Experiments". *Proceedings of the Combustion Institute*, 1982:19:pp. 181–196.

[208] **Mitani, T.** "Propagation Velocities of Two-Reactants Flames". *Combustion Science & Technology*, 1980:21:p. 175.

[209] **Molkov, V. and Makarov, D.** "Rethinking The Physics Of Large-Scale Vented Explosions And Its Mitigation". *Process Safety And Environmental Protection*, 2006:84(1):pp. 33–39.

[210] **Molkov, V., Makarov, D., and Schneider, H.** "LES Modelling Of An Unconfined Large-Scale Hydrogen-Air Deflagration". *Journal of Physics D : Applied Physics*, 2006:39:pp. 4366–4376.

[211] **Moller, S., Lundgren, E., and Fureby, C.** "Large-Eddy Simulation Of Unsteady Combustion". *Proceedings of the Combustion Institute*, 1996:26:pp. 241–248.

[212] **Moureau, V. and Desjardins, O.** "A Second-Order Ghost-Fluid Method For The Primary Atomization Of Liquid Fuel In Air-Blast Type Injectors". *Proceedings of the summer program 2008*, NASA Ames / Stanford University - Center For Turbulent Research, 2008.

[213] **Moureau, V., Fiorina, B., and Pitsch, H.** "A Level-Set Formulation For Premixed Combustion LES Considering The Turbulent Flame Structure". *Combustion and Flame*, 2009:156:pp. 801–812.

[214] **Moureau, V., Lartigue, G., Sommerer, Y., Angelberger, C., Colin, O., and Poinsot, T.** "Numerical Methods For Unsteady Compressible Multi-Component Reacting Flows On Fixed And Moving Grids". *Journal of Computational Physics*, 2005:202:pp. 710–736.

[215] **Mulder, W., Osher, S., and Sethian, J.** "Computing Interface Motion In Compressible Gas Dynamics". *Journal of Computational Physics*, 1992:100:p. 209.

[216] **Murayama, M. and Takeno, T.** "Fractal-like Character Of Flamelets In Turbulent Premixed Combustion". *Proceedings of the Combustion Institute*, 1989:22(1):pp. 551–559.

[217] **Navarro-Martinez, S. and Kronenburg, A.** "LES-CMC Simulations of a Turbulent Bluff-Body Flame". *Proceedings of the Combustion Institute*, 2007:31:pp. 1721–1728.

[218] **Navarro-Martinez, S., Kronenburg, A., and Di Mare, F.** "Conditional Moment Closure for Large Eddy Simulation". *Flow, Turbulence and Combustion*, 2005:75:pp. 245–274.

[219] **Noh, W. and Woodward, P.** *Springer Lectures Notes In Physics*, vol. 59, chap. SLIC (Simple Line Interface Calculation), pp. 330–339. Springer-Verlag, 1976:.

[220] **North, G. and Santavicca, D.** "The Fractal Nature Of Premixed Turbulent Flames". *Combustion Science & Technology*, 1990:72(4):p. 215.

[221] **Oran, E. and Gamezo, V.** "Origins Of The Deflagration-To-Detonation Transition In Gas-Phase Combustion". *Combustion and Flame*, 2007:148:pp. 4–47.

[222] **Osher, S. and Fedkiw, R.** *Level Set Methods And Dynamic Implicit Interfaces*. Springer, 2003.

[223] **Osher, S. and Sethian, J.** "Fronts Propagating With Curvature-Dependent Speed : Algorithms Based On Hamilton-Jacobi Formulations". *Journal of Computational Physics*, 1988:79:pp. 12–49.

[224] **Pakdee, W. and Mahaligan, S.** "An Accurate Method To Implement Boundary Conditions For Reacting Flows Based On Characteristic Wave Analysis". *Combustion Theory and Modelling*, 2003:7(4):pp. 705–729.

[225] **Pappas, J., Solberg, D., and Foyn, T.** "Gas Explosion Research Program - Final Report". *Tech. Rep. 83-1334*, Det Norske Veritas, 1983.

[226] **Pasman, H., Groothuizen, T., and de Gooijer, H.** "Design Of Pressure Relief Vents". In *Proceedings Of The First International Symposium On Loss Prevention*, 1974: p. 185.

[227] **Patel, S., Jarvis, S., Ibrahim, S., and Hargrave, G.** "An Experimental And Numerical Investigation Of Premixed Flame Deflagration In A Semi-Confined Explosion Chamber". *Proceedings of the Combustion Institute*, 2002:29(2):pp. 1849–1854.

[228] **Pedersen, H. and Middha, P.** "Modelling Of Vented Gas Explosions In The CFD Tool FLACS". *Chemical Engineering*, 2012:26:p. 1.

[229] **Peters, N.** "Laminar Flamelet Concepts in Turbulent Combustion". In *21st International Symposium on Combustion, The Combustion Institute*. Pittsburgh, 1988: pp. 1231–1250.

[230] **Peters, N.** "The Turbulent Burning Velocity for Large-Scale and Small-Scale Turbulence". *Journal of Fluid Mechanics*, 1999:384:pp. 107–132.

[231] **Peters, N.** *Turbulent Combustion*. Cambridge University Press, 2000.

[232] **Peters, N.** "Combustion Theory". *Tech. rep.*, Combustion Energy Frontier Research Center - Princeton University, June-July 2010.

[233] **Pitsch, H.** "A G-Equation Formulation for Large Eddy Simulation of Premixed Turbulent Combustion". *Annual Research Briefs 20030328 482*, NASA Ames / Stanford University - Center For Turbulent Research, December 2002.

[234] **Pitsch, H.** "Large Eddy Simulation of Turbulent Combustion". *Annual Review of Fluid Mechanics*, 2006:38:pp. 453–482.

[235] **Pitsch, H. and Duchamp de Lageneste, L.** "Large Eddy Simulation of Premixed Turbulent Combustion Using a Level-Set Approach". *Proceedings of the Combustion Institute*, 2002:29:pp. 2001–2008.

[236] **Poinsot, T., Echekki, T., and Mungal, M.** "A Study of the Laminar Flame Tip and Implications for Premixed Turbulent Combustion". *Combustion Science & Technology*, 1992:81:pp. 45–73.

[237] **Poinsot, T. and Lele, S.** "Boundary Conditions For Direct Numerical Simulations Of Compressible Viscous Flows". *Journal of Computational Physics*, 1992:101:pp. 104–129.

[238] **Poinsot, T. and Veynante, D.** *Theoretical and Numerical Combustion*. Edwards, 2005.

[239] **Poinsot, T., Veynante, D., and Candel, S.** "Quenching Processes And Premixed Turbulent Combustion Diagrams". *Journal of Fluid Mechanics*, 1991:228:pp. 561–605.

[240] **Popat, N., Catlin, C., Arntzen, B., Lindstedt, R., Hjertager, B., Solberg, D., Saeter, O., and Van den Berg, A.** "Investigations To Improve And Assess The Accuracy Of Computational Fluid Dynamic Based Explosion Models". *Journal of Hazardous Material*, 1996:45(1):pp. 1–25.

[241] **Pope, S.** "The Evolution of Surfaces in Turbulence". *International Journal of Engineering Sciences*, 1988:26:pp. 445–469.

[242] **Pope, S.** "PDF Methods for Turbulent Reactive Flows". *Progress in Energy and Combustion Science*, 1985:11:pp. 119–192.

[243] **Pope, S.** "Computations of Turbulent Combustion ; Progress and Challenges". In *Proceedings of the 23rd Symposium (International) on Combustion*. The Combustion Institute, Pittsburgh, Orleans, 1990: pp. 591–612.

[244] **Pope, S.** *Turbulent Flows*. Cambridge University Press, 2000.

[245] **Porumbel, I. and Menon, S.** "Large-Eddy Simulation Of Bluff-Body Stabilized Premixed Flames". In *44th AIAA Aerospace Sciences Meeting and Exhibit*, 2006: pp. 1–17.

[246] **Prasad, R. and Gore, J.** "An Evaluation Of Flame Surface Density Models For Turbulent Premixed Jet Flames". *Combustion and Flame*, 1999:116:pp. 1–14.

[247] **Probyn, M., Thornber, B., Drikakis, D., Youngs, D., and Williams, R.** "An Investigation Into Nonlinear Growth Rate of Two-Dimensional and Three-Dimensional Single-Mode Richtmyer-Meshkov Instability Using an Arbitrary-Lagrangian-Eulerian Algorithm". *ASME Journal of Fluid Engineering*, 2014:136(9):pp. 1–7.

[248] **Puttock, J., Yardley, M., and Cresswell, T.** "Prediction Of Vapour Cloud Explosions Using The SCOPE model". *Journal of Loss Prevention In The Process Industries*, 2000:13(3):pp. 419–431.

[249] **Quillatre, P.** "Simulation Aux Grandes Echelles d'Explosions En Domaine Semi-Confine". Ph.D. thesis, INP Toulouse, 2014.

[250] **Quirk, J. and Karni, S.** "On The Dynamic Of A Shock-Bubble Interaction". *Journal of Fluid Mechanics*, 1996:318:pp. 129–163.

[251] **Richard, S., Colin, O., Vermorel, O., Benkenida, A., Angelberger, C., and Veynante, D.** "Towards LES Of Combustion In Spark Ignition Engines". *Proceedings of the Combustion Institute*, 2007:31:pp. 3059–3066.

[252] **Roe, P.** "Approximate Riemann Solvers, Parameters And Difference Schemes". *Journal of Computational Physics*, 1981:43:p. 357.

[253] **Roe, P.** *Numerical Methods For Fluid Dynamics*, chap. Fluctuations And Signals - A Framework For Numerical Evolution Problems, pp. 219–257. Academic Press, 1982:.

[254] **Roe, P.** "A New Approach To Computing Discontinuous Flows Of Several Ideal Gases". *Tech. rep.*, Cranfield Institute Of Technology, 1984.

[255] **Ruuth, S. and Spiteri, R.** "Two Barriers on Strong-Stability-Preserving Time Discretisations Methods". *Journal of Scientific Computation*, 2002:17(1-4):pp. 211–220.

[256] **Sankaran, R., Hawkes, E., Chen, J., Lu, T., and Law, C.** "Structure of a Spatially Developing Turbulent Lean Methane-Air Bunsen Flame". *Proceedings of the Combustion Institute*, 2007:31:pp. 1291–1298.

[257] **Selle, L., Lartigue, G., Poinsot, T., Kaufmann, P., Krebs, W., and Veynante, D.** "LES Of Turbulent Combustion For Gas Turbines With Reduced Chemistry". *Proceedings of the summer program 2002*, NASA Ames / Stanford University - Center For Turbulent Research, 2002.

[258] **Selle, L., Lartigue, G., Poinsot, T., Koch, R., Schildmacher, K.U., Krebs, W., Prade, B., Kaufmann, P., and Veynante, D.** "Compressible LES of Turbulent Combustion in Complex Geometry on Unstructured Meshes". *Combustion and Flame*, 2004:137:pp. 489–505.

[259] **Shankar, S., Kawai, S., and Lele, S.** "Numerical Simulation Of Multi-Component Shock Accelerated Flows And Mixing Using Localized Artificial Diffusivity Method". In *48th AIAA Aerospace Science Meeting*, AIAA 2010-352, 2010: pp. 1–31.

[260] **Shyue, K.H.** "An Efficient Shock-Capturing Algorithm For Compressible Multi-Component Problems". *Journal of Computational Physics*, 1998:142:pp. 208–242.

[261] **Smagorinsky, J.** "General Circulation Experiments with the Primitive Equations - I - The Basic Experiment". *Monthly Weather Review*, 1963:91:pp. 99–164.

[262] **Smiljanovski, V., Moser, V., and Klein, R.** "A Capturing-Tracking Hybrid Scheme For Deflagration Discontinuities". *Combustion Theory and Modelling*, 1997:1-2:pp. 183–215.

[263] **Smooke, M. and Giovangigli, V.** "Formulation of the Premixed and Nonpremixed Test Problems". *Lecture Notes Physics*, 1991:384:pp. 1–28.

[264] **Spalart, P. and Allmaras, S.** "One-Equation Turbulence Model for Aerodynamic Flows". *Recherche Aerospatiale*, 1994:1:pp. 5–21.

[265] **Spalding, D.** "Mixing and Chemical Reactions in Steady Confined Turbulent Flames". *Proceedings of the Combustion Institute*, 1971:13:pp. 649–657.

[266] **Sreenevasan, K. and Meneveau, C.** "The Fractal Facet Of Turbulence". *Journal of Fluid Mechanics*, 1986:173(1):pp. 357–386.

[267] **Staffelbach, G.** "Simulation Aux Grandes Echelles Et Analyse Acoustique De Turbines A Gaz Industrielles Multi-Bruleurs". Ph.D. thesis, Institut National Polytechnique de Toulouse, 2006.

[268] **Sutherland, J. and Kennedy, C.** "Improved Boundary Conditions For Viscous, Reacting, Compressible Flows". *Journal of Computational Physics*, 2003:911:pp. 502–524.

[269] **Taylor, B., Houim, R., Kessler, D., Gamezo, V., and Oran, E.** "Detonation Initiation And Shock-Flame Interaction In Hydrogen-Air Mixtures". In *51st AIAA Aerospace Sciences Meeting*, AIAA 2013-1171. AIAA, Grapevine, US, 07-10 January 2013: pp. 1–13.

[270] **Terashima, H. and Tryggvason, G.** "A Front-Tracking / Ghost-Fluid Method For Fluid Interfaces In Compressible Flows". *Journal of Computational Physics*, 2009:228:pp. 4012–4037.

[271] **Thompson, K.** "Time Dependent Boundary Conditions For Hyperbolic Systems". *Journal of Computational Physics*, 1987:68:pp. 1–24.

[272] **Thompson, K.** "Time Dependent Boundary Conditions For Hyperbolic Systems II". *Journal of Computational Physics*, 1990:89:pp. 439–461.

[273] **Thornber, B.** "Implicit Large Eddy Simulation For Unsteady Multi-Component Compressible Turbulent Flows". Ph.D. thesis, Cranfield University, 2007.

[274] **Thornber, B., Bilger, R., Masri, A., and Hawkes, E.** "An Algorithm for LES of Premixed Compressible Flows Using the Conditional Moment Closure Model". *Journal of Computational Physics*, 2011:230:pp. 7687–7705.

[275] **Thornber, B., Drikakis, D., Williams, R., and Youngs, D.** "On Entropy Generation and Dissipation of Kinetic Energy in High-Resolution Shock-Capturing Schemes". *Journal of Computational Physics*, 2008:227:pp. 4853–4872.

[276] **Thornber, B., Mosedale, A., Drikakis, D., Youngs, D., and Williams, R.** "An Improved Reconstruction Method for Compressible Flows with Low-Mach Number Features". *Journal of Computational Physics*, 2008:227:pp. 4873–4894.

[277] **Ton, V.** "Improved Shock-Capturing Methods For Multi-component And Reacting Flows". *Journal of Computational Physics*, 1996:128:p. 237.

[278] **Toro, E.** *Riemann Solvers and Numerical Methods for Fluid Dynamics.* Springer-Verlag, Cambridge, 3rd ed., 2009.

[279] **Triantafyllidis, A.** "Large Eddy Simulation of Spark Ignition Processes with the CMC Method". Ph.D. thesis, University of Cambridge, St Edmund's College, May 2009.

[280] **Triantafyllidis, A., Mastorakos, E., and Eggels, R.** "Large Eddy Simulations of Forced Ignition of a Non-Premixed Bluff-Body Methane Flame with Conditional Moment Closure". *Combustion and Flame*, 2009:156:pp. 2328–2345.

[281] **Trouve, A. and Poinsot, T.** "The Evolution Equation for the Flame Surface Density in Turbulent Premixed Combustion". *Journal of Fluid Mechanics*, 1994:278:pp. 1–31.

[282] **United Nations, Department of Economic**. "World Population Prospects : The 2004 Revision : Volume 1 : Comprehensive Tables". *Tech. rep.*, United Nations, 2006.

[283] **Van Kalmthout, E.** "Stabilisation et Modelisation des Flammes Turbulentes et Premelangees. Etude Theorique et Simulation Directes". Ph.D. thesis, Ecole Centrale de Paris, 1996.

[284] **Van Leer, B.** "Towards The Ultimate Conservative Difference Scheme V. A Second-Order Sequel To Godunov's Method". *Journal of Computational Physics*, 1979:32(1):pp. 101–136.

[285] **Vervisch, L., Bidaux, E., Bray, K., and Kollman, W.** "Surface Density Function in Premixed Turbulent Combustion Modeling, Similarities Between Probability Density Function and Flame Surface Approaches". *Physics of Fluids*, 1995:7:p. 2496.

[286] **Veynante, D. and Vervisch, L.** "Turbulent Combustion Modelling". *Progress in Energy and Combustion Science*, 2002:28:pp. 193–266.

[287] **Vreman, B., Geurts, A., and Kuerten, H.** "A Priori Tests of Large Eddy Simulation of the Compressible Plane Mixing Layer". *Journal of Engineering Mathematics*, 1995:29:pp. 299–327.

[288] **Wang, G., Boileau, M., Veynante, D., and Truffin, K.** "LES of a growing turbulent premixed flame kernel using a dynamic FSD model". *Combustion and Flame*, 2012:159:pp. 2742–2754.

[289] **Wang, S., Anderson, M., Oakley, J., Corradini, M., and Bonazza, R.** "A Thermodynamically Consistent And Fully Conservative Treatment Of Contact Discontinuities For Compressible Multi-Component Flows". *Journal of Computational Physics*, 2004:195:pp. 528–559.

[290] **Westbrook, C.K.** "Chemical Kinetics Of Hydrocarbon Oxidation In Gaseous Detonations". *Combustion and Flame*, 1982:46:pp. 191–210.

[291] **Westbrook, C.K. and Dryer, F.L.** "Chemical Kinetic Modeling Of Hydrocarbon Combustion". *Progress in Energy and Combustion Science*, 1984:10:pp. 1–57.

[292] **Whitehouse, D., Greig, D., and Koroll, G.** "Combustion Of Stratified Hydrogen-Air Mixtures In The 10.7 m3 Combustion Test Facility Cylinder". *Nuclear Engineering And Design*, 1996: 166(3):pp. 453–462.

[293] **Wilcox, D.** "A Half Century Historical Review of the k-ω Model". In *AIAA, 29th Aerospace Science Meeting.* DCW Industries, Inc., La Canada, United States, January, 7-10 1991: p. 10.

[294] **Wilke, C.** "A Viscosity Equation for Gas Mixtures". *The Journal Of Chemical Physics*, 1950: 18:pp. 517–519.

[295] **Williams, F.** *Combustion Theory*. Benjamin Cummings, Menlo Park, CA, 1985.

[296] **Williams, F.** *The Mathematics of Combustion*, chap. Turbulent Combustion, pp. 197–318. Society For Industrial and Applied Mathematics, 1985:.

[297] **Woolley, R. and Fairweather, M.** "Conditional Moment Closure Modelling of Soot Formation in Turbulent, Non-Premixed Methane and Propane Flames". *Fuel*, 2009:88:pp. 393–407.

[298] **Yakhot, V. and Orszag, S.** "Development Of Turbulence Models For Shear Flows By A Double Expansion Technique". *Physics of Fluids A*, 1992:4(7):pp. 1510–1520.

[299] **Yoo, C. and Im, H.** "Characteristic Boundary Conditions For Simulations of Compressible Reacting Flows with Multi-dimensional, Viscous and Reaction Effects". *Combustion Theory and Modelling*, 2007:11(2):pp. 259–286.

[300] **Yoo, C., Sankaran, R., and Chen, J.** "Three-Dimensional Direct Numerical Simulation Of A Turbulent Lifted Hydrogen Jet Flame In Heated Coflow : Flame Strabilization And Structure". *Journal of Fluid Mechanics*, 2009:640:pp. 453–481.

[301] **Zeldovich, Y., Barenblatt, G., Librovich, V., and Makhviladze, G.** *The Mathematical Theory of Combustion and Explosions*. Consultants Bureau, New-York, 1985.

[302] **Zhong, B., Scheurich, F., Titarev, V., and Drikakis, D.** "Turbulent Flow Simulations Around a Multi-Element Airfoil Using URANS, DES and ILES Approaches". In *19th AIAA Computational Fluid Dynamics*, AIAA 2009-3799, 2009: pp. 1–14.

[303] **Zimont, V. and Lipatnikov, A.** "A Numerical Model Of Premixed Turbulent Combustion In Gases". *Chemical Physics Rep.*, 1995:14:p. 993.

APPENDIX **A**

Computing mixture pressure or temperature using a Newton-Raphson procedure

A.1 Finding the pressure value for thermally perfect gases with the QCVF and FCVF models

The implicit equation for pressure derived in §. 3.4.3 does not accept analytical solutions. Therefore an iterative method has to be used to find a suitable approximation of the solution. Theoretically, a 5^{th} order polynomial equations accepts 5 roots, however, they can be complex or real. In our case, only the real positive roots are relevant to us, which means that the simple iterative Newton-Raphson procedure can be applied.

This choice is also strongly supported by the fact that the derivative of the implicit equation is known exactly, hence rendering the already fast convergence rate of the method even faster and speeding up the overall process. It is to be noted that the use of variable γ gas will add an important overhead to the computations, as even if the solution is found in less than 10 iterations, it has to be repeated in each cell at each time-step.

It can be written as follows,

$$\sum_{i=0}^{5} m_i P^i = 0 \tag{A.1}$$

where,

$$m_0 = -\rho\varepsilon + \sum_{k=1}^{N} \begin{cases} -\rho_k z_k T_{0_k}^{\varepsilon} & \text{if } T_k < 1000\,[K] \\ \rho_k z_k \left(K_k^{\varepsilon} - T_{0_k}^{\varepsilon}\right) & \text{if } T_k \geqslant 1000\,[K] \end{cases} \tag{A.2}$$

$$m_i = \frac{1}{i} \sum_{k=1}^{N} \left[\rho_k z_k \left(\frac{1}{\rho_k \mathcal{R}_k} \right)^i a_{i_k}^r \right] \tag{A.3}$$

where $r \equiv (1, 2)$ depending on T_k.

An initial guess of pressure has to be made in order to compute the temperature of each species, and then chose the proper set of polynomial coefficients for each species. This assumption might introduce a small error for the species whose temperature was less than 1000K at the previous time-step and would become greater than 1000K at the next time-step. However, the changes in species temperature are expected to be small from one time-step to the next, meaning that the error will be tolerable.

For each species, the temperature is computed as,

$$T_{k_n} = \frac{P_n}{\rho_k \mathcal{R}_k} \tag{A.4}$$

Once the temperature is known, all the coefficients can be computed, and the iterative procedure is advanced from the iteration (n) to the next iteration $(n+1)$ by,

$$P_{n+1} = P_n - \frac{\sum_{i=0}^{5} m_i P_n^i}{\sum_{i=1}^{5} i\, m_i\, P_n^{i-1}} \tag{A.5}$$

The new value of pressure will allow the computation of the new species temperature, and the procedure is repeated until P_{n+1} satisfies Eq. A.1 within the set tolerance, usually set at 10^{-9}.

A.2 Finding the temperature value for thermally perfect gases with the FCMF model

In compressible reacting flows, temperature and pressure are not explicitly calculated in the governing equations, they are extracted from the knowledge of the different conserved quantities. However, pressure and temperature are explicitly needed in numerous calculations, such as the transport coefficients, reactions rates, etc. By using the definition of internal energy, enthalpy and the EoS, it is possible to write,

$$P = \rho h + \rho\varepsilon = \sum_{k=1}^{N} \rho Y_k h_k\left(T\right) - \rho E + \frac{1}{2}\rho \mathbf{u}^2 \tag{A.6}$$

By further subtracting the perfect gas equation of state, it yields an implicit relation for the mixture temperature,

$$\Theta\left(\rho,\ E,\ Y_k,\ T\right) = \rho h + \rho\varepsilon = \sum_{k=1}^{N} \rho Y_k h_k\left(T\right) - \rho E + \frac{1}{2}\rho \mathbf{u}^2 - \mathcal{R}_u T \sum_{k=1}^{N} \frac{\rho Y_k}{W_k} \tag{A.7}$$

The derivative of this term while holding density, composition, temperature, velocity and total non-chemical energy constant is then used in a Newton-Raphson procedure defined as,

$$T^{n+1} = T^n - \frac{\Theta\left(\rho,\ E,\ Y_k,\ T\right)}{\Theta'\left(\rho,\ E,\ Y_k,\ T\right)} \tag{A.8}$$

where the temperature in the cell at the beginning of the time-step is used as the initial solution for the iterative process. The tolerance is usually taken as 10^{-9}, and thanks to the exponential convergence rate of the Newton-Rahpson method, usually less than 10 iterations are required until convergence.

APPENDIX **B**

Chemical mechanisms

B.1 C_3H_8/air - One-step mechanism

Simplest mechanism considered, with 5 species and a single-step irreversible chemistry. Presented by Westbrook and Dryer (1984) [291] using a modification of the reaction order to match the laminar flame speed and ignition times with the more complex mechanisms.

	A (cgs)	β (cgs)	E_a (cal/mol)
$C_3H_8 + 5O_2 \Rightarrow 3CO_2 + 4H_2O$	8.6×10^{11}	0.0	30.0×10^3
$a = 0.1$, $b = 1.65$			
$k = AT^{\beta} \exp\left(-E_a/\mathcal{R}_u T\right) [\text{Fuel}]^a [\text{Oxidiser}]^b$			

Table B.1: *Westbrook and Dryer propane one-step mechanism*

B.2 CH_4/air - 2-step mechanism

The 2-step methane mechanism from CERFACS has been developed to be used in the Thickened Flame Model framework [258], to provide an simplified and affordable chemical mechanism for the methane combustion matching both the flame temperature and speed. It has been originally written under the form of a irreversible step consuming CH_4 to produce both CO_2 and H_2O, while the second step is a reversible reaction producing and consuming radicals. It has been also written under an entirely irreversible mechanism where the radical production and consumption have been separated in two reactions. Additionally, this mechanism relies on the modification of the reaction orders to match the laminar flame speed.

	A (cgs)	β (cgs)	E_a (cal/mol)
$CH_4 + 1.5O_2 \Rightarrow CO + 2H_2O$	2.0000×10^{15}	0.0	35.000×10^3
$a = 0.9$, $b = 1.1$			
$CO_2 \Rightarrow CO + 0.5O_2$	8.1104×10^{10}	0.0	77.194×10^3
$CO + 0.5O_2 \Rightarrow CO_2$	2.0000×10^9	0.0	12.000×10^3
$k = AT^{\beta} \exp\left(-E_a/\mathcal{R}_u T\right) [\text{Fuel}]^a [\text{Oxidiser}]^b$			

Table B.2: *2s_CM2 CERFACS CH_4 chemical mechanism*

B.3 H_2/air - 7-step mechanism

A more detailed mechanism previously used in supersonic hydrogen combustion and reported to give reasonable results. It is composed of 7 reversible reactions, or 14 irreversible steps. It has been developed by the French lab ONERA [145].

				A (cgs)	β (cgs)	E_a (kJ/mol)
1.	$H_2 + O_2$	$\Rightarrow$	$OH + OH$	1.700×10^{13}	$+0.0000$	199.9122
2.	$OH + OH$	$\Rightarrow$	$H_2 + O_2$	4.032×10^{10}	$+0.3168$	121.0074
3.	$H + O_2$	$\Rightarrow$	$OH + O$	1.987×10^{14}	$+0.0000$	70.3043
4.	$OH + O$	$\Rightarrow$	$H + O_2$	8.930×10^{11}	$+0.3383$	-0.9778
5.	$H_2 + OH$	$\Rightarrow$	$H_2O + H$	1.024×10^{8}	$+1.6000$	13.8008
6.	$H_2O + H$	$\Rightarrow$	$H_2 + OH$	7.964×10^{8}	$+1.5280$	77.3248
7.	$H_2 + O$	$\Rightarrow$	$OH + H$	5.119×10^{4}	$+2.6700$	26.3016
8.	$H + OH$	$\Rightarrow$	$H_2 + O$	2.701×10^{4}	$+2.6490$	18.6212
9.	$OH + OH$	$\Rightarrow$	$H_2O + O$	1.506×10^{9}	$+1.1400$	0.4142
10.	$H_2O + O$	$\Rightarrow$	$OH + OH$	2.220×10^{10}	$+1.0890$	71.6144
11.	$H + OH + M$	$\Rightarrow$	$H_2O + M$	2.212×10^{22}	-2.0000	0.0000
12.	$H_2O + M$	$\Rightarrow$	$H + OH + M$	8.936×10^{22}	-1.8350	496.7304
13.	$H + H + M$	$\Rightarrow$	$H_2 + M$	9.791×10^{16}	-0.6000	0.0000
14.	$H_2 + M$	$\Rightarrow$	$H + H + M$	5.086×10^{16}	-0.3624	433.2265

$k = AT^{\beta} \exp\left(-E_a/\mathcal{R}_u T\right)$

Third body efficiencies : $H_2O = 12.0$, $H_2 = 2.5$

Table B.3: *ONERA H_2 chemical mechanism*

B.4 H_2/air - 34-step mechanism

This mechanism is an H_2/O_2 mechanism also used for H_2/Air simulations and mainly used in the simulation of detonations. It has been extracted by Deiterding [73] from the hydrocarbon mechanism of Westbrook [290] used mainly for hydrocarbon detonations in gaseous mixtures.

				A (cgs)	β (cgs)	E_a (cal/mol)
1.	$H + O_2$	$\Rightarrow$	$O + OH$	1.860×10^{14}	0.00	1.6790×10^{4}
2.	$O + OH$	$\Rightarrow$	$H + O_2$	1.480×10^{13}	0.00	6.8000×10^{2}
3.	$H_2 + O$	$\Rightarrow$	$H + OH$	1.820×10^{10}	1.00	8.9000×10^{3}
4.	$H + OH$	$\Rightarrow$	$H_2 + O$	8.320×10^{9}	1.00	6.9500×10^{3}
5.	$H_2O + O$	$\Rightarrow$	$OH + OH$	3.390×10^{13}	0.00	1.8350×10^{4}
6.	$OH + OH$	$\Rightarrow$	$H_2O + O$	3.160×10^{12}	0.00	1.1000×10^{3}
7.	$H_2O + H$	$\Rightarrow$	$H_2 + OH$	9.550×10^{13}	0.00	2.0300×10^{4}
8.	$H_2 + OH$	$\Rightarrow$	$H_2O + H$	2.190×10^{13}	0.00	5.1500×10^{3}
9.	$H_2O_2 + OH$	$\Rightarrow$	$H_2O + HO_2$	1.000×10^{13}	0.00	1.8000×10^{3}
10.	$H_2O + HO_2$	$\Rightarrow$	$H_2O_2 + OH$	2.820×10^{13}	0.00	3.2790×10^{4}
11.	$HO_2 + O$	$\Rightarrow$	$OH + O_2$	5.010×10^{13}	0.00	1.0000×10^{3}
12.	$OH + O_2$	$\Rightarrow$	$HO_2 + O$	6.460×10^{13}	0.00	5.6160×10^{4}
13.	$HO_2 + H$	$\Rightarrow$	$OH + OH$	2.510×10^{14}	0.00	1.9000×10^{3}
14.	$OH + OH$	$\Rightarrow$	$HO_2 + H$	1.200×10^{13}	0.00	4.0100×10^{4}
15.	$HO_2 + H$	$\Rightarrow$	$H_2 + O_2$	2.510×10^{13}	0.00	7.0000×10^{2}
16.	$H_2 + O_2$	$\Rightarrow$	$HO_2 + H$	5.500×10^{13}	0.00	5.7800×10^{4}
17.	$HO_2 + OH$	$\Rightarrow$	$H_2O + O_2$	5.010×10^{13}	0.00	1.0000×10^{3}
18.	$H_2O + O_2$	$\Rightarrow$	$HO_2 + OH$	6.310×10^{14}	0.00	7.3860×10^{4}
19.	$H_2O_2 + O_2$	$\Rightarrow$	$HO_2 + HO_2$	3.980×10^{13}	0.00	4.2640×10^{4}
20.	$HO_2 + HO_2$	$\Rightarrow$	$H_2O_2 + O_2$	1.000×10^{13}	0.00	1.0000×10^{3}
21.	$H_2O_2 + H$	$\Rightarrow$	$HO_2 + H_2$	1.700×10^{12}	0.00	3.7500×10^{3}
22.	$HO_2 + H_2$	$\Rightarrow$	$H_2O_2 + H$	7.240×10^{11}	0.00	1.8700×10^{4}
23.	$H_2O + M$	$\Rightarrow$	$H + OH + M$	2.190×10^{16}	0.00	1.0500×10^{5}
24.	$H + OH + M$	$\Rightarrow$	$H_2O + M$	1.410×10^{23}	-2.00	0.0000×10^{0}
25.	$H + O_2 + M$	$\Rightarrow$	$HO_2 + M$	1.660×10^{15}	0.00	-1.0000×10^{3}
26.	$HO_2 + M$	$\Rightarrow$	$H + O_2 + M$	2.290×10^{15}	0.00	4.5900×10^{4}
27.	$H_2O_2 + M$	$\Rightarrow$	$OH + OH + M$	1.200×10^{17}	0.00	4.5500×10^{4}
28.	$OH + OH + M$	$\Rightarrow$	$H_2O_2 + M$	9.120×10^{14}	0.00	-5.0700×10^{3}
29.	$O + H + M$	$\Rightarrow$	$OH + M$	1.000×10^{16}	0.00	0.0000×10^{0}
30.	$OH + M$	$\Rightarrow$	$O + H + M$	7.940×10^{19}	-1.00	1.0372×10^{5}
31.	$O_2 + M$	$\Rightarrow$	$O + O + M$	5.130×10^{15}	0.00	1.1500×10^{5}
32.	$O + O + M$	$\Rightarrow$	$O_2 + M$	4.680×10^{15}	-0.28	0.0000×10^{0}
33.	$H_2 + M$	$\Rightarrow$	$H + H + M$	2.190×10^{14}	0.00	9.6000×10^{4}
34.	$H + H + M$	$\Rightarrow$	$H_2 + M$	3.020×10^{15}	0.00	0.0000×10^{0}

$k = AT^{\beta} \exp\left(-E_a/\mathcal{R}_u T\right)$

$f(O_2) = 0.40,\ f(H_2O) = 6.50$

Table B.4: *9-species / 34 reactions Hydrogen-Oxygen mechanism extracted from the hydrocarbon mechanism of Westbrook [290]*

APPENDIX C

Initial Conditions

C.1 Thermally perfect shock calculation

The initialisation of shock containing simulations requires the computations of shocked quantities, knowing the medium in which the shock travels and its Mach number (or its speed). This is relatively straightforward for a calorically perfect gas, but less so for a thermally perfect where the adiabatic index varies through the shock in a non-linear way.

In the case of calorically perfect, the relations are well established and taken from the jump conditions (conservation of energy, mass and momentum) across a shock, and using the EoS with a constant gamma index, leads to the well known Rankine-Hugoniot relationships, which can in turn be used to express the ratio of pressure, velocity and density across the discontinuity [278]. For a thermally perfect gas, an iterative procedure has to be considered to converge towards the correct solution.

Considering a right moving shock at speed S_s, the shocked quantities are noted (ρ_*, P_*, u_*), while the undisturbed quantities are noted (ρ, P, u). To simplify the analysis, it is easier to consider a stationary shock, where the shocked quantities are (ρ_*, P_*, $\hat{u_*}$), and the undisturbed variables are (ρ, P, $\hat{u}$), with $\hat{u_*} = u_* - S_s$ and $\hat{u} = u - S_s$. We can also define the relative Mach number as,

$$M_r = M - M_s = \frac{u}{c} - \frac{S_s}{c} \tag{C.1}$$

where c is the sound speed in the undisturbed medium.

C.1.1 Calorically perfect gas

Manipulation of the Rankine-Hugoniot conditions leads to,

$$\frac{\rho_*}{\rho} = \frac{(\gamma+1)\left(M - M_s\right)^2}{(\gamma-1)\left(M - M_s\right)^2 + 2} \tag{C.2}$$

$$\frac{P_*}{P} = \frac{2\gamma\left(M - M_s\right)^2 - (\gamma-1)}{\gamma+1} \tag{C.3}$$

$$S_s = u + c\sqrt{\left(\frac{\gamma+1}{2\gamma}\right)\left(\frac{P_*}{P}\right) + \left(\frac{\gamma-1}{2\gamma}\right)} \tag{C.4}$$

$$u_* = \left(1 - \frac{\rho}{\rho_*}\right) S_s + u\frac{\rho}{\rho_*} \tag{C.5}$$

C.1.2 Thermally perfect gas

The case of a thermally perfect gas is more complex as the Rankine-Hugoniot relationship do not hold true any more. Contrary to the calorically perfect gas case where the ratios of quantities across the shock are

function of the shock Mach number only, in this case, two upstream conditions are needed, both the velocity and temperature. The Mach number only plays an important role in the calorically perfect gas case.

It is worth reminding the jump conditions first, as they are the only relations true for any type of gas across the shock,

$$\rho\hat{u} = \rho_*\widehat{u_*} \tag{C.6}$$
$$\rho\hat{u}^2 + P = \rho_*\widehat{u_*}^2 + P_* \tag{C.7}$$
$$h + \hat{u}^2/2 = h_* + \widehat{u_*}^2/2 \tag{C.8}$$

If all the upstream conditions are known, this leaves 3 equations and 4 unknowns. The system is then closed with a relation of the type $h = h\left(P,\, \rho\right)$, so that $h_* = h\left(P_*,\, \rho_*\right)$. The iterative procedure is then,

1. Specify u and T, and compute $h = h\left(T\right)$
2. Guess $\nu = \rho/\rho_*$
3. Using the jump conditions (Eq. C.6 and Eq. C.8), we have,

$$\hat{u_*} = \nu\hat{u} \tag{C.9}$$
$$h_* = h + \left(\hat{u_*}^2/2\right)\left(1 - \nu^2\right) \tag{C.10}$$

4. Using the jump conditions (Eq. C.7) and the equation of state,

$$\frac{P_*}{P} = 1 + \left(1 - \nu\right)\frac{\hat{u}^2}{RT} \tag{C.11}$$
$$\frac{T_*}{T} = \nu\left(\frac{P_*}{P}\right) \tag{C.12}$$
$$\widetilde{h_*} = h\left(T_*\right) \tag{C.13}$$

5. Does $h_* = \widetilde{h_*}$? If not, use a root-finding method to modify the value of ν and continue from step 3.

C.2 Initial turbulent velocity background

C.2.1 Background

The generation of an initial turbulent flow-field is an important step in a LES calculation, especially in the case of a transient phenomena. It is indeed clear that no matter the care with which the corresponding experiment has been conducted, there is always a residual level of turbulence. Furthermore, in the current case, an initial turbulent flow field can also be considered to break the symmetry of the problem. Without any turbulent background, the numerical results feature a strong symmetry, not necessarily reflecting the actual results obtained experimentally (off-center ignition, etc.).

Several strategies exist to generate either a turbulent inflow or a turbulent background, Klein *et al.* [157] provide an overview of the different techniques, that is summarised below. It must first be mentioned that in general a turbulent inflow/initial-condition can be obtained by superimposing fluctuations onto a specified mean, which in the most simple case, is a simple random noise scaled to match the trace of the Reynolds Stress Tensor (RST).

The different techniques presented in the literature review, can thus be summarised as,

- *Random noise* : The simplest technique to generate a fluctuating field $\mathcal{U}_i$ is to apply random noise, where the value in each cell is just a random number. The energy spectrum thus created is close to $E(k) = cst$, and thus lack energy in the low wave-number range compared to the high range. Consequently, the turbulence is dampened to 0 very quickly and makes this technique quite ineffective [157].
- *Fourier transform* : To overcome the problem of energy distribution in the wave-number space, Lee *et al.* [177] proposed the use of an inverse Fourier transformation of a real (or imposed) turbulence. The main drawbacks for this method are its complexity and its difficulty of implementation. Additionally, it requires equidistant cartesian grids, and the spectrum must be applied globally. Finally, the accurate measurement of a full 3D energy spectrum is quite complex forcing the user to rely on a determined spectrum which might be less realistic.
- *Digital filters* : The method was developed by Klein *et al.* [157] to eliminate the problems encountered with the inverse Fourier transformation. This method allows the prescription of a pseudo-turbulent velocity field with a specified RST. This works by creating arrays of random data convoluted with digital, linear, non-recursive filters. The three-dimensional flow field is obtained by the convolution of three one-dimensional filters.

The methods presented above show a continuous stream of improvement towards an increased accuracy and control on the turbulent fluctuations, however, even the digital filter approach requires equidistant cells to work properly. Thus a technique is needed to create such a turbulence in the general case of complex geometries and unstructured/irregular meshes.

C.2.2 Methodology

The new technique presented by Kempf *et al.* [150] relies on the use of diffusion to generate the turbulent fluctuations, and is applied in physical space. It can therefore be extended to any geometries/meshes.

The main idea behind this approach is to rely on physical diffusion to convert white noise into a signal featuring a required length-scale (and/or RST).

It can be shown that the convolution of a white noise signal u with $\bar{u} = 0$ (zero mean) and $\hat{u} = 1$ (unity variane) with a gauss filter defined by,

$$G(x) = \frac{1}{\sqrt{4\pi Dt}} \exp\left(-\frac{x^2}{4Dt}\right) \tag{C.14}$$

leads to an autocorrelation function featuring the following shape,

$$R_{u*g,u*g}(r,t) = \exp\left(-\frac{r^2}{8Dt}\right) \tag{C.15}$$

Additionally, it can also be proven that the solution of the homogeneous diffusion equation,

$$\frac{\partial u}{\partial t} = D\nabla^2 u \;\; ; \;\; u\,(x,0) = u_0(x) \;\; ; \;\; x \in \mathbb{R} \tag{C.16}$$

is equivalent to a convolution of $u_0(x)$ with a Gaussian filter,

$$u(x,t) = \frac{1}{\sqrt{4\pi Dt}} \exp\left(-\frac{x^2}{4Dt}\right) * u_0(x) \tag{C.17}$$

The corollary of this, is that if u_i^0 is a discrete random signal with zero mean and unity variance, and u_i^n the discrete solution of Eq. C.16. By also having $\Delta x_i = cst$ and $\Delta t_n = cst$, the discrete correlation

$\overline{u_i^n u_{i+k}^n}/\overline{u_i^n u_i^n}$ can be approximated as,

$$\frac{\overline{u_i^n u_{i+k}^n}}{\overline{u_i^n u_i^n}} \approx \exp\left(-\frac{k^2}{8cn}\right) \tag{C.18}$$

$$c = \frac{D\Delta t}{\Delta x} \tag{C.19}$$

If follows that the length scale $L \approx \sqrt{2\pi cn}\Delta x$.

The flow-chart for generating a turbulent initial conditions is thus,

1. Choose a diffusion coefficient D, a time-step size Δt and calculate the number of time-step needed to achieve the required length scale
2. Generate three random fields $\mathcal{U}_\alpha$, $\alpha = x, y, z$ with the dimensions of the mesh
3. Normalise the fields so that $\overline{\mathcal{U}}_\alpha = 0$ and $\widehat{\mathcal{U}}_\alpha = 1$, where $\widehat{(\,)}$ denotes the standard deviation.
4. To compensate for the effect of cell size, rescale the fields by $\frac{1}{\sqrt{V_\mathbf{i}}}$ where $V_\mathbf{i}$ is the cell volume
5. Apply the diffusion for the number of time-steps computed in step 1.
6. Re-normalise the fields $\mathcal{U}_\alpha$ so that $\overline{\mathcal{U}}_\alpha = 0$ and $\widehat{\mathcal{U}}_\alpha = 1$

It shall be noted that inhomogeneous length-scales can be generated by this technique, by putting $D = 0$ in the areas where the length-scale has reached the desired value, while it continues growing in others.

C.2.3 Application

The case under consideration in this study is the Masri experiment conducted in Sydney. During the experiment, the experimental chamber was purged with the correct fuel-air mixtures for 10 $[s]$ allowing roughly 7 times the volume of the chamber of fresh gases to ensure that no combustion products from the previous cycle were left in the chamber. It was then allowed to settle for about 5 $[s]$ in the case of hydrogen mixture, before being ignited.

In the previous numerical studies simulating similar problems [79, 117, 249], the authors decided to initialise the velocity field with $\mathbf{u} = 0\,[m/s]$ everywhere. In this work, the above presented technique was then considered for the initialisation of a turbulent background.

The integral length scale of this flow has been estimated experimentally to about 10% of the chamber width, or $L_t \approx 5\,[mm]$ [201]. The diffusion coefficient has been set to $\mu = 1 \times 10^{-3}\,[Pa.s]$, while the time-step was chosen as $\Delta t = 2.5 \times 10^{-5}\,[s]$. With these values, the total time was found to be $t_0 = n\Delta t = 3.98\,[ms]$.

Fig. C.1 presents the initial random flow field and the final result after smoothing and reinitialisation in terms of velocity and vorticity for the BBB0 configuration. Fig. C.2 also present the initial flow field for several other configurations.

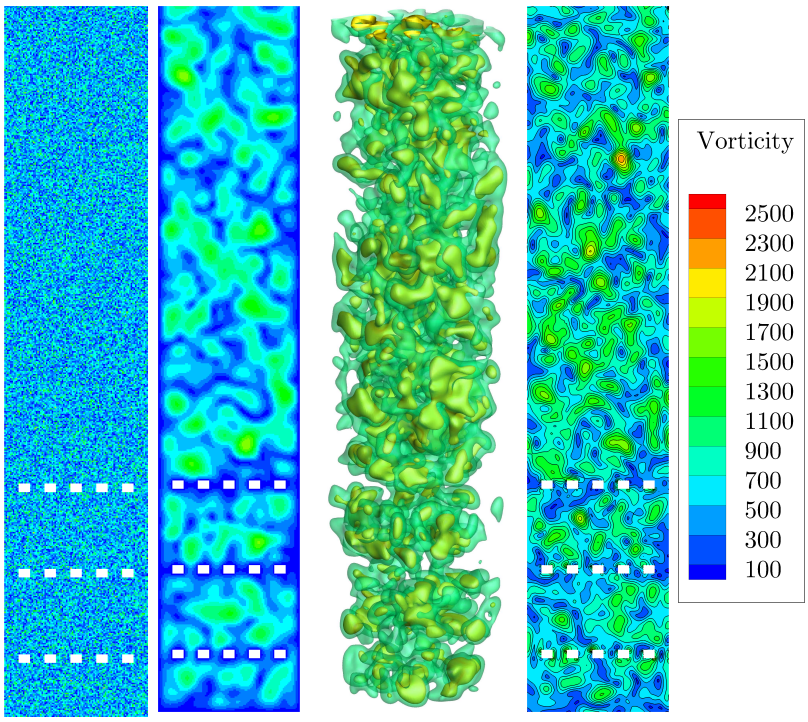

Figure C.1: *Longitudinal cut of the BBB0 configurations displaying (a) Initial random velocity field, (b) Smoothed and re-normalised turbulent velocity field, (c) Iso-surface of velocity magnitude (green - $U = 2\,[m/s]$, yellow - $U = 3\,[m/s]$), **(d)** Vorticity magnitude*

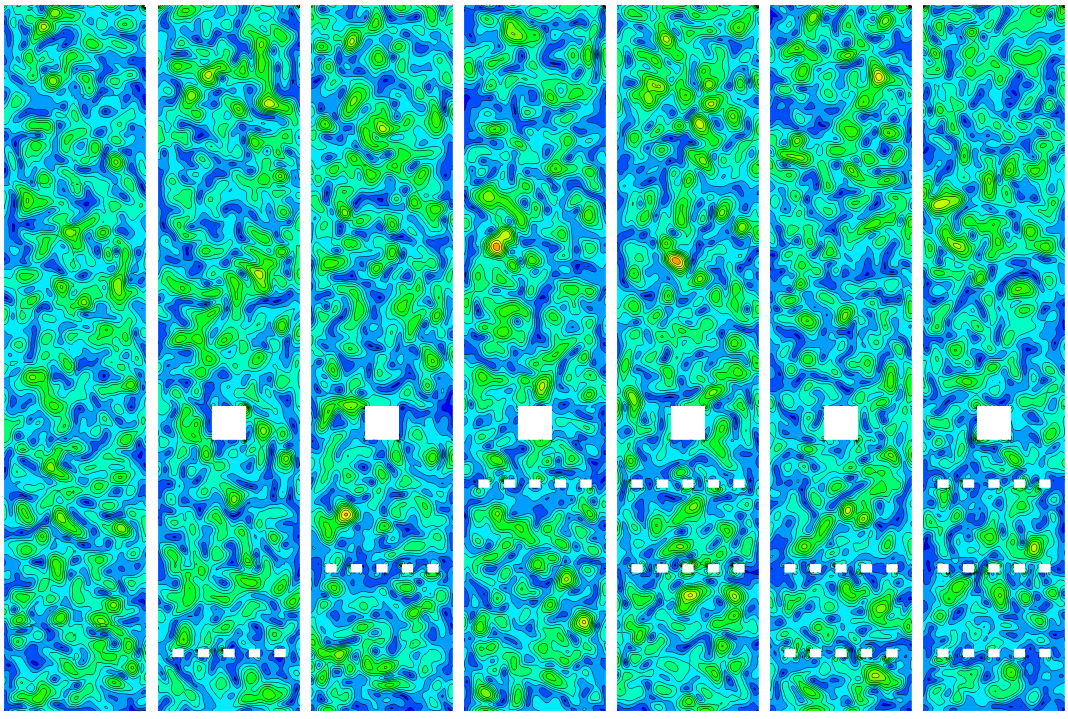

(a) *0000* **(b)** *B00S* **(c)** *0B0S* **(d)** *00BS* **(e)** *0BBS* **(f)** *BB0S* **(g)** *BBBS*

Figure C.2: *Vorticity magnitude contours for different baffle/small obstacle configurations on the fine grid*

APPENDIX **D**

Derivation of the Navier-Stokes Characteristic Boundary Conditions (NSCBC)

As pointed out in §. 4.6, the main idea of the NSCBC boundary conditions is that hyperbolic system of conservation law can be rewritten using a different set of variable such that waves moving in and out of the domain are explicitly accounted for and can be controlled to obtain the desired behaviour at the boundaries.

The derivations presented here are based on the work of Poinsot and Lele [237] and Baum and Poinsot [18] who presented the extension of the NSCBC to the mixture of thermally perfect gases. However, this extension is ill-posed, a similar problem is visible in the publication of Pakdee and Mahalingam [224]. There are three equations for the momentum (u, v, w), N equations for the species, one for the energy and a last one for the mixture density. The problem is thus over-constrained. Moureau *et al.* [214] proposes to either remove the density equation, or one species equation such that the problem becomes correctly posed. As the different models considered in this work (QCMF, QCVF, FCMF, FCVF) feature a symmetric system of equations as far as the species are concerned, the choice has been made to keep all the species equations and leave the mixture density one to keep the symmetry of the different systems.

The second difference of the derivation presented in this work compared to [18] resides in the choice of the primitive and conservative variables considered. The primitive variable associated to energy is the pressure and not the temperature, while the one related to the species is actually similar to the conserved variable, leading to $\mathbf{V} = [u,\ P,\ \rho Y_k]^T$.

Regarding the volume fraction model, the misnamed NSCBC (the system of equation is not the Navier-Stokes any more) have been derived only for the QCVF as the FCVF model was not used with the special boundary conditions as it was discarded due to its oscillating behaviour as explained in §. 5.2. The basis of the derivation can be found in the work of Allaire *et al.* [7] up to the calculation of the jacobian matrix. Everything else is the work of the author. The set of primitive variables considered is slightly different than for the mass fraction models, but is chosen to yield a very similar form of the wave equations. The primitive variables are thus $\mathbf{V} = [u,\ P,\ \rho_k,\ z_k]^T$.

For both mass and volume fractions models, the governing equations are presented in conservative, quasi-linear conservative, quasi-linear primitive and characteristic forms. The wave relations are then presented with the characteristic primitive and conservative forms of the equations, as well as the extraction of the LODI relation used to enforce the different boundary conditions. As the fundamental procedure is based on the Euler equations, the viscous and source terms are neglected here and the problem reduced to a single space dimension for simplicity.

D.1 Mass fraction models

The derivation presented in this section is based on the derivation of Moureau [214] and Staffelbach [267].

D.1.1 Definitions

The definition of the main variables considered in the derivation as well as their relations are reminded here. It shall be noted that in this section (and this section only), ρ_k corresponds to the species partial densities defined by $\rho_k = \rho Y_k$ by Poinsot [238].

- Mass density : $\rho_k = \rho Y_k$
- Momentum : $m_i = \rho u_i$
- Sensible energy : $\varepsilon_{s_k} = \int_0^{T_0} C_{v_k} \, \mathrm{d}T$
- Sensible enthalpy : $h_{s_k} = \int_0^{T_0} C_{p_k} \, \mathrm{d}T = \varepsilon_{s_k} + \dfrac{P_k}{\rho_k}$
- Sensible energy density : $\rho\varepsilon_s = \sum_{k=1}^{N} \rho_k \varepsilon_{s_k} = \rho \sum_{k=1}^{N} Y_k \varepsilon_{s_k}$
- Sensible enthalpy density : $\rho h_s = \sum_{k=1}^{N} \rho_k h_{s_k} = \rho \sum_{k=1}^{N} Y_k h_{s_k}$
- Kinetic energy density : $e_c = \dfrac{1}{2}\rho u_i^2 = \dfrac{1}{2\rho} m_i^2$
- Total energy : $\rho E = \rho e_c + \rho \varepsilon_s$
- Total enthalpy : $\rho H = \rho e_c + \rho h_s = \rho E + P$

To simplify the notation, two new parameters can be added,

$$\beta = \gamma - 1 \tag{D.1}$$

$$\chi_k = \mathcal{R}_k T - \beta \varepsilon_{s_k} \tag{D.2}$$

$$\chi = \sum_{k=1}^{N} \chi_k Y_k = \mathcal{R} T - \beta \varepsilon_s \tag{D.3}$$

$$\frac{1}{\gamma - 1} = \frac{1}{\beta} = \frac{C_v}{\mathcal{R}} = \frac{C_p}{\mathcal{R}} - 1 \tag{D.4}$$

D.1.2 Differential relations

In order to be able to calculate the Jacobian of the system without omitting any terms, is it often useful to write the differential of all the variables of interest.

$$\mathrm{d}\rho = \sum_{k=1}^{N} \mathrm{d}\rho_k \tag{D.5}$$

$$\mathrm{d}P = \rho\mathcal{R}\,\mathrm{d}T + \sum_{k=1}^{N} \mathcal{R}_k T\,\mathrm{d}\rho_k \tag{D.6}$$

$$\mathrm{d}T = \frac{1}{\rho\mathcal{R}}\,\mathrm{d}P - \sum_{k=1}^{N} \frac{\mathcal{R}_k T}{\rho\mathcal{R}}\,\mathrm{d}\rho_k \tag{D.7}$$

$$\mathrm{d}\left(\rho e_c\right) = \rho u\,\mathrm{d}u + \sum_{k=1}^{N} e_c\,\mathrm{d}\rho_k \tag{D.8}$$

$$\mathrm{d}\left(\rho\varepsilon_s\right) = \rho C_v\,\mathrm{d}T + \sum_{k=1}^{N} \varepsilon_{s_k}\,\mathrm{d}\rho_k \tag{D.9}$$

$$\mathrm{d}\left(\rho h_s\right) = \rho C_p\,\mathrm{d}T + \sum_{k=1}^{N} h_{s_k}\,\mathrm{d}\rho_k \tag{D.10}$$

$$\begin{aligned}\mathrm{d}\left(\rho E\right) =& \rho u\,\mathrm{d}u + \sum_{k=1}^{N} \left(e_c + \varepsilon_{s_k}\right)\mathrm{d}\rho_k + \rho C_v\,\mathrm{d}T \\ =& \rho u\,\mathrm{d}u + \sum_{k=1}^{N} \left(e_c + \varepsilon_{s_k} - \frac{\mathcal{R}_k}{\mathcal{R}} C_v T\right)\mathrm{d}\rho_k + \frac{1}{\beta}\,\mathrm{d}P\end{aligned} \tag{D.11}$$

$$\mathrm{d}P = \beta\left(-\rho u\,\mathrm{d}u + \mathrm{d}\left(\rho E\right) + \sum_{k=1}^{N}\left(-e_c + \frac{\chi_k}{\beta}\right)\mathrm{d}\rho_k\right) \tag{D.12}$$

D.1.3 Governing Equations

Conservative form

The inviscid one-dimensional Euler equations reads,

$$\begin{cases} \dfrac{\partial \rho u}{\partial t} + \dfrac{\partial \rho u u + P}{\partial x} = 0 \\ \dfrac{\partial \rho E}{\partial t} + \dfrac{\partial \left(\rho E + P\right) u}{\partial x} = 0 \\ \dfrac{\partial \rho_k}{\partial t} + \dfrac{\partial \rho_k u}{\partial x} = 0 \end{cases} \tag{D.13}$$

which can be rewritten in *conservative matrix form*,

$$\frac{\partial \mathbf{U}}{\partial t} + \frac{\partial \mathbf{F}\left(\mathbf{U}\right)}{\partial x} = 0 \tag{D.14}$$

with $\mathbf{U} = \left[\rho u,\ \rho E,\ \rho_k\right]^T$ and $\mathbf{F}\left(\mathbf{U}\right) = \left[\rho u^2 + P,\ \left(\rho E + P\right) u,\ \rho_k u\right]^T$, where $\mathbf{U}$ is the vector or conservative variables.

Quasi-linear conservative form

This system can also be written under a *quasi-linear conservative form*, such as,

$$\frac{\partial \mathbf{U}}{\partial t} + \underline{\mathbf{A}}^x \frac{\partial \mathbf{U}}{\partial x} = 0 \tag{D.15}$$

where $\underline{\mathbf{A}}^x$ is the Jacobian matrix of the system, and its elements are computed as, $\underline{\mathbf{A}}^x_{i,j} = \dfrac{\partial \mathbf{F}_i}{\partial \mathbf{U}_j}$, yielding,

$$\begin{aligned}
\underline{\mathbf{A}}^x &= \begin{pmatrix}
\frac{\partial F_{\rho u}}{\partial \rho u} & \frac{\partial F_{\rho u}}{\partial \rho E} & \frac{\partial F_{\rho u}}{\partial \rho_1} & \cdots & \frac{\partial F_{\rho u}}{\partial \rho_N} \\
\frac{\partial F_{\rho E}}{\partial \rho u} & \frac{\partial F_{\rho E}}{\partial \rho E} & \frac{\partial F_{\rho E}}{\partial \rho_1} & \cdots & \frac{\partial F_{\rho E}}{\partial \rho_N} \\
\frac{\partial F_{\rho_1}}{\partial \rho u} & \frac{\partial F_{\rho_1}}{\partial \rho E} & \frac{\partial F_{\rho_1}}{\partial \rho_1} & \cdots & \frac{\partial F_{\rho_1}}{\partial \rho_N} \\
\vdots & \vdots & \vdots & \ddots & \vdots \\
\frac{\partial F_{\rho_N}}{\partial \rho u} & \frac{\partial F_{\rho_N}}{\partial \rho E} & \frac{\partial F_{\rho_N}}{\partial \rho_1} & \cdots & \frac{\partial F_{\rho_N}}{\partial \rho_N}
\end{pmatrix} \\
&= \begin{pmatrix}
2u - \beta u & \beta & -u^2 + \beta e_c + \chi_1 & \cdots & -u^2 + \beta e_c + \chi_N \\
H - \beta u^2 & (1+\beta)\, u & -uH + \beta u e_c + u\chi_1 & \cdots & -uH + \beta u e_c + u\chi_N \\
Y_1 & 0 & u - uY_1 & \cdots & -uY_1 \\
\vdots & \vdots & \vdots & \ddots & \vdots \\
Y_N & 0 & -uY_N & \cdots & u - uY_N
\end{pmatrix}
\end{aligned} \tag{D.16}$$

Quasi-linear primitive form

It is clear from the previous expression that this matrix is difficult to diagonalise easily. It appears therefore more convenient to introduce the primitive variable vector defined by $\mathbf{V} = [u, P, \rho_k]^T$.

By defining the matrix $\underline{\mathbf{M}}$ to convert the primitive variables into the conservative variables, one can write,

$$\underline{\mathbf{M}} = \frac{\partial \mathbf{U}}{\partial \mathbf{V}} \tag{D.17}$$

where its elements are defined by, $\underline{\mathbf{M}}_{i,j} = \dfrac{\partial \mathbf{U}_i}{\partial \mathbf{V}_j}$, yielding,

$$\underline{\mathbf{M}} = \begin{pmatrix}
\frac{\partial \rho u}{\partial u} & \frac{\partial \rho u}{\partial P} & \frac{\partial \rho u}{\partial \rho_1} & \cdots & \frac{\partial \rho u}{\partial \rho_N} \\
\frac{\partial \rho E}{\partial u} & \frac{\partial \rho E}{\partial P} & \frac{\partial \rho E}{\partial \rho_1} & \cdots & \frac{\partial \rho E}{\partial \rho_N} \\
\frac{\partial \rho_1}{\partial u} & \frac{\partial \rho_1}{\partial P} & \frac{\partial \rho_1}{\partial \rho_1} & \cdots & \frac{\partial \rho_1}{\partial \rho_N} \\
\vdots & \vdots & \vdots & \ddots & \vdots \\
\frac{\partial \rho_N}{\partial u} & \frac{\partial \rho_N}{\partial P} & \frac{\partial \rho_N}{\partial \rho_1} & \cdots & \frac{\partial \rho_N}{\partial \rho_N}
\end{pmatrix} = \begin{pmatrix}
\rho & 0 & u & \cdots & u \\
\rho u & \frac{1}{\beta} & M_{2,2+1} & \cdots & M_{2,2+N} \\
0 & 0 & 1 & \cdots & 0 \\
\vdots & \vdots & \vdots & \ddots & \vdots \\
0 & 0 & 0 & \cdots & 1
\end{pmatrix} \tag{D.18}$$

where,

$$\begin{aligned}
M_{2,2+k} &= \frac{\partial \rho E}{\partial \rho_k} = \frac{1}{\partial \rho_k}\left(\partial \rho e_c + \partial \rho \varepsilon_s\right) \\
&= \frac{1}{\partial \rho_k}\left(\rho u \partial u + \sum_{j=1}^{N} e_c \partial \rho_j + \rho C_v \partial T + \sum_{j=1}^{N} \varepsilon_{s_j} \partial \rho_j\right) \\
&= \frac{1}{\partial \rho_k}\left(\rho u \partial u + \sum_{j=1}^{N} \left(e_c + \varepsilon_{s_j}\right) \partial \rho_j + \rho C_v \left(\frac{1}{\rho \mathcal{R}} \partial P - \sum_{j=1}^{N} \frac{\mathcal{R}_k T}{\rho \mathcal{R}} \partial \rho_j\right)\right) \\
&= e_c + \varepsilon_{s_k} + C_v \frac{\mathcal{R}_k T}{\rho} = e_c + h_k - \frac{P}{\rho_k} + C_v \frac{\mathcal{R}_k T}{\rho} \\
&= e_c + h_k - \frac{P}{\rho_k}\left(1 + \frac{1}{\beta}\right) = e_c - \frac{\chi_k}{\beta}
\end{aligned} \tag{D.19}$$

The inverse of the matrix $\underline{\mathbf{M}}$ can also be computed, and upon simplification yields,

$$\underline{\mathbf{M}}^{-1} = \begin{pmatrix} \frac{1}{\rho} & 0 & -\frac{u}{\rho} & \cdots & -\frac{u}{\rho} \\ -\beta u & \beta & M^{-1}_{2,2+1} & \cdots & M^{-1}_{2,2+N} \\ 0 & 0 & 1 & \cdots & 0 \\ \vdots & \vdots & \vdots & \ddots & \vdots \\ 0 & 0 & 0 & \cdots & 1 \end{pmatrix} \tag{D.20}$$

where the inverse elements $M^{-1}_{2,2+k}$ are given by,

$$M^{-1}_{2,2+k} = (\gamma - 1)\left(e_c - h_j + \frac{\mathcal{R}_u T}{W_k}\left(1 + \frac{1}{\gamma - 1}\right)\right) = \beta e_c + \chi_k \tag{D.21}$$

By recalling Eq. D.15, and using $\partial \mathbf{U} = \underline{\mathbf{M}} \partial \mathbf{V}$, we have,

$$\underline{\mathbf{M}} \frac{\partial \mathbf{V}}{\partial t} + \underline{\mathbf{A}}^x \underline{\mathbf{M}} \frac{\partial \mathbf{V}}{\partial x} = 0 \tag{D.22}$$

which upon left multiplication by $\underline{\mathbf{M}}^{-1}$ yields,

$$\underline{\mathbf{M}}^{-1} \underline{\mathbf{M}} \frac{\partial \mathbf{V}}{\partial t} + \underline{\mathbf{M}}^{-1} \underline{\mathbf{A}}^x \underline{\mathbf{M}} \frac{\partial \mathbf{V}}{\partial x} = 0 \tag{D.23}$$

where by noting $\underline{\mathbf{E}}^x = \underline{\mathbf{M}}^{-1} \underline{\mathbf{A}}^x \underline{\mathbf{M}}$ we obtain the *quasi-linear primitive* form of the Euler equations,

$$\frac{\partial \mathbf{V}}{\partial t} + \underline{\mathbf{E}}^x \frac{\partial \mathbf{V}}{\partial x} = 0 \tag{D.24}$$

and $\underline{\mathbf{E}}^x$ is given by,

$$\underline{\mathbf{E}}^x = \begin{pmatrix} u & \frac{1}{\rho} & 0 & \cdots & 0 \\ \rho c^2 & u & 0 & \cdots & 0 \\ \rho_1 & 0 & u & \cdots & 0 \\ \vdots & \vdots & \vdots & \ddots & \vdots \\ \rho_N & 0 & 0 & \cdots & u \end{pmatrix} \tag{D.25}$$

where $\rho c^2 = \gamma P$.

Characteristic form

The matrix $\underline{\mathbf{E}}^x$ can be easily diagonalised, and by using,

$$\underline{\mathbf{L}}\,\underline{\mathbf{E}}^x\underline{\mathbf{R}} = \underline{\mathbf{\Lambda}} \tag{D.26}$$

where $\underline{\mathbf{\Lambda}}$ is a diagonal matrix whose elements are the eigenvalues of $\underline{\mathbf{E}}^x$ as $(\Lambda_{i,i} = \lambda_i)$, and is expressed as,

$$\underline{\mathbf{\Lambda}} = \begin{pmatrix} u+c & 0 & 0 & \cdots & 0 \\ 0 & u-c & 0 & \cdots & 0 \\ 0 & 0 & u & \cdots & 0 \\ \vdots & \vdots & \vdots & \ddots & \vdots \\ 0 & 0 & 0 & \cdots & u \end{pmatrix} \tag{D.27}$$

It can be noted that N eigenvectors will be associated with the same eigenvalue, which means that any linear combination of these eigenvectors will also be an eigenvector of the system. The matrix $\underline{\mathbf{R}}$ of right eigenvectors and $\underline{\mathbf{L}} = \underline{\mathbf{R}}^{-1}$ (left eigenvectors) are given by,

$$\underline{\mathbf{R}} = \begin{pmatrix} \frac{1}{2} & -\frac{1}{2} & 0 & \cdots & 0 \\ \frac{\rho c}{2} & \frac{\rho c}{2} & 0 & \cdots & 0 \\ \frac{\rho_1}{2c} & \frac{\rho_1}{2c} & 1 & \cdots & 0 \\ \vdots & \vdots & \vdots & \ddots & \vdots \\ \frac{\rho_N}{2c} & \frac{\rho_N}{2c} & 0 & \cdots & 1 \end{pmatrix}, \quad \underline{\mathbf{L}} = \begin{pmatrix} 1 & \frac{1}{\rho c} & 0 & \cdots & 0 \\ -1 & \frac{1}{\rho c} & 0 & \cdots & 0 \\ 0 & -\frac{Y_1}{c^2} & 1 & \cdots & 0 \\ \vdots & \vdots & \vdots & \ddots & \vdots \\ 0 & -\frac{Y_N}{c^2} & 0 & \cdots & 1 \end{pmatrix} \tag{D.28}$$

The transformation from primitive to characteristic variables (denoted by $\mathbf{W}$) is defined by,

$$\partial\mathbf{W} = \underline{\mathbf{L}}\,\partial\mathbf{V} \tag{D.29}$$

$$\partial\mathbf{V} = \underline{\mathbf{R}}\,\partial\mathbf{W} = \underline{\mathbf{L}}^{-1}\partial\mathbf{W} \tag{D.30}$$

Replacing the primitive variables in Eq. D.24 by the characteristic variables using Eq. D.30, the governing equation in characteristic form reads,

$$\underline{\mathbf{L}}^{-1}\frac{\partial\mathbf{W}}{\partial t} + \underline{\mathbf{E}}^x\,\underline{\mathbf{L}}^{-1}\frac{\partial\mathbf{W}}{\partial x} = 0 \tag{D.31}$$

by further multiplying by $\underline{\mathbf{L}}$ on the left yields,

$$\underline{\mathbf{L}}\,\underline{\mathbf{L}}^{-1}\frac{\partial\mathbf{W}}{\partial t} + \underline{\mathbf{L}}\,\underline{\mathbf{E}}^x\,\underline{\mathbf{L}}^{-1}\frac{\partial\mathbf{W}}{\partial x} = 0 \tag{D.32}$$

where $\underline{\mathbf{L}}\,\underline{\mathbf{E}}^x\,\underline{\mathbf{L}}^{-1} = \underline{\mathbf{L}}\,\underline{\mathbf{E}}^x\,\underline{\mathbf{R}} = \underline{\mathbf{\Lambda}}$, finally giving the *characteristic form* of the Euler equations,

$$\frac{\partial\mathbf{W}}{\partial t} + \underline{\mathbf{\Lambda}}\frac{\partial\mathbf{W}}{\partial x} = 0 \tag{D.33}$$

D.1.4 Waves relations

Now that the conservative system has been transformed into a characteristic wave and the eigenvalues associated with each waves, it becomes possible to identify the different waves and their propagation characteristics.

Characteristic-Primitive system

Using Eq. D.30, it becomes possible to write the characteristic variables variations as functions of the primitive variables variations, yielding,

$$\begin{cases} \partial W^1 = \partial u + \dfrac{1}{\rho c}\partial P \\ \partial W^2 = -\partial u + \dfrac{1}{\rho c}\partial P \\ \partial W^{2+k} = -\dfrac{Y_k}{c^2}\partial P + \partial\left(\rho Y_k\right) \end{cases} \quad \text{with} \quad \begin{cases} \lambda_1 = u + c \\ \lambda_2 = u - c \\ \lambda_{2+k} = u \end{cases} \tag{D.34}$$

where the entropy wave identified by Poinsot and Lele [237] can be recovered by summing the species waves,

$$\partial W^S = \sum_{j=1}^{N} \partial W^{2+k} = \partial\rho - \frac{1}{c^2}\partial P \text{ with } \lambda_S = u \tag{D.35}$$

The quasi-linear primitive form of the equations (Eq. D.24) can be left multiplied by $\underline{\mathbf{L}}$ yielding,

$$\underline{\mathbf{L}}\frac{\partial \mathbf{V}}{\partial t} + \underline{\mathbf{L}}\,\underline{\mathbf{E}}^x\frac{\partial \mathbf{V}}{\partial x} = 0 \tag{D.36}$$

which by using Eq. D.26 further leads to,

$$\underline{\mathbf{L}}\frac{\partial \mathbf{V}}{\partial t} + \underline{\mathbf{\Lambda}}\,\underline{\mathbf{L}}\frac{\partial \mathbf{V}}{\partial x} = 0 \tag{D.37}$$

where we can define the wave amplitude variations by the vector $\mathcal{L} = \underline{\mathbf{\Lambda}}\,\underline{\mathbf{L}}\dfrac{\partial \mathbf{V}}{\partial x} = \underline{\mathbf{\Lambda}}\dfrac{\partial \mathbf{W}}{\partial x}$, and its elements are defined by $\mathcal{L}_i = \lambda_i L_i \dfrac{\partial V^i}{\partial x}$ with L_i being the i-th row of $\underline{\mathbf{L}}$ (the i-th left eigenvector). By further simplifying the original quasi-linear primitive equations can now be written as,

$$\frac{\partial \mathbf{V}}{\partial t} + \underline{\mathbf{L}}^{-1}\mathcal{L} = 0 \tag{D.38}$$

The wave amplitude variations can then be expressed as a function of the primitive variables derivatives and the eigenvalues of the system,

$$\begin{pmatrix} \mathcal{L}_1 \\ \mathcal{L}_2 \\ \mathcal{L}_{2+k} \end{pmatrix} = \begin{pmatrix} \mathcal{L}_+ \\ \mathcal{L}_- \\ \mathcal{L}_k \end{pmatrix} = \begin{pmatrix} (u+c)\left(\dfrac{\partial u}{\partial x} + \dfrac{1}{\rho c}\dfrac{\partial P}{\partial x}\right) \\ (u-c)\left(-\dfrac{\partial u}{\partial x} + \dfrac{1}{\rho c}\dfrac{\partial P}{\partial x}\right) \\ u\left(-\dfrac{Y_k}{c^2}\dfrac{\partial P}{\partial x} + \dfrac{\partial \rho Y_k}{\partial x}\right) \end{pmatrix} \tag{D.39}$$

The entropy wave amplitude variations identified by Poinsot and Lele [237] can be recovered as,

$$\mathcal{L}_S = \sum_{k=1}^{N}\mathcal{L}_k = u\left(-\frac{1}{c^2}\frac{\partial P}{\partial x} + \frac{\partial \rho}{\partial x}\right) \tag{D.40}$$

The quasi-linear primitive system (Eq. D.24) can also be rewritten as a function of the characteristic variables, leading to the *characteristic-primitive* form of the governing equations,

$$\frac{\partial \mathbf{V}}{\partial t} + \underline{\mathbf{E}}^x\underline{\mathbf{R}}\frac{\partial \mathbf{W}}{\partial x} = 0 \tag{D.41}$$

where $\underline{\mathbf{E}}^x\underline{\mathbf{R}}$ is given by,

$$\underline{\mathbf{E}}^x\underline{\mathbf{R}} = \begin{pmatrix} \frac{u+c}{2} & -\frac{u-c}{2} & 0 & \cdots & 0 \\ \frac{\rho c}{2}(u+c) & \frac{\rho c}{2}(u-c) & 0 & \cdots & 0 \\ \frac{\rho}{2c}(u+c)\,Y_1 & \frac{\rho}{2c}(u-c)\,Y_1 & u & \cdots & 0 \\ \vdots & \vdots & \vdots & \ddots & \vdots \\ \frac{\rho}{2c}(u+c)\,Y_N & \frac{\rho}{2c}(u-c)\,Y_N & 0 & \cdots & u \end{pmatrix} \tag{D.42}$$

Local One Dimensional Inviscid (LODI) relations

The previous system can then be expanded to express the primitive variable temporal variation as functions of the characteristic variables spatial variations and eigenvalues of the system,

$$\begin{pmatrix} \frac{\partial u}{\partial t} \\ \frac{\partial P}{\partial t} \\ \frac{\partial \rho Y_k}{\partial t} \end{pmatrix} + \begin{pmatrix} \frac{\lambda_1}{2}\frac{\partial W^1}{\partial x} - \frac{\lambda_2}{2}\frac{\partial W^2}{\partial x} \\ \frac{\rho c}{2}\left(\lambda_1\frac{\partial W^1}{\partial x} + \lambda_2\frac{\partial W^2}{\partial x}\right) \\ \frac{\rho Y_k}{2c}\left(\lambda_1\frac{\partial W^1}{\partial x} + \lambda_2\frac{\partial W^2}{\partial x}\right) + \lambda_{2+k}\frac{\partial W^{2+k}}{\partial x} \end{pmatrix} = 0 \tag{D.43}$$

By reminding that $\mathcal{L}_i = \lambda_i\frac{\partial W^i}{\partial x}$, we can simplify the previous system and write it as,

$$\begin{pmatrix} \frac{\partial u}{\partial t} \\ \frac{\partial P}{\partial t} \\ \frac{\partial \rho Y_k}{\partial t} \end{pmatrix} + \begin{pmatrix} \frac{1}{2}(\mathcal{L}_1 - \mathcal{L}_2) \\ \frac{\rho c}{2}(\mathcal{L}_1 + \mathcal{L}_2) \\ \frac{\rho Y_k}{2c}(\mathcal{L}_1 + \mathcal{L}_2) + \mathcal{L}_{2+k} \end{pmatrix} = 0 \tag{D.44}$$

where the convective wave $\mathcal{L}_+$ and $\mathcal{L}_-$ are convected at respectively $u+c$ and $u-c$. All the other waves are advected at the flow velocity u. This system represents the first three LODI relations for velocity, pressure and ρY_k respectively.

By noting $\mathbf{d}$ the vector of normal terms, we have,

$$\mathbf{d} = \underline{\mathbf{E}}^x\underline{\mathbf{R}}\frac{\partial \mathbf{W}}{\partial x} = \begin{pmatrix} d_1 \\ d_2 \\ d_{2+k} \end{pmatrix} = \begin{pmatrix} \frac{1}{2}(\mathcal{L}_1 - \mathcal{L}_2) \\ \frac{\rho c}{2}(\mathcal{L}_1 + \mathcal{L}_2) \\ \frac{\rho Y_k}{2c}(\mathcal{L}_1 + \mathcal{L}_2) + \mathcal{L}_{2+k} \end{pmatrix} \tag{D.45}$$

Additional LODI relations can be added for some other primitive or conservative variables, such as the density of the mixture obtained by summing all the species waves,

$$\begin{aligned} \frac{\partial}{\partial t}\left(\sum_{k=1}^{N}\rho_k\right) + \frac{1}{2c}\left(\sum_{k=1}^{N}\rho_k\right)(\mathcal{L}_1 + \mathcal{L}_2) + \sum_{k=1}^{N}\mathcal{L}_{2+k} &= 0 \\ \frac{\partial \rho}{\partial t} + \frac{\rho}{2c}(\mathcal{L}_1 + \mathcal{L}_2) + \mathcal{L}_S &= 0 \end{aligned} \tag{D.46}$$

the species mass fractions, by multiplying the species waves by the inverse of the mixture density wave,

$$\begin{aligned}
\frac{1}{\rho}\left(\frac{\partial \rho Y_k}{\partial t}\right) + \frac{1}{\rho}\frac{\rho Y_k}{2c}\left(\mathcal{L}_1 + \mathcal{L}_2\right) + \frac{1}{\rho}\mathcal{L}_{2+k} &= 0 \\
\frac{1}{\rho}\left(\rho\frac{\partial Y_k}{\partial t} + Y_k\frac{\partial \rho}{\partial t}\right) + \frac{\rho Y_k}{2\rho c}\left(\mathcal{L}_1 + \mathcal{L}_2\right) + \frac{1}{\rho}\mathcal{L}_{2+k} &= 0 \\
\frac{\partial Y_k}{\partial t} + \frac{\rho Y_k}{2\rho c}\left(\mathcal{L}_1 + \mathcal{L}_2\right) + \frac{1}{\rho}\mathcal{L}_{2+k} - \frac{Y_k}{\rho}\left(\frac{\rho}{2c}\left(\mathcal{L}_1 + \mathcal{L}_2\right) + \mathcal{L}_S\right) &= 0 \\
\frac{\partial Y_k}{\partial t} + \frac{1}{\rho}\left(\mathcal{L}_{2+k} - Y_k\mathcal{L}_S\right) &= 0
\end{aligned} \tag{D.47}$$

Temperature LODI can also be determined by reminding Eq. D.7 and using Eq. D.44,

$$\begin{aligned}
\frac{\partial T}{\partial t} - \frac{1}{\rho\mathcal{R}}\frac{\partial P}{\partial t} + \sum_{k=1}^{N}\frac{\mathcal{R}_k T}{\rho\mathcal{R}}\frac{\partial \rho_k}{\partial t} &= 0 \\
\frac{\partial T}{\partial t} - \frac{1}{\rho\mathcal{R}}\left(-\frac{\rho c}{2}\left(\mathcal{L}_1 + \mathcal{L}_2\right)\right) + \sum_{k=1}^{N}\frac{\mathcal{R}_k T}{\rho\mathcal{R}}\left(-\frac{\rho}{2c}Y_k\left(\mathcal{L}_1 + \mathcal{L}_2\right) - \mathcal{L}_{2+k}\right) &= 0 \\
\frac{\partial T}{\partial t} + \left(\mathcal{L}_1 + \mathcal{L}_2\right)\left(\frac{c}{2R} - \frac{T}{2c}\right) - \frac{T}{\rho\mathcal{R}}\sum_{k=1}^{N}\mathcal{R}_k\mathcal{L}_{2+k} &= 0 \\
\frac{\partial T}{\partial t} + \frac{\beta T}{2c}\left(\mathcal{L}_1 + \mathcal{L}_2\right) - \frac{T}{\rho\mathcal{R}}\sum_{k=1}^{N}\mathcal{R}_k\mathcal{L}_{2+k} &= 0
\end{aligned} \tag{D.48}$$

Using Eq. D.44 the time evolution of the primitive variables has been expressed as a direct function of the wave amplitude crossing the boundary. Additional relations have also been derived for other variables of interest such as the mixture density (Eq. D.46), the mixture composition (Eq. D.47) and the temperature (Eq. D.48). Using a similar approach, LODI relations could also be derived for gradients normal to the boundary, but as they are not used in this work, the derivation is not presented here.

Characteristic-Conservative system

The boundary conditions are used during the simulation to evolve the conservative variables in time in the ghost cells from time t^n to time t^{n+1}. The LODI relations presented in the previous paragraph allows the update of the primitive variables using the wave amplitude variations. The conservative variables could then be computed using the knowledge of the primitive variables. However, a simpler solution would be to rewrite the previous relations (Eqs. D.44-D.48) but featuring the conservative variables vector $\mathbf{U}$ instead of the primitive one $\mathbf{V}$.

The LODI relations can simply be expressed as,

$$\frac{\partial \mathbf{V}}{\partial t} + \mathbf{d} = 0 \tag{D.49}$$

where the vector of normal terms is defined in Eq. D.45. A similar approach can be used using the conservative variables and leads to,

$$\frac{\partial \mathbf{U}}{\partial t} + \underline{\mathbf{A}}^x\,\underline{\mathbf{M}}\,\underline{\mathbf{R}}\frac{\partial \mathbf{W}}{\partial x} = 0 \tag{D.50}$$

However, due to the complexity of the three matrices involved, it seems unlikely that the resulting expression will be easy to simplify to give relatively simple relation between the conservative variables and the wave amplitude variations. A side approach consists in using the characteristic primitive system

(Eq. D.41) and multiply on left by the matrix $\underline{\mathbf{M}}$, which according to Eq. D.17 yields,

$$\underline{\mathbf{M}}\frac{\partial \mathbf{V}}{\partial t} + \underline{\mathbf{M}}\,\underline{\mathbf{E}}^{x}\underline{\mathbf{R}}\frac{\partial \mathbf{W}}{\partial x} = 0 \tag{D.51}$$

$$\Leftrightarrow \frac{\partial \mathbf{U}}{\partial t} + \underline{\mathbf{M}}\mathbf{d} = 0 \tag{D.52}$$

which is obviously much simpler. This gives the final form of the *characteristic-conservative* system linking directly the time evolution of the conservative variables and the different wave amplitude variations as,

$$\begin{cases} \dfrac{\partial \rho u}{\partial t} + \rho d_1 + u\displaystyle\sum_{k=1}^{N} d_{2+k} = 0 \\ \dfrac{\partial \rho E}{\partial t} + \rho u d_1 + \dfrac{1}{\beta} d_2 + \displaystyle\sum_{k=1}^{N}\left(e_c - \frac{\chi_k}{\beta}\right) d_{2+k} = 0 \\ \dfrac{\partial \rho_k}{\partial t} + d_{2+k} = 0 \end{cases} \tag{D.53}$$

D.2 Volume Fraction Models

D.2.1 Definitions

The definition of the main variables considered in the derivation as well as their relations are reminded here.

- Equation of State : $P_k = \rho_k \mathcal{R}_k T_k$
- Density : $\rho = \displaystyle\sum_{k=1}^{N} \rho_k z_k$
- Momentum : $m_i = \rho u_i$
- Sensible energy : $\varepsilon_{s_k} = \displaystyle\int_0^{T_k} C_{v_k}(\xi)\,\mathrm{d}\xi = \frac{P_k}{\rho_k(\gamma_k - 1)}$
- Sensible enthalpy : $h_{s_k} = \displaystyle\int_0^{T_k} C_{p_k}(\xi)\,\mathrm{d}\xi = \varepsilon_{s_k} + \frac{P_k}{\rho_k}$
- Sensible energy density : $\rho\varepsilon = \displaystyle\sum_{k=1}^{N} \rho_k z_k \varepsilon_{s_k} = \rho \sum_{k=1}^{N} Y_k \varepsilon_{s_k}$
- Sensible enthalpy density : $\rho h = \displaystyle\sum_{k=1}^{N} \rho_k z_k h_{s_k} = \sum_{k=1}^{N} Y_k h_{s_k} = \rho\varepsilon + P$
- Kinetic energy density : $\rho e_c = \dfrac{1}{2}\rho u^2 = \dfrac{1}{2\rho} m_i^2$
- Total energy density : $\rho E = \rho\varepsilon + \rho e_c$
- Total enthalpy density : $\rho H = \rho h + \rho e_c = \rho E + P$

D.2.2 Derivatives and differentials

Additional variables are being defined in Allaire *et al.* [7] work and are used in the following derivations. These are the internal energy derivatives with respect to species density,

$$\delta_k = \left(\frac{\partial \rho_k \varepsilon_k}{\partial \rho_k}\right)_P \tag{D.54}$$

which yields $\delta_k = 0$ for calorically perfect gases and its expression for thermally perfect gases is presented in Eq. D.100. The internal energy derivative with respect to pressure yields,

$$\xi = \sum_{k=1}^{N} \xi_k z_k = \sum_{k=1}^{N} z_k \left(\frac{\partial \rho_k \varepsilon_k}{\partial P_k} \right)_{\rho_k} = \sum_{k=1}^{N} z_k \frac{1}{\gamma_k - 1} = \frac{1}{\gamma - 1} \tag{D.55}$$

One can also define the derivative of pressure with respect to the volume fraction as,

$$\mathcal{M} = \left(\frac{\partial P}{\partial z_k} \right) \tag{D.56}$$

Its exact expression is obtained by considering the differential of the species internal energies given in [7, Eq. 28]

$$\begin{aligned}
\mathrm{d}\rho\varepsilon =& \sum_{k=1}^{N} \left(\rho_k \varepsilon_k \, \mathrm{d}z_k + z_k \, \mathrm{d}\rho_k \varepsilon_k \right) \\
=& \sum_{k=1}^{N} \rho_k \varepsilon_k \, \mathrm{d}z_k + \sum_{k=1}^{N} z_k \left(\left(\frac{\partial \rho_k \varepsilon_k}{\partial \rho_k} \right)_P \mathrm{d}\rho_k + \left(\frac{\partial \rho_k \varepsilon_k}{\partial P} \right)_{\rho_k} \mathrm{d}P \right) \\
=& \sum_{k=1}^{N} \rho_k \varepsilon_k \, \mathrm{d}z_k + \sum_{k=1}^{N} \left(z_k \delta_k \, \mathrm{d}\rho_k + z_k \xi_k \, \mathrm{d}P \right) \\
=& \sum_{k=1}^{N} \rho_k \varepsilon_k \, \mathrm{d}z_k + \sum_{k=1}^{N} z_k \delta_k \, \mathrm{d}\rho_k + \xi \, \mathrm{d}P \\
=& \xi \, \mathrm{d}P + \sum_{k=1}^{N} \rho_k \varepsilon_k \, \mathrm{d}z_k + \sum_{k=1}^{N} z_k \delta_k \left(\mathrm{d}\rho_k z_k - \rho_k \, \mathrm{d}z_k \right) \\
=& \xi \, \mathrm{d}P + \sum_{k=1}^{N} \left(\rho_k \varepsilon_k - \delta_k \rho_k \right) \mathrm{d}z_k + \sum_{k=1}^{N} \delta_k \, \mathrm{d}\rho_k z_k
\end{aligned} \tag{D.57}$$

The pressure differential then reads,

$$\xi \, \mathrm{d}P = \mathrm{d}\rho\varepsilon - \sum_{k=1}^{N} \delta_k \, \mathrm{d}\rho_k z_k + \sum_{k=1}^{N} \left(\delta_k \rho_k - \rho_k \varepsilon_k \right) \mathrm{d}z_k \tag{D.58}$$

By identification and using $\mathcal{M} = \sum_{k=1}^{N} \mathcal{M}_k$, we have,

$$\mathcal{M}_k = \frac{1}{\xi} \left(\delta_k \rho_k - \rho_k \varepsilon_k \right) \tag{D.59}$$

and for perfect gas, it yields,

$$\xi \, \mathrm{d}P = \mathrm{d}\rho\varepsilon - \sum_{k=1}^{N} \rho_k \varepsilon_k \, \mathrm{d}z_k \tag{D.60}$$

The internal energy differential being known, this leads easily to the differential of the total energy,

$$\mathrm{d}\rho E = \mathrm{d}\rho e_c + \mathrm{d}\rho\varepsilon \tag{D.61}$$

$$= \rho u \, \mathrm{d}u + \frac{u^2}{2} \sum_{k=1}^{N} \mathrm{d}\rho_k z_k + \xi \, \mathrm{d}P + \sum_{k=1}^{N} \delta_k \, \mathrm{d}\rho_k z_k - \xi \sum_{k=1}^{N} \mathcal{M}_k \, \mathrm{d}z_k \tag{D.62}$$

$$= \rho u \, \mathrm{d}u + \sum_{k=1}^{N} \left(\frac{u^2}{2} + \delta_k \right) \mathrm{d}\rho_k z_k + \xi \, \mathrm{d}P - \xi \sum_{k=1}^{N} \mathcal{M}_k \, \mathrm{d}z_k \tag{D.63}$$

D.2.3 Governing equations

Quasi-conservative form

The QCVF model equations have been presented in details in Chapter 3. The hyperbolic system is composed of $2+N$ conservative equations and N equations for the volume fraction advection. Its one-dimensional inviscid *quasi-conservative* form reads as follows,

$$\begin{cases} \dfrac{\partial \rho_k z_k}{\partial t} + \dfrac{\partial \rho_k z_k u}{\partial x} = 0 \\ \dfrac{\partial \rho u}{\partial t} + \dfrac{\partial \rho u^2 + P}{\partial x} = 0 \\ \dfrac{\partial \rho E}{\partial t} + \dfrac{\partial \left(\rho E + P\right) u}{\partial x} = 0 \\ \dfrac{\partial z_k}{\partial t} + u \dfrac{\partial z_k}{\partial x} = 0 \end{cases} \tag{D.64}$$

Quasi-linear quasi-conservative form

Using the vector of conserved variable $\mathbf{U} = [\rho u\,,\ \rho E\,,\ \rho_k z_k\,,\ z_k]^T$, the *quasi-linear quasi-conservative* form is given by,

$$\frac{\partial \mathbf{U}}{\partial t} + \underline{\mathbf{A}}^x \frac{\partial \mathbf{U}}{\partial x} = \mathbf{0} \tag{D.65}$$

where $\underline{\mathbf{A}}^x$ is the Jacobian matrix of the system with its components defined by $\underline{\mathbf{A}}^x_{i,j} = \dfrac{\partial \mathbf{F}_i}{\partial \mathbf{U}_j}$. Its detailed expression is given below with $\beta_k = \dfrac{1}{\xi}\left(\dfrac{u^2}{2} - \delta_k\right)$,

$$\underline{\mathbf{A}}^x = \begin{pmatrix} \left(2-\frac{1}{\xi}\right)u & \frac{1}{\xi} & \beta_1 - u^2 & \cdots & \beta_N - u^2 & \mathcal{M}_1 & \cdots & \mathcal{M}_N \\ \left(H - \frac{u^2}{\xi}\right) & \left(1+\frac{1}{\xi}\right)u & (\beta_1 - H)\,u & \cdots & (\beta_N - H)\,u & u\mathcal{M}_1 & \cdots & u\mathcal{M}_N \\ Y_1 & 0 & uY_N & \cdots & -uY_1 & 0 & \cdots & 0 \\ \vdots & \vdots & \vdots & \ddots & \vdots & \vdots & \ddots & \vdots \\ Y_N & 0 & -uY_N & \cdots & uY_1 & 0 & \cdots & 0 \\ 0 & 0 & 0 & \cdots & 0 & u & \cdots & 0 \\ \vdots & \vdots & \vdots & \ddots & \vdots & \vdots & \ddots & \vdots \\ 0 & 0 & 0 & \cdots & 0 & 0 & \cdots & u \end{pmatrix} \tag{D.66}$$

Quasi-linear primitive form

Using the primitive variables vector defined by $\mathbf{V} = [u,\ P,\ \rho_k z_k,\ z_k]^T$ similar to its mass fraction counterpart at the different that the volume fraction is also a primitive variable here (note that the choice of using ρ_k and z_k independently as the primitive variables could also have been made, but at the cost of leading to a system widely different than the mass fraction one). Using this vector, it can be expected that the characteristic forms of the QCVF model will be close to their FCMF/QCMF counterparts.

The quasi-linear quasi-conservative jacobian matrix would be complex to diagonalise while leading to a relatively simple system. Similarly to the mass fraction models, the matrix $\underline{\mathbf{M}}$ allowing the transformation

between the conservative and primitive variables is defined by Eq. D.17 and yields,

$$\underline{\mathbf{M}} = \begin{pmatrix} \rho & 0 & u & \cdots & u & 0 & \cdots & 0 \\ \rho u & \xi & \frac{u^2}{2}+\delta_1 & \cdots & \frac{u^2}{2}+\delta_N & -\xi\mathcal{M}_1 & \cdots & -\xi\mathcal{M}_N \\ 0 & 0 & 1 & \cdots & 0 & 0 & \cdots & 0 \\ \vdots & \vdots & \vdots & \ddots & \vdots & \vdots & \ddots & \vdots \\ 0 & 0 & 0 & \cdots & 1 & 0 & \cdots & 0 \\ 0 & 0 & 0 & \cdots & 0 & 1 & \cdots & 0 \\ \vdots & \vdots & \vdots & \ddots & \vdots & \vdots & \ddots & \vdots \\ 0 & 0 & 0 & \cdots & 0 & 0 & \cdots & 1 \end{pmatrix} \tag{D.67}$$

Its inverse is expressed by,

$$\underline{\mathbf{M}}^{-1} = \begin{pmatrix} \frac{1}{\rho} & 0 & -\frac{u}{\rho} & \cdots & -\frac{u}{\rho} & 0 & \cdots & 0 \\ -\frac{u}{\xi} & \frac{1}{\xi} & \frac{1}{\xi}\left(\frac{u^2}{2}-\delta_1\right) & \cdots & \frac{1}{\xi}\left(\frac{u^2}{2}-\delta_N\right) & \mathcal{M}_1 & \cdots & \mathcal{M}_N \\ 0 & 0 & 1 & \cdots & 0 & 0 & \cdots & 0 \\ \vdots & \vdots & \vdots & \ddots & \vdots & \vdots & \ddots & \vdots \\ 0 & 0 & 0 & \cdots & 1 & 0 & \cdots & 0 \\ 0 & 0 & 0 & \cdots & 0 & 1 & \cdots & 0 \\ \vdots & \vdots & \vdots & \ddots & \vdots & \vdots & \ddots & \vdots \\ 0 & 0 & 0 & \cdots & 0 & 0 & \cdots & 1 \end{pmatrix} \tag{D.68}$$

Note that this derivation is valid for any value of δ_k and by definition of $\mathcal{M}_k$ as well, thus indicating that this expression is valid for both the calorically and thermally perfect EoS.

Similarly to the mass fraction models, and noting $\underline{\mathbf{E}}^x = \underline{\mathbf{M}}^{-1}\,\underline{\mathbf{A}}^x\,\underline{\mathbf{M}}$, the *quasi-linear primitive* system reads,

$$\frac{\partial \mathbf{V}}{\partial t} + \underline{\mathbf{E}}^x \frac{\partial \mathbf{V}}{\partial x} = \mathbf{0} \tag{D.69}$$

where $\underline{\mathbf{E}}^x$ is the primitive Jacobian of the system and is given by,

$$\underline{\mathbf{E}}^x = \begin{pmatrix} u & \frac{1}{\rho} & 0 & \cdots & 0 & 0 & \cdots & 0 \\ \rho c^2 & u & 0 & \cdots & 0 & 0 & \cdots & 0 \\ \rho_1 z_1 & 0 & u & \cdots & 0 & 0 & \cdots & 0 \\ \vdots & \vdots & \vdots & \ddots & \vdots & \vdots & \ddots & \vdots \\ \rho_N z_N & 0 & 0 & \cdots & u & 0 & \cdots & 0 \\ 0 & 0 & 0 & \cdots & 0 & u & \cdots & 0 \\ \vdots & \vdots & \vdots & \ddots & \vdots & \vdots & \ddots & \vdots \\ 0 & 0 & 0 & \cdots & 0 & 0 & \cdots & u \end{pmatrix} \tag{D.70}$$

where c is the speed of sound and defined by,

$$\begin{aligned} \xi c^2 =& \frac{1}{\rho}\sum_{k=1}^{N} \rho_k z_k \left(h_k - \delta_k\right) \\ =& \frac{1}{\rho}\sum_{k=1}^{N} \rho_k z_k \xi_k c_k^2 \end{aligned} \tag{D.71}$$

Characteristic form

The matrix $\underline{\mathbf{E}}^x$ is thus diagonalised using,

$$\underline{\mathbf{L}}\,\underline{\mathbf{E}}^x\underline{\mathbf{R}} = \underline{\mathbf{\Lambda}} \tag{D.72}$$

where $\underline{\mathbf{L}}$ and $\underline{\mathbf{R}}$ are the left and right eigenvector matrices respectively and $\underline{\mathbf{\Lambda}}$ is the eigenvalue matrix ($\Lambda_{i,i} = \lambda_i$), where the λ_i are the eigenvalues of $\underline{\mathbf{E}}^x$ and is given by,

$$\underline{\mathbf{\Lambda}} = \begin{pmatrix} u+c & 0 & 0 & \cdots & 0 & 0 & \cdots & 0 \\ 0 & u-c & 0 & \cdots & 0 & 0 & \cdots & 0 \\ 0 & 0 & u & \cdots & 0 & 0 & \cdots & 0 \\ \vdots & \vdots & \vdots & \ddots & \vdots & \vdots & \ddots & \vdots \\ 0 & 0 & 0 & \cdots & u & 0 & \cdots & 0 \\ 0 & 0 & 0 & \cdots & 0 & u & \cdots & 0 \\ \vdots & \vdots & \vdots & \ddots & \vdots & \vdots & \ddots & \vdots \\ 0 & 0 & 0 & \cdots & 0 & 0 & \cdots & u \end{pmatrix} \tag{D.73}$$

It can be noted that $2 \times N$ eigenvectors are associated with the same eigenvalue (u) meaning that any linear combination of them will also be an eigenvalue of the system. The left and right eigenvector matrices are as follows,

$$\underline{\mathbf{R}} = \begin{pmatrix} \frac{1}{2} & -\frac{1}{2} & 0 & \cdots & 0 & 0 & \cdots & 0 \\ \frac{\rho c}{2} & \frac{\rho c}{2} & 0 & \cdots & 0 & 0 & \cdots & 0 \\ \frac{\rho_1 z_1}{2c} & \frac{\rho_1 z_1}{2c} & 1 & \ldots & 0 & 0 & \ldots & 0 \\ \vdots & \vdots & \vdots & \ddots & \vdots & \vdots & \ddots & \vdots \\ \frac{\rho_N z_N}{2c} & \frac{\rho_N z_N}{2c} & 0 & \ldots & 1 & 0 & \ldots & 0 \\ 0 & 0 & 0 & \cdots & 0 & 1 & \cdots & 0 \\ \vdots & \vdots & \vdots & \ddots & \vdots & \vdots & \ddots & \vdots \\ 0 & 0 & 0 & \cdots & 0 & 0 & \cdots & 1 \end{pmatrix}, \quad \underline{\mathbf{L}} = \begin{pmatrix} 1 & \frac{1}{\rho c} & 0 & \cdots & 0 & 0 & \cdots & 0 \\ -1 & \frac{1}{\rho c} & 0 & \cdots & 0 & 0 & \cdots & 0 \\ 0 & -\frac{\rho_1 z_1}{\rho c^2} & 1 & \cdots & 0 & 0 & \cdots & 0 \\ \vdots & \vdots & \vdots & \ddots & \vdots & \vdots & \ddots & \vdots \\ 0 & -\frac{\rho_N z_N}{\rho c^2} & 0 & \cdots & 1 & 0 & \cdots & 0 \\ 0 & 0 & 0 & \cdots & 0 & 1 & \cdots & 0 \\ \vdots & \vdots & \vdots & \ddots & \vdots & \vdots & \ddots & \vdots \\ 0 & 0 & 0 & \cdots & 0 & 0 & \cdots & 1 \end{pmatrix} \tag{D.74}$$

Using similar transformation as used for the mass fraction models and defined by,

$$\partial\mathbf{W} = \underline{\mathbf{L}}\,\partial\mathbf{V} \tag{D.75}$$

$$\partial\mathbf{V} = \underline{\mathbf{R}}\,\partial\mathbf{W} \tag{D.76}$$

the *characteristic* form of the system of equations for the QCVF is,

$$\frac{\partial\mathbf{W}}{\partial t} + \underline{\mathbf{\Lambda}}\frac{\partial\mathbf{W}}{\partial x} = \mathbf{0} \tag{D.77}$$

D.2.4 Wave relations

The different transformations of the original quasi-conservative system of equations has been presented in the previous section. This section now discusses the derivation of the wave relations, LODI expressions needed for the NSCBC application on the QCVF model.

Characteristic-Primitive system

The characteristic relations can then be written in function of the primitive variables as,

$$\begin{cases} \partial W^1 = \partial u + \dfrac{1}{\rho c}\partial P \\ \partial W^2 = -\partial u + \dfrac{1}{\rho c}\partial P \\ \partial W^{2+k} = -\dfrac{\rho_k z_k}{\rho c^2}\partial P + \partial \rho_k z_k \\ \partial W^{2+N+k} = \partial z_k \end{cases} \quad \text{with} \quad \begin{cases} \lambda_1 = u + c \\ \lambda_2 = u - c \\ \lambda_{2+k} = u \\ \lambda_{2+N+k} = u \end{cases} \tag{D.78}$$

where the entropy wave of Poinsot and Lele [236] can be identified by summing the species waves yielding,

$$\partial W^S = \sum_{k=1}^{N} \partial W^{2+k} = \partial \rho - \frac{1}{c^2}\partial P \tag{D.79}$$

and propagates at the eigenvalue u.

By left multiplying the quasi-linear quasi-conservative Eq. D.69 with the left eigenvector matrix, we obtain,

$$\underline{\mathbf{L}}\frac{\partial \mathbf{V}}{\partial t} + \underline{\mathbf{L}}\,\underline{\mathbf{E}}^x\frac{\partial \mathbf{V}}{\partial x} = 0 \tag{D.80}$$

$$\underline{\mathbf{L}}\frac{\partial \mathbf{V}}{\partial t} + \underline{\mathbf{\Lambda}}\,\underline{\mathbf{L}}\frac{\partial \mathbf{V}}{\partial x} = 0 \tag{D.81}$$

where the vector of wave amplitude variations can be defined in a similar fashion as the mass fraction models, i.e. $\mathcal{L} = \underline{\mathbf{\Lambda}}\,\underline{\mathbf{L}}\dfrac{\partial \mathbf{V}}{\partial x} = \underline{\mathbf{\Lambda}}\dfrac{\partial \mathbf{W}}{\partial x}$ and whose elements are $\mathcal{L}_i = \lambda_i L_i \dfrac{\partial V^i}{\partial x}$. The previous systems then reads,

$$\frac{\partial \mathbf{V}}{\partial t} + \underline{\mathbf{L}}^{-1}\mathcal{L} = 0 \tag{D.82}$$

where $\mathcal{L}$ is given by,

$$\begin{pmatrix} \mathcal{L}_1 \\ \mathcal{L}_2 \\ \mathcal{L}_{2+k} \\ \mathcal{L}_{2+N+k} \end{pmatrix} = \begin{pmatrix} \mathcal{L}_+ \\ \mathcal{L}_- \\ \mathcal{L}_k \\ \mathcal{L}_{z_k} \end{pmatrix} = \begin{pmatrix} (u+c)\left(\dfrac{\partial u}{\partial x} + \dfrac{1}{\rho c}\dfrac{\partial P}{\partial x}\right) \\ (u-c)\left(-\dfrac{\partial u}{\partial x} + \dfrac{1}{\rho c}\dfrac{\partial P}{\partial x}\right) \\ u\left(-\dfrac{\rho_k z_k}{\rho c^2}\dfrac{\partial P}{\partial x} + \dfrac{\partial \rho_k z_k}{\partial x}\right) \\ \dfrac{\partial z_k}{\partial x} \end{pmatrix} \tag{D.83}$$

and the entropy wave variation is defined as,

$$\mathcal{L}_S = \sum_{k=1}^{N}\mathcal{L}_k = u\left(-\frac{1}{\rho c^2}\frac{\partial P}{\partial x} + \frac{\partial \rho}{\partial x}\right) \tag{D.84}$$

The quasi-linear primitive system (Eq. D.69) can also expressed as the following *characteristic-primitive* system,

$$\frac{\partial \mathbf{V}}{\partial t} + \underline{\mathbf{E}}^x\frac{\partial \mathbf{V}}{\partial x} = \mathbf{0} \tag{D.85}$$

$$\frac{\partial \mathbf{V}}{\partial t} + \underline{\mathbf{E}}^x\,\underline{\mathbf{R}}\frac{\partial \mathbf{W}}{\partial x} = \mathbf{0} \tag{D.86}$$

where the matrix $\underline{\mathbf{E}}^x\,\underline{\mathbf{R}}$ is given by,

$$\underline{\mathbf{E}}^x\,\underline{\mathbf{R}} = \begin{pmatrix} \frac{u+c}{2} & -\frac{u-c}{2} & 0 & \cdots & 0 & 0 & \cdots & 0 \\ \frac{\rho c}{2}(u+c) & \frac{\rho c}{2}(u-c) & 0 & \cdots & 0 & 0 & \cdots & 0 \\ \frac{\rho_1 z_1}{2c}(u+c) & \frac{\rho_1 z_1}{2c}(u-c) & u & \cdots & 0 & 0 & \cdots & 0 \\ \vdots & \vdots & \vdots & \ddots & \vdots & \vdots & \ddots & \vdots \\ \frac{\rho_N z_N}{2c}(u+c) & \frac{\rho_N z_N}{2c}(u-c) & 0 & \cdots & u & 0 & \cdots & 0 \\ 0 & 0 & 0 & \cdots & 0 & u & \cdots & 0 \\ \vdots & \vdots & \vdots & \ddots & \vdots & \vdots & \ddots & \vdots \\ 0 & 0 & 0 & \cdots & 0 & 0 & \cdots & u \end{pmatrix} \tag{D.87}$$

Local One-Dimensional Inviscid (LODI) relations

The previous characteristic-primitive system can be expanded to express the primitive variable time variations as a function of the spatial variations of the characteristic ones and the eigenvalues of the system,

$$\begin{pmatrix} \frac{\partial u}{\partial t} \\ \frac{\partial P}{\partial t} \\ \frac{\partial \rho_k z_k}{\partial t} \\ \frac{\partial z_k}{\partial t} \end{pmatrix} + \begin{pmatrix} \frac{\lambda_1}{2}\frac{\partial W^1}{\partial x} - \frac{\lambda_2}{2}\frac{\partial W^2}{\partial x} \\ \frac{\rho c}{2}\left(\lambda_1\frac{\partial W^1}{\partial x} + \lambda_2\frac{\partial W^2}{\partial x}\right) \\ \frac{\rho_k z_k}{2c}\left(\lambda_1\frac{\partial W^1}{\partial x} + \lambda_2\frac{\partial W^2}{\partial x}\right) + \lambda_{2+k}\frac{\partial W^{2+k}}{\partial x} \\ \lambda_{2+N+k}\frac{\partial W^{2+N+k}}{\partial x} \end{pmatrix} = 0 \tag{D.88}$$

by reminding that $\mathcal{L}_i = \lambda_i \frac{\partial W^i}{\partial x}$, the previous system can be simplified to give the first four LODI relations for the velocity, pressure, ρY_k and volume fraction,

$$\begin{pmatrix} \frac{\partial u}{\partial t} \\ \frac{\partial P}{\partial t} \\ \frac{\partial \rho_k z_k}{\partial t} \\ \frac{\partial z_k}{\partial t} \end{pmatrix} + \begin{pmatrix} \frac{1}{2}(\mathcal{L}_1 - \mathcal{L}_2) \\ \frac{\rho c}{2}(\mathcal{L}_1 + \mathcal{L}_2) \\ \frac{\rho_k z_k}{2c}(\mathcal{L}_1 + \mathcal{L}_2) + \mathcal{L}_{2+k} \\ \mathcal{L}_{2+N+k} \end{pmatrix} = 0 \tag{D.89}$$

By noting $\mathbf{d}$ the vector of normal terms, we have,

$$\mathbf{d} = \underline{\mathbf{E}}^x\underline{\mathbf{R}}\frac{\partial \mathbf{W}}{\partial x} = \begin{pmatrix} d_1 \\ d_2 \\ d_{2+k} \\ d_{2+N+k} \end{pmatrix} = \begin{pmatrix} \frac{1}{2}(\mathcal{L}_1 - \mathcal{L}_2) \\ \frac{\rho c}{2}(\mathcal{L}_1 + \mathcal{L}_2) \\ \frac{\rho_k z_k}{2c}(\mathcal{L}_1 + \mathcal{L}_2) + \mathcal{L}_{2+k} \\ \mathcal{L}_{2+N+k} \end{pmatrix} \tag{D.90}$$

Using the previous LODI relations and similarly to the mass fraction models, additional LODIs can be derived for the mixture density (by summing the species waves),

$$\frac{\partial \rho}{\partial t} + \frac{\rho}{2c}\left(\mathcal{L}_1 + \mathcal{L}_2\right) + \mathcal{L}_S = 0 \tag{D.91}$$

as well as for the species mass fractions by dividing the LODI for $\rho_k z_k$ by the LODI for the mixture density,

$$\frac{\partial Y_k}{\partial t} + \frac{1}{\rho}\left(\mathcal{L}_{2+k} - Y_k \mathcal{L}_S\right) = 0 \tag{D.92}$$

Using the temperature differential given by,

$$\mathrm{d}T = \frac{1}{\rho R}\,\mathrm{d}P - \sum_{k=1}^{N} \frac{R_k T}{\mathcal{R}\rho}\,\mathrm{d}\rho_k z_k \tag{D.93}$$

and using the previous LODI relations, we have,

$$\frac{\partial T}{\partial t} - \frac{1}{\rho \mathcal{R}}\frac{\partial P}{\partial t} + \sum_{k=1}^{N} \frac{\mathcal{R}_k T}{\rho \mathcal{R}}\frac{\partial \rho_k z_k}{\partial t} = 0 \tag{D.94}$$

$$\frac{\partial T}{\partial t} + \frac{c}{2\mathcal{R}}\left(\mathcal{L}_1 + \mathcal{L}_2\right) - \sum_{k=1}^{N} \frac{\mathcal{R}_k T}{2\mathcal{R}c} Y_k \left(\mathcal{L}_1 + \mathcal{L}_2\right) - \sum_{k=1}^{N} \frac{\mathcal{R}_k T}{\rho \mathcal{R}} \mathcal{L}_{2+k} = 0 \tag{D.95}$$

$$\frac{\partial T}{\partial t} + \frac{T}{2c\xi}\left(\mathcal{L}_1 + \mathcal{L}_2\right) - \sum_{k=1}^{N} \frac{\mathcal{R}_k T}{\rho \mathcal{R}} \mathcal{L}_{2+k} = 0 \tag{D.96}$$

Characteristic-Conservative system

Similarly to the mass fraction, the characteristic-conservative system is given by,

$$\frac{\partial \mathbf{U}}{\partial t} + \underline{\mathbf{M}}\,\mathbf{d} = \mathbf{0} \tag{D.97}$$

and its final form reads,

$$\begin{pmatrix} \dfrac{\partial \rho u}{\partial t} \\ \dfrac{\partial \rho E}{\partial t} \\ \dfrac{\partial \rho_k z_k}{\partial t} \\ \dfrac{\partial z_k}{\partial t} \end{pmatrix} + \begin{pmatrix} \rho d_1 + u \displaystyle\sum_{k=1}^{N} d_{2+k} \\ \rho u d_1 + \xi d_2 + \displaystyle\sum_{k=1}^{N} \left(\frac{u^2}{2} + \delta_k\right) d_{2+k} - \xi \sum_{k=1}^{N} \mathcal{M}_k d_{2+N+k} \\ d_{2+k} \\ d_{2+N+k} \end{pmatrix} = 0 \tag{D.98}$$

which is very similar to the mass fraction models.

D.2.5 Remarks on the QCVF derivation of the NSCBC

Several remarks can be made on the characteristic forms of the QCVF governing equations,

- The mass and volume fraction derivations are very close, and similar in the case of the species and momentum transport. There is a difference in the expression of the total energy, and in the case of the QCVF, the volume fraction equation is added.

- The two models are similar if,

$$\sum_{k=1}^{N}\left(\frac{u^2}{2}+\delta_k\right)d_{2+k}-\xi\sum_{k=1}^{N}\mathcal{M}_k d_{2+N+k}=\sum_{k=1}^{N}\left(\frac{u^2}{2}+\varepsilon_k-\frac{\mathcal{R}_k T}{\mathcal{R}}C_v\right)d_{2+k} \tag{D.99}$$

such that the energy fluxes are similar for all models. It can be remarked that the normal terms d_{2+k} are similar for both models, and therefore their contribution to the energy transport need to be equal, yielding,

$$\delta_k=\varepsilon_k-\frac{\mathcal{R}_k T_k}{\mathcal{R}}C_v \tag{D.100}$$

Using the definition of $\mathcal{M}_k$ (Eq. D.59) and the value of δ_k, the species contributions to the energy fluxes for the QCVF model reads,

$$\begin{aligned}\text{Eq. D.99}\Leftrightarrow&\sum_{k=1}^{N}\left(\frac{u^2}{2}+\delta_k\right)d_{2+k}-\xi\sum_{k=1}^{N}\left(\frac{1}{\xi}\left(\rho_k\delta_k-\rho_k\varepsilon_k\right)d_{2+N+k}\right)\\&=\sum_{k=1}^{N}\left(\frac{u^2}{2}+\varepsilon_k-\frac{\mathcal{R}_k T_k}{\mathcal{R}}C_v\right)d_{2+k}-\sum_{k=1}^{N}\rho_k\left(\varepsilon_k-\frac{\mathcal{R}_k T_k}{\mathcal{R}}C_v-\varepsilon_k\right)d_{2+N+k}\\&=\sum_{k=1}^{N}\left(\frac{u^2}{2}+\varepsilon_k-\frac{\mathcal{R}_k T_k}{\mathcal{R}}C_v\right)d_{2+k}+\sum_{k=1}^{N}\rho_k\frac{\mathcal{R}_k T_k}{\mathcal{R}}C_v d_{2+N+k}\end{aligned} \tag{D.101}$$

The first part of the energy contribution now look similar, but the overall energy contribution is different due to the influence of the volume fraction wave. However, one can note that when using the isobaric closure $\rho_k\mathcal{R}_k T_k=P_k=P$ and $\dfrac{C_v}{\mathcal{R}}=\xi$, thus leading to,

$$\begin{aligned}\sum_{k=1}^{N}\rho_k\frac{\mathcal{R}_k T_k}{\mathcal{R}}C_v d_{2+N+k}&=\sum_{k=1}^{N}P\xi d_{2+N+k}=\xi P\sum_{k=1}^{N}d_{2+N+k}\\&=\xi P\sum_{k=1}^{N}\frac{\partial z_k}{\partial x}=0\end{aligned} \tag{D.102}$$

The energy characteristic-conservative form of the equations are thus similar between the volume and mass fraction models.

- A last check to verify the correctness of the derivation is to compute the mixture speed of sound using Eq. D.71 and check that it gives the correct value for perfect gases. This gives,

$$\begin{aligned}c^2&=\frac{1}{\rho\xi}\sum_{k=1}^{N}\rho_k z_k\left(h_k-\varepsilon_k+\frac{\mathcal{R}_k T_k}{\mathcal{R}}C_v\right)=\frac{1}{\rho\xi}\sum_{k=1}^{N}\rho_k z_k\left(\varepsilon_k+\frac{P}{\rho_k}-\varepsilon_k+\frac{\mathcal{R}_k T_k}{\mathcal{R}}C_v\right)\\&=\frac{P}{\rho\xi}\sum_{k=1}^{N}z_k\left(1+\frac{Cv}{\mathcal{R}}\right)=\frac{P}{\rho\xi}\sum_{k=1}^{N}z_k\left(1+\frac{1}{\gamma-1}\right)=\frac{P}{\rho\xi}\gamma\xi\sum_{k=1}^{N}z_k\\&=\frac{P\gamma}{\rho}\end{aligned} \tag{D.103}$$

which corresponds to the correct value.

D.3 Validation of the NSCBC for the different models

The derivations presented above allowed to extract the informations carried by each wave entering and leaving the domain. The use of the LODI relations to adjust the behaviour of the boundary conditions is presented in §. 4.6. In this section, several tests are presented to validate the implementation of the NSCBC to the different models. The two test cases considered are the propagation of an acoustic wave (Appendix D.3.1) and of an entropy wave (Appendix D.3.2).

D.3.1 Acoustic wave propagation

Test case

A one-dimensional problem consisting of an acoustic wave propagating towards characteristic boundaries is simulated. In order to validate the different EoS, several test cases based on the same initial conditions are considered, namely, the propagation of an acoustic wave in a single species with either a calorically or thermally perfect EoS, and the propagation of the same acoustic wave in a mixture of several species, where γ is either a function of the composition only (calorically perfect gas), or a function of both the composition and temperature (thermally perfect gas).

An acoustic wave initially at the centre of the domain is given by,

$$\begin{aligned} u(x) &= u_0 + \mathcal{A} \exp\left[-\left(\mathcal{B} \frac{x - L/2}{L} \right)^2 \right] \\ P(x) &= P_0 + \rho_0 c_0 \left(u(x) - u_0 \right) \\ \rho(x) &= \rho_0 + \frac{\rho_0 \left(u(x) - u_0 \right)}{c_0} \end{aligned} \tag{D.104}$$

where the subscript 0 represent the reference quantities, based on the initial values at the left boundary. For all the acoustic wave tests, the reference parameters will be the following, $u_0 = 10\,[m/s]$, $P_0 = 101325\,[Pa]$, $T_0 = 301\,[K]$, with $\mathcal{A} = 8\,[m/s]$ and $\mathcal{B} = 10$ being the strength and stiffness of the wave respectively. The domain length is $L = 5 \times 10^{-3}\,[m]$ and it is discretised with 200 cells. The MUSCL5 and RK2-SSP schemes are used for the spatial and time discretisation respectively. The single species simulations are carried with a domain filled with pure oxygen, while the mixture considered is composed of oxygen and nitrogen. The CFL value has been chosen as $CFL = 0.5$.

As the γ and the density are different in the simulations, so is the speed of sound, which is the speed at which the acoustic wave are moving in the domain. For consistency, the results are presented at different dimensionless times defined below,

$$\tau = \frac{2c_0}{L} t \tag{D.105}$$

where $\tau = 1.0$ is the time needed for the wave to reach the boundary.

The test cases considered are summarised in Table D.1.

	Direction	EoS	Composition	Inlet	Outlet
AW1	+	$\gamma = \gamma_0$	O_2	PR	PNR
AW2	+	$\gamma = \gamma(T)$	O_2	PR	PNR
AW3	+	$\gamma = \gamma(Y_k)$	O_2/N_2	PR	PNR
AW4	+	$\gamma = \gamma(T, Y_k)$	O_2/N_2	PR	PNR
AW5	-	$\gamma = \gamma(T, Y_k)$	O_2/N_2	PR	PNR
AW6	-	$\gamma = \gamma(T, Y_k)$	O_2/N_2	NR	PNR

Table D.1: *Acoustic wave propagation test cases (PNR : Partially Non-Reflecting, PR : Perfectly Reflecting, NR : Perfectly Non-Reflecting)*

Results

The results obtained for the case AW1 and AW2 for a single species and both EoS are visible on Fig. D.1, and show that the waves are leaving the domain with very minor perturbations as no reflection and a

minimal deformation of the leaving wave are observed. Additionally, long after it left the domain, no oscillations are visible. This means that the implementation is stable. One can remark the similarity obtained for the solution using the calorically and thermally perfect gas assumptions.

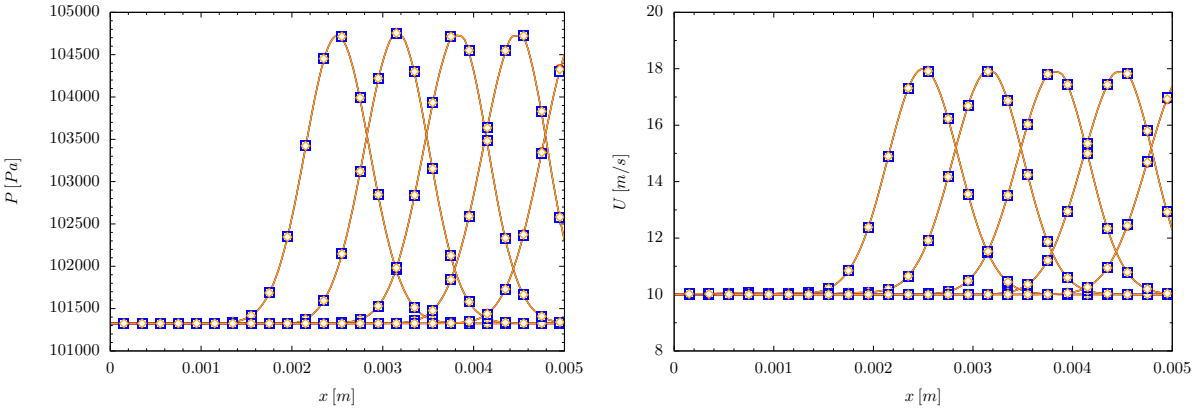

(a) $\tau = 0.0,\ 0.25,\ 0.50,\ 0.75,\ 1.0$

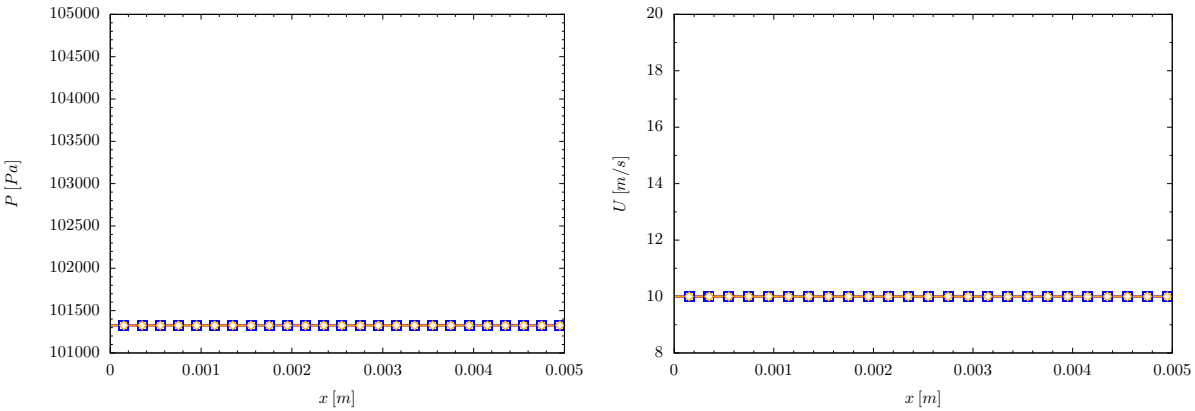

(b) $\tau = 5.0,\ 10.0$

Figure D.1: *Pressure and velocity profiles for the acoustic wave propagation test cases* AW1 *(lines) and* AW2 *(points) -* —/○ *QCVF,* —/□ *QCMF,* —/◇ *FCMF*

When using a mixture of gas, all the properties are changing across the domain, i.e. there now exists a gradient of all conserved quantities between the left and right boundaries, thus allowing one to test all the waves computations. As depicted on Fig. D.2, waves exit the domain without perturbations. Additionally, the species are also exiting the domain, without any visible perturbation on the mass fractions profiles. The long time results are also perfectly oscillations free, showing the stability of the implementation, but also the proper definition of the boundaries. Once again, it can be remarked that the boundary conditions behave similarly (and correctly) for all models and all EoS considered.

Finally, the last tests consist on an acoustic wave propagating towards the inlet (towards the left) to simulate the response of the different inlet types to an incoming wave. Two types of inlet are being tested here, a perfectly reflecting inlet, where different properties are imposed (temperature, composition and velocity) and where the pressure is free to float to adapt to the flow changes, and a second inlet where all the waves are allowed to exit the domain. Such an inlet although interesting by its non-reflecting behaviour is of somewhat limited use as no value can be imposed and by the fact that it can lead to ill-posed problems. The results are presented in Fig. D.3. It is clearly visible that the non-reflecting boundary conditions fulfil its purpose by letting the incoming wave exiting the domain without perturbation, while the perfectly reflecting inlet also behaves properly by reflecting almost perfectly the incoming wave propagate back into the domain to be evacuated by the outflow. Only a small deformation of the incoming wave is visible here, showing the correctness of the implementation. The agreement between the different models is very

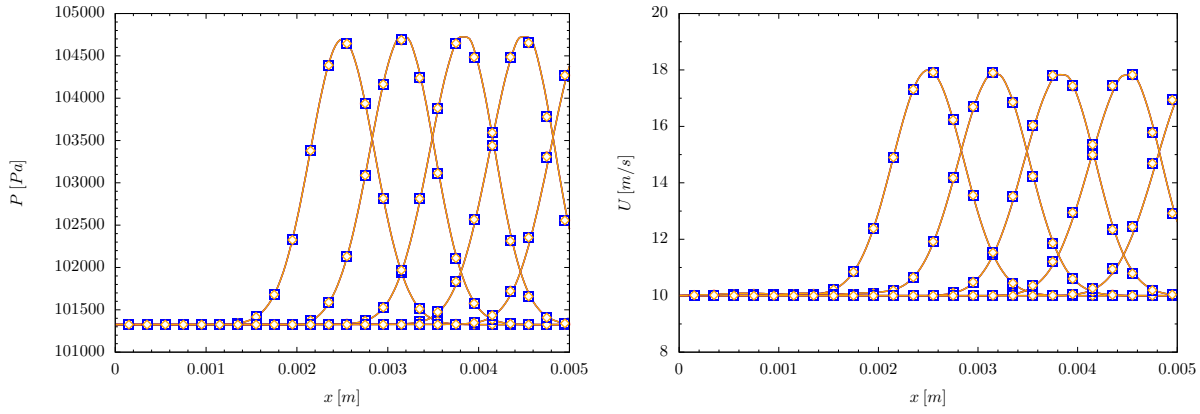

(a) $\tau = 0.0,\ 0.25,\ 0.50,\ 0.75,\ 1.0$

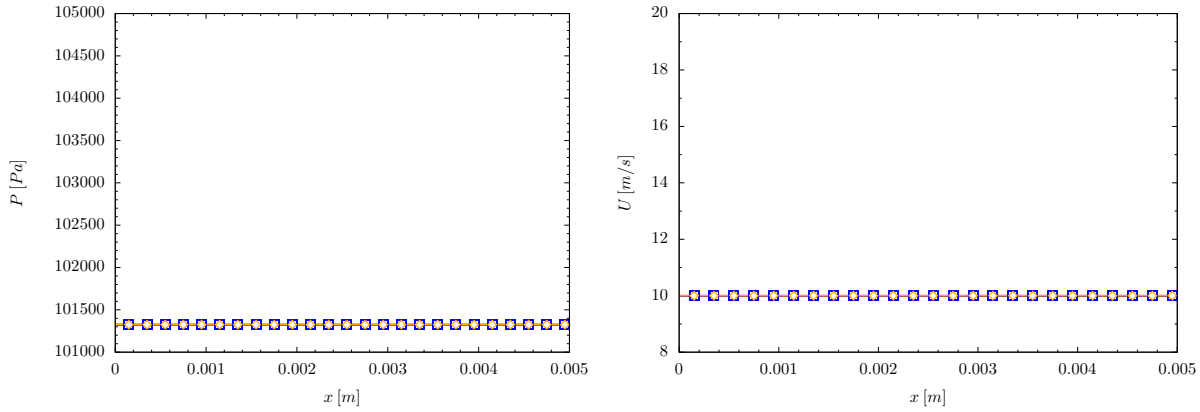

(b) $\tau = 5.0,\ 10.0$

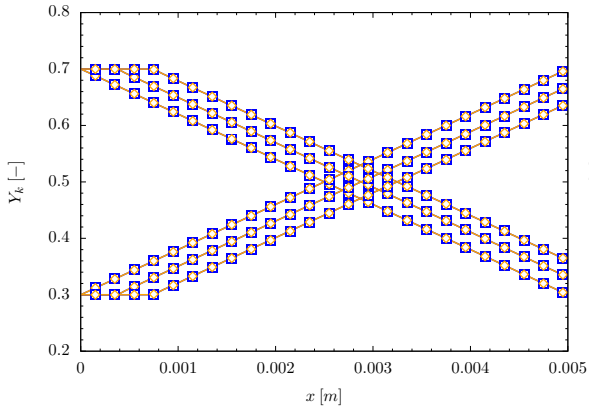

(c) Y_k - $\tau = 0.0,\ 5.0,\ 10.0$

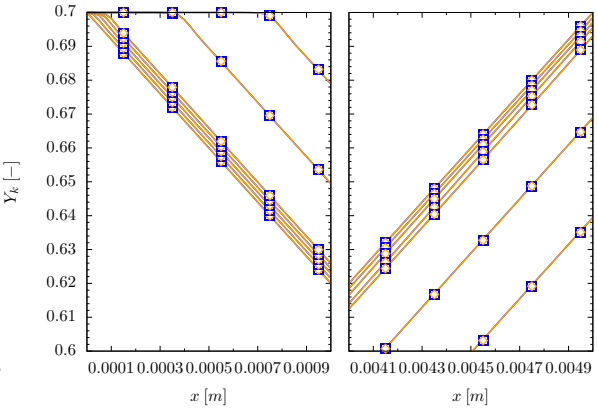

(d) Y_k - $\tau = 0.0, 0.25,\ 0.5,\ 0.75,\ 1.0,\ 5.0,\ 10.0$ - *Zoom on the boundaries*

Figure D.2: *Pressure, velocity and mass fractions profiles for the acoustic wave propagation test cases* AW3 *(lines) and* AW4 *(points) -* —/○ *QCVF,* —/□ *QCMF,* —/◇ *FCMF*

good showing the correctness of the approach for the QCVF.

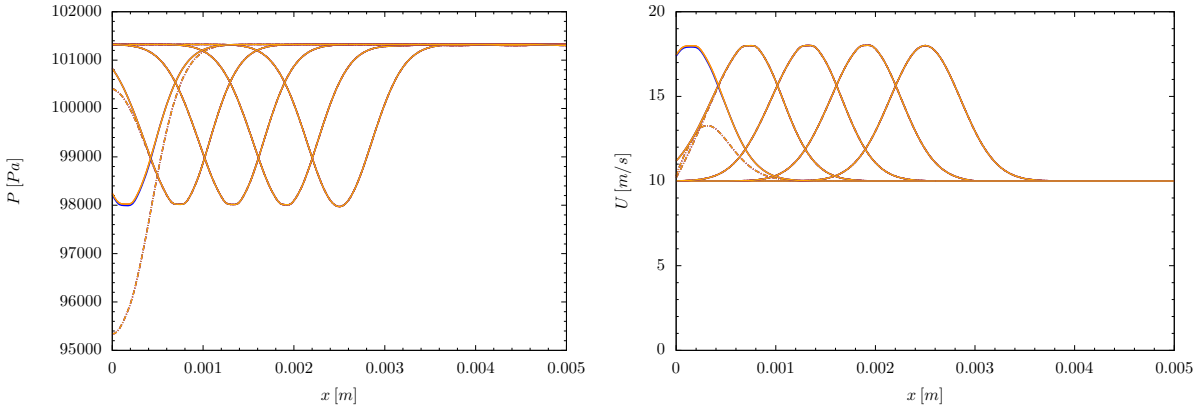

(a) $\tau = 0.0,\ 0.25,\ 0.50,\ 0.75,\ 1.0$

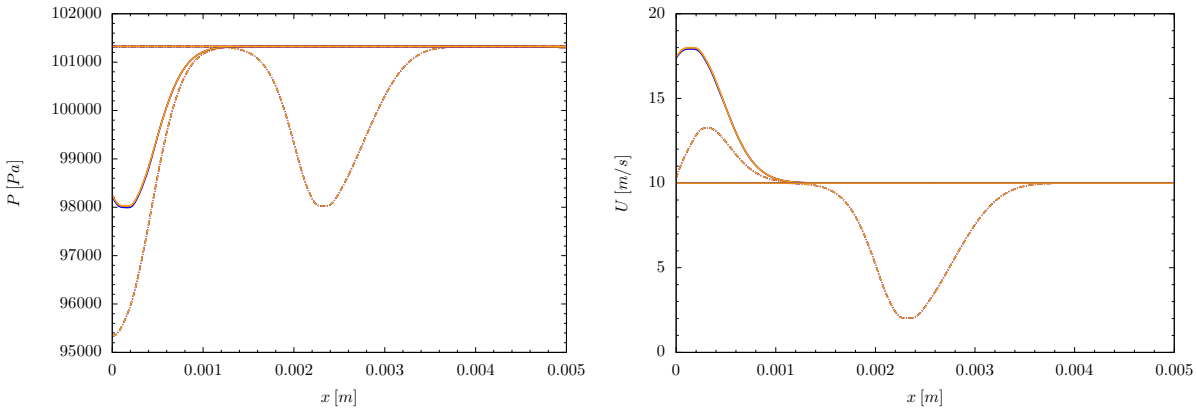

(b) $\tau = 5.0,\ 10.0$

Figure D.3: *Pressure and velocity profiles for the acoustic wave propagation test cases* AW5 *(dash-dotted lines) and* AW6 *(full lines) -* —/-·- *QCVF,* —/-·- *QCMF,* —/-·- *FCMF*

D.3.2 Entropy wave propagation

This test is analogous to the previous one, but uses an entropy wave instead of an acoustic one. It correspond to a defined bulge in temperature and the corresponding bulge in density in a uniform pressure and velocity field. The speed of this type of wave is the convection velocity of the flow, and not the speed of sound as for the acoustic wave. Similar set-up to the acoustic wave have been simulated (Table D.1), although for the sake of simplicity, only the most complex case is presented here, namely the mixture of thermally perfect gases.

The temperature field is initialised by,

$$T(x) = T_0 + \mathcal{A} \exp\left[-\left(\mathcal{B}\frac{x - L/2}{L}\right)^2\right] \tag{D.106}$$

and the density is computed using the EoS with the given pressure and composition. The reference values are as follows, $u_0 = 100\,[m/s]$, $P_0 = 101325\,[Pa]$, $T_0 = 301\,[K]$, with $\mathcal{A} = 8\,[m/s]$ and $\mathcal{B} = [10]$ being the strength and stiffness of the wave respectively. The domain length is $L = 5 \times 10^{-3}\,[m]$, and is discretised with 200 cells. The MUSCL5 and RK2-SSP schemes are used for the spatial and time discretisation respectively. The mixture considered is composed of oxygen and nitrogen. The dimensionless time is here computed such that the wave initially at the centre reaches the boundary at $\tau = 1.0$.

The results are presented in Fig. D.4, where it can be seen that the wave exit the domain without

noticeable perturbations, thus showing the correct implementation of the method in the current framework.

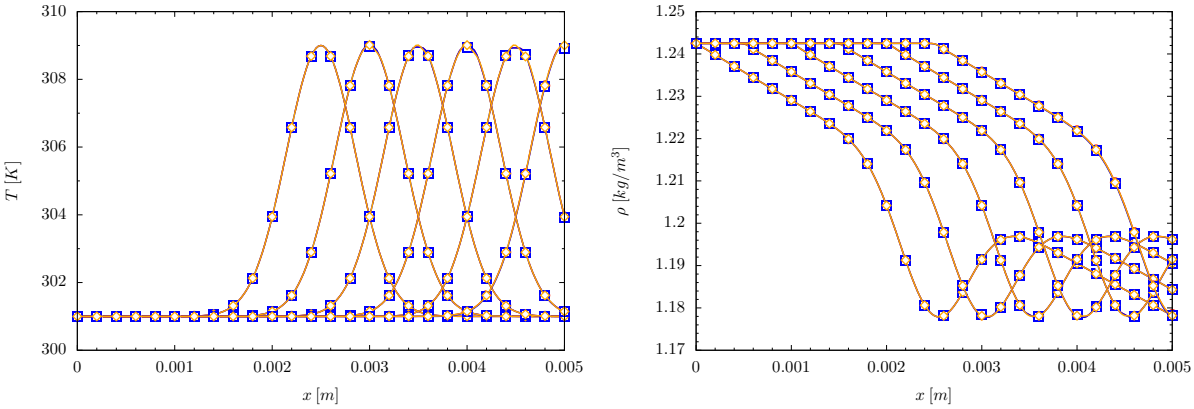

(a) $\tau = 0.0,\ 0.20,\ 0.40,\ 0.60,\ 0.80,\ 1.0$

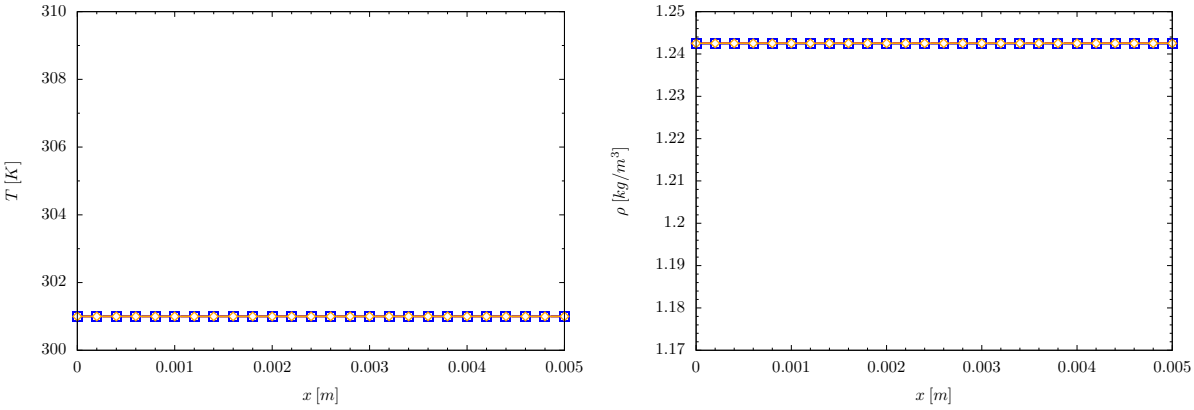

(b) $\tau = 5.0,\ 10.0$

Figure D.4: *Temperature and density profiles for the entropy wave propagation test case -* ○ *QCVF,* □ *QCMF,* ◇ *FCMF*